Université Fédérale
Toulouse Midi-Pyrénées

THÈSE

En vue de l'obtention du
DOCTORAT DE L'UNIVERSITÉ DE TOULOUSE
Délivré par l'Université Toulouse 3 - Paul Sabatier

Présentée et soutenue par

Hugo TRANIN

Le 10 novembre 2022

Recherche de populations de trous noirs non identifiées dans les archives en rayons X et multi-longueurs d'onde. Application aux trous noirs de masse intermédiaire.

Ecole doctorale : **SDU2E - Sciences de l'Univers, de l'Environnement et de l'Espace**

Spécialité : **Astrophysique, Sciences de l'Espace, Planétologie**

Unité de recherche :
IRAP - Institut de Recherche en Astrophysique et Planetologie

Thèse dirigée par
Natalie WEBB

Jury

M. Mark ALLEN, Rapporteur
Mme Marta VOLONTERI, Rapporteure
M. Jörn WILMS, Examinateur
M. Olivier GODET, Examinateur
Mme Mar MEZCUA, Examinatrice
M. Jean-Luc ATTEIA, Examinateur
Mme Natalie WEBB, Directrice de thèse

This thesis project was carried out at IRAP, in association with the XMM-SSC and XMM2ATHENA projects.

Abstract

Supermassive black holes (SMBH, $10^5 - 10^{10} M_\odot$) have regularly been found at the center of massive galaxies. However, we still know little about their formation mechanism. Extremely luminous active galactic nuclei (AGN), revealing the presence of massive SMBHs, were detected in the high redshift Universe, a few 10^8 years after the Big Bang. A rapid growth mechanism is thus needed, such as a rapid accretion (beyond the Eddington limit) onto intermediate-mass black holes (IMBH, $10^2 - 10^5 M_\odot$), or the mergers of these black holes. Some of the original IMBHs may have avoided accretion or mergers, and thus still be found in the local Universe, for example as active dwarf galaxies. However, to date, the evidence for these IMBHs remains scarce.

Conversely, stellar-mass black holes are found in the Milky Way and nearby galaxies. They are often detected in X-ray binaries (XRB), composed of a compact object - a neutron star or a black hole - accreting from a companion star. Ultraluminous X-ray sources (ULXs) may be a luminous version of the XRBs, and are thought to be powered by super-Eddington accretion above the Eddington limit onto stellar-mass compact objects, but the exact mechanism and the nature of the accretor are largely unknown. A few hyperluminous X-ray sources (HLXs, defined as ULXs with $L_X > 10^{41}$ erg/s), may be good candidates for IMBHs.

X-ray emission is a well-known signature of accreting systems, and thus X-ray surveys are the ideal place to search for new accreting black holes. The modern X-ray observatories *Swift*, *XMM-Newton* and *Chandra* have detected about a million point-like sources which are yet to be identified. With these and upcoming telescopes, an automated classification of X-ray sources becomes increasingly valuable. Using this approach could provide the cleanest samples possible, where currently contaminants limit population studies of ULXs, HLXs and active dwarf galaxy candidates.

In this thesis I develop an automated and probabilistic classification of X-ray sources. The *Swift*-XRT, *XMM-Newton* and *Chandra* catalogues are cross-correlated with each other, with optical and infrared catalogues and with the highly complete census of galaxies, *GLADE*. From these spatial, spectral, photometrical and timing properties, the classification identifies, amongst others, populations of AGN, stars and XRBs, and can be optimised to focus on one class. It efficiently retrieves AGN and stars, but other classes have small training samples limiting the classification performance. A citizen science experiment (*CLAXSON*) is proposed to enlarge these samples.

The classification is then applied to X-ray sources overlapping *GLADE* galaxies. 1901 ULX candidates are accurately identified, where analysis indicates that it is the cleanest large sample in the current literature. Their spatial distribution, hardness, variability and rates in different environments are studied. I analyse their X-ray luminosity function and confirm the presence of a powerlaw break at a luminosity of 10^{40} erg/s for spiral galaxies, tentatively proposed in previous studies. HLX candidates are inspected and cross-correlated with optical sources with redshift to remove possible contaminants. The resulting 191 HLX candidates are statistically compared to ULXs, showing tentative differences perhaps due to a different accretor mass range.

Likewise, 91 active dwarf galaxy candidates are identified, where half of them appear to have an off-centre nucleus. I analyse the active fraction of dwarf galaxies in different bins of galaxy mass and limiting luminosity, and I estimate the intrinsic fraction harbouring a black hole. Assuming that these AGN and HLX candidates are indeed black holes, their black hole mass distribution suggests a large fraction of IMBHs. I analyse how this mass compares with galaxy mass. Differences are observed between the two types of candidates and interpreted in terms of IMBH formation mechanisms.

Résumé

Les trous noirs supermassifs (TNS, $10^5 - 10^{10} M_\odot$) sont observés au centre de nombreuses galaxies massives. Pourtant, leur mécanisme de formation reste incertain. Une croissance rapide est nécessaire pour expliquer certains noyaux actifs de galaxies (AGN) vus à haut redshifts, comme une accrétion rapide (au-delà de la limite d'Eddington) sur des trous noirs de masse intermédiaire (IMBH, $10^2 - 10^5 M_\odot$), ou la fusion de ces trous noirs. Une partie de ces IMBHs pourrait avoir eu une faible croissance et se retrouver encore dans l'Univers local, par exemple sous forme de galaxies naines actives. Cependant, à ce jour, les preuves de l'existence de ces IMBHs restent rares.

À l'inverse, les trous noirs de masse stellaire sont présents dans la Voie lactée et les galaxies proches. Ils sont souvent détectés dans des binaires X (XRB), composées d'un objet compact - étoile à neutrons ou trou noir - qui accrète d'une étoile compagnon. Les sources X ultralumineuses (ULX), qui sont peut-être une version lumineuse des XRBs, seraient alimentées par l'accrétion super-Eddington sur des objets compacts de masse stellaire, mais le plus souvent sa nature et le mécanisme exact sont inconnus. Certaines sources X hyperlumineuse (HLX, défini comme un ULX ayant $L_X > 10^{41}$ erg/s) pourraient être des bons candidats pour des IMBHs.

L'émission de rayons X étant une signature importante des systèmes accrétants, les relevés en rayons X sont l'endroit idéal pour trouver de nouveaux trous noirs. Les observatoires modernes en rayons X *Swift*, *XMM-Newton* et *Chandra* ont découvert environ un million de sources ponctuelles qui n'ont pas encore été identifiées. Avec ces télescopes et ceux à venir, une classification automatisée des sources de rayons X devient indispensable. Elle pourrait notamment réduire la part de contaminants qui sont souvent un frein dans l'étude des échantillons d'ULXs, HLXs et galaxies naines actives.

Dans cette thèse, je développe une classification automatisée et probabiliste des sources de rayons X. Les catalogues *Swift*-XRT, *XMM-Newton* et *Chandra* sont corrélés entre eux et avec des catalogues optiques et infrarouges, ainsi que le recensement complet de galaxies, *GLADE*. A partir de ces propriétés spatiales, spectrales, photométriques et temporelles, la classification identifie entre autres des populations d'AGN, d'étoiles et de XRBs, et peut être optimisée pour une classe d'intérêt. Les AGN et les étoiles sont classifiés avec précision, mais les autres classes ont de petits échantillons d'entraînement limitant la classification. Une expérience de science participative (*CLAXSON*) est proposée pour les augmenter.

La classification est ensuite appliquée aux sources recouvrant les galaxies *GLADE*. 1901 candidats ULX sont identifiés, probablement l'échantillon le plus grand et propre de la littérature actuelle. Leurs distributions spatiale, spectrale et dans différents environnements sont étudiées. J'analyse leur fonction de luminosité et confirme la présence d'une cassure de la loi de puissance à $L_X \sim 10^{40}$ erg/s pour les galaxies spirales. Les candidats HLX sont inspectés et de nombreux contaminants éliminés grâce à leur redshift. Les 191 candidats HLX restants sont comparés aux ULXs, montrant de légères différences peut-être dues à une gamme de masse d'accréteur différente.

J'obtiens enfin 91 candidats galaxies naines actives. J'analyse la fraction active des galaxies dans différents intervalles de masse de galaxie et de luminosité limite, puis j'estime la fraction intrinsèque abritant un trou noir. En supposant que ces candidats AGN et HLX sont effectivement des trous noirs, leur distribution de masse de trou noir révèle une grande fraction d'IMBHs. J'analyse comment cette masse se compare à la masse de la galaxie. Des différences sont observées entre ces deux types de candidats et interprétées en termes de mécanismes de formation des IMBHs.

Remerciements

Cher lecteur, chère lectrice, bienvenue dans ma thèse. Mon premier remerciement te revient directement, à toi qui lit ces lignes, et sans qui l'écriture de l'équivalent d'un livre n'aurait que peu de sens. J'ai eu beaucoup de chance, car cette thèse, par son sujet et les outils que j'ai utilisés, s'est révélée étonnamment amusante et intéressante, et j'espère avoir bien communiqué à ces pages ce côté ludique de la recherche de trous noirs de masse intermédiaire. De ces trois ans, je ne retiendrai presque que les bons côtés : j'ai pu faire joujou avec pleins d'algorithmes de classification, créer un site de toutes pièces, découvrir qu'en fait le café c'est bon, regarder d'innombrables galaxies (toutes plus belles les unes que les autres et renfermant des trésors que personne auparavant n'avait pris le temps de publier (spoiler : moi non plus)), faire de l'activisme écologiste et des rencontres formidables, me sentir à ma place dans un groupe, me découvrir de nouvelles passions, notamment la diffusion scientifique... et en plus être payé pour ça ! Mais une thèse ne se fait pas tout seul, en tout cas pas complètement, alors il est temps pour moi de remercier toutes les personnes qui m'ont accompagnées dans cette aventure, et sans qui, sans aucun doute, je n'en serai jamais arrivé là.

Merci infiniment à mon entourage proche qui a su me soutenir tout au long de la thèse et tout particulièrement dans les derniers mois, qui n'ont pas été faciles. Merci à mes parents, qui m'ont toujours soutenu et chez qui les vacances sont de vraies vacances ! Merci à toi Lindsay, qui depuis bientôt 7 ans me supportes, me portes et m'aimes comme je suis, sans artifice. T'avoir dans ma vie est un bonheur au quotidien, je suis très fier de l'histoire que nous avons construit et très redevable de tout l'amour et le soutien que tu me donnes. J'espère en faire autant et cela pour de nombreuses années encore, quoi qu'il arrive, j'y crois fort.

Un immense merci à mes collègues de bureau Erwan, Xan, Simon, Florent et Alexei, qui ont su donner de la vie à ces murs légèrement vétustes et tristounes à grands coups de memes et de posters. *Meeeeessieurs*, vous n'êtes pas sans savoir que votre soutien et votre humour m'ont été d'une aide immense pour arriver au bout des trois ans. Grâce à vous j'ai adopté le café et abandonné l'usage d'`emacs`, je retiendrai cela et bien d'autres choses ! Xan, petite pensée à toi en particulier qui est actuellement en plein dedans, dans les affres de cette fameuse "dernière ligne droite" qui semble n'en jamais finir (et pourtant si) et en fait est on ne peut plus tortueuse, et que tout le monde se croit malin de rappeler en guise de soutien. Laisse-moi te dire, courage, c'est la dernière ligne droite ! 🤭 Bientôt ce sera à toi de répondre à ta question favorite.

Merci à William, tu m'as donné le goût de l'écriture il y a déjà plusieurs années et je le cultive avec joie (et irrégularité). Et pour ta faculté saine à remettre en question les discours et les pensées toutes-faites, je suis très reconnaissant de pouvoir refaire le monde avec un vrai ami qui ne partage pas mes opinions ! J'espère que ça continuera longtemps, viens en Espagne quand tu veux.

Merci à Matthieu Pouget, que j'ai rencontré pour une de ces fameuses formations pédagogiques *Pratiques théâtrales pour la didactique*, qui m'a tout appris pour ma première participation à *Ma thèse en 180 secondes*, et qui aujourd'hui encore (et sans doute demain) est une réelle inspiration pour ma façon d'être et de vivre mon métier. Tu fais un travail formidable et les doctorant.e.s ont beaucoup de chance de t'avoir !

Mille mercis à tous les membres actifs des associations que j'ai fréquentées, puisque ce fut une activité significative et ô combien enrichissante de mes deux premières années de thèse : merci donc aux militants d'Extinction Rebellion Toulouse, à Mathis L., Coline, Lou et Soledad, fiers fondateurs d'Action Collapse, devenu Green Sab et qui prospère désormais sur la fac (on a formé une fine équipe !), à Alix, Alex, Anouk, Sébastien, Mathilde et toutes celles et ceux qui ont cru à cette aventure et lui ont donné du temps et de l'énergie. Louis, merci de faire partie de cette équipe, et aussi d'avoir manifesté de l'intérêt pour ma thèse et toutes tes questions sur l'astrophysique, ne change rien ! Je suis bien sûr redevable à Nathalie Del Vecchio pour porter haut notre engagement, et puis plus personnellement pour m'avoir accompagné dans mon parcours pendant deux ans, comme une amie précieuse que je n'oublierai pas, et merci à Laurent Canale pour sa gentillesse, son partage d'expérience et sa bonne volonté de faire bouger les choses à la fac. Merci à Avenir Climatique pour son savoir-faire et son art de vivre l'engagement et l'éco-anxiété (merci tout particulièrement à Rémi, Rémy, Camille, Antonin, Clarisse, Thomas, Elisa, Thibaut, Gaëlle, Noé et bien d'autres, vous êtes des personnes exceptionnelles

et vous connaître m'a beaucoup apporté, et bien sûr aux organisateurices des UEDACs 2020 et 2021 qui furent pour moi les meilleures semaines de l'année !). Merci à toi Romane pour tout ton engagement, ton don de rendre toujours plus simple le passage à l'action, et ta co-animation du groupe de travail COP2 qui j'espère trouvera une suite favorable (merci à tou.te.s les participant.e.s de ce groupe qui nous ont fait confiance). Bravo et merci à Maxime, Nicolas, Antonin (encore), Hugo et Charline pour avoir porté de grands projets à l'échelle de Toulouse, au sein de Together For Earth - qu'ils aient abouti ou non !, à Julie pour les nombreux traquenards qui se sont toujours révélé utiles et passionnants, et bien sûr à Robin, Hugo (encore), Romane (encore !), Lauriane, Mathis D. et toutes celles et ceux qui ont fini par créer et porter le collectif Etudiant.e.s en Transition alors que je mettais mon activisme en pause pour finir ma thèse. Merci à toi Kim, dont l'amitié et la passion pour la nature m'a fait découvrir une autre facette de l'engagement en général, je n'oublierai jamais mes premières sorties naturalistes aux côtés des Dryades.

Pour rester sur une note associative, un grand bravo et merci à l'association Paren(thèse) Occitanie qui fait un travail formidable pour soutenir les doctorant.e.s en particulier dans la période compliquée de la rédaction, vous découvrir fut une bénédiction et plusieurs des pages à suivre n'auraient jamais été écrites sans cela ; merci en particulier à Jeanne et Marie qui m'avez fait découvrir le campus vide du Mirail le dimanche, et sa Maison de la Recherche pour continuer à travailler dans la bonne ambiance en bonne compagnie. Merci à l'Eurêkafé, celles et ceux qui ont donné le jour à ce merveilleux foyer, résidence secondaire du thésard, et à celles et ceux qui le font vivre. Merci également à Marie-Pia, Léa, Alexei (encore), Naïs, Kensya, Marguerite et Miguel d'avoir si soigneusement gardé mon petit Onyx, qui si adorable soit-il demande un peu d'organisation quand on est en déplacement !

Merci enfin à Mélanie Habouzit pour m'avoir inspiré, d'abord par son manuscrit de thèse et puis par les discussions que nous avons eues à Athènes. Merci à Chloé et Maxime, excellents stagiaires de licence promis à un grand avenir de par leur curiosité, leur grande efficacité et leurs qualités humaines, dont l'encadrement a ponctué la fin de ma thèse de la meilleure des façons et dont le travail ne sera pas vain, je m'y engage ! Merci aussi aux membres de l'"armée d'Olivier" qui m'ont précédé ou suivi dans l'étude des sources de rayons X ultralumineuses et de leurs spectres, à savoir Andrés, Maxime et Clément, beaucoup plus spécialistes que moi dans ce domaine et qui ont toujours été de bon conseil et de bonne compagnie. Merci encore à Xan et Simon pour m'avoir bien aidé à développer le site de science participative *CLAXSON* en imaginant des fonctionnalités toujours plus improbables et à le faire vivre. Tout le mérite du succès de cette expérience revient essentiellement à ses utilisateurices, envers qui je ne saurai exprimer toute ma gratitude, qui ont consacré parfois des dizaines d'heures à classer des dizaines de milliers de sources de rayons X dans le seul but de servir la science et d'apprendre en s'amusant ! Merci aussi à Roberta dont l'aide précieuse a permis de traduire le site en italien et de donner aujourd'hui une suite aux recherches sur mon échantillon de sources de rayons X hyperlumineuses.

Merci à Natalie et Olivier pour leur accompagnement tout au long de la thèse, leur façon de nous laisser apprendre par la pratique, leur pédagogie et leur tolérance envers les baisses de moral ou de productivité. Et puis merci à Mickael, Soizic, Pierrick, Frédéric, Jean-Michel, Laure et les membres de l'Atelier d'écologie politique, qui a fini de me convaincre que je pouvais concilier engagement et métier académique, ce qui me donne donc un guide, une voie "simple" à suivre pour la suite, les postdocs, les plans B et tout le reste. Si c'est surtout mon rêve d'enfant de devenir astrophysicien qui m'a poussé à commencer cette thèse, c'est surtout vous rencontrer et travailler avec vous qui me donne aujourd'hui ce feu intérieur, la volonté de continuer. Et cela n'a pas de prix.

À toi donc, chère lectrice, cher lecteur, qui fait peut-être partie de cette liste susnommée, merci encore d'accorder de ton temps à ce recueil, et je te souhaite une agréable lecture !

Contents

1 Introduction abrégée **7**
- 1.1 Considérations théoriques . . . 7
  - 1.1.1 Théorie des trous noirs . . . 7
  - 1.1.2 Les gammes de masse des trous noirs . . . 8
  - 1.1.3 Théorie de l'accrétion . . . 10
- 1.2 Signatures observationnelles des trous noirs . . . 16
  - 1.2.1 Binaires X . . . 16
  - 1.2.2 Sources X ultralumineuses . . . 17
  - 1.2.3 Sources X hyperlumineuses . . . 18
  - 1.2.4 Événements de rupture par effet de marée . . . 19
  - 1.2.5 Noyaux actifs de galaxies . . . 19
- 1.3 Astronomie en rayons X . . . 20
- 1.4 Rationale . . . 22

2 Scientific context **23**
- 2.1 Theoretical considerations . . . 23
  - 2.1.1 Theory of black holes . . . 23
  - 2.1.2 The mass ranges of black holes . . . 24
  - 2.1.3 Theory of accretion . . . 26
- 2.2 Observational signatures of black holes . . . 32
  - 2.2.1 X-ray binaries . . . 32
  - 2.2.2 Beyond the limits: ultraluminous X-ray sources . . . 32
  - 2.2.3 Hyperluminous X-ray sources . . . 33
  - 2.2.4 Tidal disruption events . . . 35
  - 2.2.5 Active galactic nuclei . . . 35
- 2.3 Finding black holes using electromagnetic signatures . . . 36
  - 2.3.1 Dynamical measurements . . . 36
  - 2.3.2 Ultraviolet and optical spectroscopy . . . 36
  - 2.3.3 X-ray diagnostics . . . 37
  - 2.3.4 Black-hole – galaxy scaling relations . . . 39
- 2.4 Relation to galaxy evolution . . . 39
  - 2.4.1 A brief history of galaxy formation and evolution . . . 40
  - 2.4.2 Co-evolution of black holes and galaxies . . . 41
  - 2.4.3 Dwarf galaxies as local analogues of primordial galaxies . . . 42
- 2.5 The missing bricks: intermediate-mass black holes . . . 43
  - 2.5.1 Formation channels . . . 43
  - 2.5.2 Observational evidence . . . 45
  - 2.5.3 Current constraints . . . 47
  - 2.5.4 Alternative scenario: primordial black holes . . . 48
- 2.6 X-ray astronomy . . . 48
- 2.7 Rationale . . . 50

3 Instruments and data **51**
3.1 X-ray observatories . . . 51
3.1.1 First generation . . . 51
3.1.2 Swift-XRT . . . 52
3.1.3 XMM-Newton . . . 54
3.1.4 Chandra . . . 55
3.2 Data . . . 57
3.2.1 Selection of reliable sources . . . 57
3.2.2 Sample enhancement . . . 57
3.2.3 Sample characterisation . . . 60
3.2.4 Visualisation tool . . . 63

4 Classification of X-ray sources **64**
4.1 Rationale and previous works . . . 64
4.2 Data used in the classification . . . 66
4.3 Method . . . 67
4.3.1 Density estimations . . . 68
4.3.2 Naive Bayes classifier . . . 69
4.3.3 Fine-tuning of the method . . . 72
4.3.4 Outlier measure . . . 73
4.4 Results . . . 73
4.4.1 Training sample . . . 74
4.4.2 Test sample . . . 77
4.4.3 Outliers . . . 81
4.5 Discussion . . . 82
4.5.1 General classification performance . . . 82
4.5.2 Comparison to machine learning results . . . 83
4.5.3 Classifications biases . . . 83
4.6 Outlook: citizen science . . . 86

5 Study of ULX and HLX **90**
5.1 Context . . . 91
5.2 Building a clean sample . . . 92
5.2.1 X-ray source – galaxy associations . . . 92
5.2.2 ULX candidates . . . 93
5.2.3 Source classification to filter contaminants . . . 94
5.2.4 Filtering remaining contaminants . . . 97
5.2.5 HLX sample . . . 97
5.2.6 Complete subsample . . . 98
5.2.7 Contaminants sample . . . 98
5.3 Results . . . 99
5.3.1 Malmquist-corrected XLF . . . 99
5.3.2 ULX rates in different environments . . . 102
5.3.3 Comparison of XRB and ULX . . . 105
5.3.4 The hyperluminous X-ray sample . . . 109
5.3.5 Comparison of ULXs and HLXs . . . 111
5.4 Discussion . . . 116
5.4.1 Comparison to other works . . . 116
5.4.2 Number of contaminants . . . 118
5.4.3 Heterogeneity of the sample and instrumental biases . . . 118
5.4.4 X-ray luminosity function . . . 119
5.4.5 Nature of HLXs . . . 123
5.4.6 Investigation of two variable HLX . . . 126
5.5 Summary . . . 129

6 Search for IMBH in dwarf galaxies **130**
6.1 Context . . . 130
6.2 Sample . . . 131
6.3 Method and results . . . 132
6.3.1 Source classification . . . 132
6.3.2 Background contaminants . . . 133
6.3.3 X-ray binaries . . . 133
6.3.4 Radio detections . . . 134
6.3.5 Off-nuclear candidates . . . 136
6.3.6 AGN candidates . . . 137
6.4 Discussion and conclusion . . . 138
6.4.1 Stellar mass and distance accuracy . . . 138
6.4.2 Metallicity effects . . . 143
6.4.3 Active fraction . . . 143
6.4.4 Nature of AGN candidates . . . 147
6.4.5 Comparison to other studies . . . 148

7 Discussion **151**
7.1 Benefits and limitations of a probabilistic approach for population studies . . . 151
7.2 Reliability of new IMBH candidates . . . 152
7.3 The black hole - galaxy co-evolution . . . 154
7.3.1 Black hole masses . . . 154
7.3.2 Stellar masses . . . 157
7.3.3 Selection bias . . . 157
7.3.4 Physical origin . . . 158
7.4 Wandering black holes . . . 158
7.5 Occupation fraction . . . 159
7.6 Local rate of accreting IMBH . . . 159
7.7 Accretion onto intermediate-mass black holes . . . 161
7.8 Comparison to formation models . . . 162
7.9 Black hole growth in dwarf galaxies . . . 164

8 Conclusion and outlook **165**
8.1 Conclusion . . . 165
8.2 Outlook . . . 168
8.2.1 Potential of our IMBH sample . . . 168
8.2.2 Potential of archival searches . . . 169
8.2.3 Citizen science, completing the classification framework . . . 171
8.2.4 Future IMBH-related population studies . . . 172

9 Conclusion et perspectives **176**
9.1 Conclusion . . . 176
9.2 Perspectives . . . 179
9.2.1 Potentiel de notre échantillon de candidats IMBH . . . 179
9.2.2 Potentiel des recherches dans les archives . . . 180
9.2.3 La science participative, complément de la classification automatique . . . 183
9.2.4 Futures études de populations liées aux IMBHs . . . 183

Appendices **188**

A List of candidates **189**

Chapter 1

Introduction abrégée

Les trous noirs furent introduits pour la première fois comme solutions mathématiques des équations d'Einstein dans les années 1910 (Einstein, 1915). Cinquante ans plus tard, la première preuve irréfutable de l'existence des trous noirs a été trouvée en rayons X, avec la découverte de la binaire X Cygnus X-1 (Bolton, 1972). Les cinq dernières décennies ont été l'âge d'or de la science des trous noirs, à bien des égards : observations de dizaines de signatures différentes de trous noirs, diversification des catégories théoriques et observationnelles de trous noirs, phénoménologie poussée de leur interaction avec les objets et milieux environnants, modélisation détaillée de leur formation et évolution... Cependant, la détection de trous noirs aussi massifs que $10^9 M_\odot$ moins d'un milliard d'années après le Big Bang (e.g. Wang et al. 2021) a conduit à des questions concernant notre compréhension de la formation des trous noirs, forçant la communauté astrophysique à postuler des mécanismes de formation extrêmement rapides dans lesquels certains trous noirs insaisissables pourraient avoir joué un rôle important : les trous noirs de masse intermédiaire. Dans ce chapitre, je résume les jalons de la science des trous noirs du point de vue des observateurs, et je montre comment la recherche et la compréhension des trous noirs de masse intermédiaire sont essentielles à notre compréhension de la formation et de l'évolution des trous noirs supermassifs.

1.1 Considérations théoriques

1.1.1 Théorie des trous noirs

Un examen de la théorie des trous noirs du point de vue de la physique théorique dépasse le cadre de cette thèse. Néanmoins, le concept de trou noir est soutenu par la théorie de la relativité générale (Einstein, 1915)[1] Les équations de champ d'Einstein décrivent comment la géométrie de l'espace et du temps est modifiée par la présence de matière, en raison de sa masse et de son contenu énergétique. Quelques mois après la publication de l'article pionnier de la relativité générale, Karl Schwarzschild a publié une solution à l'équation d'Einstein pour une masse ponctuelle M, mettant en évidence une singularité apparaissant au rayon dit de Schwarzschild $R_S = 2GM/c^2$ (Schwarzschild, 1916). Pendant des années, il n'y eut aucun consensus sur la signification physique de cette singularité. Il fut démontré par la suite qu'elle disparaissait avec un changement de système de coordonnées, alors qu'une singularité physique était en fait présente à un rayon plus petit : pour un trou noir de Schwarzschild sans rotation, la singularité est un point au centre du trou noir, alors que pour les trous noirs de Kerr en rotation maximale, c'est un anneau (Visser, 2007).

[1] L'origine du concept de trou noir peut être datée au XVIIIe siècle, lorsque le pasteur anglais John Michell et le mathématicien français Pierre Simon de Laplace ont postulé l'existence de *corps non lumineux* ou *étoiles sombres*, ayant une masse telle que leur vitesse de libération dépasse la vitesse de la lumière. Près de deux siècles plus tard, en 1968, le terme "trou noir" fut inventé lors d'une conférence et popularisé par John Wheeler.

Pour un observateur extérieur, cependant, le rayon de Schwarzschild d'un trou noir non rotatif agit comme un horizon des événements : aucune particule ou lumière contenue à l'intérieur de cette surface ne peut s'échapper, en raison de la courbure de l'espace-temps. Cette solution des équations d'Einstein a donné naissance à la théorie des trous noirs. Dans le cadre de la théorie classique de la gravitation, cela revient à dire que la vitesse de libération de cet objet dépasse la vitesse de la lumière. En théorie, toute quantité de matière, comme une planète ou une étoile, se transforme en trou noir si elle est comprimée en dessous de son rayon de Schwarzschild. En tant que tels, les trous noirs font ainsi partie de la classe plus large des objets compacts, qui ont un rayon R tel que $R_S/R > 10^{-4}$ et autour desquels les effets de la GR sont significatifs. Une autre découverte théorique de la GR est que *"les trous noirs n'ont pas de cheveux"*, suivant le commentaire de John Wheeler, ce qui signifie que les trous noirs isolés sont entièrement décrits par seulement trois paramètres : leur charge électrique, leur masse et leur spin.

En physique stellaire, les objets compacts représentent le stade final de l'évolution stellaire. Après sa naissance à partir de l'effondrement d'un nuage moléculaire dense, une étoile voit sa matière se transformer progressivement par fusion nucléaire. Lorsque son combustible nucléaire devient insuffisant pour poursuivre la fusion, le cœur de l'objet s'effondre sous l'effet de la gravité, laissant un vestige qui dépend de la masse initiale de l'étoile : une naine blanche (Anderson, 1929; Chandrasekhar, 1931), une étoile à neutrons (Landau, 1932; Baade and Zwicky, 1934) ou un trou noir (Schwarzschild, 1916; Oppenheimer and Snyder, 1939). Alors que la pression due à la gravité des naines blanches et des étoiles à neutrons est contrée par les pressions de dégénérescence des électrons et des neutrons respectivement, on ne connaît aucune preuve d'une force répulsive stabilisant les trous noirs. La gamme de masses théoriques des naines blanches, des étoiles à neutrons et des trous noirs est de $M < M_{Ch}$, $M_{Ch} < M < M_{TOV}$ et $M > M_{TOV}$, où $M_{Ch} \simeq 1.4 M_\odot$ est la limite de masse de Chandrasekhar sur une naine blanche stable (Chandrasekhar, 1931) et $M_{TOV} \in [1.6, 3.1] M_\odot$ est la limite Tolman-Oppenheimer-Volkoff (TOV) d'une étoile à neutrons froide et non rotative (Tolman, 1939; Oppenheimer and Volkoff, 1939). Récemment, des études observationnelles ont affiné cette dernière limite grâce à la détection de pulsars massifs (e.g., Cromartie et al. 2020; Riley et al. 2021 pour le pulsar milliseconde J0740+6620 de masse $\sim 2.1 M_\odot$).

1.1.2 Les gammes de masse des trous noirs

Comme nous le verrons dans les sections suivantes, les trous noirs sont observés dans une large gamme de masses. Dans cette section, nous mentionnons simplement les différentes gammes de masses théoriques et observationnelles des trous noirs et les intervalles de masse ayant peu de sources connues, comme un premier aperçu de leur population.

Trous noirs de masse stellaire

Les trous noirs de masse stellaire sont le stade final de l'évolution des étoiles massives. La figure 1.1 montre la masse du progéniteur stellaire des étoiles à neutrons et des trous noirs. Les étoiles moins massives que $140 M_\odot$ peuvent former des trous noirs dont la masse peut atteindre $\sim 65 M_\odot$ (Heger et al., 2003). Dans la gamme $140 - 260 M_\odot$, une étoile pauvre en métaux (où les métaux désignent les éléments plus lourds que He et Li) termine sa vie dans une supernova dite à instabilité de paire, ne laissant aucun vestige. Seules les étoiles très massives dépourvues de métaux (appelées étoiles de population III et présentes aux premiers stades de l'Univers, section 2.4.1) peuvent former des trous noirs plus massifs que 100 $M_\odot$ (Madau and Rees, 2001; Ohkubo et al., 2009). La formation de cette classe de trous noirs est discutée plus loin. D'autres voies de formation existent pour les trous noirs de masse stellaire, comme la coalescence de deux étoiles à neutrons.

Les trous noirs de masse stellaire ne sont détectés que dans la Voie lactée et les galaxies proches, le plus souvent lorsqu'ils se trouvent dans un système binaire avec une étoile. Ces systèmes sont appelés binaires X (XRB), en raison de leur découverte et de leur caractérisation en rayons X (Bolton, 1972), qui ont fourni certaines des premières preuves de l'existence des trous noirs.

Trous noirs de masse intermédiaire

Les trous noirs de masse intermédiaire (IMBH) ont une masse comprise dans l'intervalle $10^2 - 10^5 M_\odot$. Les mécanismes de formation de ces trous noirs sont encore incertains, mais les possibilités traditionnellement évoquées les voient comme les vestiges d'étoiles massives de population III (e.g.

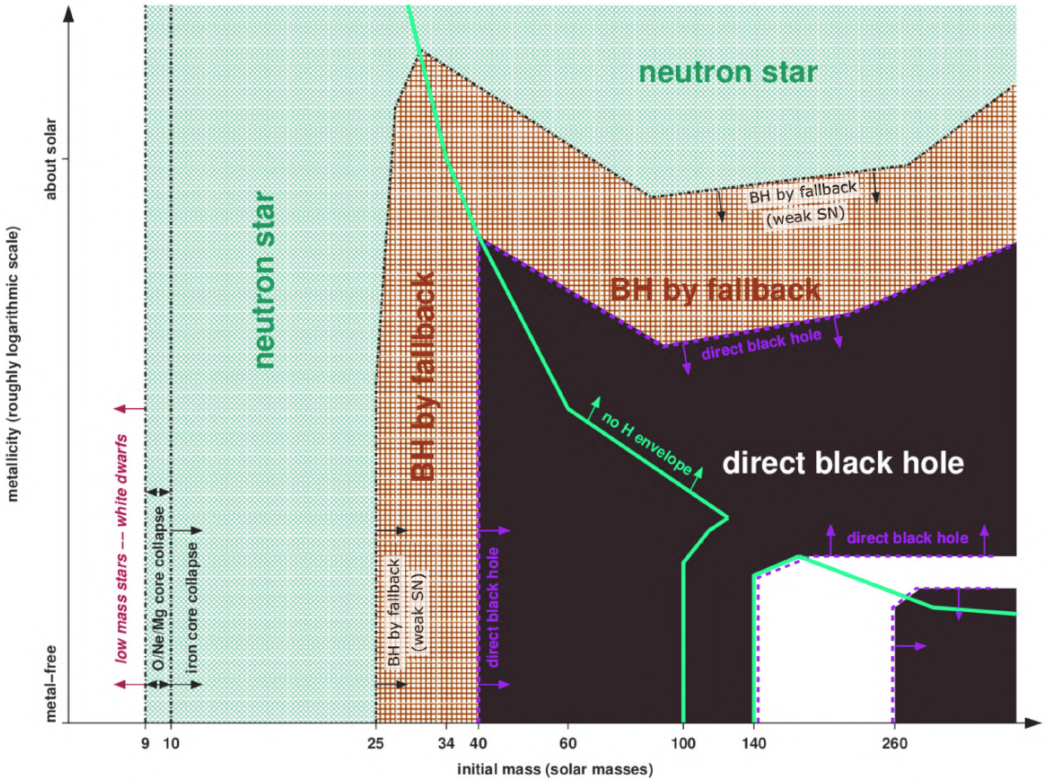

Figure 1.1: Diagramme de masse-métallicité montrant les canaux de formation atteignables par les étoiles à neutrons et les trous noirs formés à partir de l'effondrement d'étoiles isolées massives, en fonction de leur métallicité et de leur masse initiale sur la séquence principale. Reproduit à partir de Heger et al. (2003).

Madau and Rees 2001), le résultat d'un emballement des fusions de corps dans des amas stellaires denses (e.g. Portegies Zwart and McMillan 2002), ou le produit final de l'effondrement direct d'un grand nuage de gaz de faible métallicité et de faible moment angulaire (par exemple, Loeb and Rasio 1994). Ces possibilités (Mezcua 2017, section 2.5.1) pourraient déjà être en place quelques centaines de millions d'années après le Big Bang. Sur plusieurs milliards d'années, les IMBH pourraient également se former par accrétion sur un trou noir de masse stellaire, par fusion de tels trous noirs, ou par une combinaison de ces deux processus.

Jusqu'à présent, les preuves observationnelles de l'existence de ces trous noirs étaient rares, mais elles semblent s'être accumulées récemment grâce aux observatoires capables de les détecter à de plus grandes distances et à des flux plus faibles (section 2.5.2).

Trous noirs supermassifs

Les trous noirs supermassifs (TNS, $10^5 - 10^{10} M_\odot$, Section 1.2.5) se trouvent au centre de la plupart (sinon toutes) les galaxies massives. Leur formation fait l'objet d'un débat intense (section 2.5), ce qui constitue le principal moteur de la recherche et de l'étude des IMBH.

Trous noirs primordiaux

Les trous noirs primordiaux (PBHs) sont prédits comme étant un résultat possible de l'effondrement des fluctuations de densité dans l'Univers primordial, juste après le Big Bang, suivant des scénarios inflationnistes spécifiques (Carr and Kühnel, 2020). Leur masse initiale devrait dépendre linéairement de leur temps de formation, de sorte qu'ils pourraient couvrir une gamme de masse extrêmement large $10^{-10} - 10^{7} M_\odot$. S'ils sont abondants, ces trous noirs, pour la plupart isolés, devraient laisser des empreintes détectables dans l'Univers actuel. Cependant, à ce jour, les tests observationnels pour plusieurs gammes de masse de PBH, s'appuyant par exemple sur le microlentillage des étoiles (Griest et al., 2014), le fond diffus cosmologique (domaine des micro-ondes) et le fond diffus de rayons X (Poulin et al., 2017; Ballesteros et al., 2020) ou encore les signatures d'accrétion n'ont conduit qu'à des limites supérieures sur leur abondance.

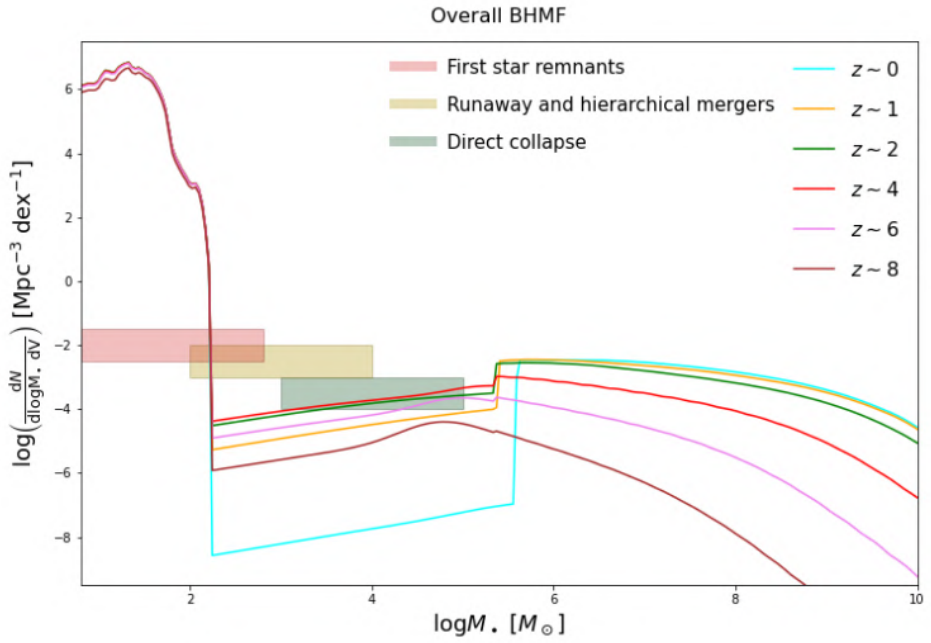

Figure 1.2: Modèle de fonction de masse des trous noirs de Sicilia et al. (2022). Reproduction de Sicilia et al. (2022).

La fonction de masse des trous noirs

Une observable fondamentale pour représenter l'abondance des trous noirs de chaque masse est le spectre de masse des trous noirs, ou fonction de masse des trous noirs (BHMF). Son étude en fonction du redshift est un outil puissant pour contraindre, par exemple, les modèles théoriques de formation des trous noirs supermassifs, ou leur rétroaction dans leur galaxie. À l'extrémité de faible masse, le BHMF est peuplé d'abondants trous noirs de masse stellaire (Section 1.2.1), vestiges de l'évolution stellaire. À l'extrémité massive, il sonde la population de TNS au centre des galaxies massives. À titre d'illustration est montré sur la figure 1.2 un exemple de BHMF issu des récents travaux semi-empiriques de Sicilia et al. (2022). L'écart de masse de l'instabilité de paire est à peine visible (il ne se manifeste que par un déclin abrupt de la BHMF à $\log M_*/M_\odot \sim 1,8$), étant peuplé de trous noirs formés dans des binaires perturbées, en particulier des binaires se terminant par une phase d'enveloppe commune s'effondrant en un trou noir massif de masse stellaire (van Son et al., 2020; Sicilia et al., 2022).

Notons que cette reconstruction peut être inexacte, en particulier dans la gamme des IMBH où leur modèle n'inclut aucun des mécanismes de croissance des IMBH les plus étudiés (superposés dans le diagramme). Comme nous le verrons plus tard, les trous noirs de différentes masses ont des environnements et des luminosités différents, de sorte que les échantillons de trous noirs détectés sont fortement biaisés vers les plus proches et les plus massifs. Ce biais de détection doit être corrigé afin d'estimer la BHMF à partir des observations. Cependant, d'un point de vue qualitatif, nous constatons que contrairement aux trous noirs stellaires et supermassifs, les IMBHs dans l'Univers local ($z = 0$) sont effectivement insaisissables.

1.1.3 Théorie de l'accrétion

Parce qu'un trou noir n'émet pas de lumière (sauf le rayonnement de Hawking Hawking 1974, au-delà des limites de détection des instruments actuels), leurs signatures observationnelles sont indirectes et dépendent largement de leur environnement. Notamment, l'accrétion joue un rôle important dans leur détectabilité et les systèmes d'accrétion constituent la plupart des trous noirs que nous avons détectés. Ces trous noirs accrétants bien étudiés sont principalement les binaires X (XRB, section 1.2.1) et les noyaux actifs de galaxie (AGN, section 1.2.5).

L'accrétion est le processus de chute de la matière vers un objet central, sous l'effet du potentiel

gravitationnel de cet objet et par dissipation visqueuse de l'énergie cinétique de la matière. Si la matière qui tombe possède un moment angulaire, elle gravitera autour de l'objet central et les processus visqueux conduiront à la formation d'un disque d'accrétion. L'énergie potentielle gravitationnelle de chaque particule de matière est convertie en énergie thermique par des processus visqueux, ce qui lui permet de perdre son moment angulaire et de tomber vers l'objet central compact. Plus la matière se rapproche de l'objet central, plus elle devient chaude, ce qui l'amène à émettre un rayonnement thermique (de Planck) de courte longueur d'onde, suivant la loi de Planck

$$\nu F_\nu \propto \frac{\nu^3}{1 - \exp(h\nu/k_B T)}$$

où ν est la fréquence du rayonnement, F_ν la densité spectrale de flux à cette fréquence, h la constante de Planck, k_B la constante de Boltzmann et T la température de la matière. Toutefois, le rayonnement thermique n'est pas le seul processus responsable de l'émission de rayons X.

Processus radiatifs

En plus du rayonnement thermique, quatre mécanismes de rayonnement non thermique dominent dans le domaine des rayons X.

- Dans un plasma à haute température (en particulier un plasma ionisé par collision), les atomes et les ions peuvent être excités (photo-ionisés) et désexcités à des niveaux d'énergie élevés, ce qui entraîne l'émission et l'absorption de raies spectrales en rayons X. (e.g. Wilms et al., 2000).
- Les particules massives chargées dans un tel plasma produisent également un champ électrique qui interagit avec les particules, les faisant décélérer et émettre des photons. Ce rayonnement est appelé "rayonnement de freinage" ou Bremsstrahlung. Pour les ions lourds déviant les électrons dans un plasma dense (tel que le milieu intra-amas, section 1.3), l'émission de Bremsstrahlung se situe dans le domaine des rayons X (Cavaliere and Fusco-Femiano, 1976; Klein, 1999).
- En présence d'un champ magnétique puissant, les particules chargées ont une trajectoire spirale autour des lignes de champ magnétique, et cette accélération entraîne l'émission du rayonnement dit synchrotron, parfois dans les rayons X (Jones et al., 1974).
- La diffusion Compton inverse ou *Compton up-scattering* est fréquente dans le domaine des rayons X. Elle désigne l'augmentation de l'énergie d'un photon de faible énergie pénétrant dans un milieu lorsqu'il est diffusé par un électron chaud. Il s'agit de l'augmentation de l'énergie d'un photon de faible énergie pénétrant dans un milieu, lorsqu'il est diffusé par un électron chaud. (Sunyaev and Titarchuk, 1980).

Les rayons X sont souvent distingués par commodité en "rayons X mous" (basse énergie, $0.1 \lesssim h_\nu \lesssim 3$ keV) et "rayons X durs" (haute énergie $h_\nu \gtrsim 1$ keV)[2]. Le rapport de flux (ou la différence relative) entre deux bandes de rayons X est alors appelé la dureté.

États d'accrétion

L'image la plus simple d'un disque d'accrétion est un disque de matière dont la température, T, décroît avec le rayon, r, ($T(r) \propto r^{-3/4}$ dans un modèle de disque d'accrétion mince en régime permanent, Shakura and Sunyaev 1973). Le rayonnement thermique d'un tel objet est décrit spectralement par un modèle de corps noir multicolore (ci-après `diskbb`), composé de l'addition du spectre de corps noir (Planck) de chaque anneau de matière. En pratique, cependant, chaque anneau de matière a une épaisseur et une densité différentes, le disque est tronqué à un certain rayon, et il peut être immergé dans un champ magnétique à grande échelle, de sorte qu'il existe une grande variété de modèles spectraux de disque d'accrétion.

L'émission thermique du disque d'accrétion peut être bloquée par un environnement optiquement épais autour du disque, la couronne, qui donne lieu à une diffusion Compton inverse de cette émission. Une autre composante de l'émission est ainsi observée, dans les rayons X durs, sous la forme d'un spectre en loi de puissance (`powerlaw`) (Titarchuk and Lyubarskij, 1995) : $F_{\nu,\texttt{powerlaw}} \propto \nu^\Gamma$

[2]Historiquement, la distinction empirique entre les rayons X mous et durs peut avoir été motivée par leur capacité à blesser la peau humaine, ou inversement à la pénétrer (Russ, 1915). Cependant, cette distinction n'est pas bien définie et, selon le contexte, les rayons X durs peuvent également désigner des photons d'une énergie de $\gtrsim$20 keV.

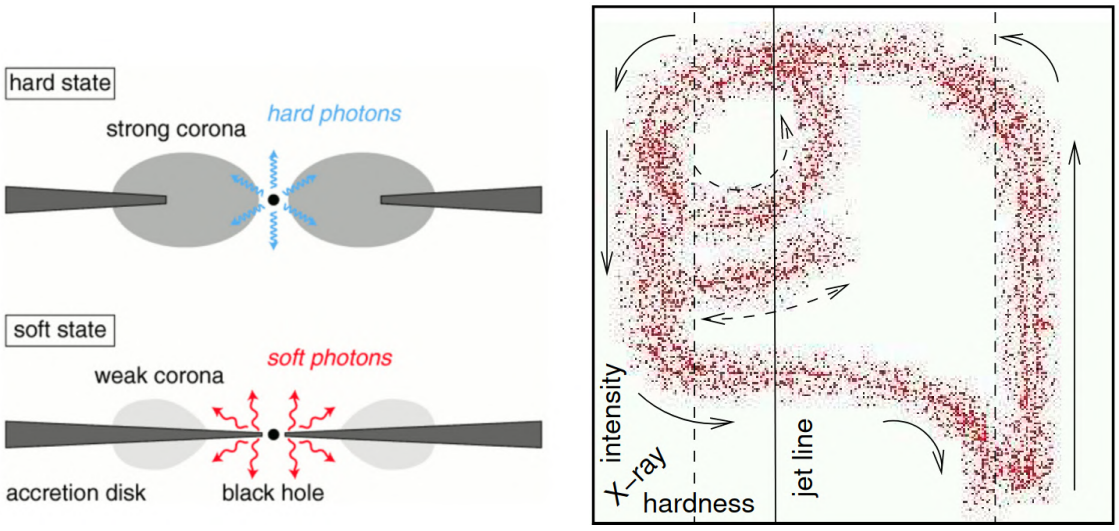

Figure 1.3: (Gauche) Schéma du modèle de disque tronqué, avec la géométrie correspondant aux états bas/dur (en haut) et haut/mou (en bas). Reproduction de Liu and Taam (2009). (Droite) Représentation schématique du diagramme dureté-intensité des binaires X à trou noir (ou "q-shape diagram"). Reproduction de Fender et al. (2004).

où ν est la fréquence de rayonnement, F_ν est la densité spectrale de flux et Γ est l'indice spectral. L'indice spectral Γ de ce modèle est un moyen de mesurer la dureté de l'émission d'une source, ce qui permet de contraindre sa nature. La plupart des AGN (section 1.2.5) ont des spectres bien ajustés par une loi de puissance absorbée avec des indices de photons dans un intervalle étroit $\Gamma = 1,7 - 2$ (e.g. Middleton et al. 2008).

Un modèle d'absorption est également nécessaire pour reproduire les spectres en rayons X. En effet, les rayons X émis par la source traversent plusieurs milieux pour atteindre l'observateur, en particulier l'environnement de la source et le milieu interstellaire de la Voie lactée. Les rayons X mous peuvent photoioniser les atomes qu'ils rencontrent, et une modélisation précise de l'absorption est obtenue en additionnant les sections efficaces de ces interactions pour chaque milieu : (typiquement, le gaz atomique neutre, les molécules et les grains de poussière Wilms et al., 2000). La section efficace totale est simplifiée comme la section efficace d'une quantité d'hydrogène présente le long de la ligne de visée, la densité de colonne d'hydrogène n_H, exprimée en cm^{-2}. Les valeurs de n_H pour le milieu interstellaire de la Voie lactée ont été cartographiées par différentes collaborations (par exemple, HI4PI Collaboration et al. 2016), et sont de l'ordre de 3×10^{20} cm^{-2} pour les lignes de visée au-dessus et au-dessous du plan galactique. Les émetteurs de rayons X intégrés dans des environnements denses ou poussiéreux, comme au centre des galaxies proches, peuvent avoir des colonnes d'hydrogène beaucoup plus élevées, de l'ordre de $10^{22} - 10^{23}$ cm^{-2} (par exemple, Risaliti et al. 2002).

En pratique, cependant, le spectre d'un système accrétant peut changer de façon radicale au fil du temps, en particulier dans les systèmes de faible masse tels que les XRB (section 1.2.1). Les premières études spectrales dans le domaine des rayons X et des ondes radio ont montré que les XRBs à trou noir suivent des états spectraux canoniques, généralement appelés haut/mou (lorsque l'émission du disque thermique domine) et bas/dur (l'émission comptonisée domine), avec parfois des états transitoires. Pour rendre compte de cette évolution spectrale, le modèle du "disque tronqué" (ou "évaporation du disque") a été développé sur la base de la théorie de l'accrétion de Shakura and Sunyaev (1973) (e.g. Meyer et al. 2000). Il est illustré dans le panneau gauche de la figure 1.3. Pendant la quiescence (état bas/dur, où le trou noir accrète à des taux très faibles et où la binaire émet des rayons X durs non thermiques), la matière s'accumule dans le disque jusqu'à ce que, dans une certaine région, la densité et la température aient augmenté à tel point que l'hydrogène devient ionisé. Cela augmente la viscosité de la matière dans le disque, ce qui entraîne sa chute vers le trou noir et son accrétion. Le rayon intérieur du disque à ce moment-là correspond à la dernière orbite circulaire stable (*innermost stable circular orbit* ou ISCO) du trou noir ($R_{in} = 6R_S$ pour un trou noir de Schwarzschild, avec R_S le rayon de Schwarzschild, et $R_{in} = R_S$ ou $R_{in} = 9R_S$ pour un trou noir de Kerr tournant respectivement dans le sens prograde ou rétrograde par rapport au disque, Bardeen et al. 1972). Cet état permet un taux d'accrétion maximal et le rayonnement thermique du disque interne chaud domine (état haut/mou).

Lorsque le disque se vide, il redevient quiescent. Les états haut/mou et bas/dur peuvent être séparés par un facteur > 1000 en luminosité.

Néanmoins, l'accrétion est aussi souvent liée à des mécanismes d'éjection, avec des preuves solides de jets relativistes dans les AGN et les XRBs (Mirabel and Rodríguez, 1999; Netzer, 2015). L'émission radio (synchrotron) d'un jet est souvent observée dans l'état dur. En outre, le chemin d'évolution entre les états présente une hystérésis dans le diagramme dureté-intensité, parfois appelé "diagramme en forme de q" (figure 1.3, panneau de droite). Pour expliquer cette hystérésis, Fender et al. (2004) a donc revisité le modèle du disque tronqué et proposé le scénario suivant : la binaire en "quiescence" (en bas à droite du diagramme dureté-intensité) commence à accréter plus de matière, ce qui provoque l'augmentation de luminosité de la source et l'apparition (ou l'intensification) d'un jet radio stable. Le jet est accéléré au fur et à mesure que le disque d'accrétion s'effondre vers des rayons internes, jusqu'à ce qu'il atteigne une limite induite par un choc (la "ligne du jet" dans la Figure 1.3) où il devient instable et transitoire. La source reste dans l'état haut/mou pendant un certain temps avant de s'estomper et de retourner progressivement à la quiescence, en perdant sa couronne et son réservoir de matière à accréter et en récupérant potentiellement un jet (Fender et al., 2004).

Bien qu'il ait été largement utilisé et qu'il ait fourni un grand nombre d'informations physiques sur l'évolution des XRBs, ce modèle fait encore débat. En outre, l'emplacement et l'étendue exacts de la couronne sont largement incertains, et font l'objet de nombreuses recherches (par exemple, Ursini et al. 2022). L'existence même d'une couronne (figure 1.3, panneau de gauche) pour reproduire l'état dur est encore débattue, et il existe des modèles alternatifs qui ne nécessitent pas l'hypothèse de deux entités indépendantes – par exemple, le modèle JED-SAD de Marcel et al. (2018) utilise une configuration de disque hybride, où le disque interne (épais) est un écoulement magnétisé chaud (disque émetteur de jet ou JED) et la périphérie est un disque mince standard non magnétisé (disque d'accrétion standard, SAD), avec un rayon de transition entre ces disques dont le déplacement provoque les différents états d'accrétion.

Cependant, une compréhension détaillée de la géométrie et des propriétés physiques du flux d'accrétion n'est pas essentielle pour ce travail de thèse, et cet aperçu des états spectraux des trous noirs en accrétion et de leur explication physique sera suffisant pour permettre de premières interprétations.

Accrétion dans le cas d'un trou noir supermassif

Des différences importantes doivent être notées entre les trous noirs accrétants de masse stellaire dans les XRBs et les trous noirs supermassifs accrétant au centre des galaxies massives.

Après la découverte des premiers quasars, de nombreuses études ont trouvé des signes d'activité nucléaire dans des galaxies massives de toutes les morphologies. Ces systèmes ont été baptisés en fonction de leurs caractéristiques observationnelles très différentes et comprennent les quasars radio-bruyants et radio-silencieux, Seyfert 1, Seyfert 2 et les Blazars. Ces objets ont ensuite été qualifiés de "noyaux actifs de galaxie" (AGN) et unifiés dans un paradigme commun, où la variable cachée expliquant cette diversité observationnelle est l'angle d'observation, comme l'illustre la figure 1.4. Dans les AGN, le système central accrétant peut lancer un jet étroit, et est lui-même entouré d'un tore de poussière et de gaz qui empêche l'émission directe du système central d'être vue le long d'une certaine ligne de visée (voir par exemple Padovani et al. 2017; Bianchi et al. 2022 pour des revues récentes). Le gaz prend la forme de nuages situés dans ce que l'on appelle la "région d'étmission des raies larges" et la "région d'émission des raies étroites" : ces nuages de gaz sont illuminés par le système central, et absorbent et réémettent ce rayonnement. Des raies spectrales sont ainsi émises par chaque nuage, et le mouvement des nuages dans différentes directions entraîne par effet Doppler un élargissement des raies dans le spectre de l'ensemble du système. Les nuages de gaz dans la région d'émission des raies larges sont les nuages les plus rapides et les plus denses près du trou noir, tandis que la région d'émission des raies étroites est située plus loin.

Lorsqu'un jet est lancé et se trouve dans la ligne de visée, l'observateur voit un Blazar. À des angles plus faibles, la luminosité de la source diminue et des raies larges et étroites deviennent visibles dans le spectre : l'objet est alors classé comme quasar radio-bruyant. En commençant à voir le système de profil, la puissante émission centrale devient cachée, mais les jets radio sont toujours détectés, d'où le nom de radiogalaxie. Pour un AGN radio-silencieux, une émission puissante est vue à toutes les longueurs d'onde sauf les ondes radio, avec des raies spectrales dans le spectre visible-UV. Les Seyfert 2 sont moins lumineuses que les Seyfert 1, et ne montrent que des raies étroites proéminentes.

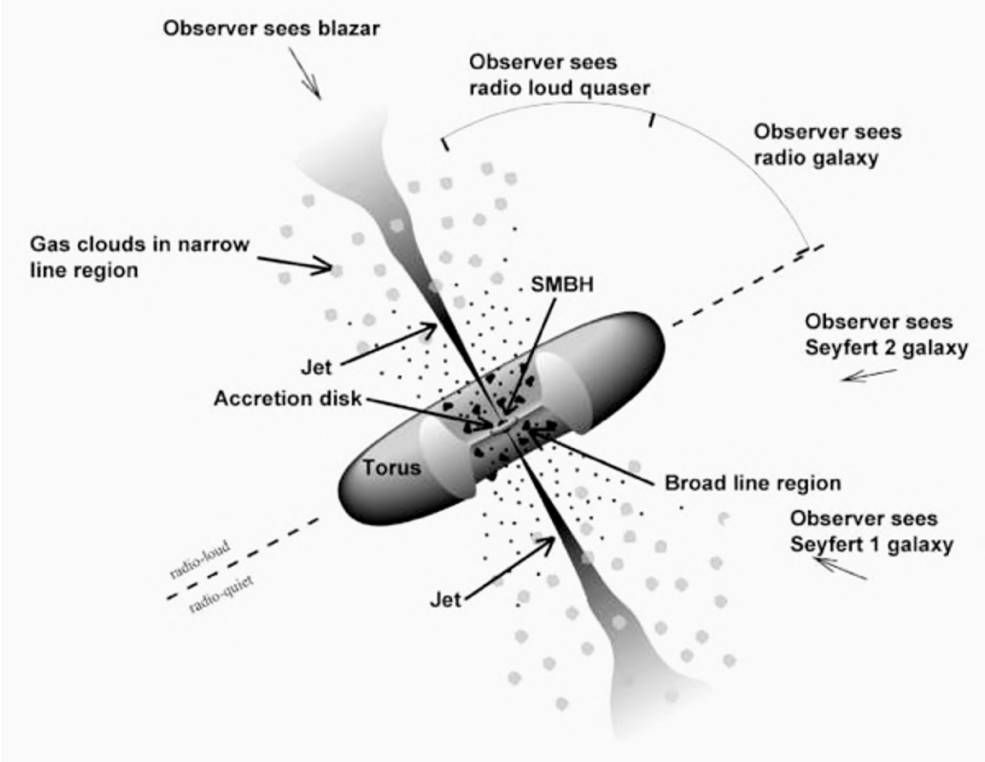

Figure 1.4: Diagramme schématique du modèle unifié des AGN (crédit : Fermi & NASA, https://fermi.gsfc.nasa.gov/science/eteu/agn/). La figure montre les différents composants d'un AGN dans ce modèle, et les caractéristiques observationnelles qu'ils provoquent en fonction de la ligne de visée.

À titre d'exemple, la figure 1.5 montre la distribution spectrale d'énergie (SED) d'un AGN de l'infrarouge moyen aux fréquences gamma (Collinson et al., 2017). Différentes composantes spectrales sont visibles, notamment l'émission thermique du disque d'accrétion, l'émission comptonisée de la couronne, un "soft excess" ou excès mou, et une composante de réflexion. La composante d'excès mou est une caractéristique spécifique des AGN, qui n'a pas encore d'explication claire et qui sort du cadre de ce travail de thèse. La composante de réflexion est produite par le rayonnement comptonisé réfléchi par l'environnement immédiat de l'AGN, et se manifeste par une augmentation du continuum dans la partie dure et des raies d'absorption et d'émission (Wilkins and Fabian, 2012). La composante du tore de poussière est liée à la région externe d'un AGN et à son angle d'observation (figure 1.4) et peut être utilisée pour sélectionner des échantillons d'AGN à partir de la photométrie dans l'infrarouge moyen (section 2.3.2). Comme le montre cette SED, l'émission d'un AGN est donc caractérisée par de multiples composantes culminant à différentes longueurs d'onde et correspondant à différentes régions autour du trou noir.

La figure 1.5 (panneau de droite) illustre un exemple de géométrie d'accrétion expliquant les différentes composantes du spectre d'un AGN (Bambi, 2021) : les photons de rayons X mous proviennent de l'émission thermique du disque chaud, et certains sont diffusés en rayons X durs dans la couronne. Ces photons comptonisés sont ensuite partiellement réfléchis par le disque, donnant lieu à la composante de réflexion (Turner and Miller, 2009). L'emplacement et la géométrie de la couronne dans la figure 1.3 (panneau de gauche) diffèrent de ceux de la figure 1.5 (panneau de droite), mais comme nous l'avons vu plus haut, cela est dû à l'existence de nombreux modèles de couronne (indépendamment de la masse du trou noir).

En plus de leur géométrie différente, une autre différence spectrale majeure entre les trous noirs XRB et les AGN est la longueur d'onde à laquelle leur émission thermique est maximale : en effet, les trous noirs plus massifs (de plusieurs ordres de grandeur) des AGN ont une dernière orbite stable plus grande, de sorte que le disque d'accrétion est plus froid. Son rayonnement thermique est donc maximal dans le domaine UV-visible (Figure 1.5, panneau de gauche). L'indice spectral des rayons X α_{ox} est donc utilisé pour paramétrer le rapport de luminosité entre les deux composantes : $\alpha_{ox} =$

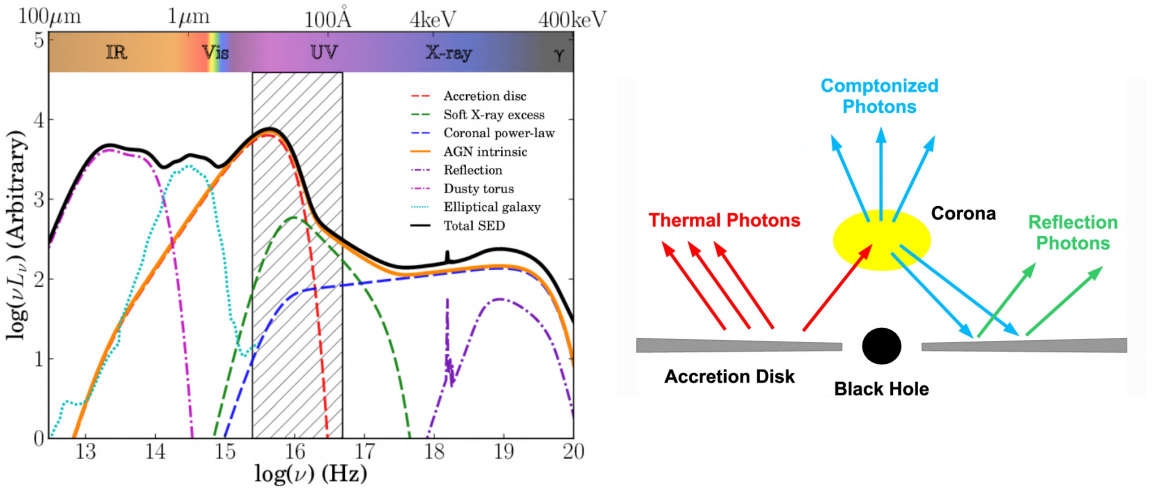

Figure 1.5: (Gauche) Diagramme simplifié de la distribution spectrale d'énergie d'un AGN. Adapté à partir de Collinson et al. (2017). (Droite) Dessin schématique de la géométrie d'accrétion dans le modèle disque-couronne. Reproduction de Bambi (2021).

$\frac{-\log(L_{2\mathrm{keV}}/L_{2500})}{2.605}$ (Bianchi et al., 2022). Pour la grande majorité des AGN, le rapport entre le flux de rayons X et le flux visible est donc compris dans une gamme étroite, 0.1–10 (Stocke et al., 1991; Lin et al., 2012), bien qu'il soit parfois significativement contaminé par la lumière des étoiles du bulbe.

De même, la transition entre les états spectraux varie avec la masse du trou noir. Les échelles de temps de transition des XRB sont de l'ordre du jour, contre plusieurs milliers d'années pour les AGN. Cependant, comme les XRB, les AGN sont parfois accompagnés de vents puissants de matière ionisée, ou de jets, ce qui ajoute à leur complexité spectrale et temporelle. Dans de nombreux AGN, une grande variabilité (facteur $\sim$ 10) peut ainsi être observée sur des échelles de temps de l'ordre de l'année, en raison de changements dans le taux d'accrétion, les colonnes d'absorption et/ou les éjections de matière (MacLeod et al., 2010; Soldi et al., 2014; Kozłowski et al., 2016; Yang et al., 2016). Les AGN pendant des épisodes d'accrétion exceptionnels ou vus sous un angle d'observation spécifique (comme les blazars) peuvent être encore plus variables sur des échelles de temps plus courtes. En particulier, une classe rare d'AGN dit *changing-look*, présentant une variabilité spectaculaire en dureté et en luminosité, a été découverte (e.g. Matt et al. 2003) et fait encore l'objet de nombreuses recherches (e.g.LaMassa et al. 2015).

La limite d'Eddington et l'état ultralumineux

Le rayonnement total libéré par un trou noir en accrétion évolue avec le taux d'accrétion, $L = \eta \dot{m} c^2$ où η est l'efficacité radiative, comprise entre 0.057 (trou noir de Schwarzschild) et 0.42 (trou noir de Kerr) (e.g. Shapiro 2005). Dans un système sphérique accrétant de l'hydrogène en équilibre hydrostatique, $\dot{m}$ est limité par les forces répulsives radiatives résultant de la matière rayonnante dans le disque, de sorte que la luminosité doit être inférieure à la limite d'Eddington : $L < L_{Edd} = 4\pi G M_{BH} m_p c/\sigma_T$, où G est la constante gravitationnelle, M_{BH} la masse du trou noir, m_p la masse du proton, c la vitesse de la lumière dans le vide et σ_T la section efficace de diffusion Thomson (Eddington, 1916). En remplaçant ces constantes par leurs valeurs, on obtient

$$L_{Edd} \approx 1.26 \times 10^{38} \left(\frac{M_{BH}}{M_\odot} \right) \text{ erg s}^{-1}$$

La luminosité observée peut cependant être augmentée en présence d'une focalisation du rayonnement, ce qui peut conduire à des luminosités apparentes super-Eddington pour des lignes de visée spécifiques : $L_b = L_{iso}/b$ (Wiktorowicz et al., 2017) où $b = 1 - cos(\theta/2)$ est le facteur de focalisation (θ étant l'angle à la base du faisceau).

Comme il est de plus en plus clair que les sources X ultralumineuses (ULX, $L_X > 10^{39}$ erg s^{-1}, section 1.2.2) observées dans les galaxies proches sont de masse stellaire (King, 2004; Stobbart et al., 2006) et présentent des spectres inhabituels avec un excès mou et une courbure spectrale autour de 5-10 keV, un autre état spectral a été postulé, l'état *ultralumineux*. (Roberts, 2007; Gladstone et al., 2009). Il est caractéristique de l'accrétion super-Eddington, et implique un durcissement modéré (en dessous de à $\sim$ 10 keV) de la source au-delà de ce seuil de luminosité. Il a été affirmé qu'une focalisation du rayonnement pourrait expliquer la luminosité des ULXs, mais ce scénario ne peut pas expliquer la présence de cavités autour de certaines d'entre elles, ou de "bulles des ULXs" (Section 1.2.2), qui suggèrent que les accréteurs des ULXs ont injecté une énergie significative dans leur environnement.

1.2 Signatures observationnelles des trous noirs

1.2.1 Binaires X

Dans les XRBs, un objet compact (étoile à neutrons ou trou noir) et une étoile forment une binaire proche, et des rayons X sont émis près de l'objet compact par l'accrétion et le chauffage de la matière de son compagnon. La matière disponible pour l'accrétion est fournie par l'étoile compagnon, soit par le vent stellaire (accrétion de Bondi-Hoyle, Bondi and Hoyle 1944; Bondi 1952), soit par le débordement de matière du lobe de Roche de l'étoile (surface équipotentielle au-dessous de laquelle la matière est liée à l'étoile par sa gravité) et forme un disque d'accrétion (e.g. van den Heuvel and De Loore 1973). Les binaires X à trou noir ou à étoile à neutrons peuvent être divisées en deux classes : les binaires X de faible masse (LMXB) et les binaires X de forte masse (HMXB), dans lesquelles le compagnon stellaire est respectivement $< 1M_\odot$ et $> 10M_\odot$ (la classe rare des binaires X de masse intermédiaire $1M_\odot < M < 10M_\odot$ complète cette nomenclature). Les HMXBs ont une durée de vie courte en raison de la courte durée de vie du donneur massif, elles se situent donc généralement loin du bulbe et près du plan galactique, où une formation d'étoile récente a eu lieu. Les LMXBs sont plus nombreuses, et se trouvent préférentiellement dans les amas globulaires et près du centre galactique (Grimm et al., 2002; Repetto et al., 2017). Les étoiles de faible masse présentes dans les LMXBs produisent peu de vent et l'accrétion se fait donc par débordement du lobe de Roche dans un disque d'accrétion. Dans les HMXB, le transfert de masse par débordement du lobe de Roche étant instable lorsque le rapport de masse de la binaire est important, l'accrétion est généralement assurée par les vents stellaires (voir par exemple Iben and Livio 1993; Nelemans et al. 2000 ; voir aussi Pavlovskii et al. 2017 où ce point est discuté).

La formation des XRBs a lieu tout au long de l'évolution d'une galaxie et suit plusieurs scénarios examinés dans Tauris and van den Heuvel (2006). Lorsqu'une étoile massive termine sa vie et subit une supernova, l'objet compact nouvellement formé a un élan natal et est éjecté de sa position initiale. Si l'étoile est dans une binaire, d'après la théorie de l'évolution stellaire, c'est toujours l'étoile la plus massive qui évolue en premier pour devenir un objet compact. Cependant, comme la majeure partie de sa masse est perdue au cours du processus, l'objet compact résultant peut être moins massif que son compagnon, formant ainsi une binaire X de forte masse. On pense que les binaires X de faible masse se forment à partir de binaires larges, de sorte que l'étoile compagnon n'est pas éjectée pendant l'explosion. Ceci est particulièrement vrai dans le cas des LMXBs à étoile à neutrons, car la fraction de masse éjectée lors de la formation d'une étoile à neutrons est plus élevée que pour les trous noirs. Autrement, dans un environnement dense, une étoile peut être capturée par l'objet compact nouvellement formé et former une binaire X. Une grande population de LMXBs est ainsi observée dans les amas globulaires, suggérant la présence de nombreuses étoiles à neutrons mais aussi de quelques trous noirs de masse stellaire (par exemple Kulkarni et al. 1993; Jonker et al. 2021).

Si différents types de XRB sont trouvés à différents endroits de la Voie lactée (Fabbiano, 2006), la même tendance se retrouve aussi dans les galaxies proches, avec une dominance de LMXB (resp. HMXB) dans les galaxies ayant un taux de formation d'étoiles spécifique faible (resp. élevé). Une observable bien connue pour caractériser les populations de XRBs dans leur ensemble est la fonction de luminosité des rayons X (XLF) : elle varie avec la fonction de masse initiale, les processus radiatifs et les durées de vie de la population, de sorte que les modèles de synthèse de population X doivent reproduire ces XLF pour être auto-consistants. De telles simulations (par exemple, Belczynski et al. 2004; Fragos et al. 2013) sont d'un intérêt majeur car elles permettent de sonder l'influence des paramètres individuels des galaxies sur l'ensemble de la population des XRBs. En particulier, on

constate que les XRBs peuvent contribuer de manière significative à la luminosité X des galaxies, même en présence d'un AGN central, et que la XLF évolue significativement avec le redshift (Tremmel et al., 2013). Les XLF observées montrent que les XRB couvrent une large gamme de luminosités, typiquement dans la gamme 10^{35-40} erg s^{-1}, avec les HMXBs généralement plus lumineuses que les LMXBs (Kim and Fabbiano, 2004; Fabbiano, 2006; Mineo et al., 2012). Une cassure est observée autour de 4×10^{38} erg s^{-1} dans la XLF des LMXBs, tandis qu'une autre cassure pourrait être présente dans la XLF des HMXBs, à $1 - 2 \times 10^{40}$ erg s^{-1} (Swartz et al., 2011; Mineo et al., 2012), mais reste à confirmer (Wang et al., 2016). Ce point est discuté dans le chapitre 5.

1.2.2 Sources X ultralumineuses

Dans les premiers relevés en rayons X des galaxies proches, des sources d'une luminosité extrême ont été trouvées en dehors du noyau de leur hôte, ce qui exclut leur interprétation comme étant des AGN. On a d'abord pensé que ces sources X ultralumineuses (ULX), dont la luminosité en rayons X était supérieure à 10^{39} erg/s, étaient de bons candidats IMBH, en se basant sur la limite d'Eddington (section 1.1.3) pour expliquer cette luminosité (e.g. Colbert and Mushotzky 1999; Liu and Bregman 2005). Cependant, on a rapidement découvert que leurs états spectraux ne ressemblaient pas à ce qu'on attendait d'une simple mise à l'échelle des XRB à trou noir de masse stellaire, comme on pourrait s'y attendre dans ce scénario. Dans les spectres d'ULX, la température interne du disque est plus froide que celle que l'on trouve habituellement dans les binaires X à trou noir ($kT = 0.1 - 0.3$ keV), tandis que la loi de puissance est plus raide ($\Gamma = 2 - 4.5$) et coupée à des énergies beaucoup plus basses ($2 - 7$ keV comparé à $\gtrsim 60$ keV dans les XRBs à trou noir). L'absorption est intermédiaire, avec des densités de colonne généralement comprises entre 1 et 3 fois 10^{21} cm^{-2}. De plus, une courbure spectrale a été trouvée dans les rayons X durs, incompatible avec une loi de puissance, laissant supposer un régime d'accrétion différent des binaires X (Bachetti et al. 2013), l'état *ultralumineux* (Gladstone et al. 2009; Kaaret et al. 2017 ; Section 1.1.3). On pensait alors que la plupart des ULX étaient des trous noirs de masse stellaire (par exemple, Sutton et al. 2013).

La découverte de pulsations en rayons X durs dans la courbe de lumière des ULXs (par exemple Bachetti et al. 2014; Fürst et al. 2016; Israel et al. 2017; Carpano et al. 2018; Quintin et al. 2021) a définitivement confirmé que l'accrétion était alimentée par un objet compact de masse stellaire, révélant que certaines de ces sources étaient même des étoiles à neutrons ($< 3M_{\odot}$) accrétant bien au-delà de la limite d'Eddington. Aujourd'hui, la fraction d'ULX abritant des étoiles à neutrons est mal connue (Gúrpide et al., 2021), bien que certains affirment qu'elle pourrait bien représenter la majorité d'entre eux (e.g. Koliopanos et al., 2017). Les ULXs à étoile à neutrons confirmées seraient les ULX les plus dures, avec un rayonnement dur très variable (Gúrpide et al., 2021). Certaines ULXs sont également variables à l'échelle de quelques kilosecondes (dans une seule observation), ce qui suggère la présence de vents, de jets ou de pulsations (par exemple Sutton et al. 2013; Koliopanos et al. 2019).

De plus, les ULX sont susceptibles de provoquer une rétroaction importante sur leur environnement, avec des signatures visible et radio d'une "bulle" les entourant, gonflée par des vents puissants et une photo-ionisation intense (e.g. Abolmasov et al. 2008; Berghea et al. 2020; Gúrpide et al. 2022). Ceci semble incompatible avec un faisceau étroit d'émission de rayons X qui pourrait expliquer une super-luminosité d'Eddington (Pakull and Mirioni, 2002; Berghea et al., 2010). Par conséquent, l'étude de ces objets est cruciale pour comprendre comment un objet peut dépasser cette limite, et parvenir à une meilleure compréhension de la croissance des premiers quasars pour lesquels l'accrétion super-Eddington est un scénario (Section 2.5).

Malgré les preuves que les ULXs possèdent des accréteurs de masse stellaire super-Eddington, le mécanisme qui sous-tend les luminosités super-Eddington est encore mal défini. Pour donner un bref aperçu, la modélisation des vingt dernières années suggère différents scénarios possibles, tels que l'émission anisotrope (par faisceau) (e.g. King 2009; Wiktorowicz et al. 2019), les disques d'accrétion supercritiques autour des trous noirs de masse stellaire avec des vents alimentés par le rayonnement (e.g. Poutanen et al. 2007; Middleton et al. 2015) ou autour des étoiles à neutrons (e.g. Erkut et al. 2019; Kuranov et al. 2020), le transfert de masse à l'échelle de temps thermique – en particulier à partir d'une étoile secondaire brûlant de l'hélium (e.g. Wiktorowicz et al. 2015; Pavlovskii et al. 2017), des écoulements d'accrétion autour d'étoiles à neutrons pulsantes fortement magnétisées (e.g. Bachetti et al. 2014; Mushtukov et al. 2015; Israel et al. 2017; Mushtukov et al. 2017) et l'accrétion de vent stellaire grumeleux renforcée par ionisation des rayons X (Krticka et al., 2022).

L'étude de nombreux échantillons d'ULXs a permis de dresser un aperçu statistique de la population des ULXs. Les ULXs sont plus fréquents dans les galaxies de type tardif et en cours de formation d'étoiles. Leur fréquence augmente avec la masse de la galaxie et leur fonction de luminosité peut être expliquée comme une simple extension en loi de puissance de la fonction de luminosité des binaires à rayons X, pour laquelle une cassure est notée à quelques 10^{38} erg/s dans les galaxies de type précoce (e.g. Kim and Fabbiano 2004, Wang et al. 2016). Une cassure ou une coupure à $1-2\times10^{40}$ erg/s peut également être présente (Swartz et al., 2011; Mineo et al., 2012) dans la XLF des galaxies de type tardif, cependant cela reste encore controversé (Wang et al., 2016). De plus, aucune cassure n'est systématiquement observée dans la fonction de luminosité de ces galaxies à la luminosité d'Eddington d'une étoile à neutrons de masse maximale ($L_{Edd}\sim2\times10^{38}$ erg s^{-1}) ou d'un trou noir stellaire de masse maximale ($L_{Edd}\sim10^{41}$ erg s^{-1} pour un trou noir de $10^2M_\odot$), comme on pourrait s'y attendre si la luminosité d'Eddington était une limite ferme (Fabbiano, 2006; Kaaret et al., 2017).

Cependant, une limitation importante des études d'ULXs est la présence d'une fraction significative de contaminants dans les grands échantillons, de l'ordre de 20% (e.g. Walton et al. 2011). Cela limite la fiabilité des informations qu'ils peuvent fournir, qui incluent, entre autres, une meilleure compréhension de l'accrétion super-Eddington (e.g. Sutton et al. 2013), de la fraction d'ULXs alimentée par des étoiles à neutrons (e. Gúrpide et al. 2021), des modèles évolutifs des binaires X (e.g. Erkut et al. 2019), et du rôle joué par les ULXs dans l'évolution des galaxies et du cosmos (e.g. Scott Barrows et al. 2022).

1.2.3 Sources X hyperlumineuses

Les HLXs, plus lumineuses ($L_X>10^{41}$ erg/s) et beaucoup plus rares, pourraient encore rester d'excellents candidats pour la recherche de IMBH.

En effet, l'un des HLXs les mieux étudiés, ESO-243-49 HLX-1 (Farrell et al., 2009) présente de très bonnes raisons d'être un IMBH. Situé à la périphérie de la galaxie lenticulaire ESO 243-49 (Figure 1.6), sa luminosité en rayons X atteint 10^{42} erg s^{-1} dans la bande 0.3–10 keV. Même avec une accrétion super-Eddington, il semble peu probable qu'une telle luminosité soit atteinte par un objet compact de masse stellaire, et les arguments d'échelle d'Eddington (détaillés dans la section 2.3.3 ainsi que d'autres estimations de masse) suggèrent une masse supérieure à $500M_\odot$. Contrairement aux ULXs, le spectre de cette source devient plus mou lorsque sa luminosité augmente, comme on le voit dans les binaires X à trou noir de notre galaxie (Godet et al., 2009; Servillat et al., 2011). La modélisation spectrale suggère une masse de l'ordre de $3000-3\times10^5M_\odot$ (Davis et al., 2011; Godet et al., 2012), ce qui la place très probablement dans la gamme de masse des IMBH. Cette estimation de masse a ensuite été affinée à $9000-9\times10^4M_\odot$ en utilisant le plan fondamental d'activité des trous noirs, grâce à la détection d'une émission radio (Webb et al., 2012). La courbe de lumière de HLX-1 est unique en son genre (Figure 1.6, panneau de droite), montrant des sursauts répétés séparés par des périodes de plus en plus longues sur près de deux décennies. Pour expliquer ce comportement, il a été proposé que le trou noir de l'ESO 243–49 HLX–1 est alimenté par des épisodes de transfert de masse induits par la dislocation partielle – ou événement partiel de rupture par effet de marée (TDE, Section 1.2.4) – d'une étoile de type naine blanche lors de son passage au périastre (Godet et al., 2014). Ce trou noir pourrait faire partie d'un amas stellaire ou être le trou noir central d'une galaxie naine en interaction avec ESO 243–49 (Webb et al., 2010, 2017; Farrell et al., 2012).

Un autre candidat IMBH fiable a été trouvé dans un amas d'étoiles excentré, après avoir subi un TDE (Section 1.2.4) qui a également atteint des luminosités hyperluminiques (Lin et al., 2018). D'autres candidats HLX ont été découverts ces dernières années, par exemple NGC 470 HLX-1 (Sutton et al., 2012) et NGC 2276-3c dans les galaxies spirales NGC 470 et NGC 2276. Contrairement à celles décrites précédemment, leur émission maximale n'est pas particulièrement molle, et on les voit atteindre des luminosités HLX de manière répétée mais apériodique. Une puissante émission radio a été trouvée dans NGC 2276-3c, de sorte que sa masse a été estimée à $\sim5\times10^4M_\odot$ à partir du plan fondamental (Mezcua et al., 2015).

Dans un travail récent, Barrows et al. (2019) a constitué un large échantillon de 169 candidats HLX grâce à la bonne résolution et à la haute sensibilité de deux relevés, à savoir *Chandra* et le relevé de galaxies SDSS. Bien que cette étude soit la première à permettre une vision statistique de la population HLX, la plupart de leurs candidats se trouvent dans des galaxies généralement plus lointaines ($D>1000$ Mpc) et ont des luminosités X élevées ($L_{2\text{–}10\text{ keV}}>10^{42}$ erg s^{-1}), ce qui les

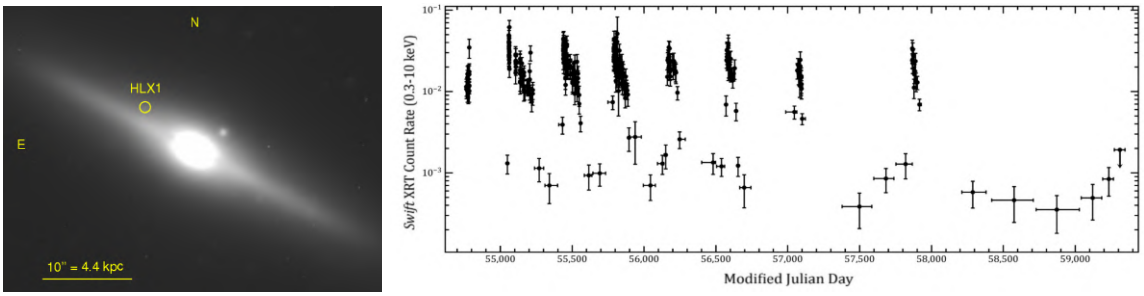

Figure 1.6: La source X hyperlumineuse ESO 243-49 HLX-1. (Gauche) Image en lumière visible (observatoire *Magellan*/IMACS, bande R) de ESO 243-49, avec la position de la source de rayons X entourée en vert. Reproduction de Soria et al. (2010). (Droite) Courbe de lumière dans la bande d'énergie 0.3–10 keV de la source pendant son suivi. Adaptation de Webb et al. (2017).

rend difficiles à comparer avec les HLXs précédemment mentionnés. Néanmoins, il est proposé qu'une fraction importante de cet échantillon pourrait être des trous noirs de masse intermédiaire en accrétion au centre d'une galaxie naine, qui subit une fusion avec la galaxie identifiée dans SDSS (Barrows et al., 2019).

Cependant, il est intéressant de noter que certains ULXs ont été observés avec une luminosité en rayons X supérieure à 10^{41} erg s^{-1} pendant une période transitoire, même lorsqu'ils sont alimentés par une étoile à neutrons (e.g. Israel et al. 2017). De même, il pourrait exister un état d'accrétion inconnu de luminosité encore plus élevée que l'état ultralumineux, ce qui permettrait d'observer des accréteurs de masse stellaire sous forme de HLX. De plus, la sélection des candidats HLX basée uniquement sur leur luminosité apparente en rayons X devrait produire des échantillons avec une grande fraction de contaminants (par exemple, 70 % de ces candidats HLX pourraient être des AGN d'arrière-plan, Zolotukhin et al. 2016), ce qui est également confirmé par certains anciens candidats maintenant connus pour être des contaminants à partir de leur mesure de redshift (e.g. Sutton et al. 2015). L'interprétation des HLXs en tant qu'IMBH doit donc encore être approfondie.

1.2.4 Événements de rupture par effet de marée

Les événements de rupture par effet de marée (*tidal disruption events* ou TDEs) sont des sursauts lumineux provoqués lorsque les forces de marée d'un trou noir dépassent l'énergie de liaison d'une étoile proche, provoquant sa dislocation et la chute d'une partie de la matière sur le trou noir, le reste se détachant du système (Rees, 1988). Leur courbe de lumière peut être utilisée pour contraindre la masse du trou noir (Section 2.3.3, Mockler et al. 2019), qui se trouve généralement dans la gamme $10^6 - 10^8 M_\odot$, mais avec des preuves récentes de détections dans la gamme de masse des IMBHs (Lin et al., 2018; Saxton et al., 2021).

Avec l'avènement de l'astronomie résolue en temps annonçant un suivi régulier du ciel transitoire dans les prochaines années (e.g. avec l'Observatoire Vera C. Rubin dans le domaine visible ou eROSITA dans les rayons X), les trous noirs dormants pourraient bientôt être observés en bien plus grand nombre grâce à des épisodes d'accrétion exceptionnels. Ces observatoires conduiront notamment à la détection de milliers de nouveaux TDEs, ce qui nous permettra d'identifier des trous noirs non détectés auparavant (e.g. van Velzen 2018; Bricman and Gomboc 2020). Étant donné que les TDEs doivent se produire à l'extérieur de l'horizon des événements pour être détectés, l'extrémité de faible masse des TNS ($M < 10^8 M_\odot$) sera sondée. Actuellement, une centaine de TDE ont été détectés en rayons X, en lumière visible et en ondes radio (Auchettl et al., 2017).

1.2.5 Noyaux actifs de galaxies

En 1963, des années avant que l'existence des trous noirs de masse stellaire ne soit confirmée, un type plus massif de trous noirs a été découvert pour la première fois à partir d'observations radio : 3C 273 et 3C 48, deux sources radio coïncidant avec des sources visibles ponctuelles (Hazard et al., 1963; Smith and Hoffleit, 1961), présentaient des raies de l'hydrogène décalées vers le rouge dans leurs spectres visibles, ce qui a permis de les situer à plusieurs centaines de mégaparsecs (Greenstein, 1963; Greenstein and Schmidt, 1964). Leur variabilité sur des échelles de temps aussi courtes qu'un jour a limité la

taille de l'émetteur à l'échelle du parsec. Ces résultats ont réfuté leur nature présumée d'étoile et les ont identifiées comme des émetteurs compacts extrêmement lumineux et distants. Salpeter (1964) a proposé que l'écoulement de matière sur un objet compact massif ($> 10^8 M_\odot$) pouvait expliquer ce comportement. Plus tard, Wolfe and Burbidge 1970 et Burbidge (1970) ont expliqué la grande dispersion de vitesse trouvée au centre des galaxies elliptiques par la présence d'un trou noir massif. Cette théorie est devenue consensuelle après la découverte d'une émission *maser* très lumineuse et de raies d'émission Kα du fer dans M106 et MCG-6-30-15 (Makishima et al., 1994; Tanaka et al., 1995), uniquement compatibles avec des trous noirs supermassifs. Depuis, les preuves indirectes de la présence de TNS au centre de toutes les galaxies massives sont omniprésentes (e.g. (Kormendy and Ho, 2013)), l'une des plus récentes étant fournie par l'imagerie haute résolution avec le télescope Event Horizon ayant détecté l'ombre du TNS au centre de M87 (Event Horizon Telescope Collaboration et al., 2019).

Les trous noirs supermassifs sont donc historiquement définis comme les trous noirs que l'on trouve dans les noyaux de galaxies (appelés dès lors noyaux actifs de galaxie ou AGN lorsqu'ils sont en accrétion, section 1.1.3), dans la gamme $10^6 - 10^{10} M_\odot$ (Kormendy and Richstone, 1995; Ferrarese and Ford, 2005). Cependant, jusqu'à récemment, les preuves de leur présence dans les galaxies de masse inférieure étaient rares. Les deux premières galaxies naines (de masse stellaire $M_* < 3 \times 10^9 M_\odot$, Section 2.4.3) dans lesquelles des trous noirs massifs ont été découverts furent NGC 4395 et Pox 52 (Filippenko and Sargent, 1989; Kunth et al., 1987) (Section 2.5). Des recherches récentes dans les galaxies naines ont augmenté cet échantillon et conduit à l'élargissement de l'intervalle de masse définissant les TNSs à $10^5 - 10^{10} M_\odot$ (e.g. Reines et al. 2013; Moran et al. 2014).

Les AGN émettent sur l'ensemble du spectre électromagnétique (section 1.1.3) et ont des luminosités bolométriques allant de 10^{38} erg/s à 10^{48} erg s^{-1} (Ho, 2008; Padovani et al., 2017). Les AGN dont la luminosité en rayons X est comprise entre 10^{38} et 10^{42} erg s^{-1} constituent la majeure partie de la population des AGN mais sont plus difficiles à détecter que les plus lumineux, et donc moins bien étudiés : ils sont regroupés sous le nom de "AGN de faible luminosité" ou LLAGN (e.g. Asmus et al. 2011).

Les AGN sont maintenant considérés comme une phase par laquelle passent tous les trous noirs supermassifs avant de retomber en quiescence, phase participant à leur évolution via plusieurs cycles d'activité d'une durée typique de 10^{7-8} ans (e.g. Merloni and Heinz 2013). Leur luminosité extrême en fait probablement les sources persistantes les plus lointaines observables depuis la Terre : les AGN sont détectés à tous les redshifts depuis l'époque de la réionisation ($z > 6$, moins de 1 Gyr après le Big Bang, section 2.4.1). Certains des plus lointains ont des masses supérieures à $10^9 M_\odot$ (e.g. Fan et al. 2006; Mortlock et al. 2011; Wang et al. 2021), ce qui rend leur formation extrêmement rapide et difficile à expliquer (Section 2.5).

1.3 Astronomie en rayons X

Afin de reconnaître les trous noirs dans le ciel en rayons X, il est d'abord nécessaire de connaître les caractéristique de chaque type de source de rayons X et leur distribution approximative. Des études préliminaires ne comportant que quelques centaines de sources ont permis une classification manuelle de la plupart d'entre elles, menant à la conclusion qu'elles étaient essentiellement constituées d'AGN et d'étoiles. Dans ce qui suit, nous donnons un bref aperçu des principaux types de sources de rayons X et de leurs principales caractéristiques, par ordre croissant de rareté, tandis qu'une description plus complète sera fournie au chapitre 4. Depuis l'avènement des observatoires X à haute résolution, les sources peuvent être commodément séparées en deux catégories, les sources ponctuelles (ce qui signifie que l'étendue de la source ne peut être résolue étant donnée la PSF de l'instrument) et les sources étendues, la première catégorie étant le sujet principal de cette thèse étant donné son contenu.

Les AGN (Sections 2.1.3, 2.2.5) constituent le type dominant parmi les sources ponctuelles de rayons X : émettant des rayons X en raison de l'accrétion sur le trou noir supermassif d'une galaxie massive, ils peuvent atteindre des luminosités énormes (jusqu'à $\sim 10^{46}$ erg/s). Cela les rend détectables même à grande distance, de sorte qu'ils représentent le plus grand volume cosmique sondé en rayons X, et la plus grande fraction des sources de rayons X (environ 60%, Lin et al. 2012; Stocke et al. 1991). Comme nous l'avons déjà mentionné, ils peuvent présenter une certaine gamme de rapports entre le flux de rayons X et le flux visible (la plupart du temps entre 0.1 et 10, Section 2.1.3), de variabilité

(mais sur des échelles de temps plus longues que les trous noirs plus petits des binaires X) et de formes spectrales.

En revanche, les étoiles ne sont visibles que dans les régions très locales de notre Galaxie. Les étoiles de notre Galaxie font partie des sources de lumière visible les plus brillantes du ciel. Certaines d'entre elles sont également de puissants émetteurs de rayons X mous, notamment à faible masse les étoiles de type G, K et M ($L_X \lesssim 10^{27}$erg/s) en raison de la très haute température de leur couronne (liée à l'activité chromosphérique magnétisée). Les étoiles les plus massives (types A, B, O) de la séquence principale présentent en général une puissante émission de rayons X (maximum pour les étoiles de type O : $L_X \sim 10^{32-34}$ erg/s, plus faible pour les types B et A, $L_X \sim 10^{27-31}$erg/s pour le type A), qui serait due à des chocs hydrodynamiques dans les vents stellaires d'origine radiative ou magnétique (Rauw et al., 2015). Dans l'ensemble, cependant, les rayons X ne représentent qu'une petite fraction de leur luminosité, la principale composante étant l'émission de corps noir du plasma dans les couches stellaires externes. Par conséquent, le rapport entre le flux de rayons X et le flux visible (resp. infrarouge), qui est généralement inférieur à 0.01 (0.03), est traditionnellement un critère de sélection dans les études de rayons X. Ceci ne concerne pas les jeunes objets stellaires (*young stellar object* ou YSO), affectés par une absorption importante dans le domaine visible. Certaines étoiles variables présentent une grande variabilité à court terme dans les rayons X, notamment sous forme d'éruptions. En raison de leur faible luminosité, la plupart des étoiles détectées en rayons X sont situées dans un rayon de 1 kpc autour du système solaire.

Les sources ponctuelles plus rares comprennent les binaires, notamment les binaires X et les variables cataclysmiques (binaires compactes contenant une naine blanche comme objet compact et une étoile de faible masse ou une autre naine blanche comme compagnon). Les premières peuvent être observées dans la Voie lactée ou dans des galaxies proches, en raison de leur luminosité de 10^{34-40} erg s^{-1}, tandis que les variables cataclysmiques ne sont visibles que dans notre Galaxie $L_X < 10^{34}$ erg s^{-1}. Les binaires X et les variables cataclysmiques peuvent présenter des signatures très diverses en rayons X, notamment en termes de spectre et de courbe de lumière. Leur caractérisation est abordée plus en détail dans le chapitre 4. De rares sources transitoires de rayons X complètent la liste des types de sources ponctuelles de rayons X, notamment les supernovae et les contreparties de sursauts gamma. Les supernovae sont produites lorsqu'une étoile a consommé tout son combustible thermonucléaire et s'effondre, formant parfois un objet compact (section 1.1.2). Les sursauts gamma sont des explosions extrêmement énergétiques qui proviendraient de l'effondrement gravitationnel du cœur de certaines étoiles très massives ($> 20\,M_\odot$, produisant une hypernova) et de la fusion d'étoiles à neutrons (Levan et al., 2016). Ces événements sont rares (quelques-uns par galaxie et par million d'années, Podsiadlowski et al. 2004) et l'émission de rayons gamma est suivie d'une rémanence à plusieurs longueurs d'onde (des rayons X aux ondes radio) également décroissante dans le temps mais visible sur des échelles de temps plus longues (de quelques minutes à quelques semaines, mois, voire années). Les novae à rayons X sont causées par la chute soudaine de gaz sur une étoile à neutrons ou un trou noir, ce qui se produit parfois dans des systèmes binaires sans accrétion (comme les LMXB quiescentes), provoquant l'émission retardée de sursauts dans les rayons X durs, les rayons X mous et d'autres longueurs d'onde (Tanaka and Shibazaki, 1996; Chen et al., 1997).

Parmi les sources étendues de rayons X, la population dominante est constituée d'amas de galaxies (e.g. Krautter et al. 1999). Les rayons X sont produits par l'émission thermique et Bremmstrahlung du plasma chaud ($> 10^7$K) qui compose le milieu intra-amas (Section 1.1.3). Les restes de supernova représentent le principal autre type de source étendue, les rayons X étant principalement dus à leur gaz chaud et parfois au rayonnement synchotron émis après l'interaction des électrons avec le champ magnétique d'une étoile à neutrons centrale. Parmi les autres objets étendus, citons enfin les nébuleuses planétaires de notre Galaxie, le contenu en gaz chaud de certaines galaxies proches, et l'interaction des rayons cosmiques avec le gaz moléculaire de notre Galaxie (en particulier dans sa région centrale).

Enfin, une compréhension plus approfondie des sources de rayons X ne peut être obtenue que sur la base de chaque instrument, en raison d'un certain nombre de phénomènes conduisant à des détections de rayons X parasites qui imitent la présence d'une source astrophysique. Le prochain chapitre traitera de l'instrumentation et du traitement des données des trois principaux observatoires modernes de rayons X qui ont observé le ciel au cours des deux dernières décennies, ainsi que des catalogues d'environ 1 million de sources qui en sont issus.

1.4 Rationale

Contrairement aux couleurs visibles et infrarouges qui sont largement utilisées pour sélectionner les AGN, mais qui peuvent manquer un grand nombre de trous noirs dans des environnements spécifiques tels que les galaxies naines, l'émission de rayons X est une caractéristique bien connue des systèmes accrétants. C'est pourquoi ils sont idéaux pour observer les trous noirs sur toute leur échelle de masse, des trous noirs de masse stellaire accrétant dans les XRBs aux trous noirs supermassifs accrétant dans les AGN. Si les rayons X sont incapables de détecter les trous noirs dormants ou en faible accrétion (sauf lorsqu'ils subissent un TDE, qui est également une bonne sonde), cela est également vrai pour les autres longueurs d'onde dans la plupart des cas. En sondant les sources X hyperlumineuses, une grande fraction des TDEs et de nombreux trous noirs dans les galaxies naines, les rayons X offrent ainsi une opportunité unique de sonder la population des IMBH dans diverses conditions.

En outre, la combinaison des rayons X avec d'autres longueurs d'onde est particulièrement puissante pour identifier les sources : cela a permis d'établir des règles empiriques faciles pour classer les sources de rayons X en général (par exemple Lin et al. 2012), ce qui est très précieux pour de nombreuses applications. Par exemple, dans les galaxies proches, les binaires X et l'AGN central sont observés dans les rayons X, mais aussi les étoiles d'avant-plan et l'AGN d'arrière-plan recouvrant la galaxie étudiée. Notamment, envion 20 % des ULXs répertoriés dans les catalogues récents seraient en fait des AGN d'arrière-plan. Des progrès considérables ont été réalisés grâce aux données multi-longueurs d'onde, notamment pour séparer les sources X ultralumineuses et hyperlumineuses valides de ces contaminants (Barrows et al., 2019; Bernadich et al., 2021). La systématisation de cette approche représenterait une grande avancée dans la science des ULXs, en multipliant la taille de l'échantillon des ULXs robustes et en permettant des études de population plus précises de ces objets mal compris.

Une autre application d'une telle classification serait de séparer les sources galactiques des sources extragalactiques, incluant respectivement les XRB et les AGN, ce qui serait utile, par exemple, pour contraindre la fonction de masse des trous noirs. En plus de ces deux types de sources, d'autres sources locales émettent des rayons X de manière ponctuelle : il s'agit d'étoiles massives qui émettent des vents forts chauffant leur environnement, d'étoiles de faible masse fortement magnétisées qui possèdent une couronne chaude, et de variables cataclysmiques. Identifier correctement toutes ces sources serait précieux pour mieux étudier les types de sources correspondants. L'histoire de l'astronomie en rayons X étant pavée de découvertes fortuites, les objets d'intérêt particulier et les sources exotiques représentent également des *trésors* à identifier. Avec le développement récent de l'astronomie en rayons X (particulièrement au cours des 20 dernières années), plus d'un million de sources ponctuelles sont présentes dans les archives, avec une sensibilité et une résolution spatiale sans précédent, attendant d'être étudiées.

Dans cette thèse, l'objectif principal sera donc d'identifier plus de candidats IMBH et d'apporter de nouvelles contraintes sur leur population. Afin de rassembler un large échantillon et d'obtenir les contraintes les plus strictes, j'adopte une approche d'exploration de données reposant sur une classification de sources polyvalente et puissante appliquée aux plus grandes archives de rayons X actuelles. Dans les sections précédentes, j'ai donné une vue d'ensemble des différents types de sources qui composent le ciel des rayons X. Dans le chapitre 3, je décris les observatoires en rayons X et les catalogues de sources de rayons X étudiés. Dans le chapitre 4, le développement d'une classification automatique des sources de rayons X est détaillé. Les résultats de cette classification sur des catalogues entiers sont décrits dans ce même chapitre, ainsi qu'un certain nombre d'applications scientifiques. Le chapitre 5 se concentre sur l'application de cette classification à la science des ULX et HLX, avec un accent particulier sur les nouveaux candidats IMBH. Dans le chapitre 6, la classification est appliquée aux sources de rayons X dans les galaxies naines, donnant un autre échantillon de candidats IMBH. Le chapitre 7 contient la discussion et les implications de mes résultats. Je conclus et donne quelques perspectives de cette étude dans le chapitre 8.

Chapter 2

Scientific context

Black holes were first introduced as mathematical solutions of Einstein's equations in the 1910s (Einstein, 1915). Fifty years later, the first compelling evidence for the existence of black holes was found in X-rays, with the discovery of the X-ray binary Cygnus X-1 (Bolton, 1972). The last five decades have been the golden age of the science of black holes, in many ways: observations of dozens of different black hole signatures, diversification of the theoretical and observed black hole zoo, extensive phenomenology of their interaction with the surrounding objects and media, detailed modelling of their formation and evolution... However, the detection of black holes as massive as $10^9 M_\odot$ less than a billion years after the Big Bang (e.g. Wang et al. 2021) has led to questions concerning our understanding of black hole formation, forcing the astrophysics community to postulate extremely fast formation mechanisms in which some elusive black holes might have played an important role: the intermediate mass black holes. In this Chapter, I summarise the milestones of the science of black holes from an observers perspective, and I show how the search for and understanding of intermediate-mass black holes is essential to our understanding of the formation and evolution of supermassive black holes.

2.1 Theoretical considerations

2.1.1 Theory of black holes

A review of black hole theory from the standpoint of theoretical physics is beyond the scope of this thesis. Nonetheless, the concept of black holes is supported by the general relativity (GR) theory (Einstein, 1915)[1]. Einstein field equations describe how the geometry of space and time is modified by the presence of matter, due to its mass and energy content. A few months after the publication of the GR pioneering paper, Karl Schwarzschild published a solution to the Einstein equation for a point mass M, pointing out a singularity appearing at the so-called Schwarzschild radius $R_S = 2GM/c^2$ (Schwarzschild, 1916). For years, there was no physical consensus about the physical meaning of this singularity. It was later shown that it disappeared with a change of coordinate system, whereas a physical singularity is actually present at a smaller radius: for a Schwarzschild non-rotating black

[1]The origin of the concept of black holes can be dated back to the eighteenth century, when the English pastor John Michell and the French mathematician Pierre Simon de Laplace postulated the existence of *non luminous bodies* or *dark stars*, having a mass such that their escape velocity exceeds the speed of light. Almost two centuries later, in 1968, the term "black hole" was coined by John Wheeler and became most popular.

hole, the singularity is a point at the black hole center, while for the maximally spinning Kerr black holes, it is a ring (Visser, 2007).

For an external observer, however, the Schwarzschild radius of a non-rotating black hole acts as an event horizon: no particle or light contained inside this surface is able to escape, because of spacetime curvature. This black hole solution of Einstein equations led to the theory of black holes. In the framework of the classical gravitation theory, this is analogous to saying that the escape speed of this object exceeds the speed of light. Theoretically, any amount of matter like a planet or a star would become a black hole if compressed below its Schwarzschild radius. As such, black holes are part of the broader class of compact objects, which have a radius R such that $R_S/R > 10^{-4}$ and around which GR effects are significant. Another theoretical finding from GR is that *"black holes have no hair"*, following the comment of John Wheeler, meaning that isolated black holes are entirely described by just three parameters: their electric charge, their mass and their spin.

In stellar physics, compact objects represent the endpoint of stellar evolution. After its birth from the collapse of a dense molecular cloud, a star has its matter progressively transformed by nuclear fusion. When its nuclear fuel becomes insufficient to continue fusion, the core of the object collapses under gravity, leaving a remnant which depends on the initial mass of the star: either a white dwarf (Anderson, 1929; Chandrasekhar, 1931), a neutron star (Landau, 1932; Baade and Zwicky, 1934) or a black hole (Schwarzschild, 1916; Oppenheimer and Snyder, 1939). While the pressure due to gravity of white dwarfs and neutron stars is opposed by electron and neutron degeneracy pressures respectively, no evidence for a repulsive force stabilising black holes is known. The theoretical mass range for white dwarfs, neutron stars and black holes is $M < M_{Ch}$, $M_{Ch} < M < M_{TOV}$ and $M > M_{TOV}$, where $M_{Ch} \simeq 1.4 M_\odot$ is the Chandrasekhar mass limit on a stable white dwarf (Chandrasekhar, 1931) and $M_{TOV} \in [1.6, 3.1] M_\odot$ is the Tolman-Oppenheimer-Volkoff (TOV) limit on a cold, non-rotating neutron star (Tolman, 1939; Oppenheimer and Volkoff, 1939). Recently, observational studies have refined the latter limit thanks to the detection of massive pulsars (e.g. Cromartie et al. 2020; Riley et al. 2021 for the $\sim 2.1 M_\odot$ millisecond pulsar J0740+6620).

2.1.2 The mass ranges of black holes

As we will see in the following sections, black holes are observed in a wide range of masses. In this Section, we simply mention the different theoretical and observational mass ranges and mass gaps of black holes, as a first overview of their population.

Stellar-mass black holes

Stellar-mass black holes are the end product of the evolution of massive stars. Figure 2.1 shows the mass of the stellar progenitor of neutron stars and black holes. Stars less massive than $140 M_\odot$ can form black holes with masses up to $\sim 65 M_\odot$ (Heger et al., 2003). In the range $140 - 260 M_\odot$, a metal-poor star (where metals refer to elements heavier than He and Li) ends its life in a pair-instability supernova, leaving no remnant. Only the metal-free, very massive stars (so-called Population III stars and present in the early stages the Universe, Section 2.4.1) can form black holes above $100 M_\odot$ (Madau and Rees, 2001; Ohkubo et al., 2009). The formation of this class of black holes is discussed later. Other formation channels exist for stellar-mass black holes, such as the fallback supernova occuring after material is supplied to a neutron star (Heger et al., 2003), making it overcome the TOV limit, or the coalescence of two neutron stars.

Stellar-mass black holes are only detected in the Milky Way and nearby galaxies, mostly when they are in a binary system with a star. These systems are called X-ray binaries (XRB), named after their discovery and characterisation in X-rays (Bolton, 1972), providing some of the first evidence for the existence of black holes.

Intermediate-mass black holes

Intermediate-mass black holes (IMBH) are in the mass range $10^2 - 10^5 M_\odot$. The formation mechanisms of these black holes are still uncertain, but traditionally discussed possibilities see them as the remnants of massive population III stars (e.g. Madau and Rees 2001), the result of runaway gravitational mergers in dense stellar clusters (e.g. Portegies Zwart and McMillan 2002), or the end product of the direct collapse of a large cloud of low-metallicity, low-angular-momentum gas (e.g. Loeb and Rasio 1994). These possibilities (Mezcua 2017, Section 2.5.1) could already be in place a

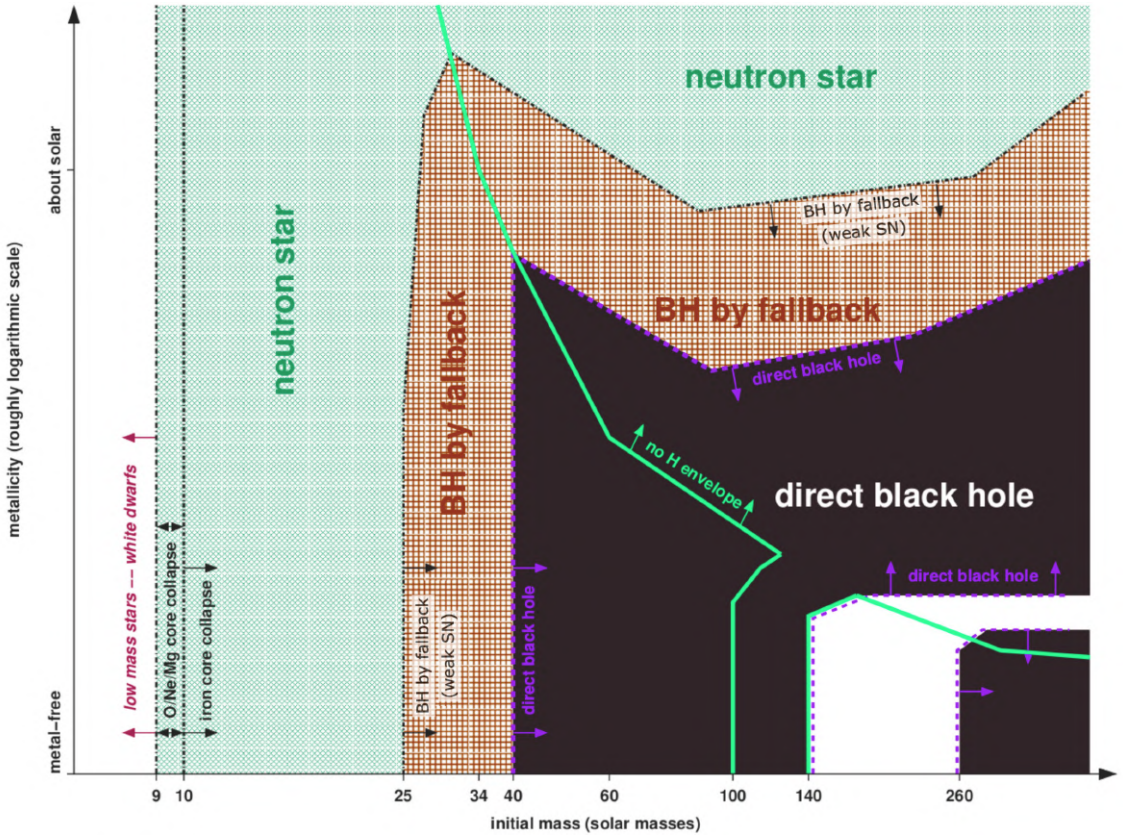

Figure 2.1: Mass-Metallicity diagram showing the formation channels reachable by neutron stars and black holes formed from the collapse of massive single stars, as a function of their metallicity and initial main-sequence mass. Reproduced from Heger et al. (2003).

few hundred million years after the Big Bang. Over several billions of years, IMBHs could also form through accretion onto a stellar mass black hole, mergers of such black holes, or a combination of both processes.

To date, the observational evidence for the existence of these black holes has been scarce, but it seems to have increased recently with observatories able to detect them at larger distances and lower fluxes (Section 2.5.2).

Supermassive black holes

Supermassive black holes (SMBH, $10^5 - 10^{10} M_\odot$, Section 2.2.5) are found at the center of most (if not all) massive galaxies. Their formation is a matter of intense debate (Section 2.5), which is the main driver of the search for and study of IMBHs.

Primordial black holes

Primordial black holes (PBHs) are predicted to be a possible result of the collapse of density fluctuations in the primordial Universe, just after the Big Bang, following specific inflationary scenarios (Carr and Kühnel, 2020). Their initial mass should depend linearly on their formation time, so they can cover an extremely wide mass range $10^{-10} - 10^{7} M_\odot$. If abundant, these mostly isolated black holes should leave detectable footprints in the present-day Universe. However, to date, observational tests for a variety of PBH mass, relying e.g. on microlensing of stars (Griest et al., 2014) or the cosmic microwave and X-ray backgrounds (Poulin et al., 2017; Ballesteros et al., 2020) or accretion signatures have only led to upper limits on their abundance.

The black hole mass function

A fundamental observable to represent the abundance of black holes of each mass is the black hole mass spectrum, or black hole mass function (BHMF). Its study as a function of redshift is a powerful

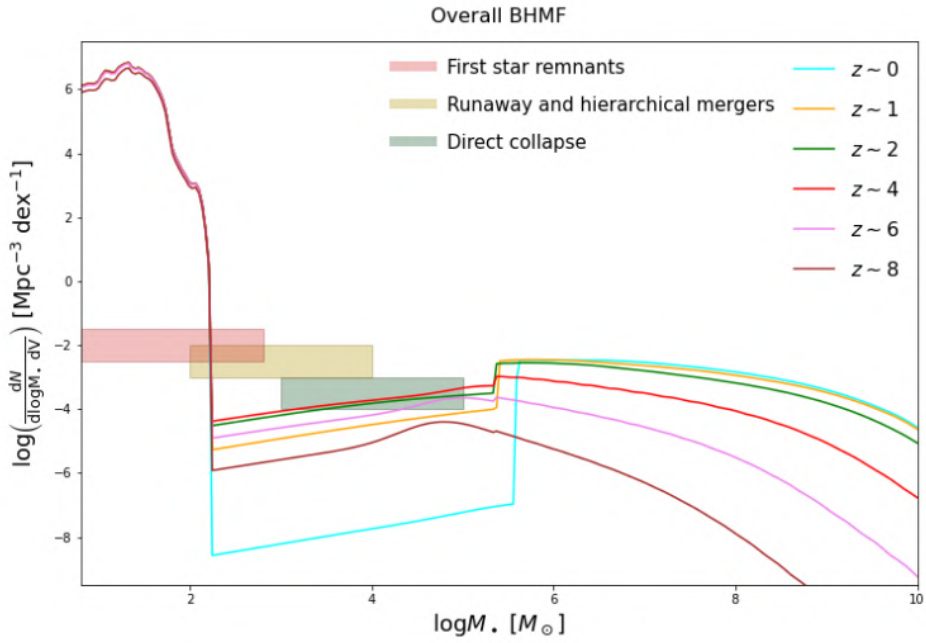

Figure 2.2: Black hole mass function model of Sicilia et al. (2022). Reproduced from Sicilia et al. (2022).

tool for constraining, for example, theoretical models of supermassive black hole formation, or their feedback in their galaxy. At the low mass end, the BHMF is populated by abundant stellar mass black holes (Section 2.2.1), remnants of stellar evolution. At the massive end, it probes the population of SMBH at the center of massive galaxies. As an illustration, we show in Figure 2.2 an example of a BHMF from the recent semi-empirical work of Sicilia et al. (2022). The pair-instability mass gap is barely visible (it only manifests itself as a steep decline in the BHMF at $\log M_*/M_\odot \sim 1.8$), being populated by black holes formed in disrupted binaries, in particular binaries ending in a common-envelope phase collapsing into a massive stellar-mass black hole (van Son et al., 2020; Sicilia et al., 2022).

Note that this reconstruction may be inaccurate, especially in the IMBH range where their model does not include any of the best studied IMBH growth mechanisms (overlaid in the diagram). As we will see later, black holes of different masses have different locations and luminosities, so that the detected black hole samples are strongly biased towards the nearest and most massive ones. This detection bias must be corrected in order to estimate the BHMF from observations. However, qualitatively, we see that unlike stellar and supermassive black holes, IMBHs in the local Universe ($z = 0$) are indeed elusive.

2.1.3 Theory of accretion

Because a black hole emits no light (except the Hawking radiation Hawking 1974, beyond the detection limits of current instruments), their observational signatures are indirect and largely depend on their environment. Notably, accretion plays an important role in their detectability and accreting systems constitute most of the black holes that we have detected. These well-studied accreting black holes are primarily the stellar-mass black hole X-ray binaries (XRB, Section 2.2.1) and the supermassive active galactic nuclei (AGN, Section 2.2.5).

Accretion is the process of matter falling towards a central object, due to the gravitational potential of this object and by viscous dissipation of the kinetic energy of the matter. If the falling material has angular momentum, it will orbit the central object and viscous processes will lead to the formation of an accretion disc. The gravitational potential energy of each particle of matter is converted into thermal energy through viscous processes, allowing it to lose angular momentum and fall towards the central compact object. The closer the material is to the central object, the hotter it becomes, causing

it to emit thermal (Planck) radiation of short wavelength, following Planck's law

$$\nu F_\nu \propto \frac{\nu^3}{1-\exp(h\nu/k_B T)}$$

where ν is the radiation frequency, F_ν the spectral flux density at this frequency, h the Planck constant, k_B the Boltzmann constant and T the temperature of the material. However, thermal radiation is not the only process responsible for X-ray emission.

Radiation processes

In addition to thermal radiation, four non-thermal radiation mechanisms dominate in the X-rays.

- In a high-temperature plasma (in particular a so-called collisionally ionised plasma), atoms and ions can be excited (photo-ionised) and de-excited to high energy levels, causing the emission and absorption of X-ray spectral lines (e.g. Wilms et al., 2000).
- Charged massive particles in such a plasma also produce an electric field which interacts with the particles, causing them to decelerate and emit photons. This radiation is called "braking radiation" or Bremsstrahlung. For heavy ions deflecting electrons in a dense plasma (such as the intracluster medium, Section 2.6), Bremsstrahlung emission is in the X-ray domain (Cavaliere and Fusco-Femiano, 1976; Klein, 1999).
- In the presence of a strong magnetic field, charged particles spiral around magnetic field lines, and this acceleration leads to the emission of the so-called synchrotron radiation, sometimes in the X-rays (Jones et al., 1974).
- Frequent in the X-ray domain is the *inverse Compton scattering* or Compton up-scattering. It refers to the increase in energy of a low-energy photon penetrating a medium, when it is scattered by a hot electron (Sunyaev and Titarchuk, 1980).

X-rays are often conveniently distinguished as "soft X-rays" (low-energy, $0.1 \lesssim h_\nu \lesssim 3$ keV) and "hard X-rays" (high-energy $h_\nu \gtrsim 1$ keV)[2]. The ratio (or relative difference) between two X-ray bands is then called the hardness.

Accretion states

The simplest picture of an accretion disc is a disc of matter with a temperature, T, decreasing with radius, r, ($T(r) \propto r^{-3/4}$ in a steady-state, thin accretion disc model, Shakura and Sunyaev 1973). The thermal radiation of such an object is described spectrally by a multicolour blackbody model (hereafter `diskbb`), composed of the addition of the blackbody (Planck) spectrum of each annulus of matter. In practice, however, each annulus of matter has a different thickness and density, the disc is truncated at a certain radius, and it may be embedded in large scale magnetic field, so that a wide variety of accretion disc spectral models exists.

The thermal emission of the accretion disc can be blocked by an optically thick environment around the disc, the corona, which gives rise to inverse Compton scattering of this emission. Another emission component is thus observed, in the hard X-rays, in the form of a power-law spectrum (`powerlaw`) (Titarchuk and Lyubarskij, 1995):

$$F_{\nu,\texttt{powerlaw}} \propto \nu^{-\alpha} \propto \nu^{-\Gamma+1}$$

where ν is the radiation frequency, F_ν is the spectral flux density, α is the spectral index and $\Gamma = \alpha + 1$ is the photon index. The photon (or spectral) index of this model is a means of measuring the hardness of a source's emission, thus constraining its nature. Most AGN (Section 2.2.5) are well-fitted by an absorbed powerlaw with photon indices in a narrow range $\Gamma = 1.7 - 2$ (e.g. Middleton et al. 2008).

An absorption model is also needed to reproduce X-ray spectra. Indeed, X-rays emitted by the source cross several environments to reach the observer, in particular the environment of the source and the Milky Way interstellar medium (ISM). Soft X-rays can photoionise the atoms they encounter, and an accurate modeling of absorption is obtained by summing the cross-sections of these interactions

[2]Historically, the empirical distinction between soft and hard X-rays may have been motivated by their ability to injure the human skin, or conversely to penetrate it (Russ, 1915). However, this distinction is not well defined and, depending on the context, hard X-rays can also refer to photons with an energy of $\gtrsim$20 keV.

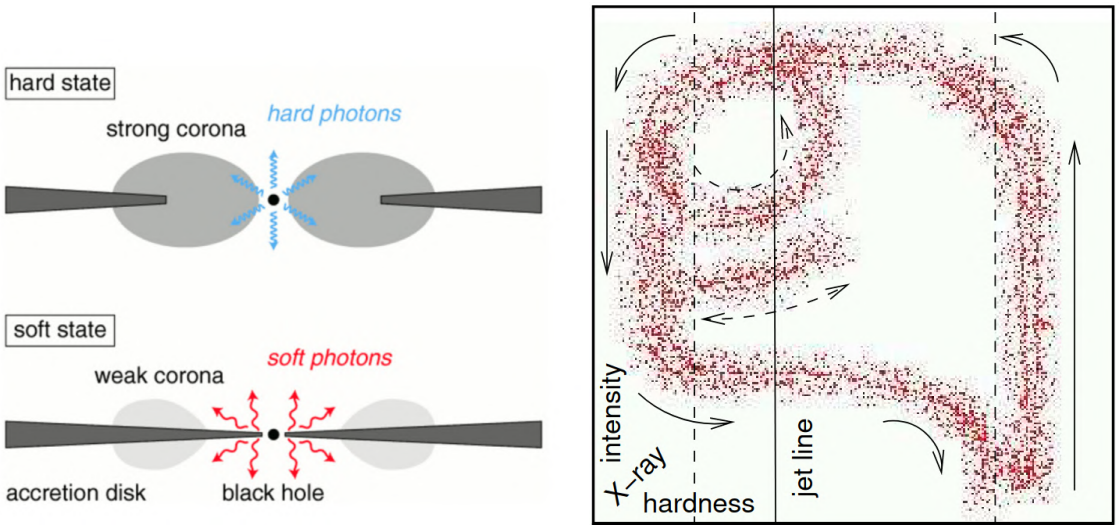

Figure 2.3: (Left) Cartoon of the truncated disc model, with the geometry corresponding to the low/hard (top) and high/soft (bottom) states. Reproduced from Liu and Taam (2009) (Right) Schematic representation of the hardness-intensity diagram (HID) of black hole XRBs (or "q-shape" diagram). Reproduced from Fender et al. (2004).

for each medium (typically, neutral atomic gas, molecules, and dust grains Wilms et al., 2000). The total cross-section is simplified as the cross-section of an effective amount of hydrogen present along the line of sight, the hydrogen column density n_H, expressed in cm^{-2}. The values of n_H for the Milky Way ISM were mapped by different collaborations (e.g. HI4PI Collaboration et al. 2016), and are of the order of 3×10^{20} cm^{-2} for lines of sight above and below the Galactic plane. X-ray emitters embedded in dense or dusty environments, such as at the center of nearby galaxies, can have much higher hydrogen columns, of typically $10^{22} - 10^{23}$ cm^{-2} (e.g. Risaliti et al. 2002).

In practice, however, the spectrum of an accretion system can dramatically change over time, in particular in low-mass systems such as XRBs (Section 2.2.1). Early spectral studies in X-ray and radio wavelengths showed that black hole XRBs follow canonical spectral states, generally called high/soft (when the thermal disc emission dominates) and low/hard (the comptonised emission dominates), with sometimes transitional states being seen. To account for this spectral evolution, the "truncated disc" (or "disc evaporation") model has been developed based on the theory of accretion of Shakura and Sunyaev (1973) (e.g. Meyer et al. 2000). It is illustrated in the left panel of Figure 2.3. During quiescence (low/hard state, where the black hole accretes at very low rates and the binary emits non-thermal hard X-rays), matter accumulates in the disc until, in a certain region, the density and temperature have increased to such an extent that the hydrogen becomes ionized. This increases the viscosity of the matter in the disc, leading it to fall inwards and being accreted. The inner disc radius at that moment is the innermost stable circular orbit (ISCO) of the black hole ($R_{in} = 6R_S$ for a Schwarzschild black hole, with R_S the Schwarzschild radius, and $R_{in} = R_S$ or $R_{in} = 9R_S$ for a Kerr black hole rotating in the prograde or retrograde direction relative to the disk, respectively, Bardeen et al. 1972). This state allows maximum accretion rate and the thermal radiation of the hot inner disc dominates (high/soft state). When the disc is emptied, it becomes quiescent again. High/soft and low/hard states can be separated by a factor > 1000 in luminosity.

Nevertheless, accretion is also often connected with ejection mechanisms, with strong evidence of relativistic jets in both AGN and XRBs (Mirabel and Rodríguez, 1999; Netzer, 2015). Radio (synchrotron) emission from a jet is often seen in the hard state. Besides, the evolutionary path between states shows a hysteresis in the hardness-intensity diagram (HID), which is sometimes called a "q-shape" diagram (Figure 2.3, right panel). To explain this hysteresis, Fender et al. (2004) therefore revisited the truncated disc model and proposed the following scenario: the binary in "quiescence" (lower right of the HID) begins to accrete more material, causing the source to brighten and a steady radio jet to appear (or brighten). The jet is accelerated as the accretion disk collapses to inner radii, until it reaches a shock-induced limit (the "jet line" in Figure 2.3) where it becomes unstable and transient. The source remains in the high soft state for some time before fading and gradually returning to quiescence, losing its corona and accretion material and potentially recovering a jet

(Fender et al., 2004).

Although it has been widely used and has provided a great deal of physical information about the evolution of XRBs, this model is still under debate. Besides, the exact location and extent of the corona is largely uncertain, and is the subject of much research (e.g. Ursini et al. 2022). The very existence of a corona (Figure 2.3, left panel) to reproduce the hard state is still debated, and alternative models exist that do not require the assumption of two independent entities – for example, the JED-SAD model of Marcel et al. (2018) uses a hybrid disc configuration, where the inner (thick) disc is a hot magnetised flow (jet-emitting disc or JED) and the periphery is a standard non-magnetised thin disc (standard accretion disc, SAD), with a transition radius between these discs whose change cause the different accretion states.

However, a detailed understanding of the geometry and physical properties of the accretion flow is not essential to this thesis work, and this overview of the spectral states of accreting black holes and their physical explanation will be sufficient to allow initial interpretation.

Accretion in supermassive black holes

Important differences should be noted between the stellar-mass accreting black holes in XRBs and the supermassive black holes accreting in the center of massive galaxies.

Following the discovery of the first quasars, numerous studies found signatures of nuclear activity in massive galaxies of all morphologies. Such systems were dubbed after their very different observational signatures and include Radio-loud and Radio-quiet quasars, Seyfert 1, Seyfert 2 and Blazars. These objects were later qualified as "active galactic nuclei" (AGN) and unified in a common paradigm, where the hidden variable explaining this observational diversity is the viewing angle, as illustrated in Figure 2.4. In AGN, the central accreting system can launch a narrow jet, and is itself surrounded by a torus of dust and gas that prevents the direct emission of the central system from being seen along a certain line of sight (e.g. Padovani et al. 2017; Bianchi et al. 2022 for recent reviews). The gas takes the form of clouds located in the so-called "broad line region" and "narrow line region": these gas clouds are illuminated by the central engine, and absorb and re-emit this radiation. Spectral lines are thus emitted by each cloud, and the motion of the clouds in different directions involves by Doppler effect a broadening of the lines in the spectrum of the whole system. Gas clouds in the broad line region are the fastest and densest clouds near the black hole, while the narrow line region is located further away.

When a jet is launched and is in the line of sight, the observer sees a Blazar. At lower angles, the source luminosity decreases and broad and narrow lines become visible in the spectrum: the object is then classified as a radio-loud quasar. Starting to see the system edge-on, the powerful central emission becomes hidden, but radio jets are still detected, hence the name of radio galaxy. For a radio-quiet AGN, a powerful emission is seen at all wavelengths but radio, with spectral lines in the optical-UV spectrum. Seyfert 2 are less luminous than Seyfert 1, and show only prominent narrow lines.

As an example, Figure 2.5 shows the spectral energy distribution (SED) of an AGN from mid-infrared to gamma frequencies (Collinson et al., 2017). Different spectral components are visible, notably the thermal emission of the accretion disc, the comptonised emission of the corona, a so-called soft excess, and a reflection component. The soft excess component is a specific feature of AGN, that still lacks a clear explanation and is outside the scope of this thesis work. The reflection component is produced by comptonised radiation reflected by the immediate surroundings of the AGN, and broadly consists of a bump in the hard part of the continuum with absorption and emission lines (Wilkins and Fabian, 2012). The dusty torus component is related to the outer region of an AGN and its viewing angle (Figure 2.4) and can be used to select samples of AGN from mid-infrared photometry (Section 2.3.2). As shown by this SED, the emission of an AGN is thus characterised by multiple components peaking at different wavelengths and corresponding to different regions around the black hole.

Figure 2.5 (right panel) illustrates an example of accretion geometry explaining the different components of an AGN spectrum (Bambi, 2021): soft X-ray photons originate from the thermal emission of the hot disc, and some are up-scattered to hard X-rays in the corona. These comptonised photons are then partly reflected by the disc, giving rise to the reflection component (Turner and Miller, 2009). The location and geometry of the corona in Figure 2.3 (left panel) differs from Figure 2.5 (right panel), but as discussed above, this is due to the existence of many corona models (regardless of black hole mass).

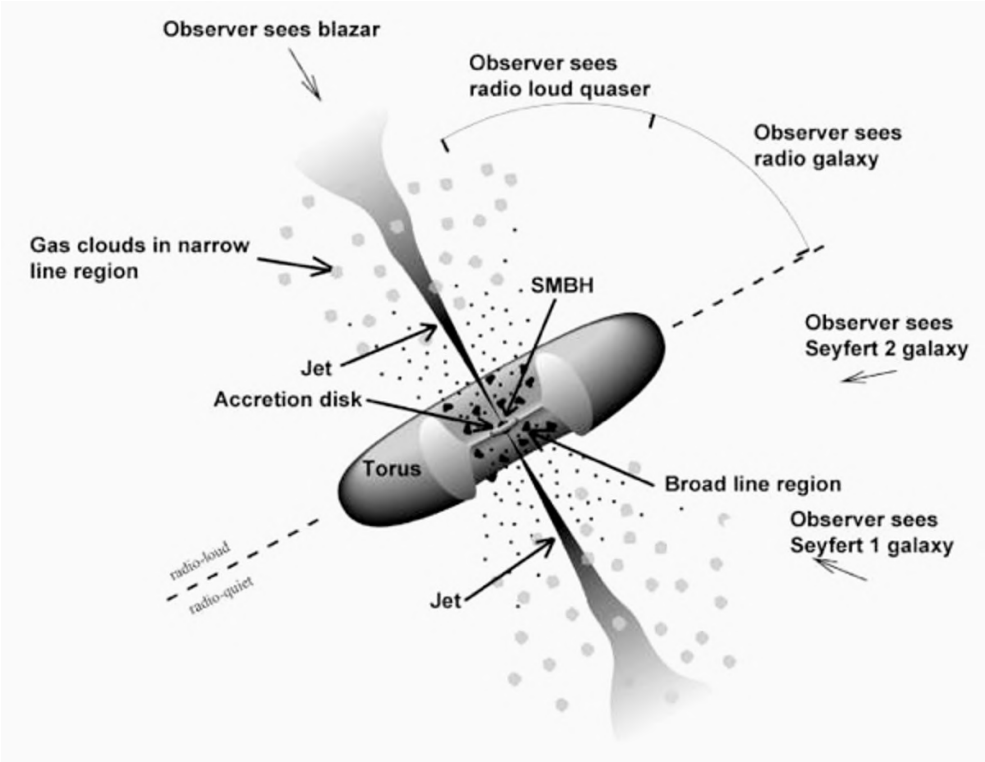

Figure 2.4: Schematic diagram of the unified model of AGN (credit: Fermi & NASA, https://fermi.gsfc.nasa.gov/science/eteu/agn/). The figure shows the different components of an AGN in this model, and the observational signatures they cause depending on the line of sight.

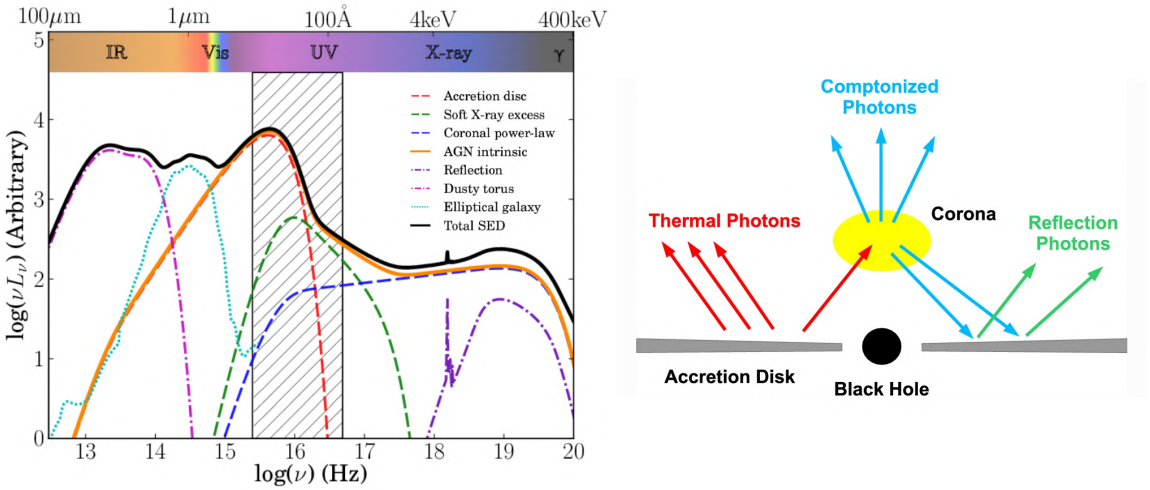

Figure 2.5: (Left) Simplified diagram of an AGN spectral energy distribution. Adapted from Collinson et al. (2017). (Right) Cartoon of the accretion geometry in the disc-corona model. Reproduced from Bambi (2021).

In addition to their differing geometry, another major spectral difference between black hole XRBs and AGN is the wavelength at which their thermal emission is peaked: indeed, the more massive (by several orders of magnitude) black holes in AGN have a larger innermost stable orbit, so that the accretion disc is colder. Its thermal radiation is thus peaked in the optical-UV (Figure 2.5, left panel). The X-ray spectral index α_{ox} is thus used to parametrise the luminosity ratio between the two components: $\alpha_{ox} = \frac{-\log(L_{2keV}/L_{2500})}{2.605}$ (Bianchi et al., 2022). For the vast majority of AGN, the X-ray to optical flux ratio is thus comprised in a narrow range, 0.1-10 (Stocke et al., 1991; Lin et al., 2012), although it is sometimes significantly contaminated by the light of bulge stars.

Likewise, the transition between spectral states scales with the mass of the black hole. XRB transition timescales are of the order of a day, translating into several thousand years for AGN. However, like XRBs, AGN are sometimes accompanied by powerful winds of ionised matter, or outflows, adding to their spectral and timing complexity. In many AGN, a large variability (factor ~ 10) can thus be seen on yearly timescales, due to changes in the accretion rate, absorption columns and/or outflows (MacLeod et al., 2010; Soldi et al., 2014; Kozłowski et al., 2016; Yang et al., 2016). AGN during exceptional accretion episodes or seen with a specific viewing angle (like blazars) can be even more variable on shorter timescales. In particular, a rare class of "changing-look" AGN showing more dramatic variability in both hardness and luminosity was discovered (e.g. Matt et al. 2003), and is still under investigation (e.g. LaMassa et al. 2015).

Eddington limit and the ultraluminous state

The total radiation released by an accreting black hole scales with the accretion rate, $L = \eta \dot{m} c^2$ where η is the radiative efficiency, comprised between 0.057 (Schwarzschild black hole) and 0.42 (Kerr black hole) (e.g. Shapiro 2005). In a spherical system accreting hydrogen under hydrostatic equilibrium, $\dot{m}$ is limited by the radiative repulsive forces resulting from radiating matter in the disc, so that the luminosity must be lower than the Eddington limit: $L < L_{Edd} = 4\pi G M_{BH} m_p c/\sigma_T$, where G is the gravitational constant, M_{BH} is the black hole mass, m_p the proton mass, c the speed of light in a vacuum and σ_T the Thomson scattering cross-section (Eddington, 1916). Replacing these constant by their values, we obtain

$$L_{Edd} \approx 1.26 \times 10^{38} \left(\frac{M_{BH}}{M_\odot} \right) \text{ erg s}^{-1}$$

The observed luminosity may be however boosted in the presence of beaming, potentially leading to seemingly super-Eddington luminosities for specific lines of sight: $L_b = L_{iso}/b$ (Wiktorowicz et al., 2017) where $b = 1 - cos(\theta/2)$ is the beaming factor (θ being the apex angle of the beam).

With growing evidence that ultraluminous X-ray sources (ULX, $L_X > 10^{39}$ erg s^{-1}, Section 2.2.2) seen in nearby galaxies are of stellar mass (King, 2004; Stobbart et al., 2006), showing unusual spectra with a soft excess and spectral curvature around 5-10 keV, another spectral state was postulated, the *ultraluminous state* (Roberts, 2007; Gladstone et al., 2009). It is characteristic of super-Eddington accretion, and implies a moderate (below ~ 10 keV) hardening of the source beyond this luminosity threshold. It has been claimed that beamed radiation could explain the luminosity of ULXs, but this scenario cannot explain the presence of cavities around some of them, or ULX "bubbles" (Section 2.2.2), which suggest that ULX accretors have injected significant energy into their surroundings.

2.2 Observational signatures of black holes

2.2.1 X-ray binaries

In XRBs, a compact object (neutron star or black hole) and a star form a close binary, and X-rays are emitted close to the compact object by the accretion and heating of matter from its companion. The matter available for accretion is supplied by the companion star, either through stellar wind (Bondi-Hoyle accretion, Bondi and Hoyle 1944; Bondi 1952) or by the star overflowing its Roche lobe (equipotential surface below which matter is bound to the star by its gravity) and forming an accretion disc (e.g. van den Heuvel and De Loore 1973). Black hole and neutron star X-ray binaries can be divided into two classes: low-mass X-ray binaries (LMXB) and high-mass X-ray binaries (HMXB), in which the stellar companion is respectively $< 1M_\odot$ and $> 10M_\odot$ (the rare class of intermediate-mass X-ray binaries $1M_\odot < M < 10M_\odot$ complete this nomenclature). HMXB are short-lived due to the short lifetime of the massive donor, so they generally lie away from the bulge and close to the Galactic plane, where recent star formation took place. LMXB are more numerous, and preferentially found in globular clusters and close to the galactic center (Grimm et al., 2002; Repetto et al., 2017). The low-mass stars present in LMXBs produce little wind and thus accretion takes place via Roche lobe overflow in an accretion disc. In HMXBs, because mass transfer by Roche lobe overflow is unstable when the binary has a large mass ratio, the accretion is generally driven by stellar winds (e.g. Iben and Livio 1993; Nelemans et al. 2000; however see Pavlovskii et al. 2017 where this point is discussed).

The formation of XRBs takes place throughout the evolution of a galaxy and follows several scenarios reviewed in Tauris and van den Heuvel (2006). As a massive star ends its life and undergoes a supernova, the newly formed compact object receives a natal kick and is ejected from its initial position. If the star is in a binary, from the theory of stellar evolution, it is always the most massive star that evolves first to become a compact object. However, because most of its mass is lost in the process, the resulting compact object can be less massive than its companion, hence forming a high-mass X-ray binary. Low-mass X-ray binaries are thought to form from wide binaries, so that the companion star is not ejected during the explosion. This is particularly true in the case of the neutron star LMXB, because the fraction of mass ejected during the formation of a neutron star is higher than for black holes. Alternatively, in a dense environment, a star can be captured by the newly formed compact object and form an X-ray binary. A large population of LMXB is thus seen in globular clusters, suggesting the presence of numerous neutron stars but also some stellar-mass black holes (e.g. Kulkarni et al. 1993; Jonker et al. 2021). X-ray binaries containing a black holes are generally called "black hole binaries" or BHB.

While different types of XRB are found in different locations of the Milky Way (Fabbiano, 2006), the same trend is found in nearby galaxies, with a dominance of LMXB (resp. HMXB) in galaxies with a low (resp. high) specific star-formation rates. A well-known observable to characterise XRB populations as a whole is the X-ray luminosity function: it scales with the initial mass function, radiative processes and lifetimes of the population, so that X-ray population synthesis models must reproduce these XLF to be self-consistent. Such simulations (e.g. Belczynski et al. 2004; Fragos et al. 2013) are of major interest since they allow to probe the influence of individual galaxy parameters on the whole XRB population. In particular, it is found that XRB can contribute significantly to the X-ray luminosity of galaxies, even in the presence of a central AGN, and that the XLF evolves significantly with redshift (Tremmel et al., 2013). Observed XLF show that XRB span a broad range of luminosities, typically in the range 10^{35-40} erg s^{-1}, with HMXB generally more luminous than LMXB (Kim and Fabbiano, 2004; Fabbiano, 2006; Mineo et al., 2012).

2.2.2 Beyond the limits: ultraluminous X-ray sources

In early X-ray surveys of nearby galaxies, sources of extreme luminosity were found outside the nucleus of their host, ruling out their interpretation as AGN. These so-called ultraluminous X-ray sources (ULXs) with X-ray luminosities $L_X > 10^{39}$ erg/s were first thought to be good IMBH candidates, based on the Eddington limit (Section 2.3.3), to account for this luminosity (e.g. Colbert and Mushotzky 1999; Liu and Bregman 2005). However, it was soon discovered that their spectral states did not resemble a scaled-up version of black hole XRB, as would be expected in this scenario. In ULX spectra, the inner temperature of the disc is cooler than usually found in black hole X-ray binaries ($kT = 0.1-0.3$ keV), while the powerlaw is steeper ($\Gamma = 2-4.5$) and cut off at much lower energies (2−7

keV compared to $\gtrsim 60$ keV in black hole XRB). The absorption is intermediate, with column densities generally in the range $1 - 3 \times 10^{21}$ cm^{-2}. Besides, a spectral curvature was found in hard X-rays, hinting at an accretion regime differing from X-ray binaries (Bachetti et al. 2013), the *ultraluminous state* (Gladstone et al. 2009; Kaaret et al. 2017; Section 2.1.3). Most ULXs were then believed to be stellar-mass black holes (e.g. Sutton et al. 2013).

The discovery of hard X-ray pulsations in the light curve of ULXs (e.g. Bachetti et al. 2014; Fürst et al. 2016; Israel et al. 2017; Carpano et al. 2018; Quintin et al. 2021) definitely confirmed that accretion was powered by a stellar-mass compact object, revealing that some of these sources were neutron stars ($< 3M_{\odot}$) accreting well above the Eddington limit. Today, the fraction of ULXs hosting neutron stars is poorly constrained (Gúrpide et al., 2021), although some claim that it may well represent the majority of them (e.g. Koliopanos et al., 2017). Confirmed neutron star ULXs were reported to be the hardest ULXs, with highly variable hard radiation (Gúrpide et al., 2021). Some ULXs are also variable on the timescale of a few kiloseconds (within a single observation), which suggests the presence of winds, outflows or pulsations (e.g Sutton et al. 2013; Koliopanos et al. 2019).

Moreover, ULXs are likely to cause important feedback on their environment, with optical and radio signatures of a "bubble" surrounding them, inflated by powerful winds and intense photo-ionisation (e.g. Abolmasov et al. 2008; Berghea et al. 2020; Gúrpide et al. 2022). This seems inconsistent with a narrow beaming of X-ray emission that could explain a super-Eddington luminosity (Pakull and Mirioni, 2002; Berghea et al., 2010). Therefore, the study of these objects is crucial to understand how an object can overcome this limit, and achieve a better understanding of the growth of the first quasars for which super-Eddington accretion is a scenario (Section 2.5).

Despite evidence for ULXs being super-Eddington stellar-mass accretors, the mechanism underlying the apparent super-Eddington luminosities is still poorly constrained. As a brief overview, modeling over the last twenty years suggests different possible scenarios such as anisotropic (beamed) emission (e.g. King 2009; Wiktorowicz et al. 2019), supercritical accretion discs around stellar-mass black holes with radiation-driven winds (e.g. Poutanen et al. 2007; Middleton et al. 2015) or around neutron stars (e.g. Erkut et al. 2019; Kuranov et al. 2020), thermal-timescale mass transfer - in particular from a Helium-burning secondary (e.g. Wiktorowicz et al. 2015; Pavlovskii et al. 2017), accretion flows around pulsating highly-magnetised neutron stars (e.g. Bachetti et al. 2014; Mushtukov et al. 2015; Israel et al. 2017; Mushtukov et al. 2017) and accretion of clumpy stellar wind enhanced by X-ray ionization (Krticka et al., 2022).

Studying ULX samples has led to a statistical picture of the ULX population. ULXs are more prominent in late-type, star-forming galaxies. Their frequency increases with galaxy mass and their luminosity function may be explained as a mere powerlaw extension of the X-ray binary luminosity function, for which a break is noted at a few 10^{38} erg/s in early-type galaxies (e.g. Kim and Fabbiano 2004, Wang et al. 2016). A break or cutoff at $1 - 2 \times 10^{40}$ erg/s may also be present (Swartz et al., 2011; Mineo et al., 2012) in the XLF of late-type galaxies, however this is still under debate (see Wang et al. 2016; this point will be discussed in Chapter 5). Moreover, no break is systematically observed in these galaxies at the Eddington luminosity of a maximum-mass neutron star ($L_{Edd} \sim 2 \times 10^{38}$ erg s^{-1}) or a maximum mass stellar black hole ($L_{Edd} \sim 10^{41}$ erg s^{-1} for a black hole of $10^2 M_{\odot}$), as would be expected if the Eddington luminosity was a hard limit (Fabbiano, 2006; Kaaret et al., 2017).

However, one important limitation in ULX studies is the presence of a significant fraction of contaminants in large ULX samples, of the order of 20% (e.g. Walton et al. 2011). This limits the reliability of the information they can provide, which includes, among other things, a better understanding of super-Eddington accretion (e.g. Sutton et al. 2013), the fraction ULXs being powered by neutron stars (e.g. Gúrpide et al. 2021), evolutionary models of X-ray binaries (e.g. Erkut et al. 2019), and the role played by ULXs in galaxy and cosmic evolution (e.g. Scott Barrows et al. 2022).

2.2.3 Hyperluminous X-ray sources

The more luminous and much rarer HLX ($L_X > 10^{41}$ erg/s) may still remain excellent candidates to look for IMBH.

Indeed, one of the best studied HLXs, ESO-243-49 HLX-1 (Farrell et al., 2009) shows very good evidence for being an IMBH. Located in the periphery of the lenticular galaxy ESO 243-49 (Figure 2.6), its X-ray luminosity reaches 10^{42} erg s^{-1} in the 0.3–10 keV band. Even with super-Eddington accretion, such a luminosity seems unlikely to be reached by a stellar-mass compact object, and

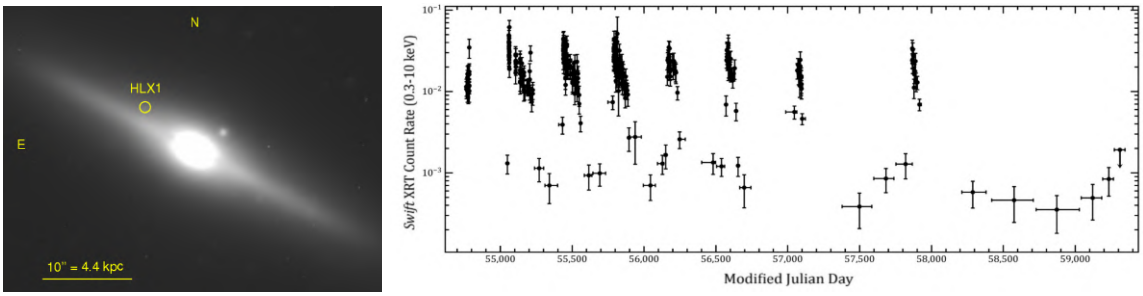

Figure 2.6: The hyperluminous X-ray source ESO 243-49 HLX-1. (Left) Optical (*Magellan*/IMACS *R*-band) image of ESO 243-49, with the position of the X-ray source circled in green. Reproduced from Soria et al. (2010). (Right) 0.3–10 keV light curve of the source during its follow-up. Adapted from Webb et al. (2017).

Eddington scaling arguments (as detailed in Section 2.3.3 along with other mass estimates) suggest a mass higher than $500 M_\odot$. Unlike ULXs, it shows signs of softening when its luminosity increases, as seen in galactic BHB (Godet et al., 2009; Servillat et al., 2011). Spectral modeling suggests a mass in the range $3000 - 3 \times 10^5 M_\odot$ (Davis et al., 2011; Godet et al., 2012), placing it most probably in the IMBH mass range. A second mass estimate was obtained using the fundamental plane of black hole activity (Section 2.3.3), $9000 - 9 \times 10^4 M_\odot$, thanks to the detection of radio emission (Webb et al., 2012) – however this method has been recently questioned in the case of intermediate-mass black holes (Gültekin et al., 2022). The light curve of HLX-1 is unique in the field (Figure 2.6, right panel), showing repeated outbursts separated by longer and longer periods of time over almost two decades. To explain this behaviour, the black hole in ESO 243–49 HLX–1 is thought to be fed by episodes of mass-transfer induced by repetitive partial stripping – or partial tidal disruption event (TDE, Section 2.2.4) – of a white dwarf-like star when passing at periapsis (Godet et al., 2014). This black hole may be embedded in a stellar cluster or be the central black hole in a dwarf galaxy stripped by or in interaction with ESO 243–49 (Webb et al., 2010, 2017; Farrell et al., 2012).

Another reliable IMBH candidate was found in an off-center star cluster, after undergoing a TDE (Section 2.2.4) that also reached hyperluminous luminosities (Lin et al., 2018). Other HLX candidates were found in recent years, for example NGC 470 HLX-1 (Sutton et al., 2012) and NGC 2276-3c in the spiral galaxies NGC 470 and NGC 2276. Unlike the ones previously described, their maximum emission is not particularly soft, and they are seen to reach repeatedly but not periodically HLX luminosities. A powerful radio emission was found in the latter, so that its mass was estimated to be $\sim 5 \times 10^4 M_\odot$ from the fundamental plane (Mezcua et al., 2015).

In a recent work, Barrows et al. (2019) put together a large sample of 169 HLX candidates thanks to the good resolution and high sensitivity of two surveys, namely *Chandra* and the SDSS galaxy catalogue. While this study is the first to allow a statistical view of the HLX population, most of their candidates are in relatively more distant galaxies ($D > 1000$ Mpc) and have high X-ray luminosities ($L_{2\text{–}10\ \mathrm{keV}} > 10^{42}$ erg s^{-1}), making them difficult to compare with the HLXs previously mentioned. Still, they find that an important fraction of them could be explained by an intermediate-mass black hole accreting at the center of a dwarf galaxy, which is undergoing a merger with the large SDSS galaxy.

However, it is worth noting that some ULXs were seen with an X-ray luminosity above 10^{41} erg s^{-1} for a transient period, even when powered by a neutron star (e.g. Israel et al. 2017). Likewise, there might be an unknown accretion state of even higher luminosity than the ultraluminous state, allowing stellar-mass accretors to be observed as HLXs. Moreover, the selection of HLX candidates based solely on their apparent X-ray luminosity is predicted to produce samples with a large fraction of contaminants (e.g. 70% of such HLX candidates may be background AGN, Zolotukhin et al. 2016), which is also confirmed by some former candidates now known to be contaminants from their redshift measurements (e.g. Sutton et al. 2015). Thus, the interpretation of HLXs as IMBHs still needs further investigation.

2.2.4 Tidal disruption events

Tidal disruption events (TDEs) are luminous bursts caused when tidal forces from a black hole exceed the binding energy of a nearby star, causing it to be disrupted and part of the matter to fall onto the black hole, with the rest becoming unbound from the system (Rees, 1988). Their light curve can be used to constrain the black hole mass (Section 2.3.3, Mockler et al. 2019), which is generally found to be in the range $10^6 - 10^8 M_\odot$, but with recent evidence for detections in the mass range of IMBHs (Lin et al., 2018; Saxton et al., 2021).

With the advent of time-domain astronomy announcing a regular monitoring of the transient sky in the next few years (e.g. with the Vera C. Rubin Observatory in the optical domain or eROSITA in the X-rays), dormant black holes may soon be observed in much larger numbers thanks to exceptional accretion episodes. In particular, these observatories will lead to the detection of thousands of new TDEs, allowing us to identify previously undetected black holes (e.g. van Velzen 2018; Bricman and Gomboc 2020). Because the TDE occurs at the tidal radius of the system, $R_t = (M_{BH}/M_{star})^{1/3} R_{star}$, it would be inside the Schwarzschild radius for a SMBH of mass $M_{BH} > 10^8 M_\odot$ disrupting a main-sequence star and its emission could not escape. Detected TDEs thus probe the low-mass end of SMBH ($M < 10^8 M_\odot$). Currently about a hundred TDEs were detected in the X-rays, optical and radio wavelengths (Auchettl et al., 2017).

2.2.5 Active galactic nuclei

In 1963, years before the existence of stellar-mass black holes was confirmed, the most massive type of black holes was discovered for the first time from radio observations: 3C 273 and 3C 48, two radio sources coincident with point-like optical sources (Hazard et al., 1963; Smith and Hoffleit, 1961), were found to show hydrogen redshifted lines in their optical spectra, locating them at several hundreds of megaparsecs (Greenstein, 1963; Greenstein and Schmidt, 1964). Their variability on timescales as short as a day constrained the size of the emitter below the parsec scale. These findings disproved their assumed stellar nature, and identified them as superluminous, distant compact emitters. Salpeter (1964) proposed that matter infalling on a massive ($> 10^8 M_\odot$) compact object would account for this behaviour. Later, Wolfe and Burbidge 1970 and Burbidge (1970) explained the large velocity dispersion found at the center of elliptical galaxies with the presence of a massive black hole. This theory became consensual after the discovery of very luminous maser emission and iron Kα emission lines in M106 and MCG-6-30-15 (Makishima et al., 1994; Tanaka et al., 1995), only consistent with supermassive black holes. Since then, indirect evidence for the presence of SMBHs at the center of all massive galaxies has been ubiquitous (e.g. Kormendy and Ho 2013), one of the most recent being provided by high-resolution imaging with the Event Horizon telescope by detecting the shadow of the SMBH at the center of M87 (Event Horizon Telescope Collaboration et al., 2019).

Supermassive black holes are thus historically defined as black holes found in galaxy nuclei (hence called active galactic nuclei or AGN when they are accreting, Section 2.1.3), in the range $10^6 - 10^{10} M_\odot$ (Kormendy and Richstone, 1995; Ferrarese and Ford, 2005). However, until recently, their evidence in lower mass galaxies has been scarce. The first two dwarf galaxies (with stellar mass $M_* < 3 \times 10^9 M_\odot$, Section 2.4.3) in which massive black holes were discovered were NGC 4395 and Pox 52 (Filippenko and Sargent, 1989; Kunth et al., 1987) (Section 2.5). Recent searches in dwarf galaxies have increased this sample and broadened the mass range defining SMBHs to $10^5 - 10^{10} M_\odot$ (e.g. Reines et al. 2013; Moran et al. 2014).

AGN emit over the entire electromagnetic spectrum (Section 2.1.3) and have bolometric luminosities ranging from 10^{38} erg/s to 10^{48} erg s^{-1} (Ho, 2008; Padovani et al., 2017). AGN whose X-ray luminosity is in the range $10^{38} - 10^{42}$ erg s^{-1} comprise the major part of the AGN population but are more difficult to detect than more luminous ones, and therefore less well studied: they are grouped under the name of "low luminosity AGN" or LLAGN (e.g. Asmus et al. 2011).

AGN are now considered as a phase through which all supermassive black holes pass before falling back into quiescence, phase participating in their evolution via several activity cycles of typical duration 10^{7-8} years (e.g. Merloni and Heinz 2013). Their enormous luminosity probably makes them the most distant persistent sources observable from Earth: AGN are detected at all redshifts since the reionisation epoch ($z > 6$, less than 1 Gyr after the Big Bang, Section 2.4.1). Some of the most distant ones have masses above $10^9 M_\odot$ (e.g. Fan et al. 2006; Mortlock et al. 2011; Wang et al. 2021), making their formation extremely rapid and challenging to explain (Section 2.5).

2.3 Finding black holes using electromagnetic signatures

The presence and the mass of a black hole can be assessed using a wide range of techniques which have different accuracies. The most reliable mass estimates, with uncertainties generally below 50%, are pulsar timing (Kızıltan et al., 2017), stellar dynamics (Kormendy, 2004) and broad Hα scaling (e.g. Chilingarian et al., 2018). Other potentially robust mass measurements are however highly model-dependant such as reverberation mapping (e.g. Negrete et al. 2013) and TDE light curve modeling (e.g. Guillochon and Ramirez-Ruiz 2013; Mockler et al. 2019). Techniques having higher uncertainties include the use of Eddington-scaling arguments, BH-galaxy scaling relations such as the $M_{BH} - \sigma_*$ (Figure 2.9), the fundamental plane of black hole activity (Figure 2.7, e.g. Plotkin et al. 2012), X-ray variability analysis (e.g. Nikolajuk et al. 2004; Kamizasa et al. 2012) and X-ray spectral analysis (e.g. (Vierdayanti et al., 2008; Davis et al., 2011; Gliozzi et al., 2021)). In the quest for intermediate-mass black holes, accurately measuring black hole masses is important, and these methods often come with large statistical or systematic uncertainties; a careful approach is then to combine several methods before concluding on the black hole mass (e.g. Koliopanos et al. 2017). We present here an overview of widely used methods to estimate black hole masses using electromagnetic signals.

2.3.1 Dynamical measurements

For the closest black holes, astrometric observations can help to constrain the orbital parameters of the system (e.g. Bolton 1972 for Cygnus X-1) even in absence of accretion. The most striking example is probably Sgr A* (Boehle et al., 2016), the supermassive black hole at the center of our own Galaxy, embedded in a cluster of stars whose orbits were used to constrain the mass of the central object very precisely ($4.154 \pm 0.014 M_\odot$, Gravity Collaboration et al. 2019). Microlensing recently proved efficient to find an isolated black hole (Sahu et al., 2022).

However, for more distant black holes, individual stars orbiting close to the black hole are beyond the capabilities of even the highest resolution telescopes, making it challenging to directly constrain the black hole mass from stellar orbits. Supermassive black holes can still be found in the absence of accretion, thanks to dynamical evidence. The mass of the central black hole in M31 was assessed using various kinematical and dynamical techniques (Kormendy and Richstone, 1995). The basic idea of these measurements is thus jointly model the mass profile (related to the surface brightness profile) and bulk motions (related to the velocity dispersion profile) in the central region of a galaxy. The mapping of the gas kinematics in a bulge region often relies on high-resolution integral-field spectroscopy.

The observation of these nearby SMBH having very low accretion rates ($\lesssim 10^{-5} M_\odot$ yr^{-1}, Eddington ratio $\sim 10^{-9}$, e.g. Garcia et al. 2010) suggests that highly accreting black holes are actually a minority, although they represent most of the population we can observe.

2.3.2 Ultraviolet and optical spectroscopy

Line broadening

Emission lines of the stellar populations orbiting an object are often used to constrain the black hole mass, as the line broadening scales with its mass (Greene and Ho, 2005). In the vicinity of a supermassive black hole, stars and gas reach high velocities scaling with the central mass, leading to a large velocity dispersion. The addition of the Doppler-shifted emission lines from each star results in a line broadening in the spectrum of the whole region, in particular for the Hα line (widely used because of its high emission), whose width can used to estimate the black hole mass (Reines et al., 2013):

$$\log\left(\frac{M_{BH}}{M_\odot}\right) = \log\epsilon + 6.57 + 0.47\log\left(\frac{L_{\mathrm{H}\alpha}}{10^{42}\ \mathrm{erg\ s^{-1}}}\right) + 2.06\log\left(\frac{\mathrm{FWHM}_{\mathrm{H}\alpha}}{10^{3}\ \mathrm{km\ s^{-1}}}\right)$$

where the scale factor ϵ is empirical with literature values in the range 0.75 – 4 (Reines et al., 2013). This mass estimator is in essence a proxy of the reverberation mapping technique presented below, and is thus subject to model dependence. Mass estimates obtained by the line broadening analysis were found to be accurate to within a factor ~ 2 compared to other mass measurement techniques (Dong et al., 2012).

Emission line diagnostics

Another way by which emission lines can reveal the presence of a black hole is the photoionisation signature produced by ionising photons emitted by the accreting black hole (Section 2.1.3), which affects the ratio of emission lines in the galaxy spectrum. This is the grounds for the classification of galaxies from the BPT diagram (Baldwin et al., 1981), distinguishing three categories (starforming, composite and active galaxies) in three loci of the $\log([\mathrm{OIII}]/\mathrm{H}_\beta) - \log([\mathrm{NII}]/\mathrm{H}_\alpha)$ plane. While it has been widely used, this observable provides no estimation of the black hole mass.

Another well-established accretion signature of AGN is the mid-infrared (MIR) emission of dust, heated by the hard emission of AGN accretion discs. Contamination by the blackbody stellar radiation is low at these MIR wavelengths (except in the case of extreme starbursts), thus enabling an efficient colour-colour selection of several millions of AGN (Secrest et al. 2015; Assef et al. 2018, but see Hainline et al. 2016).

Reverberation mapping

Time delays were found between changes in the continuum of an AGN spectrum and the same changes in its emission lines. Since emission lines originate in the broad line regions (for a Seyfert I AGN, Section 2.1.3), these delays are attributed to light echoes on such regions, and thus to the light travel time $\tau = r/c$ where r is their physical separation to the black hole. The widths of the broad lines then give access to the velocity dispersion ΔV in the broad line region and the quantity $r\Delta V^2$ (virial product) directly relates to the mass of the black hole (e.g. Greene et al. 2020, Section 2.3.4).

This technique is called reverberation mapping and relies on high-resolution spectroscopy at several epochs, but also on geometric modeling of the accretion system. These mass measurements are therefore generally accurate but considerably model-dependent.

2.3.3 X-ray diagnostics

Fundamental plane of black hole activity

Early spectral studies showed a strong link between X-ray and radio emission from accreting stellar mass black holes, attributed to the accretion and ejection processes (Section 2.1.3). This correlation was then found to extend to the supermassive regime, and to depend on the mass of the black hole. In particular, it was found that stellar mass black holes, AGN and even Sgr A* at the center of the Milky Way form a thin plane in $L_X - L_r - M_{BH}$ space, which has therefore been called the "fundamental plane of black hole activity" (Merloni et al., 2003).

This correlation is illustrated in Figure 2.7, showing the fundamental plane of Plotkin et al. (2012) who considered samples of Galactic black hole XRBs in the hard state, low-luminosity AGN, radio galaxies (FR I), blazars and Sgr A* during a hard X-ray flare. The black line they fit to these data corresponds to the following relation:

$$\log L_X = (1.45 \pm 0.04) \log L_R - (0.88 \pm 0.06) \log M_{BH} - 6.07 \pm 1.10$$

where L_X is the 0.5–10 keV unabsorbed X-ray luminosity (in erg s^{-1}), L_r is the radio luminosity at 5GHz (in erg s^{-1}), and M_{BH} is the black hole mass (in $M_\odot$). Such a fundamental plane thus allows to constrain the mass of a black hole detected in hard X-rays and radio, provided the two observations are sufficiently contemporaneous (Gültekin et al., 2019), to about ~ 1 dex.

Eddington scaling arguments

Knowing the bolometric luminosity L of the source, and assuming that accretion is capped at the Eddington limit, a lower limit on the black hole mass can be derived:

$$L < L_{Edd} \Leftrightarrow M_{BH}/M_\odot > \frac{L}{1.26 \times 10^{38} \text{ erg s}^{-1}}$$

From the Eddington ratio ($f_{Edd} = L/L_{Edd}$) distribution of a certain population, one can also assume a certain f_{Edd} value and errors of an object of this population. It is then possible to have a first order mass estimate $M_{BH}/M_\odot = L \times \left(f_{Edd} \times 1.26 \times 10^{38} \text{ erg s}^{-1}\right)^{-1}$.

In addition, a correlation was found between the L_X/L_{Edd} ratio and the best-fit powerlaw photon index Γ in Galactic XRB samples : it shows that Γ decreases from ~ 2 to ~ 1.5 with the increase

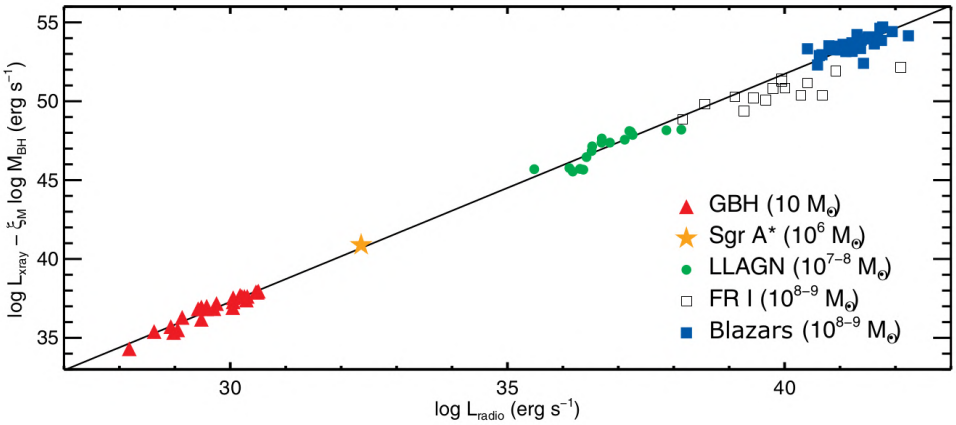

Figure 2.7: Fundamental plane of black hole activity. Adapted from Plotkin et al. (2012).

of L_X/L_{Edd} in the interval $10^{-6} - 10^{-3}$, then increases to ~ 2.5 when L_X/L_{Edd} approaches 10% (Sobolewska et al., 2011; Plotkin et al., 2013, 2017). This trend also seems to apply on AGN (Yang et al., 2015). This can help in the choice of f_{Edd} to obtain Eddington scaling mass estimates. However, this correlation presents a larger scatter and thus such mass estimates are less reliable.

Variability arguments

When no mass measurement is possible, one way to distinguish between neutron star and black hole X-ray binaries may be from their variability. Indeed, neutron stars can be pulsating, showing a regular periodic variability with a slow spin-down. In contrast, black hole binaries display aperiodic variability and are often transient (rather than persistent) sources (Tanaka, 1997). Quasi-periodic oscillations are also found in both categories, possibly caused by instabilities in the disc under Lense-Thirring precession (Stella and Vietri, 1998; Psaltis et al., 1999), although other scenarios exist and their origin is still discussed. Their correlation with the photon index modeling the XRB spectrum can however be used as a mass estimator (e.g. Molla et al. 2017).

Generally speaking, X-ray variability (e.g. the Root Mean Square variability or RMS) is expected to be anticorrelated with the black hole mass, as found in AGN (Lu and Yu, 2001). Indeed, short-term variability is produced by global coherent variations in the emission mechanism of the source (either from line-of-sight obscuration or from accretion state changes), which is easier to achieve at lower physical size. The timescale needed for the source to (intrinsically) vary significantly must be smaller than the light-crossing timescale, R/c (where R represents the size of the source).

The variability of AGN spans a wide range of timescales, from seconds (related to changes in the column density of the line of sight) to years or decades (possibly related to changes in the orbiting material), and its amplitude is anticorrelated with the black hole mass (Lu and Yu, 2001).

It is also possible to constrain the mass of a black hole causing a TDE (Section 2.2.4, Mockler et al. 2019) by using its light curve. The decay phase of TDEs is due to the decreasing fallback rate given by:

$$\dot{m} \approx \frac{1}{3}\frac{m_*}{t_{\rm fallback}}\left(\frac{t}{t_{\rm fallback}}\right)^{-5/3}$$

(Rees, 1988; Phinney, 1989), where t is the time since the TDE trigger, m_* is the mass of the disrupted star and $t_{\rm fallback}$ the characteristic dynamical fallback timescale. However, the early times of the decay do not follow this formula due to radiative feedback (Strubbe and Quataert, 2009) and the precise structure of the star (Lodato et al., 2009), so that in practice the luminosity evolution after the TDE trigger can be approximately described as

$$L(t) = \begin{cases} L_0 \text{ if } t < \tau_{Edd} \\ L_0 \left(\frac{t}{\tau_{Edd}}\right)^{-5/3} \text{ otherwise} \end{cases}$$

(Khabibullin et al., 2014), where $\tau_{Edd} \approx 0.1\big(M_{BH}/(10^6 M_\odot)\big)^{2/5}$ yr (Strubbe and Quataert, 2009; Khabibullin et al., 2014) is the time after which the fallback rate falls below the Eddington limit for a solar-type star with pericentre distance $R_p = 3R_S$, $L_0 = \eta L_{Edd}$ is the peak luminosity (η being a geometrical dilution factor).

As a result, TDEs caused by lower-mass black holes are fainter and decay faster than those around more massive black holes, making them more difficult to detect (Bricman and Gomboc, 2020).

X-ray spectra

As presented in Section 2.1.3, if a black hole accretes from a standard accretion disk (and emitting a multicolour blackbody spectrum), the inner radius of the disk depends on the mass of the black hole, as does the wavelength at the peak of its thermal emission. Actually this can be generalised to a broader range of slim disc solutions, hence allowing to constrain the black hole mass from X-ray spectral fitting.

Such an approach was carried out by Godet et al. (2012) to estimate the mass of the black hole powering ESO 243-49 HLX-1. The study of different epochs corresponding to different spectral states has given results consistent with each other, and with the Eddington scaling estimates of Farrell et al. (2009). In a numerical modeling work, Campitiello et al. (2018) extended this method to the SED of an AGN. It was found that the disc emission of an AGN depends mainly on three parameters: the mass of the black hole, the spin of the black hole and the accretion rate (or rather its product with $cos(\theta)$, where θ is the viewing angle). Mass estimates with this method can therefore be accurate, provided that the spin and accretion rate are well known, and that the thin disc solutions apply. However, this is no longer the case beyond a certain Eddington ratio threshold (~ 0.3, Campitiello et al. 2018).

2.3.4 Black-hole – galaxy scaling relations

One of the important breakthroughs of modern astrophysics was the discovery of close correlations between the properties of a galaxy and those of its central black hole, which led to theories about their strong interaction over cosmic time, or co-evolution (Section 2.4.2).

Probably the most well-known of these correlations is the $M_{BH} - \sigma$ relation (e.g. Ferrarese and Merritt 2000; Gebhardt et al. 2000) between the black hole mass and the velocity dispersion in the bulge. As shown in Figure 2.9 (right panel) reproduced from Greene et al. (2020), it allows to constrain the mass of the black hole of a galaxy knowing its velocity dispersion in the bulge, with an uncertainty of ~ 1 dex. For galaxies without bulge or dwarf galaxies, it is not possible to evaluate σ. The black hole mass - stellar mass relation ($M_{BH} - M_*$, left panel of Figure 2.9) can be used instead, but this correlation has more dispersion.

The low-mass end of these relations is very weakly constrained, however. For example, Graham and Scott (2013) suggest that the mass of black holes in low luminosity bulges scales quadratically (rather than linearly) with the mass and luminosity of the bulge, leading to a flattening in the low-luminosity regime of aforementioned correlations. While this may have important implications, particularly in the search for IMBHs and in models of galaxy and black hole formation, this result is still debated (e.g. Sahu et al. 2019), and I have studied it in this thesis work (Chapter 7).

Other scaling relations exist between black hole mass and other galactic properties, such as the spiral pitch angle (a measure of the tightness of the spiral arms) (Davis et al., 2012) or the Sersic index of the bulge n_{sph} (characterising its radial brightness profile, $\log(I(r)/I0) \propto R^{1/n_{sph}}$) (Savorgnan, 2016), further expanding the range of mass estimators (Koliopanos et al., 2017).

2.4 Relation to galaxy evolution

Different periods are distinguished in the cosmic history, leading to the structures we know in the local, present-day Universe. Of major interest is the reionisation epoch ($z \simeq 15 - 6$), during which the first generation of stars, the first galaxies and the first SMBH form and grow (e.g. Djorgovski

et al. 2001; Woods et al. 2019). Understanding the formation and co-evolution of these objects at this epoch will be of great help to physically interpret the black hole – galaxy correlations found locally (Section 2.3.4).

2.4.1 A brief history of galaxy formation and evolution

Some 380,000 years after the Big Bang, the Universe cooled enough for protons and electrons to recombine into atoms, emitting the first photons that we observe in the form of the cosmic microwave background. During the next few hundred million years (the "dark ages"), pristine, metal-free clouds of neutral gas formed and aggregated to form protogalaxies, the birthplace of the first stars. The light emitted from the first stars and galaxies then marks the beginning of the epoch of reionisation (or "cosmic dawn"), photo-ionising the hydrogen in its path (Gnedin and Ostriker 1997; Barkana and Loeb 2001).

The first stars are called Population III (Pop III) stars and were much more massive than today's stars ($40M_\odot < M < 1000M_\odot$, Ohkubo et al. 2009), because the clouds of zero metallicity that formed them could collapse at once, without being fragmented. Indeed, the Jeans mass, defining the maximum mass reachable by a gas cloud before collapsing, scales with the cube of the sound speed, and hence as $T^{3/2}$: $M_J = 700M_\odot \left(\frac{T}{200\mathrm{K}}\right)^{3/2} \left(\frac{n}{10^4\mathrm{cm}^{-3}}\right)^{-1/2}$ where n is the gas density and T is the temperature (e.g. Woods et al. 2019). The hotter the gas cloud, the larger the Jeans mass, allowing more massive objects to form. But the gas cloud is subject to various cooling processes as it collapses, becoming more efficient with increasing metallicity (e.g. Maio et al. 2007). Therefore, only metal-free and very metal-poor clouds can remain hot enough to collapse at once without fragmenting and form such stars.

After a few million years, Pop III stars will have left the main sequence and started to form metals by thermonuclear reactions, before collapsing and exploding in supernovae dispersing these metals in their environment. The next generation of less massive stars (Population II stars) then formed in this metal-enriched gas, evolved and finally collapsed, continuing the metal enrichment of the galaxy (e.g. Smith et al. 2015).

Progressively, gravitation is thought to have led to a sequence of galaxy mergers (leading in the end to the present-day galaxies). The inhomogeneities in the matter distribution of the early Universe are expected to evolve as cosmic flows of cold, dense matter, leading to the present-day large-scale structures of voids and filaments, isolated ("field") galaxies and galaxy groups or clusters. In the Λ Cold Dark Matter model, this merger history of galaxies is driven by the mergers of their dark matter halos through cosmic time. The merger history of a galaxy (or a dark matter halo) can be represented in the form of a "merger tree", showing its progenitors at different times of the Universe. An illustration of a merger tree is given in Figure 2.8. Depending notably on their mass and location, not all galaxies undergo the same number of mergers. The low-mass end of galaxies, dwarf galaxies ($M_* < 3 \times 10^9 M_\odot$), must have undergone a limited number of mergers, thus explaining their low mass and metallicity.

This scenario called "hierarchical formation" of galaxies (e.g. Cole et al. 1994; van Dokkum et al. 1999; Hopkins et al. 2006) is well illustrated by a number of observations: first of all, galaxy mergers are observed in the nearby Universe all the way to high redshifts (e.g. Conselice et al. 2003). These mergers cause intense episodes of star formation, followed by supernovae and metal enrichment, and the massive black holes of each galaxy (if any) can merge with each other, forming a larger one. This scenario thus explains the observed mass-metallicity relation among nearby galaxies, with dwarf galaxies having the lowest metal content (Section 2.4.3).

Besides, dynamical modeling suggests that the morphology of elliptical galaxies is caused by a large number of galaxy mergers (e.g. Barnes 1989). This is confirmed observationally by their preferential location in galaxy clusters (in which mergers are more frequent) and the fact that the most massive galaxies are all ellipticals. The very-low (or "quenched") star formation rates of elliptical galaxies also fit in this picture, because even if galaxy mergers cause star formation bursts, they are also thought to trigger accretion episodes on the central AGN (Villforth et al., 2017), which can then exert a galaxy-wide negative feedback (Section 2.4.2) on star formation (Khalatyan et al., 2008; Park et al., 2022).

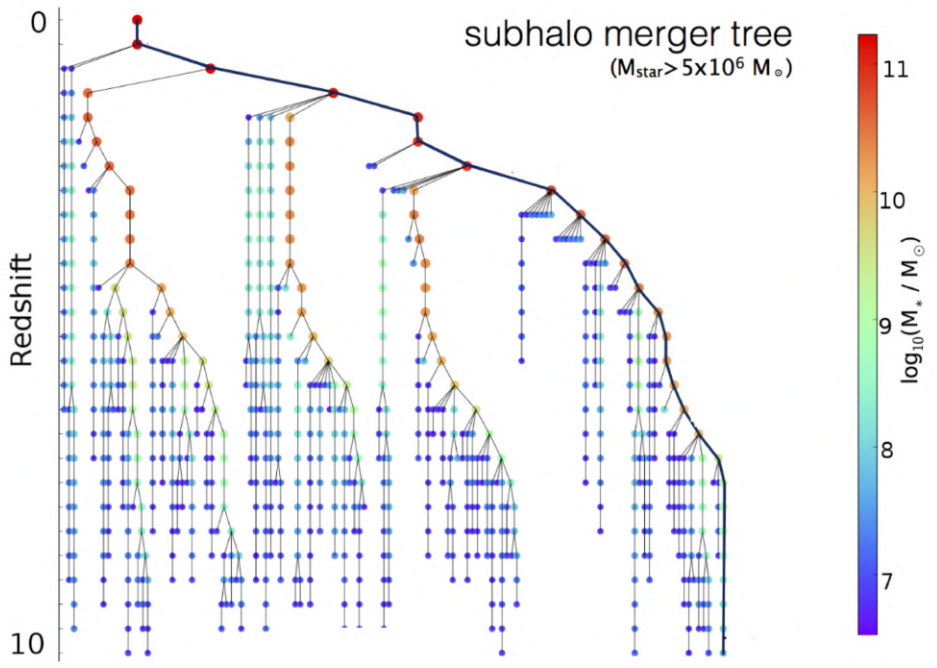

Figure 2.8: Illustration of the merger history of a galaxy, from the EAGLE cosmological simulation (McAlpine et al., 2016). Adapted from McAlpine et al. (2016).

2.4.2 Co-evolution of black holes and galaxies

In the framework of hierarchical galaxy formation and evolution, supermassive black holes are believed to co-evolve with their host. This idea is notably grounded by tight scaling relations linking the black hole mass to the galaxy properties, even on scales much larger than its sphere of influence, such as the $M_{BH} - \sigma$ relation (Ferrarese and Merritt 2000, Figure 2.9, Section 2.3.4).

One plausible explanation for these tight scaling relations is the concept of AGN feedback: their outflows can extend up to galaxy scales, sometimes manifesting as relativistic radio jets (Section 2.1.3), and can heat or remove the interstellar gas (in particular hydrogen). The energetic analysis of this feedback has shown that it is capable of suppressing (or, under specific conditions, increasing) star formation (e.g. Silk and Rees 1998; Khalatyan et al. 2008).

Consequently, they probably play an important role in the formation of cosmic structures, motivating the study of their demographics as a function of redshift. This motivated the study of their density evolution with redshift, as well as the redshift dependence of their luminosity function, notably in the UV and X-rays (Aird et al., 2010; Kulkarni et al., 2019; Bianchi et al., 2022).

However, although AGN feedback is increasingly accepted as the main cause of some galaxy evolutions (such as star formation quenching) and appears essential to explain their luminosity function (e.g. Croton et al. 2006), its role in shaping $M_{BH} - \sigma$ or $M_{BH} - M_*$ correlations is still far from being settled (Kormendy and Ho, 2013). On the one hand, luminous quasars fed by galaxy mergers release a large amount of energy on scales of up to several kiloparsecs, which is likely to heat or deplete the gas reservoir of the newly formed galaxy or even hamper the gas infall responsible for its growth (e.g. Dubois et al. 2013). This phase provides a natural explanation for the observed black hole – galaxy correlation in some galaxies.

On the other hand, it is not clear that lower luminosity AGNs, triggered outside of merger events, can have significant effects on their host mass. Peng (2007) and Jahnke and Macciò (2011) suggest instead that the observed correlations, in the majority of cases, are driven by stochastic effects after a large number of mergers, following the central limit theorem.

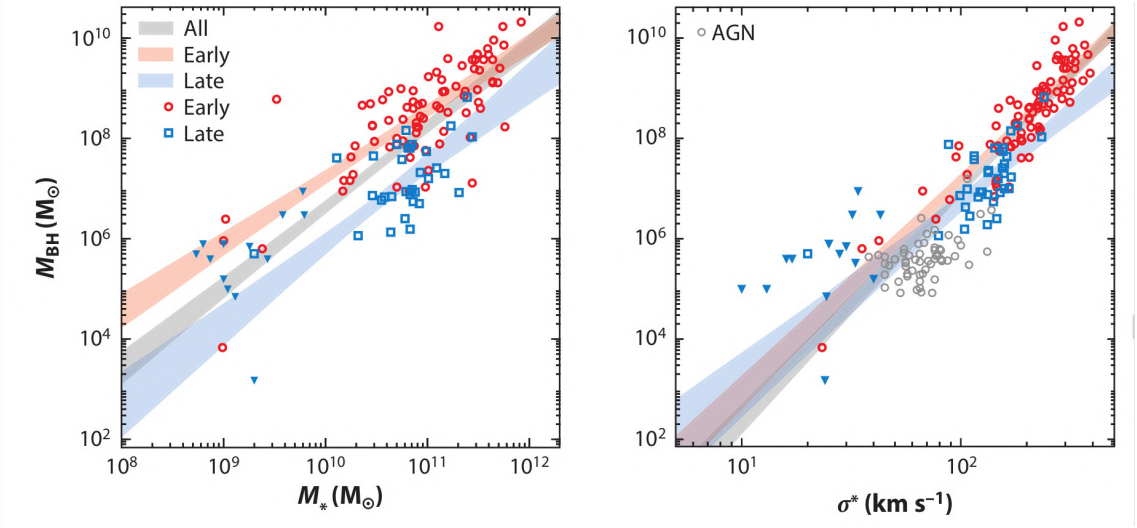

Figure 2.9: (Left) Relation between M_{BH} and the stellar mass M_* of the host galaxy, shown for early-type (red) and late-type (blue) galaxies. The shaded areas correspond to confidence intervals for the power-law fit of each sample (grey: full sample). (Right) Relation between M_{BH} and the velocity dispersion of stars in the bulge σ_* for the same sample of galaxies. The sample of AGN of Xiao et al. (2011) is shown as grey circles. Reproduced from Greene et al. (2020)

2.4.3 Dwarf galaxies as local analogues of primordial galaxies

Dwarf galaxies are defined as those of stellar mass lower than the Large Magellanic Cloud ($M_* < 3 \times 10^9 M_\odot$). The Magellanic Clouds and a number of other galaxy satellites of the Milky Way were the first dwarf galaxies to be detected and studied. These early studies have found that an important fraction of dwarf galaxies in the Local Group are satellites bound to more massive galaxies (Hodge, 1971), and under their strong tidal influence (Mayer et al., 2001). Numerical simulations showed that when merging, dwarf satellites can be tidally stripped by their host, removing up to 90% of the satellite's original stellar mass (e.g. Mayer et al. 2001; Norris et al. 2014). The remnant nucleus can however survive, left wandering in the more massive galaxy.

However, as introduced in Section 2.4.1, dwarf galaxies must have undergone a limited number of mergers since the reionisation epoch, which explains their lower metallicity (their abundance in metals is ∼10 times lower than in Milky-Way like galaxies). Therefore, they are often considered as fossils of the galaxy evolution, i.e. local analogues of high redshift galaxies.

Reinforcing this picture of weakly evolved galaxies, the feedback from AGN in dwarf galaxies was until recently considered negligible or even non-existent. First, because dwarf galaxies containing a massive black hole were initially thought to be rare, since early dynamical works found no evidence for them in nearby dwarf galaxies (Gebhardt et al., 2001; Neumayer and Walcher, 2012), and only two dwarf galaxies were reported as AGN candidates (NGC 4395 and Pox 52, Filippenko and Ho 2003; Peterson et al. 2005; Thornton et al. 2008). In the last decade, however, deeper sensitivities and larger multiwavelength surveys allowed the discovery of AGN in a large number of dwarf galaxies, suggesting that at least a fraction of such galaxies are occupied by a massive black hole (e.g. Reines et al. 2013; Lemons et al. 2015). This fraction is called the occupation fraction and is fundamental in studies of black hole formation (e.g. Volonteri et al. 2008, Section 2.5).

Still, the low-mass black holes in these galaxies are generally expected to play a minor role in the evolution of their host, compared to the dominant supernova feedback (i.e. the negative feedback exerted by supernova winds on subsequent star formation episodes). This is notably motivated by numerical simulations (Dubois et al., 2015; Habouzit et al., 2017; Bellovary et al., 2019), supporting the idea that massive black holes in present-day dwarf galaxies accreted only a small fraction of their mass since their formation. A number of observations tend to confirm this conception: in particular, star formation quenching in these galaxies is found to be extremely rare (Geha et al., 2012), and their star formation history seems essentially independent of the black hole mass (Martín-Navarro and Mezcua, 2018). Dwarf galaxies are therefore expected to have undergone few mergers and little black hole growth since their formation, and are thus ideal places to look for the seeds of supermassive black

holes. Nevertheless, in recent years, radio observations of AGN in dwarf galaxies have challenged this concept, finding in particular strong large-scale radio jets indicating stronger feedback than expected (Mezcua et al., 2019; Molina et al., 2021; Davis et al., 2022).

2.5 The missing bricks: intermediate-mass black holes

The discovery of massive quasars at the end of reionisation – including objects as massive as $\sim 10^9 M_\odot$ at $z \gtrsim 6$ (Fan et al., 2001), $1.2 \times 10^{10} M_\odot$ at $z = 6.33$ (Wu et al., 2015), $2 \times 10^9 M_\odot$ at $z = 7.085$ (Mortlock et al., 2011), $8 \times 10^8 M_\odot$ at $z = 7.54$ (Bañados et al., 2018) and $1.6 \times 10^9 M_\odot$ at $z = 7.64$ (Wang et al., 2021) – implies a rapid mechanism for forming them. If this mechanism is steady accretion at the Eddington limit, this implies the existence of massive seeds $\gtrsim 10^3 M_\odot$ already at $z \sim 15$.

This raises the question of the seeds from which they form: are they stellar-mass black holes, as seen in the local Universe? A priori, this option is ruled out. Indeed, the mass of the growing seed from gas accretion at a constant rate follows

$$M_{BH}(t) = M_0 \exp\left(\frac{1-\epsilon}{\epsilon}\lambda_{Edd}\frac{t}{0.45\mathrm{Gyr}}\right)$$

(e.g. Volonteri 2010), where M_0 is the initial mass of the seed, λ_{Edd} the Eddington ratio and ϵ the radiative efficiency. Even assuming $\epsilon = 0.1$ (typical radiative efficiency, e.g. Shakura and Sunyaev 1973) and $\lambda_{Edd} = 1$ would lead to the growth of a $M_0 = 100 M_\odot$ seed formed at $z = 20$ into a mass of only $\sim 4 \times 10^8 M_\odot$ at $z = 6$ (assuming a flat cosmology with $\Omega_m = 0.286$, $\Omega_\Lambda = 0.714$, $H_0 = 69.6$ km/s, Bennett et al. 2014). Such sustained accretion would also require a continuous supply of material, making this scenario even rarer. To grow the most massive SMBH seen in the high redshift Universe, scenarios involve direct formation as for primordial black holes (Section 2.1.2), or the accretion-fed or merger-driven formation from less massive seeds, namely intermediate-mass black holes, and/or super-Eddington accretion on such seeds. However, these formation paths remain to be clearly resolved by observations.

The discoveries of intermediate-mass black holes started with two low-mass AGN ($M \sim 3 \times 10^5 M_\odot$) identified in the dwarf galaxies NGC 4395 and Pox 52 (Filippenko and Ho, 2003; Peterson et al., 2005; Thornton et al., 2008). Later on, considerable effort was dedicated to unveil more IMBH, leading to a number of other IMBH candidates. As this effort focused on locations where IMBH are expected to reside since their formation, we review here some of their well-accepted formation paths (e.g. Mezcua, 2017; Greene et al., 2020; Volonteri et al., 2021). They are illustrated in Figure 2.10.

2.5.1 Formation channels

Stellar-mass black holes are the remnants of massive stars in the local Universe. However, these massive stars were generally formed in the last billion year ($z < 0.1$) in an environment enriched in metals. These massive stars lose mass by winds, and the mass-loss rate depends on the metal content of the matter, following the empirical relation $\dot{M} \propto Z^\alpha$ with $\alpha \simeq 0.83$ (Mokiem et al., 2007). Typically, a $100 M_\odot$ star at solar metallicity loses 80% of its mass in just 3Myr. In contrast, stars from the first generation formed during the reionisation epoch (Pop III stars) can reach a few $100 M_\odot$ (e.g. Nakamura and Umemura 2001) and end their lives collapsing into a $M_{BH} \gtrsim 200 M_\odot$ IMBH (Madau and Rees, 2001; Fryer et al., 2001; Spera and Mapelli, 2017) for the most massive ones ($M \gtrsim 230 M_\odot$). At lower masses, stars end their lives as a pulsational pair instability supernovae or a pair instability supernovae (Heger et al., 2003). Besides these Pop III stars, very metal-poor stars $Z < 10^{-3} Z_\odot$ more massive than $230 M_\odot$ (zero-age main sequence mass) may also be able to form an IMBH by direct collapse (Spera and Mapelli, 2017).

A second formation scenario, also taking place in the early Universe, relies on the direct collapse of a giant gas cloud such as a protogalaxy (e.g. Loeb and Rasio 1994; Lodato and Natarajan 2006),

with an intermediate state as a supermassive star (e.g. Woods et al. 2019). This channel only holds at very high redshifts, because pristine metal-free gas is needed to have a large enough Jeans mass (Section 2.4.1). Other specific initial conditions are required to prevent cooling, such as an intense Lyman-Werner background radiation (e.g. Omukai 2001), notably due to halo mergers (Yoshida et al., 2003; Wise et al., 2019) or an already begun star formation in local haloes (Visbal et al., 2014; Dunn et al., 2018). Recently, another possibility has emerged that they could form from the convergence of strong, cold accretion flows, without requiring a finely tuned radiation background (Latif et al., 2022). The end product of such a direct collapse is a massive black hole in the range $10^4 - 10^6 M_\odot$ (e.g. Habouzit et al. 2016).

Another formation channel is possible in compact star clusters, even at lower redshifts. In these dense environments, runaway collisions can occur and lead to the hierarchical mergers of stars and stellar-mass black holes to form larger and larger black holes (Portegies Zwart and McMillan, 2002). The main obstacle to such a scenario is the natal kicks received by the remnants, typically reaching velocities up to few 1000 km/s (Campanelli et al., 2007). Consequently, most of the remnants are kicked after before three mergers (Rodriguez et al., 2018; Mapelli et al., 2021) and the remnant black hole is of mass $M \lesssim 10^2 M_\odot$. Nevertheless, it is possible for a light IMBH to be formed through this channel (Rodriguez et al., 2019), and for more massive IMBHs to form in denser clusters such as the nuclear star clusters (Mapelli et al., 2021). In other environments such as an AGN disc, hierarchical mergers may be frequent as well and sustained for more generations (Bartos et al., 2017; Tagawa et al., 2021).

As illustrated in Figure 2.10, each seeding channel is expected to leave a different footprint on local observables such as the black hole – galaxy scaling relations.

The BHMF at high redshift (top right panel) probably shows the most significant differences between the three scenarios, but it is also hard to measure (Section 2.1.2). The BHMF of Pop III remnants resembles any stellar initial mass function, as low-mass Pop III stars make up most of the population and collapse into lower-mass black holes (Madau and Rees, 2001). Conversely, seeds formed from runaway mergers and direct collapse present mass distributions peaked at $\sim 10^3 M_\odot$ and $\sim 10^5 M_\odot$ (Volonteri et al., 2008; Volonteri, 2010). However, it is worth noting that these considerations are for the high-redshift BHMF ($z \sim 15$), and that higher masses of the BHMF are populated in a few hundred million years in case of efficient accretion (Volonteri, 2010).

Besides, direct collapse black holes require massive halo mass and fine-tuned physical conditions, they are thus particularly rare in low-mass dwarf galaxies: for instance, the occupation fraction of $10^9 M_\odot$ dwarf galaxies should be $\lesssim 50\%$ in the direct collapse model and $\sim 90\%$ in the Pop III model (Greene 2012, and middle right panel of Figure 2.10). Medium-sized runaway merger black holes should have intermediate occupation fractions, since they also require a reasonable gas reservoir to grow.

Those dwarf galaxies having a direct collapse black hole will therefore appear as overmassive outliers in the $M_{BH} - M_*$ plane (bottom right panel of Figure 2.10), given the BHMF of such seeds. In contrast, Pop III remnants may grow by accretion and mergers in a similar way to SMBH, and thus follow the classical $M_{BH} - M_*$ relation (Volonteri and Natarajan, 2009). Other works suggest instead that they may appear undermassive (from the semi-analytical model of Pacucci et al. 2018) or overmassive (from the sub-grid model in the cosmological simulation of Spinoso et al. 2022).

Regardless of their formation model, seeds are expected to grow by accretion and/or mergers. Accretion may be a viable path, since the increasing evidence for IMBHs mostly comes from accreting systems: they include low-luminosity AGN in dwarf galaxies (Chilingarian et al., 2018), hyperluminous X-ray sources (Barrows et al., 2019) and partial or total tidal disruption events (Godet et al., 2014; Lin et al., 2018). This channel also appears to provide the most mass for SMBHs, as indicated by the luminosity function of AGN (Yu and Tremaine, 2002). However, growth by accretion must be in general limited by the Eddington limit and the AGN feedback (Volonteri et al., 2021), and the accretion rate onto low-mass black holes may be even more limited (e.g. Pacucci et al. 2017).

Another channel for the seeds to grow more massive is through mergers with other massive black holes, which is naturally expected from the hierarchical galaxy formation model (Section 2.4.1). It can also be considered as a continuation of the scenario of runaway mergers, and even Pop III remnants since Pop III stars are likely to form in binaries (Sugimura et al., 2020). Besides, galaxy mergers at early times are thought to be more frequent and more rapid than today because the Universe was denser (e.g. Stott et al. 2013). On the other hand, low mass black holes are more likely to be ejected

during galaxy mergers, or to have long merger timescales, especially in the shallow potential well of low mass galaxies (Volonteri et al., 2021). Future observations of black hole mergers, notably in the gravitational wave domain (Section 2.5.2), will thus be key to compare the role of accretion and mergers in the growth of SMBHs.

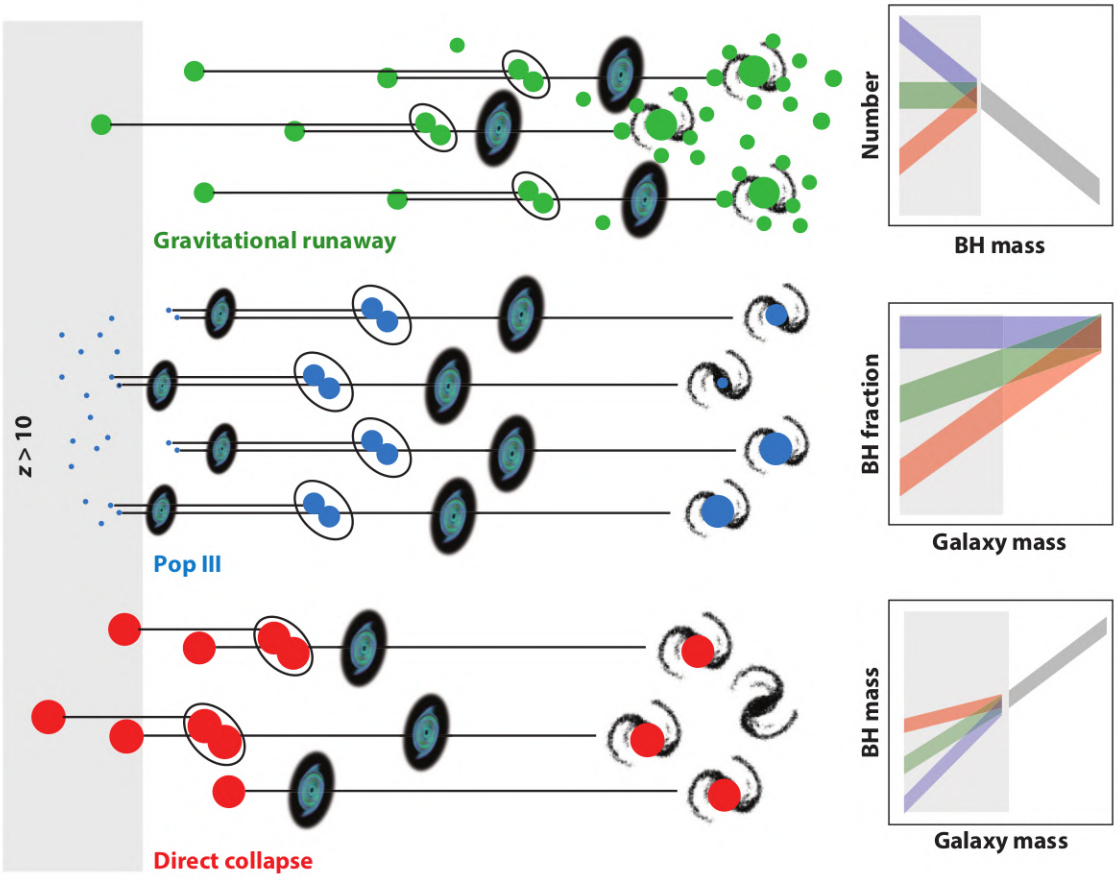

Figure 2.10: Formation paths of intermediate-mass black holes, and their consequence on several statistical observables. As galaxies and cosmic structures evolve, the seed black holes undergo mergers (black ovals), resulting in gravitational wave events, but also accretion events (blue disks) that could be observed as active galactic nuclei. At present, differences in black hole mass functions, occupation fractions and black hole – galaxy scaling relations can arise from different seeding channels. The grey shaded areas in this plot indicate where we do not yet have observational constraints. Reproduced from Greene et al. (2020).

2.5.2 Observational evidence

In the local Universe, IMBH are thus expected to reside notably in the centre of star clusters. Direct-collapse IMBH, whose mass is larger, could fall in the gravitational well of the galaxy and might now be found in the centre of dwarf galaxies. As galaxies grow by successive mergers, IMBH are also expected in the outskirts of larger galaxies having undergone a recent (minor) merger.

In practice, some IMBH candidates have indeed been found in the stellar clusters ω Cen (Noyola et al., 2008), NGC 6388 (Lützgendorf et al., 2011), M54 (Ibata et al., 2009), NGC 6624 (Perera et al., 2017) and 47 Tuc (Kızıltan et al., 2017), but their mass estimates were later refuted or dramatically reduced (Zocchi et al., 2017; Lanzoni et al., 2013; Baumgardt, 2017; Baumgardt et al., 2019; Mann et al., 2019), notably from a proper motion study of individual stars located in the cluster. Conversely, Baumgardt (2017) put upper limits on the mass of the putative central black hole for a large sample of 50 globular clusters, using dynamical modeling of their surface brightness and velocity dispersion. All except two (ω Cen and M54) of their clusters are consistent with a no-IMBH scenario. Outside the Milky Way, IMBH discoveries have been claimed in the globular clusters G1 (Gebhardt et al., 2002, 2005) and B023-G078 (Pechetti et al., 2022) of M31. However, the former candidate is debated and

was found to be consistent with a low-mass X-ray binary (Pooley and Rappaport, 2006; Miller-Jones et al., 2012). Other techniques have been proposed to trace back the existence and location of IMBH in the Milky Way, such as microlensing (Franco et al., 2021) or the kinematic modeling of hypervelocity stars (Fragione and Gualandris, 2019), but they are yet to be tested.

As massive IMBH may form or fall deep in the potential well of the galaxy, and to test the scenario in which SMBH grow by hierarchical mergers, numerous searches for new candidates have focused on the central region of the Milky Way, near Sgr A*. Among others, CO-0.40-0.22 is a millimeter continuum source consistent with a mass of about $10^5 M_\odot$ thought to be embedded in a molecular cloud and leading to the observed broad velocity width (Oka et al., 2017). Evidence for this candidate was however later refuted in an analysis of ALMA images (Tanaka, 2018). Other ALMA observations conversely suggest the presence of $10^4 M_\odot$ IMBHs to explain the kinematics of other gas streams (Takekawa et al., 2019, 2020).

More robust candidates could be found at the center of local dwarf galaxies, using accretion signatures. The first hint at the existence of a central black hole in low-mass galaxies indeed relied on optical spectroscopy of the nucleus of Pox 52 (Kunth et al., 1987), M32 (Dressler and Richstone, 1988) and NGC 4395 (Filippenko and Sargent, 1989). Because low-mass AGN have small spheres of influence and their luminosity due to accretion is expected to scale with their mass, they are difficult to detect, and their very existence was debated until the 2010s (Reines, 2022). In contrast, modern searches led to the discovery of hundreds of new IMBH candidates (defined using various thresholds between 10^5 and $10^6 M_\odot$), in particular thanks to optical spectroscopy (Reines et al., 2013; Moran et al., 2014; Chilingarian et al., 2018). Some candidates were later confirmed or newly found by accretion signatures in X-ray and UV (e.g. Baldassare et al. 2015; Mezcua et al. 2018) or MIR wavelengths (e.g. Sartori et al. 2015; Harish et al. 2021), including many IMBHs with masses lower than $10^5 M_\odot$. Synchrotron radio emission from AGN jets also proved powerful to detect new AGN candidates (Nyland et al., 2012; Latimer et al., 2019; Reines et al., 2020). Interestingly, some IMBHs were found to be wandering in the dwarf galaxy, rather than located in its bulge (Bellovary et al., 2019; Reines et al., 2020), supporting the picture in which such black holes can grow by hierarchical mergers of their galaxies.

With the success of systematic searches for a central black hole in dwarf galaxies, first constraints were drawn on the fraction of these galaxies occupied by a black hole (hereafter occupation fraction). Previous studies generally find an occupation fraction lower than 1%, using a broad range of signatures (Reines, 2022). However, these estimates may well be lower limits, as they rely on black hole signatures calibrated for massive galaxies and subject to high false negative rates in the more star-forming, metal-poor dwarf galaxy environments. This is particularly the case of line diagnostic diagrams (Groves et al., 2006; Cann et al., 2019). On the other hand, first estimates from X-ray studies suggest an occupation fraction of $\gtrsim 20\%$ (Miller et al., 2015; She et al., 2017). Dormant black holes, with low or zero accretion rates, are likely to be missed by X-ray and radio selection criteria; conversely a fraction of candidates relying on these observations may be mistaken with X-ray binaries, or AGN located in the background. Reaching more robust and representative samples seems to be possible by selecting candidates on their variability, which is a less biased estimator, thanks to which promising results are already obtained in archival optical and infrared observations (Baldassare et al., 2018, 2020; Ward et al., 2021). These samples need to be enlarged to get accurate constraints, notably thanks to upcoming observatories in radio, optical and X-rays such as the Square Kilometer Array, the Vera C. Rubin observatory and eROSITA (Greene et al., 2020; Reines, 2022).

While we now know that a large fraction of ULXs are actually powered by stellar-mass compact objects (Section 2.2.2), the more luminous HLX still represent interesting IMBH candidates (Kaaret et al., 2017) (Section 2.2.3). Among them, ESO 243-49 HLX-1 is probably the most well-established, followed by a number of candidates already introduced in Section 2.2.3. Therefore, HLXs but also off-nuclear TDEs tend to be promising probes of accreting IMBH populations.

In 2015, nearly one century after their prediction by Einstein (1916, 1918), the first gravitational wave event was officially discovered (Abbott et al., 2016), from the merger of two black holes. Since then, many black holes were found with the same technique. Figure 2.11 shows the so-called "stellar graveyard", illustrating the masses of stellar-mass black holes discovered until late 2020. Of particular interest is the event GW190521, resulting from the merger of two black holes of mass $\sim 66 M_\odot$ and $\sim 85 M_\odot$, giving a remnant of $\sim 142 M_\odot$ (Abbott et al., 2020a). The second progenitor is very likely to be in the pair-instability mass gap, and thus may be itself the result of a black hole merger in a

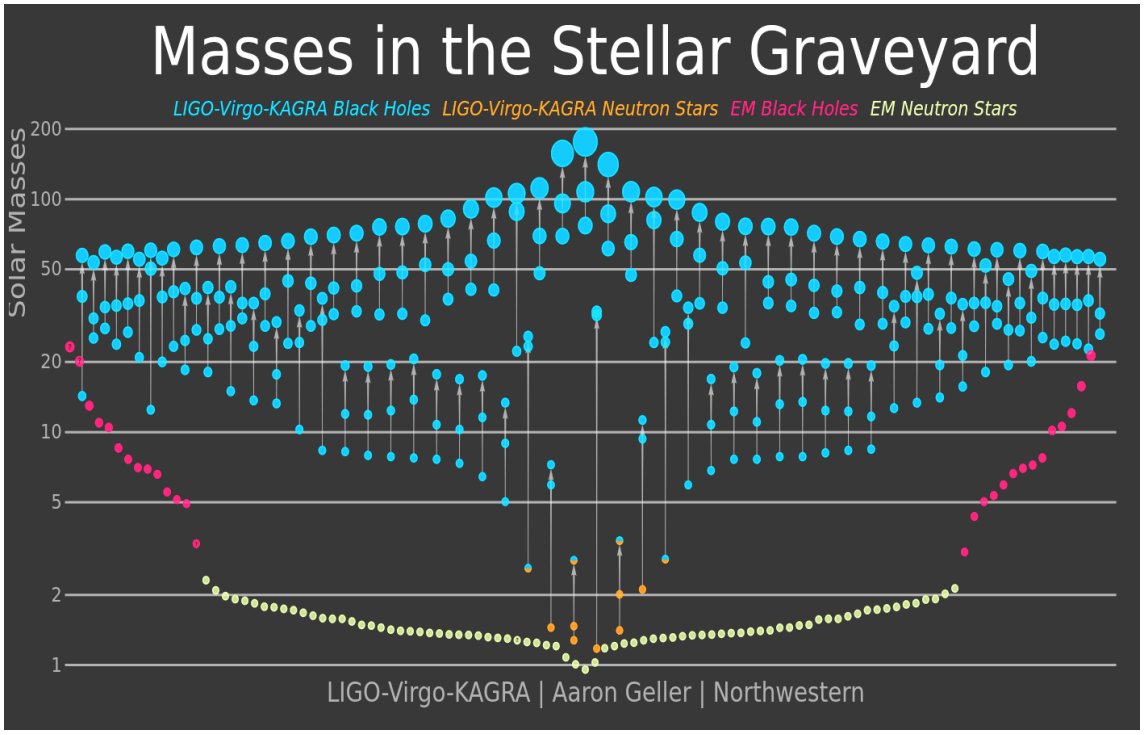

Figure 2.11: Stellar graveyard, with GW190521 highlighted. This graphic illustrates the detected neutron stars and stellar-mass black holes until late 2020, from electromagnetic or gravitational wave signatures. Image credit: LIGO-Virgo/ Northwestern U. / Frank Elavsky & Aaron Geller. Source: https://media.ligo.northwestern.edu/gallery/mass-plot

dense environment (Abbott et al., 2020b). Electromagnetic stellar-mass black holes (EM black holes in Figure 2.11) are the ones detected in XRBs. The lower mass and higher spin of EM black holes were recently discussed as a sign of them being a different population of black holes (Fishbach and Kalogera, 2022), however some $> 50M_{\odot}$ EM black holes are also found (e.g. Belczynski et al. 2020) and this observation could be explained by selection effects (Belczynski et al., 2021).

Other black hole mergers are also detectable by using gravitational wave detectors: the characteristic burst frequency is $f_b = 3.9 \left(\frac{M}{10^4 M_{\odot}}\right)^{-1} (1+z)^{-1}$ Hz (e.g Press, 1971) where M is the total mass of the merging binary, making possible the detection of black hole mergers up to $M \sim 10^2 M_{\odot}$ with current facilities but from 10^2 up to $10^9 M_{\odot}$ with future facilities such as the Laser Interferometer Space Antenna (LISA, Amaro-Seoane et al. 2017) which will cover lower frequencies 0.1mHz - 1Hz. It will allow merging black holes $> 2000M_{\odot}$ to be detected out to the very young Universe, $z > 10$ (e.g. Miller 2009; Jani et al. 2020).

2.5.3 Current constraints

As introduced in Section 2.5.1, several IMBH formation paths are possible. Several observational constraints can be inferred from the black hole mass function, occupation fraction and BH-galaxy scaling relations (Greene et al., 2020), but also the detection of high-redshift massive quasars (Pacucci and Loeb, 2022).

Current limits on the occupation fraction are insufficient to conclude. There are hints for an occupation fraction $> 50\%$ from X-ray surveys (Miller et al., 2015) and TDE detections (van Velzen, 2018), but they only concern the high-mass end of dwarf galaxies. Gravitational wave observations allow us to probe lower galaxy masses, and Sánchez-Janssen et al. (2019) derive the fraction of galaxies having a nuclear star cluster in each mass bin. However, this cannot be directly translated to black hole occupation. Nevertheless, if taken at face value, the large occupation fraction estimates and the flattening of the $M_{BH} - M_*$ relation suggest a preference for the direct collapse scenario (Mezcua et al., 2018; Martín-Navarro and Mezcua, 2018).

Recent studies however found that constraining the occupation fraction of local dwarf galaxies may not give a reliable picture of the initial IMBH population. Indeed, this requires that dwarf galaxies are "untouched relics" of the first galaxies and black holes in the epoch of reionisation, or at least that they underwent sufficiently few mergers and feedbacks to retain sufficient memory of their initial conditions (Volonteri et al., 2008; Volonteri and Natarajan, 2009; van Wassenhove et al., 2010), which might not be the case (Section 2.4.3).

Conversely, the black hole mass function at low masses is a strong signature of IMBH formation paths (Figure 2.10), but few studies were able to constrain it up to now. In particular, assuming a simple powerlaw relation between galaxy mass and black hole mass and extrapolating it to the lower masses, Greene et al. (2020) derive two models of black hole mass function using the galaxy mass function obtained in Wright et al. (2017). Large uncertainties remain, especially concerning the fraction of wandering black holes, which may considerably increase the number of low-mass IMBH, leading to poor constraints on the formation channels in the end.

Constraints inferred from the observations of high-redshift quasars may be the most reliable, provided the mass and redshift are correctly estimated, because they are direct probes of the formation timescales. Detecting even a few massive quasars formed less than half a billion years after the Big Bang is a clear indication that the initial seed of these SMBH was already massive, like in the direct collapse scenario. Pacucci and Loeb (2022) review current detections of high-redshift quasars and estimate from Monte-Carlo simulations of black hole growth that the parameter space is already well-constrained for some quasars, to $M_{seed} > 10^{3.5} M_{\odot}$ and an average radiative efficiency $\epsilon < 0.1$. However, it is to note that their study assumes a black hole growth only driven by accretion and not mergers, and that assumptions on the accretion model (i.e. slim disc accretion) are made.

2.5.4 Alternative scenario: primordial black holes

As presented in section 2.5, the observation of some high-redshift massive black holes suggests the existence of a population of massive ($> 10^3 M_{\odot}$) seeds early in the reionisation epoch ($z \sim 15$). A perhaps more exotic scenario is that this population is provided by primordial black holes (PBHs) (Düchting, 2004; Bernal et al., 2018; Volonteri et al., 2021).

To date, the failure of observational tests to find evidence for PBHs (Section 2.2) has led to the analysis that if their mass function is flat or a power law, PBHs cannot produce a sufficient population of massive seeds (Düchting, 2004). However, assuming a more complex BHMF (which is still consistent with theoretical expectations, Carr and Kühnel, 2020), PBHs are still a valid model of SMBH seeds, which we may be able to constrain by the next decade with new infrared and radio observatories (Bernal et al., 2018; Cappelluti et al., 2022).

2.6 X-ray astronomy

In order to recognise black holes in the X-ray sky, one must know the signatures of each type of X-ray source and their approximate distribution. Preliminary surveys having just a few hundred sources allowed manual classification of most of them, leading to the assessment that they were essentially made of AGN and stars. In the following, we give a rapid picture of the main types of X-ray sources and their main features, in increasing order of rarity, while a more complete description is provided in Chapter 4. Since the advent of high-resolution X-ray observatories, sources can be conveniently separated into two categories, point-like (meaning the source extent cannot be resolved at the instrument PSF) and extended, the former being the focus of this thesis given its content.

The dominant type among point-like X-ray sources is AGN (Sections 2.1.3, 2.2.5): emitting X-rays due to the accretion onto the supermassive black hole of a massive galaxy, they can reach tremendous luminosities (up to $\sim 10^{46}$ erg/s). This makes them detectable even at large distances, so that they represent the largest cosmic volume probed in X-rays, and the largest fraction of X-ray sources (about 60%, Lin et al. 2012; Stocke et al. 1991). As mentioned earlier, they can spread a wide range of X-ray

to optical flux ratio (but most of the time between 0.1 and 10, Section 2.1.3), variability (but on longer timescales than smaller black holes in XRB) and spectral shapes.

By contrast, stars are only visible in the very local regions of our Galaxy. The stars in our Galaxy are among the brightest sources of optical light in the sky. Some of them are also powerful soft X-ray emitters, especially at low mass the G-type, K-type and M-type stars ($L_X \lesssim 10^{27}$erg/s) because of the very high temperature in their corona (related to the magnetised chromospheric activity). The most massive stars (types A, B, O) of the main sequence have in general a powerful X-ray emission (maximum for the stars of type O: $L_X \sim 10^{32-34}$ erg/s, lower for types B and A, $L_X \sim 10^{27-31}$erg/s for type A), which would be due to hydrodynamic shocks in the stellar winds of radiative or magnetic origin (Rauw et al., 2015). Overall, though, X-rays represent only a small fraction of their luminosity, the main component being the blackbody emission of the plasma in outer stellar layers. Consequently, a long-standing criterion to select in X-ray surveys has been the X-ray to optical (resp. infrared) flux ratio which is generally lower than 0.01 (0.03). This does not include the more peculiar young stellar objects, affected by heavy optical absorption. Some variable stars display a large short-term X-ray variability, especially in the form of flares. As a result of their low luminosities, most of X-ray detected stars are located within a 1 kpc radius from the Solar System.

Rarer point-like sources include binaries, notably X-ray binaries and cataclysmic variables (compact binaries containing a white dwarf as compact object and a late-type star or another white dwarf as companion). The former can be seen either in the Milky Way or in nearby galaxies, due to their luminosities 10^{34-40} erg s^{-1}, while cataclysmic variables are only visible in our Galaxy $L_X < 10^{34}$ erg s^{-1}. X-ray binaries and cataclysmic variables can exhibit very diverse signatures in X-rays, notably in terms of spectrum and light curve. Their characterisation is discussed in greater detail in Chapter 4. Rare transient X-ray sources complete the list of point-like X-ray source types, including supernovae, gamma-ray burst afterglows and X-ray novae. Supernovae are produced when a star has consumed all its thermonuclear fuel and collapses, sometimes forming a compact object (section 2.1.2). Gamma-ray bursts are extremely energetic outbursts thought to originate from the gravitational collapse of the core of some very massive stars ($> 20\,M_\odot$, producing a hypernova) and from mergers of neutron stars (Levan et al., 2016). These events are rare (a few per galaxy per million years, Podsiadlowski et al. 2004) and the gamma-ray emission is followed by a multi-wavelength afterglow (from the X-ray to the radio domain) also decreasing in time but visible on longer time scales (from minutes to weeks, months, or even years). X-ray novae are caused by the sudden fall of gas onto a neutron star or a black hole, which sometimes happens in binary systems without accretion (such as quiescent LMXB), causing the delayed emission of outbursts in hard X-rays, soft X-rays and longer wavelengths (Tanaka and Shibazaki, 1996; Chen et al., 1997).

Among extended X-ray sources, the dominant population consists of clusters of galaxies (e.g. Krautter et al. 1999). X-rays are procuded by the thermal and Bremmstrahlung emission of the hot ($> 10^7$K) plasma composing the intracluster medium (Section 2.1.3). Supernova remnants represent the main other extended source type, with X-rays mostly due to their hot gas and sometimes the synchotron radiation emitted after electrons interact with the magnetic field of a central neutron star. Other extended objects include planetary nebulae in our Galaxy, the hot gas content of some nearby galaxies, and the interaction of cosmic rays with the molecular gas of our Galaxy (in particular in its central region).

Last but not least, a deeper understanding of X-ray sources can only be achieved on a per-instrument basis, due to a number of phenomena leading to spurious X-ray detections which mimick the presence of an astrophysical source. The next Chapter will address the instrumentation and data processing of the three main modern X-ray observatories observing the sky for the last two decades, and the catalogues of about 1 million sources that stem from them.

2.7 Rationale

Unlike optical and infrared colours which are widely used to select AGN, but may miss a lot of bona fide black holes in specific environment such as dwarf galaxies, X-ray emission is a probe of accretion episodes. As such, they are ideal to observe black holes over their whole mass scale, from stellar-mass black hole XRB to SMBH. While X-rays are unable to catch dormant or weakly accreting black holes (except when they undergo a TDE, which is already a good probe), this is also true for other wavelengths in most situations. Probing HLX sources, a large fraction of TDEs and numerous black holes in dwarf galaxies, X-rays offer a unique opportunity to probe the IMBH population under various conditions.

Besides, the combination of X-rays with other wavelengths is particularly powerful to identify sources: this has made it possible to establish easy empirical rules to classify X-ray sources in general (e.g. Lin et al. 2012), which is highly valuable for many applications. For example, in nearby galaxies, X-ray binaries and the possible central AGN are seen in X-rays as well as foreground stars and background AGN overlapping the galaxy under study. Notably, as many as 20% of the ULXs listed in recent catalogues may in fact be contaminated by background AGN. Considerable progress has been made thanks to multiwavelength data, in particular to separate valid ultraluminous and hyperluminous X-ray sources from these contaminants (Barrows et al., 2019; Bernadich et al., 2021). Systematising this approach would represent a great leap in ULX science, by multiplying the sample size of robust ULX and enabling more accurate population studies of these poorly understood objects.

Another application of such a classification would be to separate galactic from extragalactic sources, including XRB and AGN respectively, which would be useful e.g. to constrain the black hole mass function. Besides these two source types, other local sources are found to be point-like X-ray emitters: they include massive stars that emit strong winds heating their surroundings, low-mass highly magnetised stars that possess a hot corona, and cataclysmic variables. Identifying properly all these sources would be valuable to better study the corresponding source types. As the history of X-ray astronomy is paved with serendipitous discoveries, objects of special interest and exotic sources also represents *treasures* to identify. With the recent development of X-ray astronomy (particularly in the last 20 years), more than a million point-like sources are present in the archives, with unprecedented sensitivity and spatial resolution, waiting to be studied.

In this thesis, the primary goal will thus be to identify more IMBH candidates and make new constraints on their population. To gather a large sample and achieve the tightest constraints, I adopt a data mining approach relying on a versatile and powerful source classification applied to the largest present-day X-ray archives. In previous Sections, I gave an overview of the different types of sources composing the X-ray sky. In Chapter 3, I describe the X-ray facilities and X-ray catalogues under study. In Chapter 4, the development of an automated classification of X-ray sources is detailed. The results of this classification on whole catalogues are described in the same Section, as well as a number of science application. Chapter 5 is focused on the application of this classification to the science of ULX and HLX, with a particular highlight of new IMBH candidates. In Chapter 6, the classification is applied on X-ray sources in dwarf galaxies, giving another sample of IMBH candidates. Chapter 7 contains the discussion and implications of my findings. I conclude and give some prospects of this study in Chapter 8.

Chapter 3

Instruments and data

Since its beginning in the 1960s, X-ray astronomy has known significant breakthroughs pushing its limits in both sensitivity and angular resolution. Sources detected by *Swift*-XRT, *XMM-Newton* and *Chandra* facilities are compiled in large X-ray catalogues totalling about 1 million X-ray sources, meaning that X-ray astronomy is slowly entering the era of Big Data. This achievement would not have been possible without the rapid development of X-ray optics and space-based X-ray observatories. This chapter describes these three X-ray catalogues, as well as the enhancement we performed with supplementary data in order to develop a source classification.

3.1 X-ray observatories

Because of the Earth's atmosphere blocking X-ray radiation, astronomical X-ray sources were not observable until the launch of X-ray detectors at high altitude or into space. However, theory of stellar physics predicted that the Sun had to emit X-rays. This was confirmed thanks to the use of German V-2 rockets as sounding rockets in 1949, and subsequent missions led to the first detections of X-ray sources outside our Solar system.

In order to focus X-rays onto a detector, it is necessary to use a specific telescope design, notably the so-called Wolter telescopes. Several concentric mirrors are nested along the length of the telescope, so as to reflect incoming light at very shallow angles (grazing incidence). In this configuration, high-energy X-rays are totally reflected rather than being transmitted or absorbed by the mirror material. The development of these optics in the 1960s led to the first sensitive X-ray observatories.

3.1.1 First generation

Uhuru was the first satellite specifically dedicated to X-ray astronomy, sent into orbit in 1970. It scanned the whole sky thanks to a spin period of 12 minutes, up to a limiting sensitivity $\sim 1.5 \times 10^{-11}$ erg s^{-1} cm^{-2} in the 2–20 keV energy band achieved thanks to an imaging proportional counter, at the forefront of technology at the time of its launch.

Later missions followed the same large-coverage strategy with progressive detection innovations. They include Vela 5B (sensitive to the 3–12 keV band), Ariel V (2 keV–1.2 MeV), HEAO-1 (0.2 keV–10 MeV), EXOSAT (0.05–50 keV) and Einstein (0.2–20 keV) observatories (e.g. O'Dell et al. 2010; Saxton et al. 2022). These facilities offered a large sky coverage, at the price of shallow sensitivities ($\sim 10^{-11}$ erg s^{-1} cm^{-2}) and poor angular resolution $\gtrsim 30$'. This does not include the case of Einstein

(the first large X-ray telescope with Wolter I-type focusing mirrors) with the first high-resolution X-ray camera onboard a spacecraft, leading to competitive spatial resolution of 3" over the central 25' of the FOV.

In the 1990s, pioneering position-sensitive proportional counters allowed the development and launch of ROSAT (Pfeffermann et al., 1987), an X-ray observatory achieving an all-sky coverage in the energy band 0.1–2.4 keV with a spatial resolution $< 1'$ and limiting sensitivity $\sim 5 \times 10^{-13}$ erg s^{-1} cm^{-2} in 10^4s. This was the first X-ray image of the whole sky with a powerful X-ray telescope, including an anticoincidence system at the focal plane that reduced the particle background by 99.85%. (Pfeffermann et al., 2003). Thanks to these features, ROSAT was also the first survey overcoming the symbolic threshold of 100,000 X-ray sources (Boller et al., 2016).

In 1999, two outstanding X-ray missions – *Chandra* (energy band 0.2–10 keV, Weisskopf et al. 2002) and *XMM-Newton* (0.15–12 keV, Jansen et al. 2001) – were launched, each one having complementary capabilities and able to tackle different science goals. In 2004, the Neil Gehrels *Swift* observatory (0.3–10 keV, Gehrels et al. 2004) was sent into orbit with the aim of studying gamma-ray bursts: its X-ray instrument completes the list of powerful X-ray telescopes in service up to now, whose observations are used in this thesis work.[1]

3.1.2 Swift-XRT

Instrument

The Neil Gehrels *Swift* Observatory (Gehrels et al., 2004) is a space mission launched in November 2004 and designed to study and monitor gamma-ray bursts (Section 2.6), using three instruments. The *Swift* observatory has been designed to rapidly trigger multi-wavelength and sustained observations of these bursts: one of the three instruments of *Swift*, the Burst Alert Telescope (BAT, Barthelmy 2004), detects the prompt emission of gamma-ray bursts (in the 15−150 keV band) within its 2-steradian field of view and autonomously determines their position with a typical accuracy of 3 arcminutes. Right after this detection, the satellite is pointed in the direction measured by the BAT to perform a follow-up of the afterglow emission of the burst with the two other small-field instruments. On the one hand, the Wolter I-type X-Ray Telescope (*Swift*-XRT, Burrows et al. 2004), with a field of view of 23.6×23.6 arcmin^2 and a spatial resolution of the order of ten arcseconds, allows to measure the X-ray afterglow that follow most of the gamma-ray bursts in the 0.3–10 keV band. On the other hand, a UV/optical telescope (UVOT, Roming et al. 2005), with a field of view of 17×17 arcmin^2 and a spatial resolution of the order of an arcsecond, allows to follow the optical/UV afterglow radiation in 6 bands covering the wavelength interval 160–600 nanometres via a filter wheel.

To achieve this science goal, *Swift*-XRT is equipped with a 600px×600px CCD detector with a large collecting area (peak at 110 cm^2 at 1.5 keV) and a broad energy range (0.2–10 keV), as well as low vignetting effects: the effective area is reduced by ∼25% at the outer edge of the camera, while the PSF is almost constant (half power diameter of 18 arcsec i.e. 7.6 pixels). Most of the XRT exposure time is acquired in "photon counting" mode, the usual frame transfer operation of an X-ray CCD, retaining full imaging and spectroscopic resolution, at a time resolution of 2.5s. In this mode, the position, energy and arrival time of photons are stored in a file called the event list. Due to its low-Earth orbit, *Swift* cannot observe the same location of the sky for more than half its orbiting period (∼2.7 ks) without interruption. To achieve longer exposures, the observation of a target is thus split in several segments called *snapshots*.

During its first 13 years of activity, from January 2005 to August 2018, Swift-XRT performed more than 350 000 snapshots, observing 3790 deg^2 of the sky at a median sensitivity of $\sim 1.7 \times 10^{-13}$ erg s^{-1} cm^{-2}. It covered almost 25 000 distinct locations with considerable uniformity, 81% of which were observed at least twice (Evans et al., 2014). These features unique to *Swift*-XRT mean that a large number of serendipitous sources must have been observed by this instrument, with a large fraction observed multiple times, hence allowing to probe their variability on different timescales.

This motivated the early works of Puccetti et al. (2011); D'Elia et al. (2013) and Evans et al. (2014), who produced different catalogues such as 1SXPS, a catalogue of 151 524 point-like X-ray

[1] In July 2019, eROSITA (Merloni et al., 2012) on board the Spektrum-Roentgen-Gamma observatory was launched to perform four all-sky surveys in the 0.2–8 keV energy band. As a successor to ROSAT, it is scientifically very complementary to the three missions mentioned above. However, only a recent and early data release covering 140 deg^2 of the sky (Brunner et al., 2022) is available at the time of writing, so this survey was outside the scope of this thesis.

sources detected during the first 8 years of *Swift*-XRT observations. In 2019, this catalogue was superseded by 2SXPS (Evans et al., 2020) to include the latest observations.

Catalogue

2SXPS (Evans et al., 2020) includes all *Swift*-XRT observations having more than 100s of observations in the cleaned photon-counting mode event list. Covering 3790 deg^2, it contains 206 335 unique point-like sources detected by XRT (median exposure of $\sim$ 20ks) in the 0.3–10 keV range (broad band). This range is divided into three energy bands (soft 0.3–1 keV, medium 1–2 keV and hard 2–10 keV) allowing a first glimpse at the spectral properties of each source. This cut ensures that the detection of a typical AGN contains roughly the same number of events in each band (Evans et al., 2014).

The data preparation and the pipeline used to systematically detect X-ray sources from an event list are complex and we refer the interested reader to Evans et al. (2014) for a detailed description. This work generally relies on different specialised packages included in the software suite HEASOFT, published by the High Energy Astrophysics Science Archive Research Center (HEASARC) at NASA (2014). In brief, a sliding-cell detection algorithm is performed iteratively on the image of each X-ray snapshot. This algorithm is optimised to detect point-like sources emitting over a background, which can be of instrumental and/or astronomical origin. The typical background level in XRT observations is $\sim 10^{-6}$ counts s^{-1} px^{-1}. At each iteration, a new source is detected and the background map is refined. Count rates are computed using the exposure map. The outputs of the algorithm are the final background map, as well as the position (obtained by a PSF fit), count rate and detection likelihood of each source detected above a certain S/N threshold. This process is repeated for each of the four (broad, soft, medium and hard) energy bands.

The steps described above are used to produce the table of detections of 2SXPS, including 1 091 058 entries. It contains the positions, position uncertainty, detection likelihood, count rate and quality flags of each source detected in each energy band, during each observation. Detections are merged across bands to compute two hardness ratios for each source:

$$\mathrm{HR1} = (M - S)/(M + S)$$

$$\mathrm{HR2} = (H - M)/(H + M)$$

where S, M, H stand for the count rates in the soft, medium and hard energy bands. Due to the very nature of X-ray photon counting, the conversion of count rates into fluxes often has to rely on the use of spectral models. In 2SXPS, three sets of fluxes are provided: `FixedPowFlux` is the 0.3–10 keV flux derived from a canonical absorbed power-law model, with $\Gamma = 1.7$ and $n_H = 3 \times 10^{20}$ cm^{-2}. When the number of net source counts exceeded 50, a spectral fit was performed and the resulting model was used to compute `FittedPowFlux`. Since this is the case of only 22% of 2SXPS, a third estimate was performed based on simulations: `InterpPowFlux` is obtained by interpolating Γ and n_H from the (`HR1`, `HR2`) values.

To produce the final list of unique sources, the successive detections of a given object have to be merged in a single entry. This is performed by an internal positional crossmatch of the detections: detections whose positions are compatible within 5σ are assumed to be the same source. The final source position is taken from the detection having the lowest position errors, while other source properties are averaged between all detections. Other properties are computed as well, such as different variability indicators.

A number of detection issues may occur during an X-ray observation. We describe here common issues reported in Evans et al. (2020) that are systematically checked in the pipeline, resulting in a number of quality flags included in 2SXPS columns. In particular, spurious detections can occur due to hot rows and hot columns in the CCD or the presence of various artifacts:

- due to the *Swift* low-Earth orbit, images acquired at low angle between XRT and the so-called bright Earth limb are affected by a higher background

- when a very bright optical source is in the XRT FOV, it can charge the CCD with a large amount of photons accumulating in a 2.5s frame. This *optical loading* (or *pile-up*) effect distorts the PSF and produces ring-like artifacts in the X-ray image.

- when a very bright X-ray source lies close to the XRT FOV, its photons can reach the CCD after a single reflection in the Wolter telescope (rather than the two reflections needed to focus them). This effect produces concentric annuli of diffuse emission in the X-ray image, called *stray light*.

- diffuse X-ray emission, from specific astronomical sources such as galaxy clusters or supernovae remnants, can also lead to the spurious detection of point-like sources

A quality flag `fieldflag` is attached to each 2SXPS detection and source to inform of the presence of one of the above-mentioned effects: it takes the value 0 for clean fields, 1 for fields contaminated by stray light which was properly fitted and subtracted, 2 for fields affected by diffuse emission or artifacts, and higher values for fields affected by the presence of artifacts that could not be properly modeled and subtracted.

Statistically, background fluctuations can also mimick point-like sources: these spurious sources can be filtered out using the detection likelihood and exposure time. Evans et al. (2020) implemented a detection flag `detflag` calibrated on simulations and taking the value 0, 1 and 2 corresponding to *Good*, *Reasonable* and *Poor* quality, respectively: they estimate a false positive rate of 0.3%, 1% and $< 10\%$ among *Good*, *Good+Reasonable* and all sources, respectively.

The 206 335 resulting 2SXPS sources have a median position error of 4.5" and median flux of 4.7×10^{-14} erg cm^{-2} s^{-1} in the broad band. We note that for bright sources the position error is largely dominated by the astrometric error of *Swift*-XRT pointings, whose typical value is 3.5".

3.1.3 XMM-Newton

Instrument

The "X-ray Multi Mirror mission" *XMM-Newton* (Jansen et al., 2001) is an X-ray observatory launched in December 1999 to investigate in greater detail the distribution, spectra and temporal properties of astronomical X-ray emitters. It is equipped with three mirror modules, each one containing a Wolter 1 type grazing incidence telescope having a focal length of 7.5m, and a CCD camera. These EPIC (European Photon Imaging Camera) cameras, namely pn (Strüder et al., 2001), MOS-1 and MOS-2 (Turner et al., 2001), have a large collecting area (1550 cm^2 at 1.5 keV), a large field of view (30 arcmin in diameter), a large bandpass (0.15–12 keV) and a low vignetting – the PSF on-axis half energy width is 15" at 1.5 keV (6" FWHM), increased by 30% at an off-axis angle of 12 arcmin. While MOS cameras benefit from a better angular resolution (one of their pixels covers 1.1", versus 4.1" for pn), pn has a higher time resolution (73.4 ms in full frame mode, versus 2.6s) and is robust to the observation of brighter sources. Their spectral resolution is similar (70–80 eV at 1 keV).

Onboard *XMM-Newton*, two other types of instrument complete the scientific capabilities of the observatory: the X-ray spectrometers "RGS" (Reflection Grating Spectrometer) are placed at the focus of the mirror modules where the MOS cameras are situated (half the flux falls on the MOS detectors and half on the RGS), allowing the acquisition of high-resolution spectra (spectral resolution ~ 3 eV at 1 keV) in the energy range 0.33–.5 keV for sufficiently bright sources. Besides, the co-aligned optical-UV telescope "OM" (Optical Monitor) allows for simultaneous observations in optical/ultraviolet regime. Almost identical to *Swift*-UVOT, it images the inner 17×17 arcmin^2 of the X-ray FOV with a high angular resolution (PSF FWHM < 2") in one among six bands covering the wavelength range 180–600nm, up to a limiting magnitude ~ 21 for a 1000 s exposure.

Between 2000 February 3 and 2020 December 2020, *XMM-Newton* performed more than 12 000 observations with exposures longer than 1 ks, covering more than 1239 deg^2 of the sky. The large effective area of the three X-ray telescopes result in a very sensitive observatory, so that a single pointing of 37 ks (mean exposure time of XMM detections) lead to the detection of 70-75 serendipitous sources (Webb et al., 2020). This has motivated the production of a standardised catalogue of serendipitous sources by the *XMM-Newton* Science Survey Center (SSC[2]), a consortium of ten European institutes (Watson et al., 2001), releasing this catalogue on a yearly basis since 2015.

Catalogue

In 2020, the XMM SSC published the fourth generation of their catalogue of *XMM-Newton* serendipitous sources, 4XMM-DR9 (ninth data release since 1XMM, the first generation of this cat-

[2] xmmssc.irap.omp.eu/

alogue) (Webb et al., 2020). To this end, *XMM-Newton* data were reduced and calibrated with the software *XMM-Newton* Science Analysis System (SAS) (Gabriel et al., 2004) in a dedicated pipeline.

In brief, all observations containing at least 1 ks of clean EPIC exposure were processed with a sliding-cell detection algorithm applied simultaneously on all images and energy bands. Five energy bands are defined in XMM catalogues, used in pairs to compute four hardness ratios: 0.2–0.5 keV (band 1), 0.5–1 keV (band 2), 1–2 keV (band 3), 2–4.5 keV (band 4) and 4.5–12 keV (band 5). A maximum likelihood fitting procedure is then applied on each detected source to compute its parameters (position, position error, count rate in each band, hardness ratios...). Spectra and light curves are generated for all of those sources having at least 100 EPIC counts. Just as in 2SXPS, detections of a same source are then merged together in the catalogue of unique sources.

Unlike the 2SXPS catalogue, 4XMM contains also information on the source extent: during the fitting process, the goodness of fit of the instrumental PSF to the detected source is compared with the goodness fit of the convolution between the PSF and a β extent model (Lorentz model with a varying power law, usually well-suited to represent the X-ray emission of galaxy clusters, Cavaliere and Fusco-Femiano 1976). If the likelihood of the extended model is higher than a threshold $L_{ext,min} = 4$, and higher than the likelihood of the point-like model by at least 4 units, then the source is flagged as extended and the likelihood as well as the extent radius (in the range 6–80" as defined in the corresponding SAS subroutine) are recorded in the columns `EP_EXT_ML` and `EP_EXTENT`. Moreover, XMM point-like sources generally have a lower position error than *Swift*-XRT sources thanks to the sub-arcsecond astrometric precision of XMM pointings – the typical systematic astrometric uncertainty, estimated on point-like SDSS quasars (Pâris et al., 2018) matching a point-like XMM source, is 0.96 arcsec (Webb et al., 2020). Last, but not least, *XMM-Newton* is sensitive to sources as faint as 2×10^{-15} erg s^{-1} cm^{-2} (resp. 10^{-14} erg s^{-1} cm^{-2}) in the band 0.5–2 (resp. 2–10) keV in 20 ks (median exposure time). This is more than one order of magnitude better than *Swift*-XRT, thanks to a larger effective area while keeping a low background rate ($\sim 2 \times 10^{-6}$ cts s^{-1} arcsec^{-2}, Traulsen et al. 2019).

Similarly to *Swift* pointings, XMM observations are affected by a number of artefacts and problematic detections. A quality flag is attached to each detection in each detector, reporting twelve different detection issues, as well as a summary flag `SUM_FLAG` to sum them up. The latter is raised to the value 1 if the source lies close to the edge of a detector coverage, within an extended emission or close to another source. This means that the source is likely to be non spurious, but some of its measured parameters may be affected. `SUM_FLAG` is raised to the value 2 if the source is categorised as a possible spurious source from various criteria, or if it lies on the bright corner of MOS-1 or a bright low gain column of pn: in these cases, the source is more likely to be spurious. Other values of `SUM_FLAG` (3,4) are assigned when the source is in a field where artefacts (such as stray light and optical loading) or diffuse emission are found, notably by manual inspection.

In this work we use the most recent incremental version of 4XMM at the time of writing, 4XMM-DR11 (August 2021), covering 1239 deg^2 of the sky observed between February 2000 and December 2020. It contains 895 415 detections and 602 543 unique sources, including 10% (61 425) of extended sources. Their median flux is $\sim 1.9 \times 10^{-14}$ erg s^{-1} cm^{-2} and their median position error is 1.5".

3.1.4 Chandra

Instrument

The *Chandra* X-ray observatory (e.g., Weisskopf et al. 2000, 2002) was launched in July 1999 with the primary goal of studying the X-ray sky at faint fluxes and high angular resolution. Its Wolter type I telescope is composed of four nested mirrors with a thick coating in a specific support structure, called the "high resolution mirror assembly".

Two types of X-ray detectors can be positioned at the focal plane of the mirrors: ten Advanced CCD Imaging Spectrometers (ACIS) are analogous to the cameras onboard *Swift*-XRT and *XMM-Newton*, allowing to measure the position, arrival time and energy of incoming X-ray photons. Four of them (ACIS-I) are optimised for imaging, with their positions in the chip allowing a large FOV of 16×16 arcmin^2, while the other (ACIS-S) are optimised for spectroscopy (energy resolution of 100 eV) and have a smaller (individual) FOV (8×8 arcmin^2). On the other hand, the High Resolution Camera (HRC) has a larger FOV (31×31 arcmin^2), higher timing capabilities (temporal resolution of 16 μs) and a higher resolving power due to its 69 million glass tubes instead of pixels, but it suffers from a

low spectral resolution except in very soft X-rays. Maybe for this reason, ACIS is more widely used by the proposers. Depending on the operation mode, *Chandra* observations thus have a FOV in the range $\sim$ 60–250 arcmin^2. Both kinds of detectors are sensitive to a broad energy band, 0.1–10 keV, with best performance in the range 0.5–7 keV.

The thick, precisely polished substrate on *Chandra* mirrors is responsible for the high resolving power of Chandra: the PSF FWHM is 0.2" on-axis (0.5" for ACIS cameras), and more than 80% of the incoming X-rays are focused at the sub-arcsecond level. This comes at the cost of effective area (200cm^2 at 1 keV for each detector) and vignetting effects: the *Chandra* PSF is downgraded to 6" at an offaxis angle of 10 arcmin and 14" at 15 arcmin, and the effective area is reduced by 30% at 15 arcmin.

Thanks to their high resolving power and low operating temperature (-120°), ACIS cameras have a very low instrumental background, $\sim 10^{-7}$ cts s^{-1} px^{-1} (Markevitch et al., 2003; Revnivtsev et al., 2007) in the band 0.5–7 keV. However, the effective area of ACIS cameras was progressively decreased by the accumulation of out-gassed material (carbon, oxygene and fluorine) on its filters, increasing their temperature and damaging ACIS sensitivity. This contamination is particularly significant below 2 keV and since 2010 (e.g. Plucinsky et al. 2018).

Since the beginning of its operations, as of 2020, *Chandra* observed more than 850 deg^2 of the sky. Despite this sky coverage smaller than *Swift*-XRT and *XMM-Newton*, the deeper sensitivity of *Chandra* observations also represent a reservoir of serendipitous sources that are yet to be studied. The *Chandra* X-ray Center (CXC) operated at the Smithsonian Astrophysical Observatory published in 2010 a first release of the *Chandra* Source Catalogue (CSC). In 2020, CSC 2.0 (hereafter CSC2) was released, covering all observations that were publicly released at the end of 2014.

Catalogue

CSC2 (Evans et al., 2010, 2019) contains 928 280 detections of 317 167 unique sources extracted from 10 382 *Chandra*-ACIS and -HRC imaging observations that covers 550 deg^2 of the sky. Following a similar pipeline to 2SXPS and 4XMM, this catalogue was generated through standardised routines present in the CXCDS (*Chandra* X-ray Center data system, Evans et al. 2006) processing system and the CIAO (*Chandra* Interactive Analysis of Observations, Fruscione et al. 2006) software. This includes notably a wavelet-based source detection algorithm and a PSF fit to localise each source and measure its parameters (in particular its extent). Count rates are recorded from the X-ray images in five energy bands: 0.1–10 keV (wide) for HRC observations, and 0.5–7 keV (broad), 0.5–1.2 keV (soft), 1.2–2 keV (medium) and 2–7 keV (hard) for ACIS observations – allowing the definition of two hardness ratios. Two likelihood threshold are applied to discard most spurious sources, separating sources into 3 categories, according to the quality flag `likelihood_class`: it takes the value `FALSE` (generally below a likelihood of 10) for sources to be discarded, `MARGINAL` for marginally detected sources (this corresponds to $\sim$1 spurious source per field) and `TRUE` for well-detected sources ($\sim$0.1 spurious sources per field). 77% of CSC2 sources are in the latter category.

The strong dependence of the PSF with off-axis angle leads to several limitations. Close point sources can be well separated in an observation but confused in another one, so the process of merging detections into unique sources is less straightforward than in 2SXPS and 4XMM. The catalogue of unique sources is thus built iteratively, and when a detection is associated with several unique sources, these associations are recorded and flagged as "ambiguous" and the confusion flag `conf_flag` is set. For the same reason, the position uncertainty of each detection depends on its offaxis angle θ: it is $\sim$1 arcsec (median) for $\theta < 8$ arcmin and $\sim$5 arcsec for $8 < \theta < 15$ arcmin. Last, but not least, the flag `extent_flag` can be set for some detections of a point source, and propagated to the catalogue of unique sources.

Even if detection issues (such as pile-up) are also present in *Chandra* observations, the low background and high angular resolution of *Chandra* lead to a cleaner catalogue of X-ray sources: only a handful of sources are affected by the presence of ACIS readout streaks or saturation (425 and 20 sources, respectively).

Like in 2SXPS, several sets of CSC2 fluxes are estimated and left to the user's choice: `flux_aper_X` is the aperture-corrected source flux in band `X`, estimated by counting X-ray events, `flux_powlaw_aper_X` is the model flux inferred from a canonical absorbed power-law spectral model ($\Gamma = 2.0, n_H = 10^{20}$ cm^{-2}) and `flux_powlaw_X` is the model flux inferred from the best-fitting absorbed power-law model.

3.2 Data

3.2.1 Selection of reliable sources

Our initial sample of X-ray sources is the compilation of high-quality, well-detected, point-like X-ray sources from the three abovementioned catalogues.

From the largest of these catalogues, 4XMM-DR11, we selected the 496645 point-like sources that have a detection with a reasonable detection flag `SUM_FLAG`≤ 1 (source parameters may be affected, but spurious detections are unlikely). A few extended sources are considered as point-like by the XMM pipeline (`SC_EXTENT`$= 0$) and remain in this selection. They have typically `SC_EXT_ML`> 100 and `SC_SUM_FLAG`> 1 or `SC_EXT_ML`$> 10^4$, so we remove the 561 corresponding sources. We also remove sources below the detection likelihood `SC_DET_ML`$= 10$ threshold, to limit the false source rate while still keeping a high fraction of the catalogue sources (83%).

The *Chandra* CSC2 catalogue is treated in a similar way: removing sources flagged as extended or ambiguous (as given in the source name), saturated or overlapping a bright streak. Unlike the XMM pipeline, *Chandra* extended sources seem to be all flagged as extended, but some seemingly point-like sources are also flagged likewise: from manual inspection, we choose to exclude extended sources in a confused area, or whose median major axis across energy bands (computed in the *Chandra* pipeline) exceeds 0.5 arcsec. We keep only sources in the likelihood class `TRUE` and with a non-zero flux, having detections with a `conf_code` lower than 256 (to remove sources with unreliable parameters due to an overlapping extended source); 214757 sources remain after this filtering process.

Likewise, from the Swift-XRT catalogue 2SXPS (Evans et al., 2020) we selected sources having `detflag`$= 0$ and `fieldflag`≤ 1 to remove possibly spurious sources and sources in polluted fields, as well as sources with a zero flux.

Since *Swift*-XRT has the largest PSF among the three X-ray telescopes, some supposedly point-like sources may actually be extended at this stage, and no extent estimate is made available. This was notably confirmed by a visual inspection of some fields containing galaxy clusters. We thus flagged 2SXPS sources matching the extent of an XMM or *Chandra* extended source, unless they also match a reliable source at less than 10". In a galaxy cluster, because the cluster is extended, the *Simbad* and XRT position can be as far from each other as 20": 188 sources at less than 20" from a *Simbad* galaxy cluster were conservatively flagged as well, as possibly due to the hot gas extended emission. This leaves a sample of 130162 clean sources.

3.2.2 Sample enhancement

In our work, we make use of several source properties that are natively present in X-ray catalogues : they notably include the hardness ratios, the source flux in different energy bands, the source position and its position error. However, this thesis work also requires supplementary data in order to properly identify X-ray sources. While some of them are straightforward to compute, such as the source Galactic coordinates, others imply a substantial data processing that we describe here.

Multi-mission X-ray variability

The long-term variability of X-ray sources gives an important clue on their nature. While some variability indicators are already present in X-ray catalogues, they are specific to the detections of each instrument. To probe the source variability on a multi-mission basis, and in order to assess the number of unique sources left in our final sample, we perform a crossmatch of the three catalogues with each other using the TOPCAT software (Taylor, 2005). The *Sky with Errors* algorithm is applied, using the 3-sigma position error of each source in each catalogue. Grouped matches are found, meaning ambiguous associations, either in crowded fields (like galaxies) or because of spatial resolution issues (it is not unusual that two close CSC2 sources are merged into a single 4XMM or 2SXPS one, since these instruments cannot resolve them). We choose to remove these associations and flag the corresponding source, unless they become ungrouped when a crossmatch using the 1-sigma position error is performed. In this way, ambiguous associations in which one of the potential associations is much more likely are well retrieved, while more ambiguous associations are flagged and removed. As a result, 1.7% of 2SXPS sources (resp. 0.7% of 4XMM sources) matching a *Chandra* source are in ambiguous association.

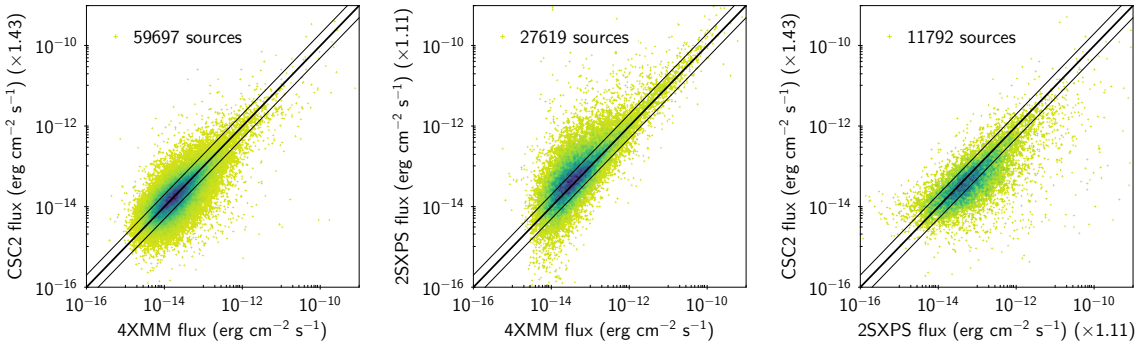

Figure 3.1: Comparison of 2SXPS, CSC2 and 4XMM fluxes, for associated sources of our X-ray samples, after calibration in the 0.2–12 keV band. The density of sources is colour-coded, in linear scale. The thick black line is identity and the thin lines correspond to a factor 2 of difference.

Since the three catalogues have different energy bands, in order to compare their fluxes, we redefine their broad band flux in the band 0.2–12 keV. This is done using an absorbed powerlaw model ($\Gamma = 1.7$, $n_H = 3 \times 10^{20}$ cm^{-2}) using the WebPIMMS tool[3], the same model as the one already used in the count-rate to flux conversion in 2SXPS and 4XMM-DR11. As a result, 2SXPS `FixedPowFlux` is increased by 11% and CSC2 `flux_aper_b` is increased by 43%. This absorbed powerlaw model is generally quite consistent with accreting sources such as AGN or XRB in the hard state, but not with soft sources such as stars. This may induce some biases later in the classification process (Section 4.5.3). Figure 3.1 shows the comparison of *Swift*, *XMM-Newton* and *Chandra* fluxes for compiled sources present in several catalogues.

Multiwavelength counterparts

X-ray catalogues generally contain cross-correlation information with external catalogues, including catalogues of optical and infrared point-like sources. Such catalogues have been published over the last two decades following the advent of sensitive all-sky surveys treated with automatic pipelines. In the optical domain, notable surveys are USNO-B1.0 (Monet et al., 2003), Gaia (Gaia Collaboration et al., 2016) and PanSTARRS (covering 76% of the sky, Chambers et al. 2016). In the infrared domain, they include 2MASS (Cutri et al., 2003) and AllWISE (Cutri and et al., 2014) surveys. These matches can be used as optical and infrared counterparts of X-ray sources, in order to compute the ratio of the X-ray flux to their optical or infrared fluxes and use it as another indicator of the source class. Such an indicator was already used, for example, to separate stars and AGN, with simple threshold rules such as "if $\log(F_X/F_{IR}) < -2$ then the source is considered as a star" (e.g., Mikles et al. 2006).

However, the crossmatching algorithm used in X-ray surveys is often simplistic (e.g. only based on positions and 3-sigma position errors) and unsuitable for dense fields. For instance, Evans et al. (2020) report 59%, 45% and 51% of spurious matches in their search for 2SXPS counterparts in 2MASS, AllWISE and USNO-B1.0, respectively. Moreover, recent optical and infrared surveys allow a much more complete census of X-ray counterparts. Besides the catalogues mentioned above, we broadened the search for optical counterparts to the catalogues of optical sources Gaia Early Data Release 3 (EDR3; Gaia Collaboration et al., 2021), Pan-STARRS Data Release 1 (DR1; Chambers et al., 2016), and DES DR1 (Abbott et al., 2018), and to the UnWISE catalogue of infrared sources (Schlafly et al., 2019).

Because of the large sky densities of these catalogues of optical and infrared sources, crossmatches between the X-ray catalog and such catalogues were obtained using the Bayesian crossmatching tool NWAY (Salvato et al., 2018) in two steps, to avoid memory and computation time issues. First we retrieved all counterpart candidates (sources from the second catalogue within 15 arcsec of an X-ray source) with the "CDS Upload X-match" tool in TOPCAT; then, we ran NWAY to obtain all possible associations and their probability. To obtain these probabilities, the sky coverage of each catalogue must be given as input: for the X-ray catalogue, we use the sky coverage values given in Section 3.1. For the second catalogue, it is assimilated to $N_m/N_{tot} \times A$, where N_m is the number of

[3] https://heasarc.gsfc.nasa.gov/cgi-bin/Tools/w3pimms/w3pimms.pl

unique sources kept as counterpart candidates, N_{tot} is the size of the initial catalogue and A is its sky coverage (41253 deg^2 for all-sky surveys, 31512 deg^2 for PanSTARRS, 5255 deg^2 for DES). Other input parameters include the maximum search radius, fixed to 8", the position error of the X-ray catalogue, for which we use the 1-sigma values given for each source, and that of the second catalogue, fixed to its typical value of 0.1" – this has little effect on the output since the X-ray error generally dominates.

NWAY allowed the use of optical (r-band) and infrared (W1-band) magnitudes to refine these probabilities. We kept only associations above a certain probability cutoff defined using the dedicated calibration tool in NWAY, to ensure a spurious match rate below 15% for each catalog. This was done by simulating new X-ray positions (initial positions plus a random offset of up to 1 degree) and performing the crossmatch again. This 15% spurious match rate is a large improvement compared to the associations provided in 2SXPS and 4XMM. When an X-ray source had more than one association, only the most likely was kept. NWAY identified about 8% (4%) of ambiguous multiple associations in the optical (resp. infrared) catalogs.

Distance measurements

As described in Section 2.6, the main types of X-ray emitters have very different luminosity regimes spanning almost 20 orders of magnitude. In order to compute it from the X-ray flux, one has to know the source distance. While distance estimation has been a long-standing problem in astronomy, leading to a succession of methods composing the so-called cosmic distance ladder, here we focus on two widely-accepted distance measurements: parallaxes obtained from the Gaia mission, with its unprecedented accuracy of tens of microarcseconds (Gaia Collaboration et al., 2016), and galaxy distances present in galaxy catalogues.

The parallax-based distance of X-ray sources is directly taken from the nearest (if any) Gaia counterpart found in the previous step. These Gaia sources are matched to the Gaia catalogue of distances for 1.47 billion stars (Bailer-Jones et al., 2021): the `rp_geo` column contains the posterior photo-geometric estimate of the source distance, in parsecs, using a Galaxy model of stellar parallaxes and a model of the distribution of extincted stellar magnitudes.

To search for X-ray source – galaxy associations, we use a recent compilation of large galaxy catalogues, GLADE (Dálya et al., 2018), intended to help locate the origin of gravitational wave events. It is 100% complete in bright galaxies (defined as those accounting for half of the integrated Schechter luminosity function, Dálya et al. 2018) up to 91 Mpc and more than 90% complete at 200 Mpc. It is thus more complete than other widely-used galaxy catalogues, such as HyperLEDA (Paturel et al., 2003) that it includes, or HECATE (Kovlakas et al., 2021) containing about 200000 entries at D<200 Mpc. Unlike more recent versions of GLADE or catalogues of galaxies extending up to larger redshifts, its 2016 version contains information on the extent of galaxies, over 270000 entries at D<200 Mpc and totals nearly 2 million entries up to redshift ~ 0.5. We found that some extended infrared sources from 2MASX (the 2MASS extended source catalogue, Skrutskie et al. 2006), included in GLADE, are actually young stellar objects or diffuse emission from nebular regions in our Galaxy: from a manual inspection of the ones matching an X-ray source, we found that their B magnitude, inferred in GLADE, is generally lower than 14, or that their Gaia colours are distinct from actual galaxies (whose G and BP Gaia magnitudes follow $G - BP > 0$). So we remove the corresponding 2MASX entries. We also remove entries matching a stellar object in *Simbad* within 10 arcsec (typical angular size of the closest young stellar objects), unless they are also categorised as a galaxy. Since the major axis of 2MASX entries is missing in the catalogue, we retrieve the `r_fe` column native of 2MASX. Last but not least, because GLADE is a compilation of catalogues, some duplicate entries are found. We retrieve 6725 such galaxies from a *Sky* internal crossmatch of 10 arcsec. Although their distances in each catalogue are generally close to each other, large differences can occur when the distance is photometrically estimated. In these cases, we favour the distance of HyperLEDA or GWGC (White et al., 2011) over the one of 2MASX, as they are more consistent with each other (Dálya et al., 2018). To remove Galactic globular clusters present in GLADE, where we do not expect the presence of ULX, we limit the sample to distances above 1 Mpc. The resulting galaxy sample is composed of ∼1.7 million galaxies essentially at $B_{mag} < 19$ (median $B_{mag} = 17.3$).

Because it is designed to search for counterparts of gravitational wave events, GLADE contains the distance of all its objects, enabling the computation of the source luminosity. We selected X-ray

sources as soon as their X-ray error circle overlapped with the ellipse representing a galaxy extent (parameterised in GLADE by the galaxy center, a major axis – which is D_{25}, the diameter of the $Bmag = 25.1\,\mathrm{mag/arcsec^2}$ isophote level – a minor axis and a position angle), using the "Sky Ellipses" algorithm in TOPCAT.

GLADE does not contain any information on the galaxy morphology, star-formation rate (SFR) or stellar mass. The latter is however estimated from infrared integrated luminosity in the latest release of GLADE, GLADE+ (Dálya et al., 2022), so we retrieve this column from this catalogue. The Hubble type of galaxies is present in HyperLEDA, so this column is retrieved as well and provides morphology information for ∼460000 galaxies. To get a more complete census of spiral and elliptical galaxies, we cross-correlate GLADE with the catalogue of galaxy morphologies inferred by machine learning on PanSTARRS images (Goddard and Shamir, 2020). As a result, we obtain stellar masses and morphologies for ∼1.5 million and ∼1 million galaxies, respectively. Last but not least, as done in HECATE and introduced by Cluver et al. (2017) (see also Kennicutt and Evans 2012), we cross-correlate GLADE with the WISE catalogue of infrared sources (Cutri and et al., 2012) to estimate the star-formation rate from the W3 magnitude and the galaxy distance. More than 99% of our GLADE subset has a WISE counterpart. This method provides an unbiased SFR (albeit with significant scatter) for late-type galaxies, while the heated dust content generally dominates in early-type galaxies, often leading to an SFR overestimation (e.g. Galliano et al. 2018; Kovlakas et al. 2021).

Reference sample of known sources

In any catalogue of X-ray sources, we expect a wide diversity of source natures, with typically AGN and stars as the most dominant populations. To implement a classification, a sample of reference objects for which this nature is already known is required. Since no such information is provided in 2SXPS, 4XMM-DR11 or CSC2, we cross-correlated them with catalogues of identified AGN, stars and other X-ray source types, as detailed in Table 3.1, in order to build our reference sample. It should be noted that the All-Sky Compiled Catalogue (ASCC) and the allWISEagn catalogue may be contaminated by CVs and stars, respectively, for about 0.4% of their sources, as inferred from matches with *Simbad* sources. The cross-correlation was done through the positional crossmatch algorithm implemented in TOPCAT, using the 3-sigma error for X-ray catalogues and a typical position error for the secondary catalog (0.1 arcsec for catalogues of AGN and stars, and 1 arcsec for other catalogues). For AGN, we combined the catalogs of Véron-Cetty and Véron 2010 (VV10) and Secrest et al. 2015 (allWISEagn). For stars, the ASCC (Kharchenko and Roeser, 2009) catalogue of 2.5 million stars was used, combining several large catalogues of stars. As a compromise between their diversity of signatures and the number counts of each class (which has to be high enough for statistics purpose), we chose to keep only two classes for stellar-mass compact objects, one gathering LMXBs, HMXBs and BHBs into the class "XRB" and the other made up of all kinds of CVs.

The reference sample is made of all these identified sources, after removing the spurious double identifications that happen, for example, in areas of high source crowding. They were identified when present in several catalogues corresponding to different natures. For instance in 2SXPS, 26 potential AGN, 51 potential stars, 29 potential XRBs, and 32 potential CVs were discarded in this process (totaling 69 unique sources).

The resulting samples contain a majority of AGN and stars, and a few percent of XRBs and CVs, as described in Table 3.2.

3.2.3 Sample characterisation

Table 3.2 summarises the main features of our enhanced samples of X-ray sources. The compilation of the three surveys contain 2 188 243 detections of 857 458 unique sources. Adding together the three sky coverage maps, accounting for intersecting fields, this compilation represents 4800 $\mathrm{deg^2}$ of the sky. Figure 3.2 shows the repartition of these sources in the sky, and Figure 3.3 illustrates the distribution of their fluxes in each survey.

Since X-ray catalogues of serendipitous sources represent a compilation of highly inhomogeneous datasets, covering only a biased selection of the sky at a wide variety of exposure times, our final sample of X-ray sources is all but a complete, unbiased census of X-ray emitters. This is visible in the difference of proportions of each type for the three surveys in Table 3.2. Figure 3.4 shows an estimation

Catalogue	Source nature	Number of sources	Sky fraction	Reference
Gaia EDR3	Optical sources	1.81×10^9	100%	Gaia Collaboration et al. (2021)
Pan-STARRS DR1	Optical sources	1.92×10^9	76.4%	Chambers et al. (2016)
DES DR1	Optical sources	3.99×10^8	12.7%	Abbott et al. (2018)
USNO-B1.0	Optical sources	1.05×10^9	100%	Monet et al. (2003)
2MASS	Infrared sources	4.71×10^8	100%	Cutri et al. (2003)
AllWISE	Infrared sources	7.48×10^8	100%	Cutri and et al. (2014)
unWISE	Infrared sources	2.21×10^9	100%	Schlafly et al. (2019)
allWISEagn	AGN	1.35×10^6	–	Secrest et al. (2015)
VV10	AGN	1.7×10^5	–	Véron-Cetty and Véron (2010)
ASCC	Stars	2.5×10^6	–	Kharchenko and Roeser (2009)
Downes 2006	CV	1830	–	Downes et al. (2005)
Ritter 2014	CV	1429	–	Ritter and Kolb (2015)
	LMXB	108		
Liu 2007	LMXB	187	–	Liu et al. (2007)
Kundu 2007	LMXB	638	–	Kundu et al. (2007)
Humphrey 2008	LMXB	1194	–	Humphrey and Buote (2008)
Zhang 2011	LMXB	185	–	Zhang et al. (2011)
Liu 2006	HMXB	114	–	Liu et al. (2006)
Mineo 2012	HMXB	1055	–	Mineo et al. (2012)
Sazonov 2017	HMXB	200	–	Sazonov and Khabibullin (2017)
BlackCAT	BHB	57	–	Corral-Santana et al. (2016)
WATCHDOG	BHB	77	–	Tetarenko et al. (2016)

Table 3.1: External catalogues cross-correlated with our X-ray samples.

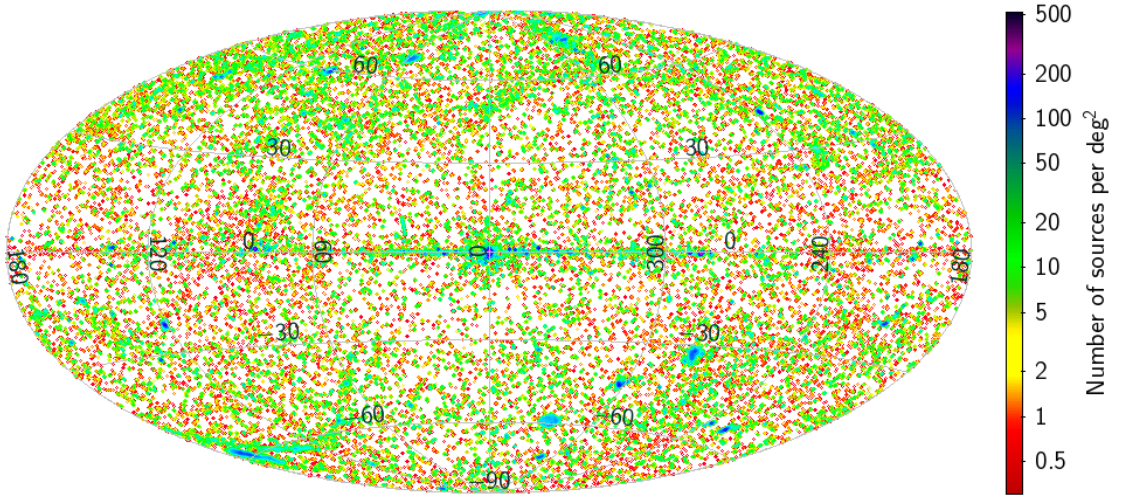

Figure 3.2: The locations, in Galactic coordinates, of X-ray sources in the compilation of our 2SXPS, 4XMM-DR11 and CSC2 samples. The color encodes the sky density of these sources.

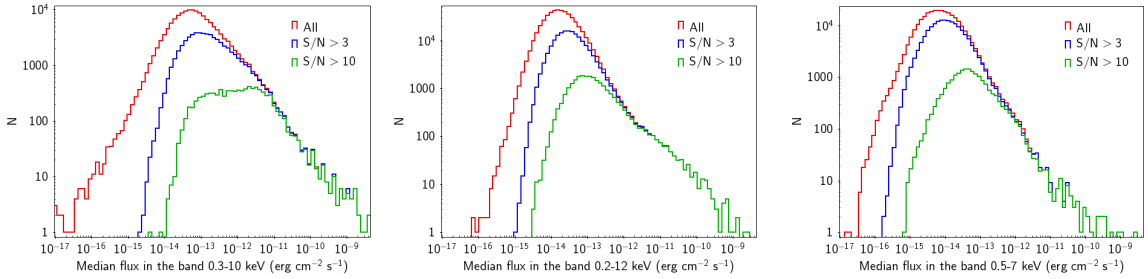

Figure 3.3: Distribution of median X-ray fluxes in the broad band, for the selected subsample of 2SXPS (left), 4XMM-DR11 (middle) and CSC2 (right) point sources. Different signal-to-noise ratio levels are shown.

Sample	2SXPS	4XMM-DR11	CSC2	Compilation
Unique sources (inc. serendipitous[(1)])	148 345 (147 307)	496 645 (493 880)	305 212 (301 441)	857 458
Detections and UL[(2)]	442 038	758 040	1,042 906	2 188 243
% multiple detections	54%	21%	46%	38%
% optical ctp	83%	75%	69%	74%
% infrared ctp	89%	85%	81%	84%
AGN	19670	44680	19959	71164
Star	3821	7910	3024	12836
XRB	316	520	1069	1209
CV	256	243	124	486

Table 3.2: Overview of the final samples. [(1)] i.e. not located in a 10" circle centered on any observed target (or the FOV center for 2SXPS). [(2)] upper limits, present in the CSC2 catalogue.

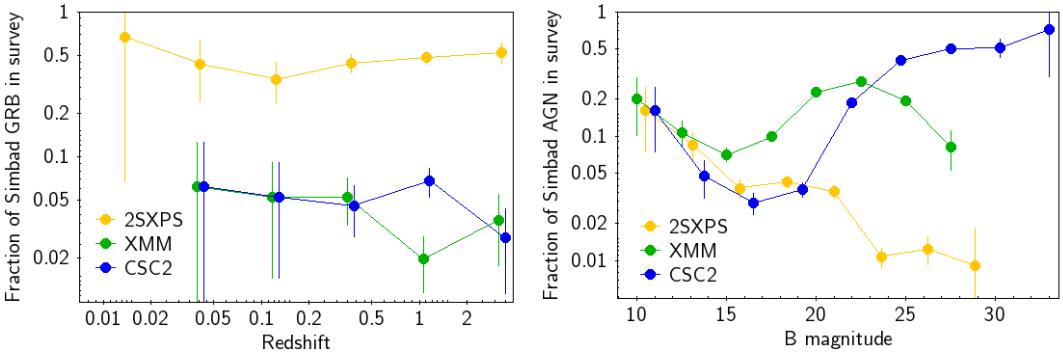

Figure 3.4: Test of completeness of each X-ray survey for two science cases. (Left) Fraction of gamma-ray bursts taken from *Simbad* that are also present in each X-ray catalogue, as a function of their redshift. (Right) Fraction of AGN taken from *Simbad* that are also present in each X-ray catalogue, as a function of their B magnitude.

of the completeness of each X-ray catalogue, in terms of the detected fraction of gamma-ray bursts and AGN found in the *Simbad* database[4]. This illustrates how the *Swift*-XRT survey is biased towards gamma-ray bursts (though they represent less than 1% of 2SXPS), and is less sensitive to fainter AGN. While the brightest, most nearby AGN are equally targeted by each X-ray telescope, there is a visible selection effect at fainter B magnitude: *XMM-Newton* can detect more AGN of medium brightness, due to its large sky coverage and sufficient sensitivity, and it is also more often used to target these objects. On the other hand, the deepest X-ray fields are taken with Chandra, and they have led to the census of some of the most distant AGN.

The various sensitivities of X-ray fields also affects the science that can be inferred from them. In particular, the computation of some observables such as the Cosmic X-ray Background (e.g. Moretti et al. 2003), or the luminosity function of X-ray binaries, ULX and galaxy clusters (e.g. Mineo et al. 2012; Walton et al. 2011; Allen et al. 2003, need a complete sample, so that the contribution of brighter objects is not overestimated. This can be achieved thanks to a cut in flux (or distance) guaranteeing that the selected subset is complete. However, defining a constant cut in all fields leads to the removal of most objects located at higher distances or in more sensitive fields. This cut is most robust and conservative when using the sensitivity map of each X-ray field. For some X-ray surveys, these sensitivity maps are provided when the catalog is published, but this is not the case for 2SXPS and their use can be computationally expensive.

In this study, we estimate the sensitivity F_{lim} for each field, and in particular each galaxy in the sky coverage of each instrument. We use here a data-driven approach, for simplicity and because sensitivity maps are not accessible for all three instruments. For each X-ray catalogue, we infer the flux – exposure time relation from subsets of sources with signal-to-noise close to 3. *Chandra* sources show the highest deviation from a simple power-law model, because a third parameter, the off-axis angle θ, is determinant in the sensitivity value. If we consider an effective exposure time $t' = 2t/max(\theta \text{ (arcmin)}, 2)$, the three X-ray subsets show a ± 0.5 dex deviation from a simple power-law model. The resulting F_{lim} relations are as follow:

[4]http://simbad.cds.unistra.fr/simbad/sim-fsam

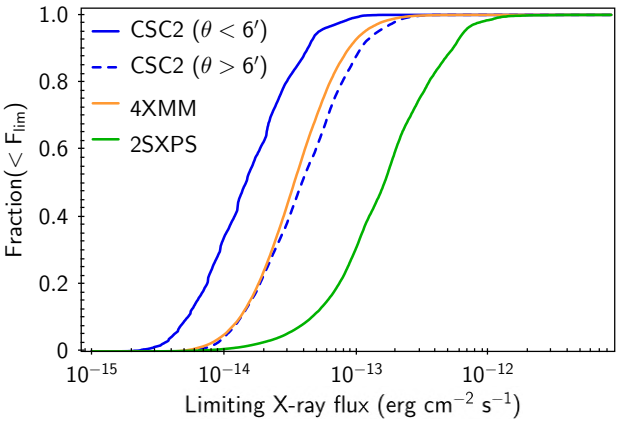

Figure 3.5: Cumulative distribution of GLADE galaxies X-ray 3σ sensitivities, computed from Eq. (3.1) as a function of flux. θ refers to the *Chandra* off-axis angle.

$$F_{lim} = \begin{cases} \left(\frac{1.2\times10^{-15}}{t'}\right)^{0.75} & \text{for CSC2} \\ \left(\frac{1\times10^{-14}}{t}\right)^{0.8} & \text{for 4XMM} \\ \left(\frac{5\times10^{-13}}{t}\right)^{0.8} & \text{for 2SXPS} \end{cases} \tag{3.1}$$

The limiting X-ray sensitivities of Chandra, XMM-Newton and Swift are illustrated in Figure 3.5, showing the cumulative distribution of the limiting X-ray flux for GLADE galaxies in their sky coverage. The difference between on-axis and off-axis *Chandra* galaxies is to be noted. Once applied to X-ray sources matching a GLADE galaxy, the $F > F_{lim}$ cut keeps 70 to 95% of sources with $S/N > 3$ and removes 80 to 90% of sources with $S/N < 3$. This empirical sensitivity can thus be considered as a proxy for the 3σ sensitivity.

3.2.4 Visualisation tool

We manually verified a large number of our selected X-ray sources, which greatly helped to develop and assess the filtering pipeline described above. To this end, we developed a virtual observatory tool based on Aladin Lite and the X-ray catalogues, available at this address: http://xmm-ssc.irap.omp.eu/claxson/xray_analyzer2.php. Our sample can be explored through this interface, as well as some outputs of the X-ray classification described in the next Chapter.

Chapter 4

Classification of X-ray sources

Serendipitous X-ray surveys have been proven to be an efficient way to find rare objects – tidal disruption events, galaxy clusters, binary quasars, etc. As X-ray astronomy slowly enters the era of Big Data, an automated classification of X-ray sources becomes increasingly valuable. As a revised and expanded version of our published article addressing this topic (Tranin et al., 2022), this chapter presents a revisited Naive Bayes Classification of X-ray sources in the *Swift*-XRT, *Chandra* and *XMM-Newton* catalogues which amongst other objects identifies different types of AGN, stars and X-ray binaries – based on their spatial, spectral and variability properties at different timescales and their multiwavelength counterparts. An outlier measure is used to identify objects of other nature. I show the reliability of the method developed and demonstrate its suitability to data mining purposes. As an outlook, I introduce how the very small populations in some object classes can be enlarged using citizen science, with the development of a new platform designed for the classification of XMM sources by volunteers.

4.1 Rationale and previous works

Changing-look active galactic nuclei (AGN), intermediate-mass black hole (IMBH) candidates, supersoft sources, magnetars, super-Eddington accretors, black holes subject to a tidal disruption event... All of these rare objects were serendipitously found in large X-ray surveys (e.g., LaMassa et al. 2015, Farrell et al. 2009, Henze et al. 2012, Zhou et al. 2014, Walton et al. 2011, Lin et al. 2018), illustrating the wide variety of X-ray emitters. Identifying new, rare sources is essential for extending and deepening our knowledge of the high-energy Universe. These populations can then be used to answer questions regarding the hierarchical evolution of galaxies or how the earliest supermassive black holes formed (e.g., Greene 2012). One possible automated way to find such rare objects serendipitously is to search for outliers in the parameter space of the catalogue (e.g., Lo et al. 2014) within the framework of X-ray source classification. X-ray source classification can also be used for population studies, for example to study the X-ray luminosity function of high-mass X-ray binaries (HMXBs; Mineo et al. 2012), to perform quick diagnostics on an object's nature for individual studies, or to spot unstudied objects in unexpected environments (e.g., Lin et al. 2014). Another useful application could be to decontaminate samples of ultraluminous or hyperluminous X-ray source candidates (i.e., sources found in the outskirts of nearby galaxies with an X-ray luminosity higher than 10^{39} erg s^{-1}), such samples often being contaminated by background AGN and/or foreground stars.

In this context, an automated, efficient way to classify X-ray sources becomes increasingly valuable as X-ray catalogues get larger and larger; for example, the recently launched eROSITA X-ray telescope is predicted to detect about a million sources per year (totaling 3 million AGN by the end of the mission; Merloni et al. 2012) and has already detected more than 1 million sources in its first 6 months[1]. Historically, X-ray sources were first classified by hand, either by knowing the nature of the visible counterpart (e.g., for a star) or using empirical laws based on the source properties (extent, location in the sky, flux in different bands and colors, or, when available, variability and spectrum; e.g., Haberl and Pietsch 1999, Prestwich et al. 2003, Pineau et al. 2011). Such a manual classification can be very accurate, but it is also tedious, repetitive, and time-consuming. A first way to automate it has been to apply simple threshold rules to source properties (i.e., quantitative selection criteria organised in a decision tree) to separate the parameter space of the sample under study into classes. This approach is often used to distinguish between source natures, typically stars, AGN, and stellar-mass compact objects (e.g., Lin et al. 2012). Formally, the choice of the criteria and their application order defines a decision tree. While being a simple, transparent, and physics-based classification model, selection criteria are often quite arbitrary and may be too rough to separate classes properly (classes are often blended for some values of the properties). Besides, this method does not properly handle the presence of missing values among the properties that are used.

Machine learning algorithms have been shown to be efficient in automatically classifying X-ray sources, for example the classification of ROSAT bright sources or *XMM-Newton* variable sources (McGlynn et al. 2004, Farrell et al. 2015). For such applications, the random forest algorithm (Breiman, 2001) is often preferred to other methods, such as neural networks or support vector machines, as it seems to show better results (e.g., Arnason et al. 2020) and is theoretically better adapted to X-ray source classification: Indeed, it can be used even with a small number of features (here the source properties) or when they are not normalised, it does not require linearly separable classes, and it is useful even when the training sample is small or unbalanced. In practice, the random forest algorithm consists of the automatic generation of a large number of decision trees similar to the one described above, each trained on a subset of the training sample with a subset of the features (i.e., source properties). Every source is then assigned the most probable identification. Taken individually, each tree performs poorly at classifying sources, but the forest as a whole is able to perform much better. Lo et al. (2014) showed that *XMM-Newton* variable sources could be reasonably classified thanks to different variability features computed from *XMM-Newton* light curves. The classification efficiency is, however, boosted as soon as the classifier takes other data into account, in particular the multiwavelength information obtained via positional crossmatch between *XMM-Newton* and optical or infrared catalogues (Pineau et al. 2017, Salvato et al. 2018). While efficient, this classification was applied to a very small fraction ($< 1\%$) of the 2XMMi-DR2 catalogue (Watson et al., 2009), that is, the variable sources with a good quality flag. Similarly, Lin et al. (2012) considered only the brightest point sources (zero extent and signal-to-noise ratio higher than 20) for their classification, totaling about 2% of 2XMMi-DR3. We still lack a well-established robust classification method to apply to large fractions of X-ray catalogues in order to achieve the full potential of X-ray classification for data mining. Progress has already been made in this direction, for example by Pineau et al. (2009), who showed encouraging results of a classification of about 10000 serendipitous sources from 2XMMi-DR2 (which contains about 220000 sources). After applying a principal component analysis (PCA) to reduce the parameter space, they classified these sources by using either a k nearest neighbors (knn) or a kernel density smoothing approach. They also pointed out two limitations: knn provides discrete class probabilities and does not properly handle a bias in the class proportions of the training sample, while kernel density classification requires a large training sample.

Here, inspired from both approaches, we present a probabilistic method for obtaining a refined classification, revisiting the naive Bayes classification algorithm and using the majority of available spatial, timing, and spectral source properties. The combination of all this information, notably obtained by positional crossmatches with multiwavelength catalogues, is likely to produce a robust classification even for faint, non-variable sources. The choice of naive Bayes is motivated by its intuitive nature, as an extension of the rough classification rules used in simplistic decision trees. This approach is also transparent as it provides a way to get an insight into the reasons for a particular classification (telling which source properties most influenced it), which is not quite possible for algorithms such as

[1] https://www.mpe.mpg.de/7461950/erass1-presskit

random forest.

We first considered the *Swift*-XRT catalogue 2SXPS (Evans et al., 2020), taking advantage of the wide sky coverage of the Neil Gehrels *Swift* Observatory (Gehrels et al., 2004), which also enables the variability to be studied on different timescales. In the literature, unlike the *XMM-Newton* and *Chandra* catalogues, no classification work has addressed the 2SXPS catalogue so far. Besides, a study preliminary to this work (Primorac, 2015) shows that the *Swift* catalogue has an interesting potential for X-ray source classification, with a classification based on selection criteria forming a decision tree with three classes: AGN, stars, and stellar-mass compact objects.

After cross-correlating 2SXPS sources with optical and infrared catalogues, we applied our algorithm: The classification of each source as an AGN, star, X-ray binary (XRB), or cataclysmic variable (CV) is then based on its location, X-ray variability, X-ray spectral features (e.g., hardness ratios), and multiwavelength properties. Most X-ray point sources in our dataset indeed fall into one of these categories, motivating this choice. Special care is given to the treatment of missing values, which are commonplace in any catalogue but can sometimes be used as a piece of information *per se*. We assess the classification performance (retrieval fractions, false positive rates) in various cases, compare it to a random forest algorithm, and finally apply it to the *XMM-Newton* (Webb et al., 2020) and *Chandra* (Evans et al., 2010, 2019) catalogues.

This chapter is organised as follows: In Section 4.2 we describe the data used by the classifier; Section 4.3 presents the classification method and how it was assessed; and various miscellaneous results are given in Section 4.4. The comparison with a random forest classification is made in Section 4.5, which also discusses the method and some results. A complementary approach using citizen science is presented in Section 4.6 as an outlook.

4.2 Data used in the classification

To develop a general-purpose classification of point-like X-ray sources, applicable to the broadest range of science cases, we selected a large fraction of *Swift*-XRT, *XMM-Newton* and *Chandra* catalogues as input, and we complete the source properties with a number of external information. This process is fully described in Section 3.2. Each catalogue is classified separately.

The classifier described in the following uses the reference sample of known sources as a training set to infer the probability distributions of each property for each class. The choice of these properties is thus important, as they typically have to trace intrinsic differences among the source types. They must be contained in previously described catalogue columns, or a combination of them: for instance, `logFratioObs` is built from the list of X-ray detections compiled from the three catalogues, as the ratio of the maximum flux to the minimum flux of a unique source, characterising its variability. `logFrObsMin` is a conservative estimate of this variability indicator, taking into account the flux uncertainties.

The final set of columns used is summarised in Table 4.1.

Short-term variability indicators are made available in several X-ray catalogues, notably the probability that the source under consideration was constant during each of its observations. However, these indicators are generally reliable only for a minority of bright sources and for extreme values, triggering the short-term variability flag (e.g. `SC_VAR_FLAG` in 4XMM-DR11) (e.g. Traulsen et al. 2020; Allak et al. 2022). For these reasons, we choose not to use them in the classification. By contrast, 2SXPS provides the mean and peak count rates among all snapshots, which are useful indicators of short-term variability and are easier to interpret.

As every classification based on a training sample, our model must be applied to a sample of unlabelled sources with similar properties if we want its results to be reliable (the "test sample"). For example, the reference sample has naturally a flux distribution shifted to the bright end compared with the bulk of X-ray sources, because faint sources are often too faint to be identified. While part of our goal is to provide a classifier that can give insight into the nature of the majority of the sources, including the faintest ones, it appears unlikely that the whole catalogue can be classified currently. Note that in this thesis work the classifier will be applied to different test samples, depending on the science case.

We thus selected as first test sample those sources following a certain number of rules: (1) the X-ray source must have a counterpart in an infrared catalog; (2) the X-ray source must have a counterpart

Column	Description	Cat.
b	Galactic latitude	0
PM_Gaia[1]	Proper motion of the Gaia association	0
sepToRadius[1,2]	Separation to the center of the associated galaxy, in units of its radius at the source angle	0
HR1[4]	Hardness ratio from X-ray first and second bands	1
L_Xgal[1,2], L_Xgaia[1,3]	X-ray luminosity from the distance of the association	1
FitPowGamma	Γ of the absorbed power-law spectral fit	1
FitAPECkT	Temperature of the APEC spectral fit	1
IntpPowGamma[5]	Γ from interpolation of HR values	1
IntpAPECkT[5]	Temperature from interpolation of HR values	1
logFxFr[1]	log. of the X-ray to red band[6] flux ratio	2
logFxFw1[1]	log. of the X-ray to W1-band[7] flux ratio	2
logFratioObs[1]	log. of the max to min flux ratio in broad band from X-ray observations[8]	3
logFrObsMin[1]	log. of the ratio $\max(F - F_{err})/\min(F + F_{err})$ among X-ray observations	3
logFratioSnap[1]	log. of the max to mean flux ratio in most variable band from *Swift*-XRT snapshots[9]	3

Table 4.1: Columns of the X-ray samples used in the classification.

The last column gives the category to which the property belongs: 0=location, 1=X-ray hardness and luminosity (hereafter *hardness*), 2=multiwavelength profile (hereafter *multiwavelength*), 3=X-ray variability (hereafter *variability*.
[1] column added during catalogue enrichment. [2] given by the GLADE (Dalya et al., 2016) association. [3] given by the catalogue of Gaia distances (Bailer-Jones et al., 2021). [4] all other available hardness ratios were used, depending on the instrument. [5] Evans et al. (2014) simulated a grid of power-law and APEC spectra and computed their corresponding HR values, so they can infer Γ and kT values from HR measurements. See Evans et al. (2014) for more details. [6] given by the best optical association as explained in the text. The blue band was used likewise to compute a column $\log_{10}(F_X/F_b)$. [7] given by the best infrared counterpart. The W2-band was used likewise to compute 1 extra column. [8] using the compilation of multi-mission X-ray detections described in Section 3.2.2. [9] the soft, medium and hard *Swift* bands were used to compute this column.

in an optical catalog; (3) the X-ray source must have been detected several times, either within the same catalogue or over different catalogues; and (4) the X-ray source must have a signal-to-noise ratio higher than 10 or its spectrum must have been acquired.

Rather than requiring each source of this test sample to follow all four rules, we selected them as soon as they followed at least two of these rules. The number of rules they follow is then stored for later use, to consider several test samples of different quality. However, we do not necessarily expect a better-quality classification for the rare sources following all four rules, because they are similar to very few sources of the training sample on which the classification is based. Consequently the first test sample of each catalogue contain ∼65–80% of 2SXPS, 4XMM-DR10 and CSC2 unlabelled sources.

The requirement of each source to follow two rules is motivated by a case-by-case analysis: a manual classification is relevant, and our algorithm seems to work well as soon as several categories (i.e., variability, hardness, and multiwavelength data) have an information. We suggest that this approach can be considered as necessary and sufficient to build up a test sample, since sources that could be reliably classified and not following at least two rules are rare. This happens, for example, for the few sources that have neither a counterpart nor multiple detections but do have a good spectrum or reliable luminosity values.

When the same selection principle is applied to the reference samples, less than 3% of sources are dismissed.

4.3 Method

In the following we consider a supervised classification method, that is, we assume the existence of a sample of known sources (called the reference sample, or training sample), thanks to which the classification method can be developed and tested.

Our probabilistic classification method can be summarised as follows. First, we estimate a probability density of each class for every property, from the normalised histogram of the same property for identified objects of the reference sample.

Second, these probability densities are used to compute the likelihoods that the source to classify belongs to a certain class *given* each of its properties. When a property value is missing, and if the property is not missing at random, this likelihood is replaced by the probability that a source of this

class has this value missing. It is computed as the frequency of such sources among all known sources of this class.

Third, to compute the probability that the source belongs to the class given its properties, we use the Bayes rule. The likelihood term is here computed as the weighted product of likelihoods given by the previous step: the weights are optimised in such a way to maximise the classification performance of one particular class (XRB in our case).

Fourth, the class giving the higher probability is assigned to this source, and the probabilities of all classes are recorded. Fifth, the classification performance is assessed by cross-validation on the reference sample.

The following sections present an intuitive reasoning leading to this classification, the kernel density estimation (KDE) it needs as input, how it is fine-tuned to maximise its performance for a chosen class, and how it can be evaluated.

4.3.1 Density estimations

One of the prerequisites of the probabilistic model described in Section 4.3.2 is to compute the densities underlying the distributions of each property for each class. A common estimate is to use the histogram of the distribution directly, but this presents a number of drawbacks: The shape of the histogram is highly sensitive to the chosen bin width, leading to spurious features if the bin width is too small compared to the size of the data set or a loss of features if it is too large, but also to the chosen bin phase (i.e., the zero point for binning). Methods exist to infer the optimal histogram bin size (e.g., Izenman 1991); however, they depend on the size of the sample, meaning a different bin size for each class, which can also bias the classification. A much more robust and modern technique to estimate the density functions underlying our sample distributions is the KDE (Sheather 2004). This nonparametric approach offers a great flexibility in effectively modeling probability density functions from a sampled data set, and thus has become increasingly popular (Botev et al., 2010). Basically, KDE consists of computing the estimate of the density f as the sum of contributions of each individual data point, where the "contribution" of a point is a bell-like curve (the kernel) centered on its value:

$$\widehat{f}(x) = \sum_{observations} K(\frac{x - observation}{h}).$$

The kernel was chosen to be exponential, $K(x;h) \propto \exp(-|x|/h)$, as a compromise to detect narrow features while keeping a smooth global density shape. Here, h represents the bandwidth of the kernel: the higher the bandwidth, the smoother the estimate of f, with potential loss of features. The Silverman (1986) rule of thumb, and a manual inspection of our sample distributions and their KDEs, led to us choosing a bandwidth such that $bandwidth = 0.2\Delta x \cdot n^{-1/5}$, where Δx is the range of the values of the property x and n is the number of sources that have a non-missing x value in the reference sample.

To solve the problem of zero probabilities, arising when a source to classify has a property for which the KDE is null, we applied Lidstone smoothing (Raschka, 2017) by adding a constant offset to the corresponding density estimates: for a given property and a given class, this offset was 0.01 times the number of sources belonging to this class and not having this property missing. Another issue was the sparsity of certain property distributions, due to the physical quantity they represent. For instance, the ratio of the X-ray to optical fluxes had to be considered in logarithmic scale to correctly sample the range which can be decades. Other such examples are the spectral fitting parameters; for example, `FitPowGamma` and `FitAPECkT` in 2SXPS have most of their data points in a low-value range (-1 to 10 and 0 to 20 keV, respectively), but some of them have significantly larger values (up to 100 and 64 keV, respectively, due to the spectral fitting algorithm not converging to a proper solution; Evans et al., 2014). These fitted spectral properties were thus considered in logarithmic scale to squeeze their values into a smaller interval.

Figure 4.1 shows four examples of KDEs applied to our 2SXPS data set, on Galactic latitude `b`, `logFxFr`, `HR1`, and `logFratioSnap` (Table 4.1). We see that classes are somewhat efficiently separated by the combination of these four properties. We inspected each output density estimation to avoid any bias: Only the Galactic latitude showed a clear bias for the XRB class, with high isolated peaks corresponding to the latitude of nearby galaxies in which many XRBs were identified. This density was corrected by replacing half of it by a uniform distribution (i.e., proportional to $cos(\mathtt{b})$), to prevent

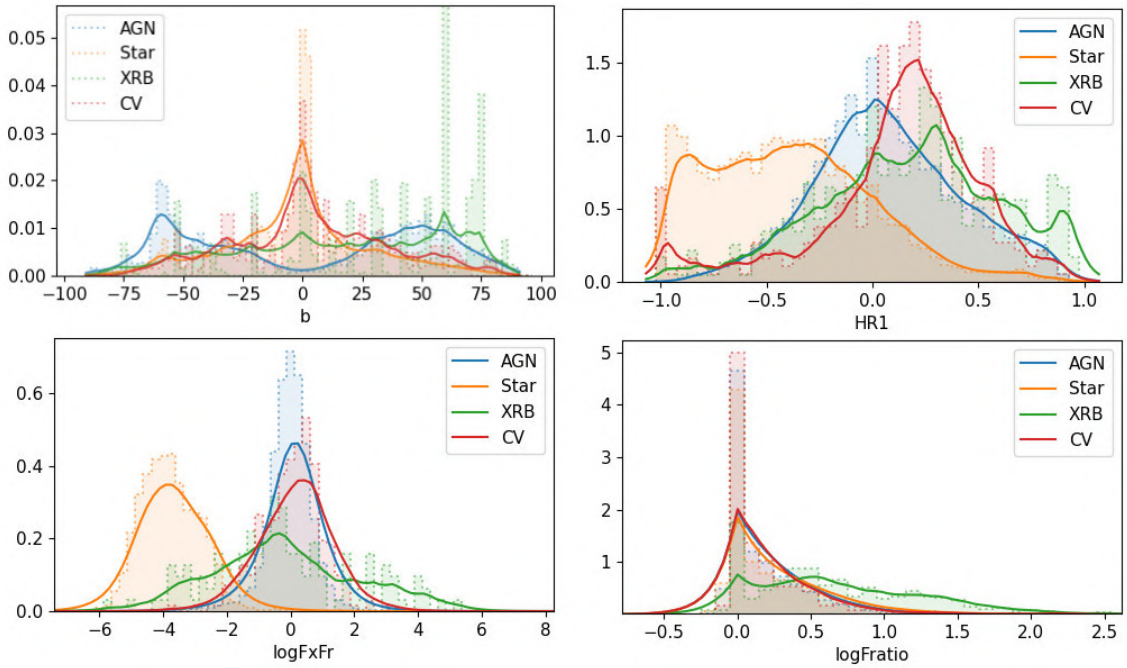

Figure 4.1: Comparisons between the distributions of different properties in the reference sample of 2SXPS and their KDE. From top to bottom, from left to right: Galactic latitude (`b`), hardness ratio between soft and medium *Swift* X-ray bands (`HR1`), X-ray to r-band flux ratio (`logFxFr`), and logarithm of the max over mean flux ratio in the most variable energy band (`logFratioSnap`). The y axis is in arbitrary units.

the classification from giving less credibility to the XRB class when handling extragalactic sources outside these few galaxies. A closer look at the other density estimations we obtained is provided in Figure 4.2, showing 4XMM-DR10 distributions.

4.3.2 Naive Bayes classifier

When dealing with an unknown source we want to classify, the manual way is to compare its properties with prior knowledge (i.e. here the distributions of the reference sample). For instance, we can consider a source with a value of the Galactic latitude `b`$= 50°$ and `logFxFr`$= -3$ (logarithm of the X-ray to optical flux ratio). Assuming we want to classify it either as an AGN or as a star, the `b`-value tends to rule out the stellar nature while the `logFxFr`-value tends to support it (Figure 4.1). In the absence of other information, the choice is then either arbitrary or based on probabilities: The class to prefer is the one that gives the highest density in the `b`–`logFxFr` plane at these coordinates, or the highest product $\mathcal{L}_{\texttt{b}}(50°) \times \mathcal{L}_{\texttt{logFxFr}}(-3)$ if the two properties are considered independent of each other. The density $\mathcal{L}_{\texttt{b}}$ (respectively $\mathcal{L}_{\texttt{logFxFr}}$) is hence considered as the likelihood for the source to belong to a certain class given its `b` (`logFxFr`) value. If we assume then that there are 60% of AGN and 40% of stars in our catalogue, following the Bayes rule with priors $\mathcal{P}(\text{AGN})$ and $\mathcal{P}(\text{Star})$, the probability that this source is an AGN given its data D follows:

$$\mathbb{P}(\text{AGN}|D) = \frac{\mathcal{P}(\text{AGN})\mathcal{L}(\text{AGN}|D)}{\mathcal{P}(\text{AGN})\mathcal{L}(\text{AGN}|D) + \mathcal{P}(Star)\mathcal{L}(Star|D)} \tag{4.1}$$

$$= \frac{0.6\ \mathcal{L}^{AGN}_{\texttt{b}}(50°)\mathcal{L}^{AGN}_{\texttt{logFxFr}}(-3)}{0.6\ \mathcal{L}^{AGN}_{\texttt{b}}(50°)\mathcal{L}^{AGN}_{\texttt{logFxFr}}(-3) + 0.4\ \mathcal{L}^{Star}_{\texttt{b}}(50°)\mathcal{L}^{Star}_{\texttt{logFxFr}}(-3)}$$

$$\approx 15\%,$$

where $\mathcal{L}^{AGN}$ and $\mathcal{L}^{Star}$ are the KDE of the AGN and star distributions shown in Figure 4.1. This is

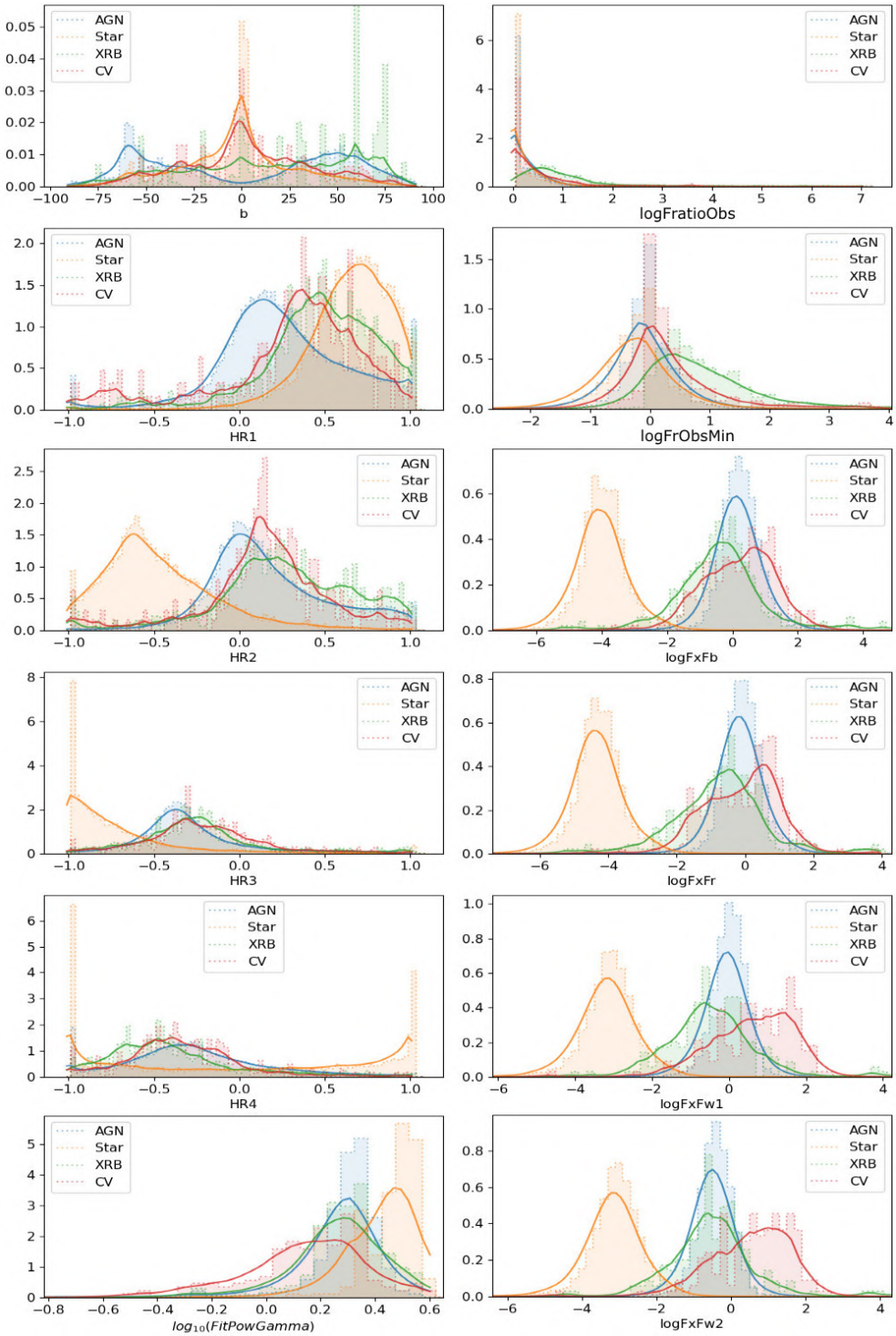

Figure 4.2: Distributions of all properties used in the classification, for the reference sample of 4XMM-DR10, and their KDE. From top to bottom, from left to right: Galactic latitude (b), the four hardness ratios (`HR1, HR2, HR3, HR4`), index of the power-law fit, X-ray variability ratios, and X-ray to other wavelength flux ratios for the optical bands b and r and the infrared bands $W1$ and $W2$. The y axis is in arbitrary units.

basically the concept of a naive Bayes classifier (Murphy et al., 2006). This model was chosen in order to address the issues of classifications based on a decision tree dividing the parameter space with rough classification rules (e.g., Lin et al. 2012), but also to still keep a simple and transparent method. In practice we considered all relevant properties of a source at once and we assigned it the probability to be a star, an AGN, an XRB, or a CV (i.e., the four classes we consider in this work). We used an outlier measure (detailed in Section 4.3.4) to be able to spot sources not belonging to any of these classes. A naive Bayes classifier relies upon the assumption of independent features, which is clearly false if we consider all columns cited in Table 4.1 at once. Any couple of highly correlated features means virtually the double-counting of a feature by the classifier. Therefore, we separated catalogue columns into categories we assumed to be more or less independent: location, hardness ratios, multiwavelength profile and variability, labeled from 1 to 5 in the last column of Table 4.1. Even if these categories are actually not independent, this is corrected by the classification optimisation, done by weighting each category (as detailed below). Thus, the likelihood of the data given a source class c, $\mathcal{L}(data|\mathrm{c})$, becomes

$$\begin{aligned}\mathcal{L}(data|\mathrm{c}) = \mathcal{L}(location|\mathrm{c}) \times \mathcal{L}(hardness|\mathrm{c}) \\ \times\ \mathcal{L}(multiwavelength|\mathrm{c}) \times \mathcal{L}(variability|\mathrm{c})\end{aligned} \tag{4.2}$$

with, for example,

$$\begin{aligned}\mathcal{L}(hardness|\mathrm{c}) =& \mathcal{L}^{\mathrm{c}}_{\mathtt{HR1}}(\mathtt{HR1})\mathcal{L}^{\mathrm{c}}_{\mathtt{HR2}}(\mathtt{HR2}) \\ &\times\ \mathcal{L}(\mathtt{HR1}\text{ present}|\mathrm{c})\mathcal{L}(\mathtt{HR2}\text{ present}|\mathrm{c}),\end{aligned} \tag{4.3}$$

where HR1 (respectively HR2) is the hardness ratio between the soft and medium (medium and hard) energy bands. $\mathcal{L}(\mathtt{HR1}\text{ present}|\mathrm{c})$ is the probability that the value is present given that the source belongs to class c. It is computed as the frequency of such sources in class c of the reference sample. If the source misses HR1 and HR2 values, then $\mathcal{L}(\mathtt{HR}|\mathrm{c})$ becomes

$$\mathcal{L}(hardness|\mathrm{c}) = \Big[\mathcal{L}(\mathtt{HR1}\text{ missing}|\mathrm{c})\mathcal{L}(\mathtt{HR2}\text{ missing}|\mathrm{c})\Big]^{1/2}.$$

When the property p under consideration is missing at random (which is the case of HR1 and HR2 in practice), $\mathcal{L}(p\text{ present}|\mathrm{c})$ and $\mathcal{L}(p\text{ missing}|\mathrm{c})$ do not depend on class c, so this term can be safely replaced by a constant (it is canceled out when computing posterior probabilities).

For data mining purpose, in this context of very unbalanced classes, it is tempting to have a flexible classification, with maximised performance for the class of highest interest. We chose to optimise the classification for XRBs, for the sake of decontaminating extragalactic X-ray sources. Indeed in the hunt for, for example, hyperluminous X-ray source (HLX) candidates (which was the initial motivation of this work), it is valuable to have both a high retrieval fraction and a low false positive rate for XRBs as opposed to their possible contaminants. A fine-tuning of the classification was done by weighting the likelihood of each category by an ad hoc coefficient α as an exponent. Eventually, the probability for the source to belong to a certain class c was computed as

$$\mathbb{P}(\mathrm{c}|data) = \frac{\mathcal{P}(\mathrm{c}) \times \left(\prod_{t\in\{\mathrm{cat}\}} \mathcal{L}(t|\mathrm{c})^{\alpha_t}\right)^{1/\sum_{t\in\{\mathrm{cat}\}}\alpha_t}}{\sum_{C\in\{\mathrm{classes}\}} \mathcal{P}(C) \times \left(\prod_{t\in\{\mathrm{cat}\}} \mathcal{L}(t|C)^{\alpha_t}\right)^{1/\sum_{t\in\{\mathrm{cat}\}}\alpha_t}}, \tag{4.4}$$

where the priors $\mathcal{P}$ of AGN, stars, XRBs, and CVs are set to 66%, 25%, 7%, and 2%, respectively (see e.g. Lin et al. 2012; McGlynn et al. 2004; Farrell et al. 2015 for various samples of classified X-ray sources expected to be comparable with our samples at least to some extent). These values are important for classification results, and this choice is based on a rough approximation of the proportions we

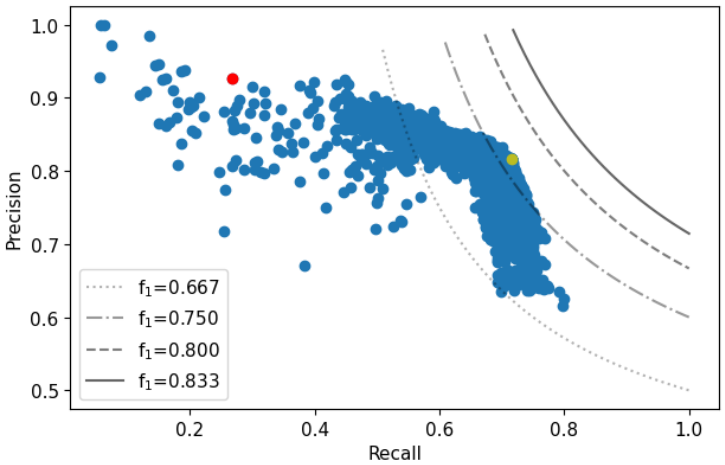

Figure 4.3: *precision* versus *recall* of the classification run at each iteration of the differential evolution algorithm. Contours of the f_1 score are shown for reference. The algorithm converges to the point closer to the contour $f_1 = 0.92$. The red and green dots correspond to the first and last iterations, respectively.

can expect in a standard X-ray catalogue (e.g.). In practice, priors put more stringent constraints for an object to be classified as a rare type: it is thus a way to avoid high false positive rates, at the expense of the *recall* rates.

4.3.3 Fine-tuning of the method

We optimised our classification to maximise its performance regarding the XRB class: coefficients α_t of Equation 4.4 are tuned to maximise the f_1 score of this class, namely, $f_1 = 2(recall^{-1}+precision^{-1})^{-1}$, where *recall* is the fraction of actual XRBs retrieved as XRBs by the classification algorithm, and *precision* is the fraction of true positives among the sources classified as XRBs. To properly estimate *precision*, the classification was performed on a reference sample with realistic proportions (i.e., the ones we used as priors in Equation 4.4). Such an optimisation is theoretically motivated by the fact that some categories of properties have more discriminant power than other. Moreover, if two categories are strongly correlated (for example if we consider hardness ratios and spectral fitting properties in two separate categories), the Bayes classifier assumption of independence will lead to the double count of such properties (they will be considered as overly important): setting coefficients α_t to an optimal value is a solution to this issue.

For this optimisation, random sets of coefficients were uniformly generated in the range $0 - 10$ for each α_t, the classification was run on a properly proportioned reference sample (i.e., a subset respecting the proportion of each class) and the f_1 score was computed. We made use of a differential evolution algorithm (Storn and Price, 1997) to derive the best set of coefficients: this optimisation method available in Scipy 1.4.1 has the advantage that it does not require the problem to be differentiable and to probe a very large space of coefficient solutions. Besides, it is barely limited by the potential presence of local minima. We saved the coefficient set at each iteration of the algorithm for manual validation, and to gain insight into the *precision–recall* compromise arising when fine-tuning our classification model.

The final coefficients after convergence of the algorithm are shown in Table 4.2. Interestingly, the most decisive properties are the ones from the "location" category: this is physically meaningful since our classification is optimised for XRBs, which overlap many of the AGN properties, but can be roughly separated using their location inside the hosting galaxy and their luminosity.

Another result shown by Figure 4.3 is that the choice of weighting coefficients is always a trade-off between *recall* and *precision*: Some sets of coefficients can have fewer false positives among sources classified as XRBs (e.g., only 10%), but they will be unable to correctly retrieve the majority of XRBs. Conversely, some known XRBs seem to be never retrieved by any choice of coefficients: they were manually inspected to try to understand the reasons for that limitation. This is detailed in Section

2SXPS	
Parameter	Value
Priors $\mathcal{P}$ (AGN, star, XRB, CV)	0.66, 0.25, 0.07, 0.02
Coefficient α_{location}	8.8
Coefficient α_{hardness}	7.3
Coefficient $\alpha_{\text{multiwavelength}}$	2.1
Coefficient $\alpha_{\text{variability}}$	3.9
4XMM-DR10	
Parameter	Value
Priors $\mathcal{P}$ (AGN, star, XRB, CV)	0.66, 0.25, 0.07, 0.02
Coefficient α_{location}	7.5
Coefficient α_{hardness}	3.2
Coefficient $\alpha_{\text{multiwavelength}}$	2.0
Coefficient $\alpha_{\text{variability}}$	6.0
CSC2	
Parameter	Value
Priors $\mathcal{P}$ (AGN, star, XRB, CV)	0.66, 0.25, 0.07, 0.02
Coefficient α_{location}	8.2
Coefficient α_{hardness}	7.5
Coefficient $\alpha_{\text{multiwavelength}}$	4.3
Coefficient $\alpha_{\text{variability}}$	8.0

Table 4.2: Parameters of the classifier after optimisation.

4.4.2, as well as the study of XRB false positives.

4.3.4 Outlier measure

Some objects do not belong to any of the classes mentioned above. Such objects can have anomalous X-ray and multiwavelength properties, in the sense that they lie outside the bulk of the distributions of AGN, stars, XRBs, and CVs. Alternatively they can have no class consistent with all their properties at once. We implemented an outlier measure to identify some of them: It consists of minus the logarithm of the product of likelihoods for the predicted class c (Equation 4.5). The lower the property distribution of the output class c at a given property value, the lower $\mathcal{L}(t|\mathrm{c})$ (where t is the category of the considered property) and the higher the outlier measure:

$$O.M. = -\log\left(\mathcal{P}(\mathrm{c}) \times \prod_{t\in\{\mathrm{cat}\}} \mathcal{L}(t|\mathrm{c})^{\alpha_t / \sum_{t\in\{\mathrm{cat}\}} \alpha_t}\right) \tag{4.5}$$

4.4 Results

To evaluate our classification method, we used two approaches: First, we looked into common classification metrics obtained from the reference sample. Then, we analysed the results obtained on the test sample, in terms of proportions and property distribution of each predicted class.

The most direct way to visualise classification results is by looking at the table showing the number counts of each output class for each input class, called the confusion matrix. A classifier is also characterised by its ability to retrieve most objects from each input class (*recall*) and to limit the number of false positives in each output class (*precision*). If the classifier is used to select a subset of a given type, *recall* and *precision* will translate into completeness and purity, respectively.

The f_1 score is often used to combine these two measures (e.g., Lukic et al. 2018), and the average of f_1 scores over all classes summarises the classifier performance in a single number. While these metrics may be difficult to interpret, they still can be compared to baselines such as their values for a "random guess" classifier or the classifier choosing always the largest class. Usually, the reference

Truth →	AGN	Star	XRB	CV	Total cl.
→AGN	19515	82	25	191	19813
→Star	44	4628	3	27	4702
→XRB	140	18	326	17	501
→CV	9	9	2	124	144
Total	19708	4737	356	359	Average
recall (%)	99.0	97.7	91.6	34.5	80.7
precision (%)	97.0	98.6	90.7	85.5	92.3
f_1 score	0.980	0.981	0.911	0.492	0.841

Table 4.3: Confusion matrix and metrics of the classification applied to the reference sample of 2SXPS.

The first four rows show the number counts of objects classified as AGN, stars, XRBs, and CVs, respectively. The last three rows give the *recall* rate, the true positive rate (*precision*), and the f_1 score associated with each class, and those averaged over all classes are given in the last column.

sample is split into a training sample on which the classifier is built (i.e., the KDEs here) and a validation sample on which it is assessed. This is useful for methods subject to important overfitting of the reference sample (e.g., neural networks). We preferred to use all the reference sample for training, since nonrepresentative features are smoothed during the KDE process. The classification was also assessed on the reference sample, computing *precision* values with a formula calibrated to reflect a sample that has the same class proportions as the priors (which is supposed to be the case in the test sample), namely

$$precision(AGN) = \frac{N_{AGN\to AGN} \times \mathcal{P}(AGN)/f_{AGN}}{\sum_{C\in\{\text{classes}\}} N_{C\to AGN} \times \mathcal{P}(C)/f_C}, \tag{4.6}$$

where f_C is the frequency of class C in the reference sample, and $N_{C\to AGN}$ is the number of sources of class C that were classified as AGN.

Regardless of the classification performance on the reference sample, it is crucial to study its results on the test sample of unknown sources, in order to characterise its biases. This is possible, for example by looking at some individual sources and comparing the classifier result to the one inferred from a manual analysis, or by comparing the statistics of output classes with the ones of the reference sample. For instance, the property distributions for each output class should be consistent with the KDEs. The results of these tests on the classification of test samples are summarised in Section 4.4.2.

4.4.1 Training sample

When applied to the 2SXPS reference sample, composed of 19708 AGN, 4737 stars, 356 XRBs, and 359 CVs, the optimised classification (i.e., the one using the best set of coefficients as described in Section 4.3.3) returns 19813 classifications as AGN, 4702 as stars, 501 as XRBs, and 144 as CVs; 97.7% of these classifications agree with the source class (96.9% when computed on a sample with the same class proportions as the priors), although this percentage varies a lot with class. To visualise the classification results in greater detail, we compute the confusion matrix and the metrics introduced before: Table 4.3 shows that the classification performs best on AGN and stars, is reasonable for XRBs and quite poor for CVs, giving lower retrieval fractions and higher false positive rates. The *precision* rates in Table 4.3 are computed using Equation 4.6.

From Table 4.3, we get the average f_1 score of 0.841. This is considerably better than the two naive baselines: a random-guess classifier would have an average f_1 score of 0.190 and a classifier that always chooses the largest class (AGN), 0.199.

Unlike a random forest method (Sect. 4.5), our model gives insight into the motives of each classification, through the likelihoods of each class for each property. This asset that we call "classification interpretability" will be used in the following to constrain as much as possible the classification performance and biases.

To begin with, we analysed the population of XRB false positives, and about 30 of them by manual inspection. These 175 sources wrongly classified as XRBs mainly consist of AGN (140), the rest being

Truth →	AGN	Star	XRB	CV	Total cl.
→AGN	18373	25	46	149	18593
→Star	15	6197	10	12	6234
→XRB	80	12	479	10	581
→CV	4	0	8	81	93
Total	18472	6234	543	252	Average
recall (%)	99.5	99.4	88.2	32.1	79.8
precision (%)	97.2	98.9	93.7	84.6	93.6
f_1 score	0.983	0.991	0.909	0.466	0.837

Table 4.4: Same as Table 4.3, but for the reference sample of 4XMM-DR10.

Truth →	AGN	Star	XRB	CV	Total cl.
→AGN	19688	15	139	37	19879
→Star	103	2990	15	10	3118
→XRB	141	4	890	1	1036
→CV	27	15	25	76	143
Total	19959	3024	1069	124	Average
recall (%)	98.6	98.9	83.3	61.3	85.6
precision (%)	97.6	97.6	91.9	76.4	90.9
f_1 score	0.981	0.982	0.874	0.680	0.879

Table 4.5: Same as Table 4.3, but for the reference sample of CSC2.

CVs (17) and stars (18). We note that 29% of them are actually misclassified by a narrow margin (there is less than 20% difference between the XRB probability and the probability of the correct class). Then after manual inspection, it appears that the reasons for misclassification as XRBs are diverse: primarily (in 60% of them), a peculiar spectrum (either too soft or too hard, or a computed luminosity in the XRB range) played an important role. About 30% presented a rather unexpected variability (typical flux ratio of 10), hence mimicking the variability of many XRBs. Figure 4.4 shows illustrations of these reasons for two typical false positives: for the source 2SXPS J095636.3+690027, which is associated with SDSS J09566+6900, a well-known quasar from Véron-Cetty and Véron (2010), we see that the X-ray luminosities are responsible for the high XRB probability given by the classifier. Because it is located 40 arcsec away from the center of M81, it was wrongly associated with this galaxy and thus its first X-ray luminosity (1.2×10^{38} erg s^{-1}) was wrongly computed. The second X-ray luminosity (1.5×10^{32} erg s^{-1}) is wrong as well, since it stems from a distance of 4 kpc given by the Gaia counterpart, as put in the catalogue of stars of Bailer-Jones et al. (2021). Regarding 2SXPS J125801.1+013431, the probability "track" (left panel) shows that its variability properties are responsible for its classification as an XRB, which is confirmed by its light curve (top right panel): Its flux varied by more than two orders of magnitude over 6 years, which is explained by the tidal disruption of a super-Jupiter (Nikołajuk and Walter, 2013). Some other XRB false positives consist of unusual objects (like AGN of low luminosity (in particular Seyfert-2) in close galaxies where the stellar bulge dominates optical emission, or absorbed distant AGN).

We also analysed in each class the sources not retrieved in their class by the classification, and about a hundred of them were manually inspected. For example, 30 XRBs are missed by the classification. They consist of 25 objects classified as AGN, 3 as stars, and 2 as CVs. Many of them (35–40%) were simply not variable enough during the X-ray detections to be classified as XRBs. Similarly, 35% have a low classification margin and would be classified as XRBs if the prior value of XRBs (7%) was somewhat higher. Another ∼25% actually have dubious identifications, and the catalogues used to form the training sample may not be trusted for these objects (e.g., some X-ray sources seemingly hosted by a galaxy and hence considered as XRBs, but also present in a catalogue of quasars). The rest (5-10%) are generally extragalactic XRBs in a globular cluster for which the multiwavelength counterpart is the whole cluster.

Likewise, 109 stars are wrongly classified as AGN (82), XRBs (18), or CVs (9). They most often consist of particularly variable types of star (eclipsing binaries, young stellar objects, etc.), X-ray sources harder than typical stars or sources with a very low proper motion (few mas/yr). A few of

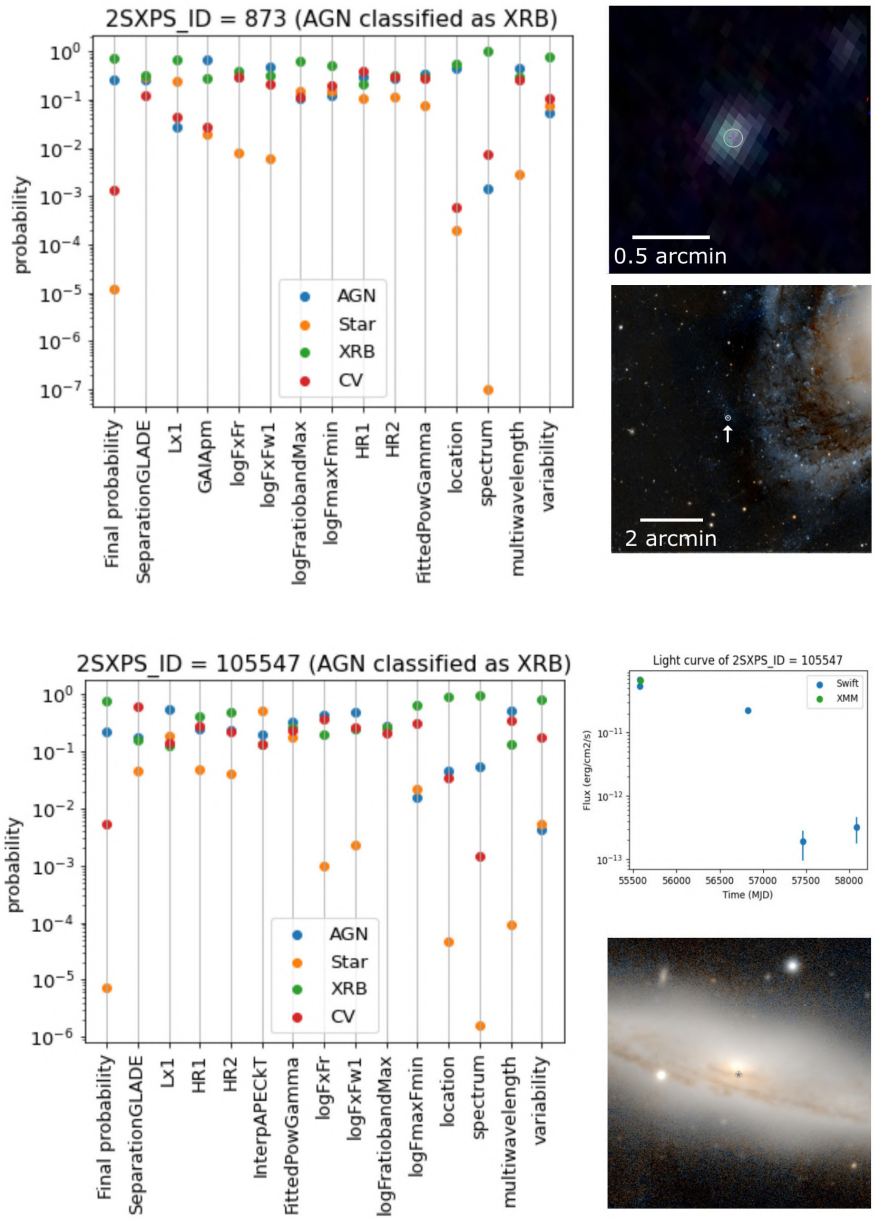

Figure 4.4: Two examples of XRB false positives. (Top) 2SXPS J095636.3+690027, a known AGN located a few arcminutes from M81. The left panel shows the probability "track", i.e., the likelihoods of each class computed as a function of the properties of the source and then used by the classifier to compute the posterior probabilities of each class (Equations 4.3 and 4.4). The top-right panel shows the XMM-EPIC image of the region, the *Swift*-XRT source location, and its error circle (reticle and gray circle). The bottom-right panel shows the Pan-STARRS image of the region and the *Swift* source location. (Bottom) 2SXPS J125801.1+013431, the central X-ray source of NGC 4845, known to host an AGN. The left panel shows the probability track, the top-right panel shows the X-ray light curve from the *Swift* and *XMM* detections, and the bottom-right panel shows the Pan-STARRS image of the galaxy and the location of the X-ray source (gray circle).

them (∼10%) are actually not stars, but HMXBs or distant Seyfert 1 galaxies according to *Simbad*.

Regarding the 235 CVs not retrieved by the classification, the misclassification seems often to be due to a lack of follow-up by X-ray observatories, or the fact that we did not characterise the light curves of single observations, so that little to no variability is detected. In particular novae are often classified as AGN (in about 60% of cases) because their X-ray hardness and multiwavelength profile are compatible with this type, which is favoured by the priors. Some types of CVs are more easily retrieved, such as polar CVs (AM Her, more than 75% retrieval).

Still, about 85% of missed CVs would have been classified as CVs if equal priors had been applied.

In 4XMM-DR10, the manual analysis of 30 XRB false positives showed that the majority of them (83%) overlap the extent of a galaxy, and hence have wrong values of X-ray luminosity and a misleading location, and 40% showed an unexpected multi-instrument variability – either physical or due to a difference in flux computation method (spectral fitting for bright Swift sources, fixed spectrum for XMM sources). Therefore, sources wrongly classified as XRBs are not misclassified for the same reasons as in 2SXPS: Fewer are primarily misclassified due to an unexpected variability, whereas more misclassifications coincide with the proximity of a galaxy. This may be due to the fact that galaxies are more often targeted by *XMM* pointings than by *Swift* pointings.

Analysing the 146 XRB false positives in the reference sample of CSC2 revealed a majority of galaxy nuclei of low luminosity (7 out of 10 have a luminosity lower than 10^{40} erg s^{-1}). The high sensitivity of *Chandra* is responsible for this high number of detected low luminosity AGN, that are non-representative of other AGN in the reference sample. Likewise, 21 of them are identified as Seyfert 2 AGN in *Simbad*, making them kind of outliers in the reference sample (Sect. 4.4.3).

A sample of so-called XRBs un-retrieved by the classification was also analysed, showing results comparable with the study on *Swift*: un-retrieved XRBs are primarily missed when they vary little between observations or when their multiwavelength ratios are consistent with an AGN. Still, about 65% of the sample would have been classified as XRBs if the XRB prior was somewhat higher. A substantial fraction (about 15%) of the sample was found to be dubious XRBs (i.e., background AGN or foreground stars contaminating the XRB reference sample).

Once applied to the 4XMM test sample of 345,000 sources, the classifier gives ∼270000 AGN (78%), ∼66000 stars (19%), ∼8200 XRBs (2.4%), and ∼1700 CVs (0.5%). These proportions are in good agreement with those obtained on the *Swift* test sample.

A closer look at sources classified as XRBs in the test sample confirmed 45% of them as being reliable and 30% as false positives with misleading data (e.g., variable AGN or AGN in the background of a galaxy); another 10% have data quality issues (e.g., a wrong optical counterpart, a spurious variability in the multi-instrument light curve or an X-ray source being actually the confusion of two distinct sources), and ∼15% are objects of another type (not AGN, stars, XRBs, or CVs, in particular young stellar objects). As expected, sources classified as AGN and stars in the test sample are more reliable: about 95% and 99% of the ones analysed manually (about 200) prove to be reliable candidates.

4.4.2 Test sample

The same classification model was applied to the 2SXPS test sample, composed of the ∼113000 unknown sources following two or more of the quality rules defined in Section 4.2. As a result we obtain 93000 objects classified as AGN (82%), 16000 as stars (14%), 4300 as XRBs (4%), and 321 as CVs (0.3%), which is globally consistent with the priors, with some discrepancies for the stellar and CV types.

The first one may be explained by an overestimation of the prior proportion of stars, while the low number of objects classified as CVs in the test sample can be explained by the CV prior being low and the reference sample being heterogeneous for this type. But also, since the classification was not optimised on this type, its retrieval is not maximised.

As expected, these proportions change with the number of quality rules followed by the sources: on the (inappropriate) test sample of unknown sources following one rule, 94% of them are classified as AGN. However, the proportions of each output class among sources following at least two quality rules seem to be rather independent of the number of followed rules.

In order to assess the results of the classifier on the test sample, we did three different studies: a manual inspection of a sample of unknown sources, an analysis of the property distribution of each

output class, and a comparison between the *Swift*, *XMM* and *Chandra* classifications.

We examined a randomly selected sample of 205 sources present in both *Swift* and *XMM* catalogues. This was done for simplicity, in order to compare both *Swift* and *XMM* classifications to the manual identification; however, this may introduce a bias toward often-pointed fields, in particular nearby galaxies. For each source, the multiwavelength images, X-ray spectrum, X-ray light curves (both within an observation and between observations) and potential *Simbad* identification were carefully inspected to infer a classification. We identified 134 AGN, 33 stars, 29 XRBs, 1 CV (confirmed by *Simbad*), and 8 objects of other nature (2 pulsars, 5 young stellar objects, and 1 supernova remnant, according to *Simbad*).

Then we classified them a second time using the classifier trained on the *Swift* reference sample, and a third time using the classifier trained on *XMM*.

Overall, among the 197 objects identified in one of the 4 classes, 86% of *Swift* classifications and 84% of *XMM* classifications agree with the manual analysis. In greater detail, the *Swift* classifier retrieves 94% of AGN, 76% of stars, 61% of XRBs, and the CV, whereas the *XMM* classifier retrieves 91% of AGN, 73% of stars, 64% of XRB, and also the CV. The false positive rates of AGN, stars and XRBs, are about 10%, 5%, and 30%. The *Swift* and *XMM* classifiers agree in 87% of the cases, and when the result differs it is in most cases due to a low or unreliable X-ray flux in one of the catalogues. An example of an XRB candidate given by all these classification methods, and unknown in the literature, is shown in Figure 4.5. 2SXPS J151604.0+561614 (4XMM J151604.0+561615) has a flux of about 2×10^{-14} erg s^{-1} cm^{-2} and a computed probability to be an XRB of about 98%, because it has no detected counterpart in optical or infrared and a pretty high variability (it varied by a factor of $\sim$6 in 2 weeks). Its mean observed X-ray luminosity (0.3–10 keV) is about 3×10^{38} erg s^{-1}, which is well in the XRB range.

The same analysis was performed on 120 *Chandra* classifications to compare them with *XMM-Newton* ones. We manually identified 81 AGN, 16 stars, 17 XRB, 5 YSO and a white dwarf (according to *Simbad*). Among the 106 objects identified as AGN, star or XRB, 91% of *Chandra* and *XMM-Newton* classifications agree with each other. This is particularly the case of AGN ($\sim$95% agreement). As a possible cause of this disagreement, among the ten disagreeing classifications, eight have more than a factor 2 difference between *Chandra* and *XMM* source fluxes, including four sources >10 times brighter in *XMM* than in *Chandra*. As suggested by Table 4.3 and 4.5, *XMM* classifications seem to be slightly more reliable than *Chandra* ones, with 92% (resp. 85%) of agreement with manual classification in this sample.

Another way to verify the self-consistency of the classification model is to statistically compare the populations of each class in the reference sample to their twin as given by the classification. Figure 4.6 shows such a comparison applied to four source properties. While all these properties show a good overall agreement, especially `HR1` and `logFratioObs`, some discrepancies are visible in the `b` and `logFxFr` panels: There is a peak of sources classified as AGN near `b`= 0°, and the star and CV distributions of the X-ray to optical flux ratio are shifted to higher (resp. lower) values. One can interpret these discrepancies as the result of two factors: biases in the reference sample (selection effects), and biases in the classification process. Indeed, the peak of `logFxFr` at very low values for reference sample stars is probably a selection effect of nearby stars, which are all well catalogued, while more distant stars at these `logFxFr` fall below the sensitivity limit of the X-ray telescope (and thus are not detected). Low-mass stars, having higher `logFxFr` values, were also identified by more recent surveys absent from the ASCC catalogue. Likewise, AGN behind the galactic plane are under-represented in the literature (e.g., Truebenbach and Darling 2017), and therefore also in the reference sample: this explains part of the 0° peak of sources classified as AGN, being actual AGN. After inspection of *Simbad* counterparts (about 10% of this AGN peak), the rest seem to mainly consist of outliers (young stellar objects, stars that are harder than typical stars of the reference sample) and XRBs and CVs with properties in the AGN range and misclassified because of the priors. Last but not least, the shifted `logFxFr` peak of CVs is probably the result of these priors since sources in the bulk of the original peak have much more of a chance of being classified as AGN.

We also compared the results of *Swift*, *XMM* and *Chandra* classifiers to a sample of X-ray sources of good quality and present in two of these catalogues. This sample consisted of sources detected on a multi-mission basis, following at least two quality rules in each catalogue, and having reasonable quality flags – *Swift*: `detflag`$\leq$ 1, `fieldflag`$\leq$ 1, *XMM*: `SC_SUM_FLAG`$\leq$ 1, *Chandra*: `conf_flag`= 0, `extent_flag`= 0 – (66667 sources at this stage), with the additional constraint of having the same

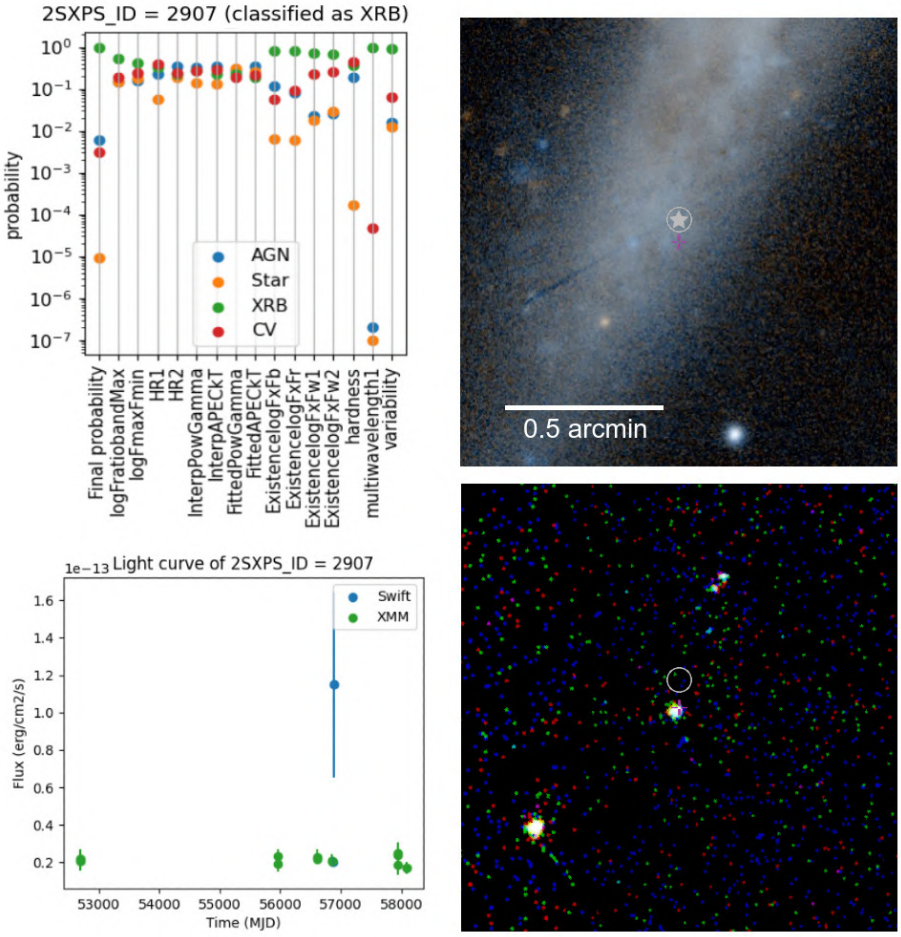

Figure 4.5: 2SXPS J151604.0+561614, an XRB candidate found in NGC 5907 by the classifier. Top left: Probability track showing the likelihood of each class as a function of the source property. Bottom left: *Swift* X-ray light curve (0.3-10 keV) and *XMM* (0.2-12 keV) observations. Bottom right: X-ray image from *Chandra*; the *Swift* location and position error are pinpointed by the gray circle. Top right: Optical image from Pan-STARRS; the *Swift* location and position error are pinpointed by the circled star.

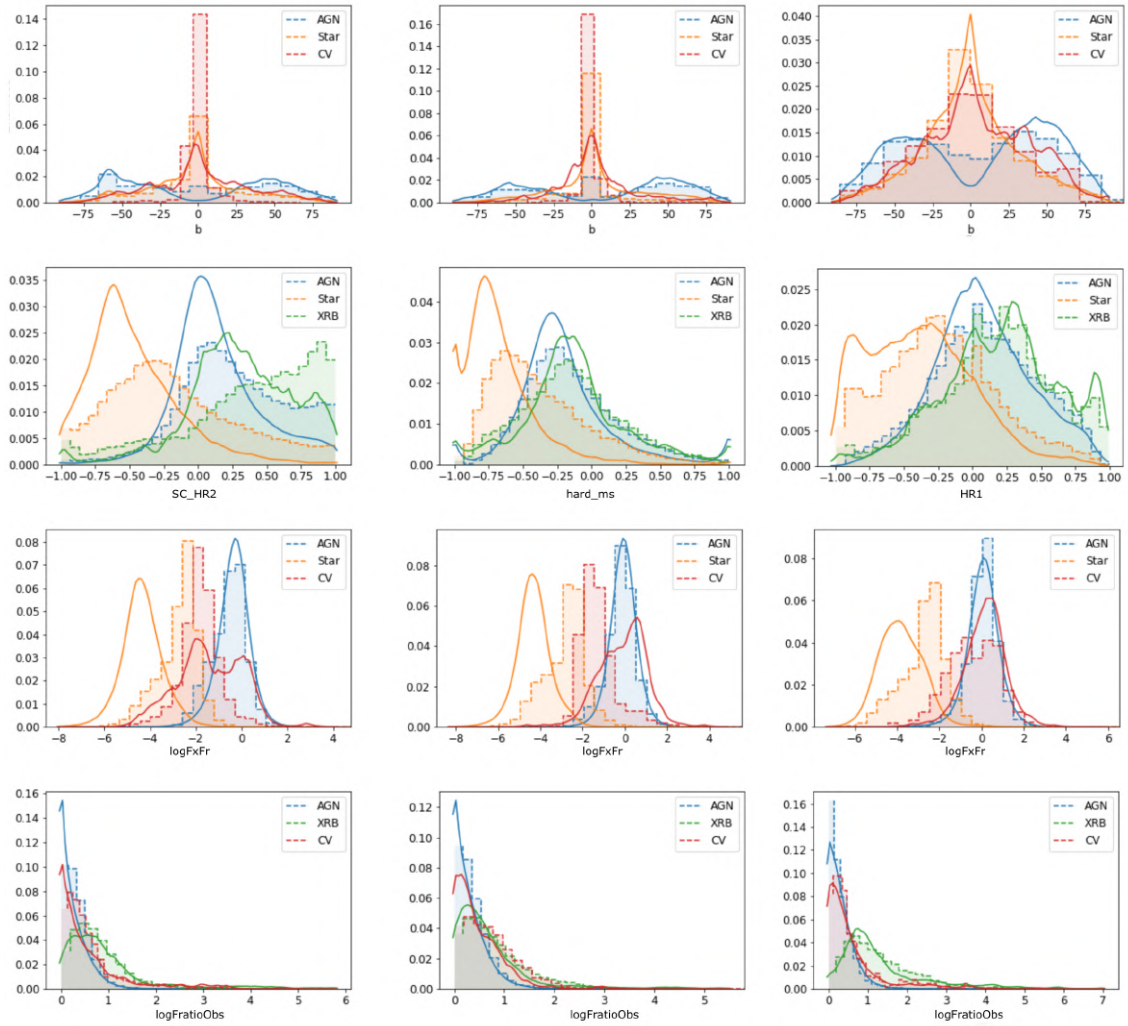

Figure 4.6: Comparisons between the distributions of different properties in the test sample and their KDE (solid line). Left column: CSC2 sample, middle column: 4XMM sample, right column: 2SXPS sample. From top to bottom, Galactic latitude (`b`), hardness ratio between a soft and a medium X-ray bands (`hard_ms`, `SC_HR2`, `HR1`), X-ray to r-band flux ratio (`logFxFr`), and logarithm of the max-to-min flux ratio among X-ray observations (`logFratioObs`). The y axis is in arbitrary units. In some panels, only three classes are shown, to ease the graph readability. Classes not present have distributions consistent with their KDE.

optical and infrared counterparts (60543 sources). Depending on the catalogue under consideration, the classifier returned ∼76–77% of AGN, 16–18% of stars, 3–7% of XRBs, and 0.5–2% of CVs. As a result, at least two classifiers agree in 91% of cases, in particular on AGN classifications (96%), then stars (83 to 88%), then XRBs (40 to 70%), and finally CVs (20 to 40%). The 3547 sources present in all three catalogues have agreeing classifications in 80% of cases. Among all three classifiers, *Chandra* and *Swift* have the smaller agreement rate (85%). The causes of differing classifications are diverse, but we note the following trends: They can occur when the candidates have ambiguous classifications ($\sim 60\%$ of such cases have a final probability of the selected class lower than 65%), when median X-ray fluxes highly differ between *Swift*, *XMM* and *Chandra* (factor of > 3 difference in $\sim 33\%$ of sources), and when two categories suggest two different classifications. In the last case the difference is thus due to the three versions of weighting coefficients resulting from the optimisation, leading e.g. the *XMM* classifier to a higher XRB retrieval fraction at the expense of the XRB false positive rate.

4.4.3 Outliers

By construction, the classifier we built has to choose a class for every object from a small selection (here AGN, stars, XRBs, and CVs). Some X-ray sources do not belong to any of these classes (e.g., spurious sources, X-ray transients, galaxy clusters, supernova remnants) and their classification will thus be misleading. However, some of these outliers may be retrieved by analyzing their outlier measure (as defined in Section 4.3.4).

This approach has already been carried out in the work of Lo et al. (2014): they considered a source as being anomalous if its classification margin (i.e., $2\mathbb{P}(\mathrm{c}|data) - 1$ where c is the preferred class and $\mathbb{P}$ is the output probability) was less than -0.3, or if its outlier measure - not the same as the one we used - was greater than 10. As a result they obtain mainly sources with data quality issues, but also an interesting HLX candidate.

Figure 4.7 shows the distribution of the outlier measure for different subsets of 4XMM-DR10 sources. AGN false positives (in red in the first panel) tend to have a higher outlier measure than actual AGN, due to some of their properties differing significantly from the bulk of AGN in the reference sample. Such objects are generally classified as AGN by default, because of the higher prior of this class (91% of them follow $\mathbb{P}(AGN) < 0.9$, against 5% of actual AGN). Some AGN from the reference sample also have high outlier measures, because their properties also deviate from the bulk of reference AGN: Indeed, as obtained after a cross-correlation with *Simbad*, more than 70% of them are actually quasi-stellar objects, and less than 13% and 1% are respectively Seyfert 2s and LINERs, which are types of AGN whose nuclear emission is absorbed by the dusty torus, while the distribution of `logFxFr` is centered on 0 for quasars and -2 for LINERs (Seyfert 2 also shine brighter in optical and are much harder in X-ray due to absorption). The same conclusions can be drawn for the stellar type, with variable stars that have the highest outlier measures. Non-stars classified as a star generally have some properties deviating from typical stars (either the hardness or the variability). The outlier measure can then be used to retrieve a substantial fraction of objects not matching one of the four classes we used.

To better characterise the outliers, we studied a sample of 85 objects that have an outlier measure higher than 10 and that match a *Simbad* source. Their analysis can be divided by their *Simbad* type, between AGN, stars, XRBs, and other types. About 55% of AGN outliers are just LINERs, Seyfert 2, and blazars, in which the outlier has a physical meaning. Another 10% of them are outliers because of their variability: these AGN vary in X-ray by a factor of 5 to 100 between observations, sometimes due to a faint flux (the variation is contained in the error bars) but most often well-founded when inspecting the light curve); the rest of outliers is due to the location of the source, for example when it is an AGN in the background of a galaxy, or a peculiar hardness in X-rays. Similarly, two thirds of star outliers are just young stellar objects and variable stars of Orion-type, and the rest of outliers are due to a large X-ray-to-optical flux ratio and/or a significant X-ray variability. X-ray binaries are numerous to have high outlier measures, due to the heterogeneity of this class, but those with a measure higher than 10 are generally those with no infrared counterpart or no counterpart at all, or with a particularly hard spectrum, or located in the Magellanic clouds.

Sources of other types considered as outliers include many transients (12 gamma-ray bursts, 17 supernovae, and 5 TDEs, 62 supernova remnants, 17 pulsars, and 11 planetary nebulae. Only 40% of sources of these types have an outlier measure higher than ten, either because the others lack critical

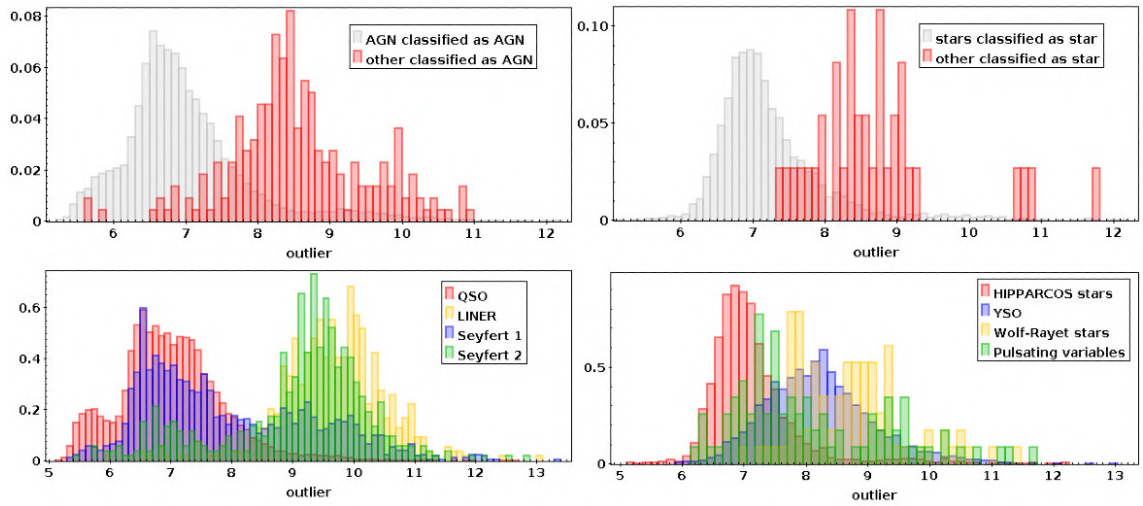

Figure 4.7: Distribution of the outlier measure, obtained from objects in the 4XMM reference sample classified as AGN (first panel), from objects in the reference sample classified as stars (second panel), from different types of AGN (third panel), and from different types of stars (fourth panel).

data (25% of transients have only one X-ray detection) or because the properties we use do not enable them to be distinguished from the four types: AGN, stars, XRBs, and CVs.

Last but not least, we analysed a sample of sources that have an outlier measure higher than ten and no counterpart in *Simbad*. After a careful inspection of *XMM* and *Chandra* fields, among the 40 sources analysed, 36% have a low detection likelihood and may be spurious. The other 64% are actual sources not present in *Simbad*, in particular XRB candidates and AGN in the background but also some galaxy clusters.

As a conclusion, our outlier measure is useful to nuance the interpretation of a particular classification, and retrieve some misclassified sources; a non-negligible part of sources deviating from the bulk of classes used as reference; and sources that have data quality issues. However, given the generality of the classes we used, we estimate that only ∼1% of the 14000 4XMM sources considered as outliers are actually sources of another type. A detailed study of outliers of special interest will be addressed in a future work.

4.5 Discussion

4.5.1 General classification performance

From the reference sample, we can expect that at least 95% of all objects are classified correctly, in each of the *Swift*, *XMM* and *Chandra* catalogues. However, our results on the test sample show a slightly lower performance, about 85–90%. This is expected due to physical differences between the reference and the test samples, biases in the classification process, and computation errors of some properties in the catalogue, as will be detailed in the rest of Section 4.5.

Manual inspection of the test samples still showed an overall good performance of our classification, with about 95% of sources classified as AGN and stars actually being reliable candidates. Despite the optimisation, XRBs remain less well classified than AGN and stars: this is partly due to their lower prior as well as the wide variety of properties they can have. Sources classified as XRBs are rarer and their reliability is lower, because they include a substantial fraction of outliers that have a particular physical nature and another substantial fraction of sources affected by data issues (spurious variability or wrongly-missing counterparts). Since the AGN and stars in the reference sample were found by crossmatching with catalogues built in the optical or infrared, we also expect more frequent matching issues in the test sample than in the reference sample. Overall, we infer an XRB true positive rate of 50–65%, 45–60% and 35–55% in the *XMM*, *Chandra* and *Swift* test samples, respectively. The large difference between these rates and the ones computed on the reference samples is notably due to the presence of sources of other nature and faint sources with data quality issues – more frequent

Truth →	AGN	Star	XRB	CV	Total cl.
→AGN	5889	7	20	39	5955
→Star	6	1404	1	3	1414
→XRB	9	5	83	5	102
→CV	7	1	1	68	77
Total	5911	1417	105	115	Average
recall (%)	99.6	99.1	79.0	59.1	84.2
precision (%)	96.8	99.2	95.2	87.9	95.2
f_1 score	0.982	0.991	0.863	0.707	0.886

Table 4.6: Same as Table 4.3, but for the random forest classification applied to the reference sample of 2SXPS.

than in the reference sample. Many of misclassified sources overlap the extent of a nearby galaxy. To overcome these issues, we implemented a version of the classifier specialised in X-ray populations of nearby galaxies, as detailed in Chapter 5.

The CV class gives a lower performance, either because a classification as CVs is difficult to infer with the properties we use (one needs either the spectrum or the light curve), or because the classification is not optimised for this class. Overall, mainly because of their low prior, sources classified as CVs have lower classification margins: about 95% of them have a probability $\mathbb{P}(\mathrm{CV}) < 60\%$. Further work is needed to better perform at the classification of this rare type.

Differences exist between *Swift*, *XMM* and *Chandra* performances, due to a better constrained variability (*Swift*) or better constrained hardness (*XMM*) and location (*XMM* and *Chandra*). The X-ray luminosity and variability and the proximity to a galaxy prove to be the most important features from the optimisation, regardless of the catalogue. However, this may change if we optimised it for, for example, AGN or CVs.

4.5.2 Comparison to machine learning results

For comparison, we performed a classification of 2SXPS sources using a random forest algorithm with the following parameters: four classes (AGN, star, XRB, CV), the same source properties as presented in Table 4.1, a maximum depth of the decision trees equal to 12, and a weighted loss function to optimise the classification for XRBs (the weight of this class is set to 1 while the weight of other classes is set to 0.01). The algorithm was trained on a sample containing 70% of the reference sample and validated on the other 30%. The confusion matrix obtained on the validation sample is shown in Table 4.6. Compared to Table 4.3, we see comparable results. The *precision* of XRBs and their *recall* seem to be slightly higher and lower, respectively, but this depends on the weight chosen for the XRB class. The f_1 score of XRBs is also higher than a recent random forest classifier of X-ray sources in the literature (0.769 for Arnason et al. 2020, however not based on the same source properties).

We compared random forest performance to our classification on the test sample, both statistically and with manual inspection of a small subsample.

Once trained on the whole reference sample and applied to the 2SXPS test sample defined in Section 4.4.2, we obtain about 97000 sources classified as AGN, 13000 as stars, 2200 as XRBs, and 330 as CVs. Compared with the naive Bayes classifier, this classification thus gives similar class proportions, with a little preference for the AGN and star classes at the expense of the XRB one. However, the results obtained with the naive Bayes classifier are more interpretable because the motives of each classification are explicitly related to the values of the source properties.

4.5.3 Classifications biases

Biases can occur both before and during a classification process, and these two types of bias are sometimes hard to disentangle. For instance, X-ray surveys naturally contain few AGN at low Galactic latitudes, so unknown sources at low latitudes are less likely to be classified as AGN than sources at higher latitudes. However, this difference in AGN frequency may not be the same in the training sample and in the whole sample, since the training sample is partly built up using surveys searching explicitly for extragalactic sources, which thus exclude lower latitudes by construction. The proportion

of each class in the training sample is thus biased in an unquantifiable way. This is partly corrected by manual choice of the priors, but this still affects the probability densities of each class.

A second type of bias refers to missing values, in particular the multiwavelength flux ratios. The non-detection of multiwavelength counterparts is considered as a feature as well as other properties, so it is important to not miss them because of statistical effects. If such a value is missing for a particular object, this means that no counterparts were found by NWAY, and manual inspection revealed that possibly missing counterparts are rare. However, when a source is in a stellar association, a spurious counterpart is identified sometimes, in particular the optical counterpart may be different to the infrared one. More importantly, while missing counterparts for an X-ray bright source give a significant piece of information, a faint source that has no counterparts is not surprising at all, whereas our model does not take the X-ray flux into account. Similarly, a source that has just one detection has the same variability parameters as a source of constant luminosity and is considered as such by the algorithm.

We expect also important biases for this study when applying a model optimised for the training sample to the test sample, which has not exactly the same properties. In particular, since most X-ray emitting stars have to be close to be detected, many of them are already in the reference sample, which thus has a higher proportion of stars than the test sample. As a consequence, the prior of the stellar class should not be the same between the two samples. Likewise, since the reference sample contains a greater proportion of bright sources, the absence of multiwavelength counterparts may be over-favoring the XRB class, when going from the training to the test sample. Moreover, because nearby, large galaxies are more studied, they are a preferred location for XRBs in the reference sample, which induce a bias in their Galactic latitude distribution. If location were considered as important by the classifier, this would have biased the classification as XRBs in the test sample.

X-ray flux

When applying the classification to faint sources, the absence of counterpart is wrongly taken as an important piece of information. Indeed, although most X-ray bright AGN have optical and infrared counterparts, this does not hold anymore at faint fluxes: an AGN following $F_X/F_r = 5$ (resp. $F_X/F_{W1} = 4$) reaches the Pan-STARRS (resp. UnWISE) limiting magnitude when its X-ray flux is about $3 - 4 \times 10^{-14}$ erg s^{-1} cm^{-2}. The fraction of 4XMM sources matching a quasar from SDSS DR14 (Pâris et al., 2018) (resp. matching an AGN in allWISEagn), and without any infrared (resp. optical) counterpart, is about 10% in this flux bin, and becomes much higher in fainter bins. This suggests that the classification of sources below this threshold and missing a counterpart may not be completely reliable; these sources represent about 15% of the CSC2 test sample (8% for 4XMM and 3% for 2SXPS), and about 38% (resp. 17% and 10%) of the sources classified as XRBs.

Spurious variability

As explained in Section 3.2.2, X-ray detections from different X-ray observatories were combined to augment the catalogue with extra variability data. However, this process has several caveats detailed in the following. First, we find some systematics in the comparison of *Swift* fluxes to other observatories: when the source is faint (typically fainter than 5×10^{-14} erg s^{-1} cm^{-2}), *Swift* fluxes are very often fainter by a factor of two to ten than *XMM-Newton* fluxes. This may be due to a caveat in the conversion from the count rate to the X-ray flux, since the conversion factor is not computed using the same hypotheses for 2SXPS, 4XMM, and CSC2.

Second, the X-ray telescopes on board *Swift*, *XMM-Newton,* and *Chandra* do not cover the same energy bands: 0.3–10 keV, 0.2–12 keV, and 0.5–7 keV, respectively. The conversion from one band to another requires the assumption of a spectral model, which is why we simply kept fluxes as computed in each X-ray catalogue. This can lead to a spurious variability in the multi-instrument light curve, especially in very soft sources: for instance among the few hundred stars present in both 2SXPS and 4XMM-DR10, about 70% have a *Swift* flux higher than the *XMM* flux, and the median ratio between these fluxes is about 1.5. These numbers become 54% and 1.05 in the case of AGN. Future works carefully comparing source flux from multi-mission observations will be crucial to correct this bias (Quintin et al. in prep).

Reference sample reliability

Despite our effort to maximise the purity of the reference sample, it stills contains a small fraction of contaminants. These are for example the presumed mid-infrared-selected AGN that actually have another type (Secrest et al. (2015) state a purity of their sample higher than 95%), some presumed XRBs that are actually flaring stars or background AGN (e.g., Guo et al., 2016; Sazonov and Khabibullin, 2017). Indeed, some of the catalogues we used to identify known XRBs estimate a low but non-negligible number of contaminants, especially background AGN (e.g., Liu et al. 2007, Kundu et al. 2007, Mineo et al. 2012 from Table 3.1).

Another issue when building such a training sample is its completeness. Our reference sample is obviously incomplete at faint fluxes, for which few X-ray sources have a known nature. For instance, only 15% of AGN in the reference sample have an X-ray flux lower than 2×10^{-14} erg s^{-1} cm^{-2}. This selection effect does not apply to stars (55% of them have a flux lower than 2×10^{-14} erg s^{-1} cm^{-2}), since X-ray visible stars are bright enough in optical or infrared to be identified as such. Moreover, other selection effects hinder the sample completeness: too few AGN are identified at low Galactic latitudes (Truebenbach and Darling, 2017; Secrest et al., 2020), too few XRBs in further, less-studied galaxies, etc.

Choice and size of the classes

The choice of the classes may be crucial to the performance of the classifier: since it is based on the correlation between the source properties and its class, the sharper the features of each property distribution for each class, the more efficient the classifier can be. Any heterogeneity in the composition of a class, like the presence of a small number of objects with very different properties (e.g., LINER-type AGN among the AGN sample, or highly variable stars among all stars), results in a large outlier measure for these objects. On the other hand, a sufficient number of objects in each class must be identified, in order to obtain reliable KDEs. From a visual inspection of the KDE obtained from different 4XMM-DR10 training samples, we estimate that a number of at least 75–100 objects is advisable to infer meaningful KDE.

In order to investigate further how the classifier is sensitive to the choice of classes, we performed the classification on two other reference samples in 4XMM-DR10: one with only two classes (binary classifier), "XRBs" and "non-XRBs", and the other with six classes: AGN, non-variable stars, variable stars and young stellar objects, XRBs in the Milky Way, extragalactic XRBs, and CVs (Table 4.7). The binary classifier returned somewhat less performing results than the standard classifier for the XRB class: a retrieval fraction of 82.4% and a *precision* of 95%. The resulting f_1 score averaged on the two classes is 0.883.

Compared with the binary classifier, the six-class classifier returned a lower retrieval fraction (73.3%) but higher *precision* (95.6%) for Galactic XRBs, because of the lower prior for this class (only one-seventh of our XRB sample corresponds to Galactic XRBs). Recombining Galactic and extragalactic XRBs after the classification has been performed, we retrieve 92.4% of them and the *precision* of XRB classification is 95.3%. Interestingly, other classes slightly benefit from the split in six classes, for example the stars (recombining young, variable and other stars in the general class of "star" after the classification) for which the retrieval fraction becomes 99.7% and the *precision* becomes 99.2%. The f_1 score averaged over all four general classes becomes 0.852 with this classifier. The detail of the number counts is shown in Table 4.7.

The optimisation of this classifier (favoring the performance on the Galactic XRBs) led to a set of weighting coefficients very similar to the four-class classifier: 7.5 for location, 4.3 for spectrum, 2.6 for multiwavelength counterparts, and 6.1 for variability. This may suggest that Galactic XRBs are critical in the optimisation of the four-class classifier on the reference sample, while most false positives in the test sample are extragalactic cases. Once applied to the test sample, the classifier returns 79% of AGN, 17% of stars, 1.2% of variable or young stars, 0.5% of Galactic XRBs, 1.6% of extragalactic XRBs, and 0.6% of CVs, which is again roughly consistent with the prior proportions of these classes.

Other model assumptions

Truth →	AGN	Star	V/Y*	CV	gXB	eXB
→ AGN	18234	9	2	147	11	18
→ Star	12	4605	137	5	2	2
→ V/Y*	1	45	53	3	0	0
→ CV	1	0	1	85	6	0
→ gXB	2	0	1	2	55	0
→ eXB	61	0	0	8	0	429
Total	18311	4659	194	250	75	449
Total cl.	18421	4659	101	60	487	99
recall	99.6	98.8	27.3	34.0	73.3	95.5
precision	97.6	93.6	68.6	87.9	95.6	95.3
f_1 score	0.986	0.961	0.391	0.490	0.830	0.954

Table 4.7: Confusion matrix and metrics of the classification with six classes, applied to the reference sample of 4XMM-DR10.

The first six rows show the number counts of objects classified as AGN, normal stars, variable or young stars, CVs, galactic XRBs, and extragalactic XRBs, respectively. The last three rows give the *recall* rate, the true positive rate (*precision*), and the f_1 score associated with each class.

Our model assumes that the different classes given as parameters correspond to specific X-ray properties that enable them to be distinguished from one another. However, the f_1 score of XRBs is still lower than the one of AGN and stars, despite the maximisation process: this may be due to the frequent overlap between AGN and XRB properties, whereas the AGN class is much more dominant in terms of number counts (and thus is favoured by the priors). A subdivision of the XRB class into smaller, more homogeneous populations may partly solve this issue; however, these populations (e.g., black hole XRBs, separated further by spectral state) are not yet identified in sufficient number to constitute a reliable training sample. Future works of manual classification, such as the inspection of our XRB or CV candidates, will be able to validate some of them and allow a refinement of each class. Such a work could be achieved e.g. thanks to the help of volunteers in a citizen science experiment (Section 4.6).

Another assumption of the model is that all multiwavelength counterparts are true and contemporaneous associations, which is limited by our crossmatch algorithm. The spurious correlation problem is fairly well addressed by the use of the Bayesian cross-correlation algorithm NWAY, selecting the most likely counterpart for each source and assigning it a flag. To retrieve contemporaneous associations we would need a large overlap between X-ray and optical surveys, as will be the case for eROSITA and Vera C. Rubin surveys[2].

For the same purpose of improving the catalogue enrichment, further improvements of our method could be to include constraining X-ray upper limits of each source. This could also enable the use of other variability properties, for example the maximum X-ray flux drop (or increase) factor over 7 days (presumably short enough to not see important variations in AGN) or other time-dependent features.

A more straightforward improvement is to consider a more homogeneous sample to classify, such as the X-ray populations detectable in nearby galaxies, which are less diverse than the ones detectable in our own Galaxy. This approach is implemented in Chapter 5.

4.6 Outlook: citizen science

Citizen science is a means of generating knowledge by engaging volunteers from the general public, usually to access or analyse a quantity of data that would otherwise be difficult to access or analyse. In astrophysics, one of the most popular citizen science experiments has been Galaxy Zoo, offering the possibility to non experts to classify the morphology of galaxies from their images in the *SDSS* survey. Originally developed by Chris Lintott and collaborators (Lintott et al., 2008), it rapidly gathered more than 200000 participants who performed more than 100 million classification of the initial sample of nearly 900000 galaxies. While the main goal of this experiment was to gather a large training sample

[2]This is of course only true if eROSITA is switched back on at the time of Vera C. Rubin first light.

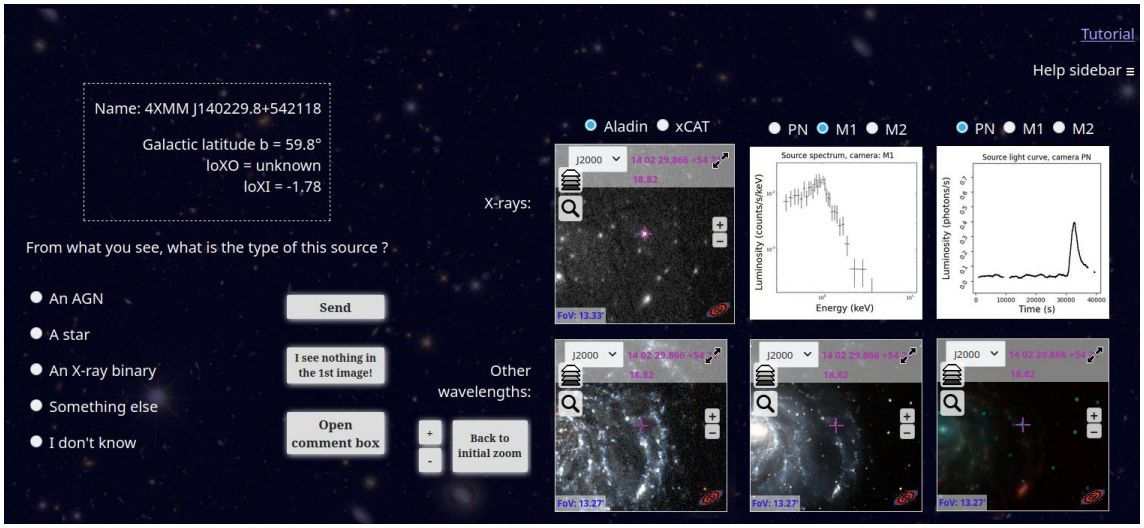

Figure 4.8: Screenshot of the classification page for the source 4XMM J140229.8+542118. In the boxed area are written the name of the source, its Galactic latitude b and the logarithm of the X-ray to optical (infrared) flux ratio $loXO = log_{10}(\frac{F_{0.2\text{-}12\ \mathrm{keV}}}{F_{\mathrm{r}}})$ (resp. $loXI = log_{10}(\frac{F_{0.2\text{-}12\ \mathrm{keV}}}{F_{\mathrm{W1}}})$). Zoomable images are presented for different wavelengths (top left: X-rays, bottom: ultraviolet, optical and infrared). The source spectrum and light-curve for OBSID = 0104260101 are shown. In the lower left part of the image, volunteers are asked to give their classification for this source.

for future machine learning experiments, the project has had a huge impact in many ways, from the construction of a large, clean training sample that is benchmarked to date (Lintott et al., 2011), to the serendipitous discovery of some objects such as the "Green Peas" galaxies, which are green-looking, extremely starforming, low metallicity compact dwarf galaxies (Cardamone et al., 2009; Izotov et al., 2011). The success of such experiments relies on the so-called "wisdom of crowds", which is the idea that a group of people asked to classify the same data will reach a consensus on the correct answer.

The accuracy of classifications presented in this Chapter and later in this thesis work was found to be limited when the training sample size is small (Section 7.1). To overcome this issue, one idea has been to develop a citizen science platform, CLAXSON (CLAssification of X-ray SOurces for Novices, https://xmm-ssc.irap.omp.eu/claxson), on which volunteers can learn how to classify point-like X-ray sources and provide their own classifications for unidentified sources. I provide here information on the platform that I developed and preliminary results of the project.

Structure

Different types of X-ray sources come with a variety of different signatures that must be simultaneously inspected to derive a valid classification. While for a machine learning classifier, these data must be reduced to scalar quantities (such as flux ratios and spectral parameters), manual classification is less tedious and more convenient on visual data (such as images at different wavelengths and the source spectrum). Therefore, in CLAXSON, the classification page (Figure 4.8) includes zoomable images (from AladinLite[3], Bonnarel et al. 2000; Boch and Fernique 2014) in X-rays (using images from the *XMM-Newton* observatory), ultraviolet (GALEX), optical (PanSTARRS, DES or DSS) and infrared (2MASS or AllWISE); as well as the source spectrum and light curve (rebinned every 100s for the pn camera) obtained from the 4XMM catalogue website[4]. For the latter, the detection having the largest number of counts is shown. The long-term light-curve, as introduced in Section 3.2.2, is also made available.

As a first run, about 20000 4XMM-DR10 point-like sources were uploaded into CLAXSON, out of a sample of $\sim$ 300000 sources considered as well-suited for a manual classification, i.e. following at least two quality rules (as defined in Section 4.2), having $SC_DET_ML > 12$ and $SC_POSERR <$ 3 arcsec.

Because they make up most of the X-ray sky, and because they can reasonably be disentangled

[3] https://aladin.u-strasbg.fr/AladinLite/
[4] http://xmm-catalog.irap.omp.eu

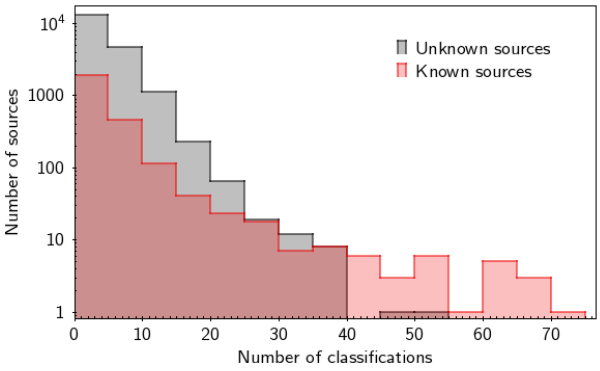

Figure 4.9: Histogram of the number of classifications received per source, as of April 2022. Only sources having more than 20 classifications can be reasonably analysed.

using this data, three classes are proposed for each source: AGN, Star, and X-ray Binary; two other possibilities (Other type or Undecided) complete the range of possibilities left to the user.

To ensure the reliability of the results, every volunteer must go through three stages:

1. During the "discovery" phase, they read a short simple presentation of each class (AGN, Star, X-ray binary and Other type) and their behaviour, before completing a quiz on their observational signatures.

2. In the "training" phase, they are given known X-ray sources to classify. The answer is given after each classification, so that they learn the basics of source classification by trial and error.

3. When they have made more than 20 classifications and achieved more than 75% accuracy on the last 20 sources, they reach the final phase. From this point on, they can classify unknown sources and their classifications are recorded.

In order to increase the interest of the volunteers and to ensure that they classify carefully, their success rate (presented as a game achievement) is always shown to them, and it also appears in the public leaderboard of the platform.

First results

To date, CLAXSON has more than 150 users who have made more than 75000 classifications (Figure 4.9). 98 unknown sources and 81 known sources were classified by at least 20 volunteers, and therefore benefit from the "wisdom of crowds" effect, allowing us to analyse their classification. The confusion matrices of these samples are shown in Table 4.8, where the reference for unknown sources is the output of the automated classifier developed in Chapter 4. Overall, we find that the classification from CLAXSON volunteers and the automated classification agree $\sim 80\%$ of the time. On a per-class basis, results are encouraging, despite a seemingly lower recall and accuracy on unknown sources. However, the results of the general classifier (which are taken as reference for this sample) are questionable for unknown sources (Section 7.1). Indeed, and most interestingly, after careful manual inspection of sources whose classifications did not match, we found that the volunteer classifications were the most reliable in the vast majority of cases.

The future of this experiment is presented in Section 8.2.3.

Known sources

	AGN	Star	XRB	Precision
→AGN	38	0	0	100%
→Star	1	31	1	94%
→XRB	1	0	8	89%
→Other	0	0	1	-
Recall	95%	100%	80%	

Unknown sources

	AGN	Star	XRB	Precision
→AGN	43	1	8	83%
→Star	5	15	4	62%
→XRB	6	1	9	60%
→Other	0	0	2	-
Recall	80%	88%	39%	

Table 4.8: Confusion matrices for known (top) and unknown (bottom) CLAXSON sources having more than 20 classifications.

Chapter 5

Study of ULX and HLX

Ultra-/hyperluminous X-ray sources (ULX and HLX) could constitute interesting laboratories to further improve our understanding of the supermassive black hole growth through super-Eddington accretion episodes and successive mergers of lighter holes. ULXs are thought to be powered by super-Eddington accretion onto stellar-mass compact objects, while HLXs are of unknown nature, but could be good candidates for accreting intermediate mass black holes (IMBH). However, a significant portion of the sample of ULX/HLX candidates derived from catalogue searches are in fact background AGN. In this chapter, which is an augmented version of an article submitted to *Astronomy and Astrophysics* (Tranin et al.), we build samples of ULXs and HLXs from the three largest X-ray catalogues available, compiled from *XMM-Newton*, *Swift*-XRT and *Chandra* detections, and the GLADE catalogue containing 1.7 million galaxies at D<1000 Mpc. We aim to characterize the frequency, environment, hardness and variability of ULXs of HLXs in order to better assess their differences and understand their populations. After a thorough classification of these X-ray sources, we were able to remove ∼42% of $S/N > 3$ sources which were shown to be contaminants, to obtain the cleanest sample of ULX/HLXs to date. From a sample of 1342 ULXs and 191 HLXs detected with a signal to noise $> 3\sigma$, we study the occupation fraction, hardness, variability, radial distribution and preferred environment of the sources. We build their Malmquist-corrected X-ray luminosity functions (XLF) and compare them with previous works. Thanks to the unprecedented size of the sample, we are able to statistically compare ULXs and HLXs and assess the differences in their nature. The interpretation of HLXs as IMBHs is investigated. A significant break is seen in the XLF at $\sim 10^{40}$ erg s^{-1}. With our ULX sample, containing $\lesssim 2\%$ of contaminants, we are able to confirm that ULXs are located preferentially in late-type galaxies and galaxies with higher star-formation rates, with an excess seen in dwarf galaxies. While X-ray binaries, ULXs and most of HLXs share common hardness and variability distributions, a fraction of HLXs appear significantly softer. Unlike ULXs, HLXs seem to reside equally in spiral and lenticular/elliptical galaxies. We report on the discovery of two variable and particularly interesting HLX candidates, sharing spectral and variability features with NGC 470 HLX-1 and the well-known IMBH candidate ESO 243-49 HLX-1. 35% of the HLX candidates have an optical counterpart, and we estimate the mass of 120 of them to be in the range of $2 \times 10^3 - 10^5 M_\odot$. Most of the HLX population is found to be consistent with an accreting massive black hole in a dwarf galaxy satellite of the primary host. This diverse nature needs to be confirmed with deeper optical and infrared observations, as well as upcoming X-ray facilities.

5.1 Context

Supermassive black holes (SMBH, in the mass range $10^6 - 10^{10} M_\odot$) are found in the centers of the most massive galaxies observed so far, and are thought to play a major role in galaxy evolution notably during their violent episodes of accretion and ejection (Fabian 2012; Padovani et al. 2017). However, the formation mechanisms of these objects are yet to be fully understood. Some SMBH observed at $z > 6$, less than 1 Gyr after the Big Bang, are more massive than $10^9\,M_\odot$ (e.g. Mortlock et al. 2011; Wang et al. 2021), implying rapid and efficient growth mechanisms that may be a mixture of intermediate-mass black hole (IMBH, $10^2 - 10^5 M_\odot$) mergers and sustained super-Eddington accretion onto these seeds (Volonteri et al., 2008; Haiman, 2013; Pacucci and Loeb, 2022). However, compelling evidence for the existence of IMBH is still missing, with the exception of some recent discoveries through gravitational waves and X-ray observations (e.g. Farrell et al. 2009; Mezcua 2017; Abbott et al. 2020a).

The search and study of X-ray sources in nearby galaxies, especially in the luminosity range $10^{39} - 10^{42}$ erg s^{-1}, could be a promising way to gain insights into the SMBH growth mechanisms. Extra-galactic and off-nuclear ultraluminous X-ray sources (ULXs) with X-ray luminosities $L_X > 10^{39}$ erg/s, at first thought to be good IMBH candidates (e.g. Colbert and Mushotzky 1999; Liu and Bregman 2005), are now widely accepted as super-Eddington accretors (Section 2.2.2).

Their high-luminosity end, the much rarer HLX ($L_X > 10^{41}$ erg/s) may however remain excellent candidates to look for IMBH, as evidenced with ESO 243–49 HLX–1 (Farrell et al., 2009), one of the best IMBH candidate known reaching at peak an X-ray luminosity of 10^{42} erg s^{-1} in the 0.3–10 keV band. It shows a spectral evolution similar with the one obserbed in Galactic black holes (Godet et al., 2009; Servillat et al., 2011; Godet et al., 2012). The black hole in ESO 243–49 HLX–1 is likely to be fed by the repeated partial tidal disruption of a white dwarf at the periastron of its very elliptical orbit, explaining the source peculiar light curve (Section 2.2.3, Godet et al. 2014). Besides, it is found coincident with an optical extended source, consistent with the tidally stripped nucleus of a dwarf galaxy in interaction with ESO 243–49 (Webb et al., 2010, 2017; Farrell et al., 2012). Very few other HLX candidates are known so far, most often located at high distance (Swartz et al., 2011; Zolotukhin et al., 2016), where confusion with a nuclear or background source is more likely. In a recent work, Barrows et al. (2019) manage to gather a large sample of 169 HLX candidates thanks to the resolution power and high sensitivity of two surveys, namely *Chandra* and the SDSS galaxy catalogue. However, most of their candidates are at $D > 1000$ Mpc where a background source is hardly seen by the deepest large optical surveys. Their median unabsorbed luminosity of 4.6×10^{42} erg/s in the band $2 - 10$ keV, as well as the significant fraction of HLXs having an optical counterpart (28%), could be also explained by an important contamination by background sources, although they interpret them as AGN in satellites of the host galaxy and report a background contamination rate of $7 - 8\%$ estimated from the cosmic X-ray background curves of Moretti et al. (2003).

In order to obtain a statistical view of the ULX population, many studies have been devoted to the collection and study of samples of ULX candidates from old (Swartz et al. 2004; Liu and Bregman 2005; Liu and Mirabel 2005; Swartz et al. 2011; Walton et al. 2011; Wang et al. 2016) and recent (Earnshaw et al. 2019; Kovlakas et al. 2020; Inoue et al. 2021; Bernadich et al. 2021; Walton et al. 2022) releases of large X-ray catalogues. Focusing either on the hardness (e.g. Earnshaw et al. 2019) and variability of ULXs (e.g. Sutton et al. 2013; Bernadich et al. 2021) or on their environment and counterparts (e.g. Kovlakas et al. 2020), or on their X-ray luminosity function (XLF, Mineo et al. 2012; Wang et al. 2016), these studies showed several features for the ULX population: ULX are more frequently found in late-type, star-forming galaxies. Their frequency increases with galaxy mass and their luminosity function may be explained as a mere powerlaw extension of the high-mass X-ray binary luminosity function, for which a break is noted at a few 10^{38} erg/s in early-type galaxies (e.g. Kim and Fabbiano 2004, Wang et al. 2016). A break or cutoff at $1 - 2 \times 10^{40}$ erg/s may also be present (Swartz et al., 2011; Mineo et al., 2012) in the XLF of late-type galaxies, however this is still under debate (in particular see Walton et al. 2011; Wang et al. 2016). Moreover, no break is systematically observed in these galaxies at the Eddington luminosity of a maximum-mass neutron star ($L_{Edd} \sim 2 \times 10^{38}$ erg s^{-1}) or a maximum mass stellar black hole ($L_{Edd} \sim 10^{41}$ erg s^{-1} for a black hole of $10^2 M_\odot$), as would be expected if the Eddington luminosity was a hard limit (Fabbiano, 2006; Kaaret et al., 2017). ULXs in late-type (resp. early-type) galaxies are found to be consistent with a dominant population of high-mass (resp. low-mass) X-ray binaries (HMXB and LMXB, Section

2.2.1), accordingly with the expected environment for these two classes.

Some differences were still reported between XRB and ULX populations. However, only a handful of the brightest (and often closest) ULXs have been studied in detail. Many of the conclusions on the population of ULXs are often drawn from simple model fitting, which does not give a physical description of the data (e.g. Swartz et al. 2004), or on easily computed quantities such as the hardness ratio between two bands. A large sample approach was carried out by Walton et al. (2011) who reported a small offset of ULXs towards harder accretion states when residing in late-type galaxies. Earnshaw et al. (2019) found no significant difference between the hardness ratio distributions of ULXs and XRB. Likewise, the larger dataset of Bernadich et al. (2021) showed similar locations for these two populations in the hardness-hardness diagrams. In contrast, ULXs seem less prone to exhibit high variability on the timescale of years compared to XRB, and the most variable ones are hosted in spiral galaxies (Bernadich et al., 2021). Confirmed neutron star ULXs were reported to be the hardest ULXs, with highly variable hard radiation (Gúrpide et al., 2021). Some ULXs are also variable on the timescale of a few kiloseconds (within a single observation), as found by Earnshaw et al. (2019) and studies of individual ULXs suggest the presence of winds, outflows or pulsations (e.g Sutton et al. 2013; Koliopanos et al. 2019).

Nevertheless, ULX population studies suffer from a moderately high contamination fraction due to foreground stars and (mainly) background AGN, often estimated to be $\sim$20% from the $\log N - \log S$ diagram of cosmic X-ray background sources (e.g. Walton et al. 2011), increasing with X-ray luminosity (e.g. Bernadich et al. 2021). Despite evidence for ULXs being super-Eddington stellar-mass accretors, the mechanism underlying the apparent super-Eddington luminosities is still poorly constrained. Modeling over the last twenty years suggests different possible scenarios such as anisotropic (beamed) emission (e.g. King 2009; Wiktorowicz et al. 2019), supercritical accretion discs around stellar-mass black holes with radiation-driven winds (e.g. Poutanen et al. 2007; Middleton et al. 2015) or around neutron stars (e.g. Erkut et al. 2019; Kuranov et al. 2020), thermal-timescale mass transfer - in particular from a Helium-burning secondary (e.g. Wiktorowicz et al. 2015; Pavlovskii et al. 2017), accretion flows around pulsating highly-magnetized neutron stars (e.g. Bachetti et al. 2014; Mushtukov et al. 2015; Israel et al. 2017; Mushtukov et al. 2017; Koliopanos et al. 2017) and accretion of clumpy stellar wind enhanced by X-ray ionization (Krticka et al., 2022).

In this work, we develop a novel approach to build cleaner ULX and HLX samples, using the probabilistic classification of X-ray sources developed in Chapter 4. We assess the added value of such a clean sample, and we conduct a statistical study of our sample – the largest to date – to offer a more complete view of ULX and HLX properties.

In Section 5.2 we explain our ULX selection method, involving the use of a classification of X-ray sources, and the way we validate the sample and build a complete subsample. The sample of contaminants and the selection of HLX candidates are also described. In Section 5.3 we present a statistical study of our clean sample, in terms of X-ray luminosity function, ULX rate evolution with the environment, hardness and variability properties. Samples of XRBs, ULXs and HLXs are compared. We discuss these results in Section 5.4 and compare them to catalogues and results obtained in previous works. The nature of HLXs is also investigated. We summarize our study in Section 5.5. Unless stated otherwise, errors are quoted at the 1-σ level.

5.2 Building a clean sample

5.2.1 X-ray source – galaxy associations

The first published ULX catalogues were constructed by cross-correlating X-ray catalogues with rather small catalogues of bright galaxies (in particular RC3, de Vaucouleurs et al. 1991). More recently, in order to achieve more complete ULX catalogues, larger galaxy catalogues were considered, such as HyperLEDA (Paturel et al., 2003), the Catalogue of Neighbouring Galaxies (Karachentsev et al., 2004) or HECATE (Kovlakas et al., 2021). In this study, using the GLADE catalogue is a mean to achieve a more complete census of ULX and HLX, as it is a compilation of large galaxy catalogues, including for example HyperLEDA (Section 3.2.2).

In order to retrieve the largest ULX sample possible, we use the three X-ray samples of 2SXPS, 4XMMDR11 and CSC2 described in Section 3.2, already augmented with external data such as the association to a GLADE galaxy. Because of the source crowding in observations of nearby galaxies,

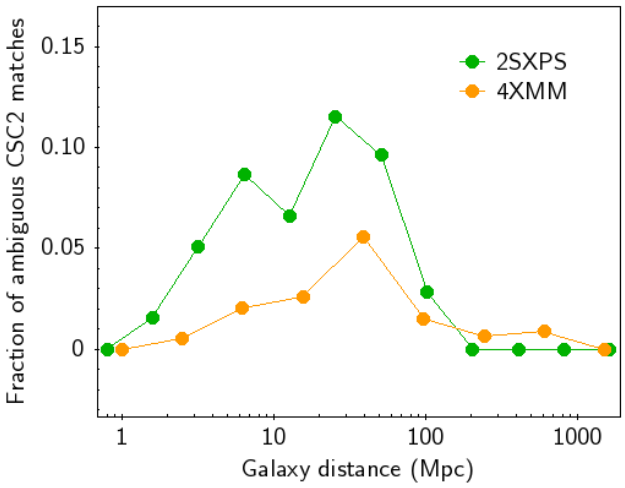

Figure 5.1: Fraction of 2SXPS-CSC2 and 4XMM-CSC2 ambiguous matches as a function of the host distance given by GLADE.

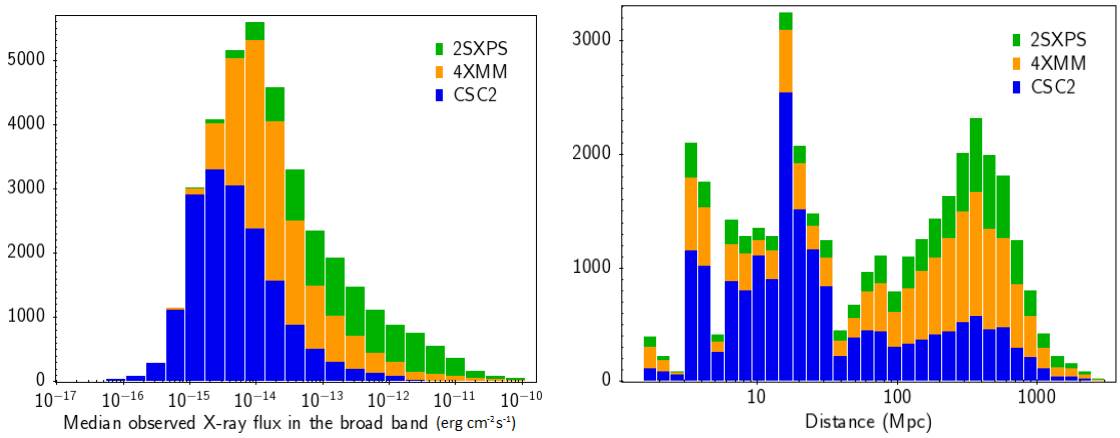

Figure 5.2: Stacked histograms of the median X-ray flux (left panel) and distance of the matched galaxy (right panel) for X-ray sources associated to a GLADE galaxy.

observations at lower spatial resolution are more subject to source confusion issues, which can be quantified by the fraction of ambiguous multi-mission X-ray associations (described in Section 3.2). This fraction increases with galaxy distance and becomes ∼10% (resp. ∼5%) in galaxies at 40 Mpc (Figure 5.1). At higher distances, some Chandra sources must be confused as well, causing an apparent decrease of the fraction of ambiguous matches (Figure 5.1). This source confusion issue is important in ULX studies because tight groups of XRB (resp. ULX) can be mistaken for ULXs (resp. HLXs) (e.g. Wolter et al. 2015).

The resulting samples of X-ray associations contain 18506, 13055 and 7243 sources from CSC2, 4XMMDR11 and 2SXPS, respectively. The distributions of their median X-ray flux and (host) distance are shown in Figure 5.2.

5.2.2 ULX candidates

To form the ULX sample, the first step is to identify X-ray sources matching a galaxy, but outside its nuclear region to avoid AGN contaminants.We used the matching tool of TOPCAT to this end, with the *Sky Ellipses* algorithm to retrieve all sources whose X-ray error circle overlap the ellipse representing the galaxy extent (with major axis being the Holmberg diameter $D_{Holm} = 1.26 \times D_{25}$ as in Kovlakas et al. 2020, where D_{25} is the isophotal diameter at surface brightness 25 mag arcsec^{-2}). The resulting samples of X-ray matches are used later as input for source classification. They contain

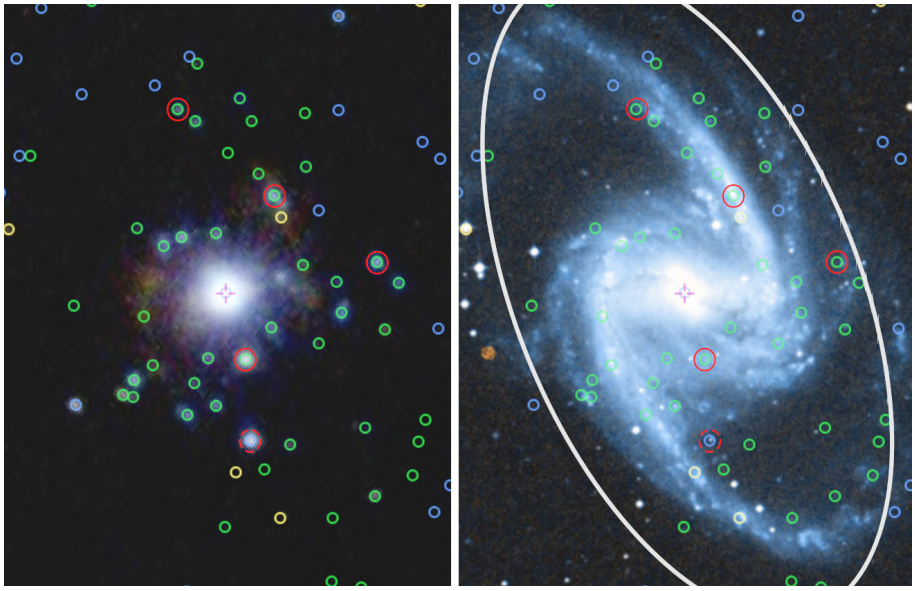

Figure 5.3: Illustration of ULX selection on the galaxy NGC 1365. (Left) *XMM-Newton* X-ray image (Right) DSS Optical image. The D_{25} ellipse of the galaxy is shown in grey. Blue, orange, green and red circles represent sources classified as AGN, soft sources, XRB and initial ULX candidates, respectively. The dashed red circle corresponds to a candidate classified as contaminant, and is indeed a background AGN. An interactive view of this figure is available at https://xmm-ssc.irap.omp.eu/claxson/xray_analyzer.php?srcquery=53.4019%20-36.1406

18506, 13055 and 7243 sources for *Chandra*, *XMM-Newton* and *Swift*, respectively.

To exclude the central region, we select sources satisfying the criterion $d > 3(POSERR + 0.5)$ where d is the angular separation to the galaxy center and $POSERR$ is the X-ray position error at 1σ. A minimal offset of 3 arcsec is required. The 0.5 arcsec term is applied to correct for astrometric errors on the galaxy center reported in GLADE – it is the typical offset between GLADE and SDSS positions. ULX candidates are those whose mean observed X-ray luminosity exceeds 10^{39} erg s^{-1}. The mean observed X-ray luminosity over the instrument broad band (0.2-12 keV for *XMM-Newton*, 0.5-7 keV for *Chandra* and 0.3-10 keV for *Swift*) is computed from the mean X-ray flux given in the X-ray catalogues and the galaxy distance.

5.2.3 Source classification to filter contaminants

One main issue in ULX studies is the high rate of contaminants in ULX samples, due to the presence of foreground (essentially stars in our Galaxy) and background (AGN) sources. Some central AGN may also pass the criterion cited above because of bad astrometry. Previous attempts to remove these contaminants mainly focused on removing known AGN and stars (e.g. Kovlakas et al. 2020; Bernadich et al. 2021) using the large existing datasets for these types. However, this is not sufficient to remove all contaminants, since many of them remain uncatalogued. Another option, applied in Bernadich et al. (2021), is to remove all sources that are too bright in optical to be a ULX. To this end, they use Gaia and PanSTARRS magnitudes obtained by a positional crossmatch with X-ray sources to compute the X-ray to optical flux ratio: any source with $\log(F_X/F_{Opt}) < -2.2$ is considered as a star, and other sources with $\log(F_X/F_{Opt}) < 0$ were manually inspected to flag likely background sources while keeping the bright HII star-forming regions where ULXs are preferentially found.

While efficient, this process is tedious and also misses all possible background AGN having $F_X > F_{Opt}$. To overcome this issue, we make use of the automated probabilistic classification of X-ray sources developed in the Chapter 4. In a nutshell, the dataset is first prepared by enriching the X-ray catalogue by completing X-ray sources with the following information: their optical and infrared counterparts from large ground-based surveys, identified with the Bayesian cross-matching tool NWAY (Salvato et al., 2018); galaxies hosting the source, as explained in Section 5.3.3; X-ray variability ratio between multi-instrument observations; and source identification given by external catalogues, to form the training sample. The classification scheme starts with a Naive Bayes Classifier based on the

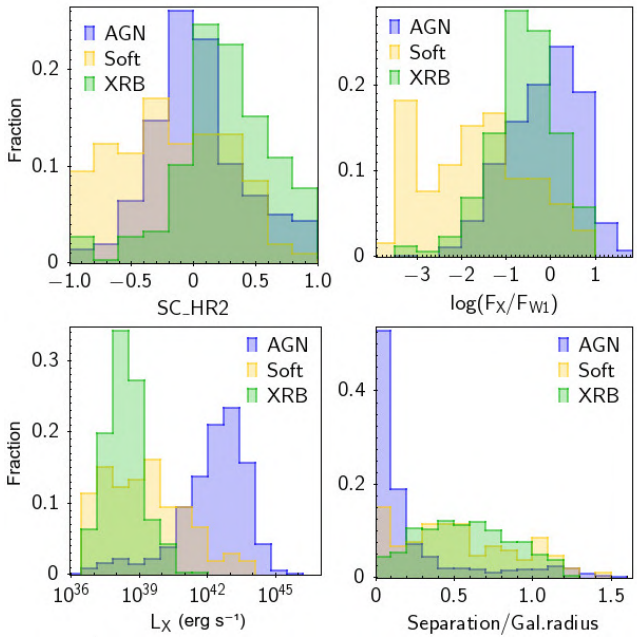

Figure 5.4: Densities of some source properties for each class of the 4XMM-DR11 training sample. SC_HR2: second hardness ratio of 4XMM-DR11 (between bands 0.5-1 and 1-2 keV), from EPIC-pn and MOS cameras. $\log(F_X/F_{W1})$: logarithm of the X-ray to infrared (W1-band, 3.4 μm) flux ratio. L_X: mean 0.2–12 keV observed luminosity. Separation/Gal. radius: galactocentric distance, i.e. the source separation to the host center, in units of the host radius at the source position angle.

densities of the training sample for all source properties obtained after this enrichment. The scheme is then fine-tuned to maximize the classification performance of a chosen class (here X-ray binaries), by increasing the weight of the most discriminating properties. The probabilities of each class as well as the final class (giving maximum probability) are computed. Here, the X-ray sample of sources matching a GLADE galaxy is divided into a training sample of known sources and a test sample to classify. The classification is based on three classes: AGN (corresponding to background contaminants and most sources located in galaxy centres), X-ray binaries (the sample of in-situ genuine sources) and soft sources (a miscellaneous class containing stars, supernovae and supernova remnants, that are in-situ and foreground contaminants). While in the Chapter 4 the stars could form a class of their own, the scarcity of foreground stars, supernovae, and supernova remnants in this sample dictated that they be combined into a single class to allow for a sufficient training sample. Cataclysmic variables are not expected in this extragalactic sample, due to their low X-ray luminosity and low sky density. The properties used in the classification process and the list of catalogues used to retrieve AGN, stars and XRB are detailed in Tables 1 and 2 of Tranin et al. (2022). Supernovae and supernova remnants are retrieved through a match with *Simbad*. The parameters of the classifier for each catalogue are summarized in Table 5.1, while the sample size of the training samples of *XMM-Newton*, *Chandra* and *Swift* are detailed in Table 5.2, as well as the classification results in the training samples. The classifier is very efficient at retrieving AGN, and retrieves more than 80% of X-ray binaries. False positive rates are also low ($\lesssim$15%) and can be further decreased by applying a probability threshold on the class under consideration.

As a sanity check, we obtain that 99% of sources at $L_X > 10^{42}$ erg/s and 94% of sources matching the galaxy center (see Eq. (1)) are classified as AGN. The vast majority of other central sources are classified as soft sources, mostly being absorbed (Seyfert II) AGN or hot gas.

To remove contaminants, the probability that the source is an XRB is simply the probability that it is not a contaminant (indeed $P_{XRB} = 1 - P_{AGN} - P_{Soft}$). It is then compared to the fraction of contaminants in the galaxy area within the source separation. This fraction is obtained with the formula:

$$f_{cont} = 2\frac{\pi a b n_{cont} sep^2}{N_{ULX}} \tag{5.1}$$

4XMM	
Priors $\mathcal{P}_{AGN}$, $\mathcal{P}_{Soft}$, $\mathcal{P}_{XRB}$	67%, 8%, 25%
Weights α_{loc}, α_{spe}, α_{ctp}, α_{var}	4.8, 9.1, 1.0, 5.5

CSC2	
Priors $\mathcal{P}_{AGN}$, $\mathcal{P}_{soft}$, $\mathcal{P}_{XRB}$	50%, 10%, 40%
Weights α_{loc}, α_{spe}, α_{ctp}, α_{var}	6.9, 5.3, 3.6, 4.2

2SXPS	
Priors $\mathcal{P}_{AGN}$, $\mathcal{P}_{soft}$, $\mathcal{P}_{XRB}$	67%, 8%, 25%
Weights α_{loc}, α_{spe}, α_{ctp}, α_{var}	9.6, 9.1, 1.3, 4.5

Table 5.1: Classification parameters for 4XMM, CSC2 and 2SXPS. For each catalogue are shown (first line) the prior proportions applied to each class and (second line) the weights for properties related to location, spectrum, multiwavelength counterparts and variability, once optimized to maximize the XRB classification performance. See Table 5.1 and Equation (3) of Tranin et al. (2022) for further details.

4XMM				
	AGN	Soft	XRB	Precision
→AGN	1482	26	10	98%
→Soft	15	33	18	50%
→XRB	29	20	320	87%
Recall	97%	42%	92%	

CSC2				
	AGN	Soft	XRB	Precision
→AGN	996	27	58	92%
→Soft	25	140	27	73%
→XRB	81	80	830	84%
Recall	90%	57%	91%	

2SXPS				
	AGN	Soft	XRB	Precision
→AGN	1568	31	14	97%
→Soft	8	43	13	67%
→XRB	65	36	363	78%
Recall	96%	39%	93%	

Table 5.2: Confusion matrixes resulting from the classification of 4XMM-DR11, CSC2 and 2SXPS training samples.

where a and b are the galaxy semi-major and semi-minor axes, n_{cont} is the density of contaminants computed with the analytical formula of the log(N)-log(S) relation in Moretti et al. (2003), for the hard cosmic X-ray background, *sep* is the galactocentric distance (i.e. the source separation in units of the galaxy radius at its position angle), and N_{ULX} is the number of ULX candidates in the considered galaxy. Regardless of this quantity, sources with a probability to be a contaminant higher than ∼95% are also classified as contaminant: it is notably the case of many foreground sources, and many of the few spurious sources remaining in the sample. Selected candidates are thus those following $P_{XRB} > max(0.05, f_{cont})$. From manual inspection of 150 sources, we estimate that more than 90% of reliable ULXs are retrieved (as detailed in Section 5.2.7) and that at most 15% of selected candidates are compatible with background contaminants. Removed candidates represent ∼42% of the initial candidates. This high fraction is the result of three factors: first, the selection out to $1.26D_{25}$ increases the galaxy extents by 60% and the number of background contaminants by the same amount. Second, foreground contaminants and spurious sources (resulting from the X-ray detection pipelines) are also removed in this process. Third, a few valid ULX candidates are removed as well, because their properties used in this work are also compatible with an AGN (e.g. NGC 3921 ULX X-2, Jonker et al. 2012).

5.2.4 Filtering remaining contaminants

We manually verified a large number of our selected ULX candidates, which greatly helped to develop and assess the filtering pipeline described above. To this end, we used the virtual observatory tools Aladin Lite[1] (Bonnarel et al., 2000; Boch and Fernique, 2014), the *Simbad* database[2] and the VizieR catalogue access tool[3] (Ochsenbein et al., 2000), developed at CDS, Strasbourg Observatory, France.

Some contaminants remain after the filtering process described above: to remove them, we match our sample with *Simbad* (3 arcsec) and exclude objects of types AGN or stellar objects (75% of these objects were already successfully identified by the classification). We also inspect manually all sources with an optical counterpart and selected as ULX, having optical colour $b - r > 0.5$, due to the redder nature of background AGN (about 700 sources). There are 135 sources from *XMM-Newton*, 139 from *Chandra* and 53 from *Swift* that are discarded in this process, bringing the expected contamination rate at about 2% (Section 5.4.2).

In the same way as the contamination rate, the false negative rate is expected to increase with luminosity, because the likelihood of the AGN class is enhanced (Figure 5.4, lower left panel).

5.2.5 HLX sample

Hyperluminous candidates were selected as described in Section 5.2.2, as off-nuclear sources with a mean observed X-ray luminosity $> 10^{41}$ erg s^{-1} in the broad energy band. To limit the fraction of spurious sources, only candidates having a $S/N > 3$ were kept. Respectively 195, 360 and 110 sources from CSC2, 4XMM and 2SXPS satisfy these criteria. Each of these HLX candidates was manually inspected to remove spurious sources (notably due to source confusion issues) and contaminants such as stars, hot gas overdensities and jet hotspots. This step led to the removal of 157 sources. Likewise, 33 sources were removed as being mistakenly associated to GLADE galaxies, whose extent was manifestly overestimated.

Unlike ULXs, which have well-constrained properties that are essentially similar to XRBs for the classifier, selecting HLXs from the classification results is unsuitable. In particular, no HLX is present in the training sample, and bright, reliable HLX candidates having a Gaia (Gaia Collaboration et al., 2021), PanSTARRS (Chambers et al., 2016) or DES (Abbott et al., 2018) optical counterpart are misclassified as background AGN. A more robust approach to eliminate background AGN is to use the redshift (spectroscopic or photometric) of the optical counterpart (as done by Barrows et al. 2019). Recently, in addition to spectroscopic measurements of the redshift for a few million sources (e.g. in the SDSS-BOSS survey, Bolton et al. 2012), large and deep surveys led to the release of several 10^9 photometric redshifts. In SDSS, this work was notably performed by Beck et al. (2016), inferring the redshift of 208 million sources up to $z \sim 0.6$ from their (u,g,r,i,z) magnitudes. Tarrío

[1] https://aladin.u-strasbg.fr/AladinLite/
[2] https://simbad.cds.unistra.fr/simbad/
[3] https://vizier.cds.unistra.fr/viz-bin/VizieR

and Zarattini (2020) computed the photometric redshift of 1.1 billion sources using the (g,r,i,z,y) PanSTARRS bands, extending up to redshift $z \sim 1$. Zou et al. (2022) performed a similar work using the (g,r,i,z,Y) and (g,r,z,W1,W2) bands from the Dark Energy Survey and the DESI Legacy Survey, respectively. These three studies provide highly reliable photometric redshifts, with a typical accuracy better than $\sigma(\Delta z_{norm}) = 0.03$. Besides, most recently, identification as quasars or galaxies and redshifts were provided for 7.8 million *Gaia* DR3 sources (Gaia Collaboration et al., 2022), using the low-resolution optical *Gaia* spectra. This set of redshift catalogues was used as input to identify background and foreground contaminants: X-ray sources at < 3 arcsec of an optical source with a redshift measurement inconsistent with the distance of the assumed host (i.e. $|z_{host} - z| > z_{err}$, with z and z_{err} the redshift value and error in the external catalogue) were discarded. This led to the removal of 283 background and 5 foreground sources, respectively. In contrast, sources having a distance match ($|z_{host} - z| < z_{err}$) have more chance to be indeed located in their associated galaxy: this is the case of 37 sources. At the end of this selection process, 115, 75 and 13 HLX candidates are found in 4XMM-DR11, CSC2 and 2SXPS respectively, totaling 191 unique sources including 11 observed by multiple X-ray instruments at the HLX level according to their mean luminosity (for X-ray sources observed with several instruments, the entry of smallest position error is kept). From them, 63% have no counterpart in Gaia, PanSTARRS and DES catalogues, 24% have a counterpart but no redshift measurement and 13% have a redshift consistent with their host.

5.2.6 Complete subsample

As introduced for example in Walton et al. (2011), ULX properties and luminosity function have to be assessed on a complete sample, so that the contribution of brighter ULX is not overestimated. Indeed, the limiting sensitivity of the instrument defines the minimum flux that a source should have to be detected; for extragalactic sources, this translates into a limiting luminosity for each distance bin. Usually, ULX surveys keep only galaxies with limiting luminosity below 10^{39} erg/s to ensure that all ULXs are well-detected. For instance, Kovlakas et al. (2020) (resp. Bernadich et al. 2021) keep galaxies closer than 40 Mpc (resp. 29 Mpc). This leads to the removal of most of bright ULXs located in more distant galaxies. In this study, we keep all sources with luminosities above the galaxy limiting luminosity $L_{lim} = 4\pi F_{lim} D^2$, where F_{lim} is the limiting sensitivity at the source position, estimated as described in Section 3.2.3. As further detailed in Section 5.3.1, the contribution of ULXs in each luminosity bin is later weighted by the number of galaxies having L_{lim} below this luminosity.

5.2.7 Contaminants sample

In order to validate the automatic filtering method of the test sample, we compiled a sample of objects classified as contaminants from the three catalogues to compare it with the compilation of selected ULX. They are ULX candidates following $d > 3(POSERR + 0.5)$ and $P_{XRB} < max(0.05, f_{cont})$, and having no identification as one of the three classes AGN, soft source or XRB in *Simbad* or other catalogues, in order not to bias the classification assessment. This results in a sample of 1431 sources (1331 unique) with 494, 715 and 222 sources from CSC2, 4XMM and 2SXPS, respectively.

We manually inspected 100 sources having S/N>3 from this sample: 83% were indeed contaminants (mostly background AGN), 7% may be reliable ULXs missed by our classification, and 10% were ambiguous cases, either lying far from the galaxy optical extent but having no optical counterpart, or having source confusion issues leading to unreliable properties.

The distributions of galactocentric distance, mean X-ray luminosities, GLADE distance and Hubble type are shown in Figure 5.5 for both selected ULXs and contaminant samples. These results agree with what is reported in previous works: sources further from the galaxy center, of higher luminosities or in elliptical galaxies are more prone to be contaminants (e.g. Kovlakas et al. 2020). In particular, before manual inspection of the HLXs, all but 6 sources above 10^{42} erg/s were classified as contaminants. One of the 6 sources is 2CXO J115324.3+493104, an AGN jet hotspot (Sambruna et al., 2006), proving the presence of unexpected types of contaminants in the ULX sample. We thus removed it from the HLX sample, as well as 2CXO J003703.9-010904, another jet hotspot in the HLX luminosity range (Martel et al., 1998; Kataoka et al., 2003).

Figure 5.6 shows the fraction of sources classified as contaminants among initial ULX candidates as a function of the mean X-ray luminosity: in particular, for a search within the Holmberg diameter

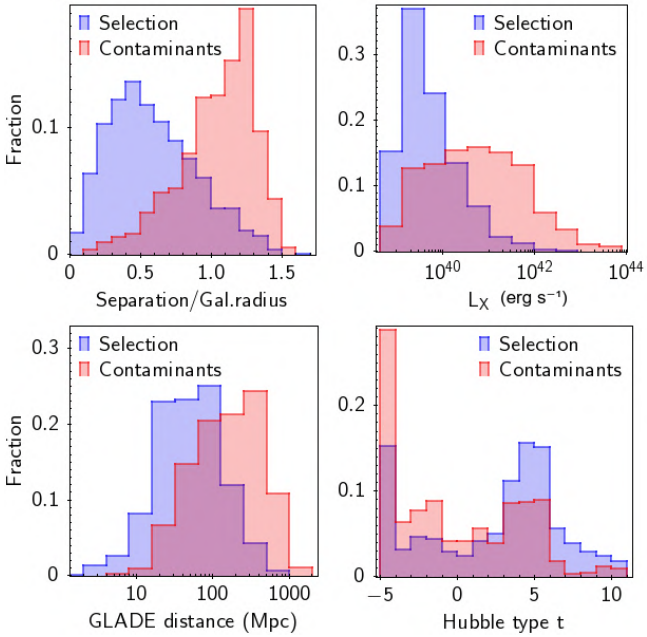

Figure 5.5: Normalised distributions of some properties of selected ULX candidates and candidates classified as contaminants, from the compilation of CSC2, 4XMM-DR11 and 2SXPS.

$1.26\times D_{25}$, more than 30% of candidates above 10^{40} erg/s are contaminants, even after removing known contaminants. This evolution is quantitatively consistent with the 70% contamination rate observed for HLX candidates (Zolotukhin et al., 2016; Kaaret et al., 2017), although this is dependent on the apparent size of selected galaxies. Consequently, previous analyses of the bright end of the X-ray luminosity function of ULXs (e.g. Swartz et al. 2011; Mineo et al. 2012; Wang et al. 2016) may be severely affected by contamination.

5.3 Results

The final ULX samples are made up of 1234, 667 and 304 sources from *Chandra*, *XMM-Newton*, and *Swift*, totaling a compiled sample of 1901 unique sources (i.e. after removing duplicate entries for sources observed by several instruments; this sample is hereafter called the compiled sample). They are detailed in 9. The rates of HLX candidates in each sample are 6%, 16% and 1.9%, respectively. This difference is expected because of the different capabilities of these X-ray facilities, as detailed in Section 5.3.1. Table 5.3 summarizes the number counts of ULXs, complete ULXs (i.e. with $L_X > L_{lim}$), HLXs, and galaxies of different morphologies in each ULX sample. To our knowledge, our work provides both the cleanest (about 2% of contaminants, Section 5.4.2) and the largest census of ULXs, just above the recently published multi-mission catalogue of Walton et al. (2022) (1843 sources). Only a handful of well-known ULXs are absent from our sample. For instance, out of the 17 well-studied ULXs compared in Gúrpide et al. (2021), only three ULXs are missed: Holmberg IX X-1 and Circinus X-5, because the $1.26 \times D_{25}$ ellipse given in GLADE are somewhat smaller than the actual galaxy extent; and NGC 55 X-1, because its mean X-ray luminosity is just below 10^{39} erg s^{-1} for each instrument. All the eight pulsating ULXs known so far, including the recent PULX candidate of Quintin et al. (2021), are retrieved in our sample. ESO 243-49 HLX-1 (along with other HLXs, Section 5.3.4) is retrieved as well. Conversely, supersoft ULXs studied by Urquhart and Soria (2016) are not in our sample because of having $\langle L_X \rangle < 10^{39}$ erg s^{-1}.

5.3.1 Malmquist-corrected XLF

Previous works on the X-ray luminosity function of ULXs only kept galaxies with limiting X-ray luminosities $L_{lim} < 10^{39}$ erg/s. While this method gives the intrinsic shape of the XLF, by probing

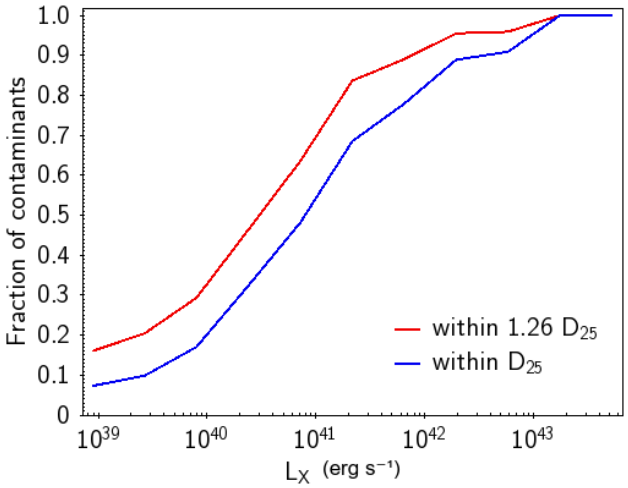

Figure 5.6: Fraction of contaminants per luminosity bin, for candidates in the D_{25} and $1.26\times D_{25}$ ellipses, among the initial ULX candidates (before filtering).

	CSC2	4XMM	2SXPS	Total (unique)
ULX	1234	667	304	2205 (1901)
cULX	925	470	266	1661 (1448)
HLX	75	115	13	203 (191)
cHLX	63	92	13	168 (158)
Galaxies	741	599	207	1547 (1303)
Spiral	377	320	171	868 (713)
Elliptical	206	112	19	337 (325)

Table 5.3: Number counts of ULXs, complete ULXs (i.e. with $L_X > L_{lim}$, Section 5.2.6), HLXs, complete HLXs and number of galaxies that host them (all types, spiral and elliptical), for CSC2, 4XMM-DR11, 2SXPS and their sum (in parenthesis: minus duplicates). In the compilation of unique sources, for X-ray sources observed with several instruments, the entry of smallest position error is kept. By construction of the HLX sample, the sources all have $S/N > 3$ and thus a higher fraction of them are complete.

the same volume in all bins, it also cuts most of the detected bright sources, located in further galaxies. Here, we keep all sources brighter than the limiting luminosity of their galaxy $L_X > L_{lim,host}$. Thus, the distribution of L_X is the XLF convolved with the survey volume, each luminosity bin $[L_X, L_X + dL_X]$ comes from a different survey volume (Malmquist bias, also known as the Eddington bias), and a $1/V_{max}$ correction has to be applied to each bin. This volume V_{max} is here given by the number of galaxies complete to the luminosity of the bin, that is having $L_{lim} < L_{X,bin}$. The deconvolved differential XLF is computed by dividing the luminosity distribution of ULXs by the cumulative limiting luminosity distribution of galaxies, $N(L_{lim} < L_{X,bin})$. Although this approach has been extensively used to constrain the luminosity functions of stars (e.g. Leggett and Hawkins 1988; Stobie et al. 1989; Kroupa 1995), galaxies (e.g. Binggeli et al. 1988; Loveday et al. 1992; Bouwens et al. 2011) and quasars (e.g. Lynden-Bell 1971; Ueda et al. 2003; Aird et al. 2010), it seems absent from the literature of XRB and ULX statistical studies at the time of writing. The underlying assumption is that a universal XLF exists and is the same in the different survey volumes, which seems reasonable since we study the very local Universe $z < 0.16$ (however see Section 5.4.4 for further discussion).

Figure 5.7 shows the deconvolved cumulative XLF (complete in each bin) for late-type (top panel) and early-type (bottom panel) galaxies. It includes selected ULXs below 10^{41} erg s^{-1} from the complete sample, and complete robust HLXs for the bright end. Poisson errors are assumed in each bin on the number of X-ray sources and the number of complete galaxies. The three datasets are in good agreement (consistent at the 90% level except at faint luminosities where the different resolution capabilities lead to substantially different numbers of detections, Section 5.4.3) after making a correction on the CSC2 sample. Indeed, we noted a deficit of *Chandra* sources at medium luminosities ($\gtrsim 10^{40}$ erg/s), which after a thorough inspection of 4XMM-CSC2 intersecting fields was found to be caused by genuine ULXs that were flagged in CSC2 as extended or confused, or not detected by the *Chandra* pipeline which is less sensitive close to the edges of the field of view. After manual inspection of 480 flagged sources, we retrieved 199 such sources including 51 at $L_X > 10^{40}$ erg/s.

We verified that both deconvolved and ULX-complete XLF had the same shape. Notably, we considered sources at low luminosities $10^{39} - 10^{40}$ erg/s in late-type galaxies, so that the sample becomes comparable to that of Wang et al. (2016) (who have only 20 candidates above this luminosity). Using a single powerlaw model, as they did in this luminosity range, we retrieve an XLF slope consistent with their result, $\alpha = 0.93 \pm 0.03$ instead of $\alpha = 0.96 \pm 0.05$ (1σ errors). In early-type galaxies, we generally find flatter slopes than in the literature; this point is discussed in Section 5.4.4.

Each XLF is then fitted with two models, a single powerlaw

$$n(> L) = n_{39}(L/10^{39})^{\alpha}$$

and a broken powerlaw

$$n(> L) = n_{39}(L/10^{39})^{\alpha_1} \text{ if } L < L_b$$
$$n(> L) = n_{39}(L/10^{39})^{\alpha_2} \text{ otherwise}$$

where n_{39} is the total ULX rate and L_b is the break luminosity. Parameters of the XLF fits and their uncertainties are probabilistically estimated in a bayesian framework, by sampling the XLF with 40000 Monte-Carlo trials using observed values and errors. Flat priors are applied on each parameter, in the ranges $n_{39} \in [0, 1]$, $\alpha \in [0, 2]$ (single powerlaw) and $n_{39} \in [0, 1]$, $\alpha_1 \in [0.3, 2]$, $\alpha_2 \in [0, 2]$, $\log(L_b) \in [39, 41]$ (broken powerlaw). Results from the single powerlaw and broken powerlaw fits of the deconvolved cumulative XLF are detailed in Tables 5.4 and 5.5. Unlike the XLF of elliptical galaxies, in spiral galaxies, the broken powerlaw fit is always preferred over a single powerlaw fit. However, the different catalogues disagree on the exact location of the break, even at the three sigma level. This discrepancy is further discussed in Section 5.4.4. However, it is to be noted that all three datasets are well-fitted by a powerlaw breaking at $L_{X,break} = 5 \times 10^{39}$ erg/s (fixed parameter), with $\chi^2_r < 1$.

Unlike the lower luminosity break seen in the XLF of early-type galaxies at a few 10^{38} erg s^{-1} which is consistent with the Eddington limit of neutron star binaries (Kim and Fabbiano, 2010), the physical origin of this higher luminosity break has been poorly understood. Previous works consider it as the suggestion for a different class of objects above the break luminosity, in particular intermediate mass black holes, as it corresponds to the Eddington luminosity of a $\sim 80 M_{\odot}$ black hole (Swartz

Sample	n_{39}	α	χ^2_r (dof)
CSC2, ETG	$0.31^{+0.01}_{-0.02}$	$0.99^{+0.02}_{-0.02}$	0.54 (28)
4XMM, ETG	$0.16^{+0.02}_{-0.03}$	$0.99^{+0.05}_{-0.04}$	0.09 (27)
2SXPS, ETG	$0.03^{+0.02}_{-0.01}$	$1.02^{+0.30}_{-0.24}$	0.68 (9)
compiled, ETG	$0.29^{+0.01}_{-0.01}$	$1.06^{+0.02}_{-0.02}$	0.67 (28)

Table 5.4: Parameters of the fits of deconvolved XLF with a single powerlaw model. "ETG" refer to the sample of complete ULXs in early-type galaxies. n_{39} and α are the amplitude and slope of the powerlaw model, respectively. See the text for more details.

Sample	n_{39}	α_1	α_2	$\log(L_{break})$	χ^2_r (dof)
CSC2, LTG	$0.45^{+0.02}_{-0.02}$	$0.67^{+0.09}_{-0.10}$	$1.36^{+0.06}_{-0.05}$	$39.45^{+0.07}_{-0.06}$	0.37 (27)
4XMM, LTG	$0.35^{+0.02}_{-0.02}$	$0.81^{+0.06}_{-0.07}$	$1.24^{+0.05}_{-0.04}$	$39.73^{+0.11}_{-0.11}$	0.19 (33)
2SXPS, LTG	$0.29^{+0.02}_{-0.02}$	$0.80^{+0.04}_{-0.05}$	$1.73^{+0.12}_{-0.10}$	$39.97^{+0.07}_{-0.08}$	0.33 (24)
compiled, LTG	$0.41^{+0.01}_{-0.01}$	$0.86^{+0.04}_{-0.06}$	$1.31^{+0.03}_{-0.03}$	$39.66^{+0.08}_{-0.09}$	0.77 (33)
CSC2, LTG39	240^{+12}_{-12}	$0.80^{+0.08}_{-0.10}$	$1.90^{+0.07}_{-0.14}$	$39.67^{+0.08}_{-0.11}$	1.13 (12)
4XMM, LTG39	168^{+10}_{-10}	$0.71^{+0.08}_{-0.09}$	$1.80^{+0.14}_{-0.17}$	$39.74^{+0.10}_{-0.10}$	0.17 (14)
2SXPS, LTG39	150^{+10}_{-10}	$0.65^{+0.10}_{-0.12}$	$1.39^{+0.25}_{-0.17}$	$39.70^{+0.20}_{-0.19}$	0.13 (18)
compiled, LTG39	424^{+15}_{-15}	$0.89^{+0.05}_{-0.06}$	$1.97^{+0.03}_{-0.06}$	$39.71^{+0.05}_{-0.06}$	0.60 (12)

Table 5.5: Parameters of the fits of the deconvolved XLFs of late-type galaxies with a broken powerlaw model. "LTG" refer to the samples of complete ULXs in late-type galaxies. "LTG39" stands for the samples of late-type galaxies having $L_{lim} < 10^{39}$ erg s^{-1}; they correspond to the classical, non-renormalised XLF. n_{39}, α_1, α_2 and $\log(L_{break})$ are the amplitude, faint-end slope, bright end slope and break luminosity of the broken powerlaw model, respectively. See the text for more details.

et al., 2011; Wang et al., 2016; Kaaret et al., 2017). The reasons for this break are further examined in Section 5.4.4.

5.3.2 ULX rates in different environments

Generally speaking, precursory studies found that late-type galaxies were more prone to host ULXs, in particular in their star-forming regions (e.g. King et al. 2001; Swartz et al. 2004; Liu and Bregman 2005). Elliptical galaxies also host a significant ULX population, especially those that have undergone a recent star-formation event (Kim and Fabbiano, 2004). The luminosity function of ULXs and their location in their host (distance to the center) seem to be consistent with the extrapolation of HMXB in late-type galaxies and LMXB in elliptical galaxies, at higher luminosities (Gilfanov et al., 2004; Swartz et al., 2011; Mineo et al., 2012; Kovlakas et al., 2020). Other demographic studies showed an excess of ULXs in dwarf galaxies and in low-metallicity galaxies (e.g. Swartz et al. 2008, Kovlakas et al. 2020). The scaling relations linking ULX rates with galaxy mass, star-formation rate and metallicity were even calibrated in recent works (Anastasopoulou et al., 2019; Kovlakas et al., 2020; Lehmer et al., 2021).

Figure 5.8 shows the evolution of ULX rates n_{ULX} with various galaxy parameters. The qualitative trends reported in the literature are also present in our cleaned ULX sample:

- ULX rates globally increase with the galaxy stellar mass, regardless of the star-formation rate; however an excess is visible for dwarf galaxies ($10^8 < M_{gal}/\mathrm{M}_\odot < 10^9$)
- ULX rates increase with the star-formation rate, at least in late-type galaxies
- ULX rates are higher in late-type galaxies, regardless of the star-formation rate; a significant ULX population does exist in elliptical galaxies

Modeling this ULX rate – SFR relation with a powerlaw, $\log(n_{ULX}) = \alpha \log(\mathrm{SFR}) + \beta$ where α is the slope and β the normalization, we obtain $\alpha = 0.43 \pm 0.04$ for late-type galaxies shown in the middle panel of Figure 5.8. This is in excellent agreement with the value obtained by Kovlakas

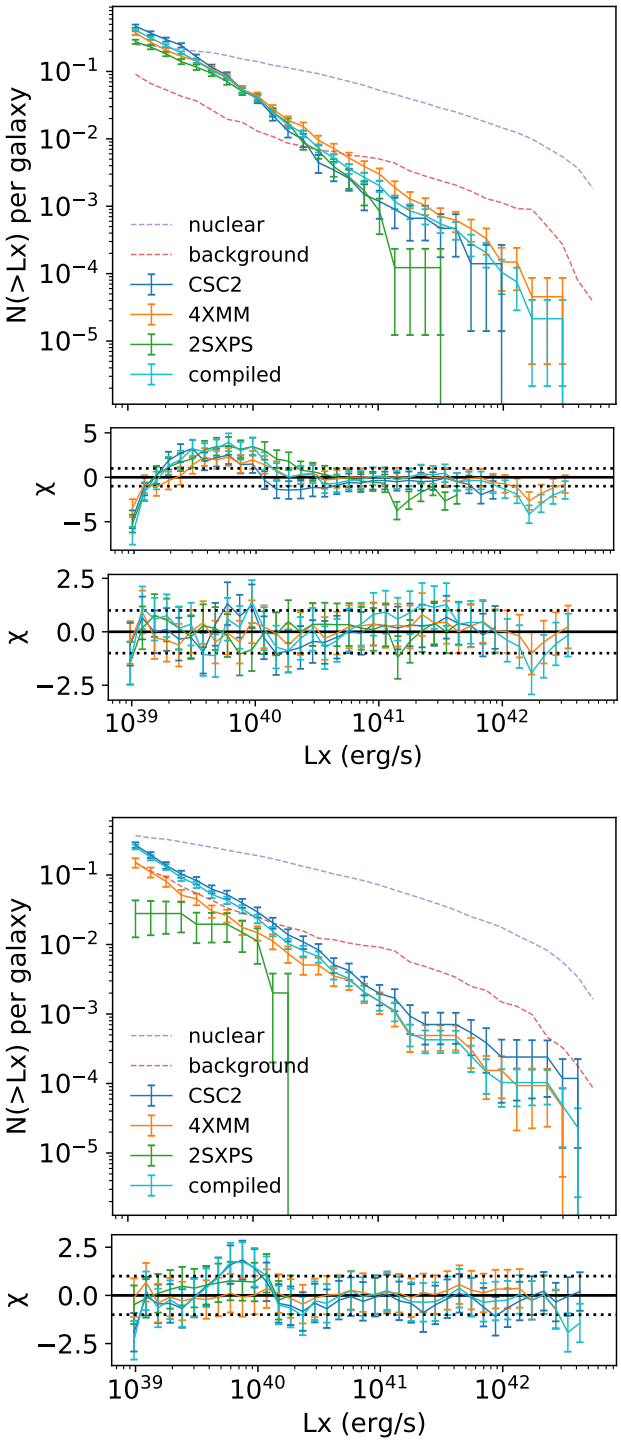

Figure 5.7: Cumulative X-ray luminosity functions of ULX candidates from 4XMM, CSC2 and 2SXPS. (Top panel) Deconvolved XLF of late-type galaxies, and residuals from the single (middle) and broken (bottom) powerlaw fits detailed in Table 5.5. (Bottom panel) Deconvolved XLF of early-type galaxies, and residuals from the single powerlaw fits detailed in Table 5.4. For comparison, we overlay the cumulative distributions of sources matching their host nucleus, and of ULX candidates classified as background contaminants.

et al. (2020) on average over all types of late-type galaxies: $\alpha = 0.45^{+0.06}_{-0.09}$. Elliptical galaxies seem to present a sharper scaling relation, with a slope $\alpha = 0.84 \pm 0.07$ at SFR < 1 M$_\odot$ yr^{-1} and a drop above this value. However, the SFR estimator we used is unreliable for early-type galaxies, being degenerate with the dust mass, so this result is inconclusive. In the top panel of Figure 5.8, we can

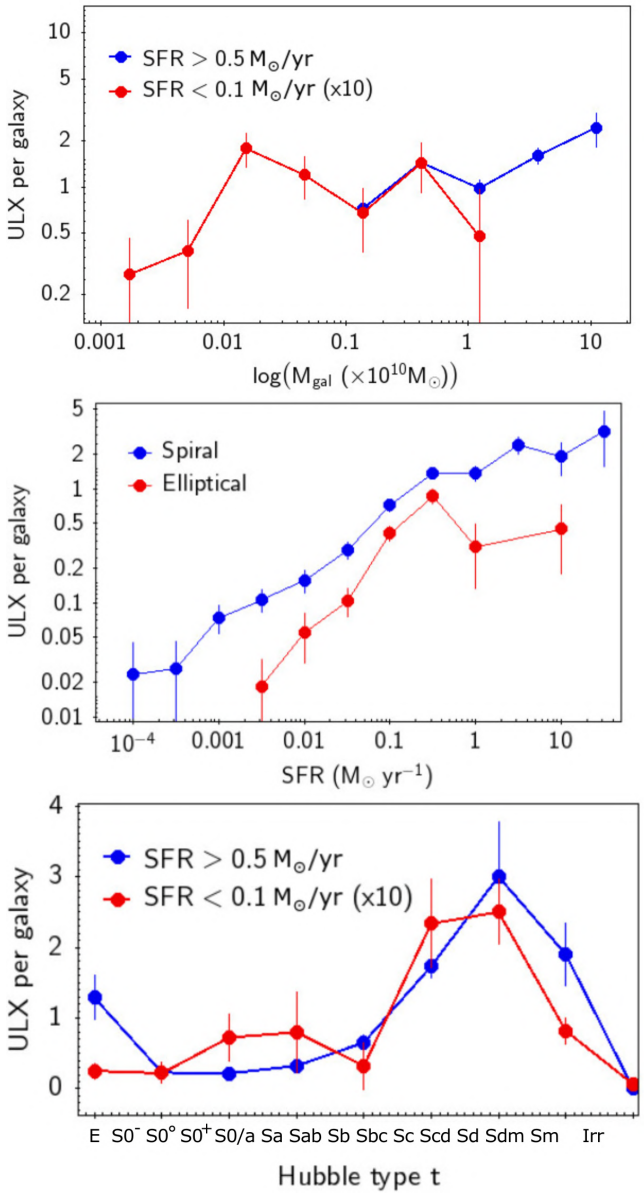

Figure 5.8: Rates of ULX as a function of different properties characterising galaxy environment.

see an excess of ULXs in dwarf galaxies and a tenfold increase of the ULX rate over five orders of magnitude in stellar masses covered by the sample: the specific ULX rate n_{ULX}/M_* thus decreases with stellar mass, in agreement with Walton et al. (2011) and Kovlakas et al. (2020).

We find tentative evidence that ULXs and HLXs do not share exactly the same environment: the latter tend to be hosted in equal rates in spiral and elliptical galaxies (Figure 5.9). Note that this trend was reported in Bernadich et al. (2021), but not found in Kovlakas et al. (2020). This trend can be interpreted in terms of the mean slope of the XLF of ULXs, which (in our sample) is shallower for early-type galaxies than for late-type galaxies. This is in tension with the trend reported in the literature (e.g. Wang et al. 2016). This point is discussed in Section 5.4.4.

The radial distribution of ULXs in their host also gives constraints on their favourable environments. However, it cannot be studied in galaxies of small angular size or large distance, due to source confusion issues and the exclusion of ULXs close to the nucleus. We thus examine the number of ULXs in spiral and elliptical galaxies having a major axis $D_{25} > 30$ arcsec, as a function of their galactocentric distance. The result is shown in Figure 5.10, where the first bin is not shown since the ULX census in this inner part of the galaxy ($\lesssim 0.15 \times D_{25}$) is incomplete. Regardless of the sample in use, the

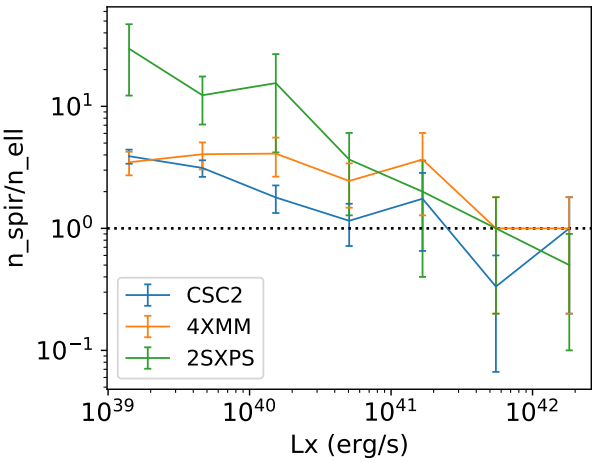

Figure 5.9: Evolution with X-ray luminosity of the ratio between ULX rates $N(L_X)$ in late-type and early-type galaxies.

surface density of ULXs in spiral galaxies smoothly decreases towards larger separations, while it becomes flatter in elliptical galaxies before being cut off beyond D_{25}. In the subsample of spiral galaxies, containing enough ULXs to probe several luminosity bins, the form of the distribution seems independent of the source luminosity. This is in agreement with the results of Kovlakas et al. (2020), performing the same analysis in galaxies closer than 40 Mpc. However, our ULX selection extending beyond the D_{25} ellipse as well as our filtering of contaminants allow us to observe for the first time the drop in ULX density in the outer part of elliptical galaxies.

5.3.3 Comparison of XRB and ULX

It is now widely accepted that most ULXs below $\sim 10^{41}$ erg/s contain either neutron stars or stellar-mass black holes accreting above the Eddington limit. However, the geometry of their accretion flow, as well as the mechanisms explaining their spectral states are still poorly understood. From the few nearby individual ULXs that have been observed multiple times with large exposures, two decades of detailed spectral study led to the results cited in the introduction.

For the three X-ray catalogues studied in this work, XRB are well-detected only in nearby galaxies ($D \lesssim 20$ Mpc) which have larger apparent sizes and thus overlap numerous background sources. For this reason, and because they correspond to a source type actually present in the training sample, we select them using a different criterion to avoid background and foreground contaminants: sources following $P_{XRB} > 0.7$, $sep < 0.8$ and $L_X < 10^{39}$ erg/s make up our sample of XRB candidates. The contamination rate among these selected candidates is 10–12% from manual inspection.

Hardness

Figure 5.11 shows three hardness – hardness diagrams comparing ULX and XRB from each survey. In all three samples, their distributions are mostly overlapping, consistently with previous studies. Except for the minority of nearby ULX sources observed for long exposure times, this hardness information is not sufficient to probe differences in the spectral shape. We also plot ULX candidates classified as background ($P_{AGN} > P_{Soft}$) and soft ($P_{AGN} < P_{Soft}$) contaminants. The locus of sources classified as background contaminants is significantly offset from these populations, and as expected, it matches precisely the locus of AGN. This gives further credit to their classification as contaminants, and is in agreement with previous works on AGN colours. Soft contaminants are fewer and dispersed at different loci of this parameter space.

More conclusive results may be found by exploring the hardness evolution when the flux varies. Indeed, hardness-luminosity studies of black hole XRBs have shown a hysteresis cycle between two canonical states, high/soft and low/hard (Shakura and Sunyaev, 1973; Remillard and McClintock, 2006) while neutron star and some black hole ULXs globally harden when they brighten (Kaaret et al., 2017; Gúrpide et al., 2021). In ULXs, a softening occurring when the ULX brighten may indicate the

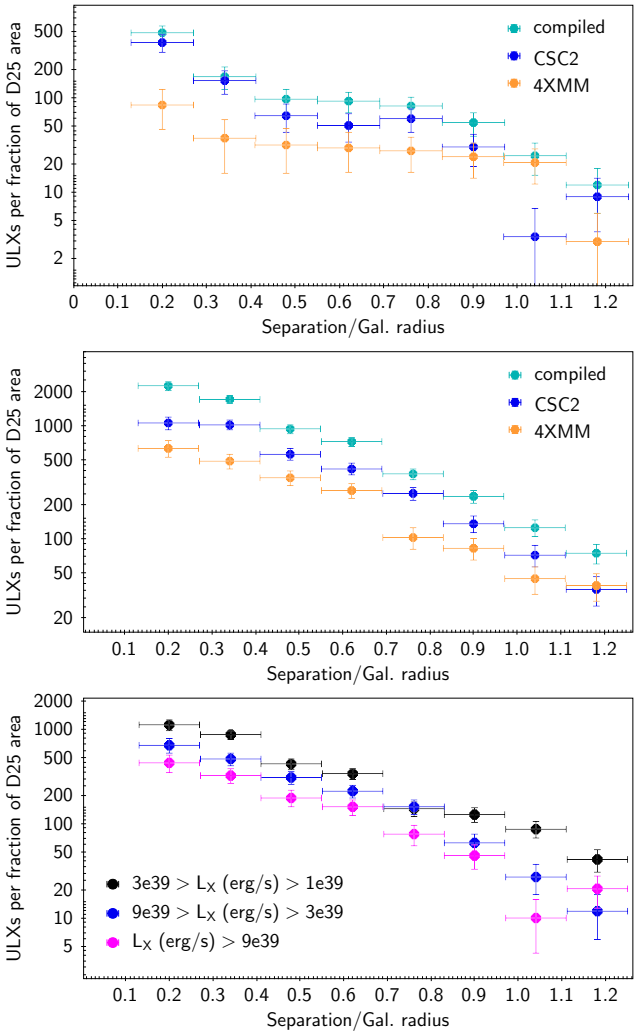

Figure 5.10: Radial distribution of ULXs in early-type (top) and late-type (middle, bottom) galaxies, showing their surface density as a function of galactocentric distance. The last panel shows the surface density of different luminosity bins in the compilation of *Chandra*, *XMM-Newton* and *Swift* selected ULXs.

presence of a black hole (e.g. Narayan et al. 2017), as found in black hole XRBs; however this does not apply to at least some ULXs (e.g. NGC 5907 ULX1, Gúrpide et al. 2021). We thus looked at the hardness evolution of a sample of XRB and ULXs having varied significantly between detections. While such a study would require a detailed spectral modeling of each source, we implement here a first approach aimed at noticing sources showing large hardness variations. In order to combine the detections coming from all three instruments, we built a flux hardness ratio $HR67$ between the bands 0.2–2 and 2–12 keV:

$$HR67 = \frac{F_{2-12} - F_{0.2-2}}{F_{2-12} + F_{0.2-2}}$$

This corresponds to existing *XMM-Newton* energy bands, and an extrapolation of *Swift* and *Chandra* energy bands, for which we used fixed conversion factors. To this end, although this is a severe approximation, we assume an absorbed powerlaw model with ($\Gamma = 1.7$, $n_H = 3 \times 10^{20}$ cm^{-2}) as already done in CSC2, 4XMM and part of *Swift* catalogues to convert count rates into fluxes. From the ULX and XRB samples in all three surveys, we select 59 unique sources that varied by a factor of at least 10 during their follow-up, and we consider their 799 detections that have $HR67_err < 0.25$. This selection targets especially high S/N sources having a good follow-up, thus most of them are already well-studied (32 have an entry in *Simbad*). Sources having their peak flux below (resp. above) 10^{39} erg/s are considered as XRB (resp. ULX). Figure 5.12 shows the detected luminosities of these 59 sources, with hardness being colour-coded.

While a subsequent fraction ($\sim$ 50%) of sources do not present a significant hardness evolution ($\Delta HR < 0.2$), most of the other sources – which have variable hardness – follow the expected trend: from the lower luminosity state to the higher luminosity state, a significant fraction of XRBs become softer and most ULXs harder. A few outliers are to be noted: some ULXs become softer instead, such as M101 ULX-1 (ObjID=38) which is a well-known supersoft ULX thought to host a black hole (Liu et al., 2013; Shen et al., 2015), or ESO 243-49 HLX-1 (ObjID=59) having a well-studied high/soft state (e.g. Servillat et al. 2011; Godet et al. 2009, 2012). NGC 4490 ULX-3 (ObjID=57) has a very low HR at peak (*Swift*) detection, which is unreliable ($L_{X,det} > 10^{41}$ erg/s), probably due to its confusion with the ambient hot gas and the vicinity of ULX-1 which is softer – indeed the *Swift* coordinates are offset in this direction, by 5 arcsec from the *Chandra* source. While 4XMM J095524.8+690113 (ObjID=24) is always very soft, it matches SN 1993J. NGC 5907 ULX-1 (ObjID=55) and 4XMM J022239.1+422328 (ObjID=25) are always very hard (this is confirmed by an inspection of their *XMM-Newton* spectra), as expected from their locations right inside a gas-rich, edge-on host galaxy suggesting an important absorption. This sample of 59 sources represents a large sample of uniformly selected, highly variable extragalactic XRBs and ULXs.

Variability

The variability within an observation is hard to characterize on a systematic basis, as it takes various forms depending on the source type and is strongly affected by the binning. Additionally, automated processing of the detailed light curve is time consuming and subject to biases. However, some variability indicators are made available as columns of the X-ray catalogues: for instance, the fractional variability F_{var} represents the dispersion of the flux between snapshots, penalized by the flux error, and is given in 4XMM-DR11. It can be used to isolate the most significantly variable objects. The probability that the source is constant within the observation is available as well in all 3 catalogues, using various tests. 2SXPS records the maximum rate among snapshots in each band, which is valuable to spot short-term outbursts. For each 2SXPS source, we compute the ratio between the maximum and the median rate among all snapshots in the most variable band. Since *Swift* snapshots are shorter (20-30 minutes) than the typical duration of our multi-mission observations ($\sim$ 10ks), this indicator probes variability on shorter timescales.

We find no significant difference between the two populations for *XMM-Newton* and *Chandra* variability indicators. However, 2SXPS ULXs clearly seem less variable than XRBs between observations and (especially) snapshots (Figure 5.13, y-axis). On average, the former varied by 0.71 dex between snapshots, while the latter varied by 1.15 dex (the standard deviation are 0.4 and 0.5 dex, respectively). This difference may be intrinsic, due to the physics behind these populations; but it may also be an observer bias, because unlike other telescopes, the *Swift* monitoring of an XRB is generally performed to track its particular variability. To remove this doubt, we also computed the variability ratio between snapshots for *XMM-Newton* sources, by rebinning the 4XMM light curves to 20 minute

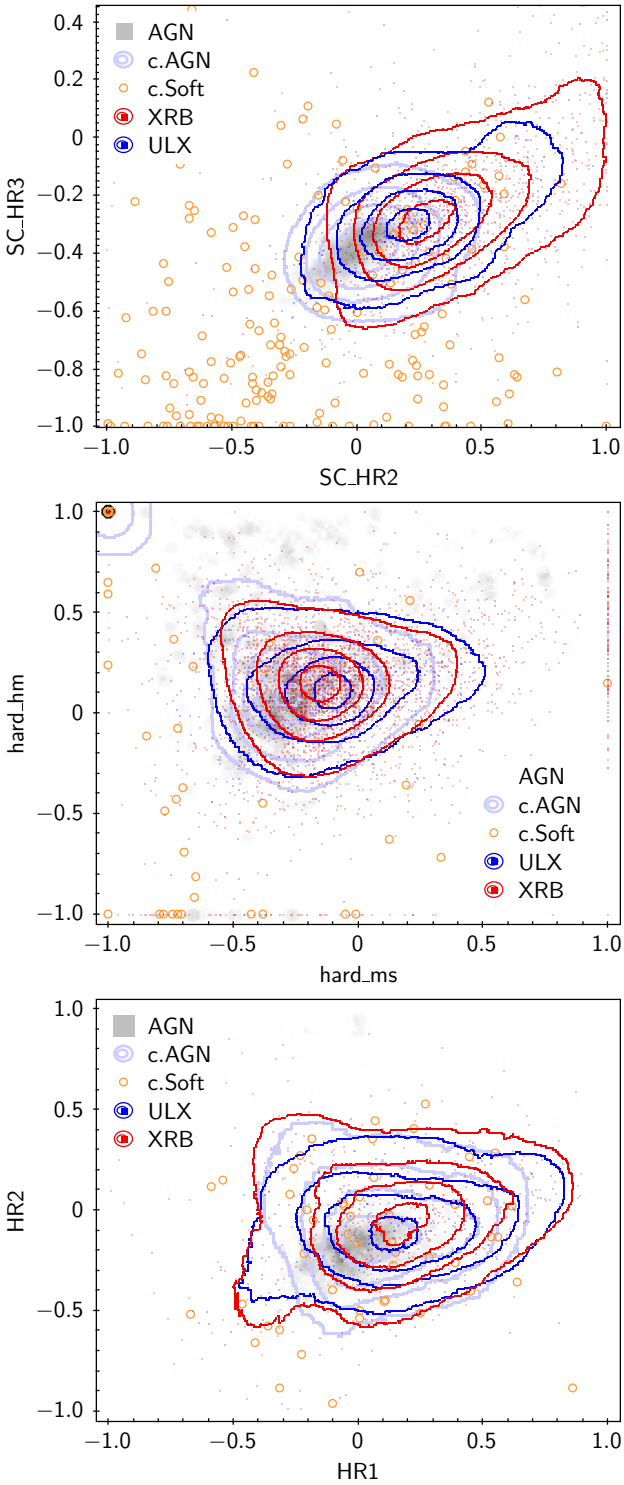

Figure 5.11: Hardness–hardness diagrams of XRB and ULX candidates from 4XMM (top panel), CSC2 (middle panel) and 2SXPS (bottom panel). Contours are shown to ease visualisation. The greyscale density in the background refers to known AGN. Candidates classified as foreground and background contaminants are shown as orange circles and pale blue contours, respectively. The hardness ratios plotted here correspond to the following energy ranges (in keV): $0.5-1/1-2$ (SC_HR2), $1-2/2-4.5$ (SC_HR3), $0.5-1.2/1.2-2$ (hard_ms), $1.2-2/2-7$ (hard_hm), $0.3-1/1-2$ (HR1) and $1-2/2-10$ (HR2).

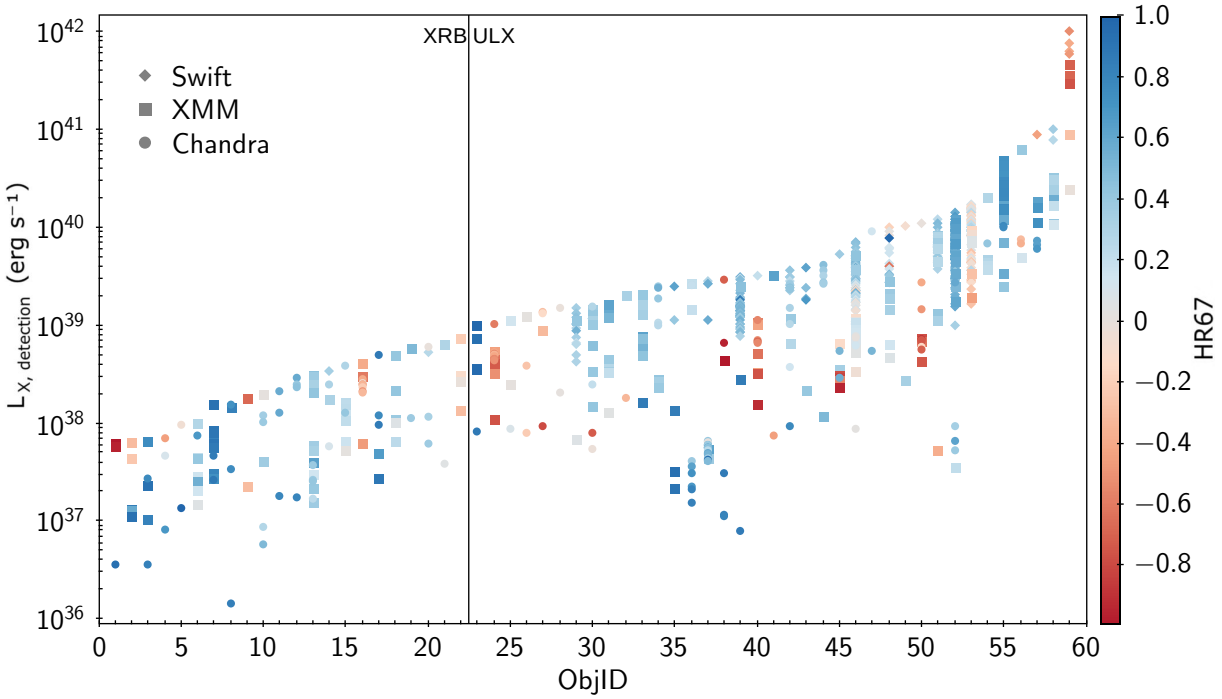

Figure 5.12: Luminosity-hardness evolution of the subset of 59 variable XRB and ULX. $HR67$ is the hardness ratio between $0.2-2$ and $2-12$ keV bands. All detections having $HR67_err < 0.25$ are shown.

long bins, and recording the peak rate of each band. The result is shown in the bottom panel of Figure 5.13: the same offset is visible, with ULXs varying of 0.56 dex between snapshots on average and XRB varying of 0.93 dex.

However, this indicator is subject to at least two biases: first, the exposure time, because episodes of high flux variations are more likely to be detected in longer exposures. XRB have to be at lower distances to be detected, in particular in better-studied galaxies, targeted by longer or more numerous observations. This is why they are detected at lower fluxes in our samples. In the *Swift* sample, 112 out of 293 XRB are located in just 4 galaxies observed for more than 200 ks: M51, M81, M101 and NGC 300. After removal of these galaxies, the ratio between the mean variability of XRBs and ULXs is reduced by 30%. The second important parameter is the flux, because the noise contribution to the source flux is more significant at low flux and equal exposure. At equal fluxes and exposure time, both populations have similar variability distributions in both surveys. This is tentative evidence that both populations undergo a short-term flux variability of equal amplitude, however this result would need a detailed treatment of the light curves to be confirmed, which is beyond the scope of our study.

5.3.4 The hyperluminous X-ray sample

In our work, thanks to the high completeness of GLADE even at several hundred Mpc, we are able to retrieve 13, 115 and 75 HLX candidates from *Swift*, *XMM-Newton* and *Chandra* samples, respectively. Of these 191 unique candidates, listed in Table A.1, 76 sources have a bright optical counterpart and are split in two categories: "galaxy pair candidates" (22 objects), if the source matches the nucleus of a known galaxy in interaction with the host; and "weak HLX candidates" (54 objects), for other point-like optical sources or sources largely offset from the galaxy extent. The latter could indeed be background AGN, as suggested by the identification of 4 such sources as MIR-detected AGN (Secrest et al., 2015). However, they could also be dwarf satellite galaxies of the host, which are a favourable environment to look for IMBH (Webb et al., 2010; Greene et al., 2020; Barrows et al., 2019); and actually 7 of them have photometric redshifts consistent with the host distance. The 115 remaining HLXs with no optical counterpart, or a faint counterpart matching the extent of the galaxy, are qualified as "robust HLX candidates". Figure 5.14 shows a random selection of 15 candidates belonging to one of these three categories, taken from the three X-ray surveys. For clarity,

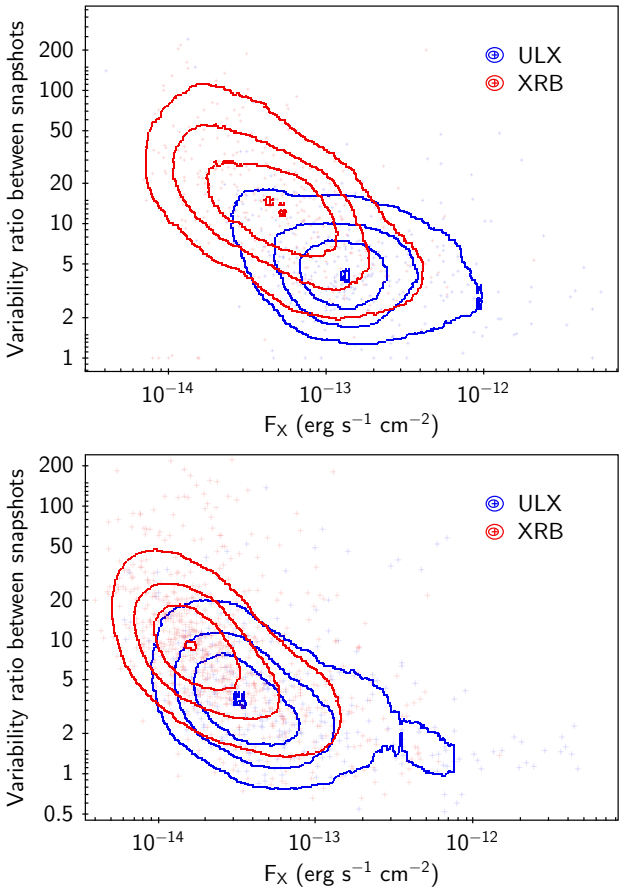

Figure 5.13: Variability between snapshots of XRB and ULX candidates from 2SXPS (top panel) and 4XMM (bottom panel), as a function of their flux. Contours are shown to ease visualisation.

	CSC2	4XMM	2SXPS	Total (unique)
Initial candidates	195	360	110	665 (619)
With redshift	96	187	41	324 (298)
Background	82	165	35	282 (259)
Foreground	2	3	0	5 (5)
Distance match	12	19	6	37 (34)
Selected candidates	75	115	13	203 (191)
Robust	51	66	5	122 (115)
Weak	15	35	7	57 (54)
Galaxy pair	9	14	1	24 (22)
With opt. counterpart	29	63	8	100 (94)
Soft ($HR67 < -0.6$)	2	5	1	8 (6)
Hard ($HR67 > -0.6$)	67	110	12	189 (179)

Table 5.6: Number counts of initial and selected HLXs in different subsamples (see Section 5.2.5 and Section 5.3.4, respectively, for details on the subsamples). The sample of "soft HLXs" is defined in Section 5.3.5, and is the complementary of "hard HLXs" (note that 6 *Chandra* candidates are not included in these samples, because their $HR67$ could not be calculated).

we summarise the number counts of each subsample of initial and selected HLX candidates in Table 5.6 .

The distributions of the distances and mean observed 0.5–10 keV X-ray luminosities of the 191 HLX candidates are shown in Figure 5.15. As usually found, HLXs are detected much further away than ULXs. Most of them have luminosities in the range $10^{41} - 10^{42}$ erg s $^{-1}$, with galaxy pair candidates being the most luminous. By construction, all candidates have $S/N > 3$. However, we note that only 17% of the sample of 169 (robust+weak) candidates have $S/N > 10$. The median S/N for this sample is 4.9.

Eight removed candidates present in the literature are reported here. Some sources are simply not present in our sample: NGC 2276 ULX-1 is located outside the GLADE $1.26 \times D_{25}$ ellipse, which does not fit the actual galaxy extent (this is the case for a small proportion of GLADE galaxies). Reported in Zolotukhin et al. (2016) as a reliable candidate, XMM0838+24 is here located outside the extent of its GLADE association, its separation being 1.5 times the galaxy radius at its position angle. The other reliable candidate cited by this study, XMM1226+12, was discarded during manual inspection as lying visibly outside the extent of the host. M82 X-1 is flagged as confused, or extended, in all three surveys. Thus these two sources are not present in our sample. The candidate in IC 4320 (an elliptical galaxy at ∼93 Mpc), proven to be a background AGN (Sutton et al., 2015), was discarded due to a PanSTARRS photometric redshift higher than the host ($z_{ph} = 0.18 \pm 0.06$, Tarrío and Zarattini 2020). Because we use the mean luminosity in each survey for selection criterion, the candidates located in NGC 5907, NGC 4077, UGC 6697 and Cartwheel are not in our HLX sample, due to their $\langle L_X \rangle < 10^{41}$ erg s^{-1}. We still retrieve some well-known candidates in our work: they include ESO 243-49 HLX-1, NGC 470 HLX-1 (Walton et al., 2011; Sutton et al., 2012) and 3XMM J161604.0-223726 in IC 4596 (Earnshaw et al., 2019).

5.3.5 Comparison of ULXs and HLXs

Because of the low number of known HLXs, few studies have attempted to characterize their typical environment. The location of ESO 243-49 HLX-1 outside the disk of its host may be due to its embedding in a stellar cluster or the stripped core of a dwarf galaxy (e.g. Webb et al. 2010) but ESO 243-49 HLX-1 in itself seems to be an outlier among HLXs (e.g. Sutton et al. 2015). Since then, different HLX discoveries led to the suggestion that HLXs and ULXs share the same type of environment, namely star-forming, spiral galaxies (Sutton et al., 2015; Barrows et al., 2019). This is at odds with the ratio of our HLX rates between spiral and elliptical (Figure 5.9), suggesting an equal rate of robust HLXs in these two morphologies. We compare the behaviour followed by ULX and HLX rates as a function of three environmental parameters (Figure 5.16): the galaxy stellar mass, its star-formation rate and its Hubble type. Unlike ULXs, our HLXs tend indeed to be hosted equally in (regular) late-type and early-type galaxies. This suggests that unlike ULXs, their rate is not related to the populations of

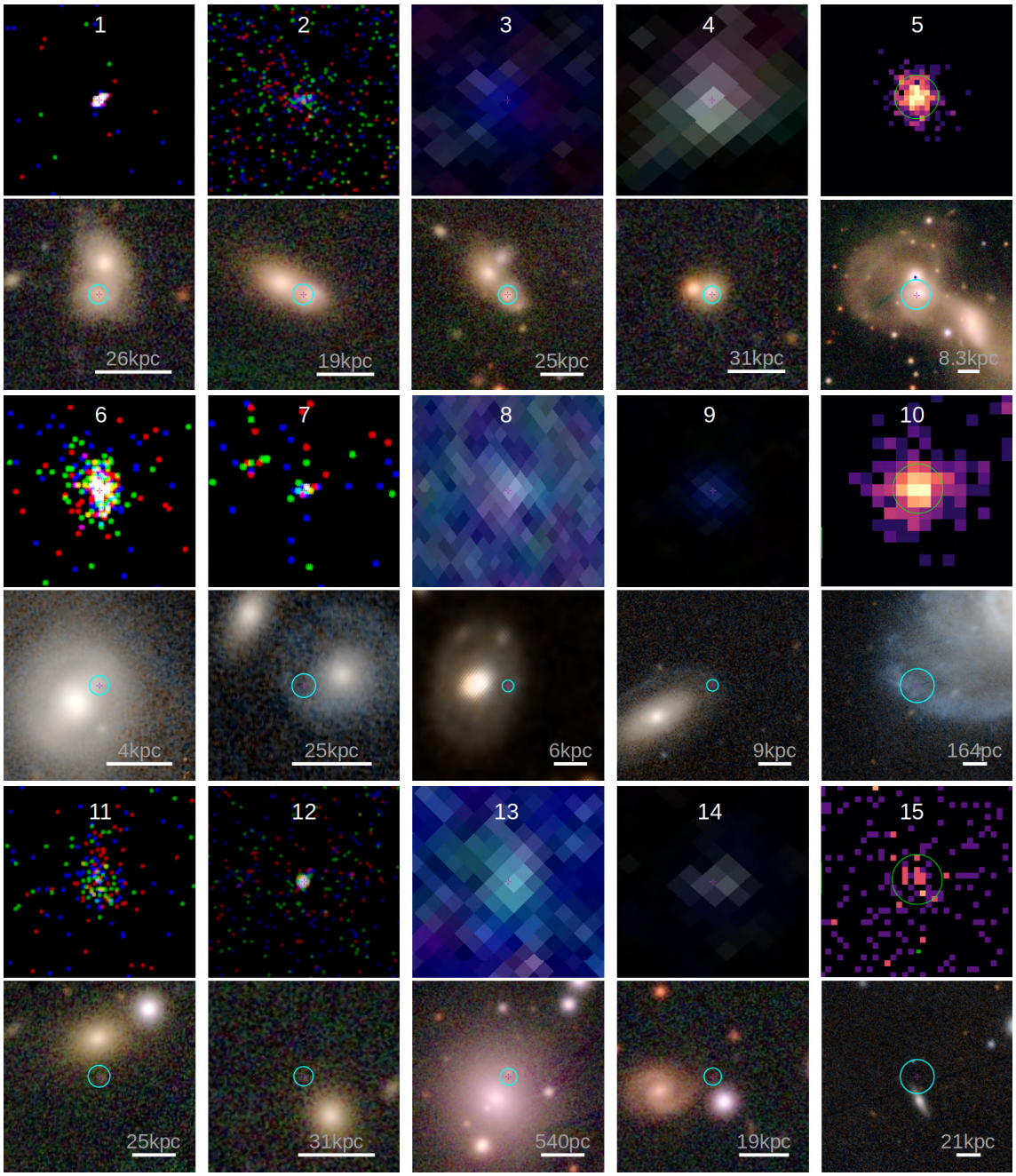

Figure 5.14: Images of a random sample of new HLX candidates. The images are structured as follows: column (1,2), (3,4) and (5) display CSC2, 4XMM-DR11 and 2SXPS candidates, respectively. (Impair) and (pair) rows show the X-ray and optical image at the same scale – the white line corresponds to 10 arcsec. Rows (1,2), (3,4) and (5,6) correspond to "galaxy pair", "robust" and "weak" candidates, respectively. These candidates have the following names: 1–2CXO J124208.4+331854, 2–2CXO J025921.5+132913, 3–4XMM J123441.0+020846, 4–4XMM J104444.7-012018, 5–2SXPS J164652.0+234011, 6–2CXO J082215.9+210535, 7–2CXO J105210.4+552243, 8–4XMM J062447.9-372122, 9–4XMM J125708.6-044144, 10–2SXPS J111416.1+481833, 11–2CXO J005151.7+474019, 12–2CXO J131133.3-011656, 13–4XMM J083235.2-225804, 14–4XMM J145753.6-113959 and 15–2SXPS J115109.2+570340. X-ray images correspond to the *Chandra* and XMM-EPIC images displayed in ESASky, or the science exposures of *Swift*-XRT where the green circle has a 10 arcsec radius. Optical images come from the PanSTARRS survey (Chambers et al., 2016), except candidate 8 (Digitized Sky Survey, McLean et al. 2000) as it lies in a region not covered by PanSTARRS. The 3σ X-ray position error circle is shown in cyan.

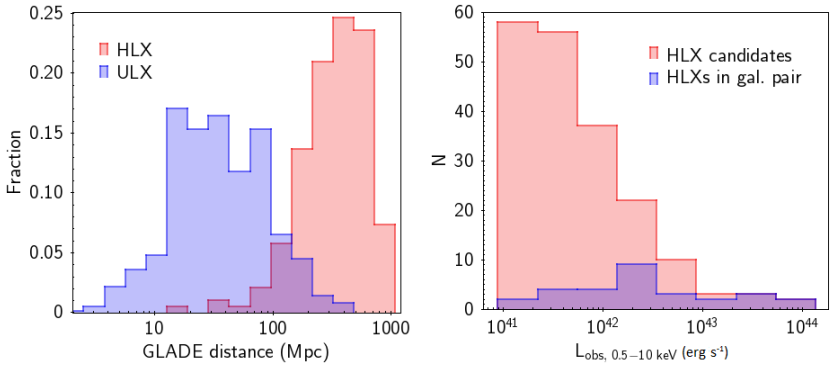

Figure 5.15: (Left) Distribution of distances for the selected samples of ULXs and HLXs. ULXs are detected up to 500 Mpc and HLXs up to 1100 Mpc. (Right) Distribution of the 0.5–10 keV observed mean X-ray luminosity of the 191 HLXs candidates, including the 22 galaxy pair candidates.

LMXBs or HMXBs, which may favour their interpretation as more massive systems. However we note that only 38 HLXs have a Hubble type value provided in HyperLEDA, and that 40% of them have errors on this type $e_t \geq 3$ (equivalent to 1.5 major graduations in Figure 5.8). On the other hand, similarly to the trends obtained on ULXs, we find a positive correlation between the HLX rate and the stellar-mass and star-formation rate.

Hardness

We investigate the locus of the 191 HLX candidates in a hardness–hardness diagram. Figure 5.17 shows the diagrams obtained from *XMM-Newton*, *Chandra* and *Swift* data, after discarding sources with $HR = -1$ or 1 to limit unreliable measurements. The HLX and ULX distributions are mainly overlapping, with only a fraction of *XMM-Newton* HLX candidates looking harder above 4.5 keV (SC_HR4). They consist mainly of 15 robust HLX candidates having $SC_HR4 > 0$ on average among detections; their low signal-to-noise ratio ($S/N < 10$) does not allow a more in depth spectral study. However, the energy range covered by SC_HR4 essentially probes the photon index of the spectrum if it were an absorbed powerlaw spectrum, and in this case such values would only be produced by $\Gamma \lesssim 2$.

Besides, in the *Swift* sample, ESO 243-49 HLX-1 is an outlier located far in the lower left of the distribution. Three other outliers are found in 4XMM: 4XMM J215022.4-055109, a well-known IMBH candidate which underwent a tidal disruption event (Lin et al., 2018), 4XMM J161534.3+192707, a variable HLX possibly consistent with another offnuclear tidal disruption event (Tranin et al., in prep), and 4XMM J085253.8+180110, a weak candidate located in a cluster of galaxies. Another soft outlier (not visible in Figure 5.17 because of having $SC_HR4 = -1$) is 4XMM J231818.7-422237, a variable soft source already cited as a candidate IMBH in Lin et al. (2014). It could actually be associated with two GLADE galaxies, and would be of ULX luminosity if belonging to the one closer to us. It is however softer than all other ULXs ($SC_HR2 = -0.73$, $SC_HR3 = -0.85$). The outlier nature of such soft HLXs is even more visible in the distribution of $HR67$, the hardness ratio between bands $0.2-2$ and $2-12$ keV, where they form the peak close to -1 ($HR67 < -0.6$) in Figure 5.18. All but two of them are also seen as outliers by the source classification, with an outlier measure > 12 (Tranin et al., 2022), higher than 99% of ULX candidates.

Variability

Some extreme ULXs were seen to approach or overcome the luminosity threshold of HLXs for transient periods. Super-Eddington radiation well above the Eddington limit seems possible for the timescale of an observation (Israel et al., 2017), and in this case the Eddington limit cannot give accurate mass estimations of the central object. HLX candidates detected only once could thus be powered by stellar-mass accretors. However, we find that out of the 191 HLX candidates, 96 were detected several times (up to 20 times, and even more for ESO 243-49 HLX-1, NGC 470 HLX-1 and the AGN in a galaxy pair XMMU J134736.6+173403). Only 26 of them have a detection below 10^{41} erg s^{-1} – including the known candidates in ESO 243-49, IC 4596 and NGC 470 – suggesting that a majority of our HLX sample is actually persistent. The time between the first and the last

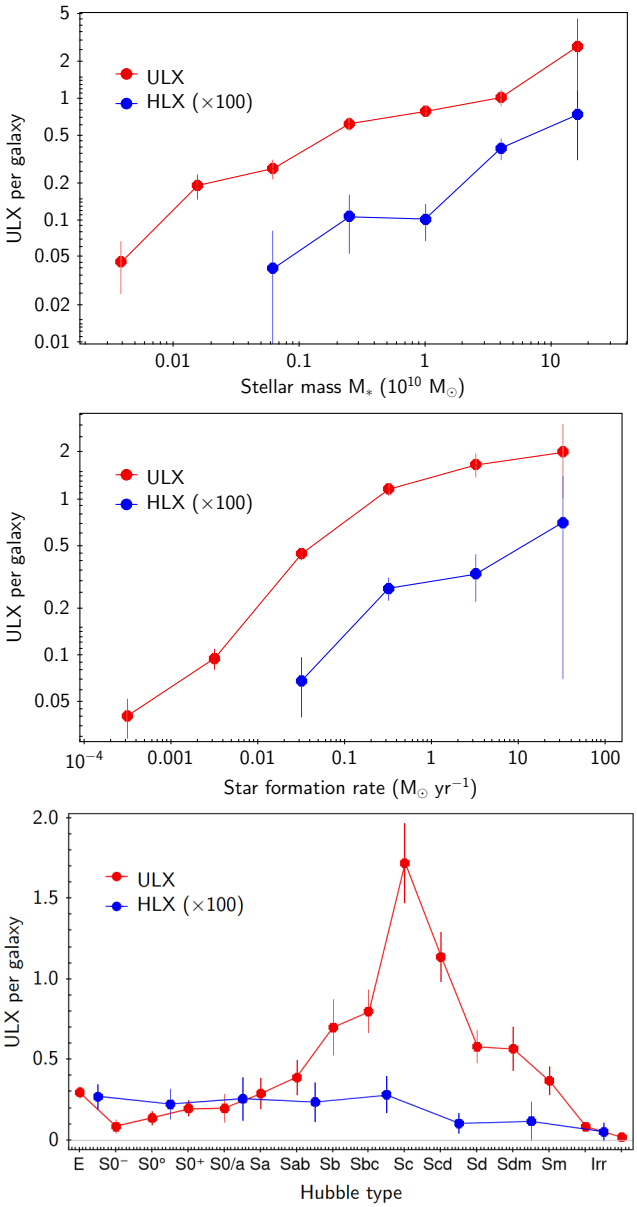

Figure 5.16: Rates of ULX and HLX as a function of different properties characterising galaxy environment.

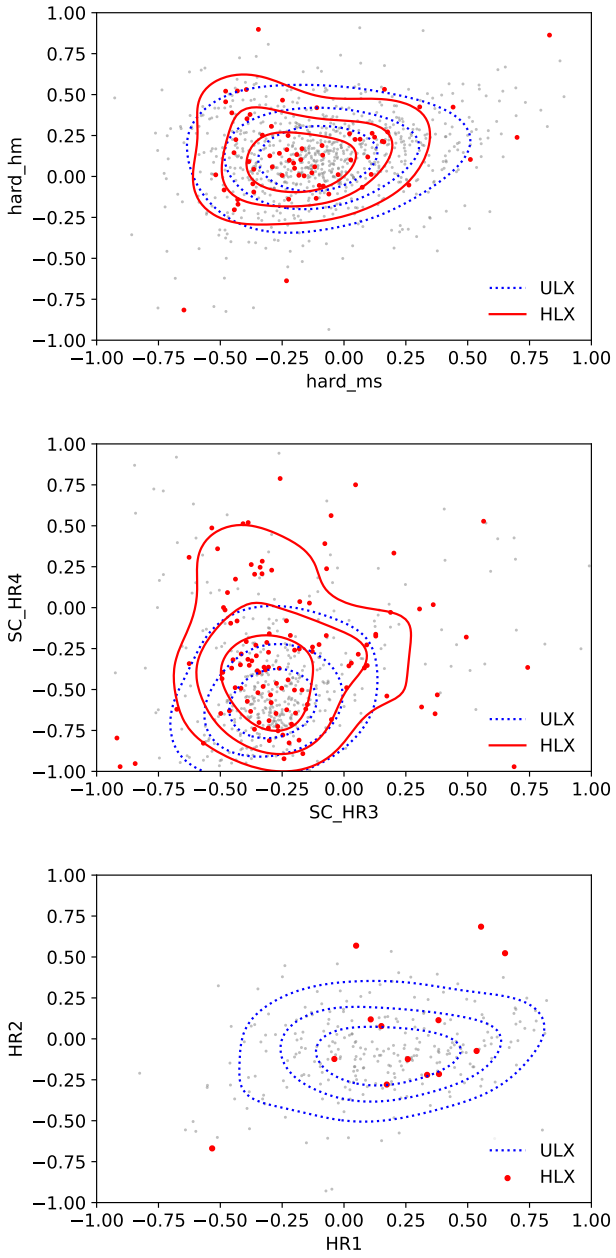

Figure 5.17: Hardness–hardness diagrams of ULX and HLX candidates from *Chandra* (top), *XMM-Newton* (middle) and *Swift* (bottom). Contours at 25th, 50th and 75th percentiles are shown to ease visualisation.

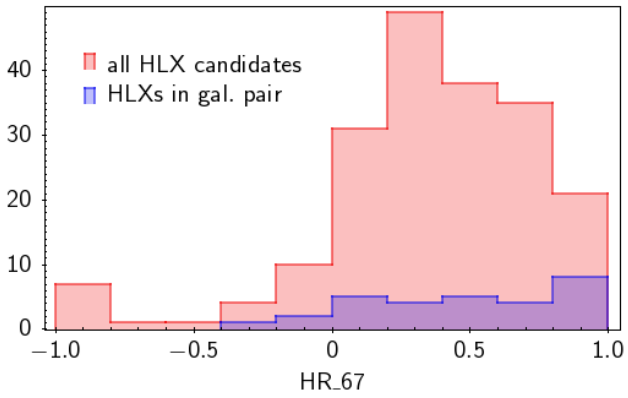

Figure 5.18: Distribution of the hardness ratio $HR67$ between the 0.2-2 and 2-12 keV energy bands for selected HLX candidates.

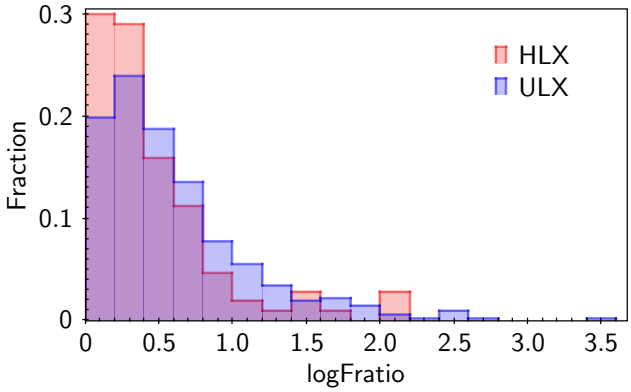

Figure 5.19: Distribution of the variability ratio between observations ($logFratio = \log\left(\frac{F_{max}}{F_{min}}\right)$), for ULXs and HLXs.

observation is $>$ 1 yr for 75% of persistent candidates. Figure 5.19 shows the distribution of their variability ratio between observations, along the one of ULXs. No significant variability excess is seen in either of these two categories.

5.4 Discussion

5.4.1 Comparison to other works

Recent releases of large X-ray surveys and complete galaxy catalogues enabled the discovery of large samples of ULXs and HLXs. We discuss our findings in the context of previous works on this subject.

Kovlakas et al. (2020) found 629 ULX candidates in 309 galaxies in the local 40 Mpc volume, from *Chandra* CSC2 catalogue matched with HECATE (Kovlakas et al., 2021). They estimated a contamination rate of 20%, using the $\log N - \log S$ method. Because of the high *Chandra* sensitivity, their sample is likely to be complete. In our work, despite the use of a different galaxy catalogue and slightly different selection criteria, we find a similar number of *Chandra* ULX candidates (567) in galaxies closer than 40 Mpc. However, we remove 58 candidates of this sample from their classification as contaminants, 16 others from their identification as another type in the literature, and 41 are also flagged during manual inspection. This leaves a sample of 442 sources located within 40 Mpc, representing 78% of the initial sample. Adding *Swift* and *XMM-Newton* candidates, the size of the sample is almost doubled (839). This outlines the need to cross-correlate several X-ray catalogues to find these sources, since focusing on one catalogue decreases the survey coverage and misses some candidates as they may have been fainter than 10^{39} erg s^{-1} at the time of the observation. Besides, we were able to confirm key results present in their work, namely the predominance of contaminants in uncleaned samples at luminosities $L_X > 10^{40.5}$ erg s^{-1}, the evolution of the ULX rate with SFR

and the decrease of specific ULX rate with galaxy stellar mass.

Bernadich et al. (2021) used a recent release of the 4XMM catalogue, 4XMM-DR10, matched with HECATE galaxies, to build a clean ULX sample. Similarly to our work, their cleaning pipeline relies on removing the known AGN and foreground contaminants, as well as manual inspection of the sources having optical counterparts (from PanSTARRS and Gaia). However, without an automatic classification, they were not able to remove contaminants having $F_X > F_{Opt}$ or no optical counterparts. Besides, we were able to improve this cleaning by manual inspection of faint counterparts in the southern hemisphere, using the DES survey. Overall, their sample of 779 candidates is somewhat larger than our cleaned sample (667 candidates). They however consider a source as ULX as soon as $L_X + L_{X,err} > 10^{39}$ erg s^{-1} in at least one detection, and only 632 of their candidates have $\langle L_X \rangle > 10^{39}$ erg s^{-1}.

Their work also focuses on the statistical study of *bright* ULXs, having $L_X + L_{X,err} > 5 \times 10^{40}$ erg cm^{-2} s^{-1} in at least one detection. While this bright sample contains 94 such sources, it is significantly different from our sample of HLXs for several reasons: first, because we use the mean luminosity to select them, and because we use the more conventional threshold of 10^{41} erg s^{-1} (only 25 of their bright candidates have $\langle L_X \rangle > 10^{41}$ erg s^{-1}). A large fraction of their sample is thus likely to be similar to luminous ULXs powered by a stellar-mass accretor. Second, because we use GLADE, which is more complete than HECATE as it is a compilation of catalogues (including HyperLEDA), and because HECATE is limited to galaxies at $D < 200$ Mpc, our HLX sample contains significantly more candidates. As a result, we find significant differences in the preferred environments and counterparts of ULXs and HLXs (Section 5.4.5). We do not find evidence in our sample for the softer average spectra for HLXs reported in Bernadich et al. (2021).

Walton et al. (2022) is similar to our work in the sense that they included the same three X-ray surveys. However, their galaxy sample is different, compiling HyperLEDA and the Catalogue of Neighbouring Galaxies. While they used the same matching limit as we do, $1.26 \times D_{25}$, the contamination rate of their sample must be high (Figure 5.6) given that they only cleaned out known contaminants. Their final sample contains 1843 unique candidates, compiled from the 4XMM-DR10, 2SXPS and CSC2 samples containing 641, 501 and 1031 sources, respectively. This total is similar to the 1901 ULXs contained in our compilation, with however slightly different proportions from each survey (667, 304 and 1185). Our slightly larger sample, despite our strict cleaning, was possible thanks to the use of GLADE. Our sample thus constitutes both the largest and the cleanest ULX catalogue to date.

We examine the classification of X-ray sources that we have in common with these three studies. We find 601 sources of Kovlakas et al. (2020) in our sample, of which only 423 pass the offnuclear and $\langle L_X \rangle > 10^{39}$ erg s^{-1} criteria. The rest are mostly discarded because of insufficient luminosities, due to their use of CSC2 fluxes from the PSF 90%-energy width ($flux_aper90_b$) instead of the source region aperture ($flux_aper_b$). 359 sources are selected as ULXs after classification and manual screening, hence ∼15% of candidates are discarded as contaminants. Similarly, in the clean ULX catalogue of Earnshaw et al. (2019) claiming a contamination rate of 24%, we find 17% of candidates removed in our pipeline. From the ULX sample of Walton et al. (2022), 1734 sources are included in this study, of which 1291 pass the first criteria (their luminosity criterion being less stringent). 27% of these sources are discarded as contaminants, higher than their estimated background contamination rate (18–23%). Most of the ULXs of Bernadich et al. (2021) are present in our sample (746), and 574 have ULX-consistent positions and luminosities in our sample. However, 27% of these sources are discarded by the classification and manual screening, considerably higher than expected from their contamination estimation (∼2%). Their estimation is however calculated for their entire X-ray sample (including non-ULXs), perhaps explaining this discrepancy.

Last but not least, Barrows et al. (2019) produced a catalogue of 169 HLX candidates from the CSC2 catalogue and SDSS images. This unprecedented sample size is allowed by their detailed treatment of optical images to detect galaxies up to greater distances and fainter surface brightness; as a result, most of their candidates are located at distances > 1000 Mpc, and present X-ray luminosities $> 10^{42}$ erg s^{-1}. Few of their galaxies are present in the GLADE catalogue: as a result, only 10 of their candidates are present in our CSC2 sample. Two of them have $\langle L_X \rangle < 10^{41}$ erg s^{-1}, and one is discarded when excluding the galaxy central region. Interestingly, 2CXO J122148.2+491131 is flagged as background contaminant due to its photometric reshift $z_{ph} = 0.46 \pm 0.1$ (Beck et al. 2016, also consistent with PanSTARRS and DESI estimates), leaving only 6 candidates out of the possible 10 in

our sample. Whilst their study has the advantage of a low contamination rate (7–8%) and probes the HLX population to greater distances in the Universe, our sample is more likely to contain candidates well-suited for a follow-up as well as HLXs of lower luminosity, probing lower IMBH masses and possibly earlier stages of black hole growth. These points are further discussed in Section 5.4.5.

5.4.2 Number of contaminants

The cosmic X-ray background (CXB) has been extensively studied for several decades by several X-ray missons, revealing that it is essentially due to radiation from unresolved point-like sources, in particular AGN (e.g., Moretti et al. 2003 and references therein). As such, its flux distribution has often been used in ULX and HLX studies to assess the number of background/foreground contaminants behind a given galaxy. For instance, the $\log N - \log S$ relation of Moretti et al. (2003), gathering wide-field and pencil-beam surveys probing six orders of magnitude in flux, was used by Walton et al. (2011), Zolotukhin et al. (2016) and Barrows et al. (2019) to compute their number of contaminants. To this aim, they converted the broad band flux of their sample to the hard energy band of Moretti et al. (2003) (2–10 keV) which yields the most contaminants, using an absorbed powerlaw spectrum with $\Gamma = 1.69$ & $n_H \sim 3 \times 10^{20}$ cm^{-2}. However, a possible caveat of this method is that CXB sources present a variety of spectra (Mushotzky et al., 2000) that cannot be accurately represented by this model. To alleviate this problem, we also compute the number of contaminants using $\log N - \log S$ distributions calibrated in an energy band similar to the broad bands of our sample, namely 0.2–12 keV (*XMM-Newton*), 0.3–10 keV (*Swift*) and 0.5–7 keV (*Chandra*). This is the case of the relations of Georgakakis et al. (2008) and Kim et al. (2007), respectively used in the ULX studies of Zolotukhin et al. (2016) and Kovlakas et al. (2020). After converting our fluxes in the proper energy band, we find excellent agreement between the results obtained from each relation.

The number of contaminants in each galaxy is computed by multiplying the cumulative flux density, $\log(N(>S))$ at a given flux S, by the extent of the galaxy used for finding ULXs (i.e. after the center exclusion criterion has been applied). The flux to consider is directly given by the galaxy distance (such that the contaminant is found in the ULX luminosity range) and the X-ray sensitivity (so that the contaminant is detectable), as $\min(f_{39}, f_{lim})$ where $f_{39} = \frac{10^{39}\text{erg s}^{-1}}{4\pi D^2}$.

Because our center exclusion radius $3(POSERR + 0.5)$ depends on the source position error, we estimate the number of contaminants using the 10%, 50% and 90% percentiles of the position error distribution in each sample of candidates. Results are given in Table 5.7 for the ULX and HLX contaminants, where error bars correspond to the variations in position error. For ULXs, it is comparable to the number of candidates known or classified as AGN, or removed by manual inspection of the optical source. For HLXs, it is similar to the number of background sources (using photometric redshifts) added to the number of HLX candidates flagged as "weak". This is a further indication that the selection of ULX and HLX candidates, and thus the automatic classification and the photometric redshifts estimates, are reliable and robust.

Except in the 4XMM sample, our filtering process identifies more ULX candidates as background contaminants than expected from the CXB. Using the CXB curves of Moretti et al. (2003), yielding the larger contamination rates, the 41 remaining background contaminants in our sample thus represent 2.2% of the sample of selected ULXs.

5.4.3 Heterogeneity of the sample and instrumental biases

Because of the different capabilities of *Swift*-XRT, *XMM-Newton* and *Chandra*, we do not expect to probe exactly the same ULX populations in each survey. *Chandra* on-axis observations are more sensitive and have a higher angular resolving power, so it can probe larger distances where the galaxies look smaller. *XMM-Newton* and *Swift* have covered larger sky areas, and the superior follow-up capabilities of *Swift* can also reveal populations of variable ULXs. The design of *Swift* as a gamma-ray burst monitor has led to a more uniform sky coverage, less biased towards galaxies of special interest, so we can expect a lower observer bias of its ULX population. However, the center-excluding criterion (Eq. 1) leads to exclude a significant fraction of actual ULXs at low galaxy angular separation. This is particularly the case of *Swift* HLX candidates, which are all offset from their host center by > 10 arcsec, while half of *XMM-Newton* and *Chandra* HLX candidates have lower separations. This probably causes the steeper slope of the 2SXPS XLF above $L_X > 10^{40}$ erg s^{-1}.

Survey	Moretti+03	Georgakakis+08	Kim+07	Identified
2SXPS ULXs	140^{+7}_{-15}	141^{+7}_{-14}	139^{+7}_{-15}	171
2SXPS HLXs	13^{+2}_{-6}	13^{+3}_{-5}	13^{+2}_{-6}	25
4XMM ULXs	582^{+55}_{-73}	558^{+53}_{-70}	554^{+53}_{-69}	541
4XMM HLXs	136^{+34}_{-44}	137^{+33}_{-44}	135^{+33}_{-43}	121
CSC2 ULXs	483^{+38}_{-67}	451^{+35}_{-62}	452^{+35}_{-62}	482
CSC2 HLXs	75^{+17}_{-31}	73^{+17}_{-30}	73^{+17}_{-30}	64

Table 5.7: Number of contaminants estimated using different published $\log N - \log S$ relations, in the ULX and HLX samples. Positive and negative errors correspond to the estimates at 10% and 90% of the exclusion radius ($3(POSERR+0.5)$) distribution. The last column gives the number of candidates filtered out by our pipeline as background contaminants, or identified as HLX "weak candidates".

Another bias in our selection of ULXs and HLXs is the significant difference between *Swift*, *XMM-Newton* and *Chandra* energy bands: in particular, the narrower energy band of the latter probably removes valid candidates just below the ULX luminosity threshold. Assuming the same absorbed powerlaw model as previously used $\Gamma = 1.7$, $n_H = 3 \times 10^{20}$ cm^{-2}, the flux conversion factor from the *XMM-Newton* 0.2–12 keV band to the *Chandra* 0.5–7 keV band is 0.7. If this conversion is valid on average, the *Chandra* XLF break in spiral galaxies would be shifted to $\sim 4 \times 10^{39}$ erg s^{-1}, better matching the other XLFs.

Nevertheless, results obtained from the XLF and the comparison with XRBs, ULXs and HLXs are comparable between instruments, showing the robustness of both our cleaning pipeline and our statistical study with respect to instrumental biases.

The XLF inferred from 2SXPS, 4XMM and CSC2 are compatible at the $2-\sigma$ level except at the faint end $L_X < 5 \times 10^{39}$. At these luminosities, most of the sample is made up of sources in galaxies in the distance range of 5–60 Mpc: those sources are most often resolved by *Chandra*, whereas a substantial fraction of *XMM-Newton* and *Swift*-XRT sources are confused (Figure 5.1). Moreover, because of the higher noise level and the poorer spatial resolution, sources hidden in diffuse X-ray emission are harder to detect with those facilities. Consequently, the intrinsic slope of the *XMM-Newton* and *Swift* XLF are substantially underestimated at the faint end.

A similar problem occurs at fainter luminosities for *Chandra* sources: as explained in Wang et al. (2016), sources fainter than 10^{38} erg/s are more likely to be below the detection threshold, in particular when located in diffuse emission. This leads to the flattening of the XLF at these luminosities, so that diagnostics on the XLF faint end of XRB must rely on deep observations of close individual galaxies, as done in Mineo et al. (2012) or include a completeness correction as in Wang et al. (2016).

Another moderately significant difference is the steeper slope in the bright end of 2SXPS XLFs, above $\sim 2 \times 10^{40}$ erg s^{-1}, while 4XMM and CSC2 are consistent with each other. A closer look at each sample above this luminosity reveals that half of 4XMM and CSC2 candidates are detected in galaxies of apparent diameter $D_{25} < 20$ Mpc, whereas 2SXPS candidates in such galaxies are systematically discarded by the center exclusion criterion due to their larger position error. There is thus a lack of HLXs in the 2SXPS sample. As a result, the XLF based on *Chandra* sources is probably the most representative of the intrinsic, "universal" XLF of late-type galaxies.

5.4.4 X-ray luminosity function

XLF break

Our work shows significant evidence of the existence of a break between 3×10^{39} and 10^{40} erg/s. This somewhat agrees with the findings of Swartz et al. (2011) and Mineo et al. (2012), suggesting a cutoff luminosity of $1 - 2 \times 10^{40}$ erg/s. In contrast, Wang et al. (2016) reported that this break is spuriously caused by the lack of statistics in these studies, and stated that no break is needed at this point of their XLF. We see two reasons for this inconsistency: first, their sample is made up by searching X-ray sources within twice the D_{25} of the galaxy, and they do not implement any procedure to remove the abundant contaminants this implies. These contaminants have an important influence at high luminosities (Figure 5.6) and thus can flatten the XLF around 10^{40} erg/s. Second, they only

considered the differential luminosity function in their XLF fits, showing higher dispersion, so that a break can be buried in this "noise". In their Figure 5.9 showing the cumulative XLF, there might be an hint for a break around 10^{40} erg/s.

The precise location of the break varies between samples, with 2SXPS sources yielding the largest value. We argue that the lack of low-luminosity ULXs due to source confusion issues, given the lower spatial resolution of *Swift*-XRT, and of HLXs due to the large *Swift* exclusion radius, are likely to distort the XLF and shift the break towards higher luminosities. This effect was already pointed out by Wang et al. (2016) when considering more distant elliptical galaxies, increasing the population of unresolved sources. Similarly, if ULXs and HLXs have different nature (see Section 5.4.5), adding HLXs in the ULX cumulative XLFs will distort it so that the break will shift towards fainter luminosities and there will be a flattening at the high-luminosity end.

We test how the location of the break is changed when sources $> 10^{41}$ erg s^{-1} are removed before fitting the XLF: while it is unchanged for 2SXPS ULXs, we obtain a best-fit break of $(5.7 \pm 1.2) \times 10^{39}$ erg/s and $(9.1 \pm 2.6) \times 10^{39}$ erg/s for the CSC2 and 4XMM samples, respectively. The single powerlaw fit is still excluded. Once converted to the *XMM-Newton* broad energy band of 0.2–12 keV (assuming an absorbed-powerlaw spectrum with $\Gamma = 1.7$, $n_H = 3 \times 10^{20}$ cm^{-2}), the CSC2 break is further moved to $\sim 8 \times 10^{39}$ erg/s, consistent with the break fitted to the 4XMM sample.

More generally, although the use of cumulative XLFs provides higher statistics and may reveal more features, it is also subject to more biases. In particular, the faint end of the cumulative XLF is impacted by all the selection biases, leading to its flattening, while having the smallest poissonian error bars. This is likely to force the faint end of the XLF fit to flatten, potentially shifting the fitted break luminosity towards fainter luminosities to alleviate the tension between the model and the data. When the differential XLF is fitted (in the form $dN/d\ln L_X$ so that the slopes of the cumulative version are conserved), the break is shifted to $(6.4 \pm 2.4) \times 10^{39}$, $(6.5 \pm 4.2) \times 10^{39}$, $(1.21 \pm 0.27) \times 10^{40}$ and $(7.9 \pm 2.5) \times 10^{39}$ erg s^{-1} for the samples of CSC2, 4XMM, 2SXPS and all ULXs, respectively. As a result, the break is probably the cutoff feature reported by Mineo et al. (2012) and Swartz et al. (2011) for late-type galaxies. Most recently, this feature was also found in the XLF from deep *Chandra* observations of the Virgo cluster (Soria et al., 2022), with a normalisation jump occurring in the range $4 - 5 \times 10^{39}$ erg/s.

We investigate the physical reasons for this break. The first possibility is that a different galaxy population is probed in each luminosity bin of the XLF. Indeed, the XLF shape was found to significantly depend on the galaxy properties, with e.g. a flatter slope for more star-forming galaxies (Wang et al., 2016). We find a moderate increase of the mean star formation rate of ULX hosts in bins of increasing luminosity, with typical values < 0.5 M$_\odot$ yr^{-1} below 5×10^{39} erg/s and > 3 M$_\odot$ yr^{-1} above 10^{41} erg/s. Extrapolating the result of Wang et al. (2016) to higher luminosities, this should produce a flattening of our XLF with luminosity, whereas we find the opposite behaviour. The stellar mass follows the same trend as the SFR, so that each bin probed similar specific SFRs. The XLF break is thus unlikely to be a selection effect of different environments.

Another possibility is that the luminosity break corresponds to the Eddington luminosity of a given class of objects, such as neutron stars or a certain population of black holes. For example, the Eddington luminosity of ~ 2M$_\odot$ neutron stars was argued to be consistent with the 5×10^{38} erg/s break seen in the luminosity function of LMXB, when accounting for beaming effects and the accretion of helium-rich material (Kim and Fabbiano, 2004; Wang et al., 2016). With the same arguments, we could expect the break found in this study to be due to the Eddington luminosity of ~ 25 M$_\odot$ black holes. Recent modeling works show that radiative processes allow a luminosity as high as 10^{40} erg/s from supercritically accreting 20M$_\odot$ stellar-mass black holes (Krticka et al., 2022). However, the > 50 M$_\odot$ black holes detected by gravitational wave facilities rule out this break to match the maximum mass of stellar-mass black holes, unless the mass distribution of stellar-mass black holes is bimodal (which could be the case if black holes in XRBs and black holes in mergers do not share the same formation channels, Fishbach and Kalogera 2022, but see Belczynski et al. 2021). Moreover, the same luminosity could be reached by the most magnetised neutron stars (Mushtukov et al., 2015), but the discovery of pulsars reaching even greater luminosities (e.g. Israel et al. 2017) may have challenged this interpretation.

On the other hand, the source spectrum, and hardness ratios, may allow better diagnostics of the source nature. Using a sample of 17 ULXs including 6 PULXs, Gúrpide et al. (2021) find that the secure neutron stars of their sample are among the hardest sources. In order to probe which

type of accretor dominate at different luminosities, and if they all present the same XLF features, we divide our samples in three bins of $HR67$: soft ($HR67 < 0.2$), medium ($0.2 < HR67 < 0.5$) and hard ($HR67 > 0.5$) ULXs. The result is plotted in Figure 5.20, showing no significant difference between each XLF. The possible reason is that $HR67$ is inefficient to distinguish NS and BH ULXs, or perhaps more interestingly, that a similar break should exist in both populations even if for different physical reasons. For instance, since the contribution of LMXB in late-type galaxies is known to be non-negligible even at ULX luminosities (e.g. Mineo et al. 2012; Lehmer et al. 2019), the break could be the manifestation of a normalisation jump in the XLF due to a luminosity cutoff at a few 10^{39} erg/s for LMXBs, as mentioned in Soria et al. (2022).

Alternatively, the HMXB XLF was found to present a large dispersion in the range $10^{38}-10^{40}$ erg/s related to galaxy metallicity (Lehmer et al., 2021), with a high luminosity cutoff located between 3×10^{39} erg/s (low metallicity galaxies, 12+log(O/H)$\simeq$7.6) and 10^{40} erg/s (galaxies of solar metallicity, 12+log(O/H)$\simeq$8.7 Allende Prieto et al. 2001). The metallicity information is absent from GLADE, but we find 106 galaxies in our ULX sample that have a match in HECATE with a metallicity value: 85% of them are in the range 8.4<12+log(O/H)<8.9, close to solar metallicity, supporting this explanation for the break. In this scenario, the XLF break we obtained may be due to the combination of an excess of luminous HMXB in low metallicity environments followed by a cutoff, and an increasingly large contribution of another type of objects at the bright end, possibly intermediate-mass black holes, corresponding to the bulk of HLXs.

XLF slopes

Throughout this Section, we compare the best-fit slopes obtained on cumulative XLFs to slope values reported in the literature. Since the latter are often obtained on differential XLF, e.g. $dN/dL_X \propto L_X^{-\alpha}$ for a simple powerlaw model, we convert these values to the cumulative case whenever needed ($N(>L_X) \propto L_X^{-\alpha'}$ where $\alpha' = \alpha - 1$).

As discussed in the previous Section, the fits to the cumulative XLFs are subject to a number of biases which affect the fitted parameters, including the XLF slopes. For example, the inclusion of HLXs flattens the bright end of the distribution. Analysing the cumulative XLF with HLXs removed, we obtain best-fit high-luminosity slopes (α_2) of 1.82 ± 0.1, 1.66 ± 0.13, 1.79 ± 0.14 and 1.80 ± 0.10 for CSC2, 4XMM, 2SXPS and all ULXs, respectively, in better agreement with the values inferred on the ULX-complete galaxies and close to the value $1.73^{+1.58}_{-0.54}$ obtained by Mineo et al. (2012) for HMXBs in the same luminosity range.

Besides, resolution effects are also likely to distort the XLF, flattening it at the faint end when two low-luminosity ULXs are mistaken for a unique, brighter source. This also explains why the number of ULXs per galaxy decreases between CSC2, 4XMM and 2SXPS samples, with decreasing spatial resolution. Similarly, given the center exclusion criterion, the larger position errors of *Swift* lead to the removal of some *bona fide* HLXs, steepening the high-luminosity slope of the XLF.

Some of these biases can be alleviated by fitting differential XLFs, rather than their cumulative version. The slopes we obtain are indeed different from the cumulative XLF fits, with (α_1, α_2) being $(0.64\pm0.16, 1.69\pm0.17)$, $(0.88\pm0.27, 1.16\pm0.12)$, $(0.58\pm0.11, 1.70\pm0.18)$ and $(0.82\pm0.09, 1.38\pm0.09)$ for CSC2, 4XMM, 2SXPS and all ULXs, respectively. These low luminosity slope values better agree with the slope of the HMXB XLF in Mineo et al. (2012) and Lehmer et al. (2019), however the high luminosity slopes are not well-constrained.

Unlike late-type galaxies, the XLF we obtained for early-type galaxies are in disagreement with the steeper ones reported in the literature. For instance, Walton et al. (2011) find a best-fit slope $\alpha = 1.5\pm0.4$ for their early-type galaxies, while Wang et al. (2016) obtain steeper slopes 1.80 ± 0.03, 2.74 ± 0.10 and 2.29 ± 0.18 for elliptical, lenticular and all early-type galaxies, respectively. In nearby galaxies, the XLF of LMXBs is found to present a break at a few 10^{38} erg/s followed by a powerlaw decrease of slope ~ 1.8 (Humphrey and Buote 2008; Kim and Fabbiano 2010).

The flatter slope of the XLF for early-type galaxies in our study is examined. One possibility is that the hot gas content, prominent in these galaxies, is drowning the signal of ULXs well above the limiting luminosity we compute, which does not depend on the background level. In that case the census of ULXs is largely incomplete, up to a higher luminosity. For instance, M86 has a CSC2 limiting luminosity of 2×10^{38} erg/s from Equation 3.1 but the only sources detected within the $D_{25}/2$ ellipse have $L_X > 2\times10^{39}$ erg/s and $S/N < 3$. At fixed hot gas density, the hot gas flux in a typical aperture increases with galaxy distance, affecting the detection of increasingly bright sources. To test

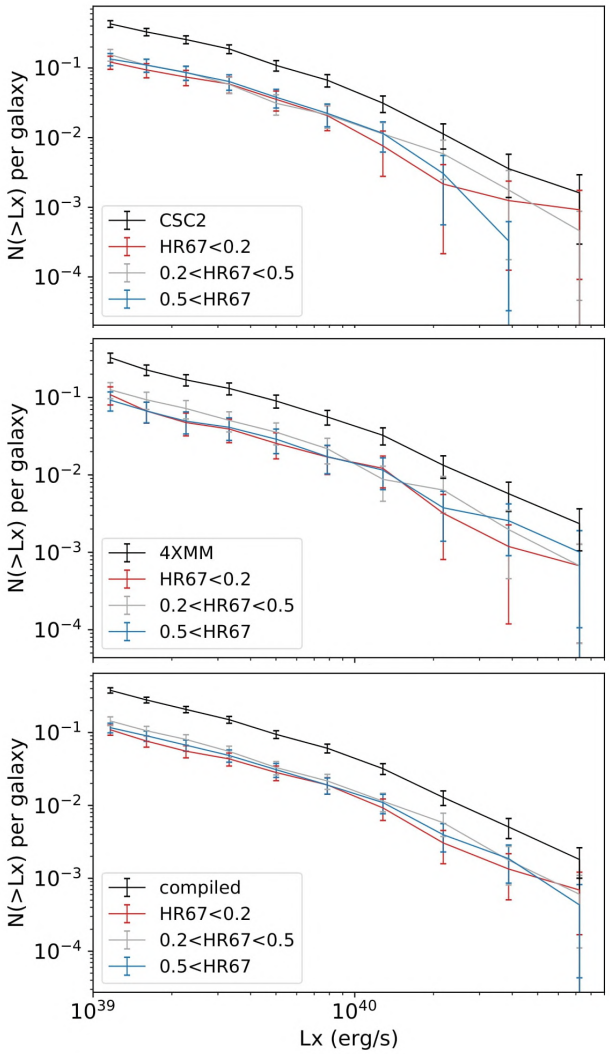

Figure 5.20: Deconvolved XLFs of *Chandra*, *XMM-Newton* and all selected ULXs in spiral galaxies, after removal of HLX candidates. Three bins of hardness ratio $HR67$ (see the text for details) are also shown, representing soft ($HR67 < 0.2$), medium ($0.2 < HR67 < 0.5$) and hard ($HR67 > 0.5$) sources.

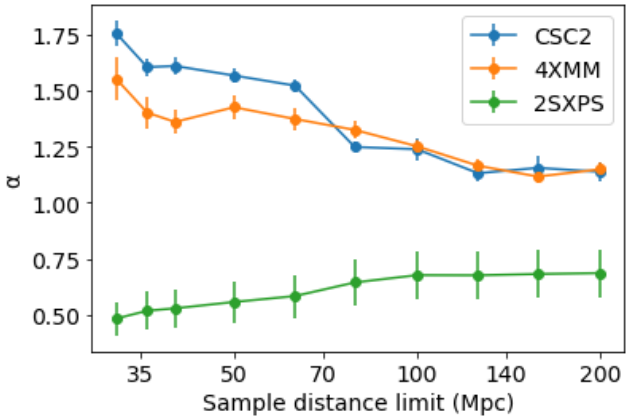

Figure 5.21: Best-fit slope of the deconvolved cumulative XLF of early-type galaxies, as a function of the distance limit of the sample.

this effect, we fit the deconvolved XLFs for samples with a range of distance limits. Figure 5.21 shows a clear flattening of the XLF when extending the sample to further distances. Below 70 Mpc, the XLF of 4XMM ULXs becomes flatter than that of CSC2, probably because of the lower spatial resolution of *XMM-Newton*. Even the closest early-type galaxies have few low-luminosity ULXs detected by *Swift*-XRT because of its lower spatial resolution, hence the flat faint end of the XLF and the inconsistent slope. For a distance limit of ~ 40 Mpc, as adopted in previous studies of this XLF (e.g. Wang et al. 2016), we find a slope in the range $1.6 - 1.8$, in good agreement with values reported in the literature.

Actually, Mineo et al. (2012) noted a large diversity of XLFs from different late-type galaxies. This diversity of XLF is arguably due to different star formation histories, metallicities and initial mass functions. Ongoing efforts to constrain these quantities for a large fraction of galaxies is thus valuable in this regard. The assumption of a universal XLF thus cannot hold regardless of the galaxy environment, and ideally the XLF should be considered in specific bins of (morphology, specific SFR, M_*, metallicity), which is beyond the scope of this study.

5.4.5 Nature of HLXs

Taking advantage of the large sky coverage and sensitivies up to faint fluxes of the compilations of three X-ray surveys, we were able to gather a sample of 191 HLX candidates. Unlike ULXs, their classification by the classifier (mostly as AGN) cannot be interpreted in terms of contaminants. Moreover, Barrows et al. (2019) (hereafter B19) found that their HLX population is at least partly consistent with accreting black holes at the center of dwarf galaxies, satellites of the matched host. Similarly, their high luminosities and galactocentric distances tend to bias the classifier towards the AGN class, particularly given that no HLX is present in the training sample of the classifier. On the other hand, because some reliable HLXs are seen to have soft spectra, with most events detected below 1 keV, some of which being explained by the total or partial tidal disruption of a star by an intermediate-mass black hole (Godet et al., 2014; Lin et al., 2018), their classification as soft sources is expected. The filtering of HLXs has thus to rely on manual inspection and the removal of known background and foreground sources.

A few contaminants may thus be left in the sample of selected HLXs. From the $\log N - \log S$ estimations reported in Table 5.7, the fraction of contaminants in the 2SXPS, 4XMM and CSC2 samples are $\sim 20\%$, $\sim 70\%$ and $\sim 60\%$, after removal of spurious sources and before removal of known background and foreground sources. The shallower sensitivity of 2SXPS implies HLX candidates located in nearer galaxies, hence the lower contamination rate. The high contamination rates obtained for other surveys agree with the 70% estimate of Zolotukhin et al. (2016), but are in contrast with the 7% of contaminants reported in B19. As they explain, this difference is mainly driven by the lower angular sizes of their galaxies, most of them being located beyond 1000Mpc, a distance range which is not probed by our sample. By using large and deep photometric redshift surveys, we were able to drastically reduce our high initial contamination fraction (identified background sources represent 85-95% of sources reported in the last column of Table 5.7). Following the reasoning of Section 5.4.2

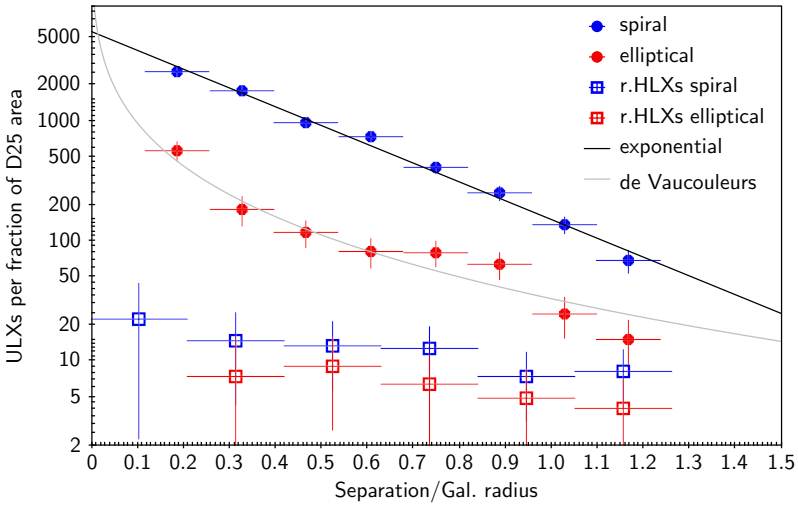

Figure 5.22: Radial distribution of all ULXs (filled circles) and robust HLXs (empty squares), showing their surface density as a function of galactocentric distance. Examples of typical galaxy light profiles are shown in solid lines.

on ULX candidates, we conservatively expect the contamination rate among robust candidates (resp. robust and weak candidates) to be $\sim$ 20% (resp. $\sim$ 30%). Thus, our slightly larger HLX sample takes advantage of the larger sky coverage of GLADE, *Swift*-XRT and *XMM-Newton*, to provide local analogues to their HLX population, better suited for future individual follow-ups.

We investigate the possible nature of our HLX candidates. First of all, the bimodality of $HR67$ as shown in Figure 5.18 suggests a difference of nature between soft and hard HLXs, the former being rarer and sometimes transient, with at least some of them consistent with partial or tidal disruption events (e.g. Godet et al. 2014; Lin et al. 2018). No such candidates were present in the sample of B19, rather showing intrinsically hard spectra or important absorption. By construction, some AGN in galaxy pairs are also included in our HLX sample, and flagged as "galaxy pair" candidates. Indeed, since HLXs are defined as off-nuclear sources, such AGN are normally discarded if their galaxy is in the GLADE catalogue; but in galaxy pairs where only the other galaxy is in GLADE, they are mistaken for HLXs. Such sources represent a minority of our HLX candidates, but their luminosity distribution is consistent with the one of "nuclear" sources (Figure 5.7). In contrast, robust and weak candidates present a steeper luminosity function consistent with the bright end slope fitted to ULXs. This maybe supports a common mechanism behind the X-ray emission of these objects, such as accreting black holes of stellar to intermediate mass. However, following the method described in Section 5.3.2 for ULXs, we find a moderately significant difference between the radial distribution of ULXs and HLXs. Figure 5.22 illustrates this discrepancy: unlike ULXs, HLXs may not follow typical light profiles and may be equally distributed in the extent of their host. This behaviour further supports the scenario in which they are the central accretor of a galaxy satellite or a globular cluster.

Unlike ULXs, a significant fraction ($\sim$ 35%) of HLXs is found to have an optical counterpart. The X-ray to optical flux ratio can often give clues on the source nature. For instance, in AGN, the optical-UV emission of the disc scales with the soft X-ray emission, so that their ratio is generally in the range 0.1–10 (e.g. Maccacaro et al. 1988; Barrows et al. 2019; Tranin et al. 2022). Following the methodology of B19, we first convert the B- and R-band fluxes given different matched optical surveys (PanSTARRS, DES, Gaia, SDSS and the Beijing Arizona Sky Survey) to the V-band, using the conversion of Jester et al. (2005). X-ray broad band fluxes are converted to the 0.3–3.5 keV band using the same fixed spectrum as above. While this is surely a limitation of our study, the heterogeneity of our sample and the low signal-to-noise levels do not allow for a more detailed spectral study. For HLXs present in both B19 and this work, we find a mean bias of our CSC2 fluxes of -0.2 dex with respect to their rest-frame unabsorbed fitted fluxes ($\pm$0.3 dex deviation), so this estimation is still reasonable for a population analysis. Finally, for X-ray sources having no counterpart, we attempt to compute an upper limit on their optical flux. B19 estimated the local background level directly from optical images, using an annulus of width being twice the radius of the host. However, we argue that such a large area is likely to contain other optical sources and thus overestimate the optical sensitivity at the HLX location, as

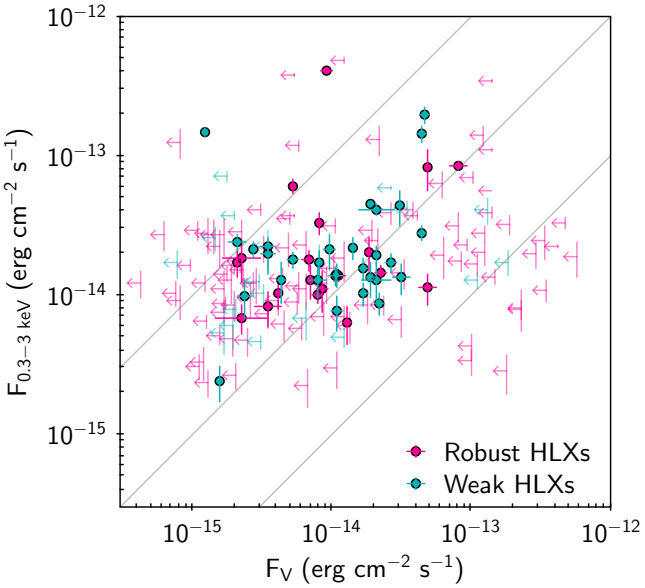

Figure 5.23: $F_X - F_V$ plane of robust and weak HLX candidates, showing their observed 0.3–3.5 keV X-ray flux as a function of the V-band flux of their optical counterpart (filled circles), or the upper limit on F_V at this location (arrows). The gray solid lines indicate ratios of $F_X/F_V = 0.1$, 1 and 10.

suggested by the bright locus of flux upper limits in their $F_X - F_V$ plane. We adopt a simpler approach in which this sensitivity is assimilated to the flux of the faintest optical source having $S/N > 5$ within a radius of 15 arcsec around the HLX candidate. Flux limits obtained with this method are found to scale well with the limits computed in B19 ($\pm$0.5 dex deviation), but are on average ten times fainter. Figure 5.23 shows the $F_X - F_V$ plane resulting from this analysis. In agreement with the finding of B19, most of F_X/F_V values in our sample are consistent with expectations for AGN (typically $0.1-10$, e.g. Stocke et al. 1991; Lin et al. 2012). The use of more optical surveys allows us to obtain more stringent constraints on the optical flux upper limit.

Considering the scenario that HLX candidates are indeed accreting black holes associated with their host, we estimate their mass and the mass of their stellar counterpart. Black hole masses are estimated using bolometric corrections of Marconi et al. (2004) and a fixed Eddington ratio. Unlike B19 who compute bolometric luminosities from their unabsorbed hard (2–10 keV) X-ray flux obtained after spectral fitting, we rather use the softer (0.5–2 keV) part of the spectrum which better matches the union of several energy bands in CSC2, 4XMM and 2SXPS, and is less affected by background emission. Since we do not correct for absorption, this approach is likely to yield some underestimated masses, but we estimate this bias to be $\lesssim 0.6$ dex from a comparison of CSC2 fluxes with B19 fluxes. The derived bolometric corrections are in the range 10–30 depending on the source luminosity (for comparison, the band 2–10 keV would yield corrections in the range 7–20, and B19 use the fixed value 10). Assuming spectral properties similar to their sample, we adopt a value $f_{Edd} = 0.24$ to derive black hole masses, and the standard formula $L_{Edd}[\mathrm{erg/s}] \simeq 1.26 \times 10^{38} M_{BH}[\mathrm{M}_\odot]$. The resulting masses are in the range $2 \times 10^3 - 2 \times 10^6 \mathrm{M}_\odot$ for robust and weak HLXs, with a median value of $4 \times 10^4 \mathrm{M}_\odot$. In particular, 122 of these 169 (robust+weak) candidates fall in the IMBH mass range, below $10^5 \mathrm{M}_\odot$. Being more luminous, HLXs in galaxy pairs have an estimated black hole mass $\gtrsim 10^4 \mathrm{M}_\odot$ with a median at $2 \times 10^5 \mathrm{M}_\odot$.

Concerning galaxy stellar masses, as done in B19, we use the mass to light ratio calibrated on optical colors (Bell et al., 2003). Point-like optical counterparts of HLXs are assimilated to their stellar associations (we note as a caveat that this neglects the optical contribution from the putative AGN, while on the contrary we previously interpreted F_V as the AGN flux). However, since some optical surveys in our sample do not provide i-band magnitudes, the relation giving M_*/L_r as a function of the $(g-r)$ color is used instead, before the computation of M_*. Another maybe important bias is that the point source flux F_r is used in this step, instead of the flux integrated over the Sérsic component. Except for HLXs in pairs, for which M_* may well be largely underestimated, we do not expect this effect to have a large impact on the computed stellar masses. Most of stellar counterparts

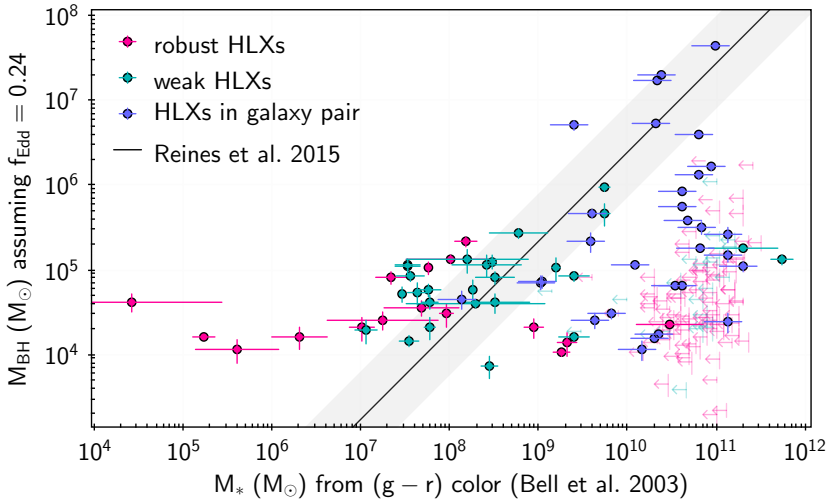

Figure 5.24: Black hole mass – stellar mass plane, estimated from the 0.5-2keV X-ray flux and the $(g-r)$ color as detailed in the text. Different types of HLX candidates are shown. Upper limits correspond to the stellar mass of the primary host.

of robust and weak HLXs are in the dwarf regime, $M_* < 3 \times 10^9 M_\odot$.

The resulting $M_{BH} - M_*$ plane is shown in Figure 5.24, also showing the scaling relation calibrated by Reines and Volonteri (2015) on local AGN in low-mass galaxies. Upper limits corresponding to the stellar mass of the host are shown for HLXs having no optical counterpart detected in both g and r bands. While some robust and weak HLXs appear under-massive, most of them are hard sources, with $F_{0.5-2\ \mathrm{keV}}$ accounting for less than 30% of their broad-band flux: their black hole mass is likely to be underestimated. A second estimation using the extrapolated band 2–10 keV gives black hole masses in the range $2 \times 10^3 - 2 \times 10^7 M_\odot$ for robust and weak HLXs (median $9 \times 10^4 M_\odot$), with these sources all above $3 \times 10^4 M_\odot$. Some HLXs in pairs are largely under-massive, possibly because of an underestimated M_{BH} (occurring for instance if $f_{Edd} < 0.24$), an overestimated M_* (occurring for instance if the optical source is dominated by the AGN), or a different nature for these candidates (such as a tight group of XRBs or ULXs, mimicking a point source). Interestingly, we find a significant proportion ($\sim 25\%$) of overmassive black holes among robust and weak HLXs, supporting a scenario in which these black holes have undergone a merger-free growth and/or that their stellar counterpart have been tidally stripped by the primary host, or is instead a globular cluster (which is likely only for stellar masses $< 10^7 M_\odot$, e.g. van de Ven et al. 2006).

This contrasts with B19 results who find a broad alignment of their HLXs to the relation of Reines and Volonteri (2015), maybe because our work is focusing on the more local Universe and thus probes lower black hole masses and an earlier growth regime. The proportion of overmassive black hole is further increased if a lower Eddington ratio is applied to compute black hole masses. For example, Baldassare et al. (2017) find a median Eddington ratio of $f_{Edd} = 0.05$ in their sample of active dwarf galaxies, that they obtain through the unabsorbed X-ray luminosity and the black hole mass inferred from the broad Hα line width (e.g. Greene and Ho 2005; Reines et al. 2013). In our study, nevertheless, a more detailed modeling of X-ray spectrum and optical emission, in particular to securely estimate galaxy masses, would be needed to confirm this overmassive locus.

5.4.6 Investigation of two variable HLX

To go more in depth in the nature of the HLX candidates, we report here the study of two candidates of special interest, given their robustness and their peculiar spectrum and/or variability.

NGC 6099 HLX-1

Because our classification is based on a training sample of standard AGN, soft sources and XRB, it is likely that some valid ULXs and HLXs are misclassified as contaminants due to their extreme properties. For instance, supersoft ULXs can be classified as soft sources due to their spectral properties, as well as HLX sharing the high/soft state of ESO 243-49 HLX-1 (and indeed its entry in 4XMM

returns $P_{Soft} > P_{XRB}$). This is notably the case of J2150-0551, an off-center TDE associated with 6dFGS gJ215022.2-055059 and likely to host an IMBH (Lin et al., 2018). An outlier measure returned by the classification can be used to spot such sources not consistent with the parameter space occupied by the training sample (Tranin et al., 2022). For our classification parameters, this measure generally takes values in the range $7 - 13$. For instance, ESO 243-49 HLX-1 returns an outlier measure of $O.M. = 12.1$ in 4XMM, while J2150-0551 has a value of $O.M. = 12.3$.

4XMM J161534.3+192707 (hereafter NGC 6099 HLX-1) is located 18" (i.e. 11 kpc) from the nucleus of NGC 6099 at a distance of 133 Mpc (Figure 5.25). It was found retrospectively in our sample of HLX candidates classified as contaminants: indeed, its peculiar spectrum led to its classification as soft source. The HLX candidate Its outlier measure is the highest among well-detected ($S/N > 5$) HLX candidates classified as contaminants ($O.M. = 12.4$). This source was first observed with *Chandra* in May 2009 with a flux of $1.3 \pm 0.2 \times 10^{-14}$ erg cm^{-2} s^{-1} in the broad energy band (0.5–7 keV), and $4 \pm 3 \times 10^{-15}$ erg cm^{-2} s^{-1} in the ultrasoft band (0.2–0.5 keV). It was then detected in February 2015 with a flux about 60 times brighter ($F_{0.2-12} = 9.2 \pm 0.1 \times 10^{-13}$ erg cm^{-2} s^{-1}), with *XMM-Newton*. Its XMM position is 0.4" away from the Chandra position, so they are consistent at the 2-σ level. *Chandra* detected some emission associated with the galaxy nucleus with a flux in the broad band of 1.2×10^{-14} erg cm^{-2} s^{-1}. *XMM-Newton* did not detect this emission being blended with the HLX candidate emission. However, even when adding the nuclear emission (supposed roughly constant), this does not account for the observed variability. In 2021, NGC 6099 was seen twice by *Swift*-XRT and also by an XMM slewing observation, showing a significant decrease in the light curve of the source. Besides, no optical counterpart is found at the source location, even in the contemporaneous XMM-OM observation, and no infrared counterpart either, out to the unWISE limiting magnitude $W1_{lim} = 16.7$. This puts a lower limit of 120 on the X-ray to infrared flux ratio, much higher than expected from a background AGN.

We find no single-component good fit for the XMM spectrum, however the spectrum has a very bright soft component just as ESO 243-49 HLX-1 in the high/soft state. When fitting the spectrum with an absorbed `powerlaw+diskbb` model (favoured for ESO 243-49 HLX-1 in the high/soft state Servillat et al. (2011)), we obtain a reasonable fit ($N_H = 3 \pm 1 \times 10^{20}$ cm^{-2}, $kT_{in} = 0.25 \pm 0.01$ keV, $\Gamma = 3.5 \pm 0.2$, χ^2/dof = 395.6/346) and a flux of 2.7×10^{-12} erg cm^{-2} s^{-1}, leading to an X-ray luminosity of $L_X = 4.6 \times 10^{42}$ erg s^{-1} assuming the same distance as the supposed host ($D = 133$ Mpc). The Chandra source 2CXO J161534.2+192707 was reported in a catalogue of extreme ULX (Gong et al., 2016), but with the luminosity from Chandra, below the HLX range. This low-luminosity state is consistent with the same spectral parameters as the high-luminosity state, only varying in flux: the Chandra hardness ratios are $hard_ms = -0.70^{+0.10}_{-0.09}$, $hard_hm = -0.37^{+0.27}_{-0.25}$, much softer than the bulk of ULX (Figure 5.17).

This source thus varied by a factor of ∼150 in 3 years (ESO 243-49 HLX-1 varied by a factor of 75 during its follow-up), has no counterparts in other wavelength and a spectrum and luminosity very similar to ESO 243-49 HLX-1, making it a very reliable HLX candidate. Conservatively assuming a radiation about 10 times above the Eddington limit (as was done for ESO 243-49 HLX-1 in Farrell et al. 2009), we obtain an estimation of the mass near $3.6 \times 10^3 M_\odot$, well in the IMBH range and about 7 times larger than ESO 243-49 HLX-1. This estimation is supported by the apparent lack of spectral change, which would tend to exclude the transition between sub-Eddington and extremely super-Eddington accretion, meaning that both regimes would be around the Eddington limit. NGC 6099 and NGC 6098 are elliptical galaxies (stellar mass $M_* = 9 \times 10^{10} M_\odot$) in interaction, favouring the idea that NGC 6099 HLX-1 may be an IMBH in a dwarf galaxy interacting with NGC 6099, in a similar way to HLX-1 with ESO 243-49.

2SXPS J111416.1+481833

2SXPS J111416.1+481833 (hereafter NGC 3583 HLX-1) (Figure 5.26) was first observed with *Swift-XRT* in November 2015 with a flux 8×10^{-13} erg cm^{-2} s^{-1}, in the outskirts of NGC 3583 ($D = 33$ Mpc). It was detected 18 times by the same facility in the next two months, with a moderately high variability between observations (maximum to minimum flux ratio of 4). Its spectrum is consistent with a power-law with photon index $\Gamma = 1.7^{+0.18}_{-0.17}$ and $n_H = 1.5^{+0.7}_{-0.6} \times 10^{21}$ cm^{-2} as given in 2SXPS. The spectrum in the low-state and the one in the high-state, as built from stacking observations having a count rate >0.02 cts/s (resp. <0.015 cts/s), are not significantly different.

This source was then imaged with *Chandra* in February 2017 as shown in the progressive survey

of the Chandra Data Archive. It is located at 3.2" from the *Swift* source, well in its 90% error circle. We extracted the source flux using CIAO v4.14 and found $2.9^{+0.9}_{-0.9} \times 10^{-14}$ erg cm^{-2} s^{-1} in the band 0.5–7keV. Converting it to the *Swift* broad band 0.3–10 keV, using the power-law model inferred from the high state, gives a flux 25% higher. The source thus dropped by a factor of at least 20 since its *Swift* observations at peak. In 2021, a large observing campaign targeted NGC 3583, showing an important variability of the source at even shorter timescales: a smooth dip by a factor 15 is visible the last 4 months of the light-curve (Figure 5.26, right panel). Still, we note a large fraction (33%) of detections at HLX luminosities.

Among our new HLX candidates, NGC 3583 HLX-1 is the only one to have been imaged by Hubble, in the long-pass (350nm), V (555nm) and I (814nm) filters. A thumbnail of the released image centered on the source location is shown in Figure 5.27. We verified that no significant (>0.5") astrometric offset is present between Chandra, PanSTARRS and HST images of this field. One bright HST source is located just 0.4" away from the Chandra position, making it a likely counterpart. It is brightest in the long-pass and V bands, totaling a luminosity $L_{opt} = 6.6^{+2}_{-2} \times 10^{34}$ erg/s which seems constant between HST observations (Parra et al. in prep.). However, numerous fainter HST sources are also located within 1" of the source. If this is the actual optical counterpart, at peak of the X-ray flux, the X-ray-to-optical flux ratio would follow $log(F_X/F_V) \simeq 5$, significantly higher than in most ULX (e.g. Tao et al. 2011).

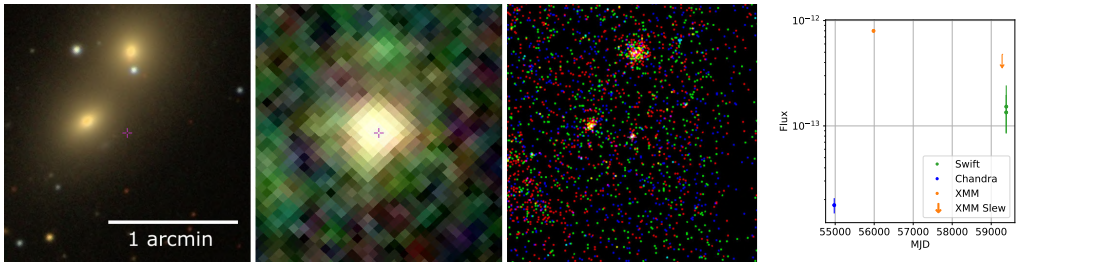

Figure 5.25: Location and light curve of the HLX 4XMM J161534.3+192707. From left to right are shown the optical (SDSS9 color) image, the X-ray image (*XMM-Newton*) in the high state, the X-ray image (Chandra) in the low state, and the light curve of X-ray observations.

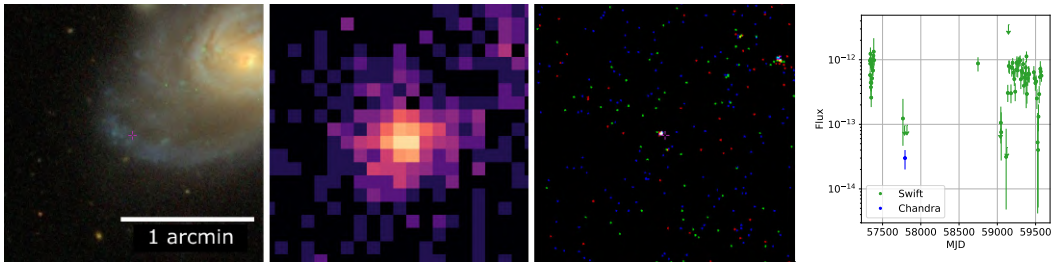

Figure 5.26: Same as Figure 5.25, but for the HLX 2SXPS J111416.1+481833. The second panel is the X-ray image from *Swift*-XRT.

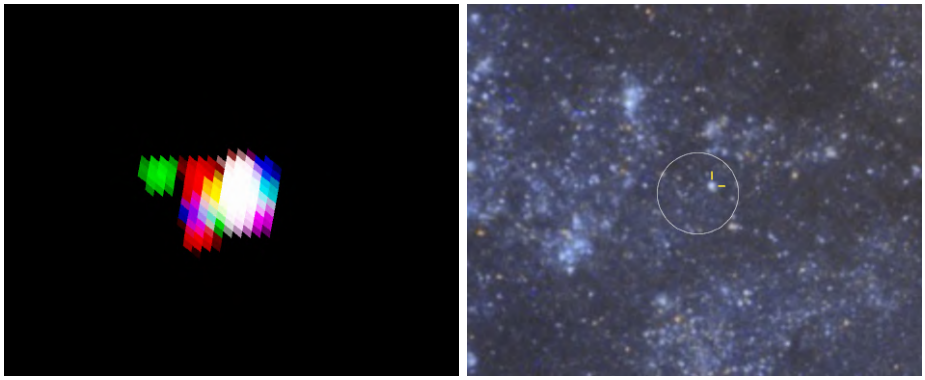

Figure 5.27: Chandra and HST close-up of NGC 3583 HLX-1 at the same scale. A circle of 1" radius centered on the source is shown in white. The brightest HST counterpart is shown with a yellow reticle.

5.5 Summary

Using the three largest X-ray surveys to date, and a galaxy catalogue of unprecedented completeness for the field, we were able to build the largest and cleanest catalogue of ULXs. It contains 1901 unique sources, compiling 304, 667 and 1185 reliable ULXs from 2SXPS, 4XMM and CSC2, respectively. They result from a strict filtering pipeline involving off-center selection, removal of all known contaminants, the use of an automatic, probabilistic classification and manual inspection. The contamination rate is estimated to be no greater than 2%, considerably improving over recent catalogues.

We conduct a statistical study of ULX luminosity function, preferred environments, and compare them with a clean XRB sample in terms of hardness and variability. We also isolate a sample of 191 HLX candidates and investigate their properties. We report the following results:

1. Thanks to the use of Malmquist-corrected XLF, considerably enlarging the number of bright sources usable in the XLF, the presence of a significant break at 10^{40} erg s^{-1} is confirmed in all three surveys, in contradiction with the recent claim of Wang et al. (2016).

2. We confirm the trends followed by the ULX rate with the galaxy environment, found in previous studies. The ULX rate is positively correlated with star-formation rate and stellar mass, with a large excess in dwarf galaxies. While low-luminosity ULXs tend to be hosted more often in spiral galaxies, the occupation fraction of spiral and elliptical galaxies becomes similar at HLX luminosities.

3. No clear hardness or variability difference is seen among the whole populations of ULXs and XRBs. However, from a sample of significantly variable sources, we confirm the opposite evolution of hardness with luminosity between ULXs and XRBs. Half of the sample shows no hardness evolution with luminosity.

4. The classification and manual inspection of sources having $\langle L_X \rangle > 10^{41}$ erg s^{-1} enables us to isolate 191 HLX candidates further divided in several categories. Their optical counterparts and radial distribution, together with the XLF break, suggest a diverse nature of the X-ray sources at such luminosities. 120 of them are consistent with an accreting IMBH in a dwarf galaxy satellite of the identified host.

In the future, we will study in greater detail the hardness-luminosity evolution of ULXs and HLXs in order to better assess their nature, and conduct individual studies of some HLX outliers. A statistical study of X-ray sources in dwarf galaxies is also in preparation, in order to seek IMBH and wandering black holes in isolated galaxies and investigate on the ULX excess found in these galaxies.

Chapter 6

Search for IMBH in dwarf galaxies

While the bright end of ULX populations has provided some of the best IMBH candidates known to date, it is not the only signature expected from these black holes, and perhaps not the best to find ungrown leftovers of some high-redshift SMBH seeds. To better constrain the nature and formation paths of these seeds, one must either directly observe them or search for their relics in the local Universe. Nearby dwarf galaxies are often believed to be suitable places to find the latter candidates, being presumably the leftover of the hierarchical formation of galaxies (however this idea is increasingly controversial, see e.g. Mezcua 2019). In this Chapter, we gather a large sample of 1139 X-ray sources located in 500 dwarf galaxies to find new active black holes up to faint X-ray luminosities ($\approx 10^{38}$ erg s^{-1}) and constrain their active fraction. Preliminary results of this study are shown, being the subject of an upcoming article (Tranin et al. in prep).

6.1 Context

As stated in Chapter 2, and in alignment with the co-evolution of black holes and galaxies, dwarf galaxies are a favourable environment to look for the seeds of SMBHs (e.g. Reines et al. 2013; Chilingarian et al. 2018; Greene et al. 2020; Reines 2022). However, their signatures in each wavelength are hard to detect and subject to important contamination in starforming environments. For example, important star formation can both produce optical emission lines characteristic of inactive galaxies (which is reinforced in low-metallicity dwarf galaxies, e.g. Polimera et al. 2022) and lead to the formation of tight groups of HMXBs mimicking an accreting massive black hole (Reines, 2022). Adding to the difficulty to identify them, unlike massive black holes that are found at the center of their galaxy, some massive black holes accreting in dwarf galaxies were found in both simulations and observations to be off-centered, wandering in the outskirts of their host (e.g. Bellovary et al. 2019; Reines et al. 2020). Such black holes were then particularly difficult to find and characterize until recently.

Unlike other wavelengths, X-rays offer a more direct probe of the accretion flow around such black holes, with low contamination from other emitters in the immediate surroundings. Spatial resolution is thus not a strong requirement as it is in other wavelengths such as optical and radio (Reines et al., 2011; Sargent et al., 2022), and a more distant population can be detected (up to redshift ~ 2.4 in the *Chandra* COSMOS Legacy survey, Mezcua et al. 2018). A clean sample of candidates is obtained after removal of other X-ray contaminants, in particular hot gas, XRBs and background AGN. The

completeness of such a sample is also limited by the sensitivity of the survey, missing candidates of low intrinsic X-ray luminosity or high obscuration. X-rays thus provide a unique tool to derive a lower limit on the fraction of dwarf galaxies containing a massive black hole (occupation fraction), and to constrain the fraction of galaxies containing an AGN (active fraction) above a limiting luminosity threshold. These quantities can provide unique constraints on the formation paths of IMBHs (Volonteri, 2010; Greene et al., 2020).

Gallo et al. (2008) studied 32 early-type galaxies in the local Universe ($D < 16$ Mpc), including 12 of low-mass ($M_* < 10^{10} M_\odot$), with archival and new (AMUSE-Virgo program) *Chandra* observations. They found 16 X-ray sources with a location consistent with the nucleus of the galaxy, and with a luminosity inconsistent with hot gas or X-ray binaries. After accounting for possible contamination, from their low-mass galaxies, they infer that $3 - 44\%$ (95 percent confidence interval) of galaxies contain an active nucleus radiating above their sensitivity 4×10^{38} erg s^{-1}. A similar work performed by Miller et al. (2015) used the latest version of the AMUSE-Virgo sample (200 early-type galaxies), finding that less than 1% of galaxies having $M_* < 10^9 M_\odot$ contain nuclear X-ray emission, and giving a lower limit of 20% on the *occupation* fraction of galaxies below $10^{10} M_\odot$, taking into account some modeling of the relation between the stellar mass of galaxies and their X-ray luminosity.

Other works focusing on dwarf galaxies ($M_* < 3 \times 10^9 M\odot$) had to rely upon larger and shallower X-ray surveys: Schramm et al. (2013) searched for AGN in 5200 dwarf galaxies located in the *Chandra* Deep Field South, finding 3 nuclear sources and deriving an active fraction of $\sim 0.1\%$ at $L_X \geq 10^{40}$ erg s^{-1}. In a comparable work probing another *Chandra* deep field, Pardo et al. (2016) provide a higher but consistent estimation of $0.6 - 3\%$. Lemons et al. (2015), using for the first time a serendipitous X-ray catalogue (CSC Release 1.1) to search AGN in the *NASA Sloan Atlas*[1] (NSA) dwarf galaxies, find at most 10 AGN candidates. Although they do not report the number of galaxies in the *Chandra* footprint, it is easily found using their samples: we find 2169 NSA dwarf galaxies in the CSC 1.1 coverage map published by the *Chandra* X-ray center[2], of which 1351 are located in the inner part of the FOV ($\theta < 12$') where *Chandra* is most sensitive and resolved and where all their candidates are found. Since they remove 39% of their galaxy sample for not being bona fide dwarf galaxies, we estimate an active fraction of $f_{AGN} \lesssim 1.2\%$, with sensitivities in the range $10^{37} - 10^{40}$ erg s^{-1}. By construction, their sample also contains off-nuclear candidates at angular distance < 5" from the nucleus. Mezcua et al. (2018) probed brighter AGN in the more distant Universe ($z \lesssim 2.4$), finding $\sim 0.4\%$ of active dwarf galaxies at $L_X \geq 10^{41}$ erg s^{-1}. Last but not least, some works extend the search to all off-nuclear (wandering) black holes, with the first constraints being derived from the 3XMM-DR7 catalogue ($2.7 < f_{AGN} < 6\%$ at $L_X \geq 10^{39}$ erg s^{-1}, Birchall et al. 2020) and the eROSITA final equatorial depth survey (eFEDS) ($f_{AGN} \leq 1.8\%$ for sensitivities in the range 10^{39}–3×10^{40} erg s^{-1}, Latimer et al. 2021).

Inspired by the above-cited X-ray studies, we perform a search for low-luminosity AGN in dwarf galaxies to find new IMBHs and better constrain the active fraction of these galaxies at faint luminosities, using the same samples of X-ray sources in GLADE galaxies as described in Chapter 3. The use of GLADE (2016 version, hereafter GLADE), 4XMM and 2SXPS catalogues is of particular interest since previous studies of AGN in dwarf galaxies most often focused on SDSS galaxies and *Chandra* sources. Nucita et al. (2017) and Birchall et al. (2020) search candidates in *XMM-Newton* observations, however they use 3XMM-DR5 and 3XMM-DR7 which cover $\sim 20\%$ less sky area than 4XMM-DR11. To our knowledge, no such study made use of *Swift* observations. This Chapter is divided as follows: in Section 6.2, we present the sample of dwarf galaxies. Section 6.3 details the cleaning pipeline adopted to select AGN candidates, as well as results obtained on the resulting sample. As in Chapter 5, much effort is devoted to remove contaminants while keeping a sample as complete as possible. The accuracy of this selection is discussed in Section 6.4, in which we also give our conclusions and outlook.

6.2 Sample

In our GLADE sample, 42115 galaxies fall in the dwarf category ($M_* \leq 3 \times 10^9 M_\odot$), including 6858 in the X-ray fields of *Chandra*, *XMM-Newton* or *Swift*-XRT. Figure 6.1 illustrates a few of their

[1] http://www.nsatlas.org
[2] https://cxc.cfa.harvard.edu/cda/cda_moc.html

properties, showing that the vast majority of them are located below 200 Mpc and are more massive than $10^9 M_\odot$. The larger, more nearby galaxies are more often found associated with an X-ray source, which is expected since the more numerous low-luminosity XRBs become undetectable in more distant galaxies. We find 500 dwarf galaxies associated with a total of 1139 unique X-ray sources, observed by *Chandra* (785 sources in 251 galaxies), *XMM-Newton* (364 sources in 247 galaxies) or *Swift*-XRT (151 sources in 112 galaxies). As in Chapter 5 for ULXs, this difference between instruments is mainly driven by sensitivity and resolution effects.

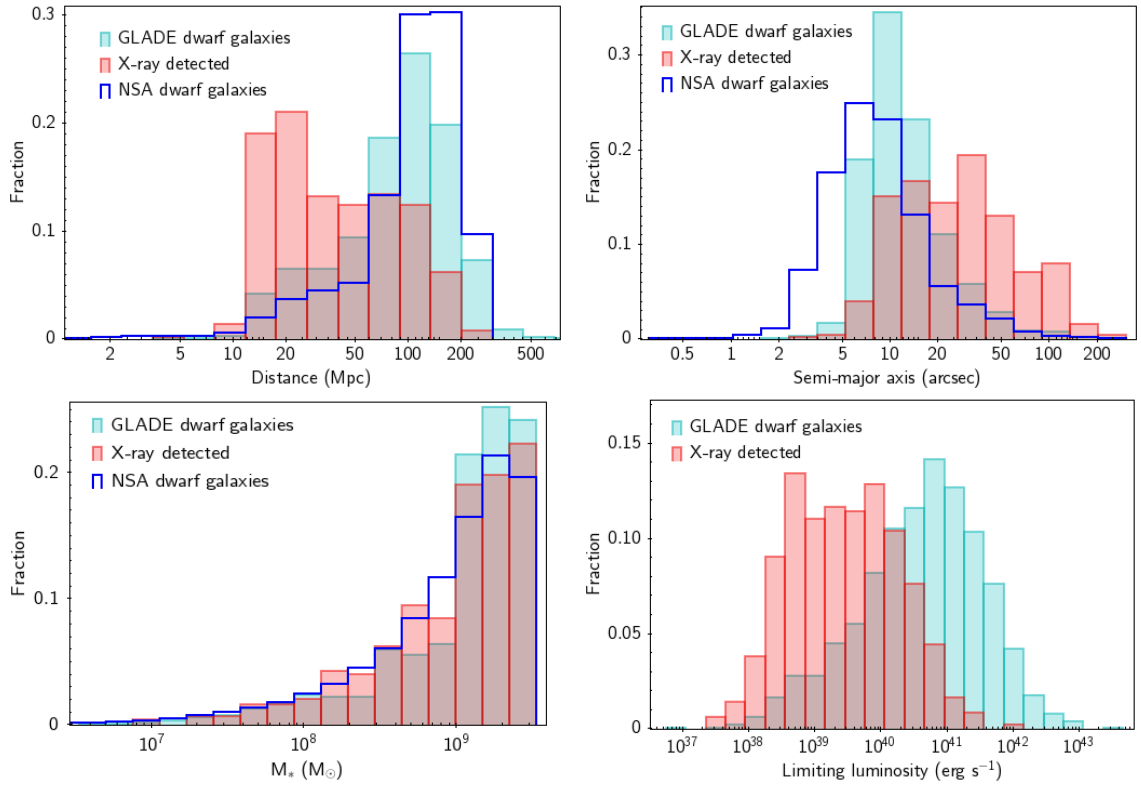

Figure 6.1: Characterisation of the sample of GLADE dwarf galaxies, showing their luminosity distance (upper left), the semi-major axis of their D_{25} ellipse (upper right), their stellar mass retrieved from GLADE+ (Dálya et al., 2022) (bottom left) and their limiting luminosity computed from Equation 3.1 (bottom right). For comparison the distributions of ∼44000 dwarf galaxies in the NASA Sloan Atlas are overlaid (version 0.1.2, Lemons et al. 2015).

6.3 Method and results

Since we expect X-ray classes and their signatures to be essentially similar between dwarf and massive galaxies, and because of the few objects available to make a training sample, the same classification as in Chapter 5 is used.

6.3.1 Source classification

Table 6.1 shows the confusion matrix of the classification for the sample of dwarf galaxies and the compiled sample of X-ray sources. It is the same as Table 5.2, but only showing sources in dwarf galaxies. For X-ray sources observed with several instruments, only the entry of smallest position error is kept. As a first approximation, precision values are given assuming the prior proportions already used for the *Chandra* catalogue, having entries for 63 out of the 91 known sources. Except for soft sources, for which a lower performance was already notable in Table 5.2 due to their small training sample size, the classification gives reasonably reliable results. The lower precision on the AGN class is due to the fact that AGN in dwarf galaxies are rarer and more difficult to find. In

	AGN	Soft	XRB	Precision
→AGN	24	6	4	78%
→Soft	0	5	1	51%
→XRB	4	15	22	78%
Recall	86%	19%	81%	

Table 6.1: Confusion matrix resulting from the classification of the compiled training sample of X-ray sources: subset in dwarf galaxies. As a first approximation, the prior proportions assumed for CSC2 (Table 5.1) are used to compute precision values.

	$L_X < 10^{39}$ erg s^{-1}		$L_X > 10^{39}$ erg s^{-1}	
	all	$L_X > L_{lim}$	all	$L_X > L_{lim}$
selected	512	210	391	236
background	111	35	64	43
soft source	38	7	23	14

Table 6.2: Number of sources selected as ULX, XRB or AGN candidates in dwarf galaxies, along with two types of identified contaminants. Columns 3 and 5 correspond to sources detected above the 3σ sensitivity threshold.

particular, half of the known sources misclassified as AGN have locations consistent with the nucleus, increasing their probability of being so classified.

Hereafter, sources are classified as ULXs and background contaminants following the same reasoning as in Chapter 5 (Sections 5.2.3 and 5.2.4). However, since Section 5.3.3 aimed at comparing XRBs and ULXs, it required reliable classifications at the expense of the recall rate. A significant fraction of XRBs was then discarded in sources with luminosities less than 10^{39} erg $^{-1}$, for not being secure XRBs. Here, in order to remove only secure background contaminants and study the integrated luminosity of the remaining sources, we need a less stringent criterion to select XRBs, fine-tuned after inspection of a random sample of candidates: $P_{XRB} > 2(sep - 0.7)$, where sep is the galactocentric distance. Table 6.2 gives the number counts of sources selected as XRB, ULX or AGN candidates, and sources classified as background or soft source (i.e. hot gas or supernova, having $P_{Soft} > 0.5$), below and above the 10^{39} erg s^{-1} threshold. As a result, 903 unique sources are selected for further analysis (including 446 above the 3σ sensitivity level), in 436 (respectively 239) galaxies.

6.3.2 Background contaminants

Following the method detailed in Section 5.4.2, we estimate the theoretical number of background contaminants using the cosmic X-ray background models of Moretti et al. (2003), Georgakakis et al. (2008) and Kim et al. (2007). As no exclusion of the nuclear region is performed, the cosmic X-ray background density is integrated over the full $1.26 \times D_{25}$ ellipse. Results are shown in Table 6.3, also showing the number of background candidates identified above the 3σ sensitivity limit and within the same ellipse. A clear effect of spatial resolution is visible: while background contaminants seem to be accurately identified among *Chandra* sources, encompassing most of the spurious sources and a few of the XRBs and ULXs, as explained in Section 5.2.3, this is not the case in the 2SXPS and 4XMM samples. This is likely due to the fact that at these luminosities, sources are more numerous and become confused or are drowned out by diffuse emission for *Swift* and *XMM-Newton*, as shown by the flattening of the XLF investigated in Section 5.4.4. As a result, background contamination in the selected sample of candidates is likely to be low ($< 10\%$).

6.3.3 X-ray binaries

Since dwarf galaxies have less regular morphologies and their massive BH can be faint and wandering, XRB contamination is a serious issue that cannot be tackled using a location criteria. Instead, a commonly used approach is to compare the X-ray luminosity integrated on the galaxy extent to the expected total luminosity of its XRBs, calibrated on massive galaxies in the nearby Universe. Such a model is given for example in the work of Lehmer et al. (2016), already used the study of AGN in

Survey	Moretti+03	Georgakakis+08	Kim+07	Identified
2SXPS $> 10^{38}$ erg s^{-1}	56	52	52	10
2SXPS $> 10^{39}$ erg s^{-1}	34	34	33	10
4XMM $> 10^{38}$ erg s^{-1}	72	66	67	17
4XMM $> 10^{39}$ erg s^{-1}	31	31	31	14
CSC2 $> 10^{38}$ erg s^{-1}	20	20	20	46
CSC2 $> 10^{39}$ erg s^{-1}	17	17	16	18

Table 6.3: Number of contaminants behind our sample of dwarf galaxies, estimated using different published $\log N - \log S$ relations, in the two luminosity bins $L_X > 10^{38}$ erg s^{-1} and $L_X > 10^{39}$ erg s^{-1}. The last column gives the number of candidates filtered out by our pipeline as background contaminants.

dwarf galaxies by Birchall et al. (2020), taking into account stellar mass, SFR and redshift:

$$L_{XRB} = \alpha_0(1+z)^\gamma M_* + \beta_0(1+z)^\delta SFR$$

where $\log_{10}(\alpha_0) = 29.04 \pm 0.17$, $\gamma = 3.78 \pm 0.82$, $\log_{10}(\beta_0) = 39.38 \pm 0.03$ and $\delta = 0.99 \pm 0.26$ in the band 0.5–2 keV, and $\log_{10}(\alpha_0) = 29.37 \pm 0.15$, $\gamma = 2.03 \pm 0.60$, $\log_{10}(\beta_0) = 39.28 \pm 0.03$ and $\delta = 1.31 \pm 0.13$ in the band 2–10 keV (Lehmer et al., 2016). In order to compare these luminosities to the broad-band luminosities in our sample, we could consider our observed luminosities in the 2–10 keV band, however this discards 85 selected sources undetected in this band. Rather, the two energy bands of Lehmer et al. (2016) are added together and converted to the broad band of each instrument using the standard spectrum assumed in the computation of catalogue fluxes (absorbed powerlaw spectrum with $\Gamma = 1.7$, $n_H = 3 \times 10^{20}$ cm^{-2}). Figure 6.2 shows the comparison of integrated luminosities in our sample to the integrated luminosity estimates for XRBs.

These scaling relations also cover the contamination by ULXs, since a representative sample of XRBs and ULXs are generally included in studies calibrating them, and these studies treat the two categories as part of the same population from considerations on their XLFs. However, one of the main drawbacks of this approach is that it assumes universal scaling relations between the physical properties of a galaxy (stellar mass, star formation rate, metallicity...) and XRB content, while a large scatter is seen between the XLFs of individual galaxies of same type (Mineo et al., 2012; Lehmer et al., 2021), resulting in important deviations from the model. A clean sample of AGN candidates is thus defined by requiring a minimal excess of the lower limit of total luminosity ($L_{X,tot} - \sigma_{L_{X,tot}}$) with respect to this standard deviation, which we choose to be twice the scatter reported in Lehmer et al. (2016), or 0.34 dex. For completeness, we also define a larger sample of candidates ("full sample"), simply requiring $L_{X,tot} > L_{XRB}$. In agreement with previous works, a large fraction of galaxies have an integrated X-ray luminosity clearly in excess of the expectation from XRBs and ULXs: it is the case of 262 galaxies, including 175 detected above the 3σ sensitivity. This may be an indication of the presence of an AGN. Alternatively, it can also be due to a poorly estimated XRB content, due to errors in M_* (which is discussed in Section 6.4.1) or SFR. Likewise, HMXB populations seem to be in excess in low-metallicity galaxies (Lehmer et al., 2021), however metallicity is not taken into account in the XRB model previously used. The effect of metallicity is investigated in Section 6.4.2

6.3.4 Radio detections

Radio wavelengths provide a complementary way to find active black holes. Combined with X-rays, assuming the X-ray luminosity is due to accretion on a black hole, we can use the fundamental plane of black hole activity to obtain an estimate of the black hole mass (e.g. Plotkin et al. 2012, Mezcua et al. 2015). The high resolution of radio interferometry can also give insight into the nature of the source by constraining the compactness of its emission or the presence of a jet, and the radio luminosity integrated over the galaxy provides another estimate of its SFR in the absence of an AGN (e.g., Mezcua et al. 2018; Sargent et al. 2022).

For all these reasons, we search for radio counterparts of the X-ray sources in the FIRST and VLASS surveys. These surveys covered more than half of the sky at $\sim$ 1 arcsec resolutions and a

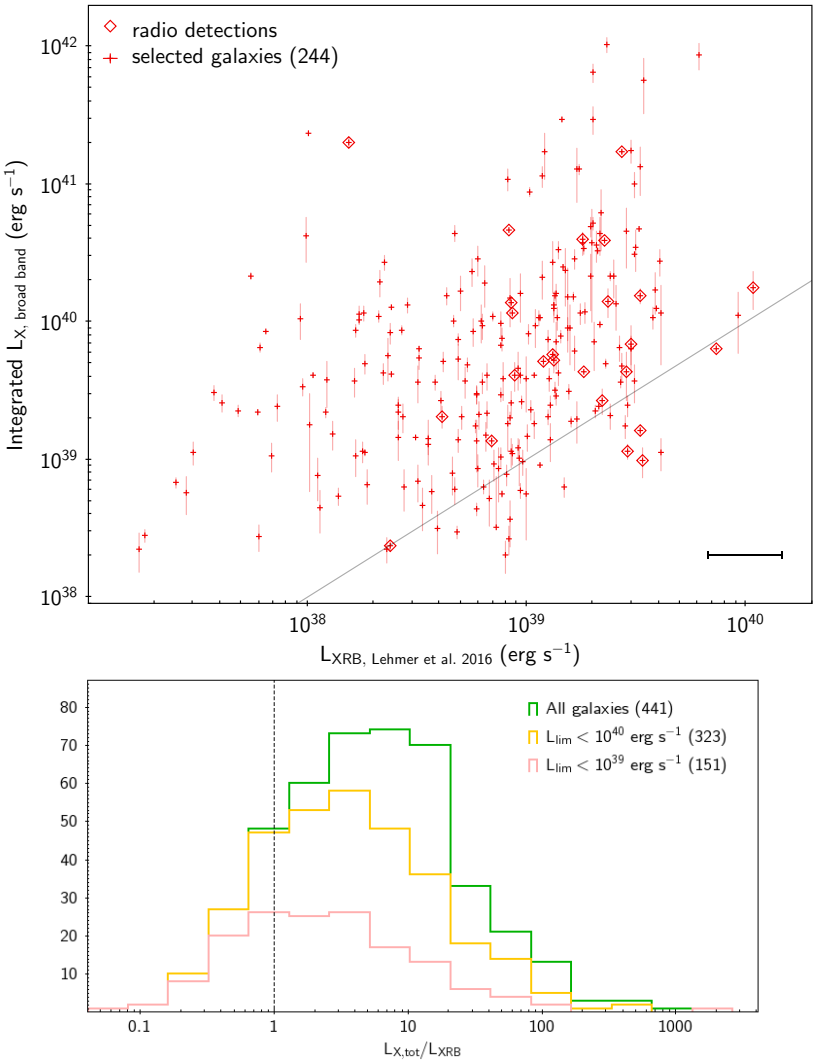

Figure 6.2: (Top) Total detected broad-band X-ray luminosity of dwarf galaxies, as a function of the predicted integrated luminosity of XRBs (Lehmer et al., 2016). Radio detections are highlighted with diamonds, and the horizontal error bar shows a ±0.17 dex deviation of XRB integrated luminosity as reported in Lehmer et al. (2016). (Bottom) Histogram of the ratio between these quantities, for different limiting luminosity bins.

typical 5σ sensitivity of 1 mJy/beam (FIRST) up to $\sim$ 0.1 mJy/beam (VLASS). To scale VLA 2–4 GHz fluxes and FIRST 1.4 GHz flux density to the 5GHz flux density, a spectral index $\alpha_R \sim -0.1$ is assumed (where $F_\nu \propto \nu^\alpha$), i.e. a flat radio spectrum, generally well-suited for both ULXs and AGN with low Eddington ratios at this spatial resolution (e.g. Plotkin et al. 2012; Sutton et al. 2012; Yang et al. 2017, 2020).

Counterparts are selected with a 3 arcsec search radius in both surveys. If a counterpart is found in both surveys, we keep the VLASS source since it is better resolved. 35 unique radio counterparts are retrieved, including 26 for selected candidates. The others are generally already identified supernovae and blazars. The distribution of their fluxes is shown in Figure 6.3.

Assuming the source under consideration is a black hole, to estimate its mass, we use the black hole mass estimator of Gültekin et al. (2019), directly derived from the fundamental plane:

$$M_{BH}(10^8 M_\odot) = 0.55 + 1.09\log_{10}(L_{5\mathrm{GHz}}[10^{38}\mathrm{erg\ s^{-1}}]) - 0.59\log_{10}(L_{2\text{-}10\ \mathrm{keV}}[10^{40}\mathrm{erg\ s^{-1}}])$$

At the median distance of our selected sample of galaxies, i.e. 33 Mpc, a 1 mJy radio source has a luminosity $L_R \approx 6 \times 10^{36}$ erg s^{-1}. For an X-ray luminosity in the range $10^{37} - 10^{41}$ erg s^{-1}, this implies a black hole mass in the range $10^6 - 10^9 M_\odot$. Consequently, these radio surveys are not sensitive enough to find new IMBHs using the fundamental plane. Therefore, these 26 radio counterparts may

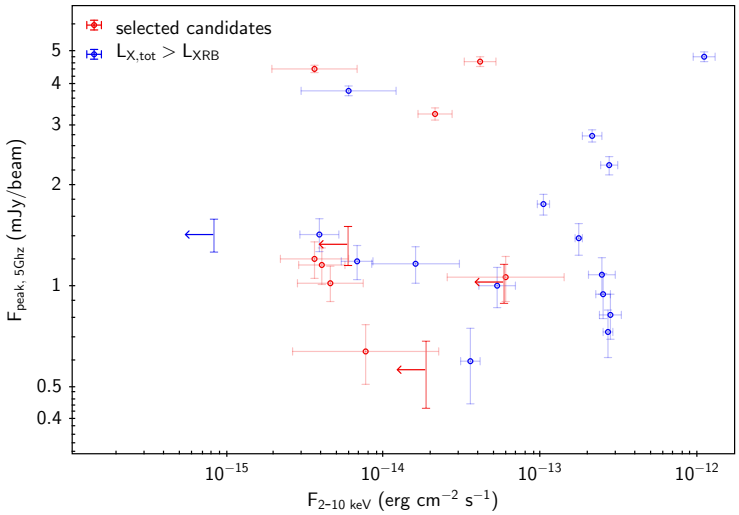

Figure 6.3: Peak radio flux density of selected candidates, as a function of their 2–10 keV flux (or 3σ upper limit for non-detections).

rather be explained by continuum emission related to star formation, and indeed two thirds of these galaxies have $SFR \gtrsim 0.25$ M$_\odot$ yr^{-1} which is the case of less than 25% of galaxies in the initial sample. More precisely, we can estimate a radio-based SFR assuming the radio emission is thermal, using the relation of Bell (2003):

$$SFR(M_\odot \text{ yr}^{-1}) = \begin{cases} 5.52 \times 10^{-22} L_{1.4\text{GHz}}, & L > L_c \\ \frac{5.52 \times 10^{-22}}{0.1 + 0.9(L/L_c)^{0.3}} L_{1.4\text{GHz}}, & L \leq L_c \end{cases}$$

where $L_c \sim 6.4 \times 10^{21}$ W Hz^{-1} is the radio luminosity at 1.4 GHz of a L_* galaxy (L_* being the characteristic luminosity of the Schechter luminosity function, Schechter 1976; Bell et al. 2003, here taken at absolute magnitude $V = -21$).

When doing so, 22 out of the 26 radio-detected galaxies have a radio-based SFR within 0.8 dex of the W3-based SFR computed for GLADE. The remaining galaxies include 3 known AGN, whose host is likely not to be a dwarf galaxy: the blazar J223812.7-394018 (Véron-Cetty and Véron, 2010), the LINER NGC 4772 (whose stellar mass is $\sim 7 \times 10^9 M_\odot$ in the NASA Sloan Atlas) and 2MASS J03354917-2749183 (Norris et al., 2006).

6.3.5 Off-nuclear candidates

Of the 903 selected sources, 683 are off-nuclear, having locations inconsistent with the host center ($d > 3(POSERR + 0.5'')$). However, this does not necessarily mean that they are XRBs or ULXs of stellar mass, since active IMBHs are sometimes seen to been wandering (Reines et al., 2020). Because of their shallower gravitational potential, we expect the low mass end of dwarf galaxies to display the larger spatial offsets. In contrast, more massive dwarf galaxies could have undergone more mergers, which are also argued to cause this offset (Bellovary et al., 2021). To investigate this, we study the radial distribution of these sources in different bins of stellar mass, for spiral and lenticular galaxies of diameter $D_{25} > 30$ arsec. As previously noted (Section 5.4.3), sources having $L_X < 10^{39}$ erg s^{-1} can be drowned out by diffuse emission, in particular in the inner regions of a galaxy, so we limit the analysis to sources above this threshold. The result is shown in Figure 6.4, where the distributions are normalised to the bin at galactocentric distance $sep \sim 0.2$ (in practice for such galaxies, sources in this bin are mostly off-nuclear). We find tentative evidence that the lower mass bin – $M_* < 4 \times 10^8 M_\odot$, containing 46 galaxies – presents an excess of sources in the outskirts, and that the profile steepens from this bin to the bin $2 \times 10^9 M_\odot < M_* < 7 \times 10^9 M_\odot$. This may be in disagreement with Bellovary et al. (2021), finding that wandering black holes are more common in more massive dwarf galaxies. However, the stellar mass range probed in their sample is essentially below $10^8 M_\odot$, so that their "massive" dwarf galaxies having undergone most mergers actually correspond to our lowest mass bin.

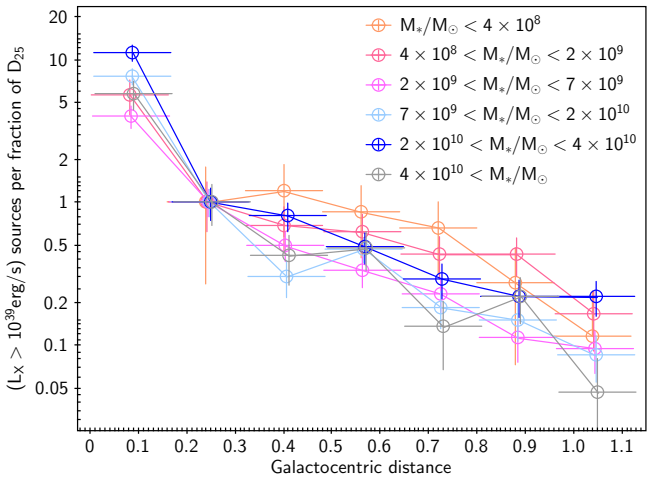

Figure 6.4: Radial distribution of X-ray sources at $L_X > 10^{39}$ erg s^{-1} in lenticular or spiral galaxies, in different bins of galaxy masses. For the purpose of comparison, each profile in normalised to the bin at galactocentric distance *sep* ~ 0.2.

Alternatively, the trend we find could also be explained by the more irregular morphologies of low-mass dwarf galaxies, with an ill-defined center, flattening the radial profile.

6.3.6 AGN candidates

In order to build a clean sample of AGN candidates, we manually inspect all selected galaxies showing an X-ray integrated luminosity in excess of the XRB model. In each galaxy, the source considered as initial AGN candidate is the one closest to the center. We analysed the 146 initial candidates having a luminosity above the 3σ limiting luminosity and at $S/N > 3$. This closer look highlighted 11 candidates as probably background AGN. To correct for stellar mass uncertainties, and the few GLADE galaxies for which M_* is underestimated (Section 6.4.1), we crossmatch GLADE galaxies with the NASA Sloan Atlas (match radius = 10 arcsec) and use the mass inferred from the best-fit Sersic profile ($SERSIC_MASS$, in units of $h^{-2}M_\odot$, where we use $h = 0.73$). Among 89 matches, another 33 galaxies are discarded because of being actually massive. To remove other massive galaxies outside the SDSS footprint, we use the catalogue of stellar and gas masses of Parkash et al. (2018) (detailed in Section 6.4.1), which identified 10 other galaxies as massive. A few other *Swift* sources were removed as well because of manifest source confusion issues or a visible extent, and two galaxies were discarded because of their underestimated distance, also impacting stellar mass estimates (NGC 1042 and J223812.7-394018, van Dokkum et al. 2019; Véron-Cetty and Véron 2010). The resulting sample is made of 91 X-ray sources (full sample) matching a dwarf galaxy, listed in Table A.4, including 77 in the clean sample (as defined from the comparison to XRB integrated luminosity). The observed 0.5–10 keV mean fluxes of the latter candidates are approximately in the range $2 \times 10^{-15} - 5 \times 10^{-13}$ erg cm^{-2} s^{-1}, with median $\approx 4 \times 10^{-14}$ erg cm^{-2} s^{-1}.

A random subset of 12 previously unreported candidates (to the best of our knowledge) is shown in Figure 6.5. Interestingly, a small fraction of candidates is found coincident with a blue, compact star-forming region, typical of ULX locations. Indeed, 4 sources of our sample are known ULXs individually studied in the literature (Thuan et al., 2004; Kaaret et al., 2011; Somers et al., 2013; Avdan et al., 2019), but all of them have a source luminosity in excess of the expected integrated luminosity of all XRBs by ≥ 0.4 dex. We note also a few notable candidates already identified as dwarf AGN or accreting IMBHs in previous works, as detailed in Table 6.4.

Among the 91 X-ray sources, 26 have $L_X > 3 \times 10^{39}$ erg s^{-1} for a sensitivity $L_{lim} < 3 \times 10^{39}$ erg s^{-1}. There are 871 GLADE dwarf galaxies that are in the footprint of X-ray instruments at this sensitivity level, so that we can derive an active fraction above this luminosity: $f_{AGN,39.5} \sim 3\%$. The same reasoning can be performed at different limiting luminosities, therefore we define three complete subsamples to conduct this study: $L_X > 5 \times 10^{38}$ erg s^{-1} (13 candidates), $L_X > 2 \times 10^{39}$ erg s^{-1} (23 candidates) and $L_X > 8 \times 10^{39}$ erg s^{-1} (17 candidates). The luminosities and limiting luminosities of the full and clean sample are shown in Figure 6.6. Active fraction estimates are further discussed in

Name	Reference
2CXO J004111.8-210752[†]	(1)
2CXO J050144.0-041718	(2)
2CXO J115237.3-022807	(2)
2CXO J122111.0+173817	(2)
2CXO J124517.0+270731	(2, 3)
2CXO J132501.3+362615	(1)
2CXO J153425.5+040806	(4)
4XMM J103410.1+580348	(1, 5)
4XMM J110912.3+612345	(4, 5)
4XMM J120746.1+430735	(5)
4XMM J192758.3-413431	(6)

Table 6.4: Known AGN candidates in dwarf galaxies present in our sample. References: (1) Miller et al. (2015), (2) Lemons et al. (2015) (3) Latimer et al. (2019) (4) Reines et al. (2013) (5) Birchall et al. (2020) (6) Oskinova et al. (2019). [†] Miller et al. (2015) choose to discard this candidate due to spectroscopic signatures of recent star formation in its region.

Section 6.4.3.

6.4 Discussion and conclusion

From an initial sample of 42115 dwarf galaxies, we are able to reliably classify 1139 X-ray sources. This represents the largest survey of the X-ray population of dwarf galaxies in the local Universe, superseding previous surveys based on the NASA Sloan Atlas (NSA) catalogue (about 44000 dwarf galaxies) which probes fainter galaxies and only covers a fraction of the sky. However, unlike NSA galaxies, the properties of GLADE objects are most often estimated photometrically. We discuss here the validity of their use.

6.4.1 Stellar mass and distance accuracy

Distances in GLADE are inferred from the redshift or Tully-Fisher estimators, when available. However, a large fraction of GLADE galaxies (in particular those retrieved from the 2MASS catalogue of extended sources, Skrutskie et al. 2006) have no such available measurements and their redshift has to be photometrically estimated (Dálya et al., 2022). Although their use of optical to infrared bands allow them to reliably estimate most redshifts with low deviation ($\sigma(\Delta z_{norm}) = 0.015$), a fraction of outliers can remain in our sample and have wrong distance or stellar mass values. To estimate this fraction, we crossmatch GLADE galaxies with three other catalogues providing distance estimates: HECATE (Kovlakas et al., 2021), the NASA Sloan Atlas and the recent galaxy catalogue of Zou et al. (2022) produced from the DESI Legacy imaging surveys. The resulting comparison is illustrated in Figure 6.7.

We find no significant bias between the GLADE, HECATE and NSA distance estimates. A small bias of ~ 0.12 dex does exist between GLADE and DESI estimates (the latter being more distant), however the photometric redshifts of Zou et al. (2022) use only optical bands and show a slightly larger standard deviation ($\sigma(\Delta z_{norm}) = 0.017$), maybe producing this bias. 90% of GLADE galaxies are within 0.04 dex of the NSA and HECATE estimates. Therefore, GLADE distances are probably accurate enough for this science case.

The same cannot be said for stellar mass estimates, taken from GLADE+ (Section 3.2.2), and computed by using k-corrected W1 magnitudes and a mass-to-light ratio depending on whether the galaxy is active (Kettlety et al., 2018; Dálya et al., 2022). A larger standard deviation is visible between the different surveys (Figure 6.8), i.e. 0.44 dex, 0.57 dex and 0.67 dex between GLADE and HECATE, NSA and DESI, respectively. This is considerably larger than the typical 0.05 dex deviation quoted in Kettlety et al. (2018) for their sample of galaxies, whose method is used to produce GLADE+ stellar masses (Dálya et al., 2022). This may be due to the range in stellar mass largely different from their sample ($M_* > 10^{10.4} M_\odot$). Additionally, HECATE stellar masses are typically offset by $\sim$0.5 dex towards larger masses. However, the same bias is seen between HECATE, NSA and DESI, so that

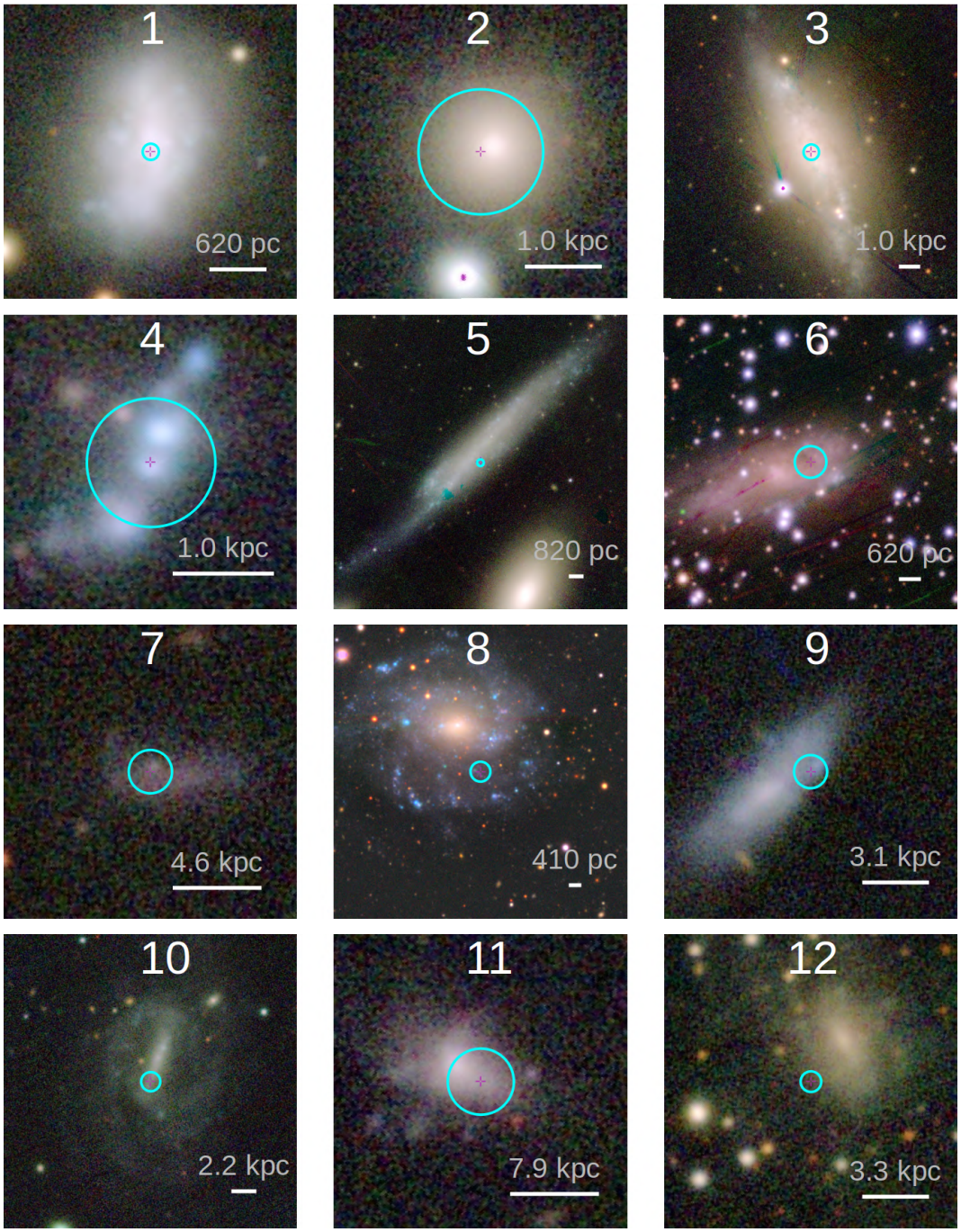

Figure 6.5: Optical (PanSTARRS) images of a random sample of 12 new AGN candidates. The image of candidate 8 is taken from DES, as its position is not covered by the PanSTARRS survey. In each image, the white line corresponds to 10 arcsec (the corresponding physical scale is written), and a 3σ X-ray position error circle is overlaid in cyan. Candidates are plotted in order of increasing physical separation to their host, and are named as follows: (1) 2CXO J023914.9+300905, (2) 2SXPS J091041.8+07122, (3) 4XMM J122858.2+123941, (4) 4XMM J094401.9-003834, (5) 4XMM J121221.1+291219, (6) 2SXPS J080707.3-28030, (7) 4XMM J024358.8-260321, (8) 2SXPS J051045.5-31362, (9) 4XMM J142758.3+255201, (10) 2CXO J135101.0+240519, (11) 4XMM J005546.6-011709, (12) 2CXO J162456.4-273637.

HECATE stellar mass estimates are likely to be less reliable. Interestingly, when considering different bins of galaxy distance, we do find a bias between GLADE and NSA masses, i.e. overestimated M_* in nearby galaxies and underestimated M_* in further galaxies (Figure 6.9). This may be due to a different implementation of the k-correction between the two catalogues. An attempt at correcting GLADE

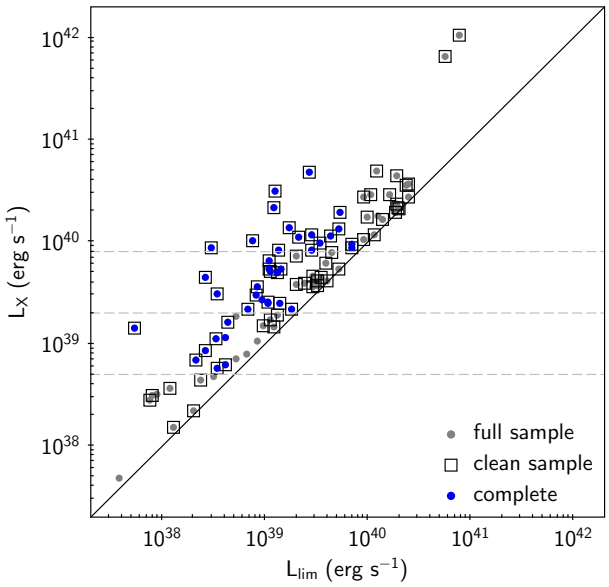

Figure 6.6: Luminosity - sensitivity dispersion of the full sample of AGN candidates. Clean candidates are circled with a black square. Complete subsamples (highlighted in blue) are defined for three luminosity thresholds (5×10^{38} erg s^{-1}, 2×10^{39} erg s^{-1} and 8×10^{39} erg s^{-1}) to study the active fraction.

stellar masses is beyond the scope of this work, but one solution may be through a machine learning estimation, arguably more precise than the analytical relation used in GLADE+ (e.g. Bonjean et al. 2019).

As a result, we identify several GLADE dwarf galaxies that are actually massive in NSA. This step removed 33 candidates out of the 146 galaxies selected initially. Given this significant correction, we search for other reliable stellar masses for dwarf galaxies outside the SDSS footprint. Parkash et al. (2018) identify ∼3000 galaxies in the intersection of WISE and Parkes HI sources, accurately probing the stellar and gas content of galaxies in the nearby Universe ($D \lesssim 100$ Mpc). While their stellar mass estimates are also based on mid-infrared data, they carefully model WISE isophotes and use a colour-dependent mass-to-light ratio rather than a fixed value, so that their estimates are accurate to ~ 0.2 dex and are unbiased even for dwarf galaxies (though with a larger scatter). After cross-correlating GLADE with their catalogue (available on *Vizier*[3]), with a cone search of radius 10 arcsec, we find an extra 10 galaxies that are not dwarf in our sample of candidates. A comparison of M_* estimates from the two catalogues and NSA is shown in Figure 6.10, confirming the bias of GLADE towards smaller masses for these nearby galaxies having $D_{25} \gtrsim 20$ arcsec, where NSA estimates seem to be unbiased. As a result, 103 galaxies are left for manual analysis, including 64 (62%) with bona fide dwarf masses.

Concerning the remaining galaxies, we note that less than 20% of GLADE dwarf galaxies have NSA masses $M_{*,Sersic}$ larger than $3 \times 10^9 M_\odot$, and only 2% of them have $M_{*,Sersic} > 10^{10} M_\odot$. Therefore, while this can bias the active fractions inferred in this work, these fractions are likely to be valid at a <0.1 dex level, provided that the considered objects are indeed massive black holes.

Additionally, while GLADE provides a > 50% complete census of galaxies up to ∼ 200 Mpc, stellar mass estimates are not given for all entries. Even if Dálya et al. (2022) state that 97% of galaxies are provided with such estimates, they are particularly lacking for low-mass galaxies. Indeed, the crossmatch of GLADE with the catalogue of ∼3000 nearby galaxies ($\lesssim 100$ Mpc) of Parkash et al. (2018) reveal that more than 30% of galaxies at $M_* < 10^9 M_\odot$ have a GLADE stellar mass, and more than 60% below $10^8 M_\odot$ (Figure 6.11). This significantly limits the possibility to compare our candidates with the recent literature (Section 6.4.5).

[3] https://vizier.cfa.harvard.edu/viz-bin/VizieR?-source=J/ApJ/864/40

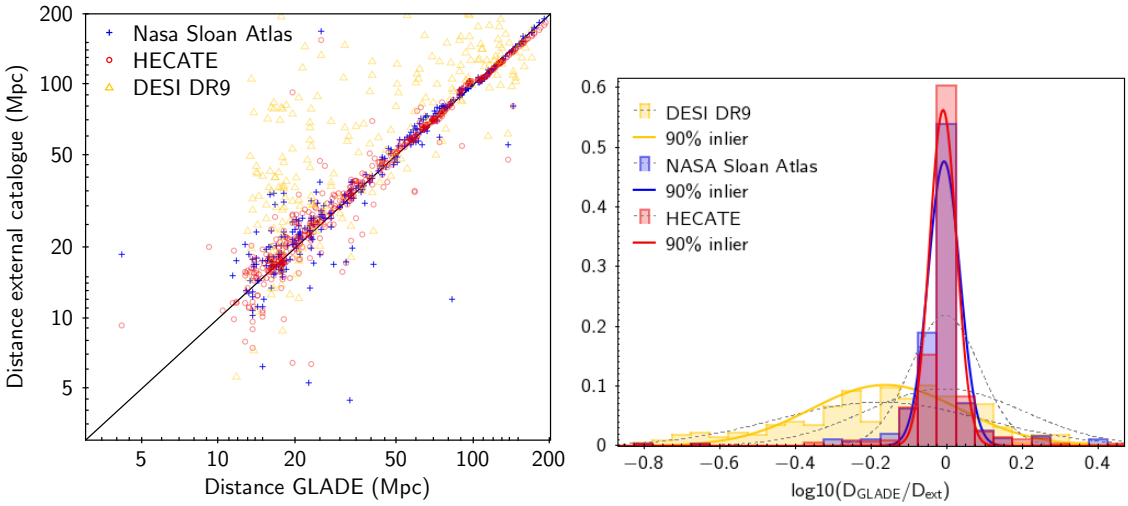

Figure 6.7: Comparison of GLADE distances with distances from external surveys, for X-ray detected dwarf galaxies in their intersection. (Right): histogram of the deviation between these quantities (in dex).

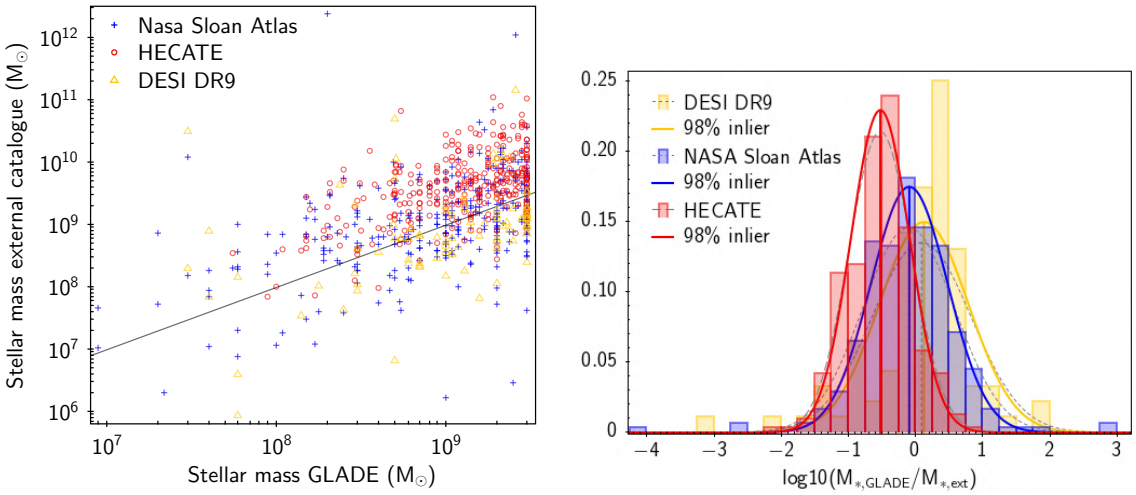

Figure 6.8: Comparison of GLADE stellar masses with stellar masses from external surveys, for X-ray detected dwarf galaxies in their intersection. (Right): histogram of the deviation between these quantities (in dex).

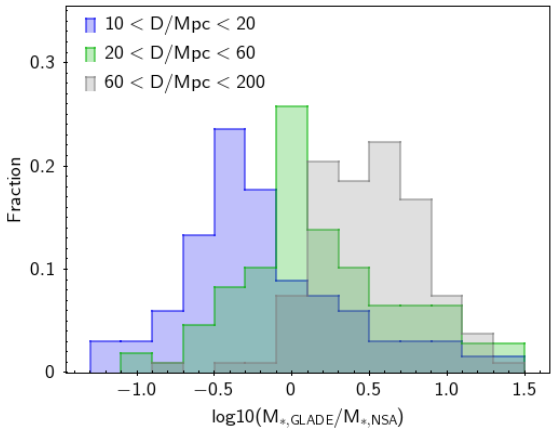

Figure 6.9: Histogram of the deviation between GLADE and NSA stellar masses (in dex), in different bins of GLADE distance.

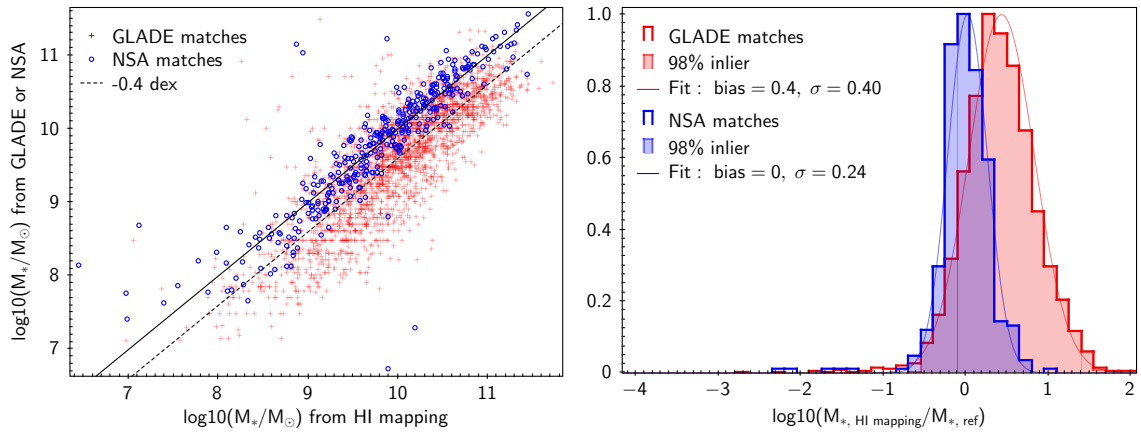

Figure 6.10: (Left) Comparison of stellar masses estimated from NSA, GLADE and Parkash et al. (2018), for dwarf galaxies in their intersection. (Right) histogram of the deviation between these quantities (in dex).

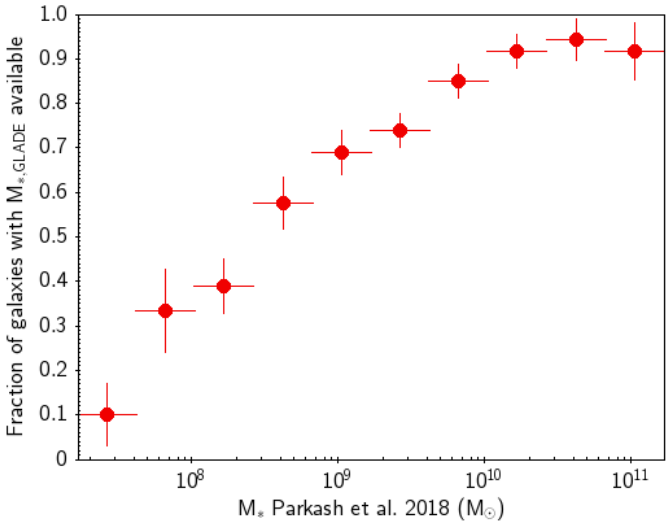

Figure 6.11: Fraction of GLADE galaxies having an available stellar mass estimate, as a function of galaxy stellar mass, for GLADE nearby galaxies present in the sample of Parkash et al. (2018).

6.4.2 Metallicity effects

As stated in Section 6.3.3, the scaling relations generally used to estimate the total XRB luminosity of a galaxy are calibrated on nearby, mostly massive galaxies. However, a clear excess of ULX rate is seen in dwarf galaxies (Kovlakas et al. 2020, Chapter 5), and these galaxies are generally found to have metallicities ~ 1 order of magnitude lower than their massive analogues (e.g. Andrews and Martini 2013). The rate of luminous HMXBs ($L_X > 10^{40}$ erg s^{-1}) (expected to be dominant in the ULX population of starforming environments at these luminosities) is higher in these low-metallicity environments (Lehmer et al., 2021), and such sources in starforming galaxies are generally responsible for most of the total X-ray luminosity of their host. This may drive the excess seen in the X-ray total luminosity of many dwarf galaxies.

To investigate this effect, we use the model of Lehmer et al. (2021) representing the total XRB emission as a function of metallicity and star-formation rate. The mass-metallicity relation of Andrews and Martini (2013) is assumed to estimate the galaxy metallicity: $12 + \log_{10}(\mathrm{O/H}) = 12 + \log_{10}(\mathrm{O/H})_{asm} - \log_{10}(1 + (M_{TO}/M_*)^{\Gamma})$ where $12 + \log_{10}(\mathrm{O/H})_{asm} = 8.798$, $\log_{10}(M_{TO}) = 8.901$ and $\Gamma = 0.640$. To estimate the total LMXB luminosity, we use the model of Lehmer et al. (2016): $L_{LMXB} = \alpha_0(1+z)^{\gamma} M_*$ where α_0 and γ are quoted in Section 6.3.3. The resulting XRB luminosity is compared to the one previously used in Figure 6.12, as a function of the galaxy stellar mass and specific SFR.

Surprisingly, only a handful of dwarf galaxies have an increased contribution of XRBs when metallicity is taken into account, notably the most starforming galaxies of the sample. Indeed, since 92% of galaxies in our sample have inferred metallicities $12 + \log_{10}(\mathrm{O/H}) > 8.2$, their XRB model are nearly independent of metallicity at all $SFR < 0.2 M_{\odot}\ yr^{-1}$, which is the case of two thirds of the sample. The downward trend at low SFR in Figure 6.12 shows that HMXB luminosities are either overestimated in Lehmer et al. (2016) or underestimated in Lehmer et al. (2021). Because the former work mostly contains massive galaxies, whereas $\sim$40% of galaxies in Lehmer et al. (2021) are dwarf galaxies, we conclude that the latter estimation is better suited for our sample. Moreover, since we use the same method as Kovlakas et al. (2021) and Cluver et al. (2017) to compute SFRs, calibrated on a sample including dwarf galaxies (down to $M_* \sim 10^7 M_{\odot}$) but in the local Universe ($D < 30$ Mpc), our SFR uncertainty should be comparable (0.15 dex). However, neither this uncertainty, nor the one on stellar mass (Section 6.4.1), are propagated to our L_{XRB} estimates, possibly leading to a small number of remaining XRB or ULX contaminants.

Perhaps more importantly, a significant fraction of galaxies in our sample of AGN candidates are blue compact dwarfs, in which the above-cited scaling relations underestimate L_{XRB}. Such galaxies typically display a ULX rate enhanced by a factor ~ 7 (Mapelli et al., 2010) and an HMXB integrated luminosity enhanced by a factor $\sim$ 10 up to $\sim$ 20 (Brorby et al., 2014; Kaaret et al., 2011). To remove XRB and ULX contribution in these galaxies, we require a clean candidate to follow $L_X > L_{LMXB} + 20 \times L_{HMXB}$, where L_{LMXB} and L_{HMXB} are computed using the relations of Lehmer et al. (2016).

6.4.3 Active fraction

Assuming that the identified candidates are indeed massive black holes, we can infer constraints on the active fraction of galaxies depending on their mass and at a certain luminosity threshold. Figure 6.13 shows the active fraction f_{AGN} obtained from clean candidates in the three complete subsamples defined above ($L_X < 5 \times 10^{38}$ erg s^{-1}, $L_X < 2 \times 10^{39}$ erg s^{-1} and $L_X < 8 \times 10^{39}$ erg s^{-1}), and in three stellar mass bins. Errors are computed using the confidence limit equations of Gehrels (1986), well-adapted to small number counts in such studies.

Our constraints are in good agreement with the ones obtained by Birchall et al. (2020) on their sample of 3XMM-DR7 candidates in NSA galaxies. The active fraction increases with decreasing limiting luminosity, consistently with a majority of AGN accreting at low rates (and hence having faint luminosities). In the upper stellar mass bin, $5 \times 10^8 < M_*/M_{\odot} < 3 \times 10^9$, f_{AGN} estimates are similar in the two fainter subsamples, maybe suggesting that this luminosity threshold offers a complete census of accreting black holes in these environments. However, the same trend could be explained by selection effects, e.g. source confusion issues at faint luminosities. The active fraction is consistent with a constant value in each stellar mass bin, but an increase cannot be ruled out in the brighter subsamples.

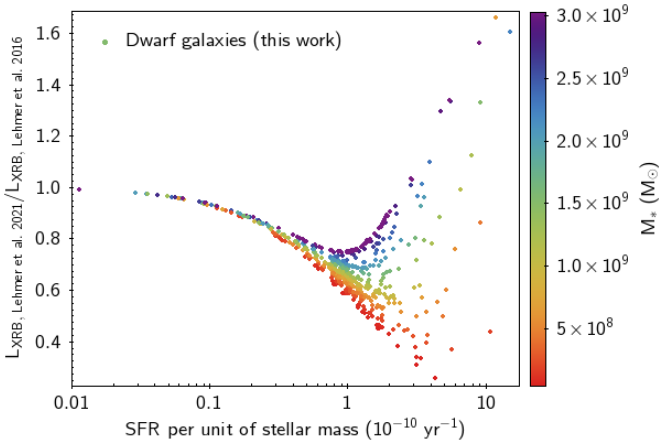

Figure 6.12: Comparison of integrated luminosities of XRB with and without accounting for metallicity (using the models of Lehmer et al. (2021) and Lehmer et al. (2016), respectively), as a function of the galaxy specific SFR and stellar mass.

Interestingly, candidates that are in the full sample but not in the clean sample (thus more likely to be XRBs or ULXs) only affect the f_{AGN} estimate in the two fainter subsamples and in the upper stellar mass bin, as shown by the cyan and blue arrows in Figure 6.4.3. This is expected, since the most massive dwarf galaxies have integrated XRB luminosities reaching the luminosity threshold of these samples. Therefore, an incomplete removal of XRBs and ULXs leads to an overestimation of f_{AGN} specifically for these galaxies. We suggest that this may cause the tentative increase of f_{AGN} with stellar mass obtained by Birchall et al. (2020). While they claim an active fraction reaching ∼6% in the upper stellar mass bin $10^9 < M_*/M_\odot < 3 \times 10^9$ at $L_X > 10^{39}$ erg s^{-1}, we find a slightly lower value $f_{AGN} \sim 3\%$ at similar luminosity and stellar mass (although consistent with their estimate at the 1σ level).

In the lower stellar mass bin, ∼25% of X-ray detected galaxies are blue compact dwarf galaxies, maybe explaining the higher f_{AGN} value obtained in the lower luminosity sample. Indeed, these galaxies are a favourable environment for ULXs in which the integrated luminosity of XRBs and ULXs is higher than expected from the usual scaling relations (Kaaret et al., 2011; Brorby et al., 2014), probably due to their lower metallicity (Brorby et al., 2016; Kovlakas et al., 2020; Lehmer et al., 2021). While the enhanced XRB luminosity at low metallicity (and in particular in blue compact dwarfs) is already taken into account to build the clean sample (Section 6.4.2), we cannot exclude at this point that some AGN candidates in this bin are actually stellar-mass ULXs, as discussed by Latimer et al. (2019).

Overall, we obtain an active fraction of dwarf galaxies of $f_{AGN} = \sim 4.3^{+1.9}_{-3.0}\%$ (1σ confidence limits) at a luminosity threshold $L_X > 5 \times 10^{38}$ erg s^{-1}. This active fraction probing the local Universe – 98% of the probed galaxies are located at $D < 40$ Mpc – is higher than typically found in previous studies, due to their shallower limiting luminosities. While Gallo et al. (2008) and Miller et al. (2015) reach such sensitivities, their galaxy sample extends to $M_* = 10^{10} M\odot$. If we assume that dwarf galaxies are local analogues of high redshift galaxies in which present-day SMBH grew and evolved (which is controversial, as reviewed by Mezcua 2019, 2021), this lower limit on the occupation fraction of dwarf galaxies is however not yet sufficient to have implications on the preferred mechanism of black hole seeding (Greene et al., 2020).

As stated above, these active fractions are only lower limits on the intrinsic black hole occupation fraction (f_{occ}) in each stellar mass bin. For a given stellar mass, the fraction of galaxies with nuclear activity detected above a given X-ray luminosity ($\equiv f_{AGN}$) depends both on the occupation fraction f_{occ} and on the distribution of black hole masses M_{BH} and Eddington fractions L/L_{Edd} at this stellar mass (more precisely, on the product of their distributions, assuming a fixed bolometric correction). To derive estimates on f_{occ}, Miller et al. (2015) model the latter $L_X - M_*$ relation of occupied galaxies by a powerlaw allowing for significant scatter: $L_X = \mathcal{N}(\alpha M_* + \beta, \sigma^2)$. f_{occ}, α, β and σ are then simultaneously fitted with a Monte-Carlo approach to their whole galaxy sample (which spans $10^{7.5} < M_*/M_\odot < 10^{12}$ in stellar mass), taking into account non-detections. This approach allow

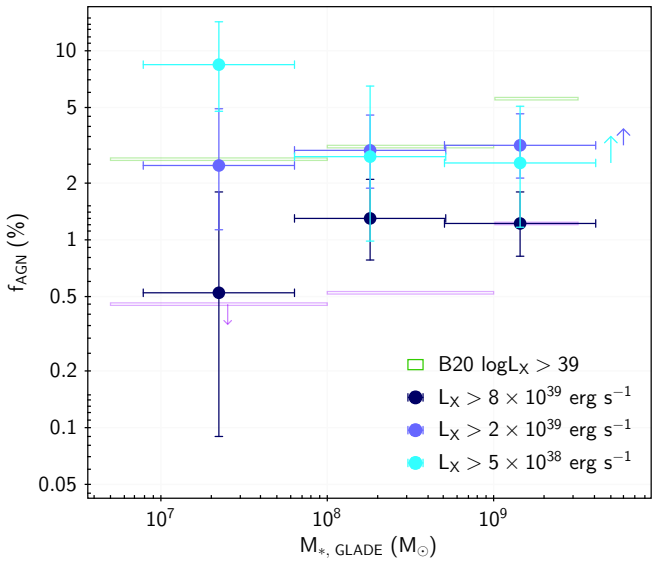

Figure 6.13: Active fraction inferred from our sample, as a function of galaxy mass. Three bins of luminosity are shown. For comparison, we overlay the constraints obtained by Birchall et al. (2020) from 3XMM-DR7 and NSA (green: $L_X > 10^{39}$ erg s^{-1}, prune: $L_X > 10^{40.5}$ erg s^{-1}). The cyan and blue arrows show the offset in f_{AGN} seen in the upper stellar mass bin if the full sample of candidates is considered, rather than the clean sample.

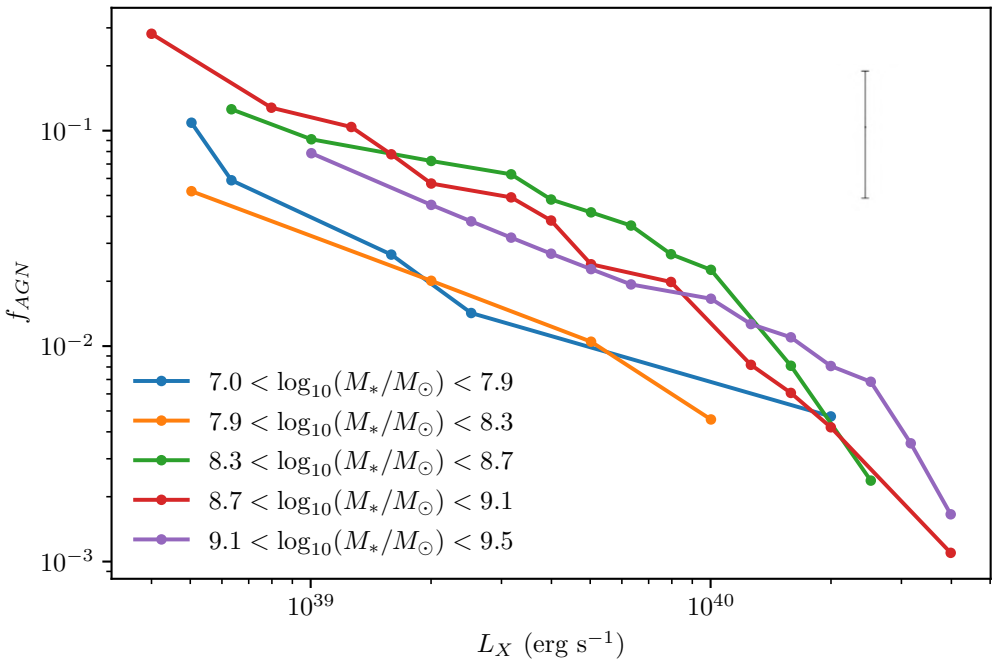

Figure 6.14: Detected active fraction as a function of limiting X-ray luminosity for the full sample of AGN candidates, in different stellar mass bins. A typical error bar is shown in the upper right part of the plot.

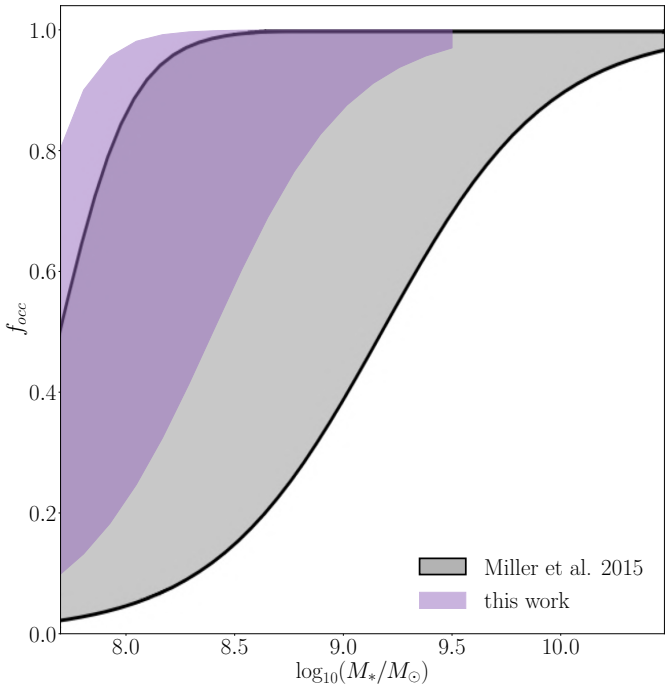

Figure 6.15: Comparison of our constraints on f_{occ} as a function of stellar mass, with the constraints of Miller et al. (2015).

them to derive $f_{occ} > 20\%$ among their sample of low-mass galaxies $M_* < 10^{10} M_\odot$. Most of their error on f_{occ} comes from the low number of detected galaxies, especially below $5 \times 10^9 M_\odot$. Besides, their upper limits are not as constraining as a detection. As they suggest, reaching deeper limiting luminosities is essential to disentangle occupation and downsizing effects.

However, as they acknowledge (concerning its scatter), this approach has the caveat to assume an $L_X - M_*$ relation valid over their full stellar mass range. It is likely that the resulting $L_X - M_*$ fit is mostly influenced by galaxies above $10^{10} M_\odot$, which are the vast majority of X-ray detected galaxies in their sample. However, if dwarf galaxies are primarily occupied by massive seeds M_{BH} $10^5 M_\odot$ (which is a possibility, Greene 2012), then their X-ray luminosity should be essentially independent of stellar mass.

As an indirect approach, we study how the active fraction depends on limiting X-ray luminosity for different bins of stellar mass (Figure 6.14). Despite the large uncertainties, some qualitative features are notable: we find tentative evidence that the shape of $f_{AGN}(L_{lim})$ is constant in the stellar mass range $10^{8.3} < M_*/M_\odot < 10^{9.5}$, and drops significantly at $M_* < 10^{8.3} M\odot$. This trend is consistent with a constant distribution of $M_{BH} \times L/L_{Edd}$, as would be the case for example for seeds of constant mass in similar accretion conditions. The characteristic mass $M_{*,0} = 2 \times 10^8 M_\odot$ below which $f_{AGN}(L_{lim})$ drops could be the typical mass having 50% of occupation fraction, as parametrised by Miller et al. (2015) (see their Figure 1, panel (b)). If extrapolated to their sample, this would imply an occupation fraction of $\sim 80\%$ among all low-mass galaxies $M_* < 10^{10} M\odot$.

However, we note that this result is dependent on the binning on stellar mass: indeed, the active fraction profile of the mass bin $7.5 < \log_{10}(M_*/M_\odot) < 7.9$ is in between the profiles of massive galaxies and the one in the bin $7.9 < \log_{10}(M_*/M_\odot) < 7.3$. Therefore, if there is indeed a drop of f_{occ} at a characteristic stellar mass, we estimate this mass to be in the range $3 \times 10^7 M_\odot < M_{*,0} < 2.5 \times 10^8 M_\odot$. In Figure 6.15, we superimpose the constraints resulting from these values to the constraints obtained by Miller et al. (2015).

We also note that this trend is in contrast with Figure 6.13 showing a rather constant active

fraction at $L_X \gtrsim 10^{39} M_\odot$ down to galaxies of $M_* \sim 10^{7.5} M_\odot$, which are again largely affected by blue compact dwarfs. Further work is needed to assess the robustness of this trend and conduct this study on different dwarf galaxy morphologies.

6.4.4 Nature of AGN candidates

Because our AGN candidates are selected not only in the nuclear region of galaxies, but also wandering in their outskirts, we can expect a small fraction of them to be ULXs. However, from the standard deviation 0.17 dex reported for the scaling relations in Lehmer et al. (2016), we can infer that 5% of GLADE dwarf galaxies will have an XRB luminosity in excess of the scaling relation value by at least 0.34 dex. In the footprint of X-ray instruments, this amounts to ~ 17 galaxies above the sensitivity limit, including ~ 2 galaxies where the excess is greater than 0.51 dex. In comparison, 72 out of 77 candidates in the clean sample are in the latter case, so that remaining ULX and XRB contaminants should be negligible. Even if we assume an XRB luminosity in dwarf galaxies enhanced by a factor 4, consistently with the excess in ULX rate seen in Figure 5.3.2, more than 60% of the clean candidates are kept.

About 50% of the clean candidates have positions inconsistent with the galaxy center reported in GLADE ($d > 3(POSERR + 0.5'')$). However, as illustrated in Figure 6.17, nearly all of them are located at less than 5 kpc from the center. This is consistent with previous simulations and observations of wandering black holes (Reines et al., 2020; Bellovary et al., 2021).

A commonly used method to estimate black hole masses is to extrapolate scaling relations obtained in the nearby Universe for massive galaxies, in particular $M_{BH} - M_*$, $M_{BH} - M_{bulge}$ or $M_{BH} - \sigma$ (e.g. Koliopanos et al. 2017; Birchall et al. 2020). While this provides first estimates that should be reliable to better than 1 dex, this implicitly assumes the same co-evolution between galaxies and black holes in both dwarf and massive galaxies, which is something that has yet to be tested, especially for off-center black holes that are expected to have their growth stunted.

On the other hand, Baldassare et al. (2017) study the X-ray emission of a sample of optically-selected low-luminosity AGN, finding a wide range of Eddington ratios $10^{-3} < f_{Edd} < 0.54$. However, the X-ray luminosities they report are notably higher than those found in our sample, so it would be bold to extrapolate these values to our candidates. Their sample being made of candidates selected from BPT diagnostics, which are known to be insensitive to most AGN in dwarfs (e.g. Mezcua and Domínguez Sánchez 2020; Polimera et al. 2022), it is possible that their sources accrete at higher levels. For sources having $L_X \lesssim 10^{40}$ erg s^{-1} (which is the case of two thirds of our clean sample), Baldassare et al. (2017) find a median Eddington ratio of 0.003 (mean of 0.005). Similarly, an independent study of the active nucleus in NGC 4395 (highly variable in X-rays but having $\langle L_X \rangle \sim 10^{40}$ erg s^{-1}) constrain its Eddington fraction to be in the range $[0.001, 0.02]$ (Montano et al., 2022).

Therefore, here we estimate black hole masses by assuming a constant Eddington ratio, $f_{Edd} = 0.004$. While we acknowledge that this estimate should not be trusted on an individual basis, it is unlikely to be biased in the same direction for a whole population. The bolometric luminosity is estimated as 10 times the X-ray luminosity in the 2–10 keV band (Marconi et al., 2004). The resulting BH mass - galaxy mass plane is shown in Figure 6.18. Black hole masses are in the range $2 \times 10^3 - 10^7 M_\odot$, with a median at $9 \times 10^4 M_\odot$. No significant difference is seen between nuclear and off-nuclear candidates. The population is globally consistent with the $M_{BH} - M_*$ relation of Reines and Volonteri (2015), especially given the ~ 1 dex uncertainty on the Eddington ratio and hence the BH mass. The candidates have masses well below 1% of their host stellar mass. This contrasts with the locus of HLX candidates, generally found above the relation of Reines and Volonteri (2015) in Figure 5.24. We suggest different mechanisms accounting for this difference. First of all, as mentioned in Section 5.4.5, stellar masses of HLX optical counterparts use the uncorrected optical fluxes of the point-like source, so they are possibly underestimated. Also, it is possible that the selected HLXs are biased towards higher Eddington ratios to be detectable, that is to say they may be lighter IMBHs accreting close to the Eddington limit, just as seen in HLX-1 (Godet et al., 2012). This bias is likely to happen when removing all sources below 10^{41} erg s^{-1} from the sample. Alternatively, HLX counterparts could be the stripped core of a dwarf galaxy having lost most of their mass during the merger. Another possibility is that our AGN candidates are also overmassive, accreting at $f_{Edd} \lesssim 0.002$, as needed to match the relation of Reines and Volonteri (2015) at stellar mass $M_* > 10^9 M_\odot$, which would place them in the locus of HLXs. These considerations are further discussed in Section 7.3.

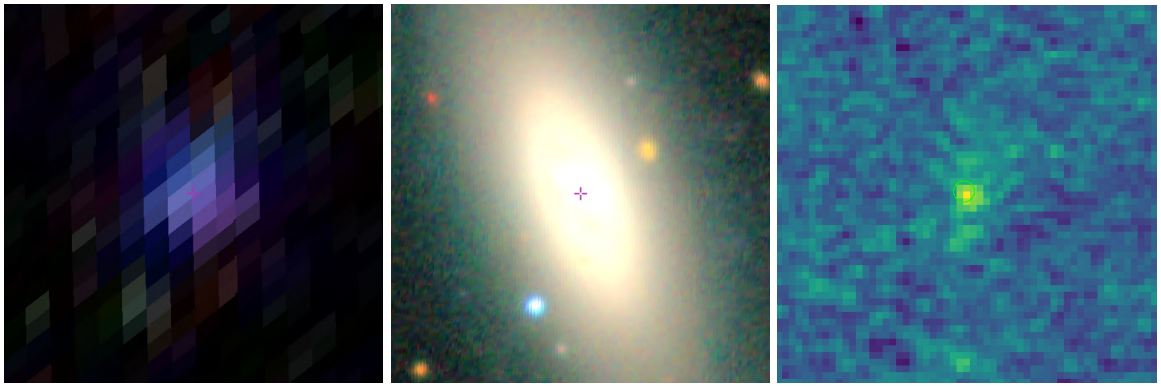

Figure 6.16: X-ray (*XMM-Newton*), optical (Beijing Arizona Sky Survey) and radio (VLA) images of 4XMM J120746.1+430735. The images are 1 arcmin on a side.

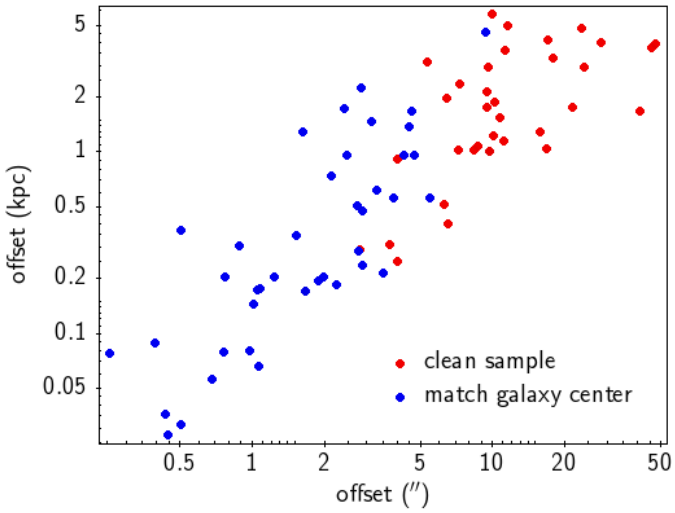

Figure 6.17: Physical and angular offset of AGN candidates to the center of their host. Candidates with positions consistent with the center ($d < 3(POSERR + 0.5'')$) are highlighted in blue.

In the clean sample, 4 sources have radio detections, but only 1 has a radio luminosity in excess of 3 times the expected thermal luminosity related to star formation: 4XMM J120746.1+430735 in NGC 4117 has a VLASS detection at 3 GHz at $S_\nu = 0.73$ mJy/beam, leading to $L_{5GHz} = 1.4 \times 10^{36}$ erg s^{-1} assuming a flat spectrum. Using the fundamental plane of Merloni et al. (2003), we find a BH mass of $\sim 1.3 \times 10^6 M_\odot$ ($3.2 \times 10^6 M_\odot$ using the mass estimator of Gültekin et al. 2019). However, the radio source seems to be extended in the radio image, which is supported by the difference of a factor ~ 6 between the peak flux and the flux integrated over the fitted radio island (6×6 arcsec^2) (Figure 6.16). In addition to the fact that X-ray and radio observations are not simultaneous, this suggests that the fundamental plane BH mass estimate is only an upper limit. It is thus in agreement with the X-ray estimate assuming $f_{Edd} = 0.004$, $M_{BH} = (2.2 \pm 0.3) \times 10^5 M_\odot$. This candidate was reported in Moran et al. (2014) and Sartori et al. (2015) as a bona fide AGN.

6.4.5 Comparison to other studies

In this study, we searched for AGN in dwarf galaxies using the largest X-ray archives and an all-sky galaxy catalogue with high completeness up to 200 Mpc. Our survey volume is thus three times larger in the optical (compared to the SDSS footprint) and $\gtrsim 3$ times larger in the X-rays compared to previous studies, allowing us to better constrain the active fraction of dwarf galaxies down to fainter luminosities and to find a large population of new IMBH candidates. Interestingly, the deep sensitivities and large survey area achieved in this allow us to probe the IMBH population at masses

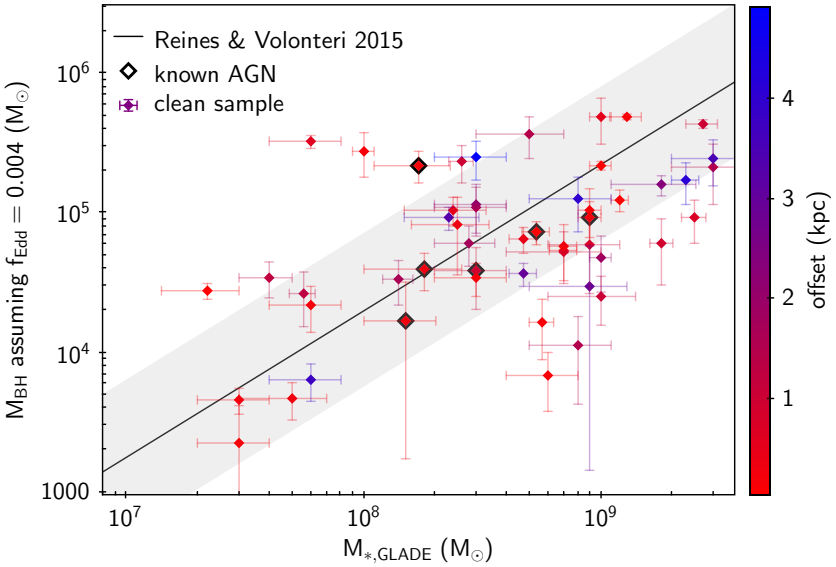

Figure 6.18: Black hole mass - galaxy mass plane for our clean sample of AGN candidates having stellar masses accurate at the 50% level. Black hole masses are computed assuming an Eddington ratio of $f_{Edd} = 0.004$ (see the text for details), where vertical error bars propagate uncertainties on the X-ray flux.

typically below $10^5 M_\odot$, which remained elusive in previous works (Greene, 2012).

Our classification-based approach also provides a tool to homogeneously select reliable AGN in dwarf galaxies. Indeed, previous works mostly relied on the removal of hot gas and sometimes known contaminants to clean up their sample of candidates, before applying a threshold on the X-ray integrated luminosity based on the XRB content of galaxies. Consequently, the remaining background sources were necessarily included in the computation of integrated luminosities, biasing their method towards the selection of background sources. Here, we were able to remove these background sources beforehand, in order to obtain clean estimations of the in-situ integrated luminosity. 146 galaxies above the 3σ sensitivity level were selected in this process, instead of 168 if we had not removed background contaminants in the first place, thus removing $\sim$1 source every 8 candidates. This is important, given the contamination rate expected from studies extending the search to off-nuclear sources at high luminosities, sometimes preventing to draw any estimate on the active fraction except an upper limit. For instance, in the eFEDS field, Latimer et al. (2021) estimate the theoretical number of background sources that they would select as candidates to be in the range $0 - 9$ (95% confidence level), while their actual sample only contains 6 candidates. The limiting luminosity of their survey is not stated, making it difficult to compare with our estimates their upper limit on the active fraction, $f_{AGN} < 1.8\%$.

However, searching for known candidates in our sample, we found that a significant fraction of them is missing in our sample. Table 6.5 lists a representative sample of X-ray detected AGN in dwarf galaxies (Reines et al., 2011; Koliopanos et al., 2017; Mezcua et al., 2018; Latimer et al., 2019; Graham et al., 2021) and their status in our study. Most of them are absent from our sample due to missing or unreliable stellar mass estimates in GLADE+.

The next step of this work will thus be to complete this census of active black holes in dwarf galaxies by considering more galaxy catalogues with reliable mass estimates (in particular NSA), in order to better compare our work with previous studies and look for unseen black holes in these surveys better covering the higher redshift Universe.

Galaxy	Status	Reference
Henize 2-10	$M_{*,GLADE}$ is missing	(1)
NGC 628	$M_{*,GLADE}$ is missing	(2)
NGC 3185	$M_{*,GLADE} > 3 \times 10^9 M_\odot$	(2)
NGC 3198	$M_{*,GLADE}$ is missing	(2)
NGC 3486	$M_{*,GLADE}$ is missing	(2)
NGC 3507	extended in CSC2†	(2)
NGC 4314	extended in CSC2†	(2)
NGC 4470	$L_{\rm X,\ tot} < L_{\rm XRB,\ Lehmer\ et\ al.\ 2016}$	(2)
SBS 0940+544	AGN candidate (clean)	(3)
Haro 9	AGN candidate (clean)	(3)
NGC 4178	$M_{*,GLADE}$ is missing	(4)
NGC 4713	$M_{*,GLADE}$ is missing	(4)
NGC 4197	$M_{*,GLADE} > 3 \times 10^9 M_\odot$	(4)
NGC 4212	$M_{*,GLADE}$ is missing	(4)
NGC 4298	AGN candidate (full)	(4)
NGC 4313	Observation not in catalogue‡	(4)
NGC 4330	$M_{*,NSA} > 3 \times 10^9 M_\odot$	(4)
NGC 4405	$M_{*,GLADE} > 3 \times 10^9 M_\odot$	(4)
NGC 4413	$M_{*,GLADE}$ is missing	(4)
NGC 4492	$M_{*,GLADE} > 3 \times 10^9 M_\odot$	(4)
NGC 4498	$M_{*,NSA} > 3 \times 10^9 M_\odot$	(4)
NGC 4519	Observation not in catalogue‡	(4)
NGC 4607	Observation not in catalogue‡	(4)

Table 6.5: List of 23 X-ray detected active dwarf galaxies from the literature, along with their status in our study. References: (1) Reines et al. (2011), (2) Koliopanos et al. (2017), (3) Latimer et al. (2019), (4) Graham et al. (2021). † the source was discarded as being extended in the CSC2 catalogue, and indeed Koliopanos et al. (2017) had to fit its spectrum with a hot gas (APEC) component. ‡ the source was observed in 2018, so it is not included in the current version of the *Chandra* catalogue.

Chapter 7

Discussion

In this thesis, I have adopted a classification-based approach to search for and study intermediate-mass black holes in X-ray data. Here I summarize the advantages and limitations of such an approach, as well as the insight it has provided into the IMBH population. Selection effects and methodological biases are highlighted, before finally comparing our results to IMBH formation channels.

7.1 Benefits and limitations of a probabilistic approach for population studies

After more than five decades of development, X-ray astronomy is now slowly entering the era of Big Data, taking a census of more than a million X-ray sources by three powerful X-ray satellites launched in the early 2000s, namely *Swift*-XRT, *XMM-Newton* and *Chandra*. Far from being limited to the study of AGN, galaxy clusters or active stars, X-ray observatories proved essential to our knowledge of the most energetic and transient phenomena of the Universe, including tidal disruption events, supernovae, neutron stars and key stages of the evolution of black holes.

The abundance of serendipitous X-ray discoveries and the growing number of X-ray detections have thus been accompanied by a gradual shift in perspective, from an empirical science governed by manual classifications and rules of thumb to distinguish several classes, to a field requiring an automatic, versatile and efficient classification. Such an approach is becoming increasingly important as current and future X-ray missions complete the census of the X-ray sky, in particular *eROSITA* (expected to detect more than 3 million sources) and future missions such as *Athena* (Nandra et al., 2013) and *Lynx* (Gaskin et al., 2019). The advent of automatic machine learning methods to classify X-ray sources has been most facilitated by the development of their systematic and rigorous cross-correlations with multiwavelength archives and the growing samples of identified AGN, stars and other X-ray emitters that could be used for training.

Such a classification proves to be increasingly relevant for a number of applications. First, it is in synergy with the development of transient astronomy and the regular monitoring of large portions of the sky in both the electromagnetic domain and gravitational waves. Specifically, the discovery of a gamma-ray counterpart for GW170817 (Abbott et al., 2017) paved the way for multimessenger astronomy. Besides, in X-rays, serendipitous transient sources are often associated with rare phenomena

(such as tidal disruption events or changing-look AGN) for which a lot of science remains to be done. But perhaps most importantly for our topic, the simplest application of an automatic classification is to gather a large sample of a certain population for study.

Indeed, X-ray population studies have so far often relied on the application of fixed, hard cuts on the source properties. This leads to some biases such as classifying all objects with $F_X/F_{opt} < 0.01$ as stars or missing most ULXs with $F_X/F_{opt} < 1$ (Bernadich et al. 2021, Section 5.2.3). One use of our automatic, probabilistic classification is thus to consider many properties at a time, and to be able to apply a given threshold to the output probability to reach a chosen recall-precision trade-off on the output class. As a result, we managed to identify more than 90% of reliable ULXs, with a lower contamination rate than previous studies. In particular, this has implications on results inferred for the X-ray luminosity function of ULXs and their radial distribution (Sections 5.4.4, 5.3.2). This ability to improve the reliability of the sample also enabled a more accurate estimation of the active fraction of dwarf galaxies (Section 6.4.5).

Besides, a (little explored) capability of our classification is the outlier measure, potentially able to identify sources not belonging to one of the classes of the training sample (e.g. spurious sources but also subtypes of AGN and stars or TDEs, Sections 4.4.3, 5.3.5).

As a result, adopting a probabilistic classification for population studies is an efficient way to obtain cleaner and less biased samples. However, important limitations appear at small sample size or low data quality. Therefore, most cataclysmic variables are classified as AGN in Chapter 4, due to their low prior probability (2%) and limited training sample ($\lesssim 300$ objects).

When the class of interest has few objects in the training sample, the histograms of their properties are likely to be biased or too noisy, leading to overfitting issues. This is the case for example in the search for possible new high-redshift quasars present in the archives (Section 8.2.2): a large fraction of such objects in the training sample have missing values for their colours or spectral parameters, hence biasing low-quality sources towards the classification as new high-redshift quasar candidate. A solution in this particular case is to impose that the coefficient β, which weights the importance of the missing values in the classification, is equal to 0.

On the other hand, if the class of interest is absent from the training sample, a fraction of this population can be retrieved as outliers as previously said. However, the majority of them are likely to be classified as the class having the highest prior, or the most similar properties. This was the case of HLX candidates (Section 5.4.5), mostly classified as AGN due to their luminosity and optical counterpart.

The issue of a small and heterogeneous training sample was also found for X-ray binaries in the classification of the whole catalogue, though their classification in nearby galaxies as consisdered in Chapter 5 is more reliable than that for the whole catalogue sample. This gain in performance is enabled by the use of more homogeneous and more balanced classes (the classifier is more "specialised"): the training sample of XRBs do not contain Galactic XRBs, and the focus on sources associated with nearby galaxies means that the proportion of XRBs is enhanced (and so does their prior). A further improvement (in preparation) of the X-ray classification will be to run it on sources inside and outside of the Galactic plane ($|b| < 20°$ and $|b| \geq 20°$, respectively) to enhance the retrieval of XRBs and CVs and remove the incorrect AGN classifications close to the Galactic center (Section 4.4.2).

However, considering specific sky areas rather than the whole catalogue obviously decreases the training sample size, often making them too small to achieve accurate results. The solution could then be to enlarge these samples of known sources. To this end, a convenient and increasingly popular approach consists of developing a citizen science experiment, as already done in the field of morphological classification of galaxies with the Galaxy Zoo experiment (Lintott et al., 2008), and as we started to do with CLAXSON (Section 8.2.3).

7.2 Reliability of new IMBH candidates

In this work, a great deal of effort was devoted to removing contaminants and assembling a sample of robust IMBH candidates. We summarise here the strategies employed to mitigate each type of contamination, and we highlight some of their caveats.

Background X-ray sources

Background sources are a serious concern when constituting a sample of HLX candidates, as they can represent 70% of the sample (Zolotukhin et al. 2016, Figure 5.6). To efficiently remove background sources among HLX candidates, we could not rely on our source classification, because it is biased towards the AGN class for sources of high luminosity and having an optical counterpart. Instead, we used large catalogues of photometric redshifts to remove bona fide background sources. As a result, *assuming that photometric redshifts and their errors are reliable*, and thus that removed sources are indeed background sources, only a small fraction of background contaminants remain in the HLX sample. This fraction should be at most 20% (30%) among robust (resp. robust and weak) candidates, from $\log N - \log S$ estimations (Section 5.4.5). These are sources for which no photometric redshift was available, or the photometric redshift was not accurate enough.

Among AGN candidates, because of their much fainter X-ray luminosities, background sources are not a major source of contamination. The majority of them should be removed by applying a selection criterion based on our classification ($P(XRB) > 2(sep - 0.7)$), where *sep* is the galactocentric distance. However, we cannot exclude that $\sim 10\%$ of the clean sample is affected by this contamination.

In situ AGN selected as HLX

By definition, ULXs are luminous sources located outside the nucleus of their host, in order to exclude the central AGN. Nearly all AGN should be excluded since we apply a stringent off-nuclear criterion, $d > 3(POSERR + 0.5)$, where d is the angular distance between the source and the galaxy center (as reported in GLADE) and $POSERR$ is the X-ray source position error. However, some AGN are still selected in the case of inaccurate GLADE positions, which sometimes happens because of astrometric errors in galaxy catalogues or the presence of a bright source across the galaxy (e.g. a star or another galaxy). Similarly, an active galaxy absent from GLADE but interacting with a GLADE galaxy is likely to be selected as an HLX candidate. This was indeed the case for 23 of our HLXs, which were flagged after manual inspection and treated separately in the analysis.

XRB/ULX selected as AGN candidate

In X-ray studies of dwarf galaxy activity, AGN are most often selected by assessing the extent to which the X-ray emission of dwarf galaxies exceeds the integrated luminosity of their expected XRB population. The latter is often estimated from scaling relations, calibrated in massive galaxies of the local Universe (e.g. Lehmer et al. 2016). However, if dwarf galaxies do not follow their trends, it is possible that a selected AGN is actually a stellar-mass XRB or ULX. And indeed, it is found that metallicity has an important effect on the XRB luminosity of a galaxy (Lehmer et al., 2021), which may be responsible for the excess of ULXs found in dwarf galaxies (Mapelli et al., 2010; Kaaret et al., 2011; Brorby et al., 2014; Kovlakas et al., 2020). More critically, we note that 32 of our 77 clean AGN candidates are also present in the sample of selected ULXs of Chapter 5. This includes some previously known AGN candidates. This shows the extreme difficulty to disentangle (stellar-mass) ULXs and wandering massive black holes. Deep resolved radio observations are needed to clearly separate these populations (Section 8.2.4). However, even the detection of a "radio bubble", that is a nebula caused by the outflows of certain ULXs (e.g. Berghea et al. 2020), may be also consistent with the feedback from an AGN (Section 7.9).

Confused X-ray sources

The comparison of *Swift*, *XMM-Newton* and *Chandra* samples of ULXs or AGN in dwarf galaxies revealed some important instrumental biases in this study.

Above all, spatial resolution effects affect the observables of some populations. The supposedly point-like sources in lower resolution (in particular *Swift*-XRT) observations were sometimes found to be extended in other surveys, or matching the position of a galaxy cluster. In nearby galaxies at $\sim$ 40 Mpc, due to tight groups of sources such as XRBs, we find that 5 to 10% of *Swift* and *XMM-Newton* sources are the result of the confusion of several (*Chandra*) sources (Figure 5.1). The confusion of tight groups of XRBs or ULXs is responsible for a flattening of their XLF (Section 5.4.3). Overall, however, this effect is unlikely to seriously affect our IMBH sample, because it does not change the integrated luminosity of XRBs used to select AGN candidates, and because the confusion of several ULXs is unlikely to produce HLX luminosities. For example, NGC 2276 ULX-1, seen as an HLX by *XMM-Newton* but as a ULX by *Chandra*, has three sources confused in the *XMM-Newton* detection. The difference in luminosity between the two observations is attributed to variability rather

than confusion (Wolter et al., 2015), so it remains a robust IMBH candidate (Mezcua et al., 2015).

7.3 The black hole - galaxy co-evolution

In massive galaxies ($M_* \gtrsim 10^{10} M_\odot$), SMBH masses are found to scale with the galaxy stellar mass, suggesting a simultaneous, symbiotic growth of galaxies and their central black hole (e.g., Ferrarese and Merritt 2000, Figure 2.9). Such a co-evolution is sometimes extrapolated to lower mass galaxies in order to approximate the mass of the central black hole, when nuclear activity is discovered. However, to this day, the low-mass end of the $M_{BH} - M_*$ relation remains highly unconstrained and is expected to depend on the seeding mechanism of SMBH.

In our work, interestingly, we find two populations of IMBH candidates from the same X-ray and galaxy surveys, with different loci in the $M_{BH} - M_*$ plane (Figure 7.1): AGN candidates are nearly consistent with an extrapolation of the $M_{BH} - M_*$ relation to lower masses, while HLX candidates appear to be overmassive. We explore here five possibilities explaining this difference:

1. HLXs are not IMBHs
2. Unreliable galaxy masses (e.g. the stellar mass of HLX hosts may be underestimated)
3. Unreliable black hole masses (e.g. the black hole mass of HLXs may be overestimated)
4. Selection bias (i.e. HLX appear to be overmassive because the bulk of their population, located at lower BH masses, is missed by our selection criteria)
5. Physical difference (i.e. intrinsic difference between the two populations)

The first possibility is already discussed at length in Sections 5.4.5 and 7.2. In summary, it is unlikely that most HLXs are in fact background sources, and some of their properties do not seem to match those of the lower luminosity ULXs, making IMBH a plausible (but not certain) explanation. However, even a low number of HLX contaminants in the overmassive locus would be sufficient to question the observed difference between AGN and HLX candidates.

7.3.1 Black hole masses

Our Eddington-based M_{BH} measurements $\left(M_{BH}\ (\mathrm{M}_\odot) \equiv \frac{L_{Edd}\ (\mathrm{erg\ s^{-1}})}{1.26\times10^{38}} = \frac{L_{bol}\ (\mathrm{erg\ s^{-1}})}{f_{Edd}\times1.26\times10^{38}}\right)$ are not very accurate since they are based on the *absorbed* X-ray luminosity in the hard band, extrapolating the $L_X - L_{bol}$ relation of Marconi et al. (2004) and assuming a fixed Eddington ratio $f_{Edd} = 0.24$ (HLXs) or $f_{Edd} = 0.004$ (AGN in dwarfs). The bolometric corrections we use (Marconi et al., 2004) are only valid with absorption-corrected luminosities and sources following a typical AGN spectrum. Thus, our mass estimate can significantly vary from an energy band to another, as shown in Figure 7.2: a bias towards a lower black hole mass is visible in the soft-band estimates (~ 0.5 dex lower than the hard-band estimates), possibly due to significant absorption. However, as we explained in Sections 5.4.5 and 6.4.4, these estimates provide physically motivated first approximations.

It could be that f_{Edd} is underestimated for HLXs, artificially placing them above the usual relation. ESO 249-43 HLX-1 reached $f_{Edd} \sim 1$ at the peak of its outbursts (Servillat et al., 2011). However, the apparent stability of X-ray emission in most of our HLXs (Section 5.3.5) disfavours this interpretation. Alternatively, M_{BH} measurements of AGN in dwarfs could be underestimated if they accrete at Eddington ratios lower than assumed.

To estimate the reliability of our Eddington ratio on a population basis, we can compare them to X-ray spectral studies of XRBs and AGN. Multi-epoch population studies of a sample of Galactic XRBs powered by a stellar-mass black hole showed a correlation between the best-fit photon index of their spectrum and their Eddington ratio, and the same was found in a sample of AGN (e.g. Yang et al. 2015). Interpolating this relation to the IMBH mass range, we could expect that most objects having $\Gamma \geq 2.1$ accrete at $L_X/L_{Edd} > 0.001$ (i.e. $f_{Edd} \gtrsim 0.01$), while objects having $\Gamma \leq 1.7$ generally have $L_X/L_{Edd} < 0.01$ ($f_{Edd} \lesssim 0.1$). In Figure 7.3, we show the $SC_HR3 - SC_HR4$ plane for HLX and AGN candidates in the *XMM-Newton* catalogue: for an absorbed powerlaw spectrum, the corresponding energy bands (1–2, 2–4.5 and 4.5–12 keV) are much affected by the photon index Γ and less by the absorption column. We overlay the expected $SC_HR3 - SC_HR4$ locus for $\Gamma = 1.7$

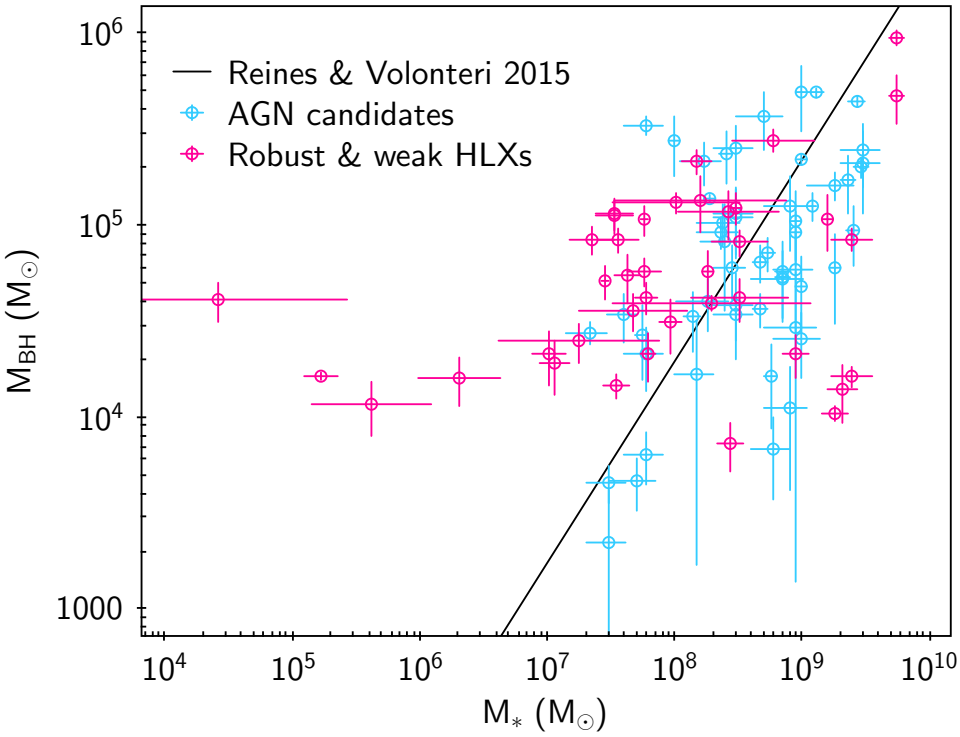

Figure 7.1: Black hole mass – stellar mass plane for the two types of IMBH candidates identified in this thesis work. HLX (resp. AGN) black hole masses are computed assuming $f_{Edd} = 0.24$ (resp. $f_{Edd} = 0.004$).

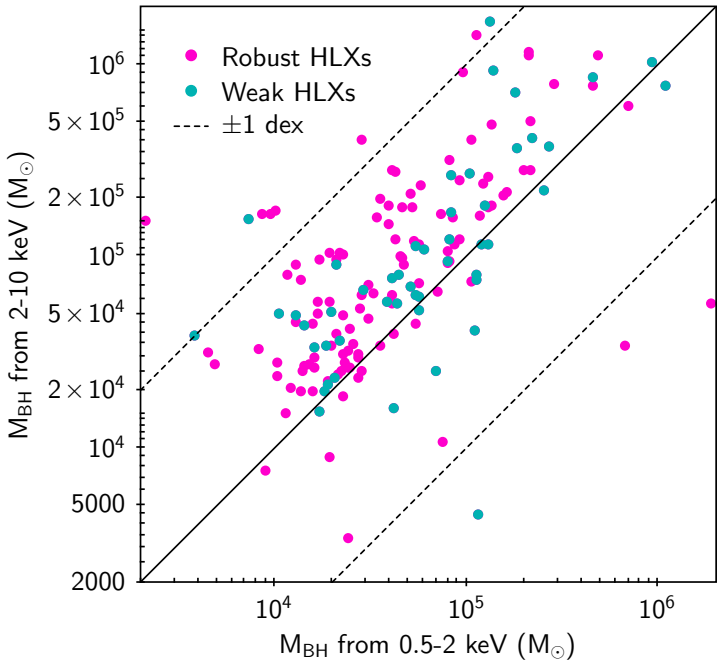

Figure 7.2: Black hole masses of HLX candidates as computed using the $0.5-2$ keV band (x-axis, bolometric correction $L_X/L_{bol} \sim 13$) and the $2-10$ keV band (y-axis, bolometric correction $L_X/L_{bol} = 10$). Weak HLX candidates (which have more chance to be active dwarf satellites but also background contaminants) present a better agreement between their soft-band and hard-band estimates, while hard-band estimates are systematically biased towards higher masses for robust candidates.

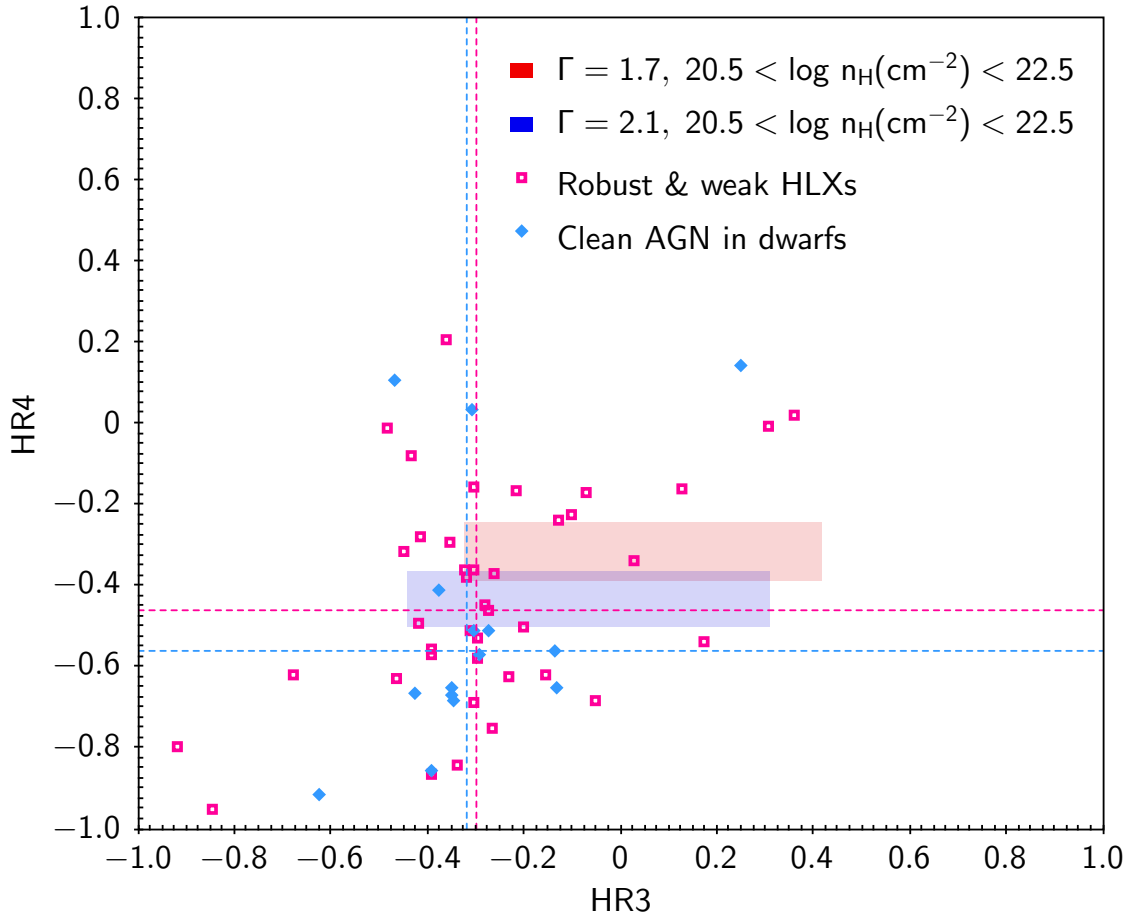

Figure 7.3: Hardness-hardness diagram of our two types of IMBH candidates, for sources above the 5σ sensitivity. The shaded areas show permitted values of pn hardness ratios for an absorbed powerlaw spectrum with $\Gamma = 1.7$ (red) or $\Gamma = 2.1$ (blue), and an absorption column in the range $3 \times 10^{20} < n_H < 3 \times 10^{22}$ cm^{-2}. The median values of HLX and AGN candidates are highlighted with magenta (resp. blue) dashed lines. AGN candidates have a lower median $HR4$ and are thus tentatively softer.

(red) and $\Gamma = 2.1$ (blue) with an absorption in the range $3 \times 10^{20} < n_H/\mathrm{cm}^{-2} < 3 \times 10^{22}$. Despite the large scatter, AGN candidates seem to be softer than HLX candidates, which are closer to the $\Gamma = 1.7$ locus.

To further investigate, we use the catalogue of spectral parameters resulting from automated fits to the 4XMM-DR11 spectra, as provided by the XMM2ATHENA consortium[1]. This presents the advantage of considering physical quantities taking absorption into account. We select 7 AGN and 11 HLXs for having less than 15% relative error on their fitted Γ, and being flagged as "clean" ($SC_SUM_FLAG = 0$) in 4XMM-DR11. The histogram of their Γ is shown in Figure 7.4. Surprisingly, it suggests that at least some HLXs have $\Gamma \lesssim 1.7$ and some AGN have $\Gamma \gtrsim 2.1$. Taken at face value, this would imply an Eddington ratio below 10% and above 1% according to the correlation found in Yang et al. (2015), respectively, hence widening the discrepancy between their loci by a factor 4. It is worth mentioning that for AGN candidates, such high values of Γ and Eddington ratio have already been reported by Baldassare et al. (2017) in their X-ray study of optically-selected active dwarf galaxies, and (for Γ) by Svoboda et al. (2019) in their X-ray study of some candidate active Green Pea galaxies. However, further work is needed to accurately model the spectra of these candidates and study their differences in nature and accretion state.

[1] http://xmm-ssc.irap.omp.eu/xmm2athena/catalogues/

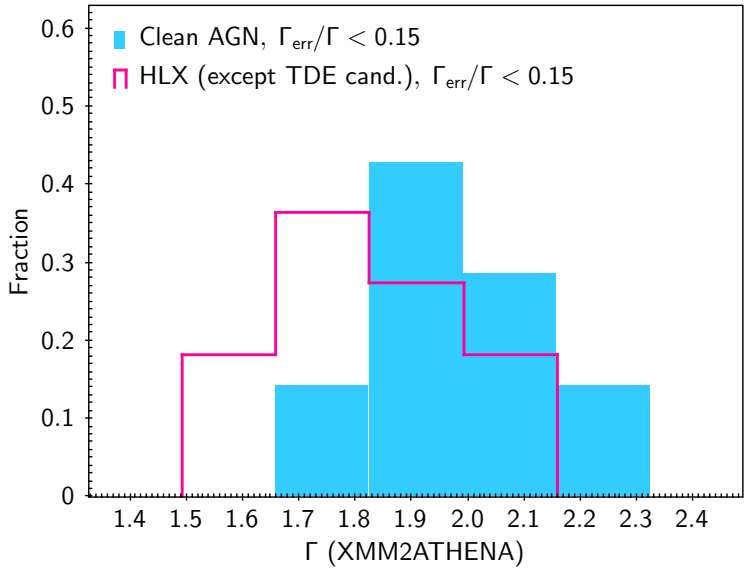

Figure 7.4: Histogram of the powerlaw photon index Γ of the best-fit absorbed powerlaw for each type of IMBH candidate, taken from XMM2ATHENA deliverables. The softest HLXs (having $HR67 < -0.6$, Figure 5.18), which possibly have a different nature, are not shown. Only sources having $SC_SUM_FLAG = 0$ and less than 15% relative error on the fitted Γ are considered.

7.3.2 Stellar masses

Previous studies have shown the importance of systematic uncertainty in stellar mass due to the lack of an unambiguous definition (e.g. Reines and Volonteri 2015). In addition to this, and to the stellar mass biases and uncertainties identified in GLADE (Section 6.4.1), our own stellar mass measurements for HLX optical counterparts are likely to be underestimated, due to their derivation from point-like fluxes. Stellar masses are indeed derived from Bell et al. (2003), allowing to estimate the stellar mass-to-light ratio from optical colours: $M_* = (M/L)_{(g-r),\text{ Bell et al. (2003)}} \times L_r$ where L_r is the r-band luminosity of the galaxy. Proper L_r estimates should be done by fitting Sersic components to the optical image (e.g. Barrows et al. 2019), but this is outside the scope of this study. We instead rely on the (*PanSTARRS* or *DES*) aperture photometry of the sources, supposing a point-like morphology. Arguably, these L_r estimates are rather accurate, given the compactness of HLX hosts.

To test this bias, we estimate stellar masses for NSA compact galaxies with our method, and compare them with the Sersic mass. To probe galaxies similar to the HLX counterparts, we require their light radius (containing 90% of the galaxy light) to be smaller than 3 arcsec. The result is shown in Figure 7.5: stellar masses are indeed biased, with 90% of them biased by a factor 1.5–15 (median 5.5). The deviation at low stellar masses ($M_{*,Bell} < 10^6 M_\odot$) is even higher. Therefore, this deviation is a plausible reason to explain why HLXs appear as overly massive outliers in the $M_{BH} - M_*$ relation. However, it should be noted that the overmassive locus of HLXs relies on two costly assumptions: (1) a negligible contribution of the putative accretor to the optical flux, which is therefore entirely attributed to the stellar mass, perhaps leading to the overestimation of the latter. On the contrary, if the X-ray source is an accreting galaxy nucleus, it is likely that its point-like optical counterpart is attributable to its thermal emission (Section 5.4.5, Barrows et al. 2019). And (2) a high Eddington ratio (24%) to calculate their mass. If this ratio is lower, $\lesssim$10% as Section 7.3.1 perhaps suggests, then this stellar mass bias becomes barely sufficient to explain the HLX locus.

7.3.3 Selection bias

Overly massive BH are commonplace in another field, namely the search for high-redshift quasars (e.g. Inayoshi et al. 2020; Bosman et al. 2022), however there is increasing evidence showing that this is a selection (or detection) bias (Matsuoka et al., 2022). It could be the case as well for our HLX sample, because fainter sources are included in the ULX population which is discarded. To assess the fraction of missed HLXs, we could inspect luminous ULXs having an optical counterpart and investigate if

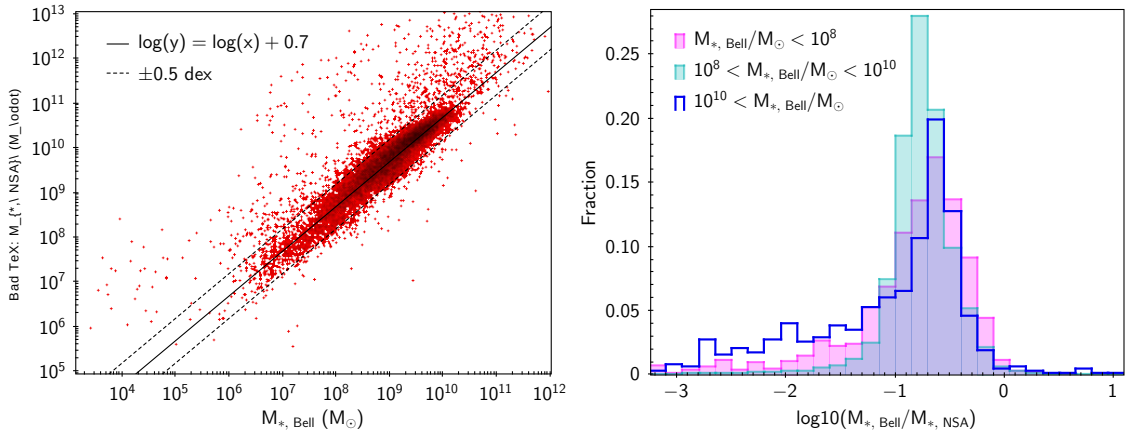

Figure 7.5: (Left) Comparison of stellar masses estimated from NSA and from Bell et al. (2003) using $g-r$ colour, for NSA galaxies having a 90%-light radius below 3 arcsec. (Right) histogram of the deviation between these quantities (in dex).

they are consistent with the same population (e.g., is the optical counterpart more consistent with a dwarf galaxy or a starforming region?). However, a proper characterisation of HLX counterparts is needed beforehand, to confirm their dwarf galaxy nature.

7.3.4 Physical origin

If all these reasons are insufficient to explain the discrepancy, then there may be an intrinsic difference between HLXs and AGN in dwarfs, with the former being overmassive.

For instance, if overly massive HLX black holes are indeed hosted by a dwarf galaxy, their optical counterpart could be the stripped core of this galaxy after a merger with the primary host. This is indeed what is expected in galaxy formation, where merging low-mass nucleated galaxies are stripped by tidal forces (e.g. Norris et al. 2014), and accretion events are triggered on the central black hole only afterwards (Seth et al., 2014; Barber et al., 2016). In this regard, HLX candidates would be analogous to (low-luminosity) AGN that are thought to be notably triggered during minor mergers (e.g. Villforth et al. 2017).

The same could happen if these BHs are not formed by the same process as AGN in dwarf galaxies. For example, HLXs could be powered by direct collapse black holes (DCBH), whereas nuclear activity in dwarf galaxies could be the signature of black holes formed after the collapse of the nuclear star cluster (Natarajan, 2021), or as remnants of Pop III stars. These considerations are discussed in Section 7.8. Efficient growth of these overmassive candidates through accretion, rather than through galaxy mergers, is also an option.

7.4 Wandering black holes

As found by Reines et al. (2020) in their radio sample, we find a significant fraction of off-nuclear AGN candidates. These are consistent with wandering black holes, claimed to be common in dwarf galaxies.

However, it is important to know that such large offsets are difficult to attribute to the shallow gravitational potential of dwarf galaxies, in particular in presence of a nuclear star cluster stabilising the BH towards the center. Studying dynamics in a large (Milky-Way like) nuclear stellar cluster and a nuclear stellar disc, Inoue (2021) argue that this potential could allow at most offsets of several 10 pc. Likewise, a scenario was proposed to rapidly form IMBH in dense gas-rich nuclear star cluster even in the present-day Universe, assuming wind-fed accretion and zero angular momentum (Natarajan, 2021). Their model could explain the presence of massive IMBH seen in local dwarf galaxies having a nuclear star cluster (NSC); in this case, the BH can be wandering in the NSC, which is however negligible ($\lesssim$ 1 pc), compared to the typical separations seen in our work and the radio-selected sample of Reines et al. (2020) ($\gtrsim$ 1 kpc). This scenario is thus unable to account for the location of most

of our candidates, except if the black hole is subsequently ejected from the cluster. Rather, dwarf galaxies undergoing many mergers may be responsible for this finding, given the long timescale needed for massive black hole to migrate to the center of the new galaxy (e.g. Ma et al. 2021 and references therein), and accordingly with the simulations of Bellovary et al. (2019).

7.5 Occupation fraction

The occupation fraction of dwarf galaxies can only be robustly constrained in the local Universe, by studying the motion of stars in the bulges of these galaxies. These dynamical studies resulted in claims of the presence of a massive black hole, or an upper limit on their mass (Greene et al., 2020).

In contrast, X-ray studies can only directly constrain the *active* fraction of dwarf galaxies, whose massive black hole is experiencing accretion. Occupation and active fractions are however not independent parameters ($f_{AGN} < f_{occ}$), and indirect constraints can be inferred from the active fraction of a large sample of galaxies. In particular, Miller et al. (2015) modeled the *downsizing* in dwarf galaxies, i.e. the weakening of the AGN emission with decreasing stellar mass, by a powerlaw with scatter ($L_X = \mathcal{N}(\alpha M_* + \beta, \sigma^2)$ where $\mathcal{N}$ is the normal distribution, M_* the stellar mass and α and β the parameters of this scaling relation, Miller et al. 2015). Assuming constant bolometric corrections, we have $L_X \propto f_{Edd} \times M_{BH}$, and thus this weakening is due to a lower black hole mass and/or a lower Eddington ratio. Miller et al. (2015) are then able to constrain the occupation fraction profile of their sample (Figure 6.15), and to obtain a lower limit of 20% on the occupation fraction of their whole sample of low-mass ($M_* < 10^{10} M_\odot$) galaxies.

In our work, we study the active fraction at different limiting luminosity thresholds and for different mass bins (Figure 6.14). Surprisingly, we find a rather constant active fraction profile $f_{AGN}(> L_X)$ over a wide range of stellar mass $10^{8.2} < M_* < 10^{9.5}$. This is at odds with the expected downsizing in these galaxies, according to which this profile should decrease by about a factor of 10 between the most massive and least massive galaxies in this subsample, if the powerlaw model of Miller et al. (2015) ($\alpha = 0.8$) is valid. However, their sample of galaxies extends to stellar masses of the order of $10^{12} M_\odot$, and most of their dwarf galaxies are undetected in X-rays. Therefore, it is very likely that the downsizing trend they fit is largely dominated by non-dwarf galaxies. Conversely, our results suggest that the downsizing flattens in the dwarf galaxy regime. This can be explained by a constant distribution of the black hole mass and the Eddington ratio, or by an anti-correlated dependence of the two quantities. AGN in dwarf galaxies may indeed have higher Eddington ratios than found in more massive galaxies (Section 7.7, and also suggested by the high Γ values shown in Figure 7.4).

Below a characteristic stellar mass $\sim 2 \times 10^8 M_\odot$, we find tentative evidence that the active fraction profile $f_{AGN}(> L_X)$ drops to lower values. Provided that the functional form of Miller et al. (2015) for the occupation fraction profile is representative of the true profile, which is motivated by the profile shapes found in modeling studies (e.g. Volonteri 2010; Bellovary et al. 2019), we are thus able to tentatively constrain the occupation fraction of dwarf galaxies in the range $10^8 - 3 \times 10^9 M_\odot$. These constraints compare well with the constraints of Miller et al. (2015) (Figure 6.15). For $\sim 10^8 M_\odot$ galaxies, they exclude total occupation, which is not the case in our study. This is most probably due to differences between our samples, since this mass bin in our sample contains many starforming late-type galaxies (notably blue compact dwarfs), which are excluded from their sample. However, we cannot exclude the possibility that a significant fraction of our AGN candidates are contaminated by ULXs, in particular wandering candidates in starforming galaxies (Section 7.2).

Figure 7.6 shows our tentative constraints superimposed on Figure 5 of Greene et al. (2020), assembling other observational and simulated constraints. Our constraints are mostly consistent with other studies, with the exception of the dynamical constraint obtained by Nguyen et al. (2019). However, their dynamical study can only constrain the presence of a $\gtrsim 10^5 M_\odot$ black hole, while our method seems to probe lower masses (Figure 7.7). Comparisons to formation models are detailed in Section 7.8.

7.6 Local rate of accreting IMBH

Although we find a larger total sample of HLX candidates than AGN candidates, the two surveys probe completely different volumes due to their different luminosity range and galaxy sample.

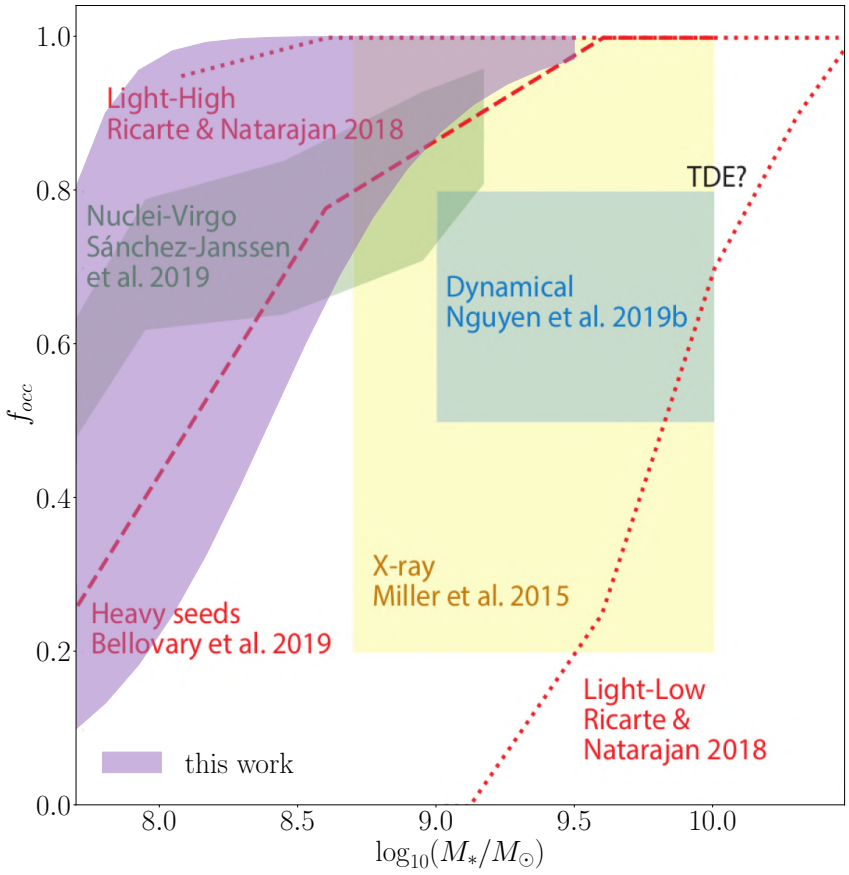

Figure 7.6: Tentative constraints obtained in this work on the occupation fraction, overlaid on Figure 5 of Greene et al. (2020), which shows various observational constraints (Miller et al., 2015; Sánchez-Janssen et al., 2019; Nguyen et al., 2019) and predictions from different models of black hole seeds (Ricarte and Natarajan, 2018; Bellovary et al., 2019).

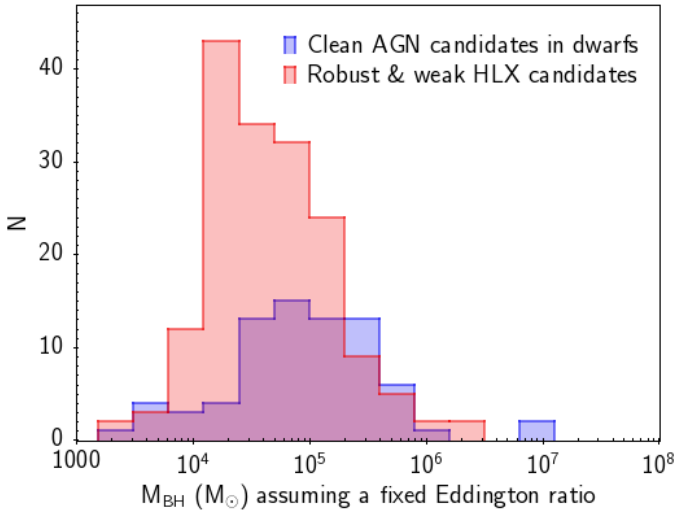

Figure 7.7: Histogram of black hole masses obtained by assuming a fixed Eddington ratio: $f_{Edd} = 0.24$ for HLX candidates and $f_{Edd} = 0.004$ for AGN candidates in dwarf galaxies.

As a first order estimate, the local rate of accreting IMBH can be inferred in each case by multiplying the corresponding XLF value to the local density of galaxies and dwarf galaxies. For robust and weak HLXs, this value is $N(L_X > 10^{41}) \approx 0.003$ HLX per galaxy, and for clean AGN candidates having stellar mass in the range $2 \times 10^8 - 3 \times 10^9 M_\odot$, it is $f_{AGN}(L_X > 10^{39}) \approx 0.05$ per galaxy.

For the local density of galaxies, we refer to the optical census made by Giodini et al. (2012) in the COSMOS field in different stellar mass bins. They also distinguish field and group galaxies, which is relevant for HLXs because a fraction of them (to be constrained in future studies) corresponds to galaxy mergers in groups. Values are taken in the redshift bin $0.2 < z < 0.4$. The GLADE primary hosts of HLXs (in which they seem to be wandering) are all massive GLADE hosts ($\gtrsim 10^{10} M_\odot$). We thus use density values $\phi(M) \sim 0.005$ Mpc^{-3} (field galaxies) and $\phi(M) \sim 8$ Mpc^{-3} (galaxies in groups), estimated from Figure 3 of Giodini et al. (2012). Likewise, for dwarf galaxies, we use the value $\phi(M) \sim 0.02$ Mpc^{-3} for field galaxies in the range $10^8 - 10^9 M_\odot$, because f_{AGN} is poorly constrained in galaxies of lower mass. The resulting rates of accreting IMBH are shown in Table 7.1. Interestingly, the rate of HLX in field galaxies is well in the IMBH density range estimated by Lin et al. (2018), $10^{-5} - 10^{-3}$ Mpc^{-3}.

7.7 Accretion onto intermediate-mass black holes

AGN in low-mass galaxies were found to have surprisingly weak X-ray hard fluxes compared to their UV flux (e.g. Dong et al. 2012; Plotkin et al. 2016). This X-ray weakness is subject to differing interpretations, such as heavy obscuration, intrinsic X-ray weakness (sometimes attributed to high Eddington ratios) or low black hole mass (Mezcua, 2017). While early studies found that only a minority of X-ray weak AGN were highly obscured (Mezcua, 2017), other studies show no dependence of the X-ray weakness on Eddington ratio, hence suggesting a non-standard accretion regime (Vito et al., 2018).

Baldassare et al. (2017), for their optically-selected AGN in dwarf galaxies that had enough counts in *Chandra* observations to constrain the photon index of an absorbed powerlaw fit, obtained values in the range $\Gamma = 2 - 2.5$, consistent with the values obtained for some of our AGN candidates (Section 7.3.1). Although these sources are brighter than the bulk of our sample ($L_X > 10^{41}$ erg s^{-1}), this may suggest a similarity in accretion state and/or Eddington ratio. If this is the case, using accordingly the Eddington ratio $\sim 10\%$ that they find for these particular AGN, it is worth noting that our AGN candidates mostly fall in the mass range $10^3 - 10^4 M_\odot$, and are thus probing much lower masses than previously accessed. However, we recall that these Eddington-based mass estimates remain highly uncertain, and that previous X-ray studies of AGN in dwarf galaxies generally refrain from making claims on the Eddington ratio based on X-ray spectra, despite their samples of sometimes similar luminosity.

Type	Density (Mpc^{-3})
HLX in field galaxies	1.5×10^{-5}
HLX in groups	2.4×10^{-2}
AGN in dwarf galaxies	1×10^{-3}

Table 7.1: Number of accreting IMBH per Mpc^3 inferred in this study, for different types of IMBH candidates.

A counter-example is Birchall et al. 2020 who estimate it as $25 L_{2\text{–}10\ \mathrm{keV}}/(1.26 \times 10^{38} \times 0.0002 M_*)$ (taken from Aird et al. 2012), which therefore supposes that the $M_{BH} - M_*$ relation can be extrapolated to the dwarf galaxy regime. We note, however, that the values of their Eddington ratio, approximately between 0.0005 and 0.01 (see their Figure 8), correspond well to our initial assumption of $f_{Edd} = 0.004$.

Perhaps more importantly, the lack of X-ray-detected dwarf galaxies was often interpreted as either a low occupation fraction, or black holes beyond current detection thresholds (Bellovary et al., 2019). In agreement with this picture, it was found from models of accretion onto IMBH that their Eddington ratio distribution should be bimodal, with a minority accreting at or above Eddington rates and the rest well below (Pacucci et al., 2018; Pezzulli et al., 2017). This bimodal distribution is motivated by the expected bimodality of the black hole mass function at high redshift, with the less massive Pop III remnants being unable to grow efficiently, whereas DCBH could reach super-critical rates (Pacucci et al., 2017). Pacucci et al. (2018) find that such a bimodal population account for the few already detected overly massive AGN in dwarf galaxies, while the bulk of them would follow a steeper (undermassive) asymptote in the $M_{BH} - M_*$ relation. Our tentatively overmassive HLXs could be related to this trend, and thus may probe a different population of BH seeds than the AGN candidates (Section 7.8). Maybe reinforcing this interpretation, AGN candidates in dwarf galaxies $\gtrsim 5 \times 10^8 M_\odot$ possibly follow a steeper slope than the classical $M_{BH} - M_*$ (Figure 7.1). This trend holds if assuming a fixed Eddington ratio (distribution) over this range of stellar masses, and would be even more pronounced if the Eddington ratio increases with decreasing stellar mass. Future facilities able to detect a large population of $< 10^4 M_\odot$ IMBH will be key to confirm or refute these trends.

In any case, the detection of a large number of (likely) highly-accreting black holes (in particular among HLXs) suggest that accretion play an important role in their growth, which is expected for high-redshift seeds (Woods et al., 2019) but not in low-redshift dwarf galaxies (Bellovary et al., 2019). And indeed, there is mounting evidence that at least a fraction of AGN in dwarf galaxies have grown significantly since their formation as seeds (see next Section). Conversely, Bellovary et al. (2019), in their simulation of the evolution and accretion luminosity of a population of (wandering) black holes in dwarf galaxies, find bolometric luminosities in the range $10^{35} - 10^{40}$ erg s^{-1} in the present-day Universe. Most of these objects have grown less than 5% of their mass through accretion. Interestingly, their luminosity range significantly overlaps the luminosities detected in our sample of AGN, reinforcing their interpretation as weakly-accreting massive black holes.

7.8 Comparison to formation models

In order to compare our results to different IMBH formation models, we recall here a few relevant observables for each of these models, previously introduced in Section 2.5.1.

Direct collapse black holes

DCBH are the so-called heavy seeds supposed to form early most massive quasars, and have masses in the range $10^4 - 10^6 M_\odot$ at birth. A large supply of gas is needed to grow such black holes, so that this model produces low occupation fraction for very low-mass dwarf galaxies. More massive dwarf galaxies could be populated by these seeds, but they would appear as overmassive outliers in the $M_{BH} - M_*$ plane (e.g. Pacucci et al. 2018; Spinoso et al. 2022). The recent zoom-in simulation of Bellovary et al. (2019) however places the characteristic mass below which galaxies are devoid of DCBH around $M_* \sim 10^8 M_\odot$ (Figure 7.6), and suggest present-day accretion luminosities below 10^{40} erg s^{-1}. In contrast, Pacucci et al. (2017) predicted them to undergo short periods of highly efficient accretion, even beyond the Eddington limit, until their gas supply is exhausted. While we still lack definitive observational evidence for these seeds (with the possible exception of the high-redshift

galaxy CR7, Agarwal et al. 2016; Woods et al. 2019), the detection of overmassive black holes has been argued to validate the existence of this scenario. Most recently, the simulations of Latif et al. (2022) have suggested than the formation of DCBH may be easier than expected, occurring especially at the intersection of cold, dense filamentary flows that subsequently form galaxy groups.

Population III remnants

Population III remnants are the so-called light seeds ($10^2 - 10^3 M_\odot$) also believed to contribute to the formation of SMBH (Madau and Rees, 2001). Unlike DCBH, they should be present in nearly all detectable dwarf galaxies, and they may appear as undermassive in the $M_{BH} - M_*$ plane (Volonteri et al., 2008; Pacucci et al., 2018), or else have had enough time to grow overmassive in the present-day Universe (Spinoso et al., 2022). According to the models of Pacucci et al. (2017, 2018), most of these seeds would accrete continuously and at low rates, so that their accretion luminosity is $L_X \lesssim 10^{40}$ erg s^{-1}.

Collapse of nuclear star cluster

The collapse of nuclear star clusters at high redshift is also proposed as a promising avenue to form SMBH seeds at high redshift. However, the presence of such seeds at low redshift is challenged by the recoil speeds that these black holes should experience, preventing their growth beyond $\sim 10^3 M_\odot$. Recently, Natarajan (2021) proposed that even present-day nuclear star clusters could collapse to form black holes in the range $10^2 - 10^5 M_\odot$, possibly explaining the population of active dwarf galaxies that is observed. This scenario could thus produce high occupation fraction of all galaxies hosting a nuclear star cluster, meaning nearly all galaxies above $10^8 M_\odot$ (Greene et al., 2020).

Comparison to our results

Before analysing these scenarios in the light of our results, we emphasize that the role of galaxy mergers in the growth of black holes is not taken into account and remains highly unconstrained. Future observations of massive black hole binary mergers, notably in the gravitational wave domain, will be key to know their importance (Section 8.2.4). Similarly, effects of AGN feedback and important growth over cosmic time are neglected, but this is discussed in Section 7.9. Therefore, the following reasoning is speculative and does not provide strong constraints on the true IMBH formation channels.

In summary, we find two populations of IMBH candidates that present different properties (due to selection biases or intrinsic differences).

HLX candidates have high luminosities, a fraction of them have an optical counterpart consistent with a dwarf galaxy undergoing a merger with their primary host, and some of them appear overmassive in the $M_{BH} - M_*$ plane. These dwarf galaxy candidates have stellar masses $\gtrsim 10^4 M_\odot$, but most probably $\gtrsim 10^{7.5} M_\odot$ given the systematic underestimations reported in Section 7.3.2. ESO 243-49 and NGC 2276, hosting two well-studied HLXs, belong to galaxy groups rather than field galaxies, and it may also be the case of most of the HLX hosts. Assuming relatively efficient accretion $f_{Edd} = 0.24$ (Barrows et al., 2019), these HLXs should be powered by black holes mostly in the mass range $10^4 - 10^5 M_\odot$. These characteristics are difficult to explain if they were formed from Population III remnants, unless they dramatically evolved since their formation, as suggested by some simulations (e.g. Spinoso et al. 2022). The large mass and efficient accretion of HLXs is more consistent with heavier seeds such as DCBHs or collapsed NSCs. The former scenario is plausible for hosts belonging to galaxy groups, which seems to be the favoured environments for DCBHs according to recent cosmological simulations (Latif et al., 2022). It also naturally explains their locus in the $M_{BH} - M_*$ plane. The NSC channel is also possible, because the final BH mass mostly depends on the mass of the gas in the NSC (rather than stellar mass), and because efficient accretion would be triggered or detectable in late stages of the galaxy merger, after the stripping of the dwarf galaxy nucleus.

AGN candidates have faint luminosities $\lesssim 10^{40}$ erg s^{-1}, part of them are found wandering in their galaxy, they seem to follow the $M_{BH} - M_*$ trend when using a fixed Eddington ratio to compute their mass, except for some undermassive candidates. Analysis of the active fraction profile suggest a nearly full occupation fraction for stellar masses higher than a few $10^8 M_\odot$, and a drop in lower-mass galaxies. The offsets of wandering AGN may be the result of previous galaxy mergers, however we cannot exclude a high ULX contamination rate among them. Preliminary spectral fits may suggest Eddington ratios higher than first assumed (but still well below Eddington), in agreement with previous findings (Baldassare et al., 2017). This would draw their mass down to $10^3 - 10^4 M_\odot$ and make

them undermassive in the $M_{BH} - M_*$ plane. However, lower Eddington ratios and thus higher masses are similarly plausible for most AGN candidates. Because of these poor constraints on f_{Edd} and M_{BH}, no formation channel is preferred. Tentative constraints on the occupation fraction profile are also consistent with all three scenarios. However, in the semi-analytic framework of Pacucci et al. (2017, 2018), these objects are much more consistent with Pop III remnants (lower luminosity, higher density, undermassive locus) than DCBHs.

Future improvements in cosmological simulations of each formation channel, and the corresponding rates of local IMBHs, are highly desirable to pursue this comparison. For instance, DeGraf and Sijacki (2020) modify the Illustris simulation to include a physically-motivated model of DCBH, and find that essentially all DCBH in the present-day Universe have grown to masses $> 10^{6.5} M_\odot$. Local dwarf galaxies would then be the leftover of high-redshift galaxies *devoid of DCBHs*. This is in contrast to classical zoom-in cosmological simulations that typically seed their galaxies with a $> 10^5 M_\odot$ black hole as soon as they exceed a dark matter halo mass threshold (Habouzit et al., 2017). In doing so, the IMBH populations are completely ignored. Our results highlight the need for more representative cosmological simulations of BH populations, especially in the IMBH range.

7.9 Black hole growth in dwarf galaxies

An important caveat of evaluating constraints on IMBH formation channels from our sample of IMBH candidates is that it implicitly assumes that local dwarf galaxies are representative of their higher redshift analogues, and that their black hole has had negligible growth throughout cosmic time (e.g. Dubois et al. 2015; Habouzit et al. 2017). In contrast, mounting evidence suggests that significant black hole growth and AGN feedback happened in some dwarf galaxies.

For instance, the dwarf galaxy J1220+3020 is a radio-selected AGN candidate in Reines et al. (2020). In the optical, Molina et al. (2021) report an iron coronal line showing signs of shocks and outflows, and argue that the radio emission is mainly due to a powerful jet. This surprising feature was later found to be frequent in a large sample of radio-selected AGN having radio jets as powerful as in massive galaxies (Mezcua et al., 2019; Davis et al., 2022), making AGN feedback plausible. Most recently, Schutte and Reines (2022) have found that a filament connects the central black hole of Henize 2-10 to a star-forming region, and is consistent with an AGN outflow, suggesting that AGN exert a positive feedback on star formation. The dominance of supernova feedback, previously taken for granted in dwarf galaxies and responsible for the hypothesis of inefficient black hole growth, is thus increasingly questioned.

However, it is worth mentioning that all these studies are intrinsically biased towards radio-loud dwarf galaxies, having radio fluxes $\gtrsim 20 \mu$Jy. From the radio-derived bolometric luminosity, a large fraction of these galaxies is predicted to host overly massive black holes in the range $4 \times 10^5 - 10^8 M_\odot$ or IMBHs accreting at super-Eddington rates (Mezcua et al., 2019). Thus, the possibility that most IMBHs in our sample may have experienced significant growth since their formation as seeds is far from settled, and even questioned by revised simulations of feedback in dwarf galaxies (Figure 3 of Koudmani et al. 2021). Another argument casting doubt on whether local AGN in dwarf galaxies are relics of high-redshift seeds is that local dwarf galaxies have undergone several mergers since then, possibly resulting in significant black hole growth (Mezcua, 2019). The overly massive BHs we found as HLXs in merging (or satellite) dwarf galaxies may be interpreted as black holes whose growth is primarily due to secular processes (such as long-term accretion), but this remains very tentative (Section 7.3). Further work is therefore needed to assess the role of feedback and mergers in the evolution of present-day AGN in dwarf galaxies, notably by achieving a more complete view of merger signatures (Nevin et al., 2019) and directly detect massive black hole mergers (Section 8.2.4).

Chapter 8

Conclusion and outlook

This chapter highlights some of the main results that I have obtained in my study of the population of intermediate mass black holes, both in terms of method and observational results. It is also the occasion to step back and to propose some future work. We consider how future observations with new observatories will be able to help address key open questions about the formation, evolution, and number of intermediate-mass black holes, whether they are sensitive to gravitational waves or to a wide range of electromagnetic signals that will reveal this population.

8.1 Conclusion

The main subject of this thesis is the search and study of intermediate-mass black holes. The aim of this work was to collect and study a large sample of intermediate-mass black hole candidates from the largest available X-ray and multi-wavelength archives, which requires efficient removal of contaminants.

To this end, we developed a probabilistic classification of X-ray sources, adaptable to a large range of samples and applications. It crossmatches a large fraction of existing X-ray catalogues with catalogues of optical and infrared sources, robustly identifying the counterparts of X-ray sources. With this information, together with X-ray spectral and timing properties and the association with *Gaia* stars or *GLADE* galaxies to estimate the source luminosity, a revisited Naive Bayes Classifier assigns to each source the probabilities of each class in an easily interpretable framework. This is the first time that a probabilistic classification scheme has been applied to such a large value-added set of X-ray sources across the sky.

We applied this method to several science cases covering a wide range of source classes: an all-sky classification (the classes are then AGN, Star, X-ray binaries and Cataclysmic variables), a classification of X-ray populations in nearby galaxies (AGN, X-ray binaries and softer sources), and also a classification for the search for high-redshift quasars (Seyfert I, Seyfert II, normal stars, YSO and high-redshift quasars) in an ongoing work (see Section 8.2.2). We have reliably identified stars and AGN in general, effectively removing contaminants among ultraluminous X-ray sources and selecting candidates for massive black holes in dwarf galaxies for further study. Since it was not possible to build up a training sample of intermediate-mass black holes, their manifestation as hyperluminous

X-ray sources and tidal disruption events could be recovered a posteriori, in particular through the use of an outlier-isolating measure.

The study of ultraluminous X-ray sources is particularly interesting for understanding how a source can sustain super-Eddington accretion and help uncover how some of the first supermassive black holes grew. Population studies of ultraluminous X-ray sources are however hindered by 15-20% of contaminants and even more among the most luminous sources and in the distant periphery of galaxies. This is therefore particularly problematic in the search for hyperluminous X-ray sources, while some of them are among the best candidates for intermediate-mass black holes known to date. In this regard, our method can be of great help to correctly identify the best candidates for follow-up studies, and to start completing a statistical view of these objects.

Indeed, we have identified 1901 ULXs and 191 HLXs among the *Swift*-XRT, *XMM-Newton* and *Chandra* catalogues, thus gathering the largest and cleanest homogeneously selected samples of these objects, to our knowledge. We were able to confirm some results already found in previous studies, such that the fact that ULXs and XRBs share the same locus in a hardness-hardness diagram. We find no sign of a difference in the variability of this population compared to XRBs, unlike for example (Bernadich et al., 2021). We do find a decrease of the ULX specific rate (i.e. per unit of stellar mass) with galaxy mass, however with a large excess of ULXs in dwarf galaxies, in agreement with recent studies. Another (rarely) studied environmental property of ULXs is their spatial distribution in their host. We find that as expected, ULXs in spiral and elliptical galaxies globally follow the respective light profile of these galaxies, with a small excess in the outskirts of the latter. In these galaxies, we were able to show the drop in ULX density beyond D_{25}, which was not possible in previous studies due to the high rate of contaminants in this region.

We also focused on the ULX X-ray luminosity function, implementing a volume-corrected calculation often used in other areas of astrophysics, but never in ULX studies, that instead adopt a volume-limited approach (requiring all sources of their sample to be observed down to limiting luminosities $\leq 10^{39}$ erg s^{-1}). After highlighting some instrumental biases due to different instrument capabilities (in particular confusion issues and other effects of angular resolution), we found clear evidence of a luminosity break in the XLF of ULXs in spiral galaxies. This feature was tentatively found in earlier studies but recently claimed to be insignificant: we interpret the high significance of our break as due to efficient removal of contaminants and better statistics. The physical origin of this break is still unclear, but it may be related to the broken XLF of HMXBs seen in low-metallicity galaxies (Lehmer et al., 2021). At higher luminosities, no cutoff is seen in the XLF which then probes the population of hyperluminous X-ray sources, though with insufficient statistics to be significantly constrained.

Hyperluminous X-ray sources ($L_X > 10^{41}$ erg s^{-1}) have such high luminosities that it is difficult for them to be powered by stellar-mass compact objects, and indeed a few of these rare sources constitute some of the best IMBH candidates. In particular, ESO 243-49 HLX-1 and 4XMM J215022.4-055109 are very soft and transient sources consistent with the TDE (or partial TDE) of a star by an IMBH. However, until this study and the work of Barrows et al. (2019), we lacked a large enough sample of HLXs to constrain their population. While the sample of 169 HLXs gathered by Barrows et al. (2019) only contains hard HLXs, our sample of 191 HLXs contains a small fraction of notably softer HLXs including the two aforementioned candidates. Essentially located at redshift $z < 0.2$ thanks to our larger sky coverage, our sample of HLX candidates is likely to contain lower mass IMBH and candidates better-suited for a follow-up than their sample. Interestingly, we find tentative differences between ULX and HLX populations, which further reinforces the interpretation that they may be massive black holes: HLXs appear to be more evenly distributed across the extent of their host, their XLF is significantly steeper than ULXs, and a significant fraction of them have an optical counterpart consistent with a dwarf galaxy. Several candidates, including a new HLX candidate compatible with a TDE, are under investigation.

Another more commonly studied location for IMBH candidates is near the center of dwarf galaxies, following an extrapolation of the black hole mass - stellar mass scaling relation. These dwarf galaxies could be leftovers of the hierarchical formation of galaxies, and thus analogous to the early galaxies in which the first black holes formed, thus providing a local probe of the poorly understood growth of SMBHs. However, it should be noted that this idea is increasingly controversial, as signs of AGN activity and possibly recent black hole growth are beginning to be discovered in these galaxies. Further work is needed to assess what fraction of dwarf galaxies is strongly affected by AGN growth feedback,

thus having a black hole mass function (and possibly an occupation fraction) that is no longer related to massive black hole formation scenarios.

In any case, the occupation fraction of dwarf galaxies by massive black holes is a hot topic, with increasing evidence of high fractions of massive black holes in galaxies of stellar mass $10^9 < M_*/M_\odot < 10^{10}$. X-ray studies of activity in dwarf galaxies must also account for a number of contaminants, including hot gas and X-ray binaries, in order to unambiguously identify nuclear activity. This problem is even more severe in small galaxies, where the massive black hole can wander to the periphery of the galaxy given its low gravitational potential, as we see in our study summarised below. AGN in the background and ultraluminous X-ray sources then become an important source of contamination. In this work, we use our classification to effectively remove all contaminants and accurately assess the active fraction of dwarf galaxies. For similar limiting luminosities, we find a somewhat lower active fraction than in previous works, probably due to the efficient removal of contaminants.

For the first time, we can study the evolution of this active fraction with limiting luminosities as low as 10^{38} erg s^{-1} and stellar masses as low as $5 \times 10^7 M_\odot$. We find tentative evidence of an X-ray luminosity function of AGN in dwarfs that is constant with stellar mass, in the range $2\times10^8-3\times10^9 M_\odot$, and a normalisation drop in the lower mass bins. Above $2 \times 10^8 M_\odot$, this result means a constant distribution of $M_{BH} f_{Edd}$ with stellar mass, at least in the bright end which is probed here. Since both M_{BH} and f_{Edd} are not supposed to increase with decreasing stellar mass, this suggests a constant occupation fraction above $2 \times 10^8 M_\odot$ and a drop below this value. Following the functional form of Miller et al. (2015) for the occupation fraction as a function of stellar mass, we are thus able to tentatively constrain the occupation fraction of dwarf galaxies in the range $10^8 - 3 \times 10^9 M_\odot$. A comparison to simulations of different seed formation channels shows complete agreement of these constraints with previous studies, except the dynamical constraints reviewed by Nguyen et al. (2019). This can be explained by various reasons summarised in Section 7.5. We recall here that further work is however needed to confirm this result, with a catalogue of galaxies having more reliable stellar masses.

In addition, a sample of 77 AGN candidates is identified as the most reliable (for being more luminous than the whole expected XRB population, and not being classified as a contaminant) and most suitable to be targeted by follow-up studies (due to their median observed flux 4×10^{-14} erg cm^{-2} s^{-1} in the range 0.5–10 keV). The spectral study of some of these candidates is already possible thanks to archival data. About half of them are found wandering at distances $\lesssim 5$ kpc from their galaxy center, as in the radio sample of Reines et al. (2020). This sample completes the growing census of low-luminosity AGNs found in dwarf galaxies, and our first-order mass estimates lead to about 50% of our AGN candidates in the $10^4-10^5 M_\odot$ range, which has been little probed to date. However, we note as a caveat that most studies searching for AGN candidates in dwarfs using X-ray data, including our work, rely on scaling relations of the total luminosity of X-ray binaries to select galaxies with excess emission. This is problematic because these relationships have been calibrated on local massive galaxies and sometimes do not take metallicity into account, and because estimates of stellar mass and star formation rate may not be reliable enough in galaxy catalogues. As a result, it is extremely difficult to distinguish between a wandering massive black hole and a ULX, since the latter are observed in great excess in low-mass galaxies. Improved scaling relations and estimates of galaxy properties, with a special focus on dwarf galaxies, could greatly improve the reliability of these samples.

Overall, the first-order estimates of the masses of the black holes in our sample show no deviation from the $M_{BH} - M_*$ relation known in the local Universe, except for a few overly massive HLX candidates. Our sample does not appear to favour any particular formation channel. This is largely due to the uncertain evolution of the resulting seeds to the present Universe, and thus their uncertain local signatures, which is due to the lack of representative cosmological simulations of BH populations, especially in the IMBH range. However, further research is needed to determine whether this result is due to inaccurate mass estimates, selection bias, or intrinsic physical differences between HLXs and AGNs in dwarf galaxies. The latter may indicate that the growth of these black holes has been primarily due to long-term processes (accretion or in situ black hole mergers) rather than processes occurring during galaxy mergers.

8.2 Outlook

8.2.1 Potential of our IMBH sample

We propose different studies as next steps of this work or as potential uses of our samples of IMBH candidates.

First, and because previous studies have proven that a number of HLX candidates are in fact background AGN (Dadina et al., 2013; Sutton et al., 2015), spectroscopic confirmation of our HLX candidates would be desirable. While our use of photometric redshifts is efficient at removing most background contaminants (including IC 4320, Sutton et al. 2015), as suggested by our estimates of the number of remaining contaminants (Section 5.4.5), they are available for only $\sim 15\%$ of our HLX sample and are necessarily less reliable than spectroscopic redshifts. The interpretation of confirmed candidates as black holes in a merging dwarf galaxy could then be robustly evaluated by searching for AGN emission lines, and compared to a scenario considering them as extreme ULXs in a star-forming region.

Our sample is the result of an extensive search for X-ray-selected IMBHs from the largest catalogues published to date, with great attention paid to the removal of contaminants. Thus, a significant number of confirmed local IMBHs would confirm the possibility of a systematic search for IMBHs in future optical and X-ray observations, capable of better constraining the growth of intermediate mass black holes by accretion. This work has suggested that accreting massive black holes are well within the reach of current observatories, in contrast with previous claims (e.g. Bellovary et al. 2019). Importantly, our sample can be compared to future HLX samples to better know our selection biases and assess the intrinsic location of IMBH in the $M_{BH} - M_*$ plane.

Second, some AGN and HLX candidates have archival contemporaneous observations in X-rays and optical/UV (from the *XMM-Newton* OM or *Swift* UVOT telescopes), including a number of sources showing signs of variability in these wavelengths. The spectral and timing analysis of such data could further refine our knowledge of these sources. For example, an ongoing work is focused on the evolution of HLXs in a hardness-intensity diagram, as already studied for ULXs by Gúrpide et al. (2021) (Amato et al. in prep). The spectra and optical counterparts of specific HLX candidates are currently being studied (Parra et al. in prep, Pellouin et al. in prep). Such studies could in the end allow us to assess the power of ongoing and future facilities of time-domain astronomy (such as the Vera Rubin observatory, Section 8.2.4) to find them.

High-resolution imaging of AGN candidates, in optical or infrared wavelengths (e.g. with HST or JWST), will provide further information on their environments, such as the presence of a nuclear star cluster or a bulge by studying their brightness profiles (as already done by Koliopanos et al. 2017 and Graham et al. 2021 on a number of low-luminosity AGN). Integral-field spectroscopy of the surroundings of the candidate can provide further constraints on the AGN nature and feedback of the source (e.g. Mezcua and Domínguez Sánchez, 2020). Similarly, a high-resolution sensitive radio follow-up will be key to constrain the mass of the accretor (using the fundamental plane and/or the source morphology), and disentangle some candidates from a stellar-mass ULX (Mezcua et al., 2013). If our first order mass estimates are reliable, the radio flux of black holes with $M_{BH} \gtrsim 5 \times 10^4 M_\odot$ starts to be just within the reach of modern radio facilities such as the VLA (the $\sim 2\mu$Jy beam^{-1} RMS noise of VLA after a ten-hour exposure results in a 4σ detection up to 20 Mpc of such a black hole having an X-ray luminosity of 3×10^{39} erg s^{-1}, using the fundamental plane of Plotkin et al. 2012). These observations should be conducted at the same time as new X-ray observations, in order to ensure the same X-ray and radio state to obtain more robust estimates (Gültekin et al., 2019).

In the clean sample of AGN candidates, 25 sources have detections with at least 100 X-ray counts, allowing their spectral study with archival data. This analysis, along with that of potentially newly observed HLXs, could constrain the thermal and comptonised components of the spectrum, and thus their accretion state, and therefore provide a better estimate of their Eddington ratio than we have done with automated spectral fits of a few candidates (Figure 7.4). It would also allow to model the absorption component and derive absorption-corrected luminosities and black hole masses. Importantly, this will reveal if the X-ray weak sources of our sample are intrinsically weak (i.e. unusual Eddington ratio or low black hole mass) or heavily obscured (Dong et al., 2012). Among the extreme ULXs in our sample ($5 \times 10^{40} < L_X < 10^{41}$ erg s^{-1}), a detailed spectral study could also uncover HLX-like candidates and reduce the current selection bias toward massive and efficiently accreting

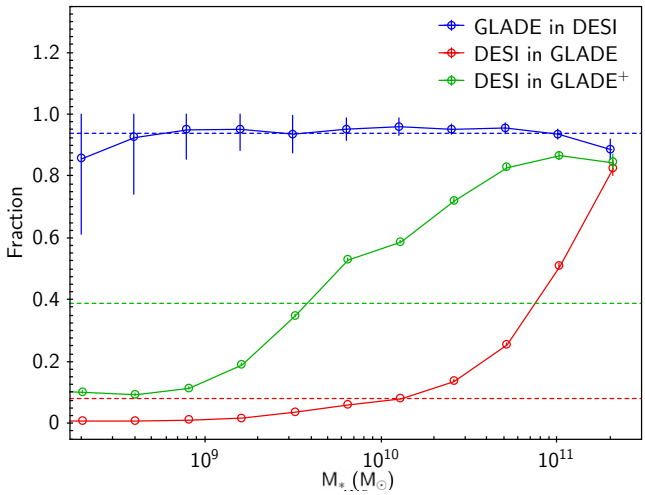

Figure 8.1: Completeness fraction of different galaxy surveys, as estimated by comparing them with each other. Blue, green: fraction of GLADE (resp. GLADE+) galaxies in the DESI galaxy sample of Zou et al. (2022) at $z < 0.2$. Green: fraction of DESI galaxies from Zou et al. (2022) in the GLADE catalogue.

black holes.

Moreover, another valuable improvement in the study of dwarf galaxies hosting AGN would be to refine estimates of their stellar mass and star formation rate, for example by using the mid-infrared based method of Parkash et al. (2018) and obtaining SFR estimates from far UV or $H\alpha$ data, as our mid-infrared estimates are not suitable for early-type galaxies and are likely to be biased in the presence of AGN (Cluver et al., 2017; Latimer et al., 2021). This would allow a robust study of the active fraction profile as a function of X-ray luminosity, and thus confirm or refute our tentative result on the occupation fraction.

8.2.2 Potential of archival searches

This study has demonstrated the potential of archival searches to find rare sources. The upcoming publication of the updated version of the *XMM-Newton*, *Swift* and *Chandra* catalogues will be of great interest to complete the current sample. This is especially true for the *Chandra* observations, included only until 2014 in the present catalogue. They provide a census with the highest sensitivities and angular resolution, which is thus well suited to extend the study to higher redshifts, as was done in Mezcua et al. 2018 for AGNs in dwarfs and Barrows et al. 2019 for HLXs.

In the search for AGN in dwarfs, the use of more complete and more reliable galaxy catalogues will be of particular interest. From Figure 6.11, at least 40% of actual dwarf galaxies have no stellar mass reported in GLADE.

Likewise, upcoming galaxy catalogues using deep optical surveys will be key to extend the search for HLXs and AGN in dwarfs to higher redshift, as already started by Barrows et al. (2019) for SDSS galaxies. This is illustrated in Figure 8.1, comparing the completeness of GLADE, GLADE+ and the catalogue of DESI galaxies (providing stellar mass estimates) of Zou et al. (2022). Unlike GLADE+, this catalogue contains information on the extent of each galaxy, thus providing an immediate perspective to extend our study.

While our local sample of IMBH may give a biased view of black hole seeds due to significant growth occuring in dwarf galaxies, an unbiased view of SMBH seeds may be achieved in the near future by searching for high-redshift quasars.

Already started in recent years, this search has mostly made use of colour cuts in optical photometric bands, using the so-called "i-dropout" technique (e.g. Fan et al. 2006; Jiang et al. 2016). Indeed, the redshift $z \gtrsim 5$ of these quasars lead to the shift of the Lyman break to the i band. However, the red sources selected with these criteria are likely to be mostly contaminants, including brown dwarfs and early-type galaxies, highlighting the need for a more probabilistic approach (Mortlock et al., 2012). Attempts have been made to develop a Bayesian (Mortlock et al., 2012) or probabilistic (Reed et al.,

	HZQ	Sy1	Sy2	YSO	Star	Precision
→HZQ	3	0	0	0	0	100%
→Sy1	18	1648	207	9	4	82%
→Sy2	2	103	349	51	20	81%
→YSO	0	0	0	810	159	91%
→Star	0	0	1	83	5489	97%
Recall	13%	94%	63%	85%	97%	

Table 8.1: Confusion matrix resulting from the classification of the 4XMM-DR11 training sample for the search for high-redshift quasars.

2017; Nanni et al., 2022) framework to select reliable high-redshift quasars using optical data. As a complement to these methods, the addition of X-ray data could be extremely useful to better remove contaminants, access the highly obscured AGNs - which are more common at high redshift (Vito et al., 2018) - and find the most massive efficiently-accreting quasars at high redshift (Vito et al., 2019; Lusso et al., 2022).

As a preliminary test, we studied a sample of $\sim$ 400000 4XMM-DR11 sources in the footprint of the large and deep optical surveys DES, BASS and PanSTARRS, in order to search for new high-redshift quasars with our classification. Optical counterparts were identified with the NWAY software (as detailed in Chapter 3) for 70% of the sample. On the basis that high-redshift quasars are often photometrically selected through their optical colours, we add a column for each of the three colours $g-r$, $r-z$ and $g-z$. For this work, as a first approximation of the types that we have to disentangle in order to isolate high-redshift quasars (here defined as redshift $z > 5$), we distinguish between the five classes: high-redshift quasar (HZQ), lower-redshift Seyfert I (Sy1), lower-redshift Seyfert II (Sy2), young stellar objects (YSO) and normal stars (Star). A training sample of such sources was identified by a crossmatch within a radius $3 \times POSERR$ (where $POSERR$ is the position error on the X-ray source) with the *Simbad* data archive. It contains 23 known high-redshift quasars, and we note as a first caveat that this is notably insufficient to infer property densities. For this reason, overfitting is an issue and we choose not to optimise the classifier. Priors on each class are arbitrarily fixed to $\mathcal{P}(\text{HZQ}) = 0.02$, $\mathcal{P}(\text{Sy1}) = 0.53$, $\mathcal{P}(\text{Sy2}) = 0.25$, $\mathcal{P}(\text{YSO}) = 0.05$ and $\mathcal{P}(\text{Star}) = 0.15$.

Two classifiers are tested, one imposing $\beta = 0$ (i.e. missing values are ignored) and one with $\beta = 1$ (i.e. the likelihood of a missing value given a class is the fraction of this class having a missing value in the training sample). The confusion matrix for the first run is shown in Table 8.1. As a result of this rough classification, we still retrieve 3 HZQ of the training sample, with no false positives. We note that this retrieval-accuracy trade-off gives a lower $f1$-score than the second run with missing values (identifying 13 HZQ plus 27 false positives), but with better accuracy, which is most relevant in this archival search.

In the test sample, 107 (87760) AGN candidates are identified from the first (resp. second) classifier. This further shows the bias introduced here by missing values, which are more present in the HZQ class than the other ones (e.g. 5 out of 23 known HZQ have missing g magnitude, due to their redshift). The distributions of S/N, $r-z$ and z for the 107 HZQ candidates are shown in Figure 8.2, with the 3 known HZQ highlighted in red.

After applying reasonable quality cuts ($S/N > 1$, $z < 23.5$ and $r < 26.5$), only three candidates are left (Figure 8.3): 4XMM J022730.3-052820, 4XMM J023127.6-072049 and 4XMM J034536.7-534020. The first two are most probably too hard to be located at high redshift, and the last one is identified as a radio-emitting galaxy in Johnston-Hollitt et al. (2008).

From this initial trial, we can conclude that our classification technique is not yet ready to identify high-redshift quasars in current archives, especially given the small training sample. However, with the wide variety of upcoming surveys (in particular from observatories such as JWST, Euclid and *Athena*, Section 8.2.4) targeting this population, such an approach is likely to become useful. Alternatively, a more natural and promising approach is to use redshift estimation rather than classification, as performed today in photometric redshift estimation works. These two approaches are likely to be more useful in combination, with the former leading to efficient contaminant removal and the latter to accurate redshift estimation. Therefore, the ongoing work of the XMM2ATHENA collaboration to

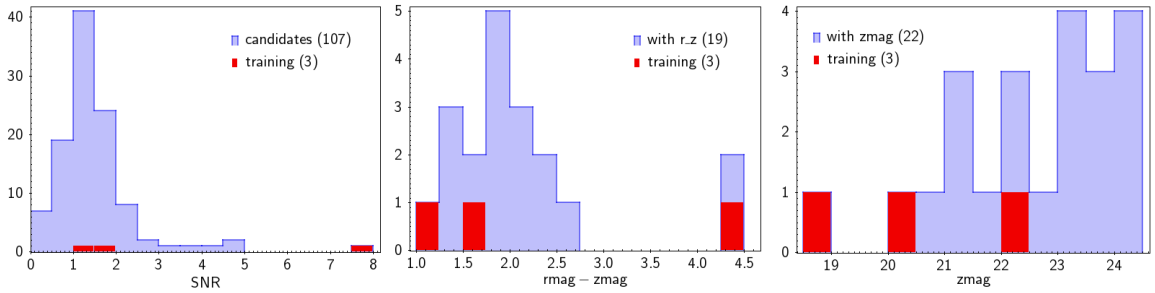

Figure 8.2: Distributions of some properties in the sample of high-redshift quasar candidates. The three known and well-classified quasars are shown in red. (Left): Signal-to-noise ratio, (Middle) $r - z$ colour, (Right): z apparent (AB) magnitude.

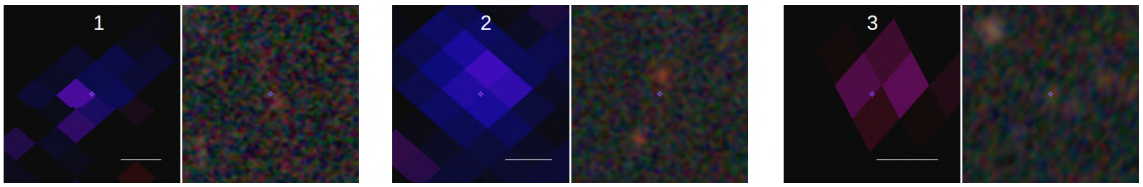

Figure 8.3: High-redshift candidates identified by the classifier in the 4XMMDR11 archive. For each candidate, the X-ray (*XMM-Newton*) and optical (DES) images are shown. The white line is 5 arcsec. (Left): 4XMM J022730.3-052820, (Middle): 4XMM J023127.6-072049, (Right): 4XMM J034536.7-534020.

stack X-ray images to reach deeper sensitivities, calculate photometric redshifts taking into account X-ray data, and automatically classify X-ray sources, may yield promising results in the near future. As for the more distant future, an outlook is presented in Section 8.2.4.

8.2.3 Citizen science, completing the classification framework

As discussed in section 7.1, efficient automatic classification of X-ray sources is hampered by small training samples. In this regard, the development of the CLAXSON (CLAssification of X-ray SOurces for Novices, https://xmm-ssc.irap.omp.eu/claxson, See section 4.6) citizen science platform, which is specifically aimed at expanding these training samples, is of particular interest. Although only four classes are included in the experiment to date, namely AGN, Star, X-ray binary and "Something else", we have found that sources being classified by a sufficiently high ($\gtrsim 20$) number of volunteers have very accurate classifications. Besides, the latter class enables the serendipitous discovery of very rare sources.

Given the encouraging preliminary results and sufficient user interest, the next step in the development of CLAXSON will be to disseminate it to a large audience, allowing us to rapidly obtain results on a larger sample. After carefully estimating the classification biases, a first data release of 4XMM source classification by visual inspection should be published. This will pave the way for finer classification studies, with the potential to allow accurate population studies of the wide range of X-ray emitters with very low contamination.

Future improvements will include extending the experiment to the *Chandra* catalogue and perhaps inviting volunteers to classify specific X-ray populations (e.g. ULX candidates, Galactic XRB candidates, TDE candidates...) from time to time. The X-ray astrophysics community could also benefit from the platform, which provides immediate access to several features of the virtual observatory. Besides, a comment section is open under each individual source on CLAXSON, which could foster useful discussions about the nature of a source and expand the range of possible serendipitous discoveries through collective intelligence.

In addition to source classifications, citizen science experiments can provide other useful information. Adding a drawing functionality to the source fields of view can allow volunteers to identify sources with particular shapes or located in particular environments, as has already been implemented in Zooniverse.[1]. This could be of particular interest to flag sources subject to source confusion, iden-

[1]The latest version of Galaxy Zoo experiments, also gathering a number of other unrelated citizen science experiments.

tify new galaxies or optical counterparts undetected by survey pipelines, or correct manifestly wrong D_{25} measurements in galaxy catalogues. Part of the value of any citizen science experience is also the opportunity to make science accessible and attractive to a wide audience, as with any outreach activity. A great effort has thus been devoted to the translation of the platform into five languages (English, French, Spanish, Italian and Greek), and to the promotion of the scientific involvement of volunteers, with the dissemination of a user survey[2] aimed at further improving the protocol and design of CLAXSON.

8.2.4 Future IMBH-related population studies

As discussed in Section 2.5.2, IMBHs can be detected from a variety of signatures, while in this thesis we primarily focused on dwarf galaxies and HLXs. A more complete knowledge of the IMBH population will be achieved over the next two decades through multi-wavelength and multi-messenger observatories.

AGN in dwarf galaxies

It may be inappropriate to seek to constrain the high-redshift black hole seeds from the properties of local active dwarf galaxies, due to the potentially large growth of their black hole since that epoch (e.g., Mezcua 2019). To overcome this issue and access a more representative view of pristine SMBH seeds, it is necessary to observe AGN at higher redshift, which have had less time to evolve. At redshifts $\gtrsim 1$ this census is limited by the depth of X-ray observations (in X-rays the most distant AGN in a dwarf galaxy was detected at redshift $z = 2.4$ in the *Chandra* COSMOS-Legacy Survey of exposure ~ 100 ks per field, Mezcua et al. 2018).

In radio, current observatories seem to already probe higher redshifts in sufficiently large and deep surveys, such as the VLA-COSMOS survey in which an AGN candidate was found at photometric redshift $z_{ph} = 3.4$ (Mezcua et al., 2019). Dwarf galaxies at the epoch of reionisation and the first black hole seeds may be soon directly accessed by JWST observations (Section 8.2.4).

An alternative way would be to study AGN candidates in carefully selected bona fide analogues of high-redshift galaxies, as could be the case of extremely metal-poor dwarf galaxies (Mezcua, 2019). Since such galaxies are necessarily rare in the local Universe, radio observations capable of observing weakly-accreting black holes with low contamination from XRBs may be best suited to construct a large population. For instance, the next-generation Very Large Array (ngVLA, e.g. Murphy et al. 2018) and the Square Kilometer Array (SKA, e.g. Lazio 2009) should achieve a few 10s of nJy sensitivities, making it possible to detect a $10^4 M_\odot$ IMBH accreting below $L_X = 10^{39}$ erg s^{-1} at 100 Mpc, or a $10^3 M_\odot$ IMBH accreting below $L_X = 10^{38}$ erg s^{-1} at 25 Mpc, according to the fundamental plane of Plotkin et al. (2012). This is particularly interesting given the large fraction ($\sim 75\%$) of the sky covered by SKA. The $\sim$10 mas resolution achieved (equivalent to 5 pc at 100 Mpc) makes it possible in many cases to distinguish the radio nebula of a ULX from the compact emission (or conversely, large radio jets) of a massive black hole (Mezcua et al., 2013; Sargent et al., 2022). On a different topic, SKA is predicted to detect nearly all quiescent IMBH in our Galaxy, or otherwise put stringent upper-limits on their mass (Acero et al., 2017).

In any case, the importance of AGN feedback and minor mergers in the evolution of dwarf galaxies and their black hole is far from being established, and a better knowledge of these faint, peculiar galaxies can only be obtained by future observatories.

Hyperluminous X-ray sources

The density of HLXs in field galaxies of the local Universe, deduced in Section 7.6, means that about 260 candidates within $\sim$160 Mpc could be detected above the 10^{-14} erg cm^{-2} s^{-1} sensitivity limit of the eROSITA all-sky survey once completed (Merloni et al., 2012), and ~ 20 HLXs in the sub-70 Mpc volume covered by the upcoming eRASS1 data release at a limiting luminosity $< 10^{41}$ erg s^{-1}[3].

https://www.zooniverse.org/

[2] https://forms.gle/tgFMujfdLUTGUjxcA

[3] A conversion factor $L_{0.5\text{–}2\text{ keV}} \approx 0.3 L_{0.2\text{–}10\text{ keV}}$, given by the absorbed powerlaw model ($\Gamma = 1.7$, $n_H = 3 \times 10^{20}$ cm^{-2}), is used to obtain these first order estimates. Note that the rare soft HLXs will be easier to detect with eROSITA, and most of other HLXs are probably harder than this model. Using the median column density of Barrows et al. (2019) $n_H = 6 \times 10^{21}$ cm^{-2} decreases these estimates by a factor 2.

The deeper sensitivities of *Athena* (Nandra et al., 2013) in the broader band $0.2-15$ keV will lead to the most significant increase in the census of HLXs. The *Athena+* WFI survey (Lanzuisi et al., 2017; Nandra et al., 2013), covering more than 50 deg^2 at a sensitivity of $\sim 7 \times 10^{-17}$ erg cm^{-2} s^{-1} and designed to achieve *Athena* science goals[4] for the observation of high-redshift quasars, will give access (in this coverage) to all HLXs of $L_X > 10^{41}$ erg s^{-1} up to redshift $z = 0.6$, and all HLXs of $L_X > 10^{42}$ erg s^{-1} up to redshift $z = 1.5$. This represents ~ 3400 and ~ 7000 objects, respectively. Some HLX dwarf hosts may be experiencing a minor merger with the primary host (Section 7.3.4), but the fraction of such HLXs is so far unconstrained. Such samples open the possibility to study how HLX numbers and properties evolve with cosmic time, and thus to further constrain the growth of SMBH seeds by accretion during galaxy mergers.

While our HLX sample is likely to have a strong selection bias towards efficiently accreting black holes, new sensitive radio antennae could detect the bulk of massive black holes in dwarf galaxies (Section 8.2.4) and separate them from the stellar mass ULX populations.

Tidal disruption events and quasi-periodic eruptions

Because off-nuclear TDEs have already revealed two of the best IMBH candidates known to date (Farrell et al., 2009; Lin et al., 2018), and because their light curves allow a preliminary estimate of the black hole mass (Mockler et al., 2019), they represent a promising avenue to search for other IMBHs. This is especially true since TDEs are only detectable for black holes of "low" mass ($\lesssim 10^8 M_\odot$), with a tidal radius beyond their event horizon for a stellar mass main-sequence star, and since TDEs offer a way to observe black holes that are usually in quiescence. So far, the reasons why no off-nuclear TDE has been detected in optical are unclear. Current and future sensitive facilities for time-domain astronomy will therefore be essential for accessing the low-mass black hole population, for constraining their properties and for better probing the intrinsic mass spectrum of black holes.

In particular, the Vera Rubin Observatory observing nearly half of the sky repeatedly is expected to yield between 3500 and 8000 TDE detections per year, depending on the SMBH mass distribution (van Velzen et al., 2011; Bricman and Gomboc, 2020). The observing cadence strategy of the Vera Rubin Observatory survey (the Large Survey of Space and Time, or LSST) is likely to be irregular and is not yet decided at the time of writing (e.g. Bricman and Gomboc 2020; Bianco et al. 2022), but is about once every 3 or 4 nights on average. It is a key parameter to estimate the number of detectable TDEs by low-mass black holes $\lesssim 10^5 M_\odot$, generally having faster decays than TDEs by higher-mass black holes (Section 2.3.3). Due to this faster decay and lower peak luminosity, about 1000–2000 TDEs by black holes of mass $\lesssim 10^5 M_\odot$ may be detected during the 10 years of the survey (Figure 7 of Bricman and Gomboc 2020). Alternatively, accreting IMBHs could well be discovered in greater numbers by this observatory using AGN variability signatures (Baldassare et al., 2020; Burke et al., 2022), however this will target black holes are that actively accrete.

In the X-ray domain, eROSITA is expected to detect several thousand TDEs once the survey will be completed[5] (Khabibullin et al., 2014). However, once again, black holes of $10^7 M_\odot$ are better sampled than lower-mass black holes (Section 2.3.3), and the 6-month cadence of eROSITA may well be insufficient to properly study them: a proper follow-up by *XMM-Newton*, *Swift* or *Chandra* observations will then be needed to analyse the most interesting candidates. Note that the IMBH candidate 4XMM J215022.4-055109 does not seem to follow this trend, as its outburst lasted several years (Lin et al., 2018), and that some TDEs are even found to last a decade (Lin et al., 2017, 2022).

However, the prospects for IMBH discovery could be even better than presented above, with the discovery of a new class of objects, rarer than TDEs, the "quasi-periodic eruptions" or QPEs (Miniutti et al., 2019). QPEs are regular explosions of soft X-rays, with a fast rise and a fast decay, which are repeated every few hours and are produced by the central black hole of some galaxies. Two of them were already detected with eROSITA observations (Arcodia et al., 2021). We still lack a robust model to describe the few QPEs discovered so far, however these objects seem to be globally consistent with partial tidal disruption events on low-mass black holes ($\sim 10^5 M_\odot$) (Miniutti et al., 2022). If confirmed, the repeating nature of QPEs will be particularly welcome in order to detect more of them and better study accretion on these low-mass, usually quiescent black holes.

[4] To date, however, it is difficult to know if the *Athena* mission or its equivalent will reach this objective, given the important redefinition of the instrument that has just begun.

[5] Unfortunately, the telescope has been put into safe mode on February 26 and the date of its restart is uncertain.

Dynamical measurements

Recently, dynamical studies led to the first stringent upper limit on the dwarf galaxy occupation fraction (Nguyen et al. 2019, discussed in Section 7.5). However, dynamical detections of IMBHs are strongly limited to their high-mass end because of a limited angular resolution and sensitivity, and many previous claims were revealed to be dubious candidates (Greene et al., 2020). In the next decade, this limit will be largely pushed with the advent of 30m-class telescope (Extremely Large Telescopes or ELTs). Their angular resolution (better than 4mas/pixel), in combination with integral field spectroscopy (such as the HARMONI instrument on the ELT), will allow the dynamical detection of many $10^3 - 10^5 M_\odot$ black holes in our Local Volume (Greene et al., 2019).

High-redshift quasars

The search for and study of quasars at high redshift is one of the most promising avenues for directly constraining the growth of supermassive black holes. Over the next two decades, many facilities are expected to tackle this scientific case in a wide range of wavelengths. Many questions remain open, such as when the first galaxies grew, how their star formation activity evolved, how they acquired their black holes, and what role galaxy mergers, AGN and supernova feedback played in these respective evolutions.

While a decade ago, only the brightest quasars could be detected at $z > 6$, recent progress in deep spectroscopic surveys (and in particular the Hyper-Supreme Cam Subaru survey) allowed the detection of more than a hundred lower luminosity quasars. Their optical lines suggest black hole masses in the range $10^{7.6} - 10^{9.3} M_\odot$, and their luminosity suggest accretion below 10% of the Eddington limit (Onoue et al., 2019; Matsuoka et al., 2022), hence reducing the detection bias and better probing the bulk of high-redshift quasars.

The X-ray census of high-redshift quasars will soar with the telescope *Athena*, detecting hundreds of AGN at $z > 6$ and even some of them at $z > 8$ (Nandra et al., 2013). This jump in performance is notably allowed by the use of silicon pore optics, allowing to combine a large field of view, a deep sensitivity and a high angular resolution (Barrière et al., 2022). In the radio band, interestingly, SKA and ngVLA should also be able to observe some direct collapse black holes at redshift $z \sim 7$ (Whalen et al., 2020).

Already beginning to yield unprecedented results on the high-redshift Universe in its early data releases, JWST is expected to revolutionize the field by its sensitivity up to AB magnitudes > 30 in the near-infrared, allowing the observations of galaxies and quasars up to $z \sim 20$ (e.g. Woods et al. 2019). Covering a much larger fraction of the sky ($\sim 1/3$) but up to shallower sensitivities, Euclid will also play a crucial role in the infrared census and study of these objects up to redshift $z \sim 8$ (Euclid Collaboration et al., 2019), with a first release planned for 2025.

Black hole mergers

In the gravitational wave domain, the LIGO/Virgo first detection of an IMBH of mass $\sim 140 M_\odot$ (Abbott et al., 2020a) has demonstrated that such seeds form at detectable rates in the local Universe, from the merger of smaller black holes. The upcoming fourth observing run, starting in 2023, will be sensitive to merging black holes of mass $\lesssim 200 M_\odot$ and is expected to detect more of these events at redshift $z < 0.5$ (at least for intermediate-mass ratio inspirals, composed of an IMBH and a stellar-mass compact object, Arca Sedda et al. 2021). Some mergers forming $10^3 M_\odot$ black holes could also be detectable by LIGO/Virgo/KAGRA at design sensitivity (Fragione et al., 2018; Mehta et al., 2022).

More massive black hole mergers may be partly uncovered in the nearby Universe using electromagnetic signals: dual AGN have already been detected in a number of galaxies showing merger signatures (Volonteri et al., 2021), including one system recently claimed to merge in the coming years from its optical light curve (Dotti et al., 2022). X-ray and optical-UV observations may provide a way to find more of these objects which are strong UV emitters, and their search in *XMM-Newton* EPIC and OM observations are the subject of an ongoing work (Foustoul, Webb et al. in prep). Preparing LISA science, these studies will be key to evaluate the importance of the merger channel of SMBH growth.

In a more distant future, LISA will represent a giant leap for the science of black holes. Its unprecedented sensitivity and passband 0.1 mHz – 1 Hz will allow the detection and study of most mergers from intermediate-mass progenitors up to extremely high redshifts, $z \sim 20$ (Bellovary et al., 2019). Particularly sensitive to IMBHs above masses $\sim 10^3 M_\odot$, it will be key to gather a large sample of black hole seeds and study their formation and evolution. Excitingly, formation channels like the

direct collapse scenario and the importance of mergers in SMBH growth will be efficiently constrained (Hartwig et al., 2018; Woods et al., 2019).

Complementary to these facilities, the Einstein Telescope, a proposed ground-based mission to operate in the band 2 Hz – 2 kHz, will probe distant ($z \sim 1-5$) black holes of mass $\lesssim 2 \times 10^3 M_\odot$ (Maggiore et al., 2020). It will thus possibly reveal Pop III remnants at moderate redshift, notably in extremely metal-poor starforming galaxies, in which the black hole growth is supposed to be essentially suppressed.

Chapter 9

Conclusion et perspectives

Ce chapitre met en avant certains des principaux résultats que j'ai obtenus dans mon étude de la population des trous noirs de masse intermédiaire, tant en termes de méthode que de résultats observationnels. C'est aussi l'occasion de prendre du recul et de proposer quelques travaux futurs. Nous donnons quelques perspectives sur la façon dont les futurs observatoires répondront aux questions ouvertes portant sur la formation, l'évolution et le nombre de trous noirs de masse intermédiaire, qu'ils soient sensibles aux ondes gravitationnelles ou à une large gamme de signaux électromagnétiques qui révéleront cette population.

9.1 Conclusion

Le sujet principal de cette thèse est la recherche et l'étude des trous noirs de masse intermédiaire. L'objectif de ce travail a été de collecter et d'étudier un large échantillon de candidats trous noirs de masse intermédiaire à partir des plus grandes archives disponbibles en rayons X et autres longueurs d'onde, ce qui nécessite une élimination efficace des contaminants.

Pour ce faire, nous avons développé une classification probabiliste des sources de rayons X, adaptable à un large éventail d'échantillons et d'applications. Pour commencer, une corrélation croisée est faite entre la plupart des sources de chaque catalogue en rayons X existant et des catalogues de sources visibles et infrarouges, identifiant ainsi de manière robuste les contreparties des sources de rayons X. À l'aide de ces informations, ainsi que des propriétés spectrales et temporelles des sources de rayons X et de leur association avec un source Gaia ou un galaxie GLADE pour estimer leur luminosité, un classificateur naïf bayésien revisité attribue à chaque source les probabilités de chaque classe dans un cadre facilement interprétable. C'est la première fois qu'un schéma de classification probabiliste est appliqué à un si grand ensemble de sources de rayons X dans le ciel entier.

Nous avons appliqué cette méthode à plusieurs cas scientifiques couvrant un large éventail de classes de sources : une classification à l'échelle du ciel entier (les classes sont alors noyau actif de galaxie (AGN), étoiles, binaires X et variables cataclysmiques), une classification des populations d'émetteurs de rayons X dans les galaxies proches (AGN, binaires X et sources molles), et aussi une classification pour la recherche de quasars à haut redshift (Seyfert I, Seyfert II, étoiles normales, YSO et quasars à haut redshift) dans un travail en cours (cf. Section 9.2.2). Nous avons identifié de manière fiable les étoiles et les AGN en général, en éliminant efficacement les contaminants parmi les sources X ultralumineuses (ULX) et en sélectionnant des candidats trous noirs massifs dans les galaxies naines pour une étude plus approfondie. Puisqu'il n'a pas été possible de constituer un échantillon d'entraînement de trous noirs de masse intermédiaire, leurs manifestations en tant que source X hyperlumineuse (HLX) ou d'événement de rupture par effet de marée (TDE) ont pu être récupérées a posteriori, notamment grâce à l'utilisation d'une mesure d'isolation des anomalies.

L'étude des sources X ultralumineuses est particulièrement intéressante pour comprendre comment une source peut soutenir une accrétion super-Eddington, et aider à comprendre la croissance de certains des premiers trous noirs supermassifs. Les études de population des sources X ultralumineuses sont toutefois entravées par la présence de 15 à 20 % de contaminants, voire davantage parmi les sources les plus lumineuses et dans la périphérie lointaine des galaxies. Ceci est donc particulièrement problématique dans la recherche de sources X hyperlumineuses, alors même que certaines d'entre elles figurent parmi les meilleurs candidats trous noirs de masse intermédiaire connus à ce jour. A cet égard, notre méthode peut être d'une grande aide pour identifier correctement les meilleurs candidats pour les études de suivi, et pour commencer à acquérir une vision statistique de ces objets.

En pratique, nous avons identifié 1901 ULXs et 191 HLXs parmi les catalogues *Swift*-XRT, *XMM-Newton* et *Chandra*, ce qui représente les échantillons les plus grands et les plus propres de ces objets obtenus à ce jour, à notre connaissance. Nous avons pu confirmer certains résultats déjà trouvés par des études de la littérature, comme le fait que les ULXs et les XRBs partagent le même emplacement dans les diagrammes dureté-dureté. Nous ne trouvons aucune différence flagrante de variabilité entre les ULXs et les XRBs, contrairement par exemple à Bernadich et al. (2021). Nous trouvons une diminution du taux spécifique d'ULX (c'est-à-dire par unité de masse stellaire) avec la masse de la galaxie, avec cependant un grand excès d'ULXs dans les galaxies naines, en accord avec plusieurs études récentes. Une autre propriété environnementale (rarement) étudiée des ULXs est leur distribution spatiale dans leur hôte. Nous constatons que, comme attendu, les ULXs dans les galaxies spirales et elliptiques suivent globalement le profil lumineux respectif de ces galaxies, avec un petit excès dans la périphérie de ces dernières. Dans ces galaxies, nous avons pu montrer la chute de la densité des ULX au-delà de D_{25}, ce qui n'était pas possible dans les études précédentes en raison du taux élevé de contaminants dans cette région.

Nous nous sommes également concentrés sur la fonction de luminosité en rayons X des ULX, en utilisant une méthode de correction des effets de volume souvent utilisée dans d'autres domaines de l'astrophysique, mais jamais dans les études sur les ULX, qui préfèrent plutôt travailler sur des échantillon limités en volume (exigeant que toutes les sources de leur échantillon soient observées avec une luminosité limite $\leq 10^{39}$ erg s^{-1}). Après avoir mis en évidence certains biais instrumentaux dus aux différentes capacités des instruments (en particulier les problèmes de confusion et d'autres effets de la résolution angulaire), nous avons prouvé l'existence d'une cassure dans la fonction de luminosité des ULX dans les galaxies spirales. Cette caractéristique avait été suggérée par des études antérieures mais avait récemment été assimilée à une fluctuation statistique. La cassure que nous obtenons est hautement significative, ce que nous interprétons comme étant dû à une élimination efficace des contaminants et à une plus grande statistique. L'origine physique de cette cassure n'est cependant pas encore claire, mais elle pourrait être liée à la cassure de la fonction de luminosité des binaires X de forte masse observée dans les galaxies de faible métallicité (Lehmer et al., 2021). A des luminosités plus élevées, aucune cassure n'est observée dans la fonction de luminosité, qui sonde alors la population des sources X hyperlumineuses, mais l'échantillon est alors insuffisant pour contraindre une telle caractéristique de manière significative.

Les sources X hyperlumineuses ($L_X > 10^{41}$ erg s^{-1}) ont des luminosités si élevées qu'il est difficile de les expliquer par de l'accrétion sur des objets compacts de masse stellaire, et en effet quelques-unes de ces rares sources constituent certains des meilleurs candidats trou noir de masse intermédiaire (IMBH). En particulier, ESO 243-49 HLX-1 et 4XMM J215022.4-055109 sont des sources très molles et transitoires compatibles avec l'événement de rupture (total ou partiel) d'une étoile par un IMBH. Cependant, jusqu'à cette étude et celle de Barrows et al. (2019), nous ne disposions pas d'un échantillon suffisamment important de HLXs pour contraindre leur population. Tandis que l'échantillon de 169 HLXs rassemblé par Barrows et al. (2019) ne contient que des HLXs durs, notre échantillon de 191 HLXs contient une petite fraction de HLXs nettement plus mous, dont les deux candidats susmentionnés. Essentiellement situé à un redshift $z < 0.2$ grâce à notre plus grande couverture du ciel, notre échantillon de candidats HLX est susceptible de contenir des IMBHs de plus faible masse et des candidats mieux adaptés à un suivi que leur échantillon. Fait intéressant, nous trouvons de légères différences entre les populations ULX et HLX, ce qui renforce l'interprétation selon laquelle ces-derniers pourraient être des trous noirs massifs : les HLXs semblent être distribués plus uniformément à travers l'étendue de leur hôte, leur fonction de luminosité est significativement plus raide que celle des ULXs, et une fraction significative d'entre eux a une contrepartie en lumière visible compatible avec une galaxie naine. Plusieurs candidats, dont un nouveau candidat HLX compatible

avec un TDE, sont en cours d'investigation.

Un autre environnement plus communément étudié pour les candidats IMBH est la zone centrale des galaxies naines, ce qui est motivé par une extrapolation de la relation d'échelle [masse du trou noir] - [masse stellaire de la galaxie]. Ces galaxies naines pourraient être des vestiges de la formation hiérarchique des galaxies, et donc analogues aux premières galaxies dans lesquelles les premiers trous noirs se sont formés, fournissant ainsi une sonde locale de la croissance des trous noirs supermassifs. Cependant, il faut noter que cette idée est de plus en plus controversée, car on commence à découvrir des signes d'activité d'AGN et peut-être de croissance récente de trous noirs dans ces galaxies. D'autres travaux sont nécessaires pour évaluer quelle fraction des galaxies naines est fortement affectée par la rétroaction exercée par les AGN et par la croissance des trous noirs, galaxies qui ont donc une fonction de masse des trous noirs (et peut-être une fraction d'occupation) qui n'est plus représentative des scénarios de formation de trous noirs massifs.

Dans tous les cas, la fraction d'occupation des galaxies naines par des trous noirs massifs est un sujet très actuel, avec des preuves croissantes de fractions élevées dans les galaxies de masse stellaire $\gtrsim 10^9 M_\odot$. Les études en rayons X de l'activité des galaxies naines doivent également tenir compte d'un certain nombre de contaminants, notamment le gaz chaud et les binaires X, afin d'identifier sans ambiguïté l'activité du noyau. Ce problème est encore plus sévère dans les petites galaxies, où le trou noir massif peut errer à la périphérie de la galaxie étant donné son faible potentiel gravitationnel, comme nous le voyons dans notre étude résumée ci-dessous. Les AGN situés en arrière-plan et les sources X ultralumineuses deviennent alors une source importante de contamination. Dans ce travail, nous utilisons notre classification pour éliminer efficacement tous les contaminants et évaluer avec précision la fraction active des galaxies naines. Pour des luminosités limites similaires, nous trouvons une fraction active un peu plus faible que dans les travaux précédents, probablement en raison de l'élimination efficace des contaminants.

Pour la première fois, nous avons pu étudier l'évolution de cette fraction active avec des luminosités limites aussi faibles que 10^{38} erg s^{-1} et des masses stellaires aussi faibles que $5\times10^7 M_\odot$. Nous trouvons des preuves ténues d'une fonction de luminosité X des AGN dans les naines qui est constante avec la masse stellaire, dans la gamme $2 \times 10^8 - 3 \times 10^9 M_\odot$, et une chute de la normalisation dans les tranches de masse inférieures. Au-dessus de $2 \times 10^8 M_\odot$, ce résultat signifie une distribution constante de $M_{BH} f_{Edd}$ avec la masse stellaire, tout du moins dans la partie brillante qui est sondée ici. Puisque M_{BH} et f_{Edd} ne sont pas supposés augmenter avec la diminution de la masse stellaire, cela suggère une fraction d'occupation constante au-dessus de $2 \times 10^8 M_\odot$ et une chute en dessous de cette valeur. En suivant la forme fonctionnelle de Miller et al. (2015) pour la fraction d'occupation en fonction de la masse stellaire, nous sommes donc en mesure de contraindre à titre provisoire la fraction d'occupation des galaxies naines dans la gamme $10^8 - 3 \times 10^9 M_\odot$. Une comparaison avec des simulations de différents canaux de formation de graines montre un accord complet de ces contraintes avec les études précédentes, à l'exception des contraintes dynamiques revues par Nguyen et al. (2019). Ceci peut s'expliquer par diverses raisons résumées dans la Section 7.5. Nous rappelons ici que des travaux complémentaires sont cependant nécessaires pour confirmer ce résultat, avec un catalogue de galaxies ayant des masses stellaires plus fiables.

De plus, un échantillon de 77 candidats AGN est identifié comme étant le plus fiable (car plus lumineux que l'ensemble de la population XRB attendue, et n'étant pas classé comme contaminant) et le plus approprié pour être ciblé par un suivi (en raison de leur flux médian observé 4×10^{-14} erg cm^{-2} s^{-1} dans la gamme 0.5–10 keV). L'étude spectrale de certains de ces candidats est déjà possible grâce aux données d'archives. Environ la moitié d'entre eux sont découverts errants à des distances $\lesssim 5$ kpc de leur centre de galaxie, comme dans l'échantillon dans le domaine des ondes radio de Reines et al. (2020). Cet échantillon complète le recensement grandissant des AGN de faible luminosité trouvés dans les galaxies naines, et nos estimations de masse approximatives conduisent à environ 50 % de nos candidats AGN dans la gamme $10^4 - 10^5 M_\odot$, qui a été peu sondée jusqu'à présent. Cependant, nous notons que la plupart des études qui recherchent des candidats AGN dans les naines à l'aide de données X, y compris notre travail, s'appuient sur des relations d'échelle de la luminosité totale des binaires X pour sélectionner les galaxies avec un excès d'émission. Ceci est problématique car ces relations ont été calibrées sur des galaxies massives locales et ne prennent parfois pas en compte la métallicité, et parce que les estimations de la masse stellaire et du taux de formation d'étoiles peuvent ne pas être assez fiables dans les catalogues de galaxies. Par conséquent, il est extrêmement difficile de faire la distinction entre un trou noir massif errant et un ULX, puisque ces derniers sont

observés en grand excès dans les galaxies de faible masse. Des relations d'échelle améliorées et des estimations plus précises des propriétés des galaxies, avec une attention particulière pour les galaxies naines, pourraient grandement améliorer la fiabilité de ces échantillons.

Globalement, les estimations au premier ordre des masses des trous noirs de notre échantillon ne montrent aucune déviation par rapport à la relation $M_{BH} - M_*$ connue dans l'Univers local, à l'exception de quelques candidats HLX trop massifs. Notre échantillon ne semble pas favoriser un canal de formation particulier. Ceci est largement dû à l'évolution incertaine des graines de trou noir jusqu'à l'Univers actuel, et donc à leurs signatures locales incertaines, qui sont dues au manque de simulations cosmologiques représentatives des populations de BH, en particulier dans la gamme des IMBH. Cependant, des recherches supplémentaires sont nécessaires pour déterminer si ce résultat est dû à des estimations de masse inexactes, à un biais de sélection, ou à des différences physiques intrinsèques entre les BH et les AGN dans les galaxies naines. Ce dernier point pourrait indiquer que la croissance de ces trous noirs a été principalement due à des processus de long terme (accrétion ou fusions de trous noirs in situ) plutôt qu'à des processus cataclysmiques se produisant pendant les fusions de galaxies.

9.2 Perspectives

9.2.1 Potentiel de notre échantillon de candidats IMBH

Nous proposons différentes études comme prochaines étapes de ce travail ou comme utilisations potentielles de nos échantillons de candidats IMBH.

Premièrement, et parce que des études précédentes ont prouvé qu'un certain nombre de candidats HLX sont en fait des AGN à l'arrière-plan (Dadina et al., 2013; Sutton et al., 2015), une confirmation spectroscopique de nos candidats HLX serait souhaitable. Bien que notre utilisation des redshifts photométriques soit efficace pour éliminer la plupart des contaminants de fond (y compris dans IC 4320, Sutton et al. 2015), comme le suggèrent nos estimations du nombre de contaminants restants (Section 5.4.5), ils ne sont disponibles que pour $\sim 15\%$ de notre échantillon HLX et sont nécessairement moins fiables que les redshifts spectroscopiques. La confirmation de certains candidats comme trous noirs dans une galaxie naine en fusion pourrait être basée sur la présence ou l'absence de raies d'émission typiques des AGN, par exemple à comparer avec un scénario les considérant comme des ULX extrêmes dans une région de formation d'étoiles.

Notre échantillon est le résultat d'une recherche étendue d'IMBHs sélectionnés en rayons X à partir des plus grands catalogues publiés à ce jour, avec une grande attention portée à l'élimination des contaminants. Ainsi, un nombre significatif d'IMBHs locaux confirmés confirmerait qu'il est possible de faire une recherche systématique d'IMBHs dans les futures observations en lumière visible et en rayons X, capable de mieux contraindre la croissance des trous noirs de masse intermédiaire par accrétion. Ce travail a suggéré que les trous noirs massifs par accrétion sont bien à la portée des observatoires actuels, contrairement aux affirmations précédentes (par exemple, Bellovary et al. 2019). Il est important de noter que notre échantillon peut être comparé aux futurs échantillons HLX pour mieux connaître nos biais de sélection et évaluer la localisation intrinsèque des IMBHs dans le plan $M_{BH} - M_*$.

Deuxièmement, certains candidats AGN et HLX disposent d'observations contemporaines archivées dans les rayons X et optiques/UV (provenant des télescopes *XMM-Newton* OM ou *Swift* UVOT), y compris un certain nombre de sources montrant des signes de variabilité dans ces longueurs d'onde. L'analyse spectrale et temporelle de ces données pourrait permettre d'affiner notre connaissance de ces sources. Par exemple, un travail en cours porte sur l'évolution des HLXs dans un diagramme dureté-intensité, comme cela a déjà été étudié pour les ULXs par Gúrpide et al. (2021) (Amato et al. in prep). Les spectres et les contreparties visibles de certains candidats HLX sont en cours d'étude (Parra et al. in prep, Pellouin et al. in prep). Ces études pourraient finalement nous permettre d'évaluer la capacité des installations actuelles et futures de l'astronomie résolue en temps (comme l'observatoire Vera Rubin, Section 9.2.4) à les trouver.

L'imagerie à haute résolution des candidats AGN, dans les longueurs d'onde visibles ou infrarouges (par exemple avec le HST ou le JWST), fournira des informations supplémentaires sur leur environnement, comme la présence d'un amas d'étoiles nucléaires ou d'un bulbe, en étudiant leurs profils de luminosité (comme l'ont déjà fait Koliopanos et al. 2017 et Graham et al. 2021 sur un certain nombre

d'AGN de faible luminosité). La spectroscopie à intégrale de champ des environs du candidat peut fournir des contraintes supplémentaires sur la nature de l'AGN et la rétroaction de la source (e.g. Mezcua and Domínguez Sánchez, 2020). De même, un suivi radio sensible et à haute résolution spatiale sera essentiel pour contraindre la masse de l'accréteur (en utilisant le plan fondamental et/ou la morphologie de la source), et pour distinguer certains candidats d'un ULX de masse stellaire (Mezcua et al., 2013). Si nos estimations de masse de premier ordre sont fiables, le flux radio des trous noirs avec $M_{BH} \gtrsim 5 \times 10^4 M_\odot$ commence à être tout juste à la portée des installations radio modernes telles que le VLA (le bruit RMS $\sim 2\mu$ Jy beam^{-1} du VLA après une exposition de dix heures résulte en une détection de 4σ jusqu'à 20 Mpc d'un tel trou noir ayant une luminosité en rayons X de 3×10^{39} erg s^{-1}, en utilisant le plan fondamental de Plotkin et al. 2012). Ces observations devraient être menées en même temps que les nouvelles observations de rayons X, afin d'assurer le même état spectral en rayons X et en radio pour obtenir des estimations plus robustes (Gültekin et al., 2019).

Dans l'échantillon propre de candidats AGN, 25 sources ont des détections avec au moins 100 coups de rayons X, permettant leur étude spectrale avec des données d'archives. Cette analyse, ainsi que celle des HLXs potentiellement nouvellement observés, pourrait contraindre les composantes thermiques et comptonisées du spectre, et donc leur état d'accrétion, et ainsi fournir une meilleure estimation de leur rapport d'Eddington que ce que nous avons fait avec les ajustements spectraux automatisés de quelques candidats (Figure 7.4). Cela permettrait également de modéliser la composante d'absorption et de dériver des luminosités et des masses de trous noirs corrigées de l'absorption. En outre, cela révélera si les sources faibles en rayons X de notre échantillon sont intrinsèquement faibles (c'est-à-dire un rapport d'Eddington inhabituel ou une faible masse de trou noir) ou fortement obscurcies (Dong et al., 2012). Parmi les ULX extrêmes de notre échantillon ($5 \times 10^{40} < L_X < 10^{41}$ erg s^{-1}), une étude spectrale détaillée pourrait également découvrir des candidats de type HLX et réduire le biais de sélection actuel envers les trous noirs massifs et à accrétion efficace.

Par ailleurs, une autre amélioration appréciable dans l'étude des galaxies naines hébergeant des AGN serait d'affiner les estimations de leur masse stellaire et de leur taux de formation stellaire, par exemple en utilisant la méthode basée sur l'infrarouge moyen de Parkash et al. (2018) et en obtenant des estimations de SFR à partir de données dans l'UV lointain ou de $H\alpha$, car nos estimations dans l'infrarouge moyen ne sont pas adaptées aux galaxies de type précoce (c'est-à-dire lenticulaires ou elliptiques) et sont susceptibles d'être biaisées en présence d'un AGN (Cluver et al., 2017; Latimer et al., 2021). Cela permettrait une étude robuste du profil de la fraction active en fonction de la luminosité en rayons X, et donc de confirmer ou d'infirmer notre résultat provisoire sur la fraction d'occupation.

9.2.2 Potentiel des recherches dans les archives

Cette étude a démontré le potentiel des recherches dans les archives pour trouver des sources rares. La publication prochaine de la version actualisée des catalogues *XMM-Newton*, *Swift* et *Chandra* sera d'un grand intérêt pour compléter l'échantillon actuel. Ceci est particulièrement vrai pour les observations *Chandra*, incluses seulement jusqu'en 2014 dans le catalogue actuel. Elles fournissent le relevé ayant la sensibilité et la résolution angulaire les plus élevées, qui est donc particulièrement adapté pour étendre l'étude à des redshifts plus élevés, comme cela a été fait dans Mezcua et al. 2018 pour les AGN dans les naines et Barrows et al. 2019 pour les HLXs.

Pour la recherche d'AGN dans les naines, l'utilisation de catalogues de galaxies plus complets et plus fiables sera particulièrement intéressante. D'après la figure 6.11, au moins 40 % des galaxies naines existantes n'ont pas de masse stellaire indiquée dans GLADE.

De même, les prochains catalogues de galaxies utilisant des études profondes en lumière visible seront essentiels pour étendre la recherche de HLX et d'AGN dans les galaxies naines à des redshifts plus élevés, comme l'a déjà fait Barrows et al. (2019) pour les galaxies SDSS. Ceci est illustré par la figure 9.1, qui compare la complétude de GLADE, GLADE+ et du catalogue de galaxies DESI (fournissant des estimations de masse stellaire) de Zou et al. (2022). Contrairement à GLADE+, ce catalogue contient des informations sur l'étendue de chaque galaxie, offrant ainsi une possibilité immédiate d'étendre notre étude.

Tandis que notre échantillon local d'IMBHs peut donner une vision biaisée des graines de trous noirs en raison de la croissance significative qui peut se produire dans les galaxies naines, une vision

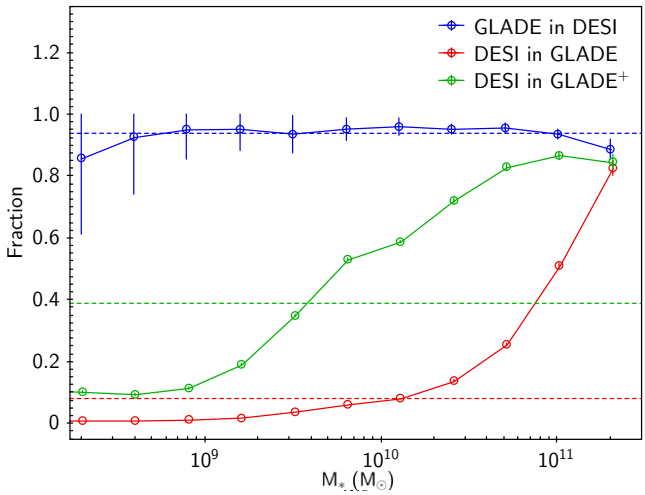

Figure 9.1: Fraction de complétude de différents relevés de galaxies, estimée en les comparant entre eux. Bleu, vert : fraction de galaxies GLADE (resp. GLADE+) dans l'échantillon de galaxies DESI de Zou et al. (2022) à $z < 0.2$. Vert : fraction des galaxies DESI de Zou et al. (2022) dans le catalogue GLADE.

non biaisée des graines de trous noirs supermassifs pourrait être obtenue dans un avenir proche en recherchant des quasars à haut redshift.

Déjà entamée ces dernières années, cette recherche a principalement utilisé des coupures de couleur dans les bandes photométriques optiques, en utilisant la technique dite du "i-dropout" (voir par exemple Fan et al. 2006; Jiang et al. 2016). En effet, le redshift $z \gtrsim 5$ de ces quasars conduit au déplacement de la cassure de Lyman vers la bande i. Cependant, les sources rouges sélectionnées avec ces critères sont susceptibles d'être pour la plupart des contaminants, notamment des naines brunes et des galaxies de type précoce, ce qui souligne la nécessité d'une approche plus probabiliste (Mortlock et al., 2012). Des tentatives ont donc été faites pour développer un cadre bayésien (Mortlock et al., 2012) ou probabiliste (Reed et al., 2017; Nanni et al., 2022) pour sélectionner des quasars fiables à haut redshift à l'aide de données visibles. En complément de ces méthodes, l'ajout de données en rayons X pourrait être extrêmement utile pour mieux éliminer les contaminants, accéder aux AGN très obscurcis - qui sont plus fréquents à haut redshift (Vito et al., 2018) - et trouver les quasars à haut redshift les plus massifs et les plus accrétants (Vito et al., 2019; Lusso et al., 2022).

En guise de test préliminaire, nous avons étudié un échantillon de ~ 400000 sources 4XMM-DR11 dans l'empreinte des relevés en lumière visible larges et profonds DES, BASS et PanSTARRS, afin de rechercher de nouveaux quasars à haut redshift avec notre classification. Des contreparties visibles ont été identifiées avec le logiciel NWAY (comme détaillé dans le chapitre 3) pour 70 % de l'échantillon. En partant du constat que les quasars à haut redshift sont souvent sélectionnés photométriquement par leurs couleurs optiques, nous ajoutons une colonne pour chacune des trois couleurs $g-r$, $r-z$ et $g-z$. Pour ce travail, en première approximation des types que nous devons distinguer afin d'isoler les quasars à haut redshift (définis ici comme un redshift $z > 5$), nous distinguons cinq classes : quasar à haut redshift (HZQ), Seyfert I à faible redshift (Sy1), Seyfert II à faible redshift (Sy2), jeunes objets stellaires (YSO) et étoiles normales (Star). Un échantillon d'entraînement de ces sources a été identifié par une corrélation croisée dans un rayon de $3 \times POSERR$ (où $POSERR$ est l'erreur de position de la source de rayons X) avec la base de données *Simbad*. Elle contient 23 quasars connus à haut redshift, et nous notons comme premier avertissement que cela est nettement insuffisant pour inférer les densités de propriétés. Pour cette raison, le surajustement devient un problème et nous choisissons de ne pas optimiser le classifieur. Les probabilités a priori sur chaque classe sont arbitrairement fixés à $\mathcal{P}(\text{HZQ}) = 0,02$, $\mathcal{P}(\text{Sy1}) = 0,53$, $\mathcal{P}(\text{Sy2}) = 0,25$, $\mathcal{P}(\text{YSO}) = 0,05$ et $\mathcal{P}(\text{Star}) = 0,15$.

Deux classifieurs sont testés, l'un imposant $\beta = 0$ (i.e. les valeurs manquantes sont ignorées) et l'autre avec $\beta = 1$ (i.e. la probabilité d'une valeur manquante donnée à une classe est la fraction de cette classe ayant une valeur manquante dans l'échantillon d'entraînement). La matrice de confusion pour le premier classifieur est présentée dans le tableau 9.1. En conséquence de cette classification approximative, nous récupérons quand même 3 HZQ de l'échantillon d'entraînement, sans aucun faux positif. Nous notons que ce compromis entre récupération et précision donne un score $f1$ inférieur à

	HZQ	Sy1	Sy2	YSO	Star	Precision
→HZQ	3	0	0	0	0	100%
→Sy1	18	1648	207	9	4	82%
→Sy2	2	103	349	51	20	81%
→YSO	0	0	0	810	159	91%
→Star	0	0	1	83	5489	97%
Recall	13%	94%	63%	85%	97%	

Table 9.1: Matrice de confusion résultant de la classification de l'échantillon d'entraînement de 4XMM-DR11 pour la recherche de quasars à haut redshift.

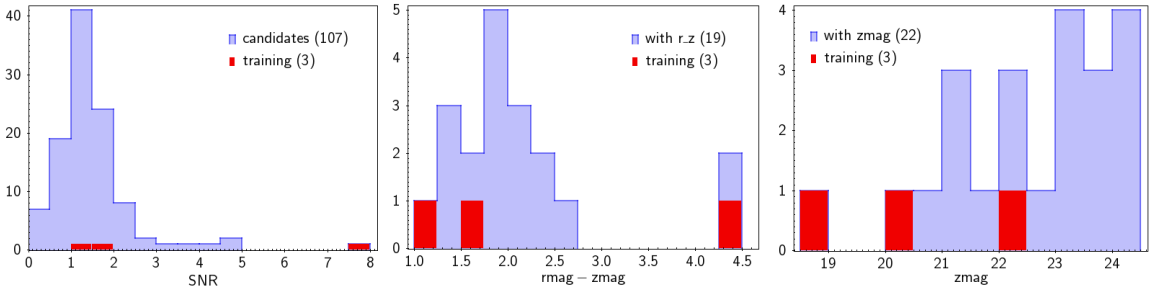

Figure 9.2: Distributions de certaines propriétés dans l'échantillon de candidats quasars à haut redshift. Les trois quasars connus et bien classés sont représentés en rouge. (Gauche) : Rapport signal/bruit, (milieu) couleur $r - z$, (droite) : Magnitude apparente z (AB).

celui du deuxième classifieur tenant compte des valeurs manquantes (identifiant 13 HZQ plus 27 faux positifs), mais avec une meilleure précision, ce qui est plus pertinent dans cette recherche.

Dans l'échantillon test, 107 (87760) candidats AGN sont identifiés par le premier (resp. le second) classifieur. Cela montre encore le biais introduit ici par les valeurs manquantes, qui sont plus présentes dans la classe des HZQ que dans les autres (par exemple, 5 des 23 HZQ connues ont une magnitude g manquante, en raison de leur redshift). Les distributions de S/N, $r - z$ et z pour les 107 candidats HZQ sont présentées sur la figure 9.2, avec les 3 HZQ connus indiqués en rouge.

Après avoir appliqué des coupures de qualité raisonnables ($S/N > 1$, $z < 23.5$ et $r < 26.5$), il ne reste que trois candidats (Figure 9.3) : 4XMM J022730.3-052820, 4XMM J023127.6-072049 et 4XMM J034536.7-534020. Les deux premiers sont très probablement trop durs pour être localisés à haut redshift, et le dernier est identifié comme une radiogalaxie (Johnston-Hollitt et al., 2008).

De ce premier essai, nous pouvons conclure que notre technique de classification n'est pas encore prête à identifier les quasars à haut redshift dans les archives actuelles, surtout en raison du petit échantillon d'entraînement. Cependant, avec la grande variété de relevés à venir ciblant cette population, une telle approche est susceptible de devenir utile. Par ailleurs, une approche plus naturelle et prometteuse consiste à utiliser l'estimation du redshift plutôt que la classification, comme cela est fait aujourd'hui dans les travaux d'estimation du redshift photométrique. Ces deux approches sont susceptibles d'être plus utiles en combinaison, la première menant à une élimination efficace des contaminants et la seconde à une estimation précise du redshift. Par conséquent, les travaux en cours

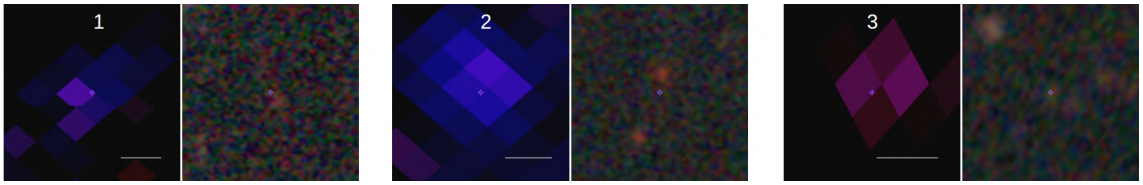

Figure 9.3: Candidats à haut redshift identifiés par le classifieur dans l'archive 4XMM-DR11. Pour chaque candidat, les images en rayons X (*XMM-Newton*) et en lumière visible (DES) sont présentées. La ligne blanche représente 5 secondes d'arc. (Gauche) : 4XMM J022730.3-052820, (Milieu) : 4XMM J023127.6-072049, (Droite) : 4XMM J034536.7-534020.

dans le cadre de la collaboration XMM2ATHENA visant à cumuler les images de rayons X pour atteindre des sensibilités plus élevées, à calculer les redshifts photométriques en tenant compte des données en rayons X, et à classer automatiquement les sources de rayons X, pourraient donner des résultats prometteurs dans un avenir proche. Quant à l'avenir plus lointain, une perspective est présentée dans la section 9.2.4.

9.2.3 La science participative, complément de la classification automatique

Comme nous l'avons vu dans la Section 7.1, l'efficacité de la classification automatique des sources de rayons X est entravée par de petits échantillons d'entraînement. À cet égard, le développement de la plateforme de science participative CLAXSON (CLAssification of X-ray SOurces for Novices, https://xmm-ssc.irap.omp.eu/claxson, voir la Section 4.6), qui vise précisément à élargir ces échantillons d'entraînement, est particulièrement intéressant. Bien que seules quatre classes soient incluses dans l'expérience à ce jour, à savoir AGN, étoile, binaire à rayons X et " autre chose", nous avons constaté que les sources classées par un nombre suffisamment élevé ($\gtrsim 20$) de volontaires présentent des classifications très précises.

Compte tenu des résultats préliminaires encourageants et de l'intérêt suffisant des utilisateurs, la prochaine étape du développement de CLAXSON sera de le diffuser auprès d'un large public, ce qui nous permettra d'obtenir rapidement des résultats sur un plus grand échantillon. Après avoir soigneusement estimé les biais de classification, une première publication de données de classification de sources 4XMM par inspection visuelle devrait être publiée. Cela ouvrira la voie à des études de classification plus fines, avec le potentiel de permettre des études de population précises de la large gamme d'émetteurs de rayons X avec une très faible contamination. Les améliorations futures comprendront une extension de l'expérience au catalogue *Chandra* et peut-être un appel à des volontaires pour classer des populations spécifiques de rayons X (par exemple, les candidats ULX, les candidats XRB galactiques, les candidats TDE...) de temps en temps. La communauté de l'astrophysique des rayons X pourrait également bénéficier de la plateforme, qui offre un accès immédiat à plusieurs fonctionnalités de l'observatoire virtuel. En outre, une section de commentaires est ouverte sous chaque source individuelle sur CLAXSON, ce qui pourrait favoriser des discussions fructueuses sur la nature d'une source et élargir l'éventail des découvertes sérendipiteuses possibles grâce à l'intelligence collective.

En plus de la classification des sources, les expériences de science participative peuvent fournir d'autres informations utiles. L'ajout d'une fonctionnalité de dessin aux champs de vue des sources peut permettre aux volontaires d'identifier des sources ayant des formes particulières ou situées dans des environnements particuliers, comme cela a déjà été mis en œuvre dans Zooniverse[1]. Cela pourrait être particulièrement intéressant pour signaler les sources sujettes à une confusion, identifier de nouvelles galaxies ou des contreparties visibles non détectées par les procédures usuelles de traitement des relevés, ou corriger des mesures de D_{25} manifestement erronées dans les catalogues de galaxies. Une partie de la valeur de toute expérience de science participative réside également dans l'opportunité de rendre la science accessible et attrayante pour un large public, comme pour toute activité de vulgarisation. Un grand effort a donc été consacré à la traduction de la plateforme en cinq langues (anglais, français, espagnol, italien et grec), et à la promotion de l'implication scientifique des volontaires, avec la diffusion d'une enquête auprès des utilisateurs[2] visant à améliorer encore le protocole et la conception de CLAXSON.

9.2.4 Futures études de populations liées aux IMBHs

Comme discuté dans la Section 2.5.2, les IMBHs peuvent être détectés à partir de signatures diverses, alors que dans cette thèse nous nous sommes concentrés sur les galaxies naines et les HLXs observés en rayons X. Une connaissance plus complète de la population des IMBHs sera probablement acquise au cours des deux prochaines décennies, grâce à des observatoires multi-longueurs d'onde et multi-messagers.

[1] La dernière version des expériences Galaxy Zoo, regroupant également un certain nombre d'autres expériences de science citoyenne sans rapport entre elles. https://www.zooniverse.org/

[2] https://forms.gle/tgFMujfdLUTGUjxcA

AGN dans les galaxies naines

Il est peut-être inapproprié de chercher à contraindre les graines de trous noirs à haut redshift à partir des propriétés des galaxies naines locales, en raison de la croissance potentiellement élevée de leur trou noir depuis cette époque (e.g., Mezcua 2019). Pour remédier à ce problème, et acquérir une vision plus représentative des graines primordiales de trous noirs supermassifs, il est nécessaire d'observer les AGN à plus grand redshift, qui ont eu moins de temps pour évoluer. À des redshifts $z \gtrsim 1$, ce recensement est actuellement limité par la sensibilité des observatoires en rayons X (en rayons X l'AGN le plus distant détecté dans une galaxie naine a été détecté à $z = 2.4$ dans le relevé *Chandra* COSMOS-Legacy Survey possédant un temps d'exposition de ~ 100 ks par champ, Mezcua et al. 2018).

En ondes radio, les observatoires actuels semblent déjà sonder de plus grands redshifts dans les relevés suffisamment larges et profonds, comme le relevé VLA-COSMOS dans lequel un candidat AGN a été trouvé à redshift photométrique $z_{ph} = 3.4$ (Mezcua et al., 2019). Les galaxies naines à l'époque de la réionisation, et les premières graines de trou noir, pourraient être révélés par les observations du JWST (Section 9.2.4).

Un moyen alternatif Une autre solution consisterait à étudier les candidats AGN dans des analogues fiables de galaxies à haut redshift soigneusement sélectionnés , comme ce pourrait être le cas des galaxies naines extrêmement pauvres en métaux (Mezcua, 2019). Puisque de telles galaxies sont nécessairement rares dans l'Univers local, les observations radio capables d'observer des trous noirs faiblement accréteurs avec une faible contamination par les XRBs pourraient être les mieux adaptées pour construire une grande population. Par exemple, le Very Large Array de nouvelle génération (ngVLA, e.g. Murphy et al. 2018) et le Square Kilometer Array (SKA, e.g. Lazio 2009) devraient atteindre des sensibilités de quelques dizaines de nJy, ce qui permettrait de détecter un IMBH de $10^4 M_\odot$ en accrétion faible $L_X \lesssim 10^{39}$ erg s^{-1} à 100 Mpc, ou un IMBH de $10^3 M_\odot$ accrétant à $L_X \lesssim 10^{38}$ erg s^{-1} à 25 Mpc, d'après le plan fondamental de Plotkin et al. (2012). Ceci est particulièrement intéressant étant donné la grande fraction ($\sim 75\%$) du ciel couverte par SKA. La résolution de ~ 10 mas atteinte (équivalente à 5 pc à 100 Mpc) permet dans de nombreux cas de distinguer la nébuleuse radio d'un ULX de l'émission compacte (ou à l'inverse, des grands jets radio) d'un trou noir massif (Mezcua et al., 2013; Sargent et al., 2022). Sur un autre sujet, SKA devrait détecter presque tous les IMBHs quiescents dans notre galaxie, ou bien fixer des limites supérieures strictes sur leur masse (Acero et al., 2017).

Quoi qu'il en soit, l'importance de la rétroaction des AGN et des fusions mineures dans l'évolution des galaxies naines et de leur trou noir est loin d'être établie, et une meilleure connaissance de ces galaxies peu lumineuses et particulières ne pourra être obtenue que par de futurs observatoires.

Sources X hyperlumineuses

La densité de HLXs dans les galaxies de champ de l'Univers local, déduite dans la section 7.6, signifie qu'environ 260 candidats dans un rayon de ∼160 Mpc pourraient être détectés au-dessus de la limite de sensibilité de 10^{-14} erg cm^{-2} s^{-1} du relevé du ciel entier eROSITA une fois terminé (Merloni et al., 2012), et ~ 20 HLXs dans le volume de rayon 70 Mpc couvert par la publication à venir des données eRASS1 à une luminosité limite $< 10^{41}$ erg s^{-1}[3].

Les sensibilités plus profondes du télescope *Athena*-WFI (Nandra et al., 2013) dans la bande plus large $0.2 - 15$ keV conduiront à l'augmentation la plus significative du recensement des HLXs. Le relevé *Athena+* WFI (Lanzuisi et al., 2017; Nandra et al., 2013), couvrant plus de 50 deg^2 à une sensibilité de $\sim 7 \times 10^{-17}$ erg cm^{-2} s^{-1} et conçu pour atteindre les objectifs scientifiques *Athena*[4] pour l'observation des quasars à haut redshift, donnera accès (dans cette couverture) à tous les HLX de $L_X > 10^{41}$ erg s^{-1} jusqu'au redshift $z = 0.6$, et à tous les HLX de $L_X > 10^{42}$ erg s^{-1} jusqu'au redshift $z = 1.5$. Cela représente respectivement ~ 3400 et ~ 7000 objets. Certains hôtes galaxie naine des HLXs peuvent subir une fusion mineure avec l'hôte massif (Section 7.3.4), mais la fraction de ces HLXs est jusqu'à présent inconnue. De tels échantillons ouvrent la possibilité d'étudier comment le

[3]Un facteur de conversion $L_{0.\ 5\text{–}2\ \mathrm{keV}} \approx 0,3 L_{0,2\text{–}10\ \mathrm{keV}}$, donné par le modèle en loi de puissance absorbée ($\Gamma = 1,7$, $n_H = 3 \times 10^{20}$ cm^{-2}), est utilisé pour obtenir ces estimations de premier ordre. Notez que les rares HLX mous seront plus faciles à détecter avec eROSITA, et que la plupart des autres HLX sont probablement plus durs que ce modèle. L'utilisation de la densité de colonne médiane de Barrows et al. (2019) $n_H = 6 \times 10^{21}$ cm^{-2} diminue ces estimations par un facteur 2.

[4]à ce jour, il est cependant difficile de savoir si la mission *Athena* ou son équivalent atteindra cet objectif, étant donné l'importante redéfinition de l'instrument qui a récemment commencé.

nombre et les propriétés des HLX évoluent avec le temps cosmique, et donc de contraindre davantage la croissance des graines de trous noirs supermassifs par accrétion pendant les fusions de galaxies.

Bien que notre échantillon HLX soit susceptible d'avoir un fort biais de sélection vers les trous noirs à accrétion efficace, de nouvelles antennes radio sensibles pourraient détecter la majeure partie des trous noirs massifs dans les galaxies naines (Section 9.2.4) et les séparer des populations ULX de masse stellaire.

Événements de rupture par effet de marée et éruptions quasi-périodiques

Parce que les TDEs off-nucléaires ont déjà révélé deux des meilleurs candidats IMBH connus à ce jour (Farrell et al., 2009; Lin et al., 2018), et parce que leurs courbes de lumière permettent une estimation préliminaire de la masse du trou noir (Mockler et al., 2019), ils représentent une voie prometteuse pour la recherche d'autres IMBHs. Ceci est d'autant plus vrai que les TDEs ne sont détectables que pour des trous noirs de "faible" masse ($\lesssim 10^8 M_\odot$), avec un rayon de marée au-delà de leur horizon des événements pour une étoile de masse stellaire de la séquence principale, et que les TDEs offrent un moyen d'observer des trous noirs qui sont habituellement en quiescence. Jusqu'à présent, les raisons pour lesquelles aucun TDE hors noyau n'a été détecté en lumière visible ne sont pas claires. Les installations sensibles actuelles et futures pour l'astronomie résolue en temps seront donc essentielles pour accéder à la population des trous noirs de faible masse, pour contraindre leurs propriétés et pour mieux sonder la fonction de masse intrinsèque des trous noirs.

En particulier, l'observatoire Vera Rubin, qui observera de manière répétée près de la moitié du ciel, devrait permettre de détecter entre 3500 et 8000 TDE par an, selon la distribution de masse des trous noirs supermassifs (van Velzen et al., 2011; Bricman and Gomboc, 2020). La stratégie de cadence d'observation du relevé de l'observatoire Vera Rubin (le Large Survey of Space and Time, ou LSST) sera probablement irrégulière et n'est pas encore décidée au moment de la rédaction de cette thèse (e.g. Bricman and Gomboc 2020; Bianco et al. 2022), mais elle sera d'environ une fois toutes les 3 ou 4 nuits en moyenne. C'est un paramètre clé pour estimer le nombre de TDE détectables par des trous noirs de faible masse $\lesssim 10^5 M_\odot$, ayant généralement des décroissances plus rapides que les TDEs par des trous noirs de masse supérieure (Section 2.3.3). En raison de cette décroissance plus rapide et d'un pic de luminosité plus faible, environ 1000-2000 TDEs par des trous noirs de masse $\lesssim 10^5 M_\odot$ pourraient être détectés pendant les 10 années du relevé (Figure 7 de Bricman and Gomboc 2020). Par ailleurs, les IMBHs en accrétion pourraient être découverts en plus grand nombre par cet observatoire en utilisant les signatures de variabilité des AGN (Baldassare et al., 2020; Burke et al., 2022), cependant cela ciblera les trous noirs qui accrètent activement.

Dans le domaine des rayons X, on s'attend à ce qu'eROSITA détecte plusieurs milliers de TDEs une fois que le relevé sera terminé (Khabibullin et al., 2014). Cependant, une fois de plus, les trous noirs de $10^7 M_\odot$ seront mieux échantillonnés que les trous noirs de masse inférieure, et la cadence de 6 mois d'eROSITA pourrait bien être insuffisante pour les étudier correctement : un suivi approprié par des observations *XMM-Newton*, *Swift* ou *Chandra* sera alors nécessaire pour analyser les candidats les plus intéressants. Notons que le candidat IMBH 4XMM J215022.4-055109 ne semble pas suivre cette tendance, puisque son éruption a duré plusieurs années (Lin et al., 2018), et que l'on trouve même des TDEs qui durent une décennie (Lin et al., 2017, 2022).

Toutefois, les perspectives de découverte d'IMBHs pourraient être encore meilleures que celles présentées ci-dessus, avec la découverte d'une nouvelle classe d'objets, plus rares que les TDEs, les "éruptions quasi périodiques" ou QPEs (Miniutti et al., 2019). Deux d'entre eux ont déjà été détectés avec les observations eROSITA (Arcodia et al., 2021). Nous manquons encore d'un modèle robuste pour décrire les quelques QPEs découverts jusqu'à présent, cependant ces objets semblent être globalement compatibles avec des événements partiels de rupture par effet de marée sur des trous noirs de faible masse ($\sim 10^5 M_\odot$) (Miniutti et al., 2022). Si cela est confirmé, la nature répétitive des QPEs sera particulièrement bienvenue afin d'en détecter davantage et de mieux étudier l'accrétion sur ces trous noirs de faible masse, habituellement quiescents.

Mesures dynamiques

Récemment, les études dynamiques ont conduit à la première limite supérieure stricte sur la fraction d'occupation des galaxies naines (Nguyen et al. 2019, discuté dans la section 7.5). Cependant, les détections dynamiques d'IMBHs sont fortement limitées aux masses élevées en raison d'une résolution angulaire et d'une sensibilité limitées, et de nombreux candidats précédents se sont révélés être peu

fiables (Greene et al., 2020). Dans la prochaine décennie, cette limite sera largement repoussée avec l'avènement des télescopes de 30m (Extremely Large Telescopes ou ELTs). Leur résolution angulaire (meilleure que 4mas/pixel), combinée à la spectroscopie à intégrale de champ (comme l'instrument HARMONI sur l'ELT), permettra la détection dynamique de nombreux trous noirs de $10^3 - 10^5 M_\odot$ dans notre Volume Local (Greene et al., 2019).

Quasars à haut redshift

La recherche et l'étude des quasars à haut redshift est l'une des voies les plus prometteuses pour contraindre directement la croissance des trous noirs supermassifs. Au cours des deux prochaines décennies, de nombreuses installations devraient s'attaquer à ce cas scientifique dans une large gamme de longueurs d'onde. De nombreuses questions restent ouvertes, comme celle de savoir quand les premières galaxies ont grandi, comment leur activité de formation d'étoiles a évolué, comment elles ont acquis leurs trous noirs, et quel rôle les fusions de galaxies, les AGN et les supernovae ont joué dans ces évolutions respectives.

Alors qu'il y a dix ans, seuls les quasars les plus brillants pouvaient être détectés à $z > 6$, les progrès récents des relevés spectroscopiques profonds (et en particulier le relevé Hyper-Supreme Cam Subaru) ont permis de détecter plus d'une centaine de quasars de plus faible luminosité. Leurs raies visibles suggèrent des masses de trous noirs de l'ordre de $10^{7.6} - 10^{9.3} M_\odot$, et leur luminosité suggère une accrétion inférieure à 10% de la limite d'Eddington (Onoue et al., 2019; Matsuoka et al., 2022), réduisant ainsi le biais de détection et permettant de mieux sonder la masse des quasars à haut redshift.

Le recensement en rayons X des quasars à haut redshift grimpera en flèche avec le télescope *Athena* s'il est maintenu à son niveau de spécification actuel, détectant des centaines d'AGN à $z > 6$ et même certains d'entre eux à $z > 8$ (Nandra et al., 2013). Ce saut de performance est notamment permis par l'utilisation d'optiques à silicium poreux, permettant de combiner un grand champ de vision, une grande sensibilité et une haute résolution angulaire (Barrière et al., 2022). Dans la bande radio, il est intéressant de noter que SKA et ngVLA devraient également être en mesure d'observer certains trous noirs à effondrement direct à redshift $z \sim 7$ (Whalen et al., 2020).

Fusions de trous noirs

Dans le domaine des ondes gravitationnelles, la première détection par LIGO/Virgo d'un IMBH de masse $\sim 140 M_\odot$ (Abbott et al., 2020a) a démontré que de tels trous noirs se forment à des taux détectables dans l'Univers local, à partir de la fusion de trous noirs plus petits. Le quatrième cycle d'observation, qui débutera en 2023, sera sensible aux fusions de trous noirs de masse $\lesssim 200 M_\odot$ et devrait permettre de détecter un plus grand nombre de ces événements à un redshift $z < 0,5$ (au moins pour les systèmes binaires à rapport de masse intermédiaire, composées d'un IMBH et d'un objet compact de masse stellaire, Arca Sedda et al. 2021). Certaines fusions formant des trous noirs de $10^3 M_\odot$ pourraient également être détectables par LIGO/Virgo/KAGRA si la sensibilité nominale est atteinte (Fragione et al., 2018; Mehta et al., 2022).

Les fusions de trous noirs plus massifs peuvent être partiellement découvertes dans l'Univers proche à l'aide de signaux électromagnétiques : des AGN binaires ont déjà été détectés dans un certain nombre de galaxies présentant des signatures de fusion (Volonteri et al., 2021), y compris un système dont il a été récemment affirmé qu'il fusionnerait dans les prochaines années d'après sa courbe de lumière visible (Dotti et al., 2022). Les observations en rayons X et en lumière visible-UV peuvent fournir un moyen de trouver davantage de ces objets qui sont de forts émetteurs UV, et leur recherche dans les observations *XMM-Newton* EPIC et les observations OM font l'objet d'un travail en cours (Foustoul, Webb et al. in prep). En préparant la science de LISA, ces études seront essentielles pour évaluer l'importance du canal des fusions dans la croissance des trous noirs supermassifs.

Dans un avenir plus lointain, LISA représentera un pas de géant pour la science des trous noirs. Sa sensibilité sans précédent et sa bande passante de 0,1 mHz – 1 Hz permettront la détection et l'étude de la plupart des fusions à partir de progéniteurs de masse intermédiaire jusqu'à des redshifts extrêmement élevés, $z \sim 20$ (Bellovary et al., 2019). Particulièrement sensible aux IMBH de masse supérieure à $\sim 10^3 M_\odot$, il sera crucial pour rassembler un grand échantillon de graines de trous noirs et d'étudier leur formation et leur évolution. Les canaux de formation tels que le scénario d'effondrement direct et l'importance des fusions dans la croissance des trous noirs supermassifs seront contraints de manière efficace (Hartwig et al., 2018; Woods et al., 2019).

Complémentaire à ces installations, le télescope Einstein, une mission terrestre proposée pour

fonctionner dans la bande 2 Hz – 2 kHz, sondera les trous noirs distants ($z \sim 1 - 5$) de masse $\lesssim 2 \times 10^3 M_\odot$ (Maggiore et al., 2020). Elle pourra ainsi révéler des fusions de rémanents d'étoiles de Population III à un redshift modéré, notamment dans des galaxies extrêmement pauvres en métaux et en étoiles, dans lesquelles la croissance des trous noirs est censée être pratiquement supprimée.

Appendices

Appendix A

List of candidates

Name	RA deg	Dec deg	$POSERR$ arcsec	F_X erg cm^{-2} s^{-1}	D Mpc	Gal. type	Sep. kpc	L_X erg s^{-1}	M_{BH} M$_\odot$	$M_{*,\mathrm{Bell}}$ M$_\odot$	Subsample
2CXO J001143.2-285548	2.9303	-28.9301	1.1	1.4×10^{-14}	267.9	E	11.2	1.2×10^{41}	2.5×10^{4}	1.8×10^{7}	robust
2CXO J002234.1+001609	5.6424	0.2693	0.7	3.7×10^{-15}	485.3	S0^{0}	15.6	1.0×10^{41}	2.3×10^{4}		robust
2CXO J005151.7+474019	12.9658	47.6720	0.8	1.8×10^{-14}	682.5		16.7	10.0×10^{41}	1.9×10^{5}		weak
2CXO J010739.2+541226	16.9134	54.2074	0.4	9.9×10^{-15}	497.8		14.3	2.9×10^{41}	4.1×10^{4}		robust
2CXO J011028.2-460422	17.6178	-46.0729	0.4	4.9×10^{-13}	90.9	S0^{+}	3.2	4.9×10^{41}			robust
2CXO J011751.9-265850	19.4664	-26.9808	1.3	8.5×10^{-15}	463.4		20.6	2.2×10^{41}	7.1×10^{4}		weak
2CXO J011854.9-010551	19.7288	-1.0976	0.5	2.0×10^{-14}	557.2	E	13.4	7.5×10^{41}	1.2×10^{5}		robust
2CXO J023659.5-511548	39.2481	-51.2636	2.8	4.7×10^{-14}	343.6		24.6	6.6×10^{41}	1.1×10^{5}	5.8×10^{7}	robust
2CXO J024106.1-081711	40.2757	-8.2865	0.6	3.3×10^{-15}	636.8		24.6	1.6×10^{41}	2.3×10^{4}		robust
2CXO J024228.5-000202	40.6188	-0.0340	0.4	7.1×10^{-15}	691.8	E	27.3	4.1×10^{41}	8.8×10^{4}		robust
2CXO J025843.0-523930	44.6794	-52.6584	0.5	4.7×10^{-15}	428.3		9.5	1.0×10^{41}			robust
2CXO J025921.5+132913	44.8398	13.4871	0.6	8.0×10^{-15}	487.5		8.2	2.3×10^{41}	3.0×10^{4}		galaxy pair
2CXO J031049.4-265431	47.7062	-26.9088	0.8	2.0×10^{-14}	597.0		14.8	8.6×10^{41}	1.6×10^{5}		robust
2CXO J034115.1+152335	55.3129	15.3932	0.4	2.7×10^{-14}	184.4		3.8	1.1×10^{41}	1.5×10^{4}	3.5×10^{7}	weak
2CXO J034231.8-533841	55.6325	-53.6449	0.4	2.3×10^{-14}	270.4	E	12.2	2.0×10^{41}	3.3×10^{4}		robust
2CXO J041338.6+102803	63.4112	10.4678	0.5	6.0×10^{-15}	405.5		10.7	1.2×10^{41}	1.7×10^{4}		robust
2CXO J043338.4-131612	68.4101	-13.2702	0.4	5.2×10^{-14}	141.9	S0^{-}	19.8	1.2×10^{41}	2.0×10^{4}		robust
2CXO J044921.6-485545	72.3403	-48.9294	0.9	6.7×10^{-15}	355.9		6.7	1.0×10^{41}	1.3×10^{4}		robust
2CXO J055107.0-570640	87.7793	-57.1111	0.5	1.5×10^{-14}	267.9		15.3	1.3×10^{41}	2.9×10^{4}		robust
2CXO J061620.8-215616	94.0867	-21.9379	0.5	1.8×10^{-14}	1.0×10^{3}		13.2	2.3×10^{42}	2.1×10^{5}		robust
2CXO J062648.6-543208	96.7028	-54.5357	0.4	7.5×10^{-14}	225.9	E	27.9	4.6×10^{41}	4.3×10^{4}		robust
2CXO J071051.5-561009	107.7150	-56.1694	0.8	1.9×10^{-14}	562.3		14.3	7.2×10^{41}	1.3×10^{5}		robust
2CXO J071644.9+372828	109.1875	37.4746	1.3	2.5×10^{-14}	317.9		14.0	3.0×10^{41}	4.0×10^{4}		robust
2CXO J074735.8+554113	116.8994	55.6870	0.5	4.0×10^{-14}	152.1		4.2	1.1×10^{41}	1.6×10^{4}	2.5×10^{9}	weak
2CXO J081654.4-073931	124.2271	-7.6588	1.4	1.3×10^{-14}	311.2		13.7	1.5×10^{41}	2.8×10^{4}		robust
2CXO J082215.9+210535	125.5665	21.0933	0.5	1.2×10^{-13}	92.3	S0^{-}	1.9	1.2×10^{41}	2.2×10^{4}	3.0×10^{10}	robust
2CXO J084128.8+322447	130.3700	32.4133	0.4	1.2×10^{-14}	295.1	S0^{0}	11.4	1.3×10^{41}	2.4×10^{4}		robust
2CXO J084135.0+010156	130.3962	1.0323	0.4	6.6×10^{-14}	503.5		7.0	2.0×10^{42}	3.8×10^{5}		galaxy pair
2CXO J091449.0+085321	138.7045	8.8892	0.4	6.8×10^{-13}	648.6	E	7.9	3.4×10^{43}	1.7×10^{7}		galaxy pair
2CXO J101239.8-010628	153.1662	-1.1078	0.5	9.5×10^{-15}	438.5	Sa	9.4	2.2×10^{41}	4.1×10^{4}	2.6×10^{4}	robust
2CXO J103619.8-273939	159.0827	-27.6610	0.9	8.6×10^{-15}	430.5	S0^{+}	27.1	1.9×10^{41}	2.9×10^{4}		robust
2CXO J103844.2+485220	159.6845	48.8724	0.4	9.2×10^{-15}	539.5		13.9	3.2×10^{41}	5.4×10^{4}		robust
2CXO J104142.2+400035	160.4262	40.0098	0.9	1.5×10^{-14}	642.7		24.7	7.6×10^{41}			galaxy pair
2CXO J105210.4+552243	163.0435	55.3786	0.5	6.9×10^{-15}	669.9	Sb	12.2	3.7×10^{41}	5.7×10^{4}		robust
2CXO J111610.0+013035	169.0418	1.5098	0.5	1.7×10^{-14}	500.9	Sbc	11.9	5.2×10^{41}	1.1×10^{5}		galaxy pair
2CXO J112002.6+132830	170.0112	13.4752	2.0	4.2×10^{-15}	586.1	Sc	20.6	1.7×10^{41}	2.2×10^{4}		robust
2CXO J112110.9+232331	170.2958	23.3922	0.6	4.2×10^{-15}	513.2	E	13.1	1.3×10^{41}	2.5×10^{4}		weak
2CXO J112255.5+010601	170.7313	1.1004	0.4	2.4×10^{-14}	342.0	E	17.5	3.4×10^{41}	8.1×10^{4}	3.3×10^{8}	weak
2CXO J121756.3+280941	184.4849	28.1615	0.5	1.2×10^{-14}	613.8	E	17.1	5.3×10^{41}	1.1×10^{5}		robust
2CXO J122155.1+271022	185.4796	27.1728	0.4	1.2×10^{-14}	363.1	E	6.4	1.9×10^{41}	2.0×10^{4}		robust
2CXO J123307.6+091942	188.2820	9.3285	0.6	3.3×10^{-14}	309.0	Sd	6.1	3.7×10^{41}	8.0×10^{4}		robust
2CXO J123605.6+163213	189.0235	16.5370	1.4	9.7×10^{-15}	318.0	E	12.5	1.2×10^{41}	1.3×10^{4}		weak
2CXO J124208.4+331854	190.5351	33.3151	0.4	8.9×10^{-14}	701.9	E	15.2	5.3×10^{42}	1.3×10^{6}		galaxy pair
2CXO J130155.9+291815	195.4833	29.3044	1.2	1.8×10^{-14}	776.2		30.3	1.3×10^{42}			robust
2CXO J131133.3-011656	197.8891	-1.2824	0.4	6.6×10^{-15}	895.4		22.3	6.3×10^{41}	1.2×10^{5}		weak
2CXO J131619.4+620610	199.0809	62.1029	0.9	1.4×10^{-14}	610.9	E	14.4	6.1×10^{41}	9.3×10^{4}		robust
2CXO J132519.7-313607	201.3324	-31.6021	0.4	5.5×10^{-14}	214.8		4.0	3.0×10^{41}	8.1×10^{4}		robust
2CXO J133338.8-314045	203.4120	-31.6792	0.5	2.3×10^{-14}	214.8	S0^{+}	55.0	1.3×10^{41}	2.2×10^{3}		robust
2CXO J134736.4+173404	206.9018	17.5680	0.4	3.2×10^{-13}	199.2	Sbc	8.2	1.5×10^{42}	4.5×10^{5}		galaxy pair
2CXO J140155.7-113809	210.4823	-11.6360	0.4	3.2×10^{-14}	230.3		5.4	2.0×10^{41}	3.1×10^{4}		robust
2CXO J142010.7+533348	215.0448	53.5635	0.6	1.2×10^{-14}	293.8	Irr	8.3	1.2×10^{41}	1.6×10^{4}	2.1×10^{6}	robust
2CXO J145409.9+183700	223.5415	18.6169	1.6	4.0×10^{-15}	520.0	Sc	24.2	1.3×10^{41}	2.3×10^{4}		robust
2CXO J150930.4+333330	227.3769	33.5585	0.6	3.1×10^{-14}	1.0×10^{3}		24.3	4.0×10^{42}	9.3×10^{5}	5.5×10^{9}	weak
2CXO J150940.1+333033	227.4172	33.5094	0.6	7.6×10^{-15}	549.5	E	13.4	2.8×10^{41}	6.9×10^{4}		weak
2CXO J152435.6+295302	231.1486	29.8841	0.7	3.2×10^{-15}	557.2		14.7	1.2×10^{41}	4.5×10^{4}		robust
2CXO J153143.2+240421	232.9304	24.0725	0.4	5.7×10^{-14}	438.5	Sab	5.9	1.3×10^{42}	6.4×10^{4}		galaxy pair
2CXO J160211.7+155437	240.5491	15.9103	0.4	3.9×10^{-14}	159.2	S0^{0}	12.5	1.2×10^{41}	2.8×10^{4}		robust
2CXO J161249.8+540832	243.2076	54.1423	0.5	3.8×10^{-14}	711.2	E	14.8	2.3×10^{42}	4.6×10^{5}		robust

Table A.1: List of HLX candidates obtained in Chapter 4.

Name	RA deg	Dec deg	$POSERR$ arcsec	F_X erg cm^{-2} s^{-1}	D Mpc	Gal. type	Sep. kpc	L_X erg s^{-1}	M_{BH} M$_\odot$	$M_{*,\mathrm{Bell}}$ M$_\odot$	Subsample
2CXO J162953.8+394601	247.4743	39.7670	6.2	4.1×10^{-14}	143.2	Sbc	21.2	1.0×10^{41}	1.7×10^{4}		robust
2CXO J163121.5-750652	247.8397	-75.1145	0.4	1.8×10^{-14}	498.9		57.1	5.3×10^{41}	8.5×10^{4}		robust
2CXO J163249.0+053852	248.2045	5.6479	0.5	7.1×10^{-15}	376.4		13.6	1.2×10^{41}	1.1×10^{4}		weak
2CXO J164237.1+272634	250.6548	27.4428	0.4	3.1×10^{-14}	469.9	E	38.7	8.3×10^{41}	1.4×10^{5}		robust
2CXO J170932.2+342542	257.3845	34.4286	0.5	1.7×10^{-14}	353.2	Sc	9.5	2.6×10^{41}	4.7×10^{4}		robust
2CXO J171215.5+640212	258.0646	64.0368	0.5	1.1×10^{-14}	335.1	E	7.1	1.5×10^{41}	2.5×10^{4}		robust
2CXO J185712.5-782830	284.3024	-78.4751	0.5	2.7×10^{-14}	181.1	Sa	14.0	1.1×10^{41}			robust
2CXO J192553.0+423807	291.4709	42.6355	1.2	9.9×10^{-14}	249.6		7.5	7.4×10^{41}	1.2×10^{5}		robust
2CXO J195142.2-550343	297.9261	-55.0621	1.3	1.8×10^{-14}	431.8		16.3	4.0×10^{41}	1.3×10^{5}	1.6×10^{8}	weak
2CXO J215022.5-055109	327.5938	-5.8526	0.4	5.4×10^{-13}	243.2	E	11.7	3.8×10^{42}	1.9×10^{6}		robust
2CXO J215543.9+084550	328.9332	8.7639	0.6	1.4×10^{-14}	757.1		20.9	9.7×10^{41}	2.2×10^{5}	1.5×10^{8}	robust
2CXO J215947.2-002644	329.9470	-0.4456	1.0	2.5×10^{-14}	598.6	E	21.3	1.1×10^{42}	2.5×10^{4}		galaxy pair
2CXO J220122.0-595323	330.3419	-59.8898	0.6	1.1×10^{-14}	485.6		15.1	3.0×10^{41}	4.6×10^{4}		robust
2CXO J224906.5-642043	342.2772	-64.3455	0.8	1.4×10^{-14}	416.9	E/S0	24.3	3.0×10^{41}	1.1×10^{5}	3.4×10^{7}	weak
2CXO J225033.7+105324	342.6408	10.8901	0.5	1.9×10^{-14}	320.4		12.2	2.3×10^{41}	4.2×10^{4}	3.3×10^{8}	weak
2CXO J225153.5-320757	342.9733	-32.1327	0.5	1.7×10^{-14}	369.9		6.4	2.8×10^{41}	5.1×10^{4}		robust
2CXO J231310.2-213531	348.2925	-21.5921	0.6	1.2×10^{-14}	355.0		11.9	1.9×10^{41}	4.2×10^{4}	6.0×10^{7}	weak
4XMM J003416.6-212430	8.5694	-21.4086	0.9	2.7×10^{-14}	269.2		8.4	2.4×10^{41}	2.2×10^{4}		weak
4XMM J011253.7+153617	18.2238	15.6047	1.9	3.6×10^{-14}	181.1	S0/a	6.7	1.4×10^{41}	8.3×10^{3}		robust
4XMM J011459.1+002519	18.7464	0.4220	0.5	2.3×10^{-14}	197.7	E	34.7	1.1×10^{41}	1.4×10^{4}		robust
4XMM J015624.1+053736	29.1007	5.6267	0.5	1.5×10^{-13}	79.2	S0^{0}	1.2	1.1×10^{41}	1.7×10^{4}		galaxy pair
4XMM J015638.3+321336	29.1596	32.2268	1.3	5.5×10^{-14}	303.3		16.6	6.0×10^{41}	8.7×10^{3}		robust
4XMM J015728.3-614120	29.3683	-61.6891	1.1	1.2×10^{-13}	87.5		2.4	1.1×10^{41}	1.1×10^{4}		robust
4XMM J020748.7-070139	31.9529	-7.0275	1.2	3.3×10^{-14}	193.2		10.7	1.5×10^{41}	2.1×10^{4}		weak
4XMM J025645.2+413508	44.1886	41.5856	0.5	6.8×10^{-14}	280.5		4.1	6.4×10^{41}	3.4×10^{4}		robust
4XMM J031054.1+095224	47.7258	9.8734	2.2	7.8×10^{-14}	1.1×10^{3}		32.8	1.1×10^{43}	2.6×10^{5}		galaxy pair
4XMM J032235.2-412623	50.6470	-41.4398	0.7	2.0×10^{-14}	284.4		9.3	1.9×10^{41}	2.3×10^{4}		robust
4XMM J032330.9-574030	50.8791	-57.6750	1.0	6.1×10^{-14}	141.8	Scd	5.6	1.5×10^{41}	1.5×10^{4}		robust
4XMM J032941.2-523115	52.4217	-52.5211	0.6	1.5×10^{-14}	276.7	S0	4.7	1.4×10^{41}	1.8×10^{4}		weak
4XMM J035555.6-421459	58.9820	-42.2498	1.1	1.9×10^{-14}	254.7	Scd	21.3	1.5×10^{41}	1.9×10^{4}	1.1×10^{7}	weak
4XMM J042058.6-484008	65.2444	-48.6690	0.6	1.4×10^{-13}	546.3		10.9	5.0×10^{42}	1.1×10^{6}		weak
4XMM J044853.2-202708	72.2220	-20.4523	0.8	3.6×10^{-14}	571.8		9.8	1.4×10^{42}	5.9×10^{4}		robust
4XMM J050107.9-384029	75.2832	-38.6749	1.1	3.3×10^{-14}	288.5		9.4	3.3×10^{41}	4.4×10^{4}		weak
4XMM J050117.1-242808	75.3215	-24.4690	0.5	8.0×10^{-14}	1.0×10^{3}		29.7	1.0×10^{43}	1.7×10^{6}		robust
4XMM J050252.9-755108	75.7205	-75.8523	1.3	3.8×10^{-13}	367.0		10.8	6.1×10^{42}	1.3×10^{5}	5.5×10^{11}	weak
4XMM J055239.0-363936	88.1628	-36.6601	1.0	3.9×10^{-14}	199.5	Sb	5.3	1.8×10^{41}	2.7×10^{4}		robust
4XMM J060737.9-614540	91.9080	-61.7613	0.9	3.3×10^{-14}	690.4		31.0	1.9×10^{42}	2.2×10^{5}		weak
4XMM J062447.9-372122	96.1996	-37.3561	0.6	6.4×10^{-14}	138.7	Sb	6.7	1.5×10^{41}	2.2×10^{4}		robust
4XMM J062536.4-535105	96.4018	-53.8516	0.7	4.2×10^{-14}	246.6		11.8	3.1×10^{41}	4.3×10^{4}		robust
4XMM J063053.0+175100	97.7212	17.8501	1.1	5.6×10^{-14}	344.2		11.0	7.9×10^{41}	7.5×10^{4}		robust
4XMM J065755.6-173046	104.4817	-17.5129	1.4	2.5×10^{-13}	415.1		15.7	5.2×10^{42}	1.1×10^{5}		robust
4XMM J071632.2+373912	109.1344	37.6535	0.7	2.6×10^{-14}	374.5		16.4	4.4×10^{41}	5.8×10^{4}	1.8×10^{8}	weak
4XMM J073733.1-694442	114.3882	-69.7452	0.9	3.9×10^{-14}	153.5	Sd	24.7	1.1×10^{41}	1.2×10^{4}		robust
4XMM J082906.3+264338	127.2765	26.7274	0.8	4.8×10^{-14}	358.1	Sbc	9.9	7.4×10^{41}	9.3×10^{4}		robust
4XMM J083235.2-225804	128.1470	-22.9680	0.6	8.1×10^{-14}	118.5	Sc	3.0	1.4×10^{41}	1.7×10^{4}		weak
4XMM J085253.8+180110	133.2243	18.0195	1.0	4.7×10^{-15}	879.0		24.5	4.4×10^{41}	1.2×10^{5}	2.7×10^{8}	weak
4XMM J085403.2+200746	133.5137	20.1295	0.5	8.7×10^{-14}	131.8	E	4.6	1.8×10^{41}	1.9×10^{4}		weak
4XMM J085859.0+542125	134.7459	54.3571	1.4	2.5×10^{-14}	381.9	E	9.1	4.3×10^{41}	2.3×10^{4}		robust
4XMM J092130.1+745304	140.3758	74.8846	1.6	4.2×10^{-14}	364.7	Sc	9.4	6.7×10^{41}	1.0×10^{4}		robust
4XMM J093233.1+472649	143.1381	47.4471	1.3	5.4×10^{-14}	907.8		23.8	5.4×10^{42}	4.9×10^{5}		robust
4XMM J100200.0-080944	150.5001	-8.1624	0.6	1.1×10^{-11}	133.6		7.5	2.3×10^{43}	5.4×10^{6}		galaxy pair
4XMM J101040.4+534719	152.6684	53.7887	0.8	5.3×10^{-14}	642.7		16.1	2.6×10^{42}	2.2×10^{5}		robust
4XMM J102440.6-184210	156.1692	-18.7031	1.3	2.4×10^{-14}	213.8	S0/a	7.8	1.3×10^{41}	4.5×10^{3}		robust
4XMM J104444.7-012018	161.1866	-1.3385	0.5	7.8×10^{-14}	897.0		10.5	7.6×10^{42}	1.7×10^{6}		galaxy pair
4XMM J105627.4+070512	164.1144	7.0869	0.9	1.2×10^{-14}	748.2		13.8	8.0×10^{41}	4.0×10^{4}		robust
4XMM J105756.4+564508	164.4852	56.7525	1.1	2.1×10^{-14}	710.0	E	13.2	1.3×10^{42}	1.4×10^{5}		robust
4XMM J110106.5+102943	165.2771	10.4954	0.5	1.1×10^{-13}	170.6	Sa	5.0	4.0×10^{41}	4.5×10^{4}		weak
4XMM J111831.5+130537	169.6314	13.0937	1.1	1.3×10^{-14}	465.6		17.9	3.3×10^{41}	2.8×10^{4}		robust
4XMM J112918.1-043548	172.3255	-4.5968	0.9	1.2×10^{-14}	426.6		10.6	2.7×10^{41}	3.1×10^{4}	9.2×10^{7}	robust
4XMM J114630.0+202728	176.6251	20.4579	0.9	7.9×10^{-14}	611.1	Sbc	23.6	3.5×10^{42}	1.4×10^{5}		weak
4XMM J114912.5+222107	177.3024	22.3520	0.9	1.1×10^{-14}	536.2	Scd	16.0	3.8×10^{41}	5.5×10^{4}		robust
4XMM J115402.8+225802	178.5118	22.9673	1.1	3.3×10^{-14}	452.9	Sbc	11.7	8.1×10^{41}	3.6×10^{4}	4.8×10^{7}	robust
4XMM J120335.1-040648	180.8963	-4.1135	0.9	2.9×10^{-13}	287.1		11.3	2.8×10^{42}	1.8×10^{5}	2.0×10^{11}	weak
4XMM J120732.8+150559	181.8868	15.0998	1.1	1.6×10^{-14}	369.8	S0^{+}	9.8	2.6×10^{41}	2.0×10^{4}		robust
4XMM J121820.1+040817	184.5841	4.1382	1.5	1.5×10^{-13}	359.7	Sd	24.4	2.4×10^{42}	1.1×10^{4}		galaxy pair
4XMM J122103.4+753121	185.2644	75.5228	1.0	2.5×10^{-14}	650.9		33.9	1.3×10^{42}	1.1×10^{5}	1.6×10^{9}	weak
4XMM J122458.3+124605	186.2433	12.7683	0.6	6.6×10^{-15}	368.1	Sa	14.3	1.1×10^{41}	2.0×10^{4}		robust
4XMM J123115.8+105320	187.8160	10.8892	0.5	2.4×10^{-14}	487.5	E	11.7	6.8×10^{41}	8.2×10^{4}		weak
4XMM J123307.1+000758	188.2798	0.1328	0.5	3.1×10^{-14}	616.6		17.7	1.4×10^{42}	2.0×10^{5}		robust
4XMM J123441.0+020846	188.6712	2.1462	0.7	7.2×10^{-14}	663.7		16.6	3.8×10^{42}	1.5×10^{5}		galaxy pair
4XMM J125225.3-290250	193.1057	-29.0473	1.2	2.5×10^{-14}	491.4		23.7	7.2×10^{41}	1.1×10^{5}		weak
4XMM J125256.2-132756	193.2345	-13.4658	1.1	2.8×10^{-14}	594.9		15.2	1.2×10^{42}	1.6×10^{5}		robust
4XMM J125424.9-290450	193.6039	-29.0806	0.6	2.1×10^{-13}	313.3	E+	12.0	2.4×10^{42}	1.8×10^{5}		galaxy pair
4XMM J125442.5-301928	193.6774	-30.3246	0.9	8.9×10^{-13}	298.8	E+	12.6	9.6×10^{42}	6.5×10^{4}		galaxy pair
4XMM J125708.6-044144	194.2859	-4.6956	0.6	2.7×10^{-14}	203.2	S0/a	17.7	1.3×10^{41}	1.0×10^{4}	1.8×10^{9}	robust
4XMM J125917.9+281107	194.8249	28.1855	0.8	4.1×10^{-14}	404.9	E	8.7	8.1×10^{41}	5.5×10^{4}	4.3×10^{7}	weak
4XMM J130256.1-022930	195.7340	-2.4919	0.7	2.7×10^{-14}	378.4	E	9.3	4.6×10^{41}	5.7×10^{4}	5.9×10^{7}	weak
4XMM J130307.6-154225	195.7818	-15.7070	2.0	2.7×10^{-13}	324.4		12.7	3.4×10^{42}	2.9×10^{5}		robust
4XMM J130543.7+350236	196.4323	35.0434	0.9	5.2×10^{-14}	459.2		13.7	1.3×10^{42}	8.3×10^{4}		robust
4XMM J132811.0-313503	202.0461	-31.5843	0.7	7.9×10^{-14}	183.7	E	8.0	3.2×10^{41}	3.9×10^{4}	2.0×10^{8}	weak
4XMM J140106.8-111128	210.2786	-11.1913	0.6	3.5×10^{-14}	379.0		8.4	6.0×10^{41}	8.3×10^{4}	2.2×10^{7}	robust

Table A.2: List of HLX candidates obtained in Chapter 4 (continued).

Name	RA	Dec	$POSERR$	F_X	D	Gal. type	Sep.	L_X	M_{BH}	$M_{*,\mathrm{Bell}}$	Subsample
	deg	deg	arcsec	erg cm^{-2} s^{-1}	Mpc		kpc	erg s^{-1}	$M_\odot$	$M_\odot$	
4XMM J141714.8+445536	214.3118	44.9267	1.1	1.0×10^{-14}	522.4	Sc	22.3	3.4×10^{41}	2.9×10^{4}		weak
4XMM J143033.0-001233	217.6379	-0.2093	1.1	1.8×10^{-14}	613.8		15.6	7.9×10^{41}	5.2×10^{4}		robust
4XMM J145753.6-113959	224.4734	-11.6665	0.6	2.0×10^{-14}	486.4		20.5	5.7×10^{41}	6.0×10^{4}		weak
4XMM J150626.4+030700	226.6103	3.1168	0.5	1.5×10^{-12}	833.2	E	19.1	1.2×10^{44}	4.3×10^{7}		galaxy pair
4XMM J150810.2+011001	227.0426	1.1670	0.9	2.2×10^{-14}	275.4	Scd	6.8	2.0×10^{41}	2.1×10^{4}	8.8×10^{8}	robust
4XMM J155851.8+272408	239.7161	27.4024	0.7	3.0×10^{-14}	195.8		8.0	1.4×10^{41}	1.9×10^{4}		robust
4XMM J160553.3+324734	241.4724	32.7928	0.5	6.0×10^{-15}	572.8	E	15.4	2.3×10^{41}	2.6×10^{4}		robust
4XMM J161342.6+470314	243.4276	47.0541	0.6	2.4×10^{-14}	399.9	E	7.7	4.6×10^{41}	4.7×10^{4}		robust
4XMM J161347.9+470809	243.4497	47.1360	0.7	1.7×10^{-14}	322.1	Scd	7.3	2.1×10^{41}	2.5×10^{4}		robust
4XMM J161534.3+192707	243.8930	19.4522	0.5	9.2×10^{-13}	133.4	S0$^-$	10.8	2.0×10^{42}	6.8×10^{5}		robust
4XMM J161604.0-223726	244.0170	-22.6240	0.5	7.3×10^{-14}	110.7	Sb	4.2	1.1×10^{41}	4.9×10^{3}		robust
4XMM J163818.7-642201	249.5783	-64.3670	0.8	4.5×10^{-14}	214.8	Sc	23.2	2.5×10^{41}	2.5×10^{4}		robust
4XMM J164727.2+345306	251.8636	34.8851	1.1	1.4×10^{-14}	457.1	Scd	12.6	3.6×10^{41}	1.3×10^{4}		robust
4XMM J165501.3+790837	253.7554	79.1438	0.7	4.8×10^{-14}	263.0		12.0	3.9×10^{41}	5.7×10^{4}		robust
4XMM J174659.3+683630	266.7474	68.6085	0.8	6.8×10^{-12}	284.4	E	11.1	6.6×10^{43}	2.0×10^{7}		galaxy pair
4XMM J174907.2-644251	267.2802	-64.7142	2.0	1.6×10^{-13}	127.5		6.4	3.1×10^{41}	1.4×10^{4}	2.1×10^{9}	robust
4XMM J175207.5+225509	268.0314	22.9192	0.6	3.0×10^{-14}	782.2		11.9	2.2×10^{42}	3.2×10^{5}		weak
4XMM J181611.6+423937	274.0485	42.6603	0.5	6.3×10^{-12}	186.2	Sbc	24.2	2.6×10^{43}	5.5×10^{5}		galaxy pair
4XMM J184724.4-631726	281.8517	-63.2907	1.1	3.4×10^{-14}	282.0		6.4	3.2×10^{41}	1.2×10^{4}		robust
4XMM J192124.0+433754	290.3501	43.6317	1.4	2.3×10^{-14}	309.4		14.9	2.6×10^{41}	2.0×10^{3}		robust
4XMM J192133.3+441322	290.3891	44.2230	0.8	2.3×10^{-13}	356.9	E	9.8	3.5×10^{42}	9.7×10^{4}		robust
4XMM J194744.7+704645	296.9363	70.7793	0.9	4.0×10^{-14}	877.5		16.9	3.7×10^{42}	7.1×10^{5}		robust
4XMM J210536.0-522300	316.4004	-52.3835	0.7	7.9×10^{-14}	154.2	Scd	13.8	2.3×10^{41}	1.7×10^{4}		robust
4XMM J213109.5-430023	322.7896	-43.0065	0.8	7.5×10^{-14}	712.3		10.7	4.5×10^{42}	2.2×10^{5}		robust
4XMM J213707.4+003834	324.2810	0.6430	1.0	2.2×10^{-14}	385.5	Sc	10.9	3.8×10^{41}	2.1×10^{4}	1.0×10^{7}	robust
4XMM J215057.1-073535	327.7381	-7.5932	0.7	4.1×10^{-14}	616.6		22.0	1.9×10^{42}	2.7×10^{5}	6.0×10^{8}	weak
4XMM J221014.5-121119	332.5605	-12.1888	2.1	4.2×10^{-14}	403.2		17.6	8.1×10^{41}	1.2×10^{5}	3.0×10^{8}	weak
4XMM J221755.3-354629	334.4808	-35.7748	0.8	3.5×10^{-14}	600.6		12.0	1.5×10^{42}	2.5×10^{5}		weak
4XMM J222248.6-290207	335.7025	-29.0355	0.6	1.7×10^{-14}	483.1		13.6	4.8×10^{41}	7.1×10^{4}		robust
4XMM J222324.0-290444	335.8501	-29.0791	0.6	6.1×10^{-14}	293.5		8.2	6.3×10^{41}	9.6×10^{3}		robust
4XMM J222837.9-245026	337.1581	-24.8406	0.5	6.9×10^{-13}	61.2	Sab	2.3	3.1×10^{41}	1.5×10^{4}		galaxy pair
4XMM J223622.4-150712	339.0934	-15.1201	1.4	8.4×10^{-14}	195.7		7.3	3.9×10^{41}	2.1×10^{4}	6.1×10^{7}	weak
4XMM J225931.7-344113	344.8823	-34.6871	0.6	1.2×10^{-13}	262.6		7.3	9.7×10^{41}	1.3×10^{5}	1.0×10^{8}	robust
4XMM J230814.5+224244	347.0608	22.7123	0.9	5.0×10^{-14}	156.3		13.4	1.5×10^{41}	3.8×10^{3}		weak
4XMM J231041.2+073427	347.6719	7.5743	1.0	2.9×10^{-14}	195.0	E	24.5	1.3×10^{41}	1.4×10^{4}		robust
4XMM J231818.7-422237	349.5780	-42.3770	0.5	4.3×10^{-14}	260.0		5.5	3.5×10^{41}	6.6×10^{4}		robust
4XMM J233342.0-151523	353.4253	-15.2564	1.9	7.2×10^{-14}	289.1		13.4	7.2×10^{41}	1.3×10^{5}		weak
4XMM J233833.7-552639	354.6408	-55.4443	0.8	3.4×10^{-14}	311.3		10.1	3.9×10^{41}	5.1×10^{4}	2.9×10^{7}	weak
4XMM J234325.8-315019	355.8576	-31.8388	0.7	4.2×10^{-13}	242.1	Sab	9.1	2.9×10^{42}	1.1×10^{5}		galaxy pair
4XMM J234427.4-541502	356.1145	-54.2506	0.8	6.2×10^{-14}	275.6		5.0	5.6×10^{41}	4.3×10^{4}		robust
4XMM J234647.1-542418	356.6963	-54.4052	0.8	4.9×10^{-14}	599.8		14.5	2.1×10^{42}	2.2×10^{5}		weak
2SXPS J002941.2-410120	7.4220	-41.0223	2.6	2.2×10^{-13}	299.2		15.2	2.4×10^{42}	2.9×10^{4}		robust
2SXPS J011942.7+032423	19.9282	3.4064	2.3	7.2×10^{-13}	36.1	Sbc	5.5	1.1×10^{41}	1.6×10^{4}	1.7×10^{5}	robust
2SXPS J021218.5-020805	33.0771	-2.1349	2.7	3.2×10^{-14}	163.7	Sbc	27.5	1.0×10^{41}	1.2×10^{4}	4.1×10^{5}	robust
2SXPS J051704.3-620923	79.2683	-62.1565	2.7	4.0×10^{-14}	206.0		9.4	2.0×10^{41}	2.0×10^{4}		weak
2SXPS J060945.1-484805	92.4382	-48.8015	2.9	1.7×10^{-13}	127.1		6.2	3.3×10^{41}	4.5×10^{4}		weak
2SXPS J101355.6+431005	153.4819	43.1682	2.4	4.2×10^{-14}	457.1		23.8	1.1×10^{42}	8.4×10^{4}	3.6×10^{7}	weak
2SXPS J103423.1+734519	158.5964	73.7555	1.4	7.2×10^{-12}	18.4	Sdm	2.8	2.9×10^{41}	5.5×10^{4}		weak
2SXPS J111416.1+481833	168.5674	48.3093	2.3	8.6×10^{-13}	33.4	Sbc	10.1	1.1×10^{41}	1.4×10^{4}		robust
2SXPS J115109.2+570340	177.7885	57.0611	2.3	1.3×10^{-14}	539.5		20.9	4.7×10^{41}	7.3×10^{3}	2.8×10^{8}	weak
2SXPS J150043.3-035223	225.1806	-3.8733	2.5	1.3×10^{-13}	210.9	S0/a	15.8	7.0×10^{41}	7.2×10^{4}		weak
2SXPS J164652.0+234011	251.7167	23.6699	2.5	9.6×10^{-13}	554.6	E	22.1	3.5×10^{43}	5.2×10^{6}		weak

Table A.3: List of HLX candidates obtained in Chapter 4 (continued).

Name	RA	Dec	$POSERR$	F_X	D	Gal. type	Sep.	L_X	M_{BH}	M_*	Subsample
	deg	deg	arcsec	erg cm^{-2} s^{-1}	Mpc		kpc	erg s^{-1}	M$_\odot$	M$_\odot$	
2CXO J003447.2-431213	8.6970	-43.2037	3.3	3.7×10^{-14}	105.7	Scd	4.5	4.9×10^{40}	9.7×10^{5}	2.0×10^{9}	clean
2CXO J004111.8-210752	10.2993	-21.1313	0.4	2.1×10^{-13}	18.3	S0$^-$	0.1	8.6×10^{39}	1.7×10^{5}	5.4×10^{8}	clean
2CXO J023914.9+300905	39.8121	30.1515	0.5	3.7×10^{-14}	13.9	Sa	0.1	8.5×10^{38}	1.7×10^{4}	1.2×10^{9}	clean
2CXO J031002.1-203611	47.5090	-20.6032	0.4	7.8×10^{-15}	19.6	Irr	1.1	3.6×10^{38}	7.1×10^{3}	6.0×10^{7}	clean
2CXO J033453.4-244731	53.7229	-24.7921	2.3	5.4×10^{-14}	21.2	E	0.6	2.9×10^{39}	5.8×10^{4}	2.0×10^{9}	clean
2CXO J033818.8-353152	54.5787	-35.5313	1.8	4.3×10^{-15}	20.6	S0$^-$	0.2	2.2×10^{38}	4.3×10^{3}	3.0×10^{7}	clean
2CXO J050144.0-041718	75.4336	-4.2886	0.4	1.5×10^{-14}	54.2	Irr	0.2	5.4×10^{39}	1.1×10^{5}	2.8×10^{9}	clean
2CXO J052004.3-132946	80.0180	-13.4961	1.7	1.5×10^{-14}	46.0		1.0	3.7×10^{39}	7.3×10^{4}	9.0×10^{8}	clean
2CXO J074653.2+390051	116.7217	39.0143	0.4	6.5×10^{-15}	58.5	Irr	0.6	2.7×10^{39}	5.3×10^{4}	1.4×10^{9}	full
2CXO J093401.9+551428	143.5082	55.2412	0.4	5.8×10^{-14}	14.3	Irr	0.0	1.4×10^{39}	2.8×10^{4}	2.2×10^{7}	clean
2CXO J094416.4+541134	146.0685	54.1929	0.4	1.4×10^{-14}	25.4	Irr	1.2	1.1×10^{39}	2.2×10^{4}	4.0×10^{7}	clean
2CXO J100339.5+474230	150.9149	47.7084	1.1	1.1×10^{-14}	64.4	Sd	2.9	5.3×10^{39}	1.1×10^{5}	9.0×10^{8}	clean
2CXO J100633.2-295606	151.6386	-29.9353	0.4	2.0×10^{-15}	13.9	E	0.0	4.7×10^{37}	935.6	1.3×10^{9}	full
2CXO J104527.5+583536	161.3647	58.5934	1.9	6.5×10^{-15}	43.3	Sdm	1.0	1.5×10^{39}	2.9×10^{4}	7.0×10^{8}	clean
2CXO J110113.6+033615	165.3069	3.6043	0.4	4.8×10^{-14}	18.0	Sd	7.7	1.9×10^{39}	3.7×10^{4}	1.2×10^{9}	full
2CXO J111738.2+174906	169.4092	17.8184	0.6	3.1×10^{-15}	20.1	S0/a	0.1	1.5×10^{38}	3.0×10^{3}	1.5×10^{8}	clean
2CXO J111934.1+513012	169.8922	51.5035	0.4	5.0×10^{-14}	22.4	Irr	0.2	3.0×10^{39}	6.0×10^{4}	6.0×10^{7}	clean
2CXO J112613.8+564809	171.5577	56.8026	1.8	1.5×10^{-14}	45.8	Sm	0.3	3.7×10^{39}	7.4×10^{4}	2.5×10^{8}	clean
2CXO J113027.7+364418	172.6156	36.7384	2.1	6.3×10^{-15}	32.4	Sdm	0.7	7.8×10^{38}	1.6×10^{4}	6.0×10^{8}	full
2CXO J115237.3-022807	178.1557	-2.4687	0.4	4.3×10^{-14}	17.6	Irr	0.3	1.6×10^{39}	3.2×10^{4}	1.8×10^{8}	clean
2CXO J115952.0+553955	179.9670	55.6654	0.5	1.3×10^{-14}	13.4	Irr	0.2	2.8×10^{38}	5.5×10^{3}	3.0×10^{7}	clean
2CXO J121326.1+543634	183.3588	54.6096	0.6	1.3×10^{-13}	37.2	Irr	0.6	2.2×10^{40}	4.3×10^{5}	6.0×10^{7}	clean
2CXO J122111.0+173817	185.2962	17.6383	1.7	1.4×10^{-13}	18.2	Sdm	0.2	5.4×10^{39}	1.1×10^{5}	9.0×10^{8}	clean
2CXO J123030.4+414142	187.6270	41.6951	0.4	2.8×10^{-13}	13.6	Irr	1.4	6.1×10^{39}	1.2×10^{5}	1.9×10^{8}	clean
2CXO J124413.0+125630	191.0544	12.9418	0.4	1.8×10^{-14}	16.5	S0$^-$	1.3	5.7×10^{38}	1.1×10^{4}	5.6×10^{7}	clean
2CXO J124517.0+270731	191.3211	27.1255	0.6	1.5×10^{-14}	13.2	Sab	0.1	3.1×10^{38}	6.2×10^{3}	5.0×10^{8}	full
2CXO J124744.5+041931	191.9358	4.3254	0.5	1.7×10^{-14}	17.6	Sdm	3.9	6.1×10^{38}	1.2×10^{4}	1.5×10^{8}	clean
2CXO J131656.3-163535	199.2348	-16.5933	0.7	7.0×10^{-15}	28.8	Sc	0.3	6.9×10^{38}	1.4×10^{4}	5.0×10^{8}	full
2CXO J132501.3+362615	201.2558	36.4377	0.7	5.2×10^{-15}	83.8	Sm	1.0	4.4×10^{39}	8.7×10^{4}	2.0×10^{9}	clean
2CXO J134943.6+263258	207.4319	26.5497	0.5	6.6×10^{-15}	163.7		0.4	2.1×10^{40}	4.2×10^{5}	3.0×10^{9}	clean
2CXO J135101.0+240519	207.7543	24.0887	1.3	3.9×10^{-14}	49.5	Sdm	2.1	1.2×10^{40}	2.3×10^{5}	3.0×10^{8}	clean
2CXO J144932.7-100950	222.3863	-10.1639	0.4	6.6×10^{-15}	19.6	Sdm	0.3	3.0×10^{38}	6.0×10^{3}	5.0×10^{7}	clean
2CXO J153425.5+040806	233.6066	4.1352	0.4	2.8×10^{-13}	175.4		1.3	1.0×10^{42}	2.1×10^{7}	3.0×10^{9}	clean
2CXO J153738.9+055845	234.4121	5.9793	0.5	2.7×10^{-14}	19.6	Sdm	4.6	1.3×10^{39}	2.5×10^{4}	4.0×10^{8}	clean
2CXO J160439.3+173656	241.1639	17.6156	1.0	1.2×10^{-14}	157.0	Scd	1.7	3.6×10^{40}	7.2×10^{5}	3.0×10^{9}	clean
2CXO J161555.3-061017	243.9805	-6.1714	0.5	2.4×10^{-15}	125.3		5.8	4.6×10^{39}	9.0×10^{4}	1.0×10^{9}	clean
2CXO J161636.5+681205	244.1521	68.2015	0.4	3.1×10^{-14}	17.5	Sbc	0.4	1.1×10^{39}	2.3×10^{4}	1.5×10^{9}	full
2CXO J162152.5+151856	245.4691	15.3156	0.5	6.2×10^{-15}	153.5	Irr	0.2	1.7×10^{40}	3.5×10^{5}	3.0×10^{9}	full
2CXO J162456.4-273637	246.2354	-27.6106	0.5	1.2×10^{-14}	69.6		2.4	7.0×10^{39}	1.4×10^{5}	1.8×10^{9}	clean
2CXO J183351.4+491642	278.4645	49.2784	0.4	2.0×10^{-14}	29.9	Sm	1.5	2.1×10^{39}	4.3×10^{4}	8.0×10^{8}	clean
2CXO J183449.5+703142	278.7065	70.5286	0.8	2.3×10^{-14}	13.1	Sd	1.1	4.8×10^{38}	9.4×10^{3}	9.0×10^{8}	full
2CXO J232744.4-020047	351.9352	-2.0131	0.5	1.1×10^{-14}	75.6		0.3	7.8×10^{39}	1.6×10^{5}	4.0×10^{8}	clean
2CXO J233622.1+020923	354.0923	2.1565	0.5	3.0×10^{-15}	34.7	Irr	0.2	4.4×10^{38}	8.7×10^{3}	6.0×10^{8}	clean
4XMM J005546.6-011709	13.9442	-1.2859	1.2	9.5×10^{-15}	175.4	Irr	2.2	3.5×10^{40}	6.9×10^{5}	3.0×10^{9}	clean
4XMM J005929.6-361109	14.8736	-36.1861	0.8	2.2×10^{-14}	48.1	Scd	0.9	6.1×10^{39}	1.2×10^{5}	1.8×10^{9}	clean
4XMM J020434.3-061209	31.1431	-6.2026	0.5	5.2×10^{-14}	17.3	Irr	3.8	1.9×10^{39}	3.7×10^{4}	6.0×10^{7}	clean
4XMM J024358.8-260321	40.9951	-26.0560	0.8	2.5×10^{-14}	98.6		1.5	2.9×10^{40}	5.7×10^{5}	5.0×10^{8}	clean
4XMM J030628.0-153352	46.6171	-15.5646	0.5	5.1×10^{-14}	24.3	Scd	2.9	3.6×10^{39}	7.1×10^{4}	4.7×10^{8}	clean
4XMM J040017.0-674815	60.0711	-67.8044	1.0	3.3×10^{-14}	16.2	Sb	1.0	1.0×10^{39}	2.1×10^{4}	1.3×10^{9}	full
4XMM J072814.6+335957	112.0610	33.9993	1.0	3.3×10^{-14}	65.2	Sbc	1.4	1.7×10^{40}	3.4×10^{5}	3.0×10^{9}	clean
4XMM J085735.4+274607	134.3975	27.7688	0.5	3.9×10^{-14}	33.0	E	0.5	5.1×10^{39}	1.0×10^{5}	4.7×10^{8}	clean
4XMM J094401.9-003834	146.0081	-0.6430	2.1	7.8×10^{-14}	20.9	Irr	0.3	4.1×10^{39}	8.1×10^{4}	1.5×10^{8}	clean
4XMM J094522.3+230419	146.3429	23.0722	1.1	2.6×10^{-14}	77.8	Irr	1.7	1.9×10^{40}	3.8×10^{5}	6.0×10^{8}	clean
4XMM J100109.0-192629	150.2876	-19.4415	1.0	2.2×10^{-12}	49.2	Sb	0.1	6.5×10^{41}	1.3×10^{7}	2.0×10^{9}	clean
4XMM J100115.0+554310	150.3127	55.7195	0.5	1.0×10^{-13}	22.7	Sbc	1.0	6.4×10^{39}	1.3×10^{5}	4.0×10^{8}	clean
4XMM J100710.3+123850	151.7930	12.6473	0.5	6.3×10^{-14}	37.9	Sm	3.3	1.1×10^{40}	2.1×10^{5}	2.3×10^{8}	clean
4XMM J102951.5-350944	157.4649	-35.1625	0.5	1.8×10^{-14}	34.0	Sa	1.1	2.5×10^{39}	4.9×10^{4}	2.5×10^{9}	full
4XMM J103410.1+580348	158.5423	58.0634	0.6	2.0×10^{-13}	33.3	Irr	0.2	2.7×10^{40}	5.3×10^{5}	1.7×10^{8}	clean
4XMM J103638.5-274250	159.1605	-27.7140	1.0	4.4×10^{-14}	50.0	S0/a	4.2	1.3×10^{40}	2.6×10^{5}	2.3×10^{9}	clean
4XMM J104925.2+324629	162.3552	32.7748	0.7	2.4×10^{-13}	26.0	Irr	1.0	1.9×10^{40}	3.8×10^{5}	2.6×10^{8}	clean
4XMM J105120.7+324558	162.8365	32.7664	0.5	1.4×10^{-13}	16.2	S0/a	0.1	4.5×10^{39}	8.8×10^{4}	7.0×10^{8}	clean
4XMM J110912.3+612345	167.3013	61.3961	1.3	1.8×10^{-14}	31.4	Sdm	0.1	2.2×10^{39}	4.3×10^{4}	3.0×10^{8}	clean
4XMM J113536.3+155831	173.9015	15.9755	0.5	1.8×10^{-14}	74.2	E	0.7	1.2×10^{40}	2.3×10^{5}	2.5×10^{9}	clean
4XMM J120746.1+430735	181.9422	43.1264	0.5	3.3×10^{-13}	18.4	S0$^+$	0.0	1.4×10^{40}	2.7×10^{5}	1.0×10^{9}	clean
4XMM J121221.1+291219	183.0882	29.2054	0.7	6.6×10^{-14}	18.0		0.5	2.6×10^{39}	5.1×10^{4}	4.0×10^{7}	clean
4XMM J121943.8+060005	184.9328	6.0014	0.7	8.9×10^{-14}	34.1	S0$^+$	4.4	1.2×10^{40}	2.4×10^{5}	2.9×10^{9}	clean
4XMM J122106.3+113538	185.2765	11.5942	0.5	3.0×10^{-14}	13.8	Sd	0.4	6.8×10^{38}	1.3×10^{4}	2.0×10^{7}	clean
4XMM J122858.2+123941	187.2427	12.6616	1.2	2.7×10^{-14}	21.0	E	0.2	1.4×10^{39}	2.9×10^{4}	5.7×10^{8}	clean
4XMM J124342.3+114054	190.9265	11.6817	0.5	1.5×10^{-14}	127.1	Sdm	3.1	2.8×10^{40}	5.6×10^{5}	2.0×10^{9}	clean
4XMM J125612.6-293002	194.0526	-29.5007	2.1	3.7×10^{-14}	28.8	Scd	1.3	3.7×10^{39}	7.3×10^{4}	2.6×10^{9}	full
4XMM J125614.1-302308	194.0591	-30.3857	1.1	4.8×10^{-14}	63.5		0.1	2.3×10^{40}	4.6×10^{5}	1.0×10^{9}	clean
4XMM J132110.6-114749	200.2944	-11.7972	1.0	2.4×10^{-14}	36.8	Scd	1.9	3.9×10^{39}	7.7×10^{4}	1.0×10^{9}	clean
4XMM J133932.2+151331	204.8846	15.2255	1.1	1.7×10^{-14}	91.2		4.9	1.6×10^{40}	3.3×10^{5}	3.0×10^{8}	clean
4XMM J135153.3+642213	207.9724	64.3705	1.1	3.3×10^{-14}	29.9	Irr	1.0	3.6×10^{39}	7.1×10^{4}	3.0×10^{8}	clean
4XMM J142758.3+255201	216.9932	25.8672	0.8	1.8×10^{-14}	66.2	Sdm	2.0	9.3×10^{39}	1.8×10^{5}	6.0×10^{8}	clean
4XMM J150027.5-262710	225.1149	-26.4528	2.2	4.6×10^{-14}	70.1	Sd	3.7	2.7×10^{40}	5.4×10^{5}	3.0×10^{9}	clean
4XMM J153632.2+162630	234.1346	16.4419	0.5	1.2×10^{-13}	26.2	Sd	1.1	1.0×10^{40}	2.0×10^{5}	2.0×10^{8}	clean
4XMM J192758.3-413431	291.9932	-41.5755	0.6	3.2×10^{-13}	34.7	Sc	0.2	4.7×10^{40}	9.3×10^{5}	1.3×10^{9}	clean
4XMM J231937.0+080514	349.9043	8.0873	0.6	4.3×10^{-14}	40.1	Sc	0.5	8.2×10^{39}	1.6×10^{5}	2.4×10^{8}	clean
2SXPS J044615.0-57202	71.5627	-57.3408	2.6	1.6×10^{-13}	16.1	Irr	1.8	4.9×10^{39}	9.7×10^{4}	2.8×10^{8}	clean
2SXPS J051045.5-31362	77.6898	-31.6073	2.6	1.9×10^{-13}	10.4	Irr	1.7	2.4×10^{39}	4.8×10^{4}	1.4×10^{8}	clean

Table A.4: List of AGN candidates in dwarf galaxies, obtained in Chapter 5.

Name	RA	Dec	$POSERR$	F_X	D	Gal. type	Sep.	L_X	M_{BH}	M_*	Subsample
	deg	deg	arcsec	erg cm^{-2} s^{-1}	Mpc		kpc	erg s^{-1}	$M_\odot$	$M_\odot$	
2SXPS J070801.2+15103	107.0053	15.1774	3.0	2.1×10^{-13}	28.8	Sd	0.6	2.1×10^{40}	4.2×10^5	1.0×10^9	clean
2SXPS J080707.3-28030	121.7808	-28.0510	2.4	6.3×10^{-14}	14.9	Sdm	1.0	1.7×10^{39}	3.4×10^4	1.0×10^9	clean
2SXPS J091041.8+07122	137.6744	7.2062	2.7	2.0×10^{-13}	20.0	Sbc	0.2	9.6×10^{39}	1.9×10^5	9.0×10^8	clean
2SXPS J104612.5+01484	161.5522	1.8137	2.8	1.0×10^{-13}	18.3	Sd	0.2	4.1×10^{39}	8.1×10^4	7.0×10^8	clean
2SXPS J114250.6+77215	175.7110	77.3648	2.8	9.0×10^{-14}	28.2	Sd	4.0	8.5×10^{39}	1.7×10^5	8.0×10^8	clean
2SXPS J122325.2+65591	185.8554	65.9867	2.4	6.0×10^{-14}	39.4	Irr	1.8	1.1×10^{40}	2.2×10^5	3.0×10^8	clean
2SXPS J130756.6-16411	196.9860	-16.6881	3.0	5.3×10^{-13}	12.7	Sm	0.2	1.0×10^{40}	2.1×10^5	10.0×10^7	clean
2SXPS J131108.3-28002	197.7848	-28.0057	2.5	1.9×10^{-13}	44.3	Irr	4.8	4.3×10^{40}	8.6×10^5	6.0×10^8	clean
2SXPS J152131.9-07224	230.3833	-7.3784	2.1	5.3×10^{-13}	21.9	Sbc	1.0	3.1×10^{40}	6.1×10^5	2.7×10^9	clean
2SXPS J221817.7+40334	334.5739	40.5625	2.4	3.7×10^{-13}	13.7	Sdm	0.0	8.2×10^{39}	1.6×10^5	1.2×10^9	clean

Table A.5: List of AGN candidates obtained in Chapter 5 (continued).

Name	RA deg	Dec deg	$POSERR$ arcsec	F_X erg cm^{-2} s^{-1}	D Mpc	Gal. type	Sep. kpc	L_X erg s^{-1}	P_{XRB}	f_{cont}
2CXO J000120.2+130641	0.3342	13.1114	0.4	5.5×10^{-15}	76.5	S0/E	1.3	3.9×10^{39}	0.56	0.01
2CXO J000125.1+130708	0.3549	13.1189	0.5	2.0×10^{-15}	75.0	S	8.8	1.3×10^{39}	0.41	0.20
2CXO J000126.7+130649	0.3616	13.1136	0.5	8.3×10^{-15}	75.0	S	3.9	5.6×10^{39}	0.82	0.08
2CXO J000131.1-574917	0.3797	-57.8215	1.9	6.5×10^{-15}	134.9	S	5.1	1.4×10^{40}	0.25	0.06
2CXO J000141.1+232949	0.4215	23.4972	0.4	2.8×10^{-15}	62.5	S	3.4	1.3×10^{39}	0.55	0.02
2CXO J000142.3+232941	0.4263	23.4947	0.4	3.9×10^{-15}	62.5	S	1.9	1.8×10^{39}	0.43	0.00
2CXO J000142.9+232935	0.4290	23.4933	0.4	3.9×10^{-15}	62.5	S	5.0	1.8×10^{39}	0.80	0.02
2CXO J000254.5-354308	0.7274	-35.7189	0.5	4.9×10^{-15}	212.8	S0/E	10.6	2.6×10^{40}	0.56	0.40
2CXO J000307.8-355428	0.7827	-35.9080	0.4	2.1×10^{-14}	223.9		9.8	1.3×10^{41}		
2CXO J000619.5-413019	1.5814	-41.5054	0.4	2.3×10^{-14}	19.5	S	1.9	1.1×10^{39}	0.58	0.00
2CXO J000620.2-413005	1.5842	-41.5016	0.4	8.9×10^{-14}	19.5	S	0.7	4.0×10^{39}	0.44	0.00
2CXO J000952.9+255547	2.4708	25.9299	0.5	4.4×10^{-15}	65.8	S	7.1	2.3×10^{39}		
2CXO J000953.2+255454	2.4720	25.9153	0.5	2.1×10^{-15}	65.8	S	9.5	1.1×10^{39}	0.83	0.29
2CXO J000955.1+255536	2.4800	25.9267	0.7	2.5×10^{-15}	65.8	S	8.1	1.3×10^{39}	0.75	0.32
2CXO J001106.9-120631	2.7788	-12.1088	0.4	8.7×10^{-15}	83.3	S	2.2	7.2×10^{39}	0.25	0.09
2CXO J001815.4+300343	4.5646	30.0620	0.7	1.9×10^{-15}	93.9	S0/E	4.3	2.0×10^{39}	0.59	0.13
2CXO J001827.1+300210	4.6131	30.0363	0.5	6.7×10^{-15}	106.7	S	11.1	9.1×10^{39}	0.63	0.34
2CXO J001849.8-102134	4.7077	-10.3596	0.4	9.7×10^{-15}	116.4	S	4.5	1.6×10^{40}	0.43	0.28
2CXO J001850.4-102228	4.7102	-10.3746	0.4	4.8×10^{-15}	119.7	S	5.7	8.2×10^{39}	0.58	0.05
2CXO J001850.9-102232	4.7122	-10.3757	0.5	1.1×10^{-14}	119.7	S	2.2	1.8×10^{40}	0.57	0.01
2CXO J001850.9-102249	4.7125	-10.3804	0.5	1.8×10^{-15}	119.7	S	7.1	3.0×10^{39}	0.76	0.12
2CXO J001851.2-102244	4.7134	-10.3791	0.4	7.5×10^{-15}	119.7	S	5.1	1.3×10^{40}	0.56	0.05
2CXO J002751.6-014813	6.9653	-1.8037	2.7	1.4×10^{-13}	57.6	S	6.9	5.4×10^{40}	0.30	0.24
2CXO J003358.1-094222	8.4922	-9.7062	0.5	1.2×10^{-14}	52.9	S	17.2	4.2×10^{39}	0.75	0.54
2CXO J003404.3-094248	8.5182	-9.7133	0.5	1.1×10^{-14}	52.9	S	9.3	3.7×10^{39}	0.79	0.35
2CXO J003404.5-094239	8.5191	-9.7110	0.6	7.8×10^{-15}	52.9	S	8.4	2.6×10^{39}	0.41	0.24
2CXO J003408.4-094140	8.5351	-9.6947	1.2	1.3×10^{-14}	67.8		2.6	7.1×10^{39}	0.29	0.02
2CXO J003413.6-212803	8.5568	-21.4676	0.7	1.5×10^{-15}	96.3	S	4.7	1.7×10^{39}	0.61	0.09
2CXO J003414.9-212455	8.5622	-21.4155	0.5	1.8×10^{-15}	270.4	S0/E	12.6	1.6×10^{40}	0.84	0.18
2CXO J003416.0-212517	8.5669	-21.4215	0.4	2.7×10^{-15}	270.4	S0/E	18.9	2.4×10^{40}	0.60	0.46
2CXO J003654.5-010737	9.2271	-1.1271	1.1	1.4×10^{-15}	326.6	S	9.8	1.7×10^{40}	0.26	0.23
2CXO J003703.9-010904	9.2665	-1.1514	0.4	1.0×10^{-14}	328.1	S0/E	5.2	1.3×10^{41}	0.24	0.07
2CXO J003737.5-334255	9.4067	-33.7153	0.4	6.3×10^{-15}	126.5	S	25.5	1.2×10^{40}		
2CXO J003738.1-334306	9.4088	-33.7183	0.4	9.0×10^{-16}	126.5	S	22.2	1.7×10^{39}	0.67	0.15
2CXO J003738.3-334309	9.4098	-33.7192	0.4	1.0×10^{-15}	126.5	S	20.8	1.9×10^{39}	0.61	0.13
2CXO J003738.7-334316	9.4114	-33.7212	0.4	7.5×10^{-15}	126.5	S	20.0	1.4×10^{40}	0.37	0.13
2CXO J003739.1-334229	9.4131	-33.7083	0.4	2.9×10^{-15}	126.5	S	22.0	5.6×10^{39}	0.75	0.13
2CXO J003739.2-334250	9.4134	-33.7139	0.4	4.4×10^{-15}	126.5	S	14.6	8.5×10^{39}	0.83	0.06
2CXO J003739.3-334323	9.4141	-33.7231	0.4	2.6×10^{-14}	126.5	S	18.9	5.0×10^{40}	0.38	0.11
2CXO J003740.2-334327	9.4177	-33.7242	0.4	1.5×10^{-15}	126.5	S	17.6	2.9×10^{39}	0.32	0.10
2CXO J003740.4-334324	9.4185	-33.7236	0.4	1.0×10^{-15}	126.5	S	15.9	2.0×10^{39}	0.66	0.08
2CXO J003740.7-334258	9.4198	-33.7161	0.4	5.3×10^{-16}	126.5	S	2.7	1.0×10^{39}	0.53	0.00
2CXO J003740.8-334331	9.4203	-33.7253	0.4	4.1×10^{-15}	126.5	S	18.8	7.8×10^{39}	0.56	0.11
2CXO J003741.2-334232	9.4218	-33.7090	0.4	1.3×10^{-15}	126.5	S	15.4	2.6×10^{39}	0.83	0.07
2CXO J003741.3-334331	9.4223	-33.7254	0.4	8.9×10^{-16}	126.5	S	19.0	1.7×10^{39}	0.68	0.11
2CXO J003742.4-334249	9.4267	-33.7138	0.4	3.7×10^{-15}	126.5	S	10.8	7.1×10^{39}	0.70	0.04
2CXO J003742.4-334304	9.4270	-33.7178	0.4	9.1×10^{-16}	126.5	S	10.4	1.7×10^{39}	0.81	0.03
2CXO J003742.7-334212	9.4283	-33.7035	0.4	1.1×10^{-15}	128.2	S	6.7	2.3×10^{39}	0.87	0.03
2CXO J003742.8-334314	9.4286	-33.7207	0.4	8.7×10^{-16}	126.5	S	15.6	1.7×10^{39}	0.80	0.07
2CXO J003742.9-334204	9.4289	-33.7012	0.4	2.4×10^{-15}	128.2	S	4.7	4.8×10^{39}	0.63	0.01
2CXO J003743.8-334209	9.4327	-33.7028	0.4	2.4×10^{-15}	128.2	S	3.0	4.7×10^{39}	0.69	0.01
2CXO J003745.3-334228	9.4388	-33.7079	0.4	2.2×10^{-15}	155.4	S0/E	6.3	6.3×10^{39}	0.82	0.20
2CXO J003747.0-333953	9.4459	-33.6647	0.5	1.8×10^{-15}	127.9		5.5	3.6×10^{39}	0.70	0.07
2CXO J003912.0+005153	9.8000	0.8650	1.2	2.7×10^{-15}	59.7	S	5.9	1.1×10^{39}	0.74	0.31
2CXO J003913.2+005142	9.8051	0.8617	0.5	2.9×10^{-14}	59.7	S	2.6	1.2×10^{40}	0.68	0.03
2CXO J003917.1+031940	9.8214	3.3279	0.4	3.4×10^{-15}	61.6	S0/E	7.2	1.5×10^{39}	0.70	0.10
2CXO J003919.7+031945	9.8324	3.3294	0.4	4.2×10^{-15}	61.6	S0/E	5.6	1.9×10^{39}	0.83	0.10
2CXO J003934.0+005127	9.8917	0.8578	0.6	8.0×10^{-15}	62.3	S	4.3	3.7×10^{39}	0.70	0.06
2CXO J003936.2+005128	9.9008	0.8578	0.6	5.8×10^{-15}	62.3	S	6.3	2.7×10^{39}	0.84	0.10
2CXO J004125.9+252945	10.3581	25.4960	0.4	5.2×10^{-15}	65.1	S	9.4	2.6×10^{39}	0.59	0.56
2CXO J004134.4-092159	10.3935	-9.3666	0.4	2.9×10^{-15}	208.9	S	11.3	1.5×10^{40}	0.71	0.50
2CXO J004136.4-091923	10.4019	-9.3233	0.4	5.3×10^{-15}	241.0	S0/E	7.6	3.7×10^{40}		
2CXO J004255.7-094505	10.7321	-9.7515	2.6	7.9×10^{-15}	227.0	S0/E	10.2	4.8×10^{40}	0.23	0.18
2CXO J004717.5-251811	11.8232	-25.3032	0.4	5.8×10^{-13}	3.9	S	4.1	1.1×10^{39}	0.95	0.02
2CXO J004722.6-252050	11.8442	-25.3475	0.5	5.9×10^{-13}	3.9	S	4.8	1.1×10^{39}	0.88	0.01
2CXO J004732.9-251748	11.8873	-25.2969	0.4	8.2×10^{-13}	3.9	S	0.6	1.5×10^{39}		
2CXO J004744.9-112754	11.9373	-11.4651	0.5	3.0×10^{-14}	18.4	S	3.3	1.2×10^{39}	0.84	0.06
2CXO J004852.6+315735	12.2194	31.9598	0.5	1.3×10^{-15}	161.2	S0/E	3.6	4.2×10^{39}	0.41	0.03
2CXO J004852.7+315739	12.2197	31.9609	0.4	1.4×10^{-15}	161.2	S0/E	6.1	4.2×10^{39}	0.68	0.06
2CXO J004953.8+321658	12.4742	32.2829	0.4	2.3×10^{-15}	67.0	S0/E	24.7	1.2×10^{39}	0.80	0.78
2CXO J005202.7+473307	13.0115	47.5522	0.4	1.1×10^{-13}	11.5	S	0.9	1.8×10^{39}		
2CXO J005402.4+730504	13.5104	73.0846	0.5	4.4×10^{-15}	69.0	S	2.1	2.5×10^{39}	0.46	0.01
2CXO J005746.5+302129	14.4440	30.3581	0.4	4.3×10^{-15}	71.0		10.9	2.6×10^{39}	0.81	0.28
2CXO J005947.4-073416	14.9479	-7.5713	0.4	3.3×10^{-14}	20.8	S	4.5	1.7×10^{39}	0.74	0.01
2CXO J005948.5-073456	14.9521	-7.5824	0.4	4.7×10^{-14}	20.8	S	2.8	2.4×10^{39}	0.68	0.01
2CXO J005949.4-073435	14.9561	-7.5766	0.4	7.8×10^{-14}	20.8	S	1.0	4.1×10^{39}	0.53	0.00
2CXO J005950.4-073454	14.9600	-7.5817	0.4	3.0×10^{-14}	20.8	S	1.4	1.6×10^{39}	0.70	0.00
2CXO J005952.2-073447	14.9679	-7.5798	0.4	3.1×10^{-14}	20.8	S	3.3	1.6×10^{39}	0.80	0.01
2CXO J010220.2-221437	15.5842	-22.2436	0.9	1.8×10^{-15}	244.3	S0/E	8.9	1.3×10^{40}	0.56	0.19
2CXO J010511.2-061207	16.2970	-6.2020	0.4	1.3×10^{-13}	11.4	S	5.6	2.1×10^{39}	0.73	0.09
2CXO J010706.5+322047	16.7774	32.3466	0.6	7.5×10^{-15}	76.0	S0/E	3.6	5.2×10^{39}	0.66	0.08

Table A.6: List of ULX candidates obtained in Chapter 4.

Name	RA deg	Dec deg	$POSERR$ arcsec	F_X erg cm^{-2} s^{-1}	D Mpc	Gal. type	Sep. kpc	L_X erg s^{-1}	P_{XRB}	f_{cont}
2CXO J010726.0+322421	16.8585	32.4060	0.5	1.5×10^{-15}	74.8	S0/E	9.6	1.0×10^{39}	0.74	0.22
2CXO J010726.8+322524	16.8621	32.4236	0.4	2.7×10^{-15}	74.8	S0/E	16.4	1.8×10^{39}	0.70	0.59
2CXO J010736.5-173210	16.9023	-17.5363	0.6	1.8×10^{-15}	86.6	S	3.5	1.6×10^{39}	0.47	0.02
2CXO J010736.5-173226	16.9024	-17.5406	0.8	1.9×10^{-15}	86.6	S	3.0	1.7×10^{39}	0.61	0.01
2CXO J010737.1-173222	16.9047	-17.5397	0.6	2.8×10^{-15}	86.6	S	3.1	2.5×10^{39}	0.81	0.02
2CXO J010737.2-173210	16.9052	-17.5364	0.5	4.5×10^{-15}	86.6	S	4.7	4.0×10^{39}	0.77	0.04
2CXO J010739.2+541226	16.9134	54.2074	0.4	9.9×10^{-15}	497.8		14.4	2.9×10^{41}	0.13	0.26
2CXO J010746.7-173027	16.9448	-17.5077	0.5	5.6×10^{-14}	83.8	S	4.7	4.7×10^{40}	0.15	0.11
2CXO J010746.8-173008	16.9453	-17.5022	0.5	1.8×10^{-15}	83.8	S	7.7	1.5×10^{39}		
2CXO J011007.5-455553	17.5313	-45.9317	0.4	2.0×10^{-14}	98.2	S0/E	4.3	2.3×10^{40}	0.80	0.15
2CXO J011020.8-455118	17.5868	-45.8551	1.0	1.0×10^{-14}	94.9	S0/E	4.1	1.1×10^{40}	0.61	0.03
2CXO J011022.4-455116	17.5934	-45.8545	1.2	1.1×10^{-14}	94.9	S0/E	11.4	1.2×10^{40}	0.69	0.28
2CXO J011028.2-460422	17.6178	-46.0729	0.4	4.9×10^{-13}	90.9	S0/E	3.2	4.9×10^{41}	0.19	0.04
2CXO J011253.2+153312	18.2219	15.5535	0.8	3.9×10^{-15}	204.2		23.5	1.9×10^{40}		
2CXO J011253.6+153622	18.2235	15.6063	1.4	4.7×10^{-15}	181.1	S0/E	11.3	1.8×10^{40}	0.55	0.53
2CXO J011253.9+153443	18.2246	15.5789	0.7	9.7×10^{-15}	177.0	S	5.3	3.6×10^{40}	0.42	0.19
2CXO J011302.1+153123	18.2591	15.5231	0.5	3.9×10^{-15}	201.4		16.1	1.9×10^{40}		
2CXO J011423.8-552332	18.5993	-55.3925	0.5	8.1×10^{-15}	49.2	S0/E	7.4	2.4×10^{39}	0.55	0.23
2CXO J011426.1-552353	18.6088	-55.3981	0.5	2.0×10^{-14}	49.0	S	2.5	5.6×10^{39}	0.63	0.04
2CXO J011524.7+001659	18.8531	0.2831	0.7	1.3×10^{-15}	206.1	S0/E	5.1	6.8×10^{39}	0.56	0.07
2CXO J011530.7+001754	18.8782	0.2983	0.6	6.3×10^{-15}	206.1	S0/E	6.2	3.2×10^{40}	0.36	0.12
2CXO J011854.9-010551	19.7288	-1.0976	0.5	2.0×10^{-14}	557.2	S0/E	13.5	7.5×10^{41}	0.31	0.24
2CXO J011942.7+032422	19.9282	3.4062	0.4	1.4×10^{-13}	36.1	S	5.9	2.2×10^{40}	0.64	0.17
2CXO J011957.1-411413	19.9881	-41.2370	0.4	3.6×10^{-15}	76.5		2.7	2.5×10^{39}	0.89	0.02
2CXO J011957.2-411357	19.9886	-41.2328	0.5	2.5×10^{-15}	76.5		3.1	1.7×10^{39}	0.78	0.04
2CXO J012002.3+142144	20.0097	14.3623	0.5	1.0×10^{-14}	137.4	S	3.3	2.3×10^{40}	0.25	0.04
2CXO J012255.7+332813	20.7323	33.4704	0.8	2.4×10^{-15}	59.4	S0/E	1.2	1.0×10^{39}	0.30	0.01
2CXO J012315.4+332748	20.8144	33.4635	0.4	1.7×10^{-14}	71.3	S0/E	17.3	1.1×10^{40}		
2CXO J012334.0+331508	20.8921	33.2523	0.4	7.8×10^{-15}	72.1	S0/E	25.3	4.9×10^{39}		
2CXO J012341.0+331652	20.9211	33.2813	0.5	4.6×10^{-15}	72.9	S0/E	2.2	2.9×10^{39}		
2CXO J012341.2+331537	20.9217	33.2603	0.6	4.2×10^{-15}	72.1	S0/E	7.3	2.6×10^{39}	0.13	0.11
2CXO J012342.2+331706	20.9259	33.2852	0.4	3.6×10^{-15}	72.9	S0/E	9.0	2.3×10^{39}	0.66	0.28
2CXO J012343.2+331655	20.9304	33.2822	0.4	3.1×10^{-15}	72.9	S0/E	11.8	2.0×10^{39}	0.69	0.55
2CXO J012358.6-350745	20.9944	-35.1292	0.7	8.4×10^{-15}	78.9	S	4.0	6.3×10^{39}	0.84	0.09
2CXO J012433.4+034748	21.1396	3.7968	0.4	5.3×10^{-14}	29.9	S	4.1	5.7×10^{39}	0.89	0.07
2CXO J012456.3+083953	21.2348	8.6648	0.8	5.5×10^{-15}	203.2	S0/E	9.0	2.7×10^{40}	0.67	0.31
2CXO J012540.7-012311	21.4198	-1.3866	0.5	1.0×10^{-14}	75.3	S0/E	20.9	7.0×10^{39}	0.76	0.45
2CXO J012542.3-012207	21.4265	-1.3687	0.5	3.1×10^{-15}	75.3	S0/E	17.2	2.1×10^{39}	0.67	0.60
2CXO J012545.0-012302	21.4378	-1.3839	0.6	1.9×10^{-15}	75.3	S0/E	7.0	1.3×10^{39}	0.80	0.10
2CXO J012545.4-012217	21.4395	-1.3715	0.6	1.9×10^{-15}	75.3	S0/E	11.9	1.3×10^{39}	0.86	0.20
2CXO J012550.5-011731	21.4605	-1.2920	0.9	4.0×10^{-15}	75.1	S0/E	3.0	2.7×10^{39}	0.43	0.02
2CXO J012558.0-011714	21.4921	-1.2875	0.4	1.8×10^{-14}	72.8	S0/E	2.4	1.1×10^{40}	0.80	0.05
2CXO J012600.5-012015	21.5021	-1.3375	0.5	2.4×10^{-15}	75.2	S0/E	7.9	1.6×10^{39}	0.81	0.10
2CXO J012600.6-012023	21.5027	-1.3400	0.5	1.5×10^{-15}	75.2	S0/E	7.9	1.0×10^{39}	0.75	0.14
2CXO J012602.0-012021	21.5087	-1.3393	0.6	1.5×10^{-15}	75.5	S0/E	10.9	1.0×10^{39}	0.81	0.37
2CXO J012602.6-012100	21.5111	-1.3503	0.5	1.7×10^{-15}	75.5	S0/E	12.9	1.2×10^{39}	0.78	0.29
2CXO J012621.9-011634	21.5913	-1.2763	0.5	3.1×10^{-14}	54.3	S	2.2	1.1×10^{40}	0.69	0.02
2CXO J013128.0+003202	22.8670	0.5341	0.5	6.2×10^{-15}	349.9	S0/E	7.9	9.1×10^{40}	0.39	0.13
2CXO J013156.8+332817	22.9871	33.4717	1.2	7.3×10^{-14}	62.4	S	6.6	3.4×10^{40}	0.41	0.23
2CXO J013424.4-154910	23.6020	-15.8196	0.5	3.5×10^{-15}	83.0	S	4.0	2.9×10^{39}	0.32	0.05
2CXO J013425.7-154902	23.6072	-15.8173	0.5	3.8×10^{-15}	83.0	S	3.9	3.1×10^{39}	0.15	0.05
2CXO J013503.5-412614	23.7646	-41.4373	0.4	3.0×10^{-14}	35.1	S	2.2	4.4×10^{39}	0.09	0.01
2CXO J013507.1-412605	23.7798	-41.4348	0.4	6.0×10^{-14}	35.1	S	4.8	8.9×10^{39}	0.37	0.05
2CXO J013651.0+154547	24.2129	15.7631	0.4	2.5×10^{-13}	7.3	S	5.4	1.6×10^{39}	0.91	0.06
2CXO J014024.4-075419	25.1020	-7.9054	0.8	8.8×10^{-15}	75.9	S	6.5	6.0×10^{39}	0.49	0.07
2CXO J014026.6-075355	25.1111	-7.8988	0.6	3.2×10^{-14}	75.9	S	7.9	2.2×10^{40}	0.48	0.07
2CXO J014430.7+170612	26.1281	17.1034	0.5	1.7×10^{-15}	120.8	S0/E	2.5	3.0×10^{39}	0.41	0.02
2CXO J015237.0+361000	28.1544	36.1669	0.4	8.3×10^{-15}	70.6	S0/E	11.6	4.9×10^{39}		
2CXO J015246.5+360936	28.1940	36.1602	0.4	7.0×10^{-15}	69.5	S	9.9	4.0×10^{39}	0.52	0.13
2CXO J015248.5+360917	28.2023	36.1547	0.4	2.5×10^{-15}	69.5	S	8.9	1.5×10^{39}	0.53	0.08
2CXO J015248.8+361454	28.2035	36.2485	0.7	6.1×10^{-15}	70.4	S0/E	2.9	3.6×10^{39}	0.20	0.06
2CXO J015249.7+360922	28.2073	36.1563	0.5	2.4×10^{-15}	69.5	S	14.0	1.4×10^{39}	0.64	0.21
2CXO J015250.1+361005	28.2090	36.1682	0.4	5.0×10^{-15}	69.5	S	24.1	2.9×10^{39}		
2CXO J015250.2+360930	28.2092	36.1584	0.4	1.8×10^{-15}	69.5	S	16.6	1.1×10^{39}	0.69	0.26
2CXO J015251.7+360955	28.2155	36.1655	0.4	5.0×10^{-15}	69.5	S	26.3	2.9×10^{39}		
2CXO J015253.3+360320	28.2223	36.0556	0.7	1.0×10^{-14}	71.3	S	4.2	6.1×10^{39}	0.59	0.18
2CXO J015301.1-134419	28.2547	-13.7388	0.4	1.5×10^{-14}	27.7	S0/E	1.2	1.4×10^{39}	0.52	0.01
2CXO J015616.7+053722	29.0700	5.6229	0.6	1.4×10^{-15}	78.8	S0/E	24.2	1.0×10^{39}	0.44	0.37
2CXO J015618.2+053835	29.0762	5.6431	0.7	1.8×10^{-15}	78.8	S0/E	24.0	1.3×10^{39}	0.57	0.43
2CXO J015619.9+053644	29.0832	5.6125	0.4	1.9×10^{-15}	78.8	S0/E	22.4	1.4×10^{39}	0.57	0.43
2CXO J015620.4+053624	29.0854	5.6068	0.4	7.0×10^{-15}	78.8	S0/E	29.3	5.2×10^{39}	0.75	0.74
2CXO J015621.1+053855	29.0883	5.6488	0.7	2.0×10^{-15}	78.8	S0/E	26.5	1.5×10^{39}	0.70	0.60
2CXO J015624.4+053702	29.1018	5.6174	0.5	1.4×10^{-15}	78.8	S0/E	24.3	1.0×10^{39}	0.83	0.41
2CXO J015627.0+053745	29.1126	5.6294	0.5	2.0×10^{-15}	78.8	S0/E	33.4	1.5×10^{39}	0.73	0.67
2CXO J015841.1+082053	29.6714	8.3481	0.4	1.6×10^{-14}	118.0	S0/E	7.4	2.6×10^{40}	0.52	0.23
2CXO J015842.0+082040	29.6751	8.3445	0.5	5.0×10^{-15}	118.0	S0/E	4.4	8.3×10^{39}	0.39	0.05
2CXO J015844.9+245344	29.6873	24.8958	0.5	3.1×10^{-14}	72.6	S0/E	14.6	2.0×10^{40}	0.64	0.53
2CXO J021404.0+275239	33.5170	27.8776	0.4	1.2×10^{-13}	9.7	S	0.3	1.3×10^{39}	0.69	0.00
2CXO J021822.6-050618	34.5944	-5.1051	0.6	8.5×10^{-16}	194.1	S	7.2	3.8×10^{39}	0.73	0.18
2CXO J021851.7-030230	34.7155	-3.0418	1.4	4.4×10^{-14}	33.3	S0/E	0.7	5.8×10^{39}	0.69	0.01
2CXO J022231.4+422023	35.6309	42.3400	0.4	2.9×10^{-13}	8.4		1.4	2.5×10^{39}		

Table A.7: List of ULX candidates obtained in Chapter 4 (continued).

Name	RA deg	Dec deg	$POSERR$ arcsec	F_X erg cm^{-2} s^{-1}	D Mpc	Gal. type	Sep. kpc	L_X erg s^{-1}	P_{XRB}	f_{cont}
2CXO J022233.4+422026	35.6394	42.3408	0.5	3.4×10^{-13}	8.4		0.9	2.8×10^{39}	0.42	0.00
2CXO J022310.6+425906	35.7943	42.9852	0.4	2.4×10^{-15}	79.3		9.4	1.8×10^{39}	0.67	0.27
2CXO J022315.2+425902	35.8135	42.9840	0.5	2.0×10^{-15}	79.3	S0/E	10.6	1.5×10^{39}	0.65	0.16
2CXO J022316.5+425831	35.8188	42.9753	0.5	3.2×10^{-15}	79.3	S0/E	22.1	2.4×10^{39}	0.69	0.42
2CXO J022320.9+430044	35.8372	43.0124	0.8	2.1×10^{-15}	90.4		6.5	2.1×10^{39}	0.47	0.26
2CXO J022503.3-244746	36.2639	-24.7961	0.5	4.7×10^{-15}	42.2	S	6.4	1.0×10^{39}		
2CXO J022503.7-244757	36.2657	-24.7993	0.4	3.1×10^{-14}	42.2	S	8.2	6.6×10^{39}		
2CXO J022503.8-244719	36.2659	-24.7886	0.4	1.1×10^{-14}	42.2	S	1.6	2.4×10^{39}		
2CXO J022504.0-244702	36.2668	-24.7841	0.4	6.1×10^{-15}	42.2	S	3.1	1.3×10^{39}		
2CXO J022504.9-244759	36.2705	-24.7998	0.4	8.2×10^{-15}	42.2	S	8.5	1.7×10^{39}		
2CXO J022505.2-244705	36.2717	-24.7849	0.4	5.2×10^{-15}	42.2	S	3.2	1.1×10^{39}		
2CXO J022505.6-244752	36.2735	-24.7979	0.4	8.1×10^{-14}	42.2	S	7.8	1.7×10^{40}		
2CXO J022505.7-244701	36.2740	-24.7838	0.4	1.1×10^{-14}	42.2	S	4.9	2.3×10^{39}		
2CXO J022721.5+333500	36.8396	33.5835	0.5	2.7×10^{-13}	9.2	S	2.6	2.7×10^{39}	0.53	0.01
2CXO J022727.5+333442	36.8647	33.5786	0.4	1.3×10^{-12}	9.2	S	5.9	1.3×10^{40}	0.66	0.03
2CXO J023603.8-512054	39.0161	-51.3484	0.7	3.7×10^{-15}	72.6	S	3.0	2.3×10^{39}	0.81	0.10
2CXO J023629.7+390014	39.1239	39.0041	0.6	9.2×10^{-14}	10.0	S	6.2	1.1×10^{39}	0.74	0.12
2CXO J023909.2+405233	39.7887	40.8759	0.4	1.1×10^{-13}	10.6	S	4.2	1.5×10^{39}	0.74	0.01
2CXO J023914.3+300854	39.8098	30.1485	0.4	1.5×10^{-13}	13.9	S	0.9	3.3×10^{39}	0.51	0.00
2CXO J024025.6-082430	40.1068	-8.4085	0.4	6.3×10^{-13}	4.2	S	1.9	1.3×10^{39}	0.89	0.00
2CXO J024228.5-000202	40.6188	-0.0340	0.4	7.1×10^{-15}	691.8	S	27.4	4.1×10^{41}	0.50	0.65
2CXO J024238.8-000055	40.6620	-0.0153	0.4	1.6×10^{-13}	10.1	S	1.4	2.0×10^{39}	0.23	0.01
2CXO J024617.2+130540	41.5721	13.0946	0.4	4.7×10^{-15}	90.7	S	1.9	4.7×10^{39}	0.40	0.01
2CXO J024618.0+130537	41.5752	13.0938	0.5	2.5×10^{-15}	90.7	S	4.6	2.5×10^{39}	0.24	0.03
2CXO J024618.2+130549	41.5760	13.0972	0.5	3.2×10^{-15}	90.7	S	5.3	3.2×10^{39}	0.70	0.09
2CXO J024619.8-301602	41.5825	-30.2675	2.4	1.2×10^{-13}	14.2	S	1.9	2.8×10^{39}	0.49	0.00
2CXO J024625.0-301719	41.6045	-30.2886	0.4	5.4×10^{-14}	14.2	S	6.3	1.3×10^{39}	0.63	0.12
2CXO J024932.1-311120	42.3842	-31.1889	0.4	1.5×10^{-14}	93.3	S0/E	9.4	1.6×10^{40}		
2CXO J024943.7-310936	42.4324	-31.1600	0.6	1.5×10^{-15}	94.0	S0/E	2.8	1.6×10^{39}	0.60	0.06
2CXO J025247.7-011156	43.1989	-1.1989	1.1	3.4×10^{-15}	97.5		3.3	3.9×10^{39}	0.23	0.07
2CXO J025249.4-011620	43.2059	-1.2723	0.5	3.5×10^{-15}	96.5	S0/E	16.5	3.9×10^{39}		
2CXO J025428.1+413435	43.6174	41.5765	0.4	1.6×10^{-14}	73.4	S0/E	4.9	1.0×10^{40}		
2CXO J025445.5+413144	43.6897	41.5291	0.5	1.5×10^{-14}	72.2		3.3	9.2×10^{39}	0.43	0.07
2CXO J025740.5+060138	44.4191	6.0274	0.5	8.6×10^{-15}	35.4	S0/E	2.5	1.3×10^{39}		
2CXO J025746.3+055657	44.4432	5.9492	0.7	1.1×10^{-14}	71.8	S	7.6	7.1×10^{39}	0.55	0.09
2CXO J025750.2+060310	44.4594	6.0530	0.4	8.4×10^{-15}	93.0	S0/E	2.7	8.7×10^{39}	0.69	0.09
2CXO J025843.0-523930	44.6794	-52.6584	0.5	4.7×10^{-15}	428.3		9.6	1.0×10^{41}	0.24	0.16
2CXO J030115.2+445230	45.3136	44.8752	0.5	2.4×10^{-14}	25.4	S0/E	9.6	1.8×10^{39}	0.52	0.20
2CXO J030133.3-145046	45.3891	-14.8461	0.4	2.5×10^{-14}	21.5	S0/E	5.3	1.4×10^{39}	0.80	0.14
2CXO J030455.0-273026	46.2293	-27.5074	0.5	1.7×10^{-15}	87.5	S	2.0	1.5×10^{39}	0.33	0.01
2CXO J030455.8-273016	46.2327	-27.5047	0.4	2.2×10^{-15}	87.5	S	3.9	2.0×10^{39}	0.37	0.02
2CXO J030456.0-273017	46.2337	-27.5049	0.5	5.2×10^{-15}	87.5	S	2.7	4.7×10^{39}	0.21	0.01
2CXO J030457.1-273017	46.2381	-27.5047	0.5	1.7×10^{-15}	87.5	S	3.1	1.5×10^{39}	0.54	0.01
2CXO J030825.6+040650	47.1068	4.1140	0.5	1.0×10^{-16}	125.3	S0/E	8.5	1.9×10^{39}	0.60	0.15
2CXO J030947.6-203531	47.4486	-20.5922	0.4	5.2×10^{-14}	14.5	S	3.9	1.3×10^{39}	0.85	0.03
2CXO J030956.7-203428	47.4864	-20.5747	0.4	4.1×10^{-14}	14.5	S	11.1	1.0×10^{39}	0.86	0.24
2CXO J031001.0-203553	47.5042	-20.5983	0.4	3.4×10^{-14}	19.6	S	1.5	1.6×10^{39}	0.85	0.01
2CXO J031049.4-265431	47.7062	-26.9088	0.8	2.0×10^{-14}	597.0		14.8	8.6×10^{41}	0.08	0.27
2CXO J031118.0+011902	47.8251	1.3173	0.4	4.7×10^{-15}	140.0	S	9.8	1.1×10^{40}	0.21	0.14
2CXO J031118.4+011848	47.8269	1.3134	0.4	2.4×10^{-15}	140.0	S	1.9	5.6×10^{39}	0.28	0.00
2CXO J031119.1+011853	47.8298	1.3149	0.4	1.9×10^{-15}	140.0	S	5.4	4.4×10^{39}	0.85	0.04
2CXO J031124.9-265617	47.8540	-26.9381	0.5	2.6×10^{-15}	302.0	S0/E	31.9	2.8×10^{40}		
2CXO J031713.8-411034	49.3077	-41.1762	0.4	2.2×10^{-13}	10.4		12.6	2.8×10^{39}	0.79	0.24
2CXO J031714.3-410717	49.3099	-41.1215	0.4	2.5×10^{-13}	10.4		3.4	3.2×10^{39}	0.92	0.02
2CXO J031741.2-572644	49.4217	-57.4458	0.4	8.3×10^{-15}	124.0		11.7	1.5×10^{40}	0.58	0.48
2CXO J031819.9-662910	49.5832	-66.4864	0.4	1.6×10^{-12}	4.1	S	1.0	3.1×10^{39}	0.85	0.00
2CXO J031948.0+413101	49.9503	41.5172	0.4	2.0×10^{-14}	76.5	S0/E	7.1	1.4×10^{40}		
2CXO J031952.1-260459	49.9671	-26.0831	0.4	2.5×10^{-14}	19.6		7.7	1.2×10^{39}	0.82	0.16
2CXO J031956.0+413315	49.9837	41.5543	0.4	1.6×10^{-14}	77.6	S0/E	14.3	1.2×10^{40}		
2CXO J032240.7-371223	50.6700	-37.2066	0.4	2.2×10^{-14}	21.5	S0/E	1.4	1.2×10^{39}		
2CXO J032251.2-370948	50.7135	-37.1636	0.5	4.6×10^{-14}	21.5	S0/E	20.2	2.5×10^{39}	0.82	0.56
2CXO J032650.7-533059	51.7114	-53.5164	1.2	1.9×10^{-15}	274.2	S	7.0	1.7×10^{40}	0.32	0.05
2CXO J032837.0+395051	52.1543	39.8477	0.9	1.8×10^{-14}	114.8		6.4	2.9×10^{40}	0.35	0.28
2CXO J032921.2+394717	52.3386	39.7883	0.5	3.1×10^{-15}	108.6		16.8	4.4×10^{39}	0.69	0.31
2CXO J032923.3+394718	52.3473	39.7886	0.5	3.2×10^{-15}	108.6		7.2	4.5×10^{39}	0.15	0.06
2CXO J033334.6-360936	53.3942	-36.1602	0.4	3.7×10^{-13}	17.9	S	6.3	1.4×10^{40}	0.63	0.03
2CXO J033336.0-360820	53.4000	-36.1390	0.4	2.7×10^{-14}	17.9	S	0.7	1.0×10^{39}		
2CXO J033338.0-360935	53.4084	-36.1597	0.4	5.0×10^{-14}	17.9	S	6.1	1.9×10^{39}	0.84	0.05
2CXO J033341.8-360731	53.4243	-36.1254	0.4	9.7×10^{-14}	17.9	S	7.3	3.7×10^{39}	0.36	0.06
2CXO J033625.2-345918	54.1052	-34.9883	0.4	7.6×10^{-14}	17.6	S0/E	4.4	2.8×10^{39}	0.93	0.09
2CXO J033713.6-354349	54.3067	-35.7303	0.4	5.8×10^{-14}	21.7	S0/E	6.4	3.3×10^{39}	0.70	0.15
2CXO J033755.1-710342	54.4800	-71.0618	0.5	6.5×10^{-15}	79.9	S	3.5	5.0×10^{39}	0.67	0.05
2CXO J033757.0-710322	54.4877	-71.0562	0.5	4.1×10^{-15}	79.9	S	6.7	3.1×10^{39}	0.68	0.15
2CXO J033827.6-352648	54.6152	-35.4469	0.4	2.8×10^{-14}	20.0	S0/E	2.1	1.3×10^{39}		
2CXO J033828.2-352710	54.6177	-35.4530	0.5	2.6×10^{-14}	20.0	S0/E	1.3	1.3×10^{39}		
2CXO J033830.7-352703	54.6280	-35.4509	0.5	2.4×10^{-14}	20.0	S0/E	1.9	1.2×10^{39}		
2CXO J033832.6-352705	54.6359	-35.4516	0.4	7.9×10^{-14}	20.0	S0/E	4.1	3.8×10^{39}		
2CXO J033833.3-352302	54.6390	-35.3840	0.5	2.5×10^{-14}	20.0	S0/E	23.5	1.2×10^{39}	0.86	0.43
2CXO J033847.7-261907	54.6991	-26.3187	0.4	6.4×10^{-14}	24.8	S	10.7	4.7×10^{39}	0.85	0.13
2CXO J033847.7-261918	54.6989	-26.3218	0.5	1.8×10^{-14}	24.8	S	9.8	1.3×10^{39}	0.59	0.10
2CXO J033848.1+095702	54.7004	9.9508	0.4	3.4×10^{-15}	241.3	S0/E	5.4	2.4×10^{40}	0.63	0.08

Table A.8: List of ULX candidates obtained in Chapter 4 (continued).

Name	RA deg	Dec deg	$POSERR$ arcsec	F_X erg cm^{-2} s^{-1}	D Mpc	Gal. type	Sep. kpc	L_X erg s^{-1}	P_{XRB}	f_{cont}
2CXO J033851.5-353542	54.7148	-35.5952	0.4	4.2×10^{-14}	21.0	S0/E	0.5	2.2×10^{39}		
2CXO J033852.0-353559	54.7167	-35.6000	0.4	2.1×10^{-14}	21.0	S0/E	2.0	1.1×10^{39}		
2CXO J033852.1-262109	54.7172	-26.3528	0.4	1.6×10^{-14}	24.8	S	6.4	1.2×10^{39}	0.58	0.07
2CXO J033853.5-261942	54.7233	-26.3285	0.4	1.8×10^{-14}	24.8	S	4.6	1.3×10^{39}	0.26	0.03
2CXO J033853.6-262053	54.7234	-26.3483	0.4	1.5×10^{-14}	24.8	S	5.1	1.1×10^{39}	0.51	0.03
2CXO J033938.1-352512	54.9090	-35.4200	0.6	5.1×10^{-15}	200.4	S	9.2	2.4×10^{40}	0.66	0.12
2CXO J033938.8-352509	54.9117	-35.4194	1.2	2.1×10^{-15}	200.4	S	5.1	1.0×10^{40}	0.25	0.04
2CXO J034008.7-353749	55.0364	-35.6303	0.4	2.6×10^{-14}	19.9	S	2.1	1.2×10^{39}	0.88	0.04
2CXO J034008.9-183447	55.0371	-18.5799	0.4	1.5×10^{-14}	28.8	S0/E	5.9	1.5×10^{39}	0.39	0.04
2CXO J034009.2-183441	55.0386	-18.5782	0.4	1.5×10^{-14}	28.8	S0/E	5.3	1.5×10^{39}	0.39	0.03
2CXO J034010.6-183543	55.0442	-18.5953	0.4	1.0×10^{-14}	28.8	S0/E	7.8	1.0×10^{39}	0.81	0.06
2CXO J034011.2-183435	55.0468	-18.5764	0.4	5.4×10^{-14}	28.8	S0/E	2.4	5.4×10^{39}	0.34	0.01
2CXO J034012.4-353740	55.0519	-35.6279	0.5	9.9×10^{-14}	19.9	S	3.8	4.7×10^{39}	0.56	0.03
2CXO J034012.5-183451	55.0522	-18.5810	0.4	1.5×10^{-13}	28.8	S0/E	1.2	1.5×10^{40}	0.19	0.00
2CXO J034014.5-183240	55.0605	-18.5446	0.4	1.4×10^{-14}	28.8	S0/E	18.5	1.4×10^{39}	0.85	0.34
2CXO J034014.5-183637	55.0605	-18.6105	0.4	2.0×10^{-14}	28.8	S0/E	15.8	2.0×10^{39}	0.88	0.28
2CXO J034117.9+152343	55.3249	15.3954	0.6	2.5×10^{-15}	129.4	S0/E	4.7	5.1×10^{39}	0.39	0.05
2CXO J034121.6+152528	55.3401	15.4247	0.9	4.5×10^{-15}	107.7	S0/E	2.3	6.3×10^{39}	0.10	0.03
2CXO J034133.0+152028	55.3878	15.3411	0.6	1.6×10^{-14}	106.7	S	3.6	2.2×10^{40}	0.30	0.07
2CXO J034218.4-352338	55.5769	-35.3940	0.4	1.8×10^{-14}	23.6	S0/E	1.4	1.2×10^{39}		
2CXO J034218.6-352240	55.5779	-35.3778	0.4	2.6×10^{-14}	23.6	S0/E	6.2	1.7×10^{39}	0.82	0.38
2CXO J034301.3-533807	55.7556	-53.6355	0.4	3.8×10^{-15}	254.7	S0/E	13.9	2.9×10^{40}	0.78	0.48
2CXO J034445.8-215434	56.1912	-21.9095	0.5	1.6×10^{-14}	26.7	S0/E	8.8	1.4×10^{39}	0.53	0.30
2CXO J034548.2-570353	56.4512	-57.0650	0.6	8.5×10^{-15}	257.0	S0/E	13.6	6.7×10^{40}	0.48	0.35
2CXO J034555.6+680455	56.4817	68.0820	0.4	1.4×10^{-12}	3.3	S	4.8	1.7×10^{39}	0.75	0.01
2CXO J034615.7+681112	56.5657	68.1869	0.4	1.5×10^{-12}	3.3	S	5.9	1.9×10^{39}	0.46	0.02
2CXO J035135.9-274432	57.8999	-27.7424	0.5	6.8×10^{-15}	289.7	S0/E	4.0	6.8×10^{40}	0.08	0.02
2CXO J035416.3+155546	58.5679	15.9296	0.5	6.1×10^{-15}	92.8	S	2.4	6.2×10^{39}	0.12	0.04
2CXO J035934.7-673756	59.8949	-67.6324	0.4	2.3×10^{-13}	15.5	S	1.1	6.6×10^{39}		
2CXO J040225.4+714218	60.6062	71.7053	0.7	8.7×10^{-15}	64.8	S	12.0	4.4×10^{39}	0.82	0.21
2CXO J040233.0+714227	60.6378	71.7076	0.6	8.6×10^{-15}	64.8	S	2.1	4.3×10^{39}	0.64	0.01
2CXO J040234.7+714234	60.6446	71.7096	0.5	6.0×10^{-15}	64.8	S	4.2	3.0×10^{39}	0.74	0.03
2CXO J040236.2+714148	60.6511	71.6968	0.6	5.8×10^{-15}	64.8	S	10.6	2.9×10^{39}	0.76	0.19
2CXO J040238.4+714241	60.6604	71.7116	0.5	1.3×10^{-14}	64.8	S	9.1	6.6×10^{39}	0.77	0.13
2CXO J040317.4+714317	60.8226	71.7214	0.4	3.1×10^{-15}	64.7	S	1.7	1.5×10^{39}	0.49	0.00
2CXO J040427.6-021029	61.1151	-2.1749	0.5	2.4×10^{-14}	90.2	S	3.0	2.3×10^{40}	0.19	0.03
2CXO J040428.1-021034	61.1172	-2.1762	0.6	1.4×10^{-14}	90.2	S	3.8	1.3×10^{40}	0.31	0.05
2CXO J040441.1+111033	61.1713	11.1760	0.9	6.1×10^{-15}	133.0		4.1	1.3×10^{40}	0.15	0.07
2CXO J040812.9-205908	62.0538	-20.9858	1.0	2.2×10^{-15}	117.1	S0/E	10.5	3.6×10^{39}	0.62	0.44
2CXO J040815.7-210253	62.0656	-21.0482	0.4	4.2×10^{-15}	56.4	S0/E	12.4	1.6×10^{39}		
2CXO J041338.6+102803	63.4112	10.4678	0.5	6.0×10^{-15}	405.5	S0/E	10.7	1.2×10^{41}	0.39	0.14
2CXO J041602.7-554657	64.0114	-55.7826	1.5	4.2×10^{-14}	18.5	S0/E	5.9	1.7×10^{39}	0.93	0.26
2CXO J042119.8-184858	65.3326	-18.8161	0.5	4.3×10^{-15}	137.4	S	2.3	9.8×10^{39}	0.21	0.02
2CXO J042922.0-534550	67.3420	-53.7641	0.5	8.1×10^{-15}	175.4	S0/E	7.8	3.0×10^{40}	0.66	0.18
2CXO J042929.1-535149	67.3716	-53.8637	0.6	2.5×10^{-15}	172.2	S0/E	7.6	8.9×10^{39}	0.77	0.20
2CXO J043039.4+004009	67.6645	0.6693	0.5	7.3×10^{-15}	49.0	S0/E	6.5	2.1×10^{39}	0.71	0.25
2CXO J043040.5+003933	67.6689	0.6594	0.6	4.5×10^{-15}	49.0	S0/E	2.9	1.3×10^{39}	0.22	0.04
2CXO J043045.0+005203	67.6878	0.8675	0.7	3.9×10^{-15}	49.4	S	3.5	1.1×10^{39}	0.25	0.03
2CXO J043138.3-050536	67.9096	-5.0936	0.4	5.2×10^{-15}	65.0	S	10.8	2.6×10^{39}		
2CXO J043139.8-050407	67.9159	-5.0686	0.4	2.5×10^{-15}	65.0	S	19.3	1.2×10^{39}	0.66	0.45
2CXO J043139.8-050552	67.9161	-5.0979	0.4	5.2×10^{-15}	65.0	S	13.0	2.6×10^{39}		
2CXO J043142.0-050551	67.9250	-5.0975	0.5	3.5×10^{-15}	65.0	S	16.0	1.8×10^{39}		
2CXO J043240.6-031403	68.1695	-3.2344	0.6	5.6×10^{-15}	121.1	S	3.1	9.8×10^{39}	0.18	0.07
2CXO J043338.4-131612	68.4101	-13.2702	0.4	5.2×10^{-14}	141.9	S0/E	19.9	1.2×10^{41}		
2CXO J043359.0-083510	68.4959	-8.5862	0.5	4.0×10^{-15}	64.6	S	9.1	2.0×10^{39}	0.41	0.20
2CXO J043400.3-083427	68.5013	-8.5744	0.4	5.5×10^{-15}	64.6	S	5.2	2.8×10^{39}	0.48	0.06
2CXO J043400.3-083432	68.5014	-8.5757	0.5	4.6×10^{-15}	64.6	S	3.9	2.3×10^{39}	0.53	0.03
2CXO J043409.5-131437	68.5399	-13.2438	0.9	7.9×10^{-15}	143.2	S	3.4	1.9×10^{40}	0.34	0.07
2CXO J044531.6-591454	71.3817	-59.2485	0.4	1.5×10^{-13}	16.1	S	6.5	4.7×10^{39}	0.90	0.05
2CXO J044533.9-591442	71.3915	-59.2450	0.4	1.2×10^{-13}	16.1	S	5.2	3.8×10^{39}	0.91	0.03
2CXO J044550.9-591422	71.4625	-59.2397	0.4	3.4×10^{-14}	16.1	S	5.5	1.1×10^{39}	0.93	0.03
2CXO J044552.8-591456	71.4701	-59.2489	0.4	2.1×10^{-13}	16.1	S	6.1	6.6×10^{39}	0.78	0.04
2CXO J044921.6-485545	72.3403	-48.9294	0.9	6.7×10^{-15}	355.9		6.7	1.0×10^{41}	0.10	0.09
2CXO J045249.8-594442	73.2076	-59.7450	0.4	4.8×10^{-14}	16.1	S	1.6	1.5×10^{39}	0.10	0.01
2CXO J045313.5+520134	73.3065	52.0262	0.7	6.9×10^{-15}	94.0		3.3	7.3×10^{39}	0.57	0.04
2CXO J045655.9-045159	74.2333	-4.8666	0.4	1.5×10^{-14}	52.6	S0/E	1.6	4.9×10^{39}		
2CXO J045659.1-044524	74.2467	-4.7568	1.0	3.0×10^{-15}	53.2	S	1.6	1.0×10^{39}	0.17	0.03
2CXO J050015.3-032053	75.0640	-3.3482	0.5	4.0×10^{-15}	49.2	S	3.8	1.2×10^{39}	0.26	0.02
2CXO J050015.4-032038	75.0646	-3.3441	0.5	8.0×10^{-15}	49.2	S	7.1	2.3×10^{39}	0.10	0.06
2CXO J050015.4-032106	75.0644	-3.3518	0.5	5.3×10^{-15}	49.2	S	0.9	1.5×10^{39}	0.29	0.00
2CXO J050017.3-032047	75.0724	-3.3467	0.5	1.2×10^{-14}	49.2	S	7.7	3.5×10^{39}	0.48	0.08
2CXO J050017.3-032111	75.0725	-3.3531	0.5	9.6×10^{-15}	49.2	S	6.0	2.8×10^{39}	0.52	0.06
2CXO J050017.6-032133	75.0737	-3.3592	0.4	4.2×10^{-14}	49.2	S	9.0	1.2×10^{40}	0.22	0.13
2CXO J050136.1-041543	75.4007	-4.2620	0.4	2.2×10^{-14}	56.6	S	2.7	8.5×10^{39}	0.59	0.05
2CXO J050138.5-041516	75.4108	-4.2546	0.4	1.7×10^{-14}	54.3	S0/E	3.2	5.9×10^{39}	0.49	0.02
2CXO J050139.7-041511	75.4157	-4.2533	0.4	9.5×10^{-15}	54.3	S0/E	7.0	3.4×10^{39}	0.33	0.06
2CXO J050143.6-041728	75.4320	-4.2912	0.4	1.5×10^{-14}	54.2	S	2.8	5.4×10^{39}	0.65	0.03
2CXO J050143.8-041714	75.4329	-4.2874	0.6	3.5×10^{-15}	54.2	S	1.5	1.2×10^{39}	0.41	0.01
2CXO J050144.9-180943	75.4374	-18.1621	0.4	1.9×10^{-14}	53.4	S	7.8	6.7×10^{39}	0.23	0.07
2CXO J050146.1-180930	75.4423	-18.1583	0.4	2.0×10^{-14}	53.4	S	2.3	6.8×10^{39}	0.12	0.01
2CXO J050147.0-180905	75.4461	-18.1514	0.5	1.1×10^{-14}	53.4	S	5.2	3.7×10^{39}	0.41	0.03

Table A.9: List of ULX candidates obtained in Chapter 4 (continued).

Name	RA deg	Dec deg	$POSERR$ arcsec	F_X erg cm^{-2} s^{-1}	D Mpc	Gal. type	Sep. kpc	L_X erg s^{-1}	P_{XRB}	f_{cont}
2CXO J050147.2-180925	75.4470	-18.1569	0.5	1.4×10^{-14}	53.4	S	2.0	4.6×10^{39}	0.10	0.01
2CXO J050147.6-180902	75.4485	-18.1508	0.5	1.1×10^{-14}	53.4	S	6.6	3.7×10^{39}	0.30	0.04
2CXO J052106.0-253005	80.2752	-25.5015	0.9	3.4×10^{-15}	139.3		6.0	7.8×10^{39}	0.52	0.10
2CXO J052907.2-392458	82.2801	-39.4164	0.4	2.0×10^{-14}	62.0	S	6.1	9.1×10^{39}	0.83	0.10
2CXO J052907.6-392524	82.2817	-39.4235	0.6	3.2×10^{-15}	62.0	S	1.9	1.5×10^{39}	0.60	0.03
2CXO J053600.9-660233	84.0039	-66.0426	0.5	2.2×10^{-15}	165.0		2.6	7.1×10^{39}	0.63	0.03
2CXO J053926.4+771827	84.8604	77.3076	0.5	7.1×10^{-15}	58.8	S	10.8	2.9×10^{39}	0.65	0.06
2CXO J053958.8+771914	84.9950	77.3208	0.4	1.9×10^{-14}	58.8	S	21.5	7.9×10^{39}	0.75	0.19
2CXO J054155.8+692259	85.4828	69.3832	0.7	3.0×10^{-15}	56.4	S	13.4	1.2×10^{39}	0.82	0.14
2CXO J054158.1+692239	85.4923	69.3778	0.8	4.7×10^{-15}	56.4	S	9.4	1.8×10^{39}	0.42	0.06
2CXO J054201.3+692239	85.5055	69.3776	0.5	2.7×10^{-14}	56.4	S	4.9	1.0×10^{40}	0.33	0.02
2CXO J054209.2+692250	85.5386	69.3808	0.8	7.7×10^{-15}	56.4	S	6.7	2.9×10^{39}	0.37	0.03
2CXO J054210.4+692308	85.5437	69.3856	1.2	3.6×10^{-15}	56.4	S	10.6	1.4×10^{39}	0.50	0.10
2CXO J054212.3+692155	85.5515	69.3656	0.5	1.3×10^{-14}	56.4	S	16.3	5.0×10^{39}	0.72	0.29
2CXO J054214.5+692202	85.5606	69.3673	0.7	6.3×10^{-15}	56.4	S	17.4	2.4×10^{39}	0.82	0.29
2CXO J054215.8+692324	85.5662	69.3901	1.3	3.6×10^{-15}	56.4	S	19.3	1.4×10^{39}	0.80	0.31
2CXO J054714.6-452849	86.8109	-45.4805	0.5	2.2×10^{-15}	178.6		6.4	8.5×10^{39}	0.32	0.09
2CXO J060105.0-234006	90.2709	-23.6686	0.4	3.2×10^{-14}	20.8	S	4.3	1.7×10^{39}	0.70	0.02
2CXO J060106.6-234008	90.2775	-23.6690	0.4	5.5×10^{-14}	20.8	S	2.2	2.8×10^{39}	0.62	0.01
2CXO J060108.7-234017	90.2864	-23.6715	0.4	6.2×10^{-14}	20.8	S	1.1	3.2×10^{39}	0.61	0.00
2CXO J060108.8-233945	90.2868	-23.6626	0.4	3.5×10^{-14}	20.8	S	3.7	1.8×10^{39}	0.75	0.03
2CXO J060208.8-395735	90.5369	-39.9598	0.4	1.1×10^{-14}	197.7	S0/E	32.5	5.1×10^{40}		
2CXO J060232.3-395700	90.6346	-39.9501	0.5	2.1×10^{-15}	297.8	S0/E	9.8	2.2×10^{40}	0.30	0.30
2CXO J061529.8+710141	93.8743	71.0282	0.4	2.0×10^{-14}	58.0	S0/E	12.8	8.1×10^{39}	0.80	0.42
2CXO J061537.0+710121	93.9044	71.0226	0.5	2.8×10^{-15}	58.0	S0/E	14.7	1.1×10^{39}	0.73	0.53
2CXO J061615.8-212203	94.0662	-21.3676	0.4	8.3×10^{-15}	32.4	S	13.7	1.0×10^{39}	0.62	0.06
2CXO J061615.9-212232	94.0663	-21.3757	0.4	5.0×10^{-14}	32.4	S	13.5	6.3×10^{39}	0.66	0.08
2CXO J061616.6-212227	94.0694	-21.3743	0.4	1.3×10^{-14}	32.4	S	11.8	1.6×10^{39}	0.55	0.06
2CXO J061616.9-212109	94.0705	-21.3527	0.4	1.9×10^{-14}	32.4	S	15.8	2.4×10^{39}	0.83	0.09
2CXO J061617.2-212250	94.0719	-21.3807	0.4	2.4×10^{-14}	32.4	S	11.4	3.0×10^{39}	0.72	0.08
2CXO J061618.0-212153	94.0751	-21.3647	0.4	8.8×10^{-15}	32.4	S	9.9	1.1×10^{39}	0.68	0.03
2CXO J061618.7-212227	94.0783	-21.3743	0.4	1.2×10^{-14}	32.4	S	7.2	1.5×10^{39}	0.77	0.02
2CXO J061620.5-212210	94.0855	-21.3697	0.4	8.1×10^{-15}	32.4	S	3.8	1.0×10^{39}	0.58	0.00
2CXO J061620.8-212250	94.0869	-21.3808	0.4	1.2×10^{-14}	32.4	S	5.3	1.5×10^{39}	0.76	0.02
2CXO J061622.6-212139	94.0944	-21.3609	0.4	1.3×10^{-14}	32.4	S	6.7	1.6×10^{39}	0.76	0.04
2CXO J061623.5-212215	94.0983	-21.3709	0.4	8.6×10^{-15}	32.4	S	3.4	1.1×10^{39}	0.30	0.01
2CXO J061623.5-212218	94.0980	-21.3719	0.4	1.6×10^{-14}	32.4	S	3.1	2.0×10^{39}	0.51	0.00
2CXO J061625.1-212229	94.1049	-21.3749	0.4	9.7×10^{-15}	32.4	S	6.8	1.2×10^{39}	0.71	0.01
2CXO J061626.5-212212	94.1106	-21.3701	0.4	1.2×10^{-14}	32.4	S	9.7	1.6×10^{39}	0.62	0.04
2CXO J061626.8-212211	94.1118	-21.3698	0.4	1.1×10^{-14}	32.4	S	10.4	1.4×10^{39}	0.84	0.05
2CXO J061628.3-212139	94.1183	-21.3609	0.4	9.9×10^{-15}	32.4	S	15.1	1.2×10^{39}	0.80	0.15
2CXO J061734.2+710442	94.3926	71.0784	4.0	1.4×10^{-14}	96.3	S	6.2	1.5×10^{40}	0.55	0.07
2CXO J061839.6+782114	94.6652	78.3540	0.4	9.6×10^{-14}	13.9	S	0.8	2.2×10^{39}		
2CXO J061914.0+782145	94.8084	78.3625	0.4	4.3×10^{-14}	13.9	S	7.4	1.0×10^{39}	0.76	0.24
2CXO J062139.2-271311	95.4134	-27.2200	0.4	3.3×10^{-14}	20.8	S0/E	5.0	1.7×10^{39}	0.75	0.05
2CXO J062536.1-535105	96.4007	-53.8516	0.6	3.0×10^{-15}	246.6		9.9	2.2×10^{40}	0.57	0.14
2CXO J062647.4-542414	96.6978	-54.4041	1.6	5.1×10^{-15}	197.7		8.5	2.4×10^{40}	0.62	0.26
2CXO J063206.5-353730	98.0274	-35.6252	0.5	2.5×10^{-15}	118.6	S	7.6	4.2×10^{39}	0.56	0.27
2CXO J063839.6-801448	99.6651	-80.2469	0.4	4.6×10^{-15}	63.5	S	1.3	2.2×10^{39}	0.76	0.01
2CXO J064258.6-741444	100.7442	-74.2457	0.4	6.2×10^{-15}	54.6		5.4	2.2×10^{39}	0.66	0.05
2CXO J064301.3-741516	100.7558	-74.2545	0.4	7.5×10^{-15}	54.6		3.4	2.7×10^{39}	0.83	0.02
2CXO J064302.2-741411	100.7595	-74.2364	0.4	1.8×10^{-14}	82.6	S	5.4	1.5×10^{40}	0.76	0.07
2CXO J064304.8-741343	100.7700	-74.2286	0.4	6.6×10^{-15}	82.6	S	12.5	5.4×10^{39}	0.84	0.17
2CXO J064306.5-741448	100.7771	-74.2469	0.5	1.3×10^{-15}	82.6	S	13.0	1.1×10^{39}	0.52	0.19
2CXO J064307.6-741502	100.7818	-74.2506	0.5	1.4×10^{-15}	82.6	S	18.3	1.2×10^{39}	0.75	0.41
2CXO J064310.5-741406	100.7940	-74.2352	0.4	3.1×10^{-15}	82.6		7.3	2.5×10^{39}	0.85	0.16
2CXO J064310.6-741434	100.7943	-74.2430	0.4	5.3×10^{-15}	82.6		12.0	4.3×10^{39}	0.52	0.24
2CXO J064846.2-641959	102.1925	-64.3332	1.3	7.4×10^{-15}	45.9	S	6.8	1.9×10^{39}	0.69	0.38
2CXO J065249.0+742922	103.2042	74.4896	0.7	4.9×10^{-15}	73.6	S	11.7	3.2×10^{39}	0.69	0.29
2CXO J065250.8+742909	103.2117	74.4860	0.7	1.8×10^{-15}	73.6	S	6.7	1.1×10^{39}	0.77	0.10
2CXO J065252.1+742833	103.2174	74.4760	0.7	2.3×10^{-15}	73.6	S	5.9	1.5×10^{39}	0.76	0.09
2CXO J070232.3+503529	105.6347	50.5915	0.5	6.7×10^{-15}	86.2	S	3.0	5.9×10^{39}	0.17	0.01
2CXO J070902.5+483427	107.2608	48.5744	0.5	2.3×10^{-14}	75.8	S	3.5	1.6×10^{40}	0.21	0.08
2CXO J071044.9+501209	107.6873	50.2027	1.0	3.2×10^{-14}	82.5	S0/E	2.6	2.6×10^{40}	0.18	0.08
2CXO J072122.1+554851	110.3422	55.8143	0.5	3.2×10^{-15}	164.1	S0/E	9.4	1.0×10^{40}	0.69	0.48
2CXO J072637.5+854534	111.6567	85.7596	0.4	8.2×10^{-14}	32.4		7.6	1.0×10^{40}		
2CXO J072648.0+854552	111.7003	85.7645	0.4	3.4×10^{-14}	32.4		8.5	4.3×10^{39}		
2CXO J073625.5+653539	114.1065	65.5944	0.4	1.0×10^{-12}	3.2	S	2.5	1.3×10^{39}	0.90	0.00
2CXO J074345.6+480816	115.9403	48.1380	0.4	1.6×10^{-14}	77.6	S0/E	1.5	1.2×10^{40}	0.15	0.02
2CXO J074651.8+390050	116.7161	39.0140	0.5	4.4×10^{-15}	53.5	S	9.6	1.5×10^{39}	0.64	0.43
2CXO J074653.2+390051	116.7217	39.0143	0.4	6.5×10^{-15}	53.5	S	5.7	2.2×10^{39}	0.51	0.12
2CXO J074655.6+390021	116.7320	39.0059	0.4	3.8×10^{-15}	53.5	S	8.7	1.3×10^{39}	0.77	0.13
2CXO J074902.3+555500	117.2600	55.9168	0.6	5.8×10^{-15}	153.5	S	6.3	1.6×10^{40}	0.43	0.16
2CXO J075117.4+501051	117.8226	50.1811	0.5	3.6×10^{-15}	91.1	S0/E	2.6	3.6×10^{39}	0.54	0.04
2CXO J075121.3+501416	117.8390	50.2380	0.5	4.3×10^{-15}	98.8		4.0	5.0×10^{39}	0.36	0.09
2CXO J075133.1+500806	117.8883	50.1352	0.7	1.4×10^{-15}	165.2	S	5.6	4.6×10^{39}	0.36	0.08
2CXO J075914.2+325514	119.8093	32.9206	1.9	6.9×10^{-15}	72.3	S	8.6	4.3×10^{39}	0.35	0.19
2CXO J080148.0+504354	120.4504	50.7319	0.4	2.6×10^{-13}	15.0	S	3.8	7.1×10^{39}	0.64	0.03
2CXO J080405.9+050655	121.0246	5.1155	0.4	3.3×10^{-15}	53.5		1.6	1.1×10^{39}	0.77	0.02
2CXO J081436.9+490326	123.6541	49.0573	0.5	1.4×10^{-13}	11.2	S	1.8	2.1×10^{39}	0.74	0.02
2CXO J081905.4+214709	124.7726	21.7858	0.9	9.8×10^{-15}	61.5	S	6.1	4.4×10^{39}	0.49	0.25

Table A.10: List of ULX candidates obtained in Chapter 4 (continued).

Name	RA deg	Dec deg	$POSERR$ arcsec	F_X erg cm^{-2} s^{-1}	D Mpc	Gal. type	Sep. kpc	L_X erg s^{-1}	P_{XRB}	f_{cont}
2CXO J081928.9+704219	124.8708	70.7054	0.4	3.2×10^{-12}	3.2		2.1	3.8×10^{39}	0.76	0.00
2CXO J082015.5+205237	125.0647	20.8770	0.5	4.7×10^{-15}	66.2	S	4.9	2.5×10^{39}	0.71	0.18
2CXO J082215.9+210535	125.5665	21.0933	0.5	1.2×10^{-13}	92.3	S	1.9	1.2×10^{41}	0.17	0.03
2CXO J082332.9+212043	125.8872	21.3454	0.6	8.7×10^{-15}	73.9	S0/E	6.9	5.7×10^{39}	0.63	0.09
2CXO J082333.7+212053	125.8905	21.3481	0.5	1.0×10^{-14}	73.9	S0/E	2.7	6.8×10^{39}	0.51	0.03
2CXO J083202.4+524717	128.0102	52.7881	0.5	3.8×10^{-15}	264.8	S	4.2	3.2×10^{40}	0.30	0.08
2CXO J083923.2+295140	129.8471	29.8613	0.5	1.0×10^{-14}	223.9	S	8.4	6.1×10^{40}	0.31	0.27
2CXO J084001.7+294846	130.0072	29.8130	0.4	1.3×10^{-14}	291.1	S	22.1	1.4×10^{41}	0.38	0.55
2CXO J084002.9+294918	130.0122	29.8219	0.4	8.9×10^{-16}	291.1	S	22.3	9.0×10^{39}	0.73	0.57
2CXO J084011.3+295146	130.0473	29.8629	0.5	4.4×10^{-15}	222.8		6.4	2.6×10^{40}	0.49	0.25
2CXO J084113.2+322454	130.3052	32.4150	0.5	3.8×10^{-15}	306.2	S0/E	7.6	4.2×10^{40}	0.18	0.04
2CXO J084113.6+322456	130.3068	32.4156	0.5	1.5×10^{-15}	306.2	S0/E	10.1	1.7×10^{40}	0.23	0.06
2CXO J084117.6+322712	130.3234	32.4536	0.5	3.5×10^{-16}	498.9		8.6	1.0×10^{40}	0.57	0.12
2CXO J084249.3+292349	130.7055	29.3970	1.0	1.5×10^{-15}	223.9		4.7	9.0×10^{39}	0.17	0.07
2CXO J084255.1+331924	130.7299	33.3234	0.5	2.2×10^{-15}	385.5		8.1	3.9×10^{40}	0.52	0.13
2CXO J084339.5+501203	130.9148	50.2009	1.3	4.3×10^{-14}	45.3	S	4.7	1.1×10^{40}	0.61	0.07
2CXO J084340.2+501149	130.9178	50.1971	1.3	2.4×10^{-14}	45.3	S	8.0	5.9×10^{39}	0.50	0.21
2CXO J085333.6+511929	133.3902	51.3249	0.4	5.2×10^{-14}	17.2	S0/E	3.4	1.8×10^{39}		
2CXO J090931.2+330821	137.3801	33.1394	0.4	1.5×10^{-14}	26.1	S	8.1	1.2×10^{39}	0.71	0.07
2CXO J090931.8+330805	137.3825	33.1347	0.4	6.5×10^{-14}	26.1	S	5.8	5.3×10^{39}	0.86	0.03
2CXO J091335.2+300011	138.3970	30.0033	0.4	5.5×10^{-15}	92.9	S	13.2	5.6×10^{39}	0.67	0.31
2CXO J091337.4+762811	138.4061	76.4699	0.4	3.1×10^{-14}	20.8	S	2.8	1.6×10^{39}	0.77	0.01
2CXO J091338.0+295958	138.4084	29.9995	0.7	2.2×10^{-15}	108.6	S	3.8	3.2×10^{39}	0.34	0.06
2CXO J091348.5+762902	138.4522	76.4840	0.4	2.3×10^{-14}	20.8	S	3.6	1.2×10^{39}	0.78	0.01
2CXO J091348.9+762828	138.4542	76.4746	0.4	6.1×10^{-14}	20.8	S	2.1	3.2×10^{39}	0.77	0.02
2CXO J091405.1+400642	138.5216	40.1118	0.4	1.7×10^{-14}	25.4	S	0.9	1.3×10^{39}		
2CXO J091405.3+400628	138.5222	40.1079	0.4	1.8×10^{-14}	25.4	S	2.6	1.4×10^{39}		
2CXO J091601.0+442108	139.0042	44.3524	0.5	4.4×10^{-15}	143.9	S	2.2	1.1×10^{40}	0.34	0.02
2CXO J091721.0+415442	139.3377	41.9118	0.4	3.1×10^{-14}	25.0	S	1.0	2.3×10^{39}	0.81	0.00
2CXO J091722.5+415433	139.3440	41.9093	0.4	1.7×10^{-14}	25.0	S	1.3	1.3×10^{39}	0.84	0.00
2CXO J092013.6+640606	140.0569	64.1017	0.4	6.9×10^{-14}	25.4	S	5.4	5.3×10^{39}	0.65	0.08
2CXO J092014.9+640435	140.0623	64.0765	0.5	2.1×10^{-14}	25.4	S	12.3	1.6×10^{39}	0.62	0.32
2CXO J092019.5+640453	140.0813	64.0817	0.5	2.6×10^{-14}	25.4	S	9.2	2.0×10^{39}	0.51	0.17
2CXO J092205.5+035335	140.5232	3.8933	1.1	1.4×10^{-14}	57.2	S	4.6	5.4×10^{39}	0.71	0.06
2CXO J092207.3+035350	140.5308	3.8974	3.8	1.2×10^{-14}	57.2	S	4.8	4.6×10^{39}	0.47	0.06
2CXO J093206.1+213058	143.0257	21.5163	0.5	2.1×10^{-13}	8.6	S	3.2	1.8×10^{39}	0.90	0.05
2CXO J093354.9+340347	143.4788	34.0633	0.6	2.2×10^{-15}	117.0	S	4.6	3.6×10^{39}	0.57	0.10
2CXO J093552.7+612112	143.9697	61.3535	0.4	2.1×10^{-15}	176.2	S	6.1	7.6×10^{39}	0.52	0.14
2CXO J093809.8+093027	144.5411	9.5077	1.4	8.8×10^{-15}	44.7	S	13.8	2.1×10^{39}	0.75	0.57
2CXO J093854.2-045131	144.7260	-4.8588	0.5	1.0×10^{-15}	91.9	S	4.5	1.0×10^{39}	0.82	0.55
2CXO J094103.9+344355	145.2665	34.7322	0.5	4.6×10^{-16}	223.9	S	3.0	2.7×10^{39}	0.31	0.05
2CXO J094129.8+412253	145.3745	41.3816	1.4	5.1×10^{-15}	75.3	S	2.8	3.5×10^{39}	0.35	0.03
2CXO J094154.7+412344	145.4782	41.3957	0.8	5.6×10^{-15}	199.6	S	4.7	2.6×10^{40}	0.25	0.14
2CXO J094253.1+092924	145.7216	9.4901	0.4	7.7×10^{-15}	42.9	S	3.2	1.7×10^{39}	0.88	0.07
2CXO J094416.4+541134	146.0685	54.1929	0.4	1.4×10^{-14}	25.4		1.2	1.1×10^{39}	0.43	0.01
2CXO J094529.2-311227	146.3720	-31.2077	0.4	1.8×10^{-13}	7.1	S	4.6	1.1×10^{39}	0.94	0.04
2CXO J094542.7-141948	146.4279	-14.3301	0.5	1.2×10^{-14}	28.8	S	2.3	1.2×10^{39}		
2CXO J094547.8-142201	146.4495	-14.3671	0.4	8.5×10^{-14}	28.8	S	1.1	8.5×10^{39}		
2CXO J094550.4-142138	146.4603	-14.3607	0.4	3.8×10^{-14}	28.8	S	5.7	3.8×10^{39}	0.74	0.26
2CXO J094619.8+030406	146.5826	3.0686	0.4	4.0×10^{-15}	81.2	S	8.2	3.1×10^{39}	0.35	0.05
2CXO J094619.9+030238	146.5831	3.0440	0.5	6.1×10^{-15}	82.3	S	3.2	5.0×10^{39}	0.71	0.04
2CXO J094620.0+030249	146.5837	3.0472	0.4	7.0×10^{-15}	82.3	S	2.8	5.6×10^{39}	0.34	0.02
2CXO J094620.1+030242	146.5839	3.0452	0.5	5.1×10^{-15}	82.3	S	1.3	4.1×10^{39}	0.32	0.00
2CXO J094620.7+030236	146.5865	3.0436	0.5	4.1×10^{-15}	82.3	S	3.5	3.3×10^{39}	0.37	0.02
2CXO J094622.3+030423	146.5931	3.0731	0.5	3.0×10^{-15}	81.2	S	7.4	2.4×10^{39}	0.26	0.04
2CXO J095532.9+690033	148.8873	69.0093	0.4	7.9×10^{-13}	3.8	S	3.7	1.3×10^{39}	0.88	0.01
2CXO J095550.9+694045	148.9624	69.6792	0.4	1.2×10^{-12}	3.9	S	0.1	2.3×10^{39}		
2CXO J095753.5+015725	149.4733	1.9571	0.9	3.3×10^{-15}	494.3		13.7	9.6×10^{40}	0.26	0.15
2CXO J095823.4-265519	149.5976	-26.9222	0.6	7.7×10^{-15}	35.2	S0/E	3.7	1.1×10^{39}	0.73	0.03
2CXO J095824.1-265523	149.6006	-26.9233	0.5	1.7×10^{-14}	35.2	S0/E	2.2	2.5×10^{39}	0.62	0.01
2CXO J095827.1-265517	149.6131	-26.9214	0.5	6.8×10^{-15}	35.2	S0/E	6.5	1.0×10^{39}	0.64	0.10
2CXO J100029.4-194005	150.1229	-19.6682	0.4	6.3×10^{-15}	51.5	S0/E	5.2	2.0×10^{39}	0.68	0.21
2CXO J100339.5+474230	150.9149	47.7084	1.1	1.1×10^{-14}	64.4	S	2.9	5.3×10^{39}	0.32	0.03
2CXO J100401.3-062819	151.0054	-6.4721	0.4	1.4×10^{-14}	67.6	S	4.9	7.7×10^{39}	0.26	0.05
2CXO J100402.4-062853	151.0102	-6.4815	0.4	1.0×10^{-14}	67.6	S	7.9	5.5×10^{39}	0.27	0.05
2CXO J100402.5-062849	151.0105	-6.4805	0.4	1.2×10^{-14}	67.6	S	6.8	6.4×10^{39}	0.24	0.04
2CXO J100402.7-062833	151.0114	-6.4759	0.4	5.7×10^{-15}	67.6	S	3.2	3.1×10^{39}	0.34	0.03
2CXO J100513.1-074238	151.3048	-7.7107	0.4	8.1×10^{-14}	10.3	S0/E	1.5	1.0×10^{39}	0.89	0.02
2CXO J100633.9-295617	151.6416	-29.9381	0.4	1.5×10^{-13}	13.9	S0/E	0.9	3.4×10^{39}	0.93	0.00
2CXO J100710.4+123848	151.7934	12.6467	0.5	4.8×10^{-14}	37.9	S	3.5	8.2×10^{39}	0.79	0.06
2CXO J100810.8+515052	152.0451	51.8481	0.4	3.3×10^{-14}	19.6	S	1.7	1.5×10^{39}	0.80	0.02
2CXO J101010.2-122627	152.5426	-12.4409	0.5	4.0×10^{-15}	48.2	S	6.0	1.1×10^{39}	0.79	0.04
2CXO J101010.6-122537	152.5443	-12.4272	0.4	4.5×10^{-15}	48.2	S	5.9	1.2×10^{39}	0.73	0.02
2CXO J101011.0-122541	152.5459	-12.4282	0.5	4.5×10^{-15}	48.2	S	6.0	1.3×10^{39}	0.58	0.03
2CXO J101011.0-122630	152.5462	-12.4418	0.5	4.5×10^{-15}	48.2	S	7.8	1.3×10^{39}	0.85	0.11
2CXO J101012.8-122524	152.5536	-12.4235	0.4	8.8×10^{-15}	48.2	S	13.1	2.4×10^{39}	0.76	0.19
2CXO J101239.8-010628	153.1662	-1.1078	0.5	9.5×10^{-15}	438.5	S	9.5	2.2×10^{41}	0.29	0.13
2CXO J101651.4+732408	154.2144	73.4024	0.6	1.8×10^{-14}	39.3	S0/E	2.1	3.3×10^{39}	0.16	0.03
2CXO J101812.0+412421	154.5502	41.4059	0.4	4.9×10^{-14}	13.2	S	5.5	1.0×10^{39}	0.92	0.06
2CXO J101825.3+215356	154.6056	21.8990	0.5	1.4×10^{-14}	34.0	S0/E	3.1	1.9×10^{39}		
2CXO J101959.1+453403	154.9966	45.5676	0.4	5.3×10^{-14}	13.8	S	5.2	1.2×10^{39}	0.89	0.04

Table A.11: List of ULX candidates obtained in Chapter 4 (continued).

Name	RA deg	Dec deg	$POSERR$ arcsec	F_X erg cm^{-2} s^{-1}	D Mpc	Gal. type	Sep. kpc	L_X erg s^{-1}	P_{XRB}	f_{cont}
2CXO J102219.7+213402	155.5823	21.5673	0.4	7.1×10^{-15}	55.8	S	2.4	2.6×10^{39}	0.72	0.01
2CXO J102219.8+213328	155.5827	21.5580	0.4	6.0×10^{-15}	55.8	S	11.0	2.2×10^{39}	0.79	0.13
2CXO J102220.1+213450	155.5839	21.5806	0.4	6.7×10^{-15}	55.8	S	9.6	2.5×10^{39}	0.78	0.10
2CXO J102221.1+213335	155.5881	21.5600	0.4	6.6×10^{-15}	55.8	S	10.1	2.5×10^{39}	0.88	0.08
2CXO J102221.6+213324	155.5904	21.5569	0.4	5.8×10^{-15}	55.8	S	13.6	2.2×10^{39}	0.71	0.16
2CXO J102440.6-184209	156.1693	-18.7026	0.6	9.6×10^{-15}	213.8	S	8.8	5.2×10^{40}	0.73	0.21
2CXO J102506.9+170913	156.2791	17.1536	0.5	1.7×10^{-14}	40.3	S	3.2	3.3×10^{39}	0.70	0.02
2CXO J102507.9+170909	156.2831	17.1527	0.4	4.2×10^{-14}	40.3	S	1.7	8.1×10^{39}	0.14	0.01
2CXO J102508.2+170948	156.2842	17.1635	0.4	8.7×10^{-14}	40.3	S	5.8	1.7×10^{40}	0.87	0.08
2CXO J102749.8-435426	156.9577	-43.9073	0.4	1.6×10^{-14}	37.0	S0/E	3.6	2.7×10^{39}		
2CXO J102750.6-435420	156.9609	-43.9056	0.4	1.6×10^{-14}	37.0	S0/E	1.7	2.7×10^{39}		
2CXO J102751.2-435358	156.9635	-43.8996	0.4	1.6×10^{-14}	37.0	S0/E	2.7	2.7×10^{39}		
2CXO J102751.5-435409	156.9650	-43.9026	0.4	3.3×10^{-14}	37.0	S0/E	0.9	5.4×10^{39}		
2CXO J102752.0-435412	156.9669	-43.9036	0.4	1.8×10^{-14}	37.0	S0/E	1.5	3.0×10^{39}		
2CXO J102752.5-435349	156.9690	-43.8972	0.4	1.4×10^{-14}	37.0	S0/E	4.8	2.3×10^{39}		
2CXO J102755.1-435446	156.9798	-43.9130	0.4	1.7×10^{-14}	37.0	S0/E	9.4	2.7×10^{39}	0.80	0.79
2CXO J103133.8-395719	157.8912	-39.9553	0.4	8.4×10^{-15}	35.8	S	3.0	1.3×10^{39}	0.79	0.03
2CXO J103135.9-395653	157.8996	-39.9482	0.5	1.4×10^{-14}	35.8	S	4.0	2.1×10^{39}	0.88	0.07
2CXO J103151.8-351243	157.9660	-35.2120	1.8	2.1×10^{-14}	31.4	S0/E	3.9	2.4×10^{39}	0.20	0.19
2CXO J103155.9-352537	157.9830	-35.4271	1.9	1.5×10^{-14}	37.8	S	11.2	2.5×10^{39}	0.71	0.53
2CXO J103409.6-351956	158.5401	-35.3323	0.7	1.5×10^{-14}	36.8	S0/E	7.3	2.4×10^{39}	0.68	0.18
2CXO J103446.2+213820	158.6926	21.6389	0.4	1.9×10^{-14}	20.8	S	3.7	1.0×10^{39}	0.92	0.04
2CXO J103619.8-273939	159.0827	-27.6610	0.9	8.6×10^{-15}	430.5	S0/E	27.1	1.9×10^{41}	0.43	0.84
2CXO J103622.8-273859	159.0951	-27.6498	0.7	7.5×10^{-15}	260.6	S	7.0	6.1×10^{40}	0.34	0.16
2CXO J103638.3-274249	159.1599	-27.7138	1.5	2.3×10^{-14}	50.0	S	3.8	6.9×10^{39}	0.73	0.14
2CXO J103844.2+485220	159.6845	48.8724	0.4	9.2×10^{-15}	539.5	S0/E	13.9	3.2×10^{41}	0.36	0.34
2CXO J103844.4+533004	159.6853	53.5013	0.4	4.8×10^{-14}	19.6	S	1.3	2.2×10^{39}		
2CXO J103845.9+533004	159.6917	53.5012	0.4	2.4×10^{-13}	19.6	S	0.7	1.1×10^{40}		
2CXO J103846.5+533038	159.6940	53.5106	0.4	5.5×10^{-14}	19.6	S	2.5	2.5×10^{39}		
2CXO J103846.6+533013	159.6942	53.5037	0.4	4.2×10^{-14}	19.6	S	0.6	1.9×10^{39}		
2CXO J103847.2+533027	159.6969	53.5077	0.4	1.3×10^{-13}	19.6	S	1.9	5.9×10^{39}		
2CXO J104230.9+050218	160.6291	5.0386	0.4	2.3×10^{-15}	120.8	S	11.5	4.1×10^{39}	0.78	0.10
2CXO J104231.3+050221	160.6307	5.0393	0.5	2.7×10^{-15}	120.8	S	9.2	4.7×10^{39}	0.82	0.12
2CXO J104319.0+313104	160.8292	31.5179	0.5	6.3×10^{-15}	160.0	S0/E	3.0	1.9×10^{40}	0.27	0.02
2CXO J104409.7+064520	161.0406	6.7557	0.4	4.7×10^{-15}	84.3	S	15.2	4.0×10^{39}	0.35	0.10
2CXO J104410.3+064533	161.0432	6.7593	0.5	1.5×10^{-15}	84.3	S	11.0	1.2×10^{39}	0.78	0.03
2CXO J104410.7+064545	161.0448	6.7626	0.4	2.0×10^{-15}	84.3	S	10.4	1.7×10^{39}	0.87	0.05
2CXO J104411.0+064539	161.0459	6.7611	0.4	9.8×10^{-15}	84.3	S	7.9	8.3×10^{39}	0.82	0.02
2CXO J104411.5+064530	161.0480	6.7585	0.4	1.9×10^{-15}	84.3	S	4.2	1.6×10^{39}	0.81	0.01
2CXO J104412.8+064545	161.0535	6.7626	0.4	5.5×10^{-15}	84.3	S	6.5	4.7×10^{39}	0.88	0.04
2CXO J104412.9+064519	161.0541	6.7553	0.4	3.2×10^{-15}	84.3	S	6.6	2.7×10^{39}	0.87	0.03
2CXO J104413.0+064553	161.0544	6.7649	0.4	2.7×10^{-15}	84.3	S	10.0	2.3×10^{39}	0.73	0.11
2CXO J104413.4+064529	161.0560	6.7582	0.4	2.8×10^{-15}	84.3	S	7.1	2.4×10^{39}	0.68	0.01
2CXO J104413.8+064546	161.0578	6.7630	0.4	1.7×10^{-15}	84.3	S	11.3	1.5×10^{39}	0.88	0.08
2CXO J104414.6+064541	161.0610	6.7616	0.4	4.4×10^{-14}	84.3	S	14.7	3.8×10^{40}	0.47	0.09
2CXO J104532.3+583522	161.3847	58.5897	1.7	5.4×10^{-15}	43.3	S	9.1	1.2×10^{39}	0.35	0.33
2CXO J104630.9+134432	161.6291	13.7424	0.4	6.0×10^{-15}	40.4	S	12.6	1.2×10^{39}	0.84	0.19
2CXO J104631.4+134503	161.6312	13.7510	0.4	5.5×10^{-15}	40.4	S	9.7	1.1×10^{39}	0.92	0.11
2CXO J104631.6+134450	161.6320	13.7473	0.4	1.3×10^{-14}	40.4	S	9.5	2.4×10^{39}	0.77	0.11
2CXO J104631.7+134524	161.6324	13.7568	0.4	6.4×10^{-15}	40.4	S	9.9	1.2×10^{39}	0.84	0.12
2CXO J104632.1+134528	161.6338	13.7580	0.4	3.6×10^{-14}	40.4	S	9.5	7.0×10^{39}	0.76	0.11
2CXO J104636.6+134522	161.6527	13.7562	0.4	7.2×10^{-15}	40.4	S	6.0	1.4×10^{39}	0.82	0.04
2CXO J104749.9+123456	161.9583	12.5825	0.4	1.8×10^{-13}	11.0	S0/E	0.3	2.7×10^{39}	0.67	0.00
2CXO J104804.0+585124	162.0168	58.8569	0.9	1.5×10^{-15}	389.0	S	17.9	2.8×10^{40}	0.49	0.26
2CXO J104826.0+123144	162.1087	12.5289	0.8	3.3×10^{-14}	21.4	S	3.1	1.8×10^{39}		
2CXO J104827.0+123138	162.1129	12.5274	0.6	3.9×10^{-14}	21.4	S	2.4	2.2×10^{39}		
2CXO J104925.2+324631	162.3553	32.7753	2.2	1.0×10^{-14}	26.0	S	1.2	8.1×10^{39}	0.53	0.01
2CXO J104946.5+325823	162.4441	32.9732	0.4	1.5×10^{-14}	23.9	S	6.4	1.0×10^{39}	0.66	0.05
2CXO J104949.7+325838	162.4574	32.9773	0.4	4.1×10^{-14}	23.9	S	2.3	2.8×10^{39}	0.74	0.01
2CXO J104949.8+325907	162.4577	32.9853	0.5	1.6×10^{-14}	23.9	S	1.1	1.1×10^{39}	0.62	0.00
2CXO J104952.1+325903	162.4674	32.9844	1.0	2.6×10^{-14}	23.9	S	3.0	1.7×10^{39}	0.93	0.07
2CXO J105120.7+324555	162.8366	32.7654	0.5	7.1×10^{-14}	16.2	S0/E	0.3	2.2×10^{39}	0.14	0.00
2CXO J105148.2+155954	162.9512	15.9985	0.4	1.1×10^{-15}	96.0	S	8.0	1.3×10^{39}	0.88	0.13
2CXO J105148.9+155951	162.9541	15.9977	0.4	5.3×10^{-15}	96.0	S	5.3	5.9×10^{39}	0.79	0.06
2CXO J105155.9+552324	162.9832	55.3901	0.4	3.7×10^{-15}	378.1	S	7.8	6.4×10^{40}	0.52	0.10
2CXO J105210.4+552243	163.0435	55.3786	0.5	6.9×10^{-15}	669.9	S	12.2	3.7×10^{41}	0.50	0.17
2CXO J105228.9+455312	163.1207	45.8869	1.2	7.4×10^{-15}	82.1	S	3.6	6.0×10^{39}	0.65	0.05
2CXO J105229.1+455322	163.1217	45.8897	1.0	1.4×10^{-14}	82.1	S	2.3	1.2×10^{40}	0.27	0.01
2CXO J105234.7+363803	163.1448	36.6342	0.8	7.7×10^{-14}	14.4	S	4.9	1.9×10^{39}	0.43	0.02
2CXO J105347.3+570651	163.4473	57.1143	3.3	1.9×10^{-14}	28.4	S	3.2	1.9×10^{39}	0.61	0.02
2CXO J105433.8+565943	163.6412	56.9955	0.6	1.3×10^{-14}	26.5	S	2.7	1.1×10^{39}	0.70	0.05
2CXO J110043.3+103307	165.1807	10.5521	0.6	3.1×10^{-15}	148.6	S0/E	20.2	8.2×10^{39}	0.87	0.76
2CXO J110113.6+033615	165.3069	3.6043	0.4	4.8×10^{-14}	18.0	S	8.1	1.9×10^{39}	0.91	0.08
2CXO J110311.9+110427	165.7998	11.0744	0.5	1.2×10^{-15}	87.7	S	6.9	1.1×10^{39}	0.62	0.04
2CXO J110313.0+110417	165.8043	11.0716	0.5	1.9×10^{-15}	87.7	S	7.7	1.8×10^{39}	0.57	0.05
2CXO J110313.0+110447	165.8042	11.0800	0.4	1.1×10^{-14}	87.7	S	4.7	1.0×10^{40}	0.79	0.02
2CXO J110313.2+110452	165.8051	11.0812	0.5	1.6×10^{-15}	87.7	S	6.7	1.4×10^{39}	0.62	0.04
2CXO J110313.6+110458	165.8068	11.0829	0.4	6.0×10^{-15}	87.7	S	9.9	5.6×10^{39}	0.78	0.08
2CXO J110315.3+110449	165.8139	11.0803	0.4	6.6×10^{-15}	87.7	S	15.3	6.1×10^{39}	0.72	0.23
2CXO J110325.7+180843	165.8573	18.1455	0.4	5.9×10^{-14}	19.1	S0/E	3.4	2.6×10^{39}	0.82	0.08
2CXO J110352.3+405101	165.9681	40.8504	0.4	2.4×10^{-15}	157.0		5.0	7.1×10^{39}	0.80	0.06

Table A.12: List of ULX candidates obtained in Chapter 4 (continued).

Name	RA deg	Dec deg	$POSERR$ arcsec	F_X erg cm^{-2} s^{-1}	D Mpc	Gal. type	Sep. kpc	L_X erg s^{-1}	P_{XRB}	f_{cont}
2CXO J110352.7+405051	165.9697	40.8476	0.5	1.7×10^{-15}	157.0		3.7	5.1×10^{39}	0.51	0.03
2CXO J110353.7+405057	165.9740	40.8492	0.5	2.3×10^{-15}	154.2	S	2.3	6.5×10^{39}	0.16	0.01
2CXO J110355.2+405053	165.9800	40.8483	0.5	9.6×10^{-16}	154.2	S	11.2	2.7×10^{39}	0.60	0.13
2CXO J110545.6+000016	166.4401	0.0045	0.4	3.2×10^{-13}	11.2	S	8.2	4.9×10^{39}	0.95	0.06
2CXO J110546.8-000809	166.4451	-0.1359	0.6	1.0×10^{-14}	137.4	S	3.8	2.3×10^{40}	0.84	0.12
2CXO J110934.7-373702	167.3949	-37.6174	1.1	1.0×10^{-14}	37.4		4.2	1.7×10^{39}	0.69	0.25
2CXO J110940.4+214422	167.4185	21.7396	0.7	2.6×10^{-15}	142.6	S0/E	6.9	6.4×10^{39}	0.34	0.28
2CXO J110956.1-373404	167.4840	-37.5679	0.5	5.5×10^{-15}	45.7	S0/E	22.7	1.4×10^{39}	0.78	0.43
2CXO J110958.3-373307	167.4930	-37.5520	0.5	4.1×10^{-15}	45.7	S0/E	10.1	1.0×10^{39}	0.77	0.10
2CXO J110959.3-373322	167.4973	-37.5563	0.5	4.3×10^{-15}	45.7	S0/E	14.1	1.1×10^{39}	0.90	0.20
2CXO J110959.6-373028	167.4984	-37.5079	0.5	1.3×10^{-14}	45.7	S0/E	24.9	3.4×10^{39}	0.59	0.51
2CXO J110959.9-373048	167.4998	-37.5133	0.4	3.1×10^{-14}	45.7	S0/E	21.0	7.9×10^{39}	0.87	0.35
2CXO J111000.8-373354	167.5037	-37.5651	0.4	7.6×10^{-15}	45.7	S0/E	21.8	1.9×10^{39}	0.85	0.50
2CXO J111006.9-373208	167.5288	-37.5358	0.5	6.5×10^{-15}	45.7	S0/E	24.0	1.6×10^{39}	0.89	0.59
2CXO J111024.8+284222	167.6037	28.7063	0.7	1.2×10^{-15}	317.7	S	9.6	1.4×10^{40}	0.30	0.18
2CXO J111126.0+554016	167.8584	55.6713	0.4	1.2×10^{-13}	10.7	S	2.2	1.7×10^{39}	0.73	0.01
2CXO J111241.2+132508	168.1719	13.4191	0.4	5.5×10^{-15}	152.8	S	4.9	1.5×10^{40}	0.84	0.12
2CXO J111241.3+132438	168.1721	13.4107	0.4	5.5×10^{-15}	152.8	S	17.6	1.5×10^{40}	0.56	0.53
2CXO J111826.5+564934	169.6108	56.8262	0.6	1.3×10^{-14}	331.1	S	5.2	1.8×10^{41}	0.18	0.11
2CXO J111858.4+130530	169.7437	13.0919	0.5	8.8×10^{-14}	12.0		2.2	1.5×10^{39}	0.88	0.06
2CXO J112015.7+133513	170.0657	13.5871	0.5	2.8×10^{-13}	9.9	S	1.0	3.3×10^{39}	0.82	0.00
2CXO J112018.3+125900	170.0763	12.9835	1.1	1.2×10^{-13}	10.0	S	2.7	1.4×10^{39}	0.90	0.02
2CXO J112020.9+125846	170.0871	12.9796	0.4	7.6×10^{-13}	10.0	S	4.6	9.2×10^{39}	0.91	0.11
2CXO J112054.2+531040	170.2262	53.1780	0.4	2.8×10^{-13}	20.1	S	8.1	1.3×10^{40}	0.53	0.11
2CXO J112110.2+531011	170.2928	53.1700	0.4	3.8×10^{-14}	20.1	S	6.4	1.9×10^{39}	0.94	0.07
2CXO J112213.0+241914	170.5545	24.3208	0.5	1.4×10^{-15}	114.3	S0/E	6.9	2.2×10^{39}	0.58	0.24
2CXO J112443.1+384737	171.1796	38.7938	0.8	1.1×10^{-14}	32.4	S	17.3	1.3×10^{39}	0.79	0.55
2CXO J112445.0+384623	171.1875	38.7731	0.5	1.1×10^{-14}	32.4	S	6.3	1.4×10^{39}	0.79	0.12
2CXO J112729.0+565301	171.8710	56.8836	0.4	3.7×10^{-14}	35.0	S	5.7	5.4×10^{39}		
2CXO J112729.9+565249	171.8749	56.8804	0.4	5.8×10^{-14}	35.0	S	3.4	8.5×10^{39}		
2CXO J112729.9+565313	171.8747	56.8871	0.4	7.3×10^{-15}	35.0	S	6.8	1.1×10^{39}	0.91	0.40
2CXO J112733.4+565227	171.8892	56.8743	0.4	1.1×10^{-14}	35.0	S	2.5	1.6×10^{39}		
2CXO J112733.8+565224	171.8911	56.8734	0.4	1.6×10^{-14}	35.0	S	3.3	2.4×10^{39}		
2CXO J112734.7+565222	171.8948	56.8729	0.4	1.9×10^{-14}	35.0	S	4.5	2.8×10^{39}		
2CXO J112826.7+583406	172.1116	58.5686	0.4	1.4×10^{-14}	35.3	S	9.6	2.0×10^{39}		
2CXO J112827.3+583450	172.1141	58.5808	0.5	9.2×10^{-16}	137.3	S0/E	5.3	2.1×10^{39}	0.80	0.16
2CXO J112830.4+583346	172.1270	58.5628	0.4	5.1×10^{-14}	35.3	S	1.3	7.6×10^{39}		
2CXO J112831.6+583349	172.1318	58.5636	0.4	2.6×10^{-14}	35.3	S	1.3	3.9×10^{39}		
2CXO J112832.2+583318	172.1345	58.5550	0.4	1.9×10^{-14}	35.3	S	5.2	2.9×10^{39}		
2CXO J112833.0+583336	172.1375	58.5602	0.4	8.3×10^{-15}	35.3	S	1.9	1.2×10^{39}		
2CXO J112833.0+583355	172.1379	58.5654	0.4	1.9×10^{-14}	35.3	S	1.6	2.8×10^{39}		
2CXO J112833.2+583402	172.1385	58.5673	0.4	2.3×10^{-14}	35.3	S	2.7	3.5×10^{39}		
2CXO J112833.6+583403	172.1402	58.5676	0.4	7.9×10^{-15}	35.3	S	2.8	1.2×10^{39}		
2CXO J112834.0+583340	172.1420	58.5612	0.4	2.2×10^{-14}	35.3	S	1.2	3.4×10^{39}		
2CXO J112834.3+583342	172.1433	58.5619	0.4	7.6×10^{-15}	35.3	S	1.2	1.1×10^{39}		
2CXO J112845.2+583539	172.1884	58.5942	0.4	1.3×10^{-15}	267.9	S	6.2	1.1×10^{40}	0.65	0.09
2CXO J113209.8+572615	173.0412	57.4376	0.4	1.2×10^{-13}	20.3	S	4.8	5.9×10^{39}	0.90	0.12
2CXO J113433.5+490527	173.6397	49.0909	1.2	1.5×10^{-15}	145.2	S0/E	8.1	3.9×10^{39}	0.46	0.23
2CXO J113447.7+490443	173.6991	49.0789	0.5	2.5×10^{-15}	150.0	S0/E	10.8	6.8×10^{39}	0.62	0.14
2CXO J113450.6+490435	173.7110	49.0764	0.5	1.9×10^{-15}	150.0	S0/E	9.1	5.0×10^{39}	0.18	0.09
2CXO J113737.0+295917	174.4042	29.9883	0.5	2.6×10^{-15}	588.8		13.9	1.1×10^{41}	0.30	0.15
2CXO J114006.9+174147	175.0288	17.6965	0.6	3.2×10^{-15}	55.1	S	5.4	1.2×10^{39}	0.70	0.15
2CXO J114046.7+174736	175.1947	17.7935	1.8	6.7×10^{-15}	47.7	S	2.4	1.8×10^{39}	0.69	0.04
2CXO J114059.2-263202	175.2468	-26.5340	0.5	6.9×10^{-15}	121.8	S0/E	4.0	1.2×10^{40}	0.50	0.02
2CXO J114059.7-263206	175.2488	-26.5353	0.7	1.8×10^{-15}	121.8	S0/E	6.2	3.2×10^{39}	0.76	0.05
2CXO J114059.8-263150	175.2493	-26.5306	0.7	1.8×10^{-15}	121.8	S0/E	4.3	3.2×10^{39}	0.74	0.03
2CXO J114346.8+195840	175.9453	19.9778	0.4	1.3×10^{-14}	89.4	S	19.3	1.3×10^{40}	0.84	0.16
2CXO J114347.0+195834	175.9462	19.9764	0.6	2.8×10^{-15}	89.4	S	16.8	2.7×10^{39}	0.81	0.12
2CXO J114347.4+195832	175.9477	19.9756	0.5	3.5×10^{-15}	89.4	S	14.5	3.4×10^{39}	0.75	0.09
2CXO J114349.4+195802	175.9561	19.9675	0.4	1.2×10^{-14}	89.4	S	2.5	1.2×10^{40}		
2CXO J114349.5+195749	175.9564	19.9638	0.4	6.8×10^{-15}	89.4	S	7.3	6.5×10^{39}		
2CXO J114356.0+195331	175.9834	19.8920	0.9	1.2×10^{-15}	88.8	S0/E	4.5	1.2×10^{39}	0.79	0.13
2CXO J114402.2+195634	176.0092	19.9428	0.5	1.3×10^{-15}	88.8	S0/E	10.4	1.3×10^{39}	0.86	0.17
2CXO J114402.6+195822	176.0112	19.9729	0.5	1.4×10^{-15}	88.9	S0/E	3.5	1.3×10^{39}	0.77	0.10
2CXO J114447.5+194619	176.1983	19.7722	0.6	2.7×10^{-15}	91.6	S	2.1	2.7×10^{39}	0.60	0.02
2CXO J114705.9-165059	176.7749	-16.8500	0.4	5.3×10^{-14}	18.2	S	2.3	2.1×10^{39}	0.84	0.03
2CXO J114833.2+124229	177.1386	12.7082	0.5	3.6×10^{-15}	62.0	S	4.8	1.6×10^{39}	0.71	0.25
2CXO J114851.2+592500	177.2136	59.4169	0.4	5.2×10^{-15}	46.5	S0/E	1.8	1.3×10^{39}	0.59	0.01
2CXO J114853.5+592556	177.2230	59.4323	0.5	6.3×10^{-15}	46.5	S0/E	14.3	1.6×10^{39}	0.84	0.40
2CXO J114911.9+560509	177.2997	56.0860	0.4	2.6×10^{-14}	19.6	S	2.8	1.2×10^{39}	0.83	0.03
2CXO J115058.6-284913	177.7444	-28.8203	0.4	1.8×10^{-14}	22.9	S0/E	7.2	1.1×10^{39}	0.86	0.06
2CXO J115237.3-022807	178.1557	-2.4687	0.4	4.3×10^{-14}	17.6	S	0.3	1.6×10^{39}	0.53	0.00
2CXO J115246.6+440648	178.1943	44.1135	0.4	8.2×10^{-14}	17.9	S	3.4	3.1×10^{39}	0.78	0.07
2CXO J115357.7-231002	178.4908	-23.1674	0.4	6.4×10^{-14}	20.8	S	1.4	3.3×10^{39}	0.83	0.01
2CXO J115558.5+232736	178.9941	23.4602	0.8	7.7×10^{-16}	232.3		5.6	5.0×10^{39}	0.78	0.10
2CXO J115627.0+550747	179.1128	55.1299	0.4	2.7×10^{-14}	20.5	S	1.9	1.4×10^{39}	0.84	0.02
2CXO J115817.1+123823	179.5714	12.6398	0.8	2.6×10^{-15}	371.5	S0/E	10.9	4.2×10^{40}	0.71	0.24
2CXO J120011.6-010656	180.0484	-1.1158	1.3	3.7×10^{-15}	331.1		9.8	4.8×10^{40}	0.55	0.16
2CXO J120022.8-010419	180.0950	-1.0720	0.5	1.7×10^{-14}	27.2	S	13.2	1.5×10^{39}	0.96	0.26
2CXO J120023.5-010626	180.0982	-1.1074	0.4	1.4×10^{-14}	27.2	S	3.5	1.2×10^{39}	0.57	0.02
2CXO J120025.7-010507	180.1074	-1.0855	0.4	2.3×10^{-14}	27.2	S	8.0	2.0×10^{39}	0.94	0.09

Table A.13: List of ULX candidates obtained in Chapter 4 (continued).

Name	RA deg	Dec deg	$POSERR$ arcsec	F_X erg cm^{-2} s^{-1}	D Mpc	Gal. type	Sep. kpc	L_X erg s^{-1}	P_{XRB}	f_{cont}
2CXO J120128.5+132643	180.3688	13.4454	1.0	6.1×10^{-15}	248.9	S	11.4	4.5×10^{40}	0.36	0.30
2CXO J120148.4-185206	180.4520	-18.8686	0.4	9.1×10^{-15}	35.3		12.4	1.4×10^{39}	0.94	0.35
2CXO J120148.8-185403	180.4534	-18.9008	0.4	8.3×10^{-15}	35.3		17.7	1.2×10^{39}	0.96	0.62
2CXO J120151.3-185224	180.4639	-18.8736	0.5	8.2×10^{-14}	35.3		4.9	1.2×10^{40}	0.80	0.03
2CXO J120152.0-185133	180.4670	-18.8592	0.5	1.3×10^{-13}	35.3		11.2	1.9×10^{40}	0.86	0.10
2CXO J120152.3-185206	180.4683	-18.8684	0.4	1.9×10^{-14}	35.3		5.7	2.9×10^{39}		
2CXO J120152.4-185313	180.4684	-18.8871	0.4	1.1×10^{-14}	35.3		6.3	1.7×10^{39}		
2CXO J120154.2-185201	180.4761	-18.8670	0.4	3.0×10^{-14}	35.3		6.7	4.5×10^{39}		
2CXO J120154.3-185209	180.4765	-18.8694	0.4	2.5×10^{-14}	35.3		5.5	3.7×10^{39}		
2CXO J120154.5-185303	180.4773	-18.8842	0.4	1.0×10^{-14}	35.3		5.4	1.5×10^{39}		
2CXO J120154.7-185251	180.4783	-18.8810	0.8	1.7×10^{-14}	35.3		4.5	2.5×10^{39}	0.72	0.02
2CXO J120154.9-185314	180.4791	-18.8873	0.4	9.3×10^{-14}	35.3		7.5	1.4×10^{40}		
2CXO J120155.4-185235	180.4812	-18.8764	0.4	7.0×10^{-15}	35.3		5.5	1.0×10^{39}		
2CXO J120155.6-185214	180.4819	-18.8707	0.5	3.2×10^{-14}	35.3		7.1	4.7×10^{39}	0.71	0.05
2CXO J120156.4-185157	180.4851	-18.8659	0.5	9.5×10^{-14}	35.3		10.4	1.4×10^{40}	0.90	0.10
2CXO J120156.7-185400	180.4864	-18.9002	0.4	6.9×10^{-15}	35.3		16.3	1.0×10^{39}	0.90	0.53
2CXO J120255.3+575152	180.7305	57.8646	0.5	3.5×10^{-15}	472.1	S	13.2	9.2×10^{40}	0.61	0.50
2CXO J120408.7+201052	181.0366	20.1811	0.7	1.1×10^{-14}	111.7	S	8.7	1.6×10^{40}	0.43	0.06
2CXO J120532.3+503245	181.3847	50.5460	0.4	7.5×10^{-14}	14.3	S	1.9	1.8×10^{39}	0.80	0.04
2CXO J120627.3+524303	181.6140	52.7176	0.8	2.8×10^{-14}	19.1	S	3.9	1.2×10^{39}	0.89	0.06
2CXO J120652.1-315650	181.7171	-31.9475	0.4	4.3×10^{-15}	92.6	S	3.6	4.4×10^{39}	0.52	0.04
2CXO J120807.4+651028	182.0311	65.1746	0.9	8.2×10^{-14}	23.9	S0/E	1.1	5.6×10^{39}	0.49	0.00
2CXO J120922.1+295559	182.3424	29.9332	0.4	1.0×10^{-13}	10.1	S0/E	0.4	1.2×10^{39}	0.85	0.00
2CXO J121033.7+302357	182.6405	30.3994	0.4	1.6×10^{-13}	13.7	S0/E	0.5	3.6×10^{39}	0.56	0.00
2CXO J121104.5+502850	182.7689	50.4807	0.4	1.5×10^{-13}	17.6	S	1.2	5.7×10^{39}	0.90	0.04
2CXO J121216.8+131223	183.0701	13.2064	0.5	1.6×10^{-14}	30.9	S0/E	1.0	1.8×10^{39}	0.59	0.01
2CXO J121244.5+105113	183.1854	10.8538	0.4	1.1×10^{-13}	14.0	S	3.5	2.6×10^{39}	0.90	0.02
2CXO J121345.2+363754	183.4386	36.6319	0.4	3.4×10^{-12}	3.5	S	0.1	4.9×10^{39}	0.62	0.00
2CXO J121409.7+543215	183.5405	54.5377	0.4	7.5×10^{-14}	35.8		6.8	1.1×10^{40}	0.79	0.15
2CXO J121510.9+203912	183.7954	20.6535	0.4	1.3×10^{-13}	10.4	S	2.6	1.7×10^{39}	0.36	0.02
2CXO J121530.0+093441	183.8753	9.5781	0.6	2.5×10^{-14}	20.0	S	2.4	1.2×10^{39}	0.90	0.06
2CXO J121549.0+470520	183.9546	47.0890	0.4	2.7×10^{-14}	19.5	S	2.0	1.2×10^{39}	0.46	0.01
2CXO J121554.6+130821	183.9779	13.1393	0.5	4.9×10^{-14}	14.1	S	2.5	1.2×10^{39}	0.91	0.03
2CXO J121618.9+602103	184.0790	60.3508	0.7	2.8×10^{-15}	271.6	S0/E	10.1	2.4×10^{40}	0.56	0.29
2CXO J121634.2+602145	184.1429	60.3628	0.7	5.5×10^{-15}	195.0	S	6.9	2.5×10^{40}	0.78	0.24
2CXO J121707.8+034020	184.2829	3.6724	1.9	1.2×10^{-14}	29.9	S	6.1	1.3×10^{39}	0.67	0.29
2CXO J121752.4+471204	184.4687	47.2013	2.3	3.1×10^{-14}	110.7		5.3	4.6×10^{40}	0.35	0.11
2CXO J121851.8+142421	184.7161	14.4060	0.5	2.7×10^{-14}	17.8	S	4.3	1.0×10^{39}	0.95	0.05
2CXO J121856.1+142419	184.7338	14.4054	0.4	3.8×10^{-13}	17.8	S	8.7	1.4×10^{40}	0.95	0.22
2CXO J121857.8+471607	184.7411	47.2688	0.4	2.1×10^{-13}	7.5	S	4.5	1.4×10^{39}	0.68	0.04
2CXO J122019.8+752216	185.0828	75.3712	0.4	2.2×10^{-14}	26.2	S0/E	1.0	1.8×10^{39}		
2CXO J122027.8+752124	185.1161	75.3568	0.4	2.5×10^{-14}	26.2	S0/E	8.0	2.1×10^{39}		
2CXO J122117.3+043616	185.3221	4.6045	0.4	1.5×10^{-14}	34.3	S0/E	5.5	2.2×10^{39}	0.93	0.18
2CXO J122151.8+042803	185.4662	4.4676	0.4	2.7×10^{-14}	18.0	S	4.4	1.0×10^{39}		
2CXO J122155.1+271022	185.4796	27.1728	0.4	1.2×10^{-14}	363.1	S	6.3	1.9×10^{41}	0.46	0.08
2CXO J122155.4+042858	185.4810	4.4830	0.4	2.8×10^{-14}	18.0	S	3.0	1.1×10^{39}		
2CXO J122158.3+042812	185.4930	4.4702	3.2	2.6×10^{-14}	18.0	S	4.5	1.0×10^{39}	0.62	0.02
2CXO J122201.2+042937	185.5052	4.4939	0.4	4.1×10^{-14}	18.0	S	10.3	1.6×10^{39}	0.96	0.28
2CXO J122224.2+144444	185.6008	14.7457	0.5	1.3×10^{-14}	59.2		1.7	5.7×10^{39}	0.44	0.02
2CXO J122228.5+291159	185.6189	29.1999	0.6	2.6×10^{-14}	17.9	S	3.7	1.0×10^{39}	0.87	0.04
2CXO J122301.6+103514	185.7568	10.5874	1.3	3.7×10^{-15}	99.5	S	4.6	4.4×10^{39}	0.86	0.12
2CXO J122308.3+103720	185.7847	10.6222	0.4	5.5×10^{-15}	114.8	S0/E	13.0	8.6×10^{39}		
2CXO J122426.3+071653	186.1098	7.2815	0.7	2.7×10^{-14}	23.3	S0/E	14.8	1.8×10^{39}	0.93	0.65
2CXO J122518.6+144545	186.3277	14.7627	0.4	1.9×10^{-14}	197.7	S	3.4	9.0×10^{40}	0.22	0.04
2CXO J122601.9+153941	186.5080	15.6615	1.6	1.4×10^{-13}	17.8	S	4.6	5.2×10^{39}	0.82	0.04
2CXO J122609.3+125558	186.5391	12.9328	0.5	6.3×10^{-14}	16.8	S0/E	4.8	2.1×10^{39}	0.89	0.01
2CXO J122609.4+125705	186.5393	12.9515	0.4	6.1×10^{-14}	16.8	S0/E	3.2	2.1×10^{39}	0.82	0.00
2CXO J122609.7+125604	186.5407	12.9345	0.7	1.2×10^{-13}	16.8	S0/E	4.1	3.9×10^{39}	0.69	0.01
2CXO J122609.9+125644	186.5413	12.9456	0.7	2.8×10^{-13}	16.8	S0/E	2.3	9.3×10^{39}	0.64	0.00
2CXO J122609.9+125655	186.5415	12.9488	0.6	2.5×10^{-13}	16.8	S0/E	2.3	8.5×10^{39}	0.61	0.00
2CXO J122611.0+125648	186.5460	12.9467	0.6	2.7×10^{-13}	16.8	S0/E	0.9	9.1×10^{39}		
2CXO J122611.6+125702	186.5485	12.9507	0.5	2.7×10^{-13}	16.8	S0/E	1.4	9.2×10^{39}	0.69	0.00
2CXO J122611.7+125615	186.5492	12.9377	0.6	1.3×10^{-13}	16.8	S0/E	2.4	4.3×10^{39}	0.69	0.00
2CXO J122612.3+125640	186.5516	12.9445	0.5	2.4×10^{-13}	16.8		0.4	8.0×10^{39}	0.64	0.00
2CXO J122612.6+125645	186.5525	12.9461	0.5	2.9×10^{-13}	16.8		0.4	9.7×10^{39}	0.63	0.00
2CXO J122612.8+125657	186.5537	12.9493	0.8	1.7×10^{-13}	16.8	S0/E	1.6	5.8×10^{39}	0.64	0.00
2CXO J122613.1+125652	186.5549	12.9480	0.6	2.6×10^{-13}	16.8		1.3	8.7×10^{39}	0.75	0.00
2CXO J122613.5+125700	186.5563	12.9500	0.6	2.7×10^{-13}	16.8	S0/E	2.3	9.0×10^{39}	0.66	0.00
2CXO J122613.9+125701	186.5580	12.9505	0.6	2.7×10^{-13}	16.8	S0/E	2.8	9.3×10^{39}	0.69	0.00
2CXO J122623.4+125456	186.5976	12.9158	0.6	3.5×10^{-14}	16.8		15.8	1.2×10^{39}		
2CXO J122627.8+085144	186.6161	8.8625	0.4	2.8×10^{-14}	20.1	S	4.4	1.4×10^{39}	0.91	0.09
2CXO J122814.6+114717	187.0610	11.7883	0.4	3.2×10^{-14}	16.7	S	0.5	1.1×10^{39}	0.90	0.00
2CXO J122827.2+170417	187.1136	17.0714	0.4	5.0×10^{-14}	15.3	S	4.4	1.4×10^{39}		
2CXO J122959.9+080114	187.4998	8.0207	0.4	3.0×10^{-14}	17.1	S	17.2	1.0×10^{39}	0.97	0.63
2CXO J123029.4+413927	187.6228	41.6577	0.4	7.8×10^{-14}	13.6	S	6.1	1.7×10^{39}	0.63	0.03
2CXO J123030.4+414142	187.6270	41.6951	0.4	2.8×10^{-13}	13.6	S	1.5	6.1×10^{39}	0.85	0.00
2CXO J123030.7+413911	187.6281	41.6532	0.4	2.3×10^{-13}	13.6	S	4.7	5.1×10^{39}	0.18	0.02
2CXO J123031.6+414140	187.6319	41.6947	0.4	9.6×10^{-14}	13.6	S	1.6	2.1×10^{39}	0.84	0.00
2CXO J123032.1+413918	187.6341	41.6551	0.4	2.6×10^{-13}	13.6	S	4.1	5.7×10^{39}	0.94	0.01
2CXO J123035.1+413846	187.6464	41.6464	0.4	1.4×10^{-13}	13.6	S	1.1	3.0×10^{39}	0.81	0.00
2CXO J123038.4+413831	187.6602	41.6422	0.4	1.3×10^{-13}	13.6	S	1.6	3.0×10^{39}	0.62	0.00

Table A.14: List of ULX candidates obtained in Chapter 4 (continued).

Name	RA deg	Dec deg	$POSERR$ arcsec	F_X erg cm^{-2} s^{-1}	D Mpc	Gal. type	Sep. kpc	L_X erg s^{-1}	P_{XRB}	f_{cont}
2CXO J123043.1+413818	187.6799	41.6385	0.4	4.9×10^{-13}	13.6	S	5.1	1.1×10^{40}	0.82	0.04
2CXO J123047.1+122415	187.6964	12.4044	0.4	3.3×10^{-14}	17.2	S0/E	4.9	1.2×10^{39}	0.94	0.04
2CXO J123048.8+122330	187.7037	12.3919	0.4	6.7×10^{-14}	17.2	S0/E	0.7	2.4×10^{39}	0.69	0.00
2CXO J123050.7+122502	187.7117	12.4172	0.4	4.4×10^{-14}	17.2	S0/E	8.0	1.6×10^{39}	0.96	0.11
2CXO J123057.4+121621	187.7394	12.2726	0.4	3.0×10^{-14}	18.3	S0/E	0.8	1.2×10^{39}		
2CXO J123058.8+080451	187.7453	8.0811	0.4	3.4×10^{-14}	17.8	S	1.5	1.3×10^{39}	0.90	0.01
2CXO J123200.3+142442	188.0017	14.4118	0.4	6.6×10^{-14}	18.6	S	3.2	2.7×10^{39}	0.71	0.01
2CXO J123200.9+142502	188.0039	14.4174	0.4	7.3×10^{-14}	18.6	S	2.4	3.0×10^{39}	0.43	0.01
2CXO J123209.7-022356	188.0406	-2.3990	0.5	3.9×10^{-15}	261.8	S0/E	12.1	3.2×10^{40}	0.73	0.49
2CXO J123307.6+091942	188.2820	9.3285	0.6	3.3×10^{-14}	309.0	S	6.1	3.7×10^{41}	0.39	0.09
2CXO J123348.1+150917	188.4507	15.1549	0.4	2.1×10^{-13}	6.4	S	1.5	1.0×10^{39}	0.81	0.00
2CXO J123410.9+023925	188.5456	2.6570	0.4	1.8×10^{-13}	13.4	S	2.5	3.8×10^{39}	0.46	0.00
2CXO J123411.4+023928	188.5477	2.6580	0.4	1.5×10^{-13}	13.4	S	3.0	3.2×10^{39}	0.90	0.01
2CXO J123535.3-395438	188.8973	-39.9107	0.4	5.5×10^{-15}	46.4	S	3.4	1.4×10^{39}	0.80	0.09
2CXO J123542.8+263435	188.9284	26.5764	0.5	7.5×10^{-15}	96.2	S0/E	6.8	8.3×10^{39}	0.41	0.23
2CXO J123551.7+275604	188.9655	27.9345	0.4	1.1×10^{-12}	7.0	S	4.1	6.1×10^{39}	0.24	0.03
2CXO J123558.5+275742	188.9940	27.9617	0.4	6.7×10^{-13}	7.0	S	0.5	3.9×10^{39}	0.74	0.00
2CXO J123607.7+191921	189.0322	19.3226	0.4	3.4×10^{-14}	16.1	S	0.5	1.1×10^{39}	0.81	0.00
2CXO J123608.9+191955	189.0371	19.3322	0.4	9.3×10^{-14}	16.1	S	2.8	2.9×10^{39}	0.91	0.02
2CXO J123614.5+260053	189.0608	26.0147	0.4	4.7×10^{-14}	17.5	S	10.8	1.7×10^{39}	0.91	0.03
2CXO J123617.4+255855	189.0725	25.9821	0.4	3.1×10^{-13}	17.5	S	4.2	1.1×10^{40}	0.89	0.09
2CXO J123619.0+260026	189.0792	26.0075	0.4	7.7×10^{-14}	17.5	S	6.4	2.8×10^{39}	0.87	0.06
2CXO J123627.3+255732	189.1141	25.9592	0.4	3.0×10^{-14}	17.5	S	11.3	1.1×10^{39}	0.84	0.03
2CXO J123628.0+260000	189.1171	26.0002	0.4	3.1×10^{-14}	17.5	S	9.1	1.1×10^{39}	0.91	0.45
2CXO J123740.3+114727	189.4180	11.7911	0.4	2.3×10^{-13}	18.8	S	9.8	9.9×10^{39}	0.95	0.33
2CXO J123743.2+114901	189.4300	11.8171	0.4	2.5×10^{-14}	18.8	S	0.6	1.0×10^{39}	0.93	0.00
2CXO J123904.7+144400	189.7699	14.7335	0.4	4.0×10^{-14}	18.4	S	1.0	1.6×10^{39}	0.91	0.01
2CXO J123920.0-003147	189.8336	-0.5298	0.6	4.5×10^{-14}	13.9	S	1.4	1.0×10^{39}	0.90	0.01
2CXO J124053.6-364512	190.2234	-36.7535	0.5	9.4×10^{-15}	43.1	S	2.5	2.1×10^{39}	0.64	0.05
2CXO J124129.1+410757	190.3714	41.1327	0.4	1.5×10^{-13}	13.6	S	4.7	3.4×10^{39}	0.94	0.06
2CXO J124133.0+410731	190.3875	41.1255	0.4	5.6×10^{-14}	63.5		1.9	2.7×10^{40}	0.16	0.02
2CXO J124155.5+323216	190.4815	32.5380	0.4	2.8×10^{-13}	5.7	S	4.3	1.1×10^{39}	0.58	0.00
2CXO J124238.5-111923	190.6606	-11.3233	0.5	1.3×10^{-15}	269.6	S0/E	3.9	1.1×10^{40}	0.51	0.04
2CXO J124241.2+024022	190.6718	2.6728	0.6	2.0×10^{-14}	387.3	S0/E	16.2	3.7×10^{41}	0.54	0.33
2CXO J124251.2+131439	190.7135	13.2444	0.8	3.1×10^{-14}	22.0	S	5.3	1.8×10^{39}	0.88	0.22
2CXO J124252.9+023749	190.7205	2.6305	0.4	4.0×10^{-14}	14.7	S0/E	14.9	1.0×10^{39}	0.82	0.79
2CXO J124255.8+112605	190.7329	11.4348	1.4	5.6×10^{-15}	78.2	S	10.7	4.1×10^{39}	0.72	0.28
2CXO J124342.3+114053	190.9265	11.6817	0.5	1.9×10^{-14}	127.1		3.2	3.7×10^{40}	0.84	0.03
2CXO J124427.8+111121	191.1162	11.1893	0.4	4.7×10^{-14}	15.0	S0/E	4.3	1.3×10^{39}	0.91	0.07
2CXO J124610.3+304422	191.5431	30.7395	0.5	5.9×10^{-15}	147.1		4.9	1.5×10^{40}	0.38	0.02
2CXO J124611.0+304315	191.5462	30.7210	0.5	1.6×10^{-15}	90.7	S	3.2	1.6×10^{39}	0.60	0.03
2CXO J124611.0+304324	191.5460	30.7236	0.7	3.4×10^{-15}	90.7	S	1.5	3.4×10^{39}	0.22	0.01
2CXO J124747.7+134617	191.9488	13.7715	0.4	6.6×10^{-14}	14.7	S	3.2	1.7×10^{39}	0.60	0.05
2CXO J124749.8+041929	191.9577	4.3249	0.4	6.0×10^{-14}	17.6	S	5.5	2.2×10^{39}	0.92	0.18
2CXO J124813.0-031959	192.0544	-3.3333	2.7	5.6×10^{-13}	11.5	S	0.5	8.9×10^{39}	0.10	0.00
2CXO J124831.2-411826	192.1303	-41.3074	0.4	5.7×10^{-15}	39.5	S0/E	0.9	1.1×10^{39}	0.84	0.01
2CXO J125010.5-411759	192.5442	-41.2999	0.5	2.1×10^{-14}	55.8	S0/E	3.9	7.7×10^{39}	0.68	0.12
2CXO J125026.3+253319	192.6099	25.5553	0.4	5.9×10^{-14}	12.8	S	12.1	1.2×10^{39}	0.96	0.55
2CXO J125132.8-262656	192.8868	-26.4490	0.5	5.9×10^{-15}	42.9	S0/E	3.5	1.3×10^{39}	0.76	0.12
2CXO J125254.1+111041	193.2256	11.1783	3.1	4.3×10^{-14}	17.8	S	16.4	1.6×10^{39}	0.72	0.52
2CXO J125303.7-091207	193.2656	-9.2021	0.4	3.8×10^{-15}	57.2	S0/E	7.9	1.5×10^{39}		
2CXO J125306.8-091152	193.2784	-9.1980	0.4	3.1×10^{-15}	57.2	S0/E	7.4	1.2×10^{39}		
2CXO J125306.9-091525	193.2788	-9.2570	0.9	4.1×10^{-15}	57.8	S0/E	1.4	1.6×10^{39}	0.76	0.01
2CXO J125329.4+021009	193.3729	2.1694	0.6	8.7×10^{-15}	40.9	S0/E	1.2	1.7×10^{39}	0.34	0.02
2CXO J125412.1+273726	193.5508	27.6241	0.4	3.8×10^{-15}	387.3	S0/E	12.2	6.8×10^{40}	0.30	0.10
2CXO J125436.6-123349	193.6527	-12.5637	0.4	2.6×10^{-15}	57.5	S0/E	4.9	1.0×10^{39}		
2CXO J125437.4-123417	193.6562	-12.5716	0.4	5.8×10^{-15}	61.4	S	8.2	2.6×10^{39}		
2CXO J125438.3-123411	193.6600	-12.5699	0.4	8.8×10^{-15}	57.5	S0/E	12.9	3.5×10^{39}		
2CXO J125512.3+000751	193.8013	0.1311	0.4	5.9×10^{-14}	12.7	S	3.2	1.1×10^{39}	0.87	0.02
2CXO J125700.6-171901	194.2528	-17.3172	1.0	7.0×10^{-15}	54.4	S	3.0	2.5×10^{39}	0.81	0.04
2CXO J125700.9-171923	194.2539	-17.3232	1.6	6.3×10^{-15}	54.4	S	2.9	2.2×10^{39}	0.79	0.03
2CXO J125707.3-465220	194.2806	-46.8725	0.7	2.6×10^{-14}	64.9	S0/E	1.5	1.3×10^{40}	0.44	0.01
2CXO J125707.8-465216	194.2827	-46.8712	0.8	1.2×10^{-14}	64.9	S0/E	2.8	6.2×10^{39}	0.53	0.01
2CXO J125708.2-465213	194.2844	-46.8705	0.8	1.7×10^{-14}	64.9	S0/E	4.2	8.8×10^{39}	0.54	0.02
2CXO J125718.4-171441	194.3270	-17.2449	0.7	9.7×10^{-15}	199.5	S0/E	5.6	4.6×10^{40}	0.60	0.11
2CXO J125814.0+281101	194.5587	28.1836	0.8	4.9×10^{-15}	107.6	S0/E	2.3	6.8×10^{39}	0.31	0.02
2CXO J125853.1-013526	194.7215	-1.5906	0.8	5.3×10^{-15}	392.6	S	6.7	9.8×10^{40}	0.55	0.08
2CXO J125901.8+345114	194.7577	34.8541	0.4	5.0×10^{-13}	7.6	S	0.9	3.4×10^{39}	0.73	0.00
2CXO J125928.8+275110	194.8701	27.8528	0.8	1.0×10^{-14}	97.7	S0/E	5.3	1.2×10^{40}	0.69	0.09
2CXO J125939.8+275716	194.9158	27.9546	0.4	1.6×10^{-14}	120.2	S	1.8	2.8×10^{40}	0.39	0.02
2CXO J130008.2+275845	195.0345	27.9793	0.5	6.4×10^{-15}	95.0	S0/E	3.7	6.9×10^{39}		
2CXO J130040.7+023001	195.1697	2.5005	0.4	3.9×10^{-14}	17.6	S	2.0	1.4×10^{39}	0.73	0.01
2CXO J130053.2+274937	195.2218	27.8271	0.4	6.9×10^{-15}	71.3		2.7	4.2×10^{39}	0.58	0.08
2CXO J130056.5+274742	195.2357	27.7951	1.0	2.2×10^{-15}	97.0	S	7.6	2.5×10^{39}	0.64	0.14
2CXO J130056.6+274729	195.2362	27.7914	0.6	2.7×10^{-15}	97.0	S	3.7	3.0×10^{39}	0.44	0.03
2CXO J130056.9+274736	195.2372	27.7934	0.5	3.2×10^{-15}	97.0	S	6.5	3.5×10^{39}	0.73	0.10
2CXO J130117.8+274812	195.3244	27.8035	0.6	2.6×10^{-15}	96.1	S	8.9	2.9×10^{39}	0.46	0.21
2CXO J130118.8+274821	195.3285	27.8061	0.6	2.0×10^{-15}	96.1	S	8.5	2.2×10^{39}	0.54	0.16
2CXO J130126.2+275249	195.3594	27.8803	1.2	2.7×10^{-15}	82.0	S	7.8	2.2×10^{39}	0.59	0.14
2CXO J130216.0-154610	195.5670	-15.7695	0.9	2.8×10^{-15}	64.7	S	19.1	1.4×10^{39}	0.25	0.24
2CXO J130218.3-154622	195.5765	-15.7729	0.6	2.7×10^{-15}	64.7	S	11.3	1.4×10^{39}	0.64	0.18

Table A.15: List of ULX candidates obtained in Chapter 4 (continued).

Name	RA deg	Dec deg	$POSERR$ arcsec	F_X erg cm^{-2} s^{-1}	D Mpc	Gal. type	Sep. kpc	L_X erg s^{-1}	P_{XRB}	f_{cont}
2CXO J130219.0-154602	195.5794	-15.7675	0.4	3.8×10^{-15}	64.7	S	5.8	1.9×10^{39}	0.33	0.02
2CXO J130228.7-154641	195.6197	-15.7782	0.6	3.5×10^{-15}	66.6	S	5.1	1.8×10^{39}	0.45	0.18
2CXO J130401.0-302153	196.0043	-30.3649	1.4	3.0×10^{-14}	48.2	S0/E	3.7	8.4×10^{39}	0.59	0.09
2CXO J130413.8-102126	196.0579	-10.3574	2.5	3.2×10^{-14}	34.7	S	10.6	4.6×10^{39}	0.56	0.09
2CXO J130414.0-102050	196.0587	-10.3475	0.5	8.6×10^{-15}	34.7	S	4.7	1.2×10^{39}	0.48	0.02
2CXO J130414.9-102005	196.0624	-10.3348	0.4	9.4×10^{-15}	34.7	S	3.2	1.4×10^{39}	0.75	0.02
2CXO J130415.3-303357	196.0639	-30.5661	0.8	4.9×10^{-15}	129.7	S	9.7	9.8×10^{39}	0.43	0.18
2CXO J130416.3-303340	196.0683	-30.5613	0.4	7.3×10^{-15}	129.7	S	13.2	1.5×10^{40}	0.60	0.28
2CXO J130416.7-303142	196.0699	-30.5286	0.9	5.4×10^{-15}	42.2	S0/E	1.8	1.1×10^{39}	0.58	0.01
2CXO J130416.8-303352	196.0702	-30.5646	0.5	4.2×10^{-15}	129.7	S	6.4	8.5×10^{39}	0.59	0.06
2CXO J130417.0-303151	196.0712	-30.5310	0.5	8.4×10^{-15}	42.2	S0/E	3.4	1.8×10^{39}	0.64	0.02
2CXO J130417.6-302951	196.0736	-30.4977	0.5	5.3×10^{-15}	42.2	S0/E	20.7	1.1×10^{39}	0.67	0.63
2CXO J130419.1-303031	196.0799	-30.5088	0.5	9.4×10^{-15}	42.2	S0/E	13.7	2.0×10^{39}	0.75	0.28
2CXO J130446.3+532955	196.1932	53.4986	1.8	8.3×10^{-15}	128.2		4.8	1.6×10^{40}	0.33	0.13
2CXO J130522.2-492912	196.3428	-49.4867	0.4	6.0×10^{-13}	3.8	S	1.5	1.0×10^{39}		
2CXO J131255.6-193039	198.2317	-19.5111	0.4	4.5×10^{-14}	34.7	S0/E	13.3	6.5×10^{39}	0.90	0.32
2CXO J131302.0-193105	198.2585	-19.5182	0.4	3.9×10^{-14}	34.7	S0/E	2.4	5.6×10^{39}		
2CXO J131304.3-193152	198.2681	-19.5312	0.4	7.4×10^{-15}	34.7	S0/E	10.9	1.1×10^{39}	0.90	0.31
2CXO J131324.7+363503	198.3532	36.5844	0.4	2.6×10^{-14}	18.8	S	4.2	1.1×10^{39}	0.86	0.05
2CXO J131329.4+363517	198.3727	36.5882	0.4	6.1×10^{-14}	18.8	S	2.7	2.6×10^{39}	0.76	0.02
2CXO J131329.6+363523	198.3736	36.5898	0.4	8.3×10^{-14}	18.8	S	2.6	3.5×10^{39}	0.79	0.02
2CXO J131331.5-193228	198.3813	-19.5413	1.1	1.9×10^{-14}	32.1	S	3.3	2.4×10^{39}	0.54	0.01
2CXO J131331.5-193238	198.3816	-19.5440	0.9	1.3×10^{-14}	32.1	S	2.3	1.6×10^{39}	0.78	0.03
2CXO J131342.0+471800	198.4250	47.3001	0.4	4.6×10^{-15}	126.5	S	3.4	8.8×10^{39}	0.86	0.05
2CXO J131516.9-162317	198.8208	-16.3882	0.5	9.4×10^{-15}	31.2	S0/E	15.0	1.1×10^{39}		
2CXO J131517.8+442434	198.8243	44.4097	0.4	3.1×10^{-15}	158.5	S0/E	7.8	9.3×10^{39}	0.74	0.31
2CXO J131519.5+420301	198.8313	42.0505	0.5	9.2×10^{-13}	7.9	S	13.1	7.0×10^{39}	0.91	0.24
2CXO J131521.9-162327	198.8415	-16.3911	0.4	1.4×10^{-14}	31.2	S0/E	5.2	1.6×10^{39}		
2CXO J131527.9-162342	198.8664	-16.3952	0.4	1.0×10^{-14}	31.2	S0/E	9.9	1.2×10^{39}		
2CXO J131619.4+620610	199.0809	62.1029	0.9	1.4×10^{-14}	610.9	S0/E	14.4	6.1×10^{41}	0.19	0.43
2CXO J131934.7-123944	199.8950	-12.6623	0.4	7.1×10^{-15}	34.7	S0/E	8.3	1.0×10^{39}	0.83	0.70
2CXO J132008.7+330530	200.0365	33.0918	0.6	5.3×10^{-15}	176.2	S	4.8	2.0×10^{40}	0.54	0.08
2CXO J132013.3-215102	200.0556	-21.8508	0.5	2.5×10^{-14}	23.1	S	10.8	1.6×10^{39}	0.72	0.64
2CXO J132029.6+330854	200.1234	33.1486	0.6	7.3×10^{-15}	78.4	S	4.8	5.4×10^{39}	0.83	0.04
2CXO J132029.8+330848	200.1242	33.1468	0.7	5.4×10^{-15}	78.4	S	2.3	3.9×10^{39}	0.42	0.01
2CXO J132218.3-164246	200.5764	-16.7130	0.4	4.9×10^{-14}	68.6	S	6.3	2.8×10^{40}	0.74	0.14
2CXO J132404.9-314100	201.0208	-31.6834	0.6	1.1×10^{-14}	225.9		5.5	7.0×10^{40}	0.50	0.14
2CXO J132409.8+135754	201.0411	13.9651	0.4	1.8×10^{-14}	97.1	S0/E	18.4	2.0×10^{40}		
2CXO J132500.4+362617	201.2520	36.4382	0.9	8.7×10^{-15}	83.8	S	3.7	7.3×10^{39}	0.70	0.06
2CXO J132518.2-430304	201.3262	-43.0514	0.4	6.4×10^{-13}	3.8		2.9	1.1×10^{39}		
2CXO J132519.7-313607	201.3324	-31.6021	0.4	5.5×10^{-14}	214.8		4.0	3.0×10^{41}	0.56	0.07
2CXO J132544.6-295004	201.4361	-29.8345	0.4	1.3×10^{-14}	55.2	S	2.2	4.8×10^{39}		
2CXO J132544.8-295013	201.4368	-29.8372	0.4	5.3×10^{-15}	55.2	S	4.2	1.9×10^{39}	0.37	0.07
2CXO J132646.5+021434	201.6938	2.2429	0.8	1.0×10^{-14}	99.1		3.4	1.2×10^{40}	0.43	0.09
2CXO J132723.2-270839	201.8470	-27.1444	1.3	1.6×10^{-14}	202.3	S0/E	7.6	7.8×10^{40}	0.27	0.20
2CXO J132733.3-293356	201.8888	-29.5658	0.9	7.5×10^{-15}	52.1	S	10.8	2.4×10^{39}	0.58	0.51
2CXO J132754.8-293657	201.9786	-29.6160	0.4	1.6×10^{-14}	57.6	S0/E	2.8	6.2×10^{39}	0.22	0.03
2CXO J132921.3+114425	202.3388	11.7405	0.9	2.6×10^{-15}	96.1	S0/E	8.7	2.8×10^{39}	0.70	0.36
2CXO J132929.6+114425	202.3737	11.7403	0.4	1.2×10^{-14}	112.7	S	13.6	1.8×10^{40}	0.78	0.68
2CXO J132935.7-175542	202.3989	-17.9285	0.4	1.4×10^{-13}	19.6	S	21.8	6.5×10^{39}	0.87	0.18
2CXO J132938.6+582505	202.4108	58.4182	0.4	1.2×10^{-12}	4.1	S	0.4	2.5×10^{39}	0.25	0.00
2CXO J132941.7-175651	202.4239	-17.9478	0.4	1.0×10^{-14}	19.6	S	11.5	4.6×10^{39}	0.76	0.05
2CXO J132956.9-175903	202.4872	-17.9842	0.4	8.2×10^{-14}	19.6	S	12.4	3.8×10^{39}	0.88	0.06
2CXO J132959.0+471318	202.4961	47.2218	0.4	1.6×10^{-13}	8.0	S	4.5	1.2×10^{39}	0.94	0.05
2CXO J133001.0+471343	202.5042	47.2289	1.5	3.0×10^{-13}	8.0	S	5.7	2.3×10^{39}	0.59	0.02
2CXO J133007.5+471106	202.5315	47.1851	0.5	2.6×10^{-13}	8.0	S	6.0	2.0×10^{39}	0.95	0.05
2CXO J133011.3-020608	202.5474	-2.1024	0.5	3.7×10^{-15}	396.3	S	11.2	7.0×10^{40}	0.41	0.38
2CXO J133037.1-223015	202.6546	-22.5044	1.2	8.6×10^{-15}	75.0	S	4.8	5.8×10^{39}	0.59	0.12
2CXO J133051.5-014638	202.7148	-1.7775	0.7	5.2×10^{-15}	158.5	S	3.4	1.6×10^{40}	0.55	0.04
2CXO J133212.5+060828	203.0523	6.1413	1.3	3.2×10^{-15}	96.8	S	8.2	3.6×10^{39}	0.46	0.20
2CXO J133342.7-313217	203.4283	-31.5381	1.3	3.9×10^{-15}	220.8	S	8.0	2.3×10^{40}	0.44	0.09
2CXO J133639.4-335713	204.1643	-33.9537	0.4	5.7×10^{-15}	49.1	S0/E	10.3	1.6×10^{39}	0.65	0.18
2CXO J133644.1-335707	204.1838	-33.9522	0.4	3.8×10^{-15}	49.1	S0/E	18.6	1.1×10^{39}	0.54	0.34
2CXO J133705.1-295207	204.2714	-29.8687	0.4	1.4×10^{-12}	4.5	S	1.2	3.4×10^{39}	0.75	0.00
2CXO J133730.1+085233	204.3755	8.8759	0.4	7.5×10^{-14}	12.7	S	2.7	1.4×10^{39}	0.50	0.05
2CXO J133802.9-175113	204.5125	-17.8537	0.4	3.3×10^{-13}	19.5	S	10.2	1.5×10^{40}	0.51	0.10
2CXO J133804.7-175415	204.5198	-17.9042	0.4	5.3×10^{-14}	19.5	S	7.2	2.4×10^{39}	0.65	0.05
2CXO J133804.9-175616	204.5207	-17.9380	0.5	2.5×10^{-14}	19.5	S	18.4	1.1×10^{39}	0.69	0.31
2CXO J133806.1-175250	204.5258	-17.8806	0.4	4.0×10^{-14}	19.5	S	4.4	1.8×10^{39}	0.83	0.03
2CXO J133807.5-175343	204.5316	-17.8953	0.4	1.8×10^{-13}	19.5	S	7.2	8.1×10^{39}	0.90	0.06
2CXO J133815.6+043255	204.5651	4.5488	0.4	1.1×10^{-14}	95.7	S0/E	10.1	1.2×10^{40}	0.87	0.16
2CXO J133816.3+043148	204.5681	4.5301	0.4	3.3×10^{-15}	95.7	S0/E	20.1	3.6×10^{39}	0.72	0.62
2CXO J133816.3+043241	204.5679	4.5448	0.4	1.1×10^{-15}	95.7	S0/E	4.7	1.2×10^{39}	0.82	0.04
2CXO J133953.5+005030	204.9729	0.8417	0.4	2.6×10^{-14}	93.8	S	5.4	2.8×10^{40}	0.25	0.07
2CXO J133953.9+005016	204.9747	0.8379	0.5	1.8×10^{-15}	93.8	S	7.9	1.9×10^{39}	0.67	0.17
2CXO J133955.9+004959	204.9831	0.8333	0.4	1.8×10^{-14}	93.2	S	11.8	1.9×10^{40}	0.72	0.17
2CXO J133957.0+004938	204.9878	0.8274	0.5	2.2×10^{-15}	93.2	S	6.8	2.3×10^{39}	0.51	0.05
2CXO J133957.2+004947	204.9884	0.8298	0.5	3.8×10^{-15}	93.2	S	3.5	4.0×10^{39}		
2CXO J133957.4+004954	204.9895	0.8318	0.5	5.2×10^{-15}	93.2	S	1.8	5.5×10^{39}	0.48	0.00
2CXO J133957.8+004947	204.9910	0.8298	0.5	3.6×10^{-15}	93.2	S	2.1	3.7×10^{39}	0.54	0.00
2CXO J133958.7+005006	204.9948	0.8352	0.4	1.3×10^{-14}	93.2	S	9.7	1.3×10^{40}	0.73	0.10

Table A.16: List of ULX candidates obtained in Chapter 4 (continued).

Name	RA deg	Dec deg	$POSERR$ arcsec	F_X erg cm^{-2} s^{-1}	D Mpc	Gal. type	Sep. kpc	L_X erg s^{-1}	P_{XRB}	f_{cont}
2CXO J133959.2+004938	204.9967	0.8274	0.5	1.7×10^{-15}	93.2	S	11.5	1.8×10^{39}	0.66	0.15
2CXO J134547.0-053009	206.4460	-5.5026	0.6	3.2×10^{-15}	233.3	S	8.7	2.1×10^{40}	0.62	0.09
2CXO J135023.9+683311	207.5996	68.5531	0.5	1.4×10^{-15}	142.6	S	6.0	3.5×10^{39}	0.78	0.10
2CXO J135101.0+240519	207.7543	24.0887	1.3	3.9×10^{-14}	49.5	S	2.2	1.2×10^{40}	0.10	0.03
2CXO J135253.7-283147	208.2239	-28.5298	0.9	1.7×10^{-14}	182.2	S0/E	4.7	6.6×10^{40}	0.23	0.07
2CXO J135324.1+402208	208.3505	40.3691	1.1	1.4×10^{-14}	37.0	S	6.1	2.3×10^{39}	0.85	0.12
2CXO J135535.2+402658	208.8968	40.4497	0.5	2.9×10^{-14}	37.0	S	12.3	4.7×10^{39}	0.24	0.20
2CXO J135535.2+402706	208.8970	40.4519	0.5	2.2×10^{-14}	37.0	S	11.4	3.5×10^{39}	0.80	0.18
2CXO J135537.1+402750	208.9046	40.4640	0.5	8.3×10^{-15}	37.0	S	6.0	1.4×10^{39}	0.86	0.07
2CXO J135538.9+402607	208.9124	40.4356	0.5	7.1×10^{-15}	37.0	S	16.8	1.2×10^{39}	0.88	0.21
2CXO J135542.0+402634	208.9254	40.4431	0.5	1.4×10^{-14}	37.0	S	12.6	2.2×10^{39}	0.87	0.16
2CXO J135700.5+415126	209.2521	41.8575	0.4	8.0×10^{-14}	37.0	S	11.5	1.3×10^{40}	0.77	0.23
2CXO J135703.3+415034	209.2638	41.8430	0.4	6.8×10^{-14}	37.0	S	3.8	1.1×10^{40}	0.75	0.03
2CXO J135706.9+414752	209.2789	41.7978	1.0	1.3×10^{-14}	36.3	S	3.2	2.1×10^{39}	0.81	0.09
2CXO J135706.9+415122	209.2791	41.8562	0.4	2.3×10^{-14}	37.0	S	7.6	3.7×10^{39}	0.84	0.16
2CXO J135837.8+372533	209.6577	37.4259	0.5	4.2×10^{-15}	49.5	S	1.1	1.2×10^{39}	0.26	0.00
2CXO J135837.9+372440	209.6580	37.4114	0.5	4.1×10^{-15}	49.5	S	11.2	1.2×10^{39}	0.81	0.18
2CXO J135838.7+372531	209.6614	37.4255	0.4	6.5×10^{-15}	49.5	S	2.4	1.9×10^{39}	0.59	0.03
2CXO J140015.8+550705	210.0662	55.1182	0.9	3.1×10^{-15}	401.8		11.5	6.0×10^{40}	0.61	0.21
2CXO J140135.1-114311	210.3967	-11.7198	0.7	3.0×10^{-15}	179.5	S0/E	5.0	1.1×10^{40}	0.44	0.06
2CXO J140155.7-113809	210.4823	-11.6360	0.4	3.2×10^{-14}	230.3	S0/E	5.4	2.0×10^{41}	0.49	0.05
2CXO J140156.5-114058	210.4856	-11.6828	0.5	5.3×10^{-15}	160.6	S	3.3	1.6×10^{40}	0.68	0.07
2CXO J140228.2+541626	210.6177	54.2742	0.5	2.0×10^{-13}	6.7	S	15.3	1.1×10^{39}	0.86	0.09
2CXO J140303.9+542735	210.7664	54.4597	0.5	5.1×10^{-13}	6.7	S	13.2	2.7×10^{39}	0.95	0.07
2CXO J140319.6-412258	210.8317	-41.3830	0.4	1.9×10^{-12}	3.7		0.4	3.2×10^{39}	0.66	0.00
2CXO J140324.6-060244	210.8527	-6.0456	0.4	3.6×10^{-14}	26.5	S	7.3	3.0×10^{39}	0.80	0.35
2CXO J140325.7-335749	210.8572	-33.9639	0.8	6.1×10^{-15}	55.5	S0/E	1.4	2.3×10^{39}	0.30	0.02
2CXO J140336.1-335830	210.9006	-33.9750	0.5	5.1×10^{-15}	56.8	S0/E	9.4	2.0×10^{39}	0.62	0.08
2CXO J140336.5-335819	210.9023	-33.9720	0.5	6.3×10^{-15}	56.8	S0/E	9.6	2.4×10^{39}	0.32	0.11
2CXO J140336.7-335754	210.9031	-33.9652	0.6	4.1×10^{-15}	56.8	S0/E	14.4	1.6×10^{39}	0.60	0.28
2CXO J140338.5-335754	210.9105	-33.9652	0.4	3.1×10^{-14}	56.8	S0/E	12.7	1.2×10^{40}	0.67	0.22
2CXO J140340.9-335847	210.9207	-33.9800	0.5	3.9×10^{-15}	56.8	S0/E	7.5	1.5×10^{39}	0.20	0.05
2CXO J140341.5-335840	210.9233	-33.9780	0.4	8.3×10^{-15}	56.8	S0/E	9.4	3.2×10^{39}	0.45	0.07
2CXO J140414.2+542604	211.0592	54.4346	0.5	4.0×10^{-13}	6.7	S	20.1	2.1×10^{39}	0.95	0.15
2CXO J140429.2+542353	211.1217	54.3981	0.5	3.2×10^{-14}	157.8	S	4.5	9.6×10^{40}	0.24	0.07
2CXO J140459.7+533809	211.2489	53.6358	0.4	1.1×10^{-12}	7.3		1.1	7.1×10^{39}	0.86	0.00
2CXO J140732.6-270041	211.8860	-27.0116	0.4	5.8×10^{-15}	92.1	S0/E	19.0	5.9×10^{39}		
2CXO J141022.2-431753	212.5927	-43.2983	0.4	2.2×10^{-14}	24.2	S	11.6	1.5×10^{39}	0.74	0.18
2CXO J141029.6-431835	212.6235	-43.3097	0.4	6.5×10^{-14}	24.2	S	8.5	4.5×10^{39}	0.85	0.09
2CXO J141030.9-432026	212.6288	-43.3407	0.4	3.5×10^{-14}	24.2	S	10.0	2.4×10^{39}	0.74	0.15
2CXO J141311.9-031232	213.2998	-3.2091	0.4	2.4×10^{-14}	19.6	S	4.2	1.1×10^{39}	0.80	0.03
2CXO J141544.8+361029	213.9370	36.1748	0.8	2.9×10^{-15}	111.7	S	6.3	4.4×10^{39}	0.65	0.15
2CXO J141600.6+520622	214.0027	52.1063	0.7	4.0×10^{-15}	346.7	S	8.2	5.7×10^{40}	0.75	0.37
2CXO J141748.6+524142	214.4525	52.6950	0.4	5.5×10^{-15}	102.0	S0/E	4.0	6.8×10^{39}	0.93	0.08
2CXO J141939.3+564137	214.9141	56.6938	0.4	3.0×10^{-13}	8.6	S	6.0	2.6×10^{39}	0.84	0.06
2CXO J142010.7+533348	215.0448	53.5635	0.6	1.2×10^{-14}	293.8		8.3	1.2×10^{41}	0.57	0.20
2CXO J142220.1-002340	215.5839	-0.3945	0.4	4.9×10^{-14}	20.8	S	6.1	2.5×10^{39}	0.43	0.30
2CXO J142235.9+595616	215.6499	59.9378	0.5	8.2×10^{-15}	132.4	S0/E	15.9	1.7×10^{40}	0.74	0.42
2CXO J142238.3+595546	215.6598	59.9295	0.4	3.8×10^{-15}	132.4	S0/E	6.8	8.1×10^{39}	0.74	0.07
2CXO J142238.5+595532	215.6607	59.9256	0.4	1.2×10^{-14}	132.4	S0/E	13.4	2.5×10^{40}	0.83	0.29
2CXO J142404.8+345152	216.0204	34.8646	0.5	3.1×10^{-15}	54.9	S	10.2	1.1×10^{39}	0.67	0.26
2CXO J142407.0+345130	216.0296	34.8586	0.5	3.2×10^{-15}	54.9	S	1.6	1.2×10^{39}	0.46	0.01
2CXO J142409.7+345041	216.0407	34.8450	0.4	9.7×10^{-15}	54.9	S	14.8	3.5×10^{39}	0.72	0.51
2CXO J142519.7+322851	216.3322	32.4811	0.8	1.2×10^{-14}	59.0	S	3.2	5.2×10^{39}	0.41	0.06
2CXO J142709.1+331503	216.7882	33.2509	0.4	8.6×10^{-15}	47.7	S0/E	1.8	2.3×10^{39}	0.49	0.04
2CXO J142732.4+343040	216.8852	34.5114	0.5	4.4×10^{-14}	309.0	S	5.3	5.0×10^{41}	0.14	0.06
2CXO J142843.5+342242	217.1816	34.3784	1.3	1.2×10^{-14}	135.8	S	7.9	2.6×10^{40}	0.24	0.20
2CXO J142940.4+031633	217.4184	3.2761	0.5	3.2×10^{-14}	22.9	S0/E	4.5	2.0×10^{39}	0.48	0.11
2CXO J143009.4+311254	217.5394	31.2152	0.5	4.8×10^{-15}	49.8	S	2.9	1.4×10^{39}	0.20	0.07
2CXO J143119.4+030418	217.8311	3.0719	0.9	4.3×10^{-15}	123.6	S	5.0	7.8×10^{39}	0.47	0.09
2CXO J143126.6+030022	217.8611	3.0063	0.4	3.4×10^{-14}	23.0	S	1.5	2.1×10^{39}	0.51	0.01
2CXO J143201.0+361828	218.0042	36.3078	0.9	3.2×10^{-15}	54.4	S	2.3	1.1×10^{39}	0.77	0.06
2CXO J143207.6+575531	218.0318	57.9253	0.5	1.4×10^{-14}	29.2	S	3.0	1.4×10^{39}	0.75	0.04
2CXO J143208.2+575510	218.0342	57.9196	0.5	3.0×10^{-14}	29.2	S	3.1	3.1×10^{39}	0.88	0.07
2CXO J143240.8-440744	218.1704	-44.1290	0.5	2.9×10^{-14}	18.4	S	14.5	1.2×10^{39}	0.71	0.45
2CXO J143242.2-440939	218.1761	-44.1609	0.5	7.1×10^{-13}	18.4	S	4.6	2.9×10^{40}	0.64	0.04
2CXO J143435.3-361715	218.6475	-36.2876	0.4	7.3×10^{-15}	53.3	S0/E	5.5	2.5×10^{39}		
2CXO J143439.2-361745	218.6636	-36.2960	0.5	3.8×10^{-15}	53.3	S0/E	11.3	1.3×10^{39}		
2CXO J143518.1+350713	218.8258	35.1204	0.7	2.7×10^{-15}	127.6	S	3.7	5.2×10^{39}	0.35	0.02
2CXO J143753.4-002359	219.4726	-0.3999	0.4	4.8×10^{-14}	20.8	S	0.4	2.5×10^{39}	0.34	0.00
2CXO J143754.3-002356	219.4766	-0.3990	0.4	2.7×10^{-14}	20.8	S	1.6	1.4×10^{39}	0.56	0.01
2CXO J144326.3+585315	220.8597	58.8876	1.2	8.2×10^{-15}	176.2	S	5.4	3.0×10^{40}	0.33	0.19
2CXO J144521.0+384336	221.3379	38.7269	0.4	4.6×10^{-14}	62.7	S	6.8	2.2×10^{40}	0.57	0.36
2CXO J144932.6-100947	222.3862	-10.1632	0.4	7.4×10^{-14}	19.6		0.4	3.4×10^{39}	0.14	0.00
2CXO J145123.2+000022	222.8467	0.0062	0.7	6.7×10^{-15}	97.6	S0/E	2.2	7.6×10^{39}	0.48	0.03
2CXO J145129.4+580508	222.8727	58.0856	0.8	3.7×10^{-15}	169.8		7.0	1.3×10^{40}		
2CXO J145350.8+032909	223.4620	3.4861	0.8	2.6×10^{-15}	114.6	S	4.2	4.1×10^{39}	0.74	0.04
2CXO J145355.7+033327	223.4823	3.5576	0.4	5.4×10^{-14}	20.8	S	5.5	2.8×10^{39}		
2CXO J145355.8+033429	223.4829	3.5749	0.4	2.3×10^{-15}	432.5	S	6.4	5.2×10^{40}	0.37	0.03
2CXO J145358.8+033216	223.4954	3.5378	0.4	3.6×10^{-13}	20.8	S	3.0	1.8×10^{40}		
2CXO J145359.4+033156	223.4977	3.5324	0.4	5.6×10^{-14}	20.8	S	5.1	2.9×10^{39}		

Table A.17: List of ULX candidates obtained in Chapter 4 (continued).

Name	RA deg	Dec deg	$POSERR$ arcsec	F_X erg cm^{-2} s^{-1}	D Mpc	Gal. type	Sep. kpc	L_X erg s^{-1}	P_{XRB}	f_{cont}
2CXO J145400.9+033128	223.5040	3.5247	0.4	2.2×10^{-14}	20.8	S	8.7	1.1×10^{39}		
2CXO J145925.3-164159	224.8556	-16.7000	0.4	3.9×10^{-15}	48.2	S	5.6	1.1×10^{39}	0.68	0.07
2CXO J145926.0-164154	224.8584	-16.6985	0.4	7.0×10^{-15}	48.2	S	5.7	2.0×10^{39}	0.67	0.06
2CXO J150105.5+014330	225.2733	1.7252	0.4	1.6×10^{-14}	32.2	S0/E	18.3	2.0×10^{39}		
2CXO J150110.8+014142	225.2953	1.6952	0.4	2.6×10^{-14}	32.2	S0/E	3.8	3.2×10^{39}		
2CXO J150119.2+014540	225.3302	1.7612	0.6	1.6×10^{-15}	197.7	S	19.7	7.4×10^{39}	0.37	0.23
2CXO J150119.2+014550	225.3302	1.7640	0.4	1.9×10^{-15}	197.7	S	20.2	8.8×10^{39}	0.43	0.25
2CXO J150119.4+014552	225.3312	1.7645	0.5	2.5×10^{-16}	197.7	S	17.9	1.2×10^{39}	0.80	0.21
2CXO J150121.2+014554	225.3384	1.7652	0.5	8.2×10^{-16}	197.7	S	11.8	3.8×10^{39}	0.81	0.16
2CXO J150442.6+260645	226.1777	26.1127	1.2	4.9×10^{-15}	237.0	S	11.3	3.3×10^{40}	0.20	0.17
2CXO J150527.5+020654	226.3646	2.1151	0.4	8.3×10^{-14}	20.8	S0/E	6.0	4.3×10^{39}	0.67	0.15
2CXO J150949.5+570000	227.4567	57.0001	0.4	5.6×10^{-14}	15.8	S	1.8	1.7×10^{39}	0.94	0.04
2CXO J151558.6+561810	228.9943	56.3029	0.4	3.2×10^{-13}	13.4	S	6.6	7.0×10^{39}	0.66	0.03
2CXO J151643.5+070045	229.1815	7.0126	0.4	2.7×10^{-15}	150.0	S	24.0	7.4×10^{39}		
2CXO J151646.4+070025	229.1935	7.0070	0.5	1.4×10^{-15}	137.4	S	8.5	3.2×10^{39}	0.75	0.38
2CXO J151805.0+424447	229.5210	42.7465	0.5	2.7×10^{-15}	181.1	S	9.9	1.0×10^{40}	0.40	0.12
2CXO J151805.2+424458	229.5218	42.7495	0.5	4.6×10^{-15}	181.1	S	13.5	1.8×10^{40}	0.63	0.11
2CXO J152127.5+303759	230.3647	30.6333	0.5	3.4×10^{-15}	340.4	S0/E	5.7	4.7×10^{40}	0.15	0.07
2CXO J152327.0+283729	230.8628	28.6247	0.5	3.2×10^{-15}	375.0	S0/E	5.8	5.4×10^{40}	0.14	0.09
2CXO J153434.9+151148	233.6456	15.1969	0.4	2.8×10^{-14}	26.5	S	0.7	2.3×10^{39}	0.13	0.00
2CXO J153456.9+233005	233.7373	23.5015	0.4	5.3×10^{-15}	78.2	S0/E	2.4	3.9×10^{39}		
2CXO J153504.9+232850	233.7704	23.4808	0.6	9.4×10^{-16}	161.4	S	3.8	2.9×10^{39}	0.41	0.05
2CXO J153547.4-285444	233.9476	-28.9124	0.7	2.9×10^{-14}	92.3	S	4.2	3.0×10^{40}	0.71	0.29
2CXO J153738.9+055845	234.4121	5.9793	0.5	2.7×10^{-14}	19.6	S	4.2	1.3×10^{39}	0.75	0.14
2CXO J155911.8+204454	239.7994	20.7484	0.4	6.8×10^{-15}	65.9	S	0.9	3.5×10^{39}	0.14	0.01
2CXO J155922.1+650631	239.8424	65.1088	1.6	3.4×10^{-15}	316.0	S	15.0	4.1×10^{40}	0.58	0.54
2CXO J160211.7+155437	240.5491	15.9103	0.8	3.9×10^{-14}	159.2	S0/E	12.6	1.2×10^{41}	0.38	0.62
2CXO J160308.1-401922	240.7841	-40.3228	0.5	1.4×10^{-15}	158.0		9.6	4.1×10^{39}	0.25	0.19
2CXO J160310.3-401901	240.7931	-40.3172	0.5	3.5×10^{-16}	158.0		13.9	1.0×10^{39}	0.52	0.44
2CXO J160435.2+174404	241.1468	17.7346	0.5	2.6×10^{-14}	156.3	S0/E	33.9	7.6×10^{40}		
2CXO J160455.0+235537	241.2292	23.9271	0.4	2.8×10^{-15}	580.8	S0/E	69.6	1.1×10^{41}		
2CXO J161040.3+543622	242.6679	54.6063	0.5	3.5×10^{-15}	331.3	S	18.4	4.6×10^{40}	0.55	0.53
2CXO J161123.6+522704	242.8487	52.4514	0.5	1.2×10^{-14}	133.0	S0/E	7.7	2.4×10^{40}	0.42	0.22
2CXO J161218.3+293257	243.0765	29.5494	0.6	6.3×10^{-15}	238.8	S0/E	7.4	4.3×10^{40}	0.21	0.16
2CXO J161249.8+540832	243.2076	54.1423	0.5	3.8×10^{-14}	711.2	S0/E	14.9	2.3×10^{42}	0.19	0.45
2CXO J161324.4-604545	243.3518	-60.7625	0.4	5.7×10^{-15}	66.7	S	6.8	3.0×10^{39}		
2CXO J161534.2+192707	243.8929	19.4521	0.5	1.2×10^{-14}	133.4	S0/E	11.1	2.6×10^{40}	0.05	0.26
2CXO J161555.3-061017	243.9805	-6.1714	0.5	2.4×10^{-15}	125.3		5.7	4.6×10^{39}	0.72	0.04
2CXO J161616.8+470233	244.0702	47.0425	1.6	9.1×10^{-14}	15.0	S	1.3	2.5×10^{39}	0.14	0.01
2CXO J161636.5+681205	244.1521	68.2015	0.4	3.1×10^{-14}	17.5	S	0.4	1.1×10^{39}	0.41	0.00
2CXO J161911.4-075403	244.7977	-7.9009	0.4	7.2×10^{-15}	119.7		2.9	1.2×10^{40}	0.35	0.03
2CXO J161948.0+050953	244.9502	5.1648	0.5	7.3×10^{-15}	111.2	S0/E	6.0	1.1×10^{40}	0.35	0.17
2CXO J162108.6+380212	245.2861	38.0368	1.6	6.2×10^{-15}	151.4	S0/E	8.2	1.7×10^{40}	0.46	0.28
2CXO J162123.2+380414	245.3468	38.0708	0.5	6.0×10^{-15}	147.9	S	8.8	1.6×10^{40}	0.53	0.30
2CXO J162455.5-273636	246.2317	-27.6100	0.5	1.4×10^{-14}	69.6		2.6	8.4×10^{39}	0.75	0.03
2CXO J162456.4-273637	246.2354	-27.6106	0.5	1.2×10^{-14}	69.6		2.4	7.0×10^{39}	0.69	0.03
2CXO J162703.4+432831	246.7645	43.4755	0.5	6.9×10^{-15}	208.9	S0/E	9.6	3.6×10^{40}	0.52	0.34
2CXO J162825.2+393401	247.1053	39.5671	0.4	6.8×10^{-15}	131.8	S0/E	15.3	1.4×10^{40}		
2CXO J162839.4+393338	247.1644	39.5606	0.4	1.1×10^{-14}	120.2	S0/E	19.9	1.9×10^{40}		
2CXO J162843.2+393410	247.1803	39.5696	0.5	5.6×10^{-15}	153.5	S0/E	2.0	1.6×10^{40}	0.16	0.02
2CXO J163121.5-750652	247.8397	-75.1145	0.4	1.8×10^{-14}	498.9		57.0	5.3×10^{41}		
2CXO J163244.8+823436	248.1868	82.5769	0.5	1.5×10^{-15}	93.6	S	3.6	1.6×10^{39}	0.25	0.07
2CXO J163249.0+053852	248.2045	5.6479	0.9	7.1×10^{-15}	376.4		13.5	1.2×10^{41}	0.28	0.25
2CXO J163603.1+661942	249.0132	66.3285	1.3	1.6×10^{-15}	149.6	S	5.3	4.4×10^{39}	0.29	0.12
2CXO J163604.9+661941	249.0206	66.3281	0.9	2.2×10^{-15}	149.6	S	3.3	5.9×10^{39}	0.46	0.02
2CXO J163614.1+661410	249.0590	66.2362	0.4	2.7×10^{-14}	109.6	S	8.0	3.9×10^{40}	0.70	0.20
2CXO J164147.8+395904	250.4492	39.9847	0.4	5.0×10^{-15}	144.5	S0/E	5.6	1.2×10^{40}	0.23	0.14
2CXO J164239.8-094310	250.6661	-9.7196	0.4	5.3×10^{-15}	118.6		1.8	8.9×10^{39}	0.24	0.01
2CXO J165259.6+022423	253.2485	2.4064	0.4	1.2×10^{-15}	108.1		11.3	1.7×10^{39}	0.34	0.18
2CXO J165300.3+022358	253.2515	2.3997	0.4	2.9×10^{-15}	108.1		11.5	4.1×10^{39}	0.58	0.54
2CXO J165823.4+585722	254.5977	58.9562	0.4	1.6×10^{-14}	82.1	S	1.7	1.3×10^{40}	0.23	0.01
2CXO J165824.5+585718	254.6024	58.9551	0.5	3.3×10^{-15}	82.1	S	2.0	2.7×10^{39}	0.35	0.01
2CXO J170932.2+342542	257.3845	34.4286	0.5	1.7×10^{-14}	353.2	S	9.5	2.6×10^{41}	0.16	0.20
2CXO J171215.5+640212	258.0646	64.0368	0.5	1.1×10^{-14}	335.1	S0/E	7.1	1.5×10^{41}	0.45	0.10
2CXO J171548.4+572218	258.9517	57.3717	0.9	2.2×10^{-15}	136.1	S	14.7	5.0×10^{39}	0.49	0.32
2CXO J171636.1-102024	259.1507	-10.3401	0.5	1.1×10^{-14}	73.9	S	5.5	7.3×10^{39}	0.24	0.21
2CXO J171648.2-624923	259.2010	-62.8233	0.4	9.1×10^{-14}	13.1	S	4.9	1.9×10^{39}	0.84	0.05
2CXO J171705.4-624910	259.2726	-62.8196	0.4	7.9×10^{-14}	13.1	S	2.6	1.6×10^{39}	0.07	0.01
2CXO J171856.4+600352	259.7353	60.0645	0.7	1.9×10^{-15}	121.3		3.9	3.3×10^{39}	0.45	0.03
2CXO J173303.0+434527	263.2629	43.7576	0.4	1.5×10^{-14}	147.2	S0/E	9.1	3.8×10^{40}		
2CXO J181340.7-574318	273.4197	-57.7219	0.5	3.5×10^{-15}	70.9	S	4.7	2.1×10^{39}	0.09	0.06
2CXO J181342.3-574318	273.4265	-57.7218	0.4	5.2×10^{-15}	70.9	S	8.0	3.1×10^{39}	0.36	0.16
2CXO J181649.0-571358	274.2046	-57.2328	0.4	1.1×10^{-14}	35.2		2.9	1.6×10^{39}	0.44	0.04
2CXO J181950.9+743512	274.9624	74.5868	0.4	3.2×10^{-14}	20.6	S	6.8	1.6×10^{39}	0.91	0.07
2CXO J181955.7+743448	274.9822	74.5800	0.4	6.3×10^{-14}	20.6	S	5.6	3.2×10^{39}	0.83	0.03
2CXO J183337.0+595321	278.4045	59.8893	0.5	4.1×10^{-15}	130.6	S0/E	2.8	8.4×10^{39}	0.39	0.05
2CXO J183351.4+491642	278.4645	49.2784	0.4	2.0×10^{-14}	29.9	S	1.5	2.1×10^{39}	0.44	0.02
2CXO J183826.3+171139	279.6098	17.1942	0.5	7.7×10^{-15}	73.6	S0/E	3.6	5.0×10^{39}	0.52	0.06
2CXO J184739.8-631741	281.9161	-63.2950	0.5	8.3×10^{-15}	63.5	S	8.9	4.0×10^{39}	0.63	0.22
2CXO J185317.1+330358	283.3215	33.0663	0.7	1.3×10^{-14}	74.0	S	7.3	8.6×10^{39}	0.34	0.30
2CXO J190611.2+685029	286.5467	68.8415	0.7	2.5×10^{-15}	353.1	S0/E	9.5	3.7×10^{40}	0.64	0.19

Table A.18: List of ULX candidates obtained in Chapter 4 (continued).

Name	RA deg	Dec deg	$POSERR$ arcsec	F_X erg cm^{-2} s^{-1}	D Mpc	Gal. type	Sep. kpc	L_X erg s^{-1}	P_{XRB}	f_{cont}
2CXO J193121.0-723929	292.8378	-72.6581	0.4	5.0×10^{-15}	270.4		9.7	4.4×10^{40}	0.42	0.09
2CXO J195944.6+404702	299.9358	40.7840	0.9	1.4×10^{-15}	194.6		5.1	6.2×10^{39}	0.25	0.15
2CXO J200751.3+593811	301.9641	59.6367	0.5	7.9×10^{-15}	166.7	S	3.4	2.6×10^{40}	0.53	0.05
2CXO J200954.9-482400	302.4789	-48.4002	0.4	2.1×10^{-14}	26.8	S0/E	9.6	1.8×10^{39}	0.65	0.39
2CXO J201012.8-481658	302.5535	-48.2830	0.6	1.0×10^{-14}	33.4	S	4.0	1.4×10^{39}	0.79	0.13
2CXO J201225.5-564951	303.1064	-56.8309	0.4	1.3×10^{-13}	244.3	S0/E	21.9	9.4×10^{41}		
2CXO J201645.7-704709	304.1907	-70.7860	0.5	2.3×10^{-15}	64.6	S	25.2	1.1×10^{39}	0.60	0.22
2CXO J201649.1-704648	304.2046	-70.7801	0.4	5.7×10^{-15}	64.6	S	17.1	2.8×10^{39}	0.47	0.10
2CXO J201653.1-704638	304.2215	-70.7772	0.5	2.2×10^{-15}	64.6	S	11.0	1.1×10^{39}	0.61	0.06
2CXO J201653.3-704605	304.2223	-70.7682	0.4	5.1×10^{-15}	62.7		2.3	2.4×10^{39}	0.45	0.01
2CXO J201655.6-704626	304.2319	-70.7740	0.4	4.0×10^{-15}	64.6	S	6.4	2.0×10^{39}	0.61	0.04
2CXO J201656.7-704636	304.2366	-70.7769	0.4	1.2×10^{-14}	64.6	S	9.5	5.8×10^{39}	0.69	0.13
2CXO J201657.8-704703	304.2408	-70.7843	0.4	9.5×10^{-15}	64.6	S	17.7	4.8×10^{39}	0.71	0.48
2CXO J201700.9-704609	304.2538	-70.7692	0.4	7.9×10^{-15}	64.6	S	6.7	3.9×10^{39}	0.43	0.07
2CXO J203402.3-525828	308.5097	-52.9746	1.9	3.3×10^{-14}	31.2	S	3.6	3.9×10^{39}	0.53	0.10
2CXO J203419.6-320007	308.5820	-32.0021	0.5	1.3×10^{-14}	28.3	S	10.5	1.2×10^{39}	0.55	0.04
2CXO J203420.7-315742	308.5866	-31.9617	0.4	4.3×10^{-14}	28.3	S	9.4	4.1×10^{39}	0.71	0.03
2CXO J203420.7-320002	308.5863	-32.0008	0.4	1.4×10^{-14}	28.3	S	9.7	1.3×10^{39}	0.58	0.04
2CXO J203420.8-315913	308.5870	-31.9871	0.5	2.5×10^{-14}	28.3	S	3.1	2.4×10^{39}	0.21	0.01
2CXO J203421.6-315832	308.5903	-31.9757	0.4	1.5×10^{-14}	28.3	S	3.2	1.4×10^{39}	0.60	0.02
2CXO J203500.7+601130	308.7531	60.1919	0.4	1.0×10^{-13}	5.7	S	4.2	3.9×10^{39}	0.76	0.03
2CXO J203717.2+253142	309.3218	25.5285	0.5	7.6×10^{-15}	148.1	S	5.4	2.0×10^{40}	0.11	0.03
2CXO J203717.7+253130	309.3238	25.5253	0.5	4.2×10^{-15}	148.1	S	4.6	1.1×10^{40}	0.23	0.03
2CXO J203717.9+253149	309.3247	25.5303	0.4	3.3×10^{-15}	148.1	S	7.8	8.7×10^{39}	0.31	0.08
2CXO J205155.5-523752	312.9815	-52.6313	0.6	6.2×10^{-15}	205.1	S0/E	12.2	3.1×10^{40}	0.31	0.28
2CXO J205200.6-570417	313.0026	-57.0715	0.4	4.3×10^{-15}	46.4	S0/E	3.8	1.1×10^{39}		
2CXO J205409.7-690234	313.5407	-69.0429	0.4	5.4×10^{-15}	158.5	S	6.5	1.6×10^{40}	0.50	0.08
2CXO J205826.5-423908	314.6106	-42.6523	0.4	1.3×10^{-14}	185.4	S0/E	7.1	5.5×10^{40}		
2CXO J210333.9+295317	315.8914	29.8883	0.4	1.7×10^{-13}	15.0	S	2.4	4.5×10^{39}	0.50	0.01
2CXO J211900.8-483348	319.7534	-48.5635	0.7	2.5×10^{-14}	30.6	S0/E	1.6	2.8×10^{39}	0.43	0.03
2CXO J213610.7-383245	324.0450	-38.5459	0.5	5.7×10^{-15}	79.5	S	1.3	4.3×10^{39}	0.24	0.00
2CXO J214115.5-635402	325.3148	-63.9007	0.4	2.1×10^{-14}	35.8	S	6.5	3.2×10^{39}	0.74	0.34
2CXO J214638.0-463034	326.6584	-46.5095	0.6	4.6×10^{-15}	133.0	S	11.2	9.8×10^{39}	0.41	0.25
2CXO J215701.8+662601	329.2577	66.4338	0.5	4.2×10^{-15}	261.3		10.4	3.4×10^{40}	0.40	0.40
2CXO J215704.1-694147	329.2672	-69.6964	0.4	8.8×10^{-15}	120.2	S0/E	14.0	1.5×10^{40}		
2CXO J215707.1-694115	329.2798	-69.6876	0.4	4.4×10^{-15}	120.2	S0/E	5.7	7.6×10^{39}		
2CXO J220207.8-315920	330.5329	-31.9891	0.4	1.0×10^{-14}	32.4	S0/E	1.2	1.3×10^{39}	0.41	0.01
2CXO J220244.6-315952	330.6862	-31.9979	0.8	1.5×10^{-14}	33.3	S0/E	4.4	2.1×10^{39}	0.43	0.19
2CXO J220325.6-345633	330.8570	-34.9427	0.4	6.0×10^{-15}	62.0	S0/E	4.8	2.8×10^{39}		
2CXO J221608.0-365019	334.0337	-36.8389	0.5	5.1×10^{-15}	48.1	S	4.9	1.4×10^{39}	0.19	0.05
2CXO J221609.7-365040	334.0404	-36.8445	0.4	9.6×10^{-15}	48.1	S	1.8	2.7×10^{39}	0.63	0.00
2CXO J221610.0-365034	334.0420	-36.8428	0.4	3.9×10^{-15}	48.1	S	2.8	1.1×10^{39}	0.39	0.00
2CXO J221610.1-365020	334.0425	-36.8389	0.4	2.3×10^{-14}	48.1	S	5.0	6.4×10^{39}	0.62	0.02
2CXO J221610.2-365024	334.0428	-36.8401	0.5	3.8×10^{-15}	48.1	S	4.4	1.1×10^{39}	0.75	0.01
2CXO J221610.8-365014	334.0450	-36.8375	0.5	3.9×10^{-15}	48.1	S	7.0	1.1×10^{39}	0.56	0.03
2CXO J221611.6-365023	334.0484	-36.8400	0.5	8.7×10^{-15}	48.1	S	7.6	2.4×10^{39}	0.59	0.03
2CXO J221827.6-593847	334.6151	-59.6465	0.9	2.3×10^{-14}	62.5	S	6.1	1.1×10^{40}	0.47	0.29
2CXO J221944.7-272219	334.9364	-27.3722	0.6	4.8×10^{-15}	251.2		5.8	3.6×10^{40}	0.51	0.06
2CXO J222044.3-244103	335.1846	-24.6843	0.4	8.4×10^{-15}	65.9	S0/E	6.9	4.4×10^{39}	0.48	0.08
2CXO J222044.6-244001	335.1859	-24.6670	0.5	2.0×10^{-15}	65.9	S0/E	12.6	1.0×10^{39}	0.64	0.26
2CXO J223546.3-260429	338.9430	-26.0749	0.8	4.7×10^{-14}	15.8	S	6.8	1.4×10^{39}	0.56	0.05
2CXO J223547.8-260239	338.9494	-26.0443	0.7	4.0×10^{-14}	15.8	S	2.3	1.2×10^{39}	0.62	0.02
2CXO J223548.1-260129	338.9506	-26.0248	0.5	3.1×10^{-13}	15.8	S	7.2	9.3×10^{39}		
2CXO J223555.7+335738	338.9821	33.9608	0.4	4.3×10^{-14}	83.2	S	14.6	3.6×10^{40}		
2CXO J223556.5+335704	338.9855	33.9512	0.5	1.3×10^{-15}	83.2	S	22.5	1.1×10^{39}	0.81	0.66
2CXO J223557.1+335758	338.9880	33.9663	0.4	1.1×10^{-15}	99.1		3.1	1.3×10^{39}	0.15	0.06
2CXO J223557.5+335859	338.9900	33.9833	0.4	4.9×10^{-15}	83.2	S	24.4	4.0×10^{39}		
2CXO J223600.7+335801	339.0031	33.9671	0.4	8.0×10^{-15}	83.2	S	11.9	6.6×10^{39}		
2CXO J223603.6+335825	339.0153	33.9736	0.4	9.6×10^{-15}	96.9		3.5	1.1×10^{40}		
2CXO J223604.8+335901	339.0201	33.9837	0.4	5.0×10^{-15}	96.9		14.7	5.7×10^{39}		
2CXO J223728.6-455528	339.3692	-45.9245	1.1	1.1×10^{-15}	221.8		7.8	6.2×10^{39}	0.56	0.25
2CXO J224514.9+394439	341.3122	39.7444	0.7	2.9×10^{-15}	364.9		8.4	4.6×10^{40}	0.29	0.14
2CXO J224718.1+033821	341.8254	3.6393	0.5	2.7×10^{-15}	122.9	S	14.1	4.9×10^{39}	0.59	0.39
2CXO J224954.9+113638	342.4791	11.6108	0.5	2.5×10^{-15}	115.3	S0/E	5.3	4.0×10^{39}	0.58	0.07
2CXO J224956.5-642548	342.4857	-64.4302	0.5	1.9×10^{-14}	420.7	S0/E	18.3	4.1×10^{41}		
2CXO J225002.1+114129	342.5090	11.6915	1.0	4.8×10^{-15}	107.6	S0/E	13.1	6.7×10^{39}	0.50	0.32
2CXO J225153.5-320757	342.9733	-32.1327	0.5	1.7×10^{-14}	369.9		6.5	2.8×10^{41}	0.08	0.08
2CXO J225709.5-362824	344.2897	-36.4734	0.4	1.2×10^{-14}	29.2	S0/E	5.8	1.2×10^{39}	0.68	0.21
2CXO J225724.7-410343	344.3530	-41.0622	0.4	3.3×10^{-13}	12.7	S	4.8	6.3×10^{39}	0.24	0.11
2CXO J230153.2+155823	345.4720	15.9731	0.4	1.3×10^{-14}	27.7	S	0.9	1.1×10^{39}	0.82	0.01
2CXO J230245.9+084822	345.6913	8.8063	0.6	1.5×10^{-15}	176.2	S	9.7	5.5×10^{39}	0.45	0.14
2CXO J230247.2+084823	345.6970	8.8066	0.4	4.7×10^{-15}	176.2	S	8.1	1.7×10^{40}	0.51	0.15
2CXO J230451.1+121842	346.2130	12.3118	0.4	2.7×10^{-14}	30.2	S	13.1	3.0×10^{39}	0.68	0.21
2CXO J230451.5+121826	346.2148	12.3072	0.4	8.2×10^{-14}	30.2	S	13.5	8.9×10^{39}	0.45	0.20
2CXO J230452.2+121944	346.2177	12.3291	0.4	3.8×10^{-14}	30.2	S	9.9	4.1×10^{39}	0.68	0.17
2CXO J230457.6+122028	346.2403	12.3414	0.4	4.5×10^{-14}	30.2	S	9.8	4.9×10^{39}	0.78	0.10
2CXO J230458.4+121915	346.2435	12.3211	0.4	1.0×10^{-14}	30.2	S	3.9	1.1×10^{39}	0.61	0.03
2CXO J231206.9-283223	348.0291	-28.5399	0.4	1.5×10^{-14}	25.0	S0/E	1.0	1.1×10^{39}	0.17	0.00
2CXO J231434.3+042956	348.6429	4.4990	0.5	7.9×10^{-15}	35.5	S	0.6	1.2×10^{39}	0.58	0.01
2CXO J231438.8+043204	348.6619	4.5345	0.4	1.0×10^{-15}	32.5	S	11.6	1.3×10^{39}	0.91	0.11
2CXO J231439.1+043204	348.6632	4.5345	0.4	9.2×10^{-15}	32.5	S	10.9	1.2×10^{39}	0.60	0.10

Table A.19: List of ULX candidates obtained in Chapter 4 (continued).

Name	RA deg	Dec deg	$POSERR$ arcsec	F_X erg cm^{-2} s^{-1}	D Mpc	Gal. type	Sep. kpc	L_X erg s^{-1}	P_{XRB}	f_{cont}
2CXO J231546.1-590306	348.9425	-59.0519	0.4	2.2×10^{-15}	193.2	S0/E	12.3	9.8×10^{39}		
2CXO J231613.6-423502	349.0567	-42.5839	0.4	9.5×10^{-14}	18.4	S	2.8	3.9×10^{39}		
2CXO J231855.9-421400	349.7330	-42.2333	0.4	2.5×10^{-14}	18.4	S	2.1	1.0×10^{39}	0.31	0.01
2CXO J231924.2-421432	349.8512	-42.2424	0.5	4.0×10^{-14}	18.4	S	5.5	1.6×10^{39}	0.68	0.06
2CXO J231925.1-421432	349.8547	-42.2423	0.5	1.0×10^{-13}	18.4	S	6.1	4.1×10^{39}	0.83	0.05
2CXO J232009.1+425810	350.0383	42.9697	1.6	1.3×10^{-14}	81.3	S	3.4	9.9×10^{39}	0.55	0.07
2CXO J232014.3+081125	350.0599	8.1903	0.7	3.0×10^{-15}	53.5	S0/E	14.5	1.0×10^{39}	0.87	0.79
2CXO J232015.6+081203	350.0653	8.2011	0.5	3.5×10^{-15}	53.5	S0/E	6.4	1.2×10^{39}		
2CXO J232041.1+081228	350.1714	8.2079	1.0	4.3×10^{-15}	53.0	S0/E	9.8	1.5×10^{39}	0.73	0.17
2CXO J232041.3+081258	350.1723	8.2162	0.8	8.5×10^{-15}	53.0	S0/E	4.4	2.9×10^{39}	0.73	0.05
2CXO J232043.0+081312	350.1795	8.2202	1.8	9.5×10^{-15}	53.0	S0/E	3.5	3.2×10^{39}	0.51	0.02
2CXO J232104.3-691310	350.2679	-69.2195	0.5	3.7×10^{-15}	182.8		10.7	1.5×10^{40}	0.47	0.29
2CXO J232353.2+093959	350.9720	9.6666	0.5	1.4×10^{-14}	50.9	S	2.8	4.2×10^{39}	0.31	0.04
2CXO J232645.1+263619	351.6883	26.6055	0.6	2.3×10^{-15}	80.6		4.5	1.8×10^{39}	0.58	0.12
2CXO J232646.5+263620	351.6941	26.6056	0.5	3.9×10^{-15}	81.0	S	3.9	3.1×10^{39}	0.66	0.04
2CXO J232647.0+263602	351.6961	26.6007	0.5	4.7×10^{-15}	81.0	S	3.3	3.7×10^{39}	0.60	0.03
2CXO J232740.7+233516	351.9199	23.5880	0.4	6.4×10^{-15}	49.8	S	1.2	1.9×10^{39}		
2CXO J232741.3+233525	351.9224	23.5905	0.4	3.1×10^{-14}	49.8	S	1.6	9.4×10^{39}		
2CXO J232741.4+233515	351.9226	23.5877	0.4	4.4×10^{-14}	49.8	S	1.6	1.3×10^{40}		
2CXO J232741.8+233507	351.9244	23.5855	0.4	7.6×10^{-15}	49.8	S	3.9	2.3×10^{39}		
2CXO J232741.9+233513	351.9248	23.5870	0.4	3.3×10^{-14}	49.8	S	3.3	9.7×10^{39}		
2CXO J232742.0+233522	351.9252	23.5895	0.4	1.0×10^{-14}	49.8	S	3.2	3.0×10^{39}		
2CXO J232944.4+001732	352.4351	0.2924	1.5	6.0×10^{-15}	255.9	S	7.1	4.7×10^{40}	0.30	0.10
2CXO J233624.5+210847	354.1025	21.1466	0.4	8.3×10^{-15}	245.5	S	17.8	6.0×10^{40}		
2CXO J233639.5+210603	354.1648	21.1009	0.5	1.4×10^{-15}	263.0		5.0	1.2×10^{40}	0.70	0.07
2CXO J233726.0+002255	354.3587	0.3820	0.5	1.3×10^{-14}	34.7	S	7.7	1.9×10^{39}	0.70	0.17
2CXO J234137.3-033351	355.4058	-3.5644	0.9	3.9×10^{-15}	90.1	S0/E	1.8	3.8×10^{39}	0.33	0.02
2CXO J234200.7-033648	355.5032	-3.6134	0.6	5.7×10^{-15}	98.2	S	3.0	6.6×10^{39}	0.47	0.05
2CXO J234204.2-033453	355.5179	-3.5815	0.9	6.4×10^{-15}	94.8	S	1.9	6.9×10^{39}	0.31	0.01
2CXO J234420.0+095548	356.0837	9.9301	0.4	3.8×10^{-14}	20.7	S0/E	2.1	2.0×10^{39}	0.80	0.03
2CXO J234524.2-640320	356.3510	-64.0556	0.6	1.0×10^{-15}	177.0	S	4.0	3.9×10^{39}	0.22	0.06
2CXO J234658.0+292734	356.7420	29.4595	0.4	1.7×10^{-14}	70.6	S	2.1	1.0×10^{40}	0.36	0.02
2CXO J234702.0+292848	356.7585	29.4802	0.5	5.4×10^{-15}	74.3	S	13.3	3.6×10^{39}	0.44	0.18
2CXO J234703.2+292828	356.7636	29.4746	0.5	4.3×10^{-15}	74.3	S	13.1	2.8×10^{39}	0.51	0.42
2CXO J234705.7+292916	356.7738	29.4880	0.6	4.2×10^{-15}	74.3	S	7.1	2.8×10^{39}	0.35	0.11
2CXO J234737.3-021851	356.9057	-2.3143	0.5	4.5×10^{-15}	95.8	S	5.0	5.0×10^{39}	0.19	0.03
2CXO J235122.4+200639	357.8437	20.1109	0.4	1.3×10^{-14}	61.7	S	9.8	5.9×10^{39}	0.66	0.16
2CXO J235123.0+200558	357.8462	20.0996	0.4	1.6×10^{-14}	61.8	S0/E	3.5	7.3×10^{39}	0.81	0.11
2CXO J235123.6+200637	357.8486	20.1105	0.4	7.1×10^{-15}	61.7	S	5.2	3.2×10^{39}		
2CXO J235127.0+200653	357.8627	20.1149	0.6	2.8×10^{-15}	61.7	S	9.4	1.3×10^{39}	0.63	0.12
2CXO J235127.5+200651	357.8647	20.1144	0.4	1.5×10^{-14}	61.7	S	11.1	6.9×10^{39}	0.77	0.18
2CXO J235655.3-345018	359.2306	-34.8384	0.8	7.8×10^{-16}	206.1		9.1	3.9×10^{39}	0.49	0.28
4XMM J001237.0+053018	3.1545	5.5052	1.4	5.1×10^{-15}	124.2	S	9.8	9.5×10^{39}	0.41	0.32
4XMM J002238.3-483445	5.6599	-48.5792	1.9	1.6×10^{-14}	43.6	S	1.6	3.6×10^{39}	0.18	0.02
4XMM J002646.1-713206	6.6923	-71.5350	1.7	1.6×10^{-14}	34.9		2.8	2.3×10^{39}	0.36	0.05
4XMM J003746.6-333951	9.4445	-33.6643	1.1	4.0×10^{-15}	127.9		3.0	7.8×10^{39}	0.41	0.03
4XMM J003844.5+415952	9.6857	41.9978	1.7	1.4×10^{-14}	80.1	S	5.0	1.1×10^{40}	0.40	0.25
4XMM J004118.0-433827	10.3251	-43.6408	1.5	5.2×10^{-15}	52.0	S	7.3	1.7×10^{39}	0.78	0.25
4XMM J004142.8-092626	10.4285	-9.4406	0.4	6.4×10^{-14}	248.9	S0/E	5.6	4.7×10^{41}	0.21	0.16
4XMM J004820.0-251010	12.0837	-25.1695	0.7	6.6×10^{-13}	3.9	S	14.6	1.2×10^{39}	0.79	0.03
4XMM J005328.6-084607	13.3693	-8.7687	0.9	2.5×10^{-14}	79.8	S	7.4	1.9×10^{40}	0.83	0.30
4XMM J005504.8-374143	13.7703	-37.6955	0.3	3.9×10^{-12}	1.9	S	1.3	1.6×10^{39}	0.18	0.00
4XMM J005746.2-272952	14.4425	-27.4978	1.2	2.2×10^{-14}	78.4	S	6.1	1.6×10^{40}	0.54	0.15
4XMM J005929.6-361109	14.8736	-36.1861	0.8	2.2×10^{-14}	48.1	S	0.9	6.1×10^{39}	0.54	0.00
4XMM J010904.2-454628	17.2677	-45.7745	1.0	4.4×10^{-14}	110.7	S0/E	2.5	6.4×10^{40}	0.08	0.03
4XMM J011001.2-455801	17.5054	-45.9670	1.0	2.1×10^{-14}	116.8		3.7	3.5×10^{40}	0.56	0.06
4XMM J011036.2-461324	17.6509	-46.2235	0.9	3.9×10^{-15}	130.0	S0/E	3.2	8.0×10^{39}	0.48	0.05
4XMM J011810.3+112302	19.5429	11.3841	1.8	7.8×10^{-15}	73.5	S	7.9	5.1×10^{39}	0.61	0.38
4XMM J011907.1-340705	19.7799	-34.1181	1.3	1.4×10^{-15}	77.3	S0/E	18.9	1.0×10^{39}	0.83	0.71
4XMM J011948.6+032322	19.9525	3.3897	0.3	1.0×10^{-13}	36.1	S	15.9	1.6×10^{40}	0.58	0.33
4XMM J012002.6+032501	20.0110	3.4171	0.8	1.7×10^{-14}	29.9	S0/E	8.7	1.8×10^{39}	0.83	0.30
4XMM J012007.0+032533	20.0296	3.4261	1.0	3.2×10^{-14}	29.9	S0/E	5.6	3.4×10^{39}	0.51	0.12
4XMM J012115.1+035154	20.3131	3.8651	1.4	8.6×10^{-15}	74.4	S	4.7	5.7×10^{39}	0.59	0.13
4XMM J012217.8+010027	20.5743	1.0076	0.3	2.9×10^{-14}	246.6	S	5.3	2.1×10^{41}	0.13	0.11
4XMM J012306.1-350416	20.7755	-35.0711	1.3	2.9×10^{-15}	75.2	S	2.1	2.0×10^{39}	0.25	0.02
4XMM J012307.8+331131	20.7828	33.1922	1.1	8.4×10^{-15}	63.6		5.7	4.1×10^{39}	0.77	0.33
4XMM J012357.9+335438	20.9916	33.9108	1.9	3.5×10^{-14}	71.9	S	8.4	2.2×10^{40}	0.21	0.13
4XMM J012446.8+093039	21.1952	9.5109	1.1	1.5×10^{-14}	24.0	S0/E	11.6	1.0×10^{39}	0.79	0.31
4XMM J012450.7+093116	21.2114	9.5212	1.6	1.6×10^{-14}	24.0	S0/E	8.9	1.1×10^{39}	0.79	0.18
4XMM J012624.6+344220	21.6028	34.7058	1.4	1.7×10^{-14}	74.1	S	12.9	1.1×10^{40}	0.43	0.33
4XMM J012644.0-011832	21.6837	-1.3089	1.2	7.4×10^{-15}	74.8	S	4.6	4.9×10^{39}	0.64	0.09
4XMM J012714.3+021027	21.8097	2.1743	1.3	1.2×10^{-14}	194.1	S	7.0	5.5×10^{40}	0.25	0.10
4XMM J013411.8-292404	23.5496	-29.4013	0.7	1.7×10^{-14}	26.4	S	13.1	1.4×10^{39}	0.91	0.25
4XMM J013413.8-292413	23.5578	-29.4038	1.2	2.4×10^{-14}	26.4	S	9.8	2.0×10^{39}	0.63	0.14
4XMM J013423.9-292740	23.5997	-29.4612	0.6	1.5×10^{-14}	26.4	S	21.6	1.3×10^{39}	0.82	0.77
4XMM J013459.1-412521	23.7464	-41.4227	1.2	2.6×10^{-14}	35.1	S	13.1	3.9×10^{39}	0.65	0.49
4XMM J013508.5+310219	23.7856	31.0387	0.7	1.3×10^{-14}	154.9	S	2.6	3.9×10^{40}	0.37	0.05
4XMM J014644.3-093121	26.6848	-9.5226	1.7	9.1×10^{-15}	229.1	S	9.6	5.7×10^{40}	0.38	0.18
4XMM J014730.9+352340	26.8788	35.3947	1.7	1.2×10^{-14}	83.5	S	3.1	1.0×10^{40}	0.26	0.07
4XMM J015132.5-084714	27.8856	-8.7874	1.5	6.5×10^{-15}	156.3	S	9.2	1.9×10^{40}	0.57	0.35
4XMM J015154.1-084015	27.9756	-8.6710	2.1	7.9×10^{-15}	182.8		6.6	3.2×10^{40}	0.28	0.20

Table A.20: List of ULX candidates obtained in Chapter 4 (continued).

Name	RA deg	Dec deg	$POSERR$ arcsec	F_X erg cm^{-2} s^{-1}	D Mpc	Gal. type	Sep. kpc	L_X erg s^{-1}	P_{XRB}	f_{cont}
4XMM J015301.8-134249	28.2579	-13.7138	1.3	1.2×10^{-14}	27.7	S0/E	12.2	1.1×10^{39}	0.84	0.50
4XMM J015306.5-134538	28.2772	-13.7607	0.6	2.0×10^{-14}	27.7	S0/E	15.7	1.8×10^{39}	0.91	0.34
4XMM J015325.3-012330	28.3558	-1.3918	0.6	2.1×10^{-14}	357.2	S	6.8	3.2×10^{41}	0.29	0.15
4XMM J015638.3+321336	29.1596	32.2268	1.3	5.5×10^{-14}	303.3	S	16.7	6.0×10^{41}	0.07	0.74
4XMM J015652.4+054625	29.2187	5.7737	1.5	7.1×10^{-15}	78.6	S0/E	2.6	5.2×10^{39}	0.19	0.06
4XMM J015728.3-614120	29.3683	-61.6891	1.1	1.2×10^{-13}	87.5		2.4	1.1×10^{41}	0.35	0.09
4XMM J020019.5+311852	30.0815	31.3146	1.3	2.0×10^{-14}	77.1	S	2.2	1.4×10^{40}	0.26	0.05
4XMM J020213.0-060425	30.5544	-6.0738	0.9	8.8×10^{-14}	67.8	S	6.0	4.9×10^{40}	0.39	0.06
4XMM J020420.7-045504	31.0865	-4.9179	1.2	4.2×10^{-14}	53.9	S	2.3	1.5×10^{40}	0.19	0.02
4XMM J020434.3-061209	31.1431	-6.2026	0.4	5.2×10^{-14}	17.3	S	3.8	1.9×10^{39}	0.53	0.04
4XMM J021716.7-052839	34.3196	-5.4775	1.4	6.7×10^{-15}	73.1	S	14.1	4.3×10^{39}	0.48	0.47
4XMM J021718.0-052828	34.3253	-5.4745	1.5	3.8×10^{-15}	73.1	S	10.1	2.5×10^{39}	0.71	0.14
4XMM J022052.7-541603	35.2197	-54.2676	1.6	1.5×10^{-14}	77.5		2.8	1.0×10^{40}	0.76	0.05
4XMM J022643.7+202944	36.6822	20.4956	0.7	1.6×10^{-14}	65.8	S0/E	13.7	8.2×10^{39}	0.81	0.64
4XMM J022646.2+203013	36.6927	20.5037	0.5	5.0×10^{-14}	65.8	S0/E	7.5	2.6×10^{40}	0.79	0.36
4XMM J022948.3+312707	37.4516	31.4521	1.3	4.1×10^{-14}	73.9	S	2.9	2.7×10^{40}	0.41	0.05
4XMM J023036.2-004918	37.6511	-0.8219	1.7	2.3×10^{-14}	166.7	S	6.7	7.6×10^{40}	0.34	0.26
4XMM J023101.2-442543	37.7553	-44.4288	3.0	4.2×10^{-14}	69.7	S	4.9	2.5×10^{40}	0.36	0.09
4XMM J023444.0+325042	38.6834	32.8452	1.2	9.6×10^{-15}	67.2	S0/E	11.8	5.2×10^{39}	0.54	0.30
4XMM J024102.9+084456	40.2624	8.7491	1.9	6.5×10^{-15}	89.9	S0/E	3.4	6.3×10^{39}	0.73	0.06
4XMM J024914.1-310306	42.3090	-31.0517	1.5	2.4×10^{-14}	91.0	S	4.3	2.4×10^{40}	0.38	0.12
4XMM J025645.2+413508	44.1886	41.5856	0.5	6.8×10^{-14}	280.5		4.1	6.4×10^{41}	0.18	0.03
4XMM J025820.7+060534	44.5865	6.0930	1.2	4.4×10^{-14}	94.5	S0/E	3.9	4.7×10^{40}	0.37	0.08
4XMM J030324.5-153748	45.8524	-15.6301	1.8	1.6×10^{-14}	33.6	S	3.9	2.2×10^{39}	0.29	0.04
4XMM J030617.0-094914	46.5712	-9.8207	1.1	1.0×10^{-14}	68.3		2.2	5.8×10^{39}	0.50	0.06
4XMM J030628.0-153352	46.6171	-15.5646	0.4	5.1×10^{-14}	24.3	S	2.8	3.6×10^{39}	0.56	0.06
4XMM J031554.4-022545	48.9769	-2.4293	1.6	2.2×10^{-15}	259.4		11.6	1.8×10^{40}	0.49	0.15
4XMM J031747.4-663009	49.4478	-66.5027	0.7	6.6×10^{-13}	4.1	S	3.4	1.3×10^{39}	0.90	0.01
4XMM J032004.9-664213	50.0206	-66.7038	0.5	3.8×10^{-14}	73.2	S	3.6	2.4×10^{40}	0.60	0.03
4XMM J032100.9+412600	50.2538	41.4335	1.3	3.7×10^{-14}	60.0		1.9	1.6×10^{40}	0.38	0.03
4XMM J032235.2-412623	50.6470	-41.4398	0.7	2.0×10^{-14}	284.4		9.4	1.9×10^{41}	0.48	0.20
4XMM J032237.7-371323	50.6572	-37.2231	0.4	1.6×10^{-13}	21.5	S0/E	7.5	8.7×10^{39}	0.54	0.02
4XMM J032242.1-371121	50.6755	-37.1894	0.5	2.6×10^{-14}	21.5	S0/E	7.0	1.4×10^{39}	0.75	0.03
4XMM J032308.7-370730	50.7863	-37.1251	0.5	2.1×10^{-14}	21.5	S0/E	45.3	1.1×10^{39}	0.83	0.68
4XMM J032330.9-574030	50.8791	-57.6750	1.0	6.1×10^{-14}	141.8	S	5.6	1.5×10^{41}	0.55	0.12
4XMM J032821.7-310319	52.0907	-31.0553	1.3	2.4×10^{-14}	19.8	S0/E	5.1	1.1×10^{39}	0.77	0.08
4XMM J032916.6-273919	52.3193	-27.6554	0.8	1.5×10^{-14}	60.0	S	1.2	6.6×10^{39}	0.15	0.02
4XMM J032941.2-523115	52.4217	-52.5211	0.6	1.5×10^{-14}	276.7	S0/E	4.7	1.4×10^{41}	0.40	0.04
4XMM J033323.1-360753	53.3463	-36.1315	0.2	2.8×10^{-14}	17.9	S	14.2	1.1×10^{39}	0.93	0.42
4XMM J033332.1-360642	53.3840	-36.1118	0.5	3.8×10^{-14}	17.9	S	10.0	1.5×10^{39}	0.70	0.14
4XMM J033338.2-050549	53.4093	-5.0972	0.6	1.9×10^{-14}	55.4	S0/E	9.2	7.0×10^{39}	0.75	0.54
4XMM J033340.6-360511	53.4193	-36.0865	0.3	2.6×10^{-14}	17.9	S	17.4	1.0×10^{39}	0.93	0.17
4XMM J033623.2-345835	54.0968	-34.9765	0.5	3.3×10^{-14}	17.6	S0/E	4.6	1.2×10^{39}	0.89	0.11
4XMM J033647.9-344450	54.1998	-34.7474	1.7	6.0×10^{-14}	15.8	S0/E	2.2	1.8×10^{39}	0.28	0.01
4XMM J033929.6-184204	54.8735	-18.7013	0.9	1.8×10^{-14}	26.4	S0/E	6.4	1.5×10^{39}	0.75	0.14
4XMM J033933.8-184040	54.8909	-18.6778	1.3	1.3×10^{-14}	26.4	S0/E	7.1	1.1×10^{39}	0.66	0.16
4XMM J034013.2-183328	55.0553	-18.5579	1.4	1.6×10^{-14}	28.8	S0/E	11.5	1.6×10^{39}	0.78	0.16
4XMM J034406.1-535359	56.0256	-53.8998	1.2	2.1×10^{-14}	158.5		5.9	6.4×10^{40}	0.16	0.10
4XMM J035318.7-102652	58.3280	-10.4480	1.0	1.6×10^{-14}	32.8	S	1.3	2.0×10^{39}	0.62	0.00
4XMM J035936.9-673736	59.9038	-67.6268	0.5	2.9×10^{-13}	15.5	S	2.5	8.3×10^{39}	0.87	0.02
4XMM J035941.9-673820	59.9247	-67.6390	0.5	9.9×10^{-14}	15.5	S	1.9	2.8×10^{39}	0.91	0.00
4XMM J040017.0-674815	60.0711	-67.8044	1.0	3.3×10^{-14}	16.2	S	0.9	1.0×10^{39}	0.90	0.01
4XMM J040708.9-545101	61.7871	-54.8504	1.5	6.2×10^{-15}	193.4		5.2	2.8×10^{40}	0.24	0.12
4XMM J041616.1-554618	64.0672	-55.7718	1.5	2.5×10^{-14}	18.5	S0/E	5.0	1.0×10^{39}	0.82	0.10
4XMM J041728.1-624817	64.3671	-62.8049	0.6	1.7×10^{-13}	12.6	S	5.6	3.2×10^{39}	0.92	0.03
4XMM J041730.7-624722	64.3781	-62.7896	0.6	3.0×10^{-13}	12.6	S	2.5	5.7×10^{39}	0.77	0.00
4XMM J041731.6-624647	64.3818	-62.7798	0.7	8.2×10^{-14}	12.6	S	1.9	1.6×10^{39}	0.89	0.01
4XMM J041826.0+285837	64.6084	28.9771	0.9	5.0×10^{-14}	22.8		0.7	3.1×10^{39}	0.44	0.00
4XMM J043256.2-130101	68.2345	-13.0171	1.0	1.4×10^{-14}	123.0		2.6	2.5×10^{40}	0.26	0.03
4XMM J043320.5-132634	68.3357	-13.4429	1.0	1.6×10^{-14}	143.2	S	8.6	4.0×10^{40}	0.61	0.28
4XMM J044534.2-591256	71.3929	-59.2156	0.4	1.0×10^{-13}	16.1	S	10.2	3.2×10^{39}	0.86	0.27
4XMM J045833.0-750442	74.6376	-75.0785	1.6	8.8×10^{-15}	83.6	S	2.7	7.3×10^{39}	0.55	0.07
4XMM J053607.1-475529	84.0298	-47.9249	0.8	1.1×10^{-14}	153.5		7.9	3.0×10^{40}	0.67	0.26
4XMM J054205.2+692353	85.5219	69.3981	1.4	4.1×10^{-15}	56.4	S	18.9	1.5×10^{39}	0.78	0.59
4XMM J054541.2-255507	86.4218	-25.9188	1.3	1.5×10^{-14}	173.8	S0/E	5.6	5.4×10^{40}	0.12	0.10
4XMM J055239.0-363936	88.1628	-36.6601	1.0	3.9×10^{-14}	199.5		5.3	1.8×10^{41}	0.21	0.15
4XMM J060048.2-394851	90.2011	-39.8143	1.1	2.4×10^{-14}	185.4		5.8	9.8×10^{40}	0.24	0.06
4XMM J061406.9-332949	93.5290	-33.4972	1.8	6.0×10^{-15}	166.0	S	15.3	2.0×10^{40}	0.22	0.09
4XMM J061617.9-212204	94.0750	-21.3678	0.6	4.4×10^{-14}	32.4	S	9.3	5.6×10^{39}	0.45	0.05
4XMM J061630.0-212243	94.1251	-21.3787	0.9	1.1×10^{-14}	32.4	S	4.7	1.4×10^{39}	0.32	0.06
4XMM J062447.9-372122	96.1996	-37.3561	0.6	6.4×10^{-14}	138.7		6.6	1.5×10^{41}	0.30	0.28
4XMM J062502.0-372244	96.2584	-37.3790	1.3	8.9×10^{-15}	36.4		1.4	1.4×10^{39}	0.46	0.04
4XMM J070949.7-273435	107.4571	-27.5766	1.1	4.8×10^{-14}	33.6	S	1.4	6.4×10^{39}	0.24	0.00
4XMM J071638.2-622013	109.1595	-62.3370	0.6	1.3×10^{-13}	37.0	S	4.4	2.1×10^{40}	0.49	0.07
4XMM J072902.1+335135	112.2591	33.8599	0.6	8.2×10^{-15}	52.7	S	7.7	2.7×10^{39}	0.63	0.10
4XMM J072903.8+335204	112.2661	33.8679	0.9	8.1×10^{-15}	52.7	S	6.7	2.7×10^{39}	0.71	0.21
4XMM J072906.0+335129	112.2750	33.8582	0.7	3.7×10^{-14}	52.7	S	4.9	1.2×10^{40}	0.57	0.07
4XMM J073314.8+854254	113.3120	85.7151	1.3	9.2×10^{-15}	32.4	S0/E	10.1	1.2×10^{39}	0.87	0.31
4XMM J073815.6-692927	114.5651	-69.4911	1.4	5.5×10^{-14}	18.3	S0/E	5.3	2.2×10^{39}	0.48	0.07
4XMM J075336.5+250209	118.4025	25.0359	2.1	1.3×10^{-14}	187.9	S0/E	6.6	5.5×10^{40}	0.28	0.17
4XMM J075508.9-762438	118.7874	-76.4106	1.7	1.7×10^{-14}	24.2	S	2.1	1.2×10^{39}	0.83	0.12

Table A.21: List of ULX candidates obtained in Chapter 4 (continued).

Name	RA deg	Dec deg	$POSERR$ arcsec	F_X erg cm^{-2} s^{-1}	D Mpc	Gal. type	Sep. kpc	L_X erg s^{-1}	P_{XRB}	f_{cont}
4XMM J080859.9+395130	122.2500	39.8584	1.6	1.2×10^{-14}	88.3	S	5.6	1.1×10^{40}	0.67	0.08
4XMM J081150.1-181759	122.9588	-18.2998	1.6	1.4×10^{-14}	61.5	S	9.8	6.2×10^{39}	0.75	0.13
4XMM J081301.8-310842	123.2575	-31.1450	1.4	2.1×10^{-14}	92.4	S	4.4	2.2×10^{40}	0.43	0.16
4XMM J082253.2+033402	125.7219	3.5673	1.2	2.2×10^{-14}	53.3	S	3.7	7.7×10^{39}	0.43	0.13
4XMM J082311.1+224002	125.7964	22.6673	1.0	1.1×10^{-14}	37.7	S	1.8	1.9×10^{39}	0.56	0.01
4XMM J082311.3+224035	125.7974	22.6766	0.8	3.3×10^{-14}	37.7	S	7.8	5.5×10^{39}	0.60	0.16
4XMM J084142.1+185157	130.4257	18.8661	1.4	5.0×10^{-14}	62.9	S	7.4	2.4×10^{40}	0.35	0.10
4XMM J084221.6+705759	130.5902	70.9665	0.7	3.7×10^{-14}	62.4	S	7.3	1.7×10^{40}	0.90	0.45
4XMM J084716.1-200106	131.8173	-20.0183	1.2	2.9×10^{-15}	60.8	S	18.2	1.3×10^{39}	0.73	0.26
4XMM J084717.1-200236	131.8215	-20.0435	1.2	3.3×10^{-15}	60.8	S	8.2	1.5×10^{39}	0.78	0.08
4XMM J084730.7-195704	131.8783	-19.9512	1.1	3.8×10^{-15}	105.9	S	4.3	5.1×10^{39}	0.74	0.03
4XMM J084810.2+740535	132.0427	74.0932	1.0	1.8×10^{-14}	28.8	S	4.2	1.8×10^{39}	0.90	0.05
4XMM J084839.3+735626	132.1640	73.9407	1.3	3.4×10^{-14}	28.3	S	0.9	3.3×10^{39}	0.63	0.00
4XMM J085540.3+584305	133.9182	58.7181	1.0	7.9×10^{-14}	16.1	S0/E	5.7	2.5×10^{39}	0.85	0.28
4XMM J085735.4+394821	134.3979	39.8059	1.4	9.7×10^{-15}	230.1		6.2	6.1×10^{40}	0.32	0.10
4XMM J085833.5+135544	134.6399	13.9290	1.3	6.5×10^{-15}	70.8		2.6	3.9×10^{39}	0.54	0.04
4XMM J085859.0+542125	134.7459	54.3571	1.4	2.5×10^{-14}	381.9	S0/E	9.1	4.3×10^{41}	0.16	0.13
4XMM J090101.4+354533	135.2560	35.7592	0.7	1.8×10^{-14}	44.4	S	2.3	4.2×10^{39}	0.52	0.04
4XMM J091031.8+542342	137.6326	54.3951	0.8	1.9×10^{-14}	57.1	S0/E	1.9	7.5×10^{39}	0.82	0.04
4XMM J091443.3+405254	138.6807	40.8818	2.0	2.1×10^{-14}	25.2	S	1.0	1.6×10^{39}	0.27	0.01
4XMM J091700.6+292058	139.2525	29.3495	1.6	6.9×10^{-15}	160.7	S	5.5	2.1×10^{40}	0.39	0.13
4XMM J091948.8-121429	139.9537	-12.2414	2.1	7.9×10^{-13}	25.4		2.2	6.1×10^{40}	0.21	0.01
4XMM J092020.7-073813	140.0863	-7.6372	2.4	2.2×10^{-14}	145.9	S	6.6	5.5×10^{40}	0.12	0.11
4XMM J092056.5+285241	140.2358	28.8781	1.8	6.5×10^{-15}	93.2	S	5.6	6.7×10^{39}	0.71	0.06
4XMM J092138.0+750717	140.4084	75.1217	2.2	7.2×10^{-15}	44.1	S	2.9	1.7×10^{39}	0.28	0.05
4XMM J093518.1+353844	143.8256	35.6456	1.8	4.0×10^{-15}	184.5	S	6.1	1.6×10^{40}	0.26	0.14
4XMM J094330.4+332302	145.8770	33.3839	0.5	8.0×10^{-14}	168.3	S0/E	6.1	2.7×10^{41}	0.18	0.16
4XMM J094434.6+040009	146.1443	4.0027	0.9	1.7×10^{-14}	81.7		1.8	1.3×10^{40}	0.63	0.01
4XMM J094521.9+094558	146.3413	9.7661	0.8	1.9×10^{-14}	43.9	S	2.7	4.5×10^{39}	0.77	0.05
4XMM J094522.5+094638	146.3440	9.7774	0.4	1.6×10^{-14}	43.9	S	7.6	3.6×10^{39}	0.76	0.09
4XMM J094523.7+094604	146.3490	9.7680	1.5	1.1×10^{-14}	43.9	S	3.2	2.5×10^{39}	0.69	0.06
4XMM J094834.7-130253	147.1449	-13.0483	1.1	2.4×10^{-14}	147.0	S	3.7	6.3×10^{40}	0.46	0.04
4XMM J094845.7+001620	147.1904	0.2724	1.8	7.6×10^{-15}	83.6	S	3.3	6.3×10^{39}	0.58	0.13
4XMM J094957.7-250018	147.4906	-25.0052	0.8	1.2×10^{-13}	33.2	S	3.8	1.5×10^{40}	0.62	0.08
4XMM J095007.6-735524	147.5321	-73.9235	1.0	6.1×10^{-14}	15.0	S	0.4	1.6×10^{39}	0.32	0.00
4XMM J095336.7+013516	148.4031	1.5879	0.4	2.1×10^{-14}	21.7	S	7.1	1.2×10^{39}	0.86	0.01
4XMM J095342.1+013434	148.4257	1.5761	0.2	2.1×10^{-13}	21.7	S	2.4	1.2×10^{40}	0.78	0.00
4XMM J095343.8+013416	148.4328	1.5713	0.2	1.2×10^{-13}	21.7	S	5.6	6.7×10^{39}	0.82	0.02
4XMM J095349.6+013347	148.4571	1.5633	0.4	2.5×10^{-14}	21.7	S	15.0	1.4×10^{39}	0.85	0.06
4XMM J095524.2+690957	148.8511	69.1659	0.2	6.0×10^{-13}	3.8	S	6.7	1.0×10^{39}	0.93	0.01
4XMM J095620.4+271335	149.0850	27.2265	0.5	6.8×10^{-14}	20.8	S	0.5	3.5×10^{39}	0.51	0.00
4XMM J100115.0+554310	150.3127	55.7195	0.2	1.0×10^{-13}	22.7	S	1.1	6.4×10^{39}	0.91	0.01
4XMM J100726.9+121623	151.8625	12.2731	1.7	7.7×10^{-14}	38.0	S	2.1	1.3×10^{40}	0.38	0.06
4XMM J101040.4+534719	152.6684	53.7887	0.8	5.3×10^{-14}	642.7	S0/E	16.1	2.6×10^{42}	0.05	0.25
4XMM J101737.3+214144	154.4057	21.6957	0.8	2.9×10^{-14}	22.6	S	3.4	1.8×10^{39}	0.81	0.05
4XMM J101822.9+412741	154.5957	41.4615	0.5	7.3×10^{-14}	13.2	S	9.6	1.5×10^{39}	0.91	0.12
4XMM J101904.7+462716	154.7698	46.4545	0.4	3.6×10^{-14}	136.1	S	2.9	8.0×10^{40}	0.33	0.03
4XMM J102220.1+213420	155.5842	21.5724	0.9	2.7×10^{-14}	55.8	S	2.0	1.0×10^{40}	0.61	0.02
4XMM J102234.3+435057	155.6432	43.8494	3.2	9.3×10^{-15}	75.7	S	4.4	6.4×10^{39}	0.37	0.22
4XMM J102335.8+195150	155.8994	19.8641	0.6	2.4×10^{-14}	20.8		7.4	1.2×10^{39}	0.77	0.61
4XMM J102421.9+002751	156.0915	0.4643	1.1	1.2×10^{-14}	440.6	S	11.7	2.9×10^{41}	0.62	0.28
4XMM J102858.4-353549	157.2435	-35.5970	1.4	1.2×10^{-14}	32.1	S0/E	10.2	1.4×10^{39}	0.88	0.33
4XMM J102909.5-353555	157.2897	-35.5988	0.6	7.3×10^{-14}	37.0	S0/E	7.1	1.2×10^{40}	0.71	0.24
4XMM J102924.6+293037	157.3526	29.5105	0.8	4.6×10^{-14}	19.4	S	8.6	2.1×10^{39}	0.87	0.15
4XMM J102951.5-350944	157.4649	-35.1625	0.5	1.8×10^{-14}	34.0	S0/E	1.1	2.5×10^{39}	0.91	0.02
4XMM J103031.1-352159	157.6297	-35.3667	0.4	2.0×10^{-14}	36.4	S0/E	11.8	3.1×10^{39}	0.89	0.66
4XMM J103549.0-034438	158.9543	-3.7441	1.2	6.7×10^{-15}	283.1	S0/E	8.5	6.4×10^{40}	0.20	0.13
4XMM J103704.3-272358	159.2682	-27.3996	1.2	1.5×10^{-14}	49.9	S0/E	1.4	4.4×10^{39}	0.46	0.01
4XMM J103805.5+014441	159.5230	1.7449	1.2	2.5×10^{-14}	152.1	S	3.9	7.0×10^{40}	0.26	0.10
4XMM J103911.1-002448	159.7965	-0.4136	2.2	1.7×10^{-14}	76.1	S	6.2	1.2×10^{40}	0.64	0.17
4XMM J103923.9-002318	159.8498	-0.3886	0.9	5.7×10^{-14}	76.1	S	2.5	3.9×10^{40}	0.29	0.02
4XMM J104626.6+631326	161.6111	63.2239	1.7	2.2×10^{-14}	22.6	S	7.5	1.3×10^{39}	0.89	0.51
4XMM J104634.9+631231	161.6455	63.2087	0.7	7.3×10^{-13}	22.6	S	6.0	4.4×10^{40}	0.59	0.07
4XMM J105334.7-054621	163.3946	-5.7725	1.4	1.2×10^{-14}	140.0	S0/E	6.1	2.7×10^{40}	0.19	0.16
4XMM J105529.8+575407	163.8744	57.9022	1.9	1.7×10^{-14}	99.9	S	8.2	2.1×10^{40}	0.62	0.30
4XMM J105627.4+070512	164.1144	7.0869	0.9	1.2×10^{-14}	748.2	S0/E	13.8	8.0×10^{41}	0.09	0.24
4XMM J105756.4+564508	164.4852	56.7525	1.1	2.1×10^{-14}	710.0	S0/E	13.2	1.3×10^{42}	0.19	0.17
4XMM J110250.1-233542	165.7090	-23.5951	2.9	2.9×10^{-14}	47.3	S	2.9	7.8×10^{39}	0.47	0.07
4XMM J110426.4+405028	166.1100	40.8412	1.8	2.3×10^{-14}	143.9		4.6	5.6×10^{40}	0.22	0.11
4XMM J110615.2-181515	166.5634	-18.2543	1.1	2.3×10^{-14}	51.7	S	5.0	7.2×10^{39}	0.61	0.11
4XMM J110817.5-050801	167.0733	-5.1339	1.0	2.7×10^{-14}	166.6	S0/E	4.6	9.0×10^{40}	0.26	0.09
4XMM J111133.1+062630	167.8880	6.4419	2.6	1.2×10^{-14}	182.8	S0/E	7.8	4.7×10^{40}	0.23	0.15
4XMM J111815.3-324817	169.5639	-32.8048	0.4	3.5×10^{-13}	6.6		1.2	1.9×10^{39}	0.74	0.00
4XMM J111816.0-324910	169.5668	-32.8197	0.5	4.3×10^{-13}	6.6		0.7	2.2×10^{39}	0.48	0.00
4XMM J111828.9+575944	169.6207	57.9957	0.5	5.3×10^{-14}	29.1	S0/E	8.2	5.4×10^{39}	0.94	0.38
4XMM J111845.4+212826	169.6896	21.4740	0.8	1.5×10^{-14}	90.2		2.0	1.5×10^{40}	0.52	0.01
4XMM J112012.6+671442	170.0526	67.2450	1.6	3.3×10^{-14}	19.7	S	1.1	1.5×10^{39}	0.65	0.00
4XMM J112037.3+133429	170.1558	13.5748	0.3	1.0×10^{-13}	9.9	S	14.4	1.2×10^{39}	0.93	0.10
4XMM J112443.8+384449	171.1828	38.7472	1.2	9.6×10^{-15}	32.4	S	8.7	1.2×10^{39}	0.73	0.14
4XMM J112809.5+165533	172.0397	16.9259	1.3	1.3×10^{-14}	25.2	S	2.4	1.0×10^{39}	0.88	0.03
4XMM J112851.7+171604	172.2154	17.2678	0.5	5.3×10^{-14}	49.9		1.3	1.6×10^{40}	0.65	0.01

Table A.22: List of ULX candidates obtained in Chapter 4 (continued).

Name	RA deg	Dec deg	$POSERR$ arcsec	F_X erg cm^{-2} s^{-1}	D Mpc	Gal. type	Sep. kpc	L_X erg s^{-1}	P_{XRB}	f_{cont}
4XMM J112903.7+171405	172.2654	17.2349	1.2	3.4×10^{-14}	53.1	S	5.5	1.1×10^{40}	0.55	0.06
4XMM J112927.0+240546	172.3629	24.0964	1.7	1.5×10^{-13}	41.1	S	5.3	3.1×10^{40}	0.59	0.10
4XMM J112929.2+240527	172.3717	24.0909	2.7	7.6×10^{-15}	41.1	S	2.0	1.5×10^{39}	0.24	0.01
4XMM J113014.4+234811	172.5604	23.8033	0.9	1.9×10^{-14}	112.2	S	2.1	2.9×10^{40}	0.31	0.02
4XMM J113136.4-301639	172.9018	-30.2778	3.4	7.2×10^{-14}	16.9	S	9.9	2.5×10^{39}	0.43	0.08
4XMM J113151.3-302446	172.9638	-30.4128	0.9	3.6×10^{-14}	21.9	S0/E	0.8	2.1×10^{39}	0.63	0.00
4XMM J113328.6+550657	173.3695	55.1160	1.7	1.8×10^{-14}	169.8		8.8	6.1×10^{40}	0.37	0.32
4XMM J113609.2+155048	174.0386	15.8469	0.7	1.1×10^{-14}	510.5	S	9.1	3.5×10^{41}	0.18	0.13
4XMM J113751.3+215823	174.4640	21.9731	1.2	1.7×10^{-14}	134.3	S0/E	3.3	3.8×10^{40}	0.17	0.07
4XMM J113752.3+214818	174.4682	21.8050	1.4	1.5×10^{-14}	128.2	S0/E	12.4	2.9×10^{40}	0.67	0.32
4XMM J113752.7+214741	174.4698	21.7949	1.8	1.0×10^{-14}	128.2	S0/E	9.2	2.0×10^{40}	0.25	0.18
4XMM J113944.2+315632	174.9344	31.9425	2.1	2.6×10^{-14}	42.3	S	8.1	5.5×10^{39}	0.31	0.16
4XMM J114052.9+030830	175.2206	3.1417	1.6	1.0×10^{-14}	116.4		3.9	1.7×10^{40}	0.62	0.11
4XMM J114153.4+101807	175.4728	10.3020	1.7	2.9×10^{-14}	83.6	S	4.5	2.4×10^{40}	0.36	0.12
4XMM J114313.4+200016	175.8061	20.0045	0.9	3.7×10^{-14}	98.8	S	2.5	4.3×10^{40}	0.32	0.02
4XMM J114336.5+193625	175.9023	19.6071	2.7	2.7×10^{-14}	93.5	S0/E	4.7	2.8×10^{40}	0.49	0.16
4XMM J114402.1+195717	176.0091	19.9548	1.6	1.2×10^{-14}	88.8	S0/E	7.4	1.1×10^{40}	0.62	0.08
4XMM J114430.2+200441	176.1262	20.0781	1.6	1.5×10^{-14}	90.0	S0/E	2.8	1.4×10^{40}	0.13	0.03
4XMM J114507.8+195755	176.2826	19.9655	1.3	1.3×10^{-14}	87.1	S	5.2	1.2×10^{40}	0.75	0.08
4XMM J114552.9+193622	176.4707	19.6062	1.3	3.2×10^{-14}	95.5	S	8.2	3.5×10^{40}	0.39	0.29
4XMM J114912.5+222107	177.3024	22.3520	0.9	1.1×10^{-14}	536.2	S	16.0	3.8×10^{41}	0.58	0.32
4XMM J115057.9-284642	177.7413	-28.7784	0.6	1.9×10^{-14}	22.9	S0/E	12.4	1.2×10^{39}	0.94	0.21
4XMM J115103.4-284749	177.7645	-28.7970	0.9	1.9×10^{-14}	22.9	S0/E	4.4	1.2×10^{39}	0.89	0.01
4XMM J115342.3+521840	178.4264	52.3114	0.4	1.1×10^{-13}	17.8	S	7.0	4.2×10^{39}	0.93	0.25
4XMM J115444.3-135854	178.6847	-13.9818	1.4	1.3×10^{-14}	35.3	S0/E	11.2	2.0×10^{39}	0.79	0.70
4XMM J115551.9+064350	178.9666	6.7308	1.5	2.7×10^{-14}	37.0	S	18.3	4.5×10^{39}	0.62	0.50
4XMM J115601.2+064517	179.0052	6.7548	1.3	4.4×10^{-14}	37.0	S	10.9	7.3×10^{39}	0.71	0.24
4XMM J120152.4-185139	180.4686	-18.8609	1.2	3.9×10^{-14}	35.3		10.0	5.8×10^{39}	0.74	0.08
4XMM J120203.2+295100	180.5135	29.8502	0.8	4.1×10^{-14}	42.8	S	1.6	9.0×10^{39}	0.76	0.01
4XMM J120438.5+014716	181.1604	1.7878	0.4	8.4×10^{-14}	84.6	S0/E	2.6	7.2×10^{40}	0.26	0.06
4XMM J120732.8+150559	181.8868	15.0998	1.1	1.6×10^{-14}	369.8	S	9.9	2.6×10^{41}	0.32	0.13
4XMM J120754.4+651040	181.9769	65.1779	1.8	1.7×10^{-14}	23.9	S0/E	8.5	1.2×10^{39}	0.45	0.10
4XMM J120807.1+651149	182.0300	65.1972	1.3	1.5×10^{-14}	23.9	S0/E	9.5	1.0×10^{39}	0.90	0.20
4XMM J120817.3+651125	182.0722	65.1905	1.4	1.7×10^{-14}	23.9	S0/E	10.6	1.2×10^{39}	0.93	0.20
4XMM J121059.6+502831	182.7486	50.4755	0.5	1.0×10^{-13}	17.6	S	4.7	3.7×10^{39}	0.97	0.02
4XMM J121111.1+502936	182.7965	50.4935	0.8	2.8×10^{-14}	17.6	S	6.1	1.0×10^{39}	0.86	0.01
4XMM J121157.0+273840	182.9876	27.6445	1.5	5.1×10^{-15}	59.1	S0/E	1.7	2.1×10^{39}	0.43	0.01
4XMM J121213.9+131248	183.0580	13.2134	1.4	9.4×10^{-15}	30.9	S0/E	8.3	1.1×10^{39}	0.97	0.43
4XMM J121221.1+291219	183.0882	29.2054	0.7	6.6×10^{-14}	18.0		0.5	2.6×10^{39}	0.87	0.01
4XMM J121325.2+023625	183.3551	2.6072	1.6	1.5×10^{-14}	613.8	S	18.2	6.9×10^{41}	0.40	0.27
4XMM J121503.7+140149	183.7657	14.0304	0.5	1.2×10^{-14}	40.0	S	2.3	2.3×10^{39}	0.75	0.01
4XMM J121638.1+072803	184.1591	7.4677	1.2	3.4×10^{-14}	29.9	S	9.8	3.6×10^{39}	0.52	0.45
4XMM J121640.0+033215	184.1670	3.5376	1.2	2.8×10^{-14}	369.8	S	10.2	4.6×10^{41}	0.45	0.25
4XMM J121756.6+071104	184.4859	7.1846	2.2	4.7×10^{-14}	50.7	S	5.5	1.4×10^{40}	0.45	0.13
4XMM J121843.8+471731	184.6828	47.2922	0.1	1.6×10^{-13}	7.5	S	5.3	1.1×10^{39}	0.93	0.03
4XMM J121847.6+472054	184.6986	47.3485	0.4	3.3×10^{-13}	7.5	S	6.9	2.2×10^{39}	0.93	0.01
4XMM J121850.5+142649	184.7104	14.4471	0.8	2.9×10^{-14}	17.8	S	9.5	1.1×10^{39}	0.94	0.12
4XMM J121852.6+142549	184.7193	14.4305	0.6	3.5×10^{-14}	17.8	S	5.7	1.3×10^{39}	0.58	0.04
4XMM J121920.8+055105	184.8369	5.8514	0.8	2.3×10^{-14}	31.6	S0/E	15.5	2.8×10^{39}	0.95	0.51
4XMM J121924.6+055104	184.8528	5.8513	0.6	2.2×10^{-14}	31.6	S0/E	14.8	2.6×10^{39}	0.84	0.54
4XMM J121943.8+060005	184.9328	6.0014	0.7	8.9×10^{-14}	34.1	S0/E	4.3	1.2×10^{40}	0.83	0.10
4XMM J122016.2+333938	185.0678	33.6606	1.6	2.3×10^{-14}	89.3	S	3.1	2.2×10^{40}	0.23	0.05
4XMM J122018.0+290600	185.0751	29.1003	0.7	6.3×10^{-14}	12.1	S0/E	0.6	1.1×10^{39}	0.74	0.00
4XMM J122116.1+113108	185.3171	11.5191	0.2	3.5×10^{-13}	17.8	S	3.2	1.3×10^{40}	0.94	0.02
4XMM J122136.0+143544	185.4002	14.5957	0.4	3.4×10^{-14}	17.8	S	5.1	1.3×10^{39}	0.93	0.08
4XMM J122151.9+042810	185.4665	4.4697	0.9	3.1×10^{-14}	18.0	S	4.1	1.2×10^{39}	0.90	0.02
4XMM J122156.3+042926	185.4850	4.4906	0.8	3.5×10^{-14}	18.0	S	5.6	1.3×10^{39}	0.78	0.04
4XMM J122204.3+281109	185.5180	28.1861	0.8	1.8×10^{-14}	113.2	S	6.7	2.8×10^{40}	0.74	0.27
4XMM J122226.9+295405	185.6125	29.9016	0.8	4.5×10^{-14}	17.9	S	5.9	1.8×10^{39}	0.90	0.19
4XMM J122313.2+112125	185.8052	11.3571	0.7	3.0×10^{-14}	19.5	S	6.6	1.3×10^{39}	0.95	0.07
4XMM J122425.6+071745	186.1067	7.2959	0.8	2.0×10^{-14}	23.3	S0/E	9.7	1.3×10^{39}	0.97	0.24
4XMM J122458.3+124605	186.2433	12.7683	0.6	6.6×10^{-15}	368.1	S	14.3	1.1×10^{41}	0.66	0.45
4XMM J122514.3+045451	186.3099	4.9144	0.6	6.2×10^{-14}	29.9	S	9.7	6.7×10^{39}	0.89	0.39
4XMM J122515.3+045543	186.3139	4.9287	0.8	2.7×10^{-14}	29.9	S	6.2	2.9×10^{39}	0.93	0.15
4XMM J122539.1+124008	186.4130	12.6691	0.4	5.0×10^{-14}	17.8	S	9.9	1.9×10^{39}	0.98	0.21
4XMM J122601.4+333131	186.5060	33.5253	0.1	5.9×10^{-13}	4.6	S	3.9	1.5×10^{39}	0.76	0.02
4XMM J122629.7+311301	186.6239	31.2171	0.8	2.9×10^{-14}	17.7	S	3.5	1.1×10^{39}	0.96	0.07
4XMM J122740.6+130447	186.9195	13.0799	0.6	1.9×10^{-13}	16.7	S	0.3	6.3×10^{39}	0.47	0.00
4XMM J122744.7+130020	186.9363	13.0056	1.5	3.0×10^{-14}	17.8	S	1.5	1.1×10^{39}	0.62	0.01
4XMM J122806.0+135447	187.0252	13.9131	1.2	2.1×10^{-14}	108.1	S	5.9	2.9×10^{40}	0.62	0.17
4XMM J122903.4+135816	187.2642	13.9712	0.3	4.5×10^{-14}	16.1	S0/E	4.3	1.4×10^{39}	0.98	0.07
4XMM J122954.3+075612	187.4764	7.9368	0.2	3.5×10^{-14}	17.1	S	21.0	1.2×10^{39}	0.98	0.37
4XMM J122959.8+133756	187.4994	13.6323	0.9	2.7×10^{-14}	17.8	S0/E	3.2	1.0×10^{39}	0.94	0.03
4XMM J123000.0+133815	187.5002	13.6378	1.6	4.7×10^{-14}	17.8	S0/E	2.7	1.8×10^{39}	0.78	0.02
4XMM J123032.4+413923	187.6354	41.6565	0.6	2.2×10^{-13}	13.6	S	4.2	4.8×10^{39}	0.92	0.01
4XMM J123038.9+413810	187.6623	41.6362	0.5	7.1×10^{-14}	13.6	S	2.6	1.6×10^{39}	0.94	0.00
4XMM J123040.3+413814	187.6681	41.6372	0.5	6.5×10^{-14}	13.6	S	3.3	1.4×10^{39}	0.98	0.01
4XMM J123200.6+142436	188.0028	14.4102	1.2	4.4×10^{-14}	18.6	S	3.8	1.8×10^{39}	0.54	0.02
4XMM J123242.7+000655	188.1779	0.1153	0.2	7.6×10^{-13}	9.7	S	2.0	8.6×10^{39}	0.77	0.00
4XMM J123307.1+000758	188.2798	0.1328	0.5	3.1×10^{-14}	616.6		17.6	1.4×10^{42}	0.41	0.35
4XMM J123430.2+093730	188.6260	9.6251	0.8	4.4×10^{-14}	18.2	S0/E	1.6	1.7×10^{39}	0.98	0.03

Table A.23: List of ULX candidates obtained in Chapter 4 (continued).

Name	RA deg	Dec deg	$POSERR$ arcsec	F_X erg cm^{-2} s^{-1}	D Mpc	Gal. type	Sep. kpc	L_X erg s^{-1}	P_{XRB}	f_{cont}
4XMM J123432.5+021054	188.6356	2.1819	0.4	1.2×10^{-13}	14.9	S	6.0	3.1×10^{39}	0.85	0.03
4XMM J123436.9+020851	188.6538	2.1476	0.4	2.4×10^{-13}	14.9	S	14.8	6.4×10^{39}	0.81	0.20
4XMM J123512.6+263149	188.8027	26.5304	0.8	8.2×10^{-15}	89.9	S	4.4	7.9×10^{39}	0.78	0.05
4XMM J123653.6+131153	189.2234	13.1981	0.5	3.0×10^{-14}	17.8	S	11.8	1.2×10^{39}	0.98	0.17
4XMM J123753.8+115019	189.4744	11.8388	0.4	2.8×10^{-14}	18.8	S	15.2	1.2×10^{39}	0.94	0.56
4XMM J124248.3+131542	190.7017	13.2619	0.9	2.1×10^{-14}	22.0	S	6.3	1.2×10^{39}	0.95	0.13
4XMM J124252.6+112619	190.7192	11.4388	0.9	2.7×10^{-14}	78.2	S	8.1	2.0×10^{40}	0.49	0.15
4XMM J124338.3+113525	190.9098	11.5906	0.3	6.3×10^{-14}	17.8		11.8	2.4×10^{39}	0.93	0.18
4XMM J124358.1+164221	190.9925	16.7060	1.5	9.9×10^{-15}	464.5	S	11.5	2.6×10^{41}	0.27	0.22
4XMM J124506.5-002817	191.2774	-0.4717	0.6	4.3×10^{-14}	15.7	S	3.6	1.3×10^{39}	0.76	0.01
4XMM J124507.7-002802	191.2823	-0.4674	0.5	5.7×10^{-14}	15.7	S	1.8	1.7×10^{39}	0.92	0.00
4XMM J124813.5-054653	192.0566	-5.7815	0.9	1.7×10^{-14}	90.9	S	7.6	1.7×10^{40}	0.80	0.39
4XMM J124820.7+082919	192.0863	8.4887	0.5	5.4×10^{-14}	23.7	S0/E	3.8	3.6×10^{39}	0.96	0.07
4XMM J124823.0+082803	192.0960	8.4677	0.5	2.9×10^{-14}	23.7	S0/E	8.0	2.0×10^{39}	0.94	0.07
4XMM J124926.6-412917	192.3611	-41.4882	0.8	6.1×10^{-15}	49.2	S0/E	1.3	1.8×10^{39}	0.76	0.02
4XMM J124936.8-410316	192.4035	-41.0546	1.6	3.7×10^{-14}	27.3	S0/E	3.4	3.3×10^{39}	0.73	0.05
4XMM J125000.8-412227	192.5034	-41.3744	1.3	6.2×10^{-15}	50.1	S0/E	10.7	1.9×10^{39}	0.77	0.34
4XMM J125025.7+253129	192.6072	25.5248	0.5	1.0×10^{-13}	12.8	S	5.4	2.0×10^{39}	0.86	0.06
4XMM J125036.8+253028	192.6536	25.5080	0.6	7.3×10^{-14}	12.8	S	8.7	1.4×10^{39}	0.93	0.15
4XMM J125042.2-412544	192.6762	-41.4289	1.0	1.2×10^{-14}	47.4	S0/E	2.1	3.1×10^{39}	0.72	0.04
4XMM J125048.6+410742	192.7026	41.1284	0.3	5.7×10^{-13}	4.2		1.2	1.2×10^{39}	0.95	0.00
4XMM J125103.3+272203	192.7639	27.3676	1.5	1.3×10^{-14}	124.2	S	4.7	2.4×10^{40}	0.33	0.08
4XMM J125212.3-295102	193.0514	-29.8508	1.7	8.8×10^{-14}	34.9	S0/E	6.5	1.3×10^{40}	0.47	0.13
4XMM J125216.2+273149	193.0679	27.5305	1.2	7.5×10^{-15}	82.8	S	3.6	6.2×10^{39}	0.87	0.12
4XMM J125243.0+155146	193.1794	15.8628	1.4	1.2×10^{-13}	20.1	S	6.0	5.9×10^{39}	0.72	0.06
4XMM J125351.6+310634	193.4653	31.1096	1.0	2.4×10^{-14}	133.0	S	6.4	5.1×10^{40}	0.64	0.34
4XMM J125612.6-293002	194.0526	-29.5007	2.1	3.7×10^{-14}	28.8	S	1.2	3.7×10^{39}	0.64	0.01
4XMM J125646.9+271738	194.1956	27.2941	0.7	2.3×10^{-14}	115.9		5.0	3.8×10^{40}	0.32	0.12
4XMM J125708.6-044144	194.2859	-4.6956	0.6	2.7×10^{-14}	203.2	S	17.7	1.3×10^{41}	0.75	0.50
4XMM J125919.6+311855	194.8319	31.3155	0.9	1.2×10^{-14}	467.7	S	11.6	3.2×10^{41}	0.30	0.10
4XMM J130002.2+282558	195.0095	28.4329	0.6	6.6×10^{-15}	120.2	S0/E	4.4	1.1×10^{40}	0.71	0.09
4XMM J130030.3+282108	195.1264	28.3523	1.5	1.3×10^{-15}	94.0	S0/E	9.7	1.4×10^{39}	0.57	0.43
4XMM J130145.9+275736	195.4416	27.9602	0.6	5.9×10^{-14}	67.7	S0/E	3.0	3.2×10^{40}	0.63	0.08
4XMM J130318.7-303117	195.8280	-30.5217	1.6	3.3×10^{-14}	34.1	S0/E	1.1	4.7×10^{39}	0.46	0.00
4XMM J130501.7+351107	196.2574	35.1853	0.6	3.4×10^{-14}	66.5	S0/E	8.6	1.8×10^{40}	0.89	0.29
4XMM J130502.4+533908	196.2601	53.6525	1.4	1.4×10^{-13}	130.6	S	4.0	2.8×10^{41}	0.09	0.08
4XMM J130538.0-492544	196.4086	-49.4291	0.3	6.7×10^{-13}	3.8	S	3.2	1.2×10^{39}	0.92	0.00
4XMM J131019.6+322830	197.5817	32.4752	1.3	5.7×10^{-15}	75.9	S	8.7	3.9×10^{39}	0.78	0.12
4XMM J131218.1-192630	198.0756	-19.4418	1.3	8.9×10^{-15}	34.4	S	3.1	1.3×10^{39}	0.93	0.02
4XMM J131329.1+363157	198.3713	36.5326	1.0	2.4×10^{-14}	18.8	S	19.9	1.0×10^{39}	0.86	0.53
4XMM J131355.7-161626	198.4824	-16.2740	1.1	9.4×10^{-15}	33.1	S0/E	1.0	1.2×10^{39}	0.76	0.00
4XMM J131505.9-162048	198.7747	-16.3467	0.7	8.7×10^{-15}	39.3	S0/E	1.1	1.6×10^{39}	0.92	0.01
4XMM J131549.4+420128	198.9562	42.0247	1.1	1.4×10^{-13}	7.9	S	0.6	1.1×10^{39}	0.56	0.00
4XMM J132110.6-114749	200.2944	-11.7972	1.0	2.4×10^{-14}	36.8	S	1.8	3.9×10^{39}	0.61	0.01
4XMM J132116.2-434140	200.3176	-43.6946	2.5	3.3×10^{-14}	37.7	S0/E	9.2	5.6×10^{39}	0.85	0.83
4XMM J132342.1+313851	200.9255	31.6477	1.1	5.3×10^{-15}	70.2	S	2.9	3.1×10^{39}	0.61	0.06
4XMM J132542.2-425943	201.4261	-42.9954	0.3	9.0×10^{-13}	3.8		3.3	1.5×10^{39}	0.80	0.01
4XMM J132621.1+123627	201.5879	12.6076	1.8	2.3×10^{-14}	89.6	S0/E	7.2	2.3×10^{40}	0.37	0.34
4XMM J132920.5+334929	202.3355	33.8248	1.7	2.9×10^{-14}	114.8	S	4.5	4.6×10^{40}	0.18	0.11
4XMM J132939.7+471239	202.4157	47.2110	0.1	1.6×10^{-13}	8.0	S	5.5	1.2×10^{39}	0.90	0.04
4XMM J133001.2-180018	202.5052	-18.0050	1.0	2.7×10^{-14}	19.6	S	21.2	1.2×10^{39}	0.78	0.19
4XMM J133047.1+111157	202.6966	11.1994	0.6	6.9×10^{-14}	90.5	S0/E	2.1	6.8×10^{40}	0.07	0.04
4XMM J133104.3+110134	202.7682	11.0264	1.4	1.1×10^{-14}	108.6	S	4.0	1.5×10^{40}	0.68	0.12
4XMM J133243.3-315507	203.1805	-31.9188	1.7	1.3×10^{-14}	211.8	S	7.1	7.0×10^{40}	0.70	0.19
4XMM J133446.4-341907	203.6936	-34.3187	2.8	8.1×10^{-15}	49.4	S0/E	5.8	2.4×10^{39}	0.85	0.26
4XMM J133522.8-340932	203.8454	-34.1589	0.6	1.6×10^{-14}	96.4	S	2.2	1.7×10^{40}	0.62	0.03
4XMM J133719.8-295348	204.3326	-29.8968	0.1	4.7×10^{-13}	4.5	S	5.8	1.1×10^{39}	0.90	0.02
4XMM J133810.3-094752	204.5432	-9.7978	2.3	1.3×10^{-13}	11.5	S	0.8	2.1×10^{39}	0.69	0.00
4XMM J133844.3+042730	204.6850	4.4585	0.9	1.2×10^{-14}	97.4	S	2.2	1.3×10^{40}	0.57	0.04
4XMM J133922.8-313152	204.8453	-31.5312	0.8	2.6×10^{-14}	94.5	S	3.4	2.7×10^{40}	0.62	0.08
4XMM J133932.2+151331	204.8846	15.2255	1.1	1.7×10^{-14}	91.2		4.9	1.6×10^{40}	0.36	0.12
4XMM J134221.7+353733	205.5907	35.6261	1.2	1.6×10^{-14}	76.2	S	2.9	1.1×10^{40}	0.17	0.04
4XMM J134336.9-381214	205.9041	-38.2041	1.1	1.5×10^{-14}	147.9	S	7.9	4.0×10^{40}	0.54	0.49
4XMM J134842.7-301310	207.1782	-30.2195	0.7	2.5×10^{-14}	66.0	S	4.7	1.3×10^{40}	0.53	0.09
4XMM J134900.0+601206	207.2502	60.2019	1.1	1.7×10^{-14}	31.2	S0/E	17.9	2.0×10^{39}	0.93	0.87
4XMM J135118.0-334907	207.8252	-33.8187	0.9	4.8×10^{-14}	14.0	S	2.7	1.1×10^{39}	0.82	0.02
4XMM J135153.3+642213	207.9724	64.3705	1.1	3.3×10^{-14}	29.9	S	1.0	3.6×10^{39}	0.74	0.00
4XMM J135241.8+401149	208.1744	40.1971	1.5	1.2×10^{-14}	275.3	S0/E	10.4	1.1×10^{41}	0.32	0.24
4XMM J135319.3+402147	208.3306	40.3632	0.9	3.1×10^{-14}	37.0	S	4.6	5.0×10^{39}	0.87	0.05
4XMM J135328.4+401842	208.3687	40.3119	1.0	1.7×10^{-14}	38.0	S0/E	6.9	2.9×10^{39}	0.91	0.52
4XMM J135457.7+051923	208.7407	5.3233	0.5	2.0×10^{-13}	19.5	S	3.6	9.1×10^{39}	0.75	0.01
4XMM J135457.8+051934	208.7410	5.3261	1.8	3.1×10^{-14}	19.5	S	2.6	1.4×10^{39}	0.65	0.00
4XMM J140314.2+541806	210.8095	54.3018	0.3	3.5×10^{-13}	6.7	S	5.5	1.9×10^{39}	0.91	0.01
4XMM J140335.9-411743	210.8998	-41.2955	0.3	9.7×10^{-15}	224.9		6.2	5.9×10^{40}	0.44	0.18
4XMM J140511.7-334524	211.2988	-33.7567	1.5	2.0×10^{-14}	57.4	S	3.4	8.0×10^{39}	0.62	0.05
4XMM J140612.6+250839	211.5529	25.1443	1.7	7.9×10^{-15}	227.0	S0/E	6.8	4.9×10^{40}	0.21	0.18
4XMM J140743.8-270415	211.9329	-27.0711	0.5	1.2×10^{-14}	85.7	S0/E	1.4	1.0×10^{40}	0.43	0.02
4XMM J141004.0+173311	212.5169	17.5532	1.5	7.7×10^{-15}	144.5	S	4.4	1.9×10^{40}	0.77	0.08
4XMM J141117.5+553033	212.8230	55.5093	2.9	1.7×10^{-14}	27.8	S	1.5	1.5×10^{39}	0.79	0.01
4XMM J141443.4+435843	213.6809	43.9788	1.7	1.2×10^{-14}	158.5	S	5.0	3.6×10^{40}	0.28	0.11
4XMM J141532.7+361346	213.8863	36.2294	2.0	8.7×10^{-15}	44.5	S	4.3	2.1×10^{39}	0.22	0.02

Table A.24: List of ULX candidates obtained in Chapter 4 (continued).

Name	RA deg	Dec deg	$POSERR$ arcsec	F_X erg cm^{-2} s^{-1}	D Mpc	Gal. type	Sep. kpc	L_X erg s^{-1}	P_{XRB}	f_{cont}
4XMM J141931.5+515527	214.8813	51.9244	1.3	1.4×10^{-14}	130.6		4.4	2.8×10^{40}	0.77	0.08
4XMM J142642.3-012140	216.6763	-1.3613	1.4	1.1×10^{-14}	375.0		13.2	1.8×10^{41}	0.32	0.14
4XMM J142758.3+255201	216.9932	25.8672	0.8	1.8×10^{-14}	66.2	S	2.0	9.3×10^{39}	0.38	0.02
4XMM J142805.4+254936	217.0229	25.8269	1.0	9.3×10^{-15}	65.5	S0/E	4.3	4.8×10^{39}	0.53	0.18
4XMM J142830.4+255138	217.1271	25.8606	1.1	1.1×10^{-14}	70.7	S	2.6	6.5×10^{39}	0.50	0.04
4XMM J142833.4+390024	217.1394	39.0069	2.0	1.4×10^{-14}	40.3	S	9.2	2.7×10^{39}	0.72	0.22
4XMM J142833.7+385958	217.1408	38.9996	1.9	3.2×10^{-14}	40.3	S	6.8	6.2×10^{39}	0.54	0.12
4XMM J143104.5-005511	217.7691	-0.9199	1.7	4.1×10^{-14}	112.2	S	3.6	6.1×10^{40}	0.07	0.04
4XMM J143235.6-441003	218.1486	-44.1676	0.5	4.7×10^{-14}	18.4	S	5.3	1.9×10^{39}	0.77	0.05
4XMM J143536.0+034133	218.9002	3.6927	1.4	1.6×10^{-14}	123.6	S	7.2	2.8×10^{40}	0.44	0.12
4XMM J143932.1+620006	219.8839	62.0019	2.1	1.6×10^{-13}	95.5	S	3.5	1.7×10^{41}	0.42	0.07
4XMM J144525.6-204114	221.3571	-20.6874	1.4	1.9×10^{-14}	25.8	S	1.0	1.5×10^{39}	0.63	0.01
4XMM J145354.6+033343	223.4776	3.5621	0.9	3.3×10^{-14}	20.8	S	7.8	1.7×10^{39}	0.84	0.03
4XMM J145921.7-163751	224.8406	-16.6311	1.1	3.1×10^{-14}	29.9	S0/E	6.1	3.4×10^{39}	0.74	0.27
4XMM J145940.4-164221	224.9185	-16.7059	1.7	1.6×10^{-14}	39.5		3.1	3.0×10^{39}	0.70	0.07
4XMM J150000.9+015310	225.0040	1.8862	1.7	2.3×10^{-14}	22.5	S	2.1	1.4×10^{39}	0.46	0.01
4XMM J150001.5+015412	225.0064	1.9035	1.3	2.3×10^{-14}	22.5	S	5.1	1.4×10^{39}	0.78	0.07
4XMM J150027.5-262710	225.1149	-26.4528	2.2	4.6×10^{-14}	70.1	S	3.7	2.7×10^{40}	0.59	0.04
4XMM J150113.3+014124	225.3055	1.6902	1.4	1.8×10^{-14}	32.2	S0/E	8.0	2.2×10^{39}	0.30	0.11
4XMM J150203.7+015017	225.5155	1.8382	2.7	2.7×10^{-14}	20.3	S	1.0	1.3×10^{39}	0.48	0.01
4XMM J150527.9+013815	226.3666	1.6376	1.4	3.2×10^{-14}	22.6	S0/E	1.4	2.0×10^{39}	0.59	0.01
4XMM J150634.8+013508	226.6453	1.5858	0.7	1.5×10^{-14}	24.9	S0/E	13.2	1.1×10^{39}	0.93	0.42
4XMM J150644.5+035141	226.6857	3.8615	1.5	2.0×10^{-14}	113.0		3.9	3.1×10^{40}	0.21	0.13
4XMM J150810.2+011001	227.0426	1.1670	0.9	2.2×10^{-14}	275.4	S	6.9	2.0×10^{41}	0.43	0.07
4XMM J150932.8+055213	227.3868	5.8703	0.9	3.8×10^{-14}	147.2		6.9	1.0×10^{40}	0.27	0.25
4XMM J151210.8+051441	228.0454	5.2449	1.3	1.7×10^{-14}	117.0	S	3.5	2.8×10^{40}	0.35	0.04
4XMM J151551.2+562054	228.9636	56.3484	0.7	2.0×10^{-13}	13.4	S	4.7	4.3×10^{39}	0.84	0.01
4XMM J151641.6+552506	229.1736	55.4184	0.6	3.5×10^{-14}	48.0	S	8.1	9.6×10^{39}	0.69	0.14
4XMM J151644.8+552345	229.1870	55.3959	1.4	4.6×10^{-15}	48.0	S	11.4	1.3×10^{39}	0.94	0.30
4XMM J151834.3-240442	229.6433	-24.0785	0.7	1.6×10^{-14}	33.9	S0/E	7.5	2.2×10^{39}	0.83	0.53
4XMM J151837.1-240718	229.6550	-24.1217	0.4	1.1×10^{-13}	25.4	S0/E	2.2	8.4×10^{39}	0.63	0.02
4XMM J152254.4+082047	230.7269	8.3465	1.9	7.5×10^{-15}	138.0	S	6.3	1.7×10^{40}	0.30	0.24
4XMM J152754.5+541620	231.9772	54.2722	1.1	1.8×10^{-14}	181.1	S	6.6	7.2×10^{40}	0.82	0.48
4XMM J153237.5-081853	233.1564	-8.3148	2.2	9.9×10^{-15}	96.4	S	7.5	1.1×10^{40}	0.18	0.14
4XMM J153632.2+162630	234.1346	16.4419	0.3	1.2×10^{-13}	26.2	S	1.1	1.0×10^{40}	0.47	0.01
4XMM J154415.4-112507	236.0646	-11.4188	2.3	1.1×10^{-14}	202.9		9.9	5.6×10^{40}	0.26	0.19
4XMM J154420.1-112616	236.0840	-11.4378	1.4	6.1×10^{-14}	111.2		3.4	9.1×10^{40}	0.37	0.07
4XMM J154618.6+022458	236.5776	2.4163	1.4	1.8×10^{-14}	53.5	S	8.5	6.2×10^{39}	0.69	0.44
4XMM J154858.2-453617	237.2429	-45.6047	1.3	7.3×10^{-14}	62.9		2.0	3.4×10^{40}	0.55	0.02
4XMM J160222.7+510905	240.5947	51.1517	0.8	9.3×10^{-15}	288.4		6.5	9.2×10^{40}	0.57	0.12
4XMM J160533.8+323939	241.3912	32.6609	0.3	3.9×10^{-14}	133.0	S	5.5	8.2×10^{40}	0.27	0.17
4XMM J160553.3+324734	241.4724	32.7928	0.5	6.0×10^{-15}	572.8	S0/E	15.5	2.3×10^{41}	0.20	0.18
4XMM J161342.6+470314	243.4276	47.0541	0.6	2.4×10^{-14}	399.9		7.7	4.6×10^{41}	0.35	0.17
4XMM J161347.9+470809	243.4497	47.1360	0.7	1.7×10^{-14}	322.1	S	7.3	2.1×10^{41}	0.29	0.16
4XMM J161604.0-223726	244.0170	-22.6240	0.4	7.3×10^{-14}	110.7	S	4.3	1.1×10^{41}	0.24	0.03
4XMM J163224.6+781111	248.1029	78.1866	0.6	2.9×10^{-14}	23.1	S0/E	6.8	1.9×10^{39}	0.79	0.40
4XMM J163515.2-580558	248.8137	-58.0995	0.9	2.9×10^{-14}	33.4	S0/E	11.3	3.9×10^{39}	0.70	0.50
4XMM J163818.7-642201	249.5783	-64.3670	0.8	4.5×10^{-14}	214.8	S	23.4	2.5×10^{41}	0.26	1.41
4XMM J164002.9+434131	250.0123	43.6920	1.3	5.5×10^{-15}	157.0	S	6.0	1.6×10^{40}	0.29	0.17
4XMM J165103.5-585948	252.7647	-58.9969	0.8	5.0×10^{-14}	19.6	S	2.7	2.3×10^{39}	0.29	0.01
4XMM J165105.9-590048	252.7750	-59.0134	1.1	2.3×10^{-14}	19.6	S	6.8	1.1×10^{39}	0.30	0.10
4XMM J165222.0+173538	253.0919	17.5940	1.2	1.4×10^{-14}	144.4		4.8	3.6×10^{40}	0.32	0.15
4XMM J165501.3+790837	253.7554	79.1438	0.7	4.8×10^{-14}	263.0	S	12.0	3.9×10^{41}	0.43	0.17
4XMM J171449.9+573411	258.7080	57.5700	0.6	2.1×10^{-14}	121.9	S	3.7	3.8×10^{40}	0.22	0.05
4XMM J171613.9+602449	259.0579	60.4137	1.6	2.6×10^{-14}	50.3	S	1.6	7.9×10^{39}	0.79	0.01
4XMM J175135.5+230429	267.8983	23.0748	1.5	2.1×10^{-15}	139.8		5.1	4.9×10^{39}	0.18	0.09
4XMM J175348.3+680257	268.4513	68.0494	1.2	8.7×10^{-15}	250.1	S	10.6	6.5×10^{40}	0.61	0.41
4XMM J181519.6+495302	273.8318	49.8840	1.1	4.6×10^{-14}	212.3	S	7.9	2.5×10^{41}	0.18	0.11
4XMM J181959.2+743513	274.9970	74.5872	2.5	2.5×10^{-13}	20.6	S	8.4	1.3×10^{40}	0.50	0.11
4XMM J184810.0-631230	282.0417	-63.2086	1.2	7.1×10^{-15}	55.2	S0/E	3.7	2.6×10^{39}	0.31	0.10
4XMM J191113.6-570347	287.8068	-57.0631	0.4	1.2×10^{-14}	42.1	S	19.0	2.6×10^{39}	0.56	0.49
4XMM J191117.3-570359	287.8221	-57.0665	0.5	1.0×10^{-15}	42.1	S	16.0	2.1×10^{39}	0.71	0.32
4XMM J191118.6-570316	287.8276	-57.0546	1.2	1.2×10^{-14}	42.1	S	8.9	2.6×10^{39}	0.61	0.11
4XMM J191125.8-570322	287.8575	-57.0562	0.5	3.3×10^{-14}	42.1	S	5.9	6.9×10^{39}	0.55	0.05
4XMM J191127.7-570331	287.8656	-57.0587	0.3	2.8×10^{-14}	42.1	S	9.4	5.9×10^{39}	0.16	0.14
4XMM J191220.3-571215	288.0850	-57.2042	1.0	5.7×10^{-15}	46.5	S	2.1	1.5×10^{39}	0.57	0.02
4XMM J192108.6+431922	290.2859	43.3230	1.6	7.4×10^{-15}	79.2	S	3.4	5.6×10^{39}	0.10	0.08
4XMM J192133.3+441322	290.3891	44.2230	0.8	2.3×10^{-13}	356.9	S0/E	9.7	3.5×10^{42}	0.20	0.19
4XMM J193317.8-580718	293.3245	-58.1218	1.0	4.3×10^{-15}	57.5	S	7.7	1.7×10^{39}	0.47	0.25
4XMM J194225.8+502732	295.6078	50.4590	1.0	1.9×10^{-14}	188.7		10.1	7.9×10^{40}	0.46	0.16
4XMM J201938.2+664324	304.9093	66.7233	2.5	6.1×10^{-14}	28.3	S	2.5	5.8×10^{39}	0.59	0.07
4XMM J202739.4-470136	306.9144	-47.0268	1.4	1.1×10^{-14}	35.5	S0/E	1.0	1.7×10^{39}	0.06	0.01
4XMM J203456.8+600811	308.7370	60.1365	0.4	3.5×10^{-13}	5.7	S	1.9	1.4×10^{39}	0.82	0.00
4XMM J204520.3-673216	311.3348	-67.5379	1.1	1.3×10^{-14}	141.7	S	3.6	3.0×10^{40}	0.21	0.05
4XMM J205119.2-005306	312.8303	-0.8851	0.8	1.3×10^{-13}	238.8		5.1	8.7×10^{41}	0.00	0.08
4XMM J205216.9-691316	313.0707	-69.2213	1.9	1.0×10^{-12}	6.3	S	2.6	4.8×10^{39}	0.86	0.00
4XMM J210136.5-280316	315.4024	-28.0544	1.6	1.4×10^{-14}	177.8	S0/E	6.1	5.1×10^{40}	0.35	0.17
4XMM J210527.8-523421	316.3661	-52.5727	0.8	1.4×10^{-14}	34.7	S0/E	12.3	1.9×10^{39}	0.76	0.46
4XMM J211833.1-483321	319.6379	-48.5559	1.7	9.1×10^{-15}	154.2	S0/E	6.6	2.6×10^{40}	0.24	0.21
4XMM J211942.6-073229	319.9275	-7.5416	1.3	1.5×10^{-14}	39.9		1.2	2.8×10^{39}	0.42	0.02
4XMM J213109.5-430023	322.7896	-43.0065	0.8	7.5×10^{-14}	712.3		10.7	4.5×10^{42}	0.07	0.14

Table A.25: List of ULX candidates obtained in Chapter 4 (continued).

Name	RA deg	Dec deg	$POSERR$ arcsec	F_X erg cm^{-2} s^{-1}	D Mpc	Gal. type	Sep. kpc	L_X erg s^{-1}	P_{XRB}	f_{cont}
4XMM J213631.8-543357	324.1329	-54.5659	0.4	6.8×10^{-13}	6.3	S	1.2	3.2×10^{39}	0.90	0.00
4XMM J220633.0-002048	331.6378	-0.3467	1.4	1.6×10^{-14}	118.6	S	5.3	2.7×10^{40}	0.15	0.14
4XMM J222315.5-285846	335.8147	-28.9795	1.2	2.6×10^{-14}	19.4	S	2.2	1.2×10^{39}	0.31	0.00
4XMM J222324.0-290444	335.8501	-29.0791	0.6	6.1×10^{-14}	293.5	S	8.3	6.3×10^{41}	0.04	0.13
4XMM J222521.2-312114	336.3386	-31.3542	0.6	3.7×10^{-14}	131.8	S	3.4	7.7×10^{40}	0.06	0.04
4XMM J223436.7+001035	338.6533	0.1764	1.4	2.7×10^{-14}	65.1		3.3	1.4×10^{40}	0.53	0.20
4XMM J223545.0-260451	338.9379	-26.0809	0.2	3.6×10^{-14}	15.8	S	8.5	1.1×10^{39}	0.38	0.07
4XMM J223705.3+342534	339.2725	34.4263	0.8	4.6×10^{-14}	13.9	S	2.7	1.1×10^{39}	0.81	0.03
4XMM J224054.3+750924	340.2265	75.1567	2.1	2.2×10^{-14}	24.2	S	3.4	1.6×10^{39}	0.87	0.06
4XMM J225204.3+011454	343.0182	1.2484	1.2	1.1×10^{-14}	214.8	S	6.5	6.2×10^{40}	0.43	0.13
4XMM J225637.1-370229	344.1549	-37.0415	0.6	1.0×10^{-13}	16.6	S	3.4	3.4×10^{39}	0.68	0.03
4XMM J225746.1-365104	344.4422	-36.8514	0.9	8.4×10^{-15}	164.4	S	10.7	2.7×10^{40}	0.41	0.13
4XMM J225747.8-365122	344.4492	-36.8564	1.1	3.8×10^{-15}	164.4	S	9.3	1.2×10^{40}	0.59	0.10
4XMM J230205.7-393615	345.5241	-39.6044	0.5	1.8×10^{-13}	14.2	S	9.4	4.2×10^{39}	0.50	0.06
4XMM J230209.8-393325	345.5410	-39.5571	0.6	3.1×10^{-13}	14.2	S	3.1	7.5×10^{39}	0.58	0.02
4XMM J230455.1+122101	346.2300	12.3503	0.6	1.1×10^{-14}	30.2	S	14.6	1.2×10^{39}	0.82	0.33
4XMM J230726.2+224835	346.8592	22.8099	1.5	9.5×10^{-15}	87.1	S	5.2	8.6×10^{39}	0.69	0.07
4XMM J231616.2-423517	349.0675	-42.5882	0.4	7.9×10^{-14}	18.4	S	5.4	3.2×10^{39}	0.70	0.15
4XMM J231652.9-424246	349.2206	-42.7130	1.5	1.5×10^{-14}	192.7		5.6	6.8×10^{40}	0.17	0.11
4XMM J231818.7-422237	349.5780	-42.3770	0.4	4.3×10^{-14}	260.0		5.5	3.5×10^{41}	0.01	0.10
4XMM J231822.2-422130	349.5927	-42.3584	1.2	2.6×10^{-14}	18.4	S	3.8	1.0×10^{39}	0.44	0.02
4XMM J231916.9-421539	349.8204	-42.2609	1.4	3.1×10^{-14}	18.4	S	4.4	1.3×10^{39}	0.40	0.02
4XMM J231920.0-421519	349.8334	-42.2555	0.8	4.6×10^{-14}	18.4	S	1.2	1.9×10^{39}	0.52	0.00
4XMM J231924.8-421432	349.8536	-42.2425	0.2	1.4×10^{-13}	18.4	S	5.9	5.8×10^{39}	0.81	0.03
4XMM J231925.6-421501	349.8567	-42.2505	1.2	1.2×10^{-13}	18.4	S	4.8	4.8×10^{39}	0.44	0.01
4XMM J232023.6+271900	350.0986	27.3168	1.9	5.2×10^{-14}	62.0	S	4.2	2.4×10^{40}	0.29	0.15
4XMM J232100.8+081048	350.2535	8.1802	1.8	1.3×10^{-14}	59.1	S	3.1	5.5×10^{39}	0.42	0.21
4XMM J233225.5-005054	353.1064	-0.8484	1.6	4.1×10^{-14}	73.1	S	2.5	2.6×10^{40}	0.33	0.05
4XMM J233317.1-540500	353.3216	-54.0835	0.8	7.8×10^{-14}	26.3	S	5.0	6.5×10^{39}	0.80	0.20
4XMM J233615.6+020923	354.0652	2.1565	0.5	1.4×10^{-13}	34.7	S	4.0	2.1×10^{40}	0.79	0.17
4XMM J233623.3+020927	354.0971	2.1576	1.1	9.8×10^{-15}	34.7	S	3.0	1.4×10^{39}	0.49	0.01
4XMM J233740.0-472913	354.4170	-47.4870	1.2	4.8×10^{-15}	43.1	S0/E	16.9	1.1×10^{39}	0.79	0.52
4XMM J233741.4-474231	354.4228	-47.7087	1.2	4.7×10^{-14}	41.3	S	20.7	9.6×10^{39}	0.64	0.20
4XMM J233906.8-121330	354.7786	-12.2251	1.3	2.1×10^{-14}	24.2	S	0.7	1.5×10^{39}	0.29	0.00
4XMM J233954.3-121700	354.9766	-12.2834	1.3	2.3×10^{-14}	23.1	S	3.9	1.5×10^{39}	0.20	0.08
4XMM J234427.4-541502	356.1145	-54.2506	0.8	6.2×10^{-14}	275.6		5.0	5.6×10^{41}	0.08	0.05
4XMM J235118.2+203455	357.8258	20.5821	1.6	1.3×10^{-14}	75.4	S	5.8	8.9×10^{39}	0.64	0.04
4XMM J235118.7+203429	357.8282	20.5748	1.1	1.4×10^{-14}	75.4	S	4.0	9.6×10^{39}	0.68	0.03
4XMM J235727.2-324303	359.3637	-32.7177	0.4	8.1×10^{-15}	185.4		3.9	3.3×10^{40}	0.67	0.04
4XMM J235747.9-323457	359.4496	-32.5826	0.3	2.0×10^{-12}	3.9		0.7	3.6×10^{39}	0.78	0.00
4XMM J235922.1+083153	359.8424	8.5315	1.0	2.2×10^{-14}	118.5	S	4.2	3.7×10^{40}	0.45	0.07
2SXPS J000621.4-412915	1.5896	-41.4877	3.2	4.1×10^{-14}	19.5	S	3.6	1.9×10^{39}	0.62	0.02
2SXPS J001430.6-004413	3.6279	-0.7370	3.4	1.3×10^{-13}	56.4	S	4.8	4.9×10^{40}	0.11	0.10
2SXPS J001735.3-093249	4.3974	-9.5472	2.7	3.4×10^{-14}	94.0	S0/E	6.4	3.6×10^{40}	0.28	0.25
2SXPS J003013.5-331629	7.5565	-33.2749	2.6	1.1×10^{-13}	17.6	S	12.9	4.2×10^{39}	0.28	0.06
2SXPS J003015.3-331545	7.5639	-33.2626	3.4	3.5×10^{-14}	17.6	S	9.0	1.3×10^{39}	0.32	0.02
2SXPS J003020.8-331430	7.5867	-33.2418	3.0	1.0×10^{-13}	17.6	S	1.3	3.8×10^{39}	0.07	0.01
2SXPS J003024.2-331423	7.6012	-33.2399	2.3	2.7×10^{-13}	17.6	S	2.9	1.0×10^{40}	0.27	0.01
2SXPS J003404.0-094222	8.5170	-9.7062	2.3	9.7×10^{-14}	52.9	S	4.9	3.3×10^{40}	0.64	0.04
2SXPS J004226.6-233754	10.6112	-23.6318	2.9	3.6×10^{-14}	91.8	S	5.5	3.6×10^{40}	0.20	0.07
2SXPS J004722.4-252042	11.8435	-25.3452	1.8	6.5×10^{-13}	3.9	S	4.7	1.2×10^{39}	0.64	0.00
2SXPS J004735.1-251503	11.8963	-25.2510	1.8	5.9×10^{-13}	3.9	S	2.6	1.1×10^{39}	0.56	0.01
2SXPS J005949.6-073426	14.9567	-7.5741	4.2	2.4×10^{-13}	20.8	S	1.6	1.2×10^{40}	0.08	0.00
2SXPS J011118.4-455549	17.8267	-45.9303	1.6	7.2×10^{-14}	88.0	S	4.7	6.7×10^{40}	0.35	0.12
2SXPS J021316.5-073936	33.3190	-7.6600	2.9	4.1×10^{-14}	66.6	S	4.3	2.2×10^{40}	0.22	0.20
2SXPS J022232.4+422027	35.6350	42.3410	1.3	1.0×10^{-12}	8.4		1.0	8.6×10^{39}	0.74	0.00
2SXPS J022234.4+422024	35.6437	42.3402	3.1	5.4×10^{-13}	8.4		1.1	4.5×10^{39}	0.93	0.00
2SXPS J022236.2+422237	35.6511	42.3770	1.7	1.3×10^{-13}	8.4		4.5	1.1×10^{39}	0.73	0.00
2SXPS J022552.1+182913	36.4672	18.4871	3.0	4.5×10^{-14}	16.1	S	2.9	1.4×10^{39}	0.19	0.02
2SXPS J022720.0+333413	36.8334	33.5705	2.4	2.1×10^{-13}	9.2	S	2.2	2.1×10^{39}	0.83	0.00
2SXPS J023531.7-092200	38.8825	-9.3668	3.0	5.6×10^{-14}	17.3	S	6.0	2.0×10^{39}	0.47	0.03
2SXPS J024242.9-000030	40.6791	-0.0085	2.0	1.0×10^{-14}	10.1	S	1.8	1.2×10^{39}	0.17	0.01
2SXPS J024323.0+372037	40.8458	37.3436	3.2	1.2×10^{-13}	10.0	S	4.1	1.4×10^{39}	0.80	0.03
2SXPS J024559.3-073419	41.4975	-7.5720	2.9	2.8×10^{-13}	24.0	S	2.9	1.9×10^{40}	0.30	0.02
2SXPS J024601.1-073407	41.5050	-7.5687	4.5	1.5×10^{-13}	24.0	S	4.7	1.1×10^{40}	0.06	0.03
2SXPS J024601.7-073453	41.5072	-7.5814	3.1	3.1×10^{-13}	24.0	S	3.3	2.1×10^{40}	0.23	0.03
2SXPS J024607.5-301441	41.5313	-30.2449	2.6	7.6×10^{-14}	14.2	S	12.6	1.8×10^{39}	0.77	0.09
2SXPS J024624.5-301726	41.6022	-30.2907	2.6	8.2×10^{-14}	14.2	S	6.2	2.0×10^{39}	0.81	0.02
2SXPS J024636.5-301939	41.6524	-30.3275	2.6	4.7×10^{-14}	14.2	S	20.2	1.1×10^{39}	0.26	0.23
2SXPS J030828.0-230314	47.1167	-23.0540	3.6	4.8×10^{-14}	34.7	S	2.0	6.9×10^{39}	0.06	0.04
2SXPS J030940.3-410134	47.4183	-41.0263	3.3	5.4×10^{-13}	10.9	S	1.6	7.6×10^{39}	0.21	0.02
2SXPS J032206.2-152338	50.5262	-15.3941	2.3	1.0×10^{-13}	23.1	S	2.4	6.6×10^{39}	0.56	0.04
2SXPS J032405.1+174454	51.0214	17.7485	2.2	8.8×10^{-13}	6.5	S	1.2	4.4×10^{39}	0.36	0.00
2SXPS J033340.1-360720	53.4171	-36.1222	3.7	4.5×10^{-14}	17.9	S	6.9	1.7×10^{39}	0.89	0.03
2SXPS J033728.9-243001	54.3706	-24.5005	2.3	2.5×10^{-13}	10.9	S	0.5	3.6×10^{39}	0.05	0.00
2SXPS J034429.4-443838	56.1228	-44.6440	4.0	7.2×10^{-14}	13.7	S	1.7	1.6×10^{39}	0.21	0.05
2SXPS J034811.8+700739	57.0496	70.1276	2.2	4.3×10^{-13}	15.5	S	3.7	1.2×10^{40}	0.72	0.04
2SXPS J034832.1+700722	57.1341	70.1228	3.0	5.0×10^{-14}	15.5	S	5.1	1.4×10^{39}	0.14	0.03
2SXPS J035427.2-355801	58.6134	-35.9670	2.3	1.3×10^{-13}	20.8	S0/E	1.5	6.6×10^{39}	0.76	0.01
2SXPS J041730.1-624701	64.3758	-62.7838	2.3	5.6×10^{-13}	12.6	S	2.3	1.1×10^{40}	0.60	0.00
2SXPS J041739.2-624627	64.4137	-62.7744	3.0	1.4×10^{-13}	12.6	S	2.5	2.7×10^{39}	0.37	0.00

Table A.26: List of ULX candidates obtained in Chapter 4 (continued).

Name	RA deg	Dec deg	$POSERR$ arcsec	F_X erg cm^{-2} s^{-1}	D Mpc	Gal. type	Sep. kpc	L_X erg s^{-1}	P_{XRB}	f_{cont}
2SXPS J044554.7-591406	71.4780	-59.2350	3.0	6.4×10^{-14}	16.1	S	8.0	2.0×10^{39}	0.16	0.10
2SXPS J044615.0-572026	71.5627	-57.3408	2.6	1.6×10^{-13}	16.1	S	1.7	4.9×10^{39}	0.56	0.02
2SXPS J044822.4-032210	72.0935	-3.3695	2.9	5.6×10^{-14}	33.8	S	1.7	7.7×10^{39}	0.25	0.02
2SXPS J050515.5-375826	76.3148	-37.9741	2.6	2.6×10^{-13}	11.0	S	1.4	3.7×10^{39}	0.23	0.01
2SXPS J051045.5-313626	77.6898	-31.6073	2.6	1.9×10^{-13}	10.4	S	2.0	2.4×10^{39}	0.24	0.01
2SXPS J053900.6-440919	84.7527	-44.1554	2.6	1.5×10^{-14}	227.0		14.2	9.4×10^{40}	0.46	0.35
2SXPS J055135.0-590217	87.8961	-59.0382	3.2	1.7×10^{-13}	49.2	S	6.3	4.9×10^{40}	0.14	0.11
2SXPS J055303.7-175229	88.2656	-17.8750	2.6	6.3×10^{-14}	36.6	S	9.2	1.0×10^{40}	0.78	0.55
2SXPS J060945.1-484805	92.4382	-48.8015	2.9	1.7×10^{-13}	127.1		6.2	3.3×10^{41}	0.01	0.20
2SXPS J061206.3-214849	93.0263	-21.8139	3.2	5.6×10^{-14}	32.4	S	8.4	7.0×10^{39}	0.32	0.23
2SXPS J061617.5-212222	94.0733	-21.3730	1.3	1.2×10^{-13}	32.4	S	9.8	1.5×10^{40}	0.69	0.12
2SXPS J061619.3-212219	94.0805	-21.3721	1.3	1.3×10^{-13}	32.4	S	6.0	1.6×10^{40}	0.83	0.04
2SXPS J061626.7-212227	94.1115	-21.3743	1.3	1.1×10^{-13}	32.4	S	2.8	1.4×10^{40}	0.58	0.01
2SXPS J061846.8+782127	94.6953	78.3576	3.2	6.9×10^{-14}	13.9	S	1.9	1.6×10^{39}	0.34	0.01
2SXPS J062057.7-082939	95.2405	-8.4943	3.2	1.5×10^{-13}	11.2	S	1.6	2.3×10^{39}	0.41	0.00
2SXPS J062140.6-271235	95.4193	-27.2098	2.3	6.6×10^{-14}	20.8	S0/E	8.7	3.4×10^{39}	0.84	0.13
2SXPS J062140.9-594432	95.4207	-59.7424	3.1	5.1×10^{-14}	37.0	S	3.4	8.3×10^{39}	0.17	0.04
2SXPS J062147.1-271524	95.4464	-27.2569	3.2	3.0×10^{-14}	20.8	S0/E	12.9	1.5×10^{39}	0.42	0.23
2SXPS J062149.3-271459	95.4554	-27.2500	2.2	3.6×10^{-14}	20.8	S0/E	14.0	1.8×10^{39}	0.59	0.27
2SXPS J065042.6-520749	102.6776	-52.1304	2.8	1.0×10^{-14}	12.0	S	3.0	1.7×10^{39}	0.17	0.02
2SXPS J070254.0+503510	105.7253	50.5862	2.3	2.4×10^{-14}	187.9	S0/E	15.3	1.0×10^{41}	0.86	0.66
2SXPS J071735.8+232206	109.3992	23.3684	4.1	5.6×10^{-14}	31.5	S	12.5	6.7×10^{39}	0.61	0.19
2SXPS J072634.8+431756	111.6453	43.2990	2.3	4.7×10^{-14}	43.6	S0/E	2.3	1.1×10^{40}	0.15	0.04
2SXPS J073451.8-691831	113.7160	-69.3087	3.2	4.7×10^{-14}	21.6	S0/E	9.1	2.6×10^{39}	0.90	0.51
2SXPS J073625.6-473750	114.1070	-47.6306	2.6	1.5×10^{-13}	10.6	S	1.6	2.1×10^{39}	0.31	0.00
2SXPS J080707.3-280303	121.7808	-28.0510	2.4	6.3×10^{-14}	14.9	S	1.2	1.7×10^{39}	0.21	0.00
2SXPS J081359.2+454327	123.4967	45.7244	3.1	9.4×10^{-14}	11.5	S	3.5	1.5×10^{39}	0.08	0.01
2SXPS J082617.1+113010	126.5713	11.5029	3.2	4.0×10^{-14}	139.3	S	7.4	9.3×10^{40}	0.12	0.11
2SXPS J083634.5-202802	129.1440	-20.4675	3.3	4.0×10^{-14}	70.5	S0/E	4.1	2.4×10^{40}	0.20	0.06
2SXPS J085509.3+201538	133.7889	20.2607	2.4	3.2×10^{-14}	140.6	S	5.6	7.5×10^{40}	0.75	0.18
2SXPS J090934.1+330713	137.3925	33.1205	2.3	1.5×10^{-14}	26.1	S	1.6	1.2×10^{39}	0.16	0.00
2SXPS J090945.0+071023	137.4377	7.1733	3.1	2.0×10^{-13}	73.9	S	4.6	1.3×10^{41}	0.11	0.09
2SXPS J091346.4+762836	138.4436	76.4769	2.3	2.4×10^{-13}	20.8	S	1.3	1.2×10^{40}	0.72	0.00
2SXPS J091720.2+415427	139.3342	41.9078	2.8	8.4×10^{-14}	25.0	S	2.4	6.3×10^{39}	0.89	0.06
2SXPS J091750.3-222145	139.4596	-22.3626	3.7	1.4×10^{-13}	8.1	S	1.8	1.1×10^{39}	0.53	0.01
2SXPS J093209.8+213106	143.0412	21.5185	2.7	1.2×10^{-13}	8.6	S	2.6	1.0×10^{39}	0.20	0.01
2SXPS J094252.9+092916	145.7204	9.4879	3.1	2.3×10^{-14}	42.9	S	4.9	5.0×10^{39}	0.81	0.16
2SXPS J094605.5+013954	146.5233	1.6653	3.3	1.7×10^{-13}	25.8	S	3.8	1.3×10^{40}	0.08	0.04
2SXPS J101445.0-285055	153.6876	-28.8487	2.7	1.1×10^{-13}	13.9	S	6.2	2.5×10^{39}	0.28	0.16
2SXPS J103220.0+274001	158.0834	27.6670	2.6	1.6×10^{-13}	9.0		0.7	1.6×10^{39}	0.20	0.00
2SXPS J103423.1+734519	158.5964	73.7555	1.4	7.2×10^{-12}	18.4	S	3.0	2.9×10^{41}	0.49	0.06
2SXPS J103522.9-244510	158.8456	-24.7531	1.2	5.6×10^{-13}	7.0	S	0.2	3.3×10^{39}	0.40	0.00
2SXPS J103715.4-413749	159.3143	-41.6305	2.3	1.2×10^{-13}	34.7	S	1.7	1.8×10^{40}	0.09	0.04
2SXPS J104028.8+091106	160.1202	9.1852	2.8	4.6×10^{-14}	79.9	S0/E	4.6	3.5×10^{40}	0.23	0.17
2SXPS J104352.8+114225	160.9701	11.7071	2.5	1.6×10^{-13}	10.0	S	3.5	1.9×10^{39}	0.63	0.06
2SXPS J104635.7+631204	161.6491	63.2011	2.8	1.1×10^{-13}	22.6	S	8.8	6.8×10^{39}	0.29	0.13
2SXPS J104702.0+171702	161.7585	17.2840	3.2	1.0×10^{-13}	23.6	S	5.3	6.8×10^{39}	0.11	0.11
2SXPS J105224.7+363551	163.1032	36.5975	3.3	5.3×10^{-14}	14.4	S	7.5	1.3×10^{39}	0.33	0.05
2SXPS J105233.9+363805	163.1416	36.6347	2.3	1.8×10^{-13}	14.4	S	4.6	4.4×10^{39}	0.59	0.01
2SXPS J110547.6-000106	166.4487	-0.0184	3.0	1.5×10^{-13}	11.2	S	3.5	2.2×10^{39}	0.77	0.01
2SXPS J111141.3+554053	167.9222	55.6816	2.7	8.3×10^{-14}	10.7	S	4.7	1.1×10^{39}	0.78	0.02
2SXPS J111416.1+481833	168.5674	48.3093	2.3	8.6×10^{-13}	33.4	S	9.8	1.1×10^{41}	0.50	0.44
2SXPS J111531.7+180647	168.8821	18.1133	3.4	2.2×10^{-14}	20.3	S0/E	6.7	1.1×10^{39}	0.75	0.25
2SXPS J112013.6+130023	170.0571	13.0065	2.0	1.0×10^{-13}	10.0	S	2.8	1.3×10^{39}	0.13	0.00
2SXPS J112013.7+125950	170.0575	12.9974	4.1	1.7×10^{-13}	10.0	S	1.4	2.0×10^{39}	0.12	0.00
2SXPS J112014.1+125907	170.0591	12.9855	4.3	1.1×10^{-13}	10.0	S	1.2	1.4×10^{39}	0.14	0.00
2SXPS J112016.2+125929	170.0676	12.9915	3.3	1.7×10^{-13}	10.0	S	0.9	2.0×10^{39}	0.45	0.00
2SXPS J112017.6+130015	170.0735	13.0043	2.8	2.3×10^{-13}	10.0	S	2.9	2.7×10^{39}	0.74	0.01
2SXPS J112418.2+480906	171.0760	48.1518	2.8	1.7×10^{-14}	82.0	S	6.9	1.3×10^{40}	0.86	0.16
2SXPS J112803.4+785953	172.0144	78.9983	2.4	8.0×10^{-13}	4.3	S	0.4	1.8×10^{39}	0.73	0.00
2SXPS J114250.6+772153	175.7110	77.3648	2.8	9.0×10^{-14}	28.2	S	3.8	8.5×10^{39}	0.31	0.07
2SXPS J115246.4+440755	178.1934	44.1322	2.6	3.9×10^{-14}	17.9	S	4.5	1.5×10^{39}	0.60	0.03
2SXPS J115252.0+440548	178.2169	44.0967	2.3	4.0×10^{-14}	17.9	S	7.8	1.5×10^{39}	0.36	0.08
2SXPS J115253.9+440613	178.2248	44.1038	2.4	4.4×10^{-14}	17.9	S	6.7	1.7×10^{39}	0.30	0.06
2SXPS J115255.4+440753	178.2310	44.1315	2.9	4.6×10^{-14}	17.9	S	6.4	1.7×10^{39}	0.35	0.06
2SXPS J115340.2+475210	178.4177	47.8695	3.0	3.3×10^{-13}	19.1	S	3.8	1.4×10^{40}	0.14	0.09
2SXPS J115349.6+522030	178.4569	52.3418	2.6	4.5×10^{-14}	17.8	S	4.7	1.7×10^{39}	0.84	0.02
2SXPS J115352.1+522016	178.4672	52.3378	3.0	8.7×10^{-14}	17.8	S	4.2	3.3×10^{39}	0.57	0.02
2SXPS J120149.7-185213	180.4572	-18.8705	3.3	8.4×10^{-14}	35.3		9.2	1.3×10^{40}	0.76	0.11
2SXPS J120153.6-185234	180.4737	-18.8764	2.0	1.4×10^{-13}	35.3		1.3	2.0×10^{40}	0.81	0.00
2SXPS J120530.3+503218	181.3765	50.5386	2.3	1.5×10^{-13}	14.3	S	2.3	3.5×10^{39}	0.57	0.01
2SXPS J121009.7+462716	182.5406	46.4545	2.6	1.9×10^{-13}	6.7	S	3.7	1.0×10^{39}	0.41	0.01
2SXPS J121855.5+471913	184.7314	47.3204	2.7	1.8×10^{-13}	7.5	S	2.3	1.2×10^{39}	0.28	0.00
2SXPS J121900.6+471750	184.7529	47.2975	2.3	1.7×10^{-13}	7.5	S	1.4	1.2×10^{39}	0.23	0.00
2SXPS J122153.3+042738	185.4724	4.4608	5.5	4.7×10^{-14}	18.0	S	4.5	1.8×10^{39}	0.66	0.02
2SXPS J122155.0+042859	185.4795	4.4832	2.7	1.6×10^{-13}	18.0	S	3.0	6.2×10^{39}	0.15	0.01
2SXPS J122156.3+042750	185.4848	4.4641	4.7	4.8×10^{-14}	18.0	S	3.5	1.9×10^{39}	0.67	0.01
2SXPS J122325.2+655911	185.8554	65.9867	2.4	6.0×10^{-14}	39.4	S	1.8	1.1×10^{40}	0.27	0.02
2SXPS J122625.7+311335	186.6071	31.2267	3.2	2.0×10^{-13}	10.4		0.7	2.5×10^{39}	0.06	0.00
2SXPS J122627.8+311329	186.6159	31.2249	2.3	4.5×10^{-13}	17.7	S	0.9	1.7×10^{40}	0.40	0.01
2SXPS J122651.2+093525	186.7136	9.5905	3.1	8.3×10^{-14}	16.0	S0/E	1.9	2.5×10^{39}	0.20	0.02

Table A.27: List of ULX candidates obtained in Chapter 4 (continued).

Name	RA deg	Dec deg	$POSERR$ arcsec	F_X erg cm^{-2} s^{-1}	D Mpc	Gal. type	Sep. kpc	L_X erg s^{-1}	P_{XRB}	f_{cont}
2SXPS J122851.7-015631	187.2156	-1.9421	5.2	4.5×10^{-14}	29.9	S0/E	2.6	4.8×10^{39}	0.08	0.06
2SXPS J122952.3+080103	187.4680	8.0178	2.3	3.2×10^{-14}	17.1	S	8.5	1.1×10^{39}	0.67	0.45
2SXPS J123029.1+413929	187.6214	41.6581	2.4	1.2×10^{-13}	13.6	S	6.3	2.6×10^{39}	0.74	0.04
2SXPS J123038.5+413740	187.6607	41.6280	3.0	6.5×10^{-14}	13.6	S	4.0	1.4×10^{39}	0.90	0.00
2SXPS J123510.0-001311	188.7918	-0.2200	3.0	3.6×10^{-14}	94.4	S	4.6	3.9×10^{40}	0.22	0.09
2SXPS J123648.0+130841	189.2001	13.1448	2.7	5.4×10^{-14}	17.8	S	6.0	2.1×10^{39}	0.71	0.03
2SXPS J124206.3+323243	190.5265	32.5454	2.2	2.8×10^{-13}	5.7	S	0.7	1.1×10^{39}	0.79	0.00
2SXPS J124211.3+323233	190.5472	32.5425	2.2	5.6×10^{-13}	5.7	S	1.2	2.2×10^{39}	0.50	0.00
2SXPS J124506.9-002801	191.2790	-0.4669	2.4	1.2×10^{-13}	15.7	S	2.4	3.6×10^{39}	0.73	0.00
2SXPS J124509.5-002732	191.2896	-0.4591	2.1	2.5×10^{-13}	15.7	S	1.2	7.5×10^{39}	0.06	0.00
2SXPS J124509.7-002720	191.2905	-0.4556	2.2	1.4×10^{-13}	15.7	S	2.1	4.1×10^{39}	0.67	0.00
2SXPS J125029.4-105154	192.6229	-10.8651	1.8	6.8×10^{-14}	26.9	S	4.9	5.9×10^{39}	0.60	0.03
2SXPS J125030.9-105106	192.6290	-10.8518	2.2	1.9×10^{-14}	26.9	S	3.2	1.7×10^{39}	0.19	0.11
2SXPS J130212.6+783212	195.5527	78.5367	2.8	2.9×10^{-14}	94.3	S	11.2	3.1×10^{40}	0.94	0.80
2SXPS J130411.1-102211	196.0463	-10.3700	3.0	2.9×10^{-14}	34.7	S	19.7	4.2×10^{39}	0.84	0.47
2SXPS J130411.4-101952	196.0477	-10.3313	2.6	7.4×10^{-14}	34.7	S	8.7	1.1×10^{40}	0.47	0.32
2SXPS J130532.9-492732	196.3874	-49.4590	2.0	7.8×10^{-13}	3.8	S	1.2	1.4×10^{39}	0.72	0.00
2SXPS J130845.9-064628	197.1913	-6.7746	2.9	9.9×10^{-14}	21.0	S	4.4	5.2×10^{39}	0.08	0.07
2SXPS J131108.3-280020	197.7848	-28.0057	2.5	1.9×10^{-13}	44.3	S	4.9	4.3×10^{40}	0.18	0.10
2SXPS J131546.7+420201	198.9447	42.0337	2.5	1.4×10^{-13}	7.9	S	1.3	1.0×10^{39}	0.52	0.00
2SXPS J131858.7-210233	199.7448	-21.0427	2.6	2.6×10^{-13}	6.6	S	1.8	1.4×10^{39}	0.41	0.01
2SXPS J132501.6-431132	201.2568	-43.1923	1.6	4.9×10^{-12}	3.8		12.5	8.3×10^{39}	0.91	0.06
2SXPS J132950.6+471154	202.4609	47.1985	3.1	1.5×10^{-13}	8.0	S	0.9	1.2×10^{39}	0.88	0.00
2SXPS J132957.8+471610	202.4909	47.2697	3.4	2.1×10^{-13}	7.7		0.8	1.5×10^{39}	0.93	0.00
2SXPS J133008.2+471053	202.5342	47.1816	2.2	1.4×10^{-13}	8.0	S	6.4	1.1×10^{39}	0.85	0.03
2SXPS J133720.4-295350	204.3352	-29.8975	1.4	5.9×10^{-13}	4.5	S	6.0	1.4×10^{39}	0.88	0.02
2SXPS J133804.4-175259	204.5185	-17.8833	4.3	1.3×10^{-13}	19.5	S	1.5	5.8×10^{39}	0.66	0.00
2SXPS J134619.8+460744	206.5827	46.1290	3.2	5.3×10^{-14}	21.7	S	9.6	3.0×10^{39}	0.09	0.04
2SXPS J134624.2+460711	206.6010	46.1198	3.8	1.2×10^{-13}	21.7	S	4.7	6.5×10^{39}	0.44	0.05
2SXPS J134624.9+460607	206.6039	46.1022	2.6	4.3×10^{-13}	21.7	S	2.0	2.4×10^{40}	0.12	0.01
2SXPS J140328.0+092810	210.8670	9.4695	3.2	3.5×10^{-14}	78.1	S	6.4	2.6×10^{40}	0.15	0.13
2SXPS J140634.7-052657	211.6446	-5.4494	2.9	2.7×10^{-13}	29.9	S	2.0	2.9×10^{40}	0.09	0.02
2SXPS J141847.3+245619	214.6975	24.9386	2.2	9.7×10^{-14}	73.7	S	3.2	6.3×10^{40}	0.13	0.03
2SXPS J142226.0-002341	215.6086	-0.3950	2.5	3.2×10^{-14}	20.8	S	4.3	1.7×10^{39}	0.51	0.03
2SXPS J142226.5-002313	215.6106	-0.3872	2.8	2.8×10^{-14}	20.8	S	4.1	1.4×10^{39}	0.74	0.03
2SXPS J142448.0+023950	216.2004	2.6641	2.3	2.3×10^{-13}	238.8	S0/E	10.4	1.6×10^{42}	0.44	0.41
2SXPS J143240.5+095249	218.1691	9.8803	2.6	4.8×10^{-14}	19.7	S	5.7	2.2×10^{39}	0.35	0.15
2SXPS J144226.2-171426	220.6093	-17.2407	3.0	2.8×10^{-14}	24.5	S	6.6	2.0×10^{39}	0.68	0.22
2SXPS J150110.4+444144	225.2936	44.6957	2.4	3.9×10^{-13}	12.0	S	0.8	6.7×10^{39}	0.38	0.00
2SXPS J150626.4+554556	226.6101	55.7656	3.0	9.3×10^{-14}	15.3	S0/E	2.0	2.6×10^{39}	0.61	0.01
2SXPS J150915.2-111858	227.3136	-11.3164	2.3	9.3×10^{-14}	28.1	S	3.0	8.7×10^{39}	0.69	0.01
2SXPS J150915.5-111842	227.3148	-11.3117	3.1	5.4×10^{-14}	28.1	S	4.9	5.1×10^{39}	0.16	0.04
2SXPS J150916.2-111950	227.3176	-11.3308	2.6	1.2×10^{-13}	28.1	S	4.4	1.1×10^{40}	0.44	0.04
2SXPS J151550.7+562026	228.9615	56.3406	1.4	9.0×10^{-14}	13.4	S	3.2	2.0×10^{39}	0.81	0.00
2SXPS J152131.9-072242	230.3833	-7.3784	2.1	5.3×10^{-13}	21.9		1.0	3.1×10^{40}	0.55	0.00
2SXPS J152133.6-072738	230.3901	-7.4606	2.7	4.7×10^{-14}	22.7	S	5.1	2.9×10^{39}	0.38	0.05
2SXPS J152319.6-040927	230.8318	-4.1576	4.3	7.2×10^{-14}	21.9	S	2.4	4.1×10^{39}	0.06	0.02
2SXPS J162150.2-021629	245.4595	-2.2750	3.6	6.3×10^{-14}	21.0	S	4.0	3.3×10^{39}	0.07	0.06
2SXPS J163106.1+234945	247.7755	23.8294	3.0	5.8×10^{-14}	166.0	S	10.1	1.9×10^{41}	0.48	0.43
2SXPS J164719.4-572736	251.8309	-57.4603	4.7	1.8×10^{-13}	12.7	S	4.4	3.5×10^{39}	0.07	0.04
2SXPS J171710.2+405043	259.2926	40.8454	2.5	1.2×10^{-13}	24.7	S	5.0	9.1×10^{39}	0.81	0.26
2SXPS J175927.2+061719	269.8634	6.2887	3.2	7.2×10^{-14}	27.7	S	3.9	6.6×10^{39}	0.17	0.05
2SXPS J191002.3-635004	287.5099	-63.8345	2.4	5.6×10^{-13}	7.1	S	4.7	3.4×10^{39}	0.89	0.05
2SXPS J195419.9-584419	298.5831	-58.7387	3.4	2.8×10^{-14}	17.9	S	7.9	1.1×10^{39}	0.24	0.22
2SXPS J195420.0-584301	298.5836	-58.7171	3.4	7.4×10^{-14}	17.9	S	2.2	2.8×10^{39}	0.49	0.02
2SXPS J212900.3-524612	322.2516	-52.7700	2.4	1.3×10^{-12}	10.3		1.3	1.6×10^{40}	0.09	0.00
2SXPS J215628.6+731520	329.1194	73.2558	2.9	5.6×10^{-14}	14.4	S	1.9	1.4×10^{39}	0.81	0.02
2SXPS J221515.0-653302	333.8126	-65.5508	2.6	1.3×10^{-13}	43.0	S	2.1	2.8×10^{40}	0.13	0.02
2SXPS J221816.5+403414	334.5691	40.5706	3.0	1.4×10^{-13}	13.7	S	2.1	3.2×10^{39}	0.09	0.01
2SXPS J221846.6-032938	334.6945	-3.4941	3.0	7.4×10^{-14}	70.9	S	3.8	4.5×10^{40}	0.24	0.11
2SXPS J223541.4+012917	338.9226	1.4882	2.3	4.1×10^{-13}	257.0	S0/E	17.0	3.3×10^{42}	0.72	0.42
2SXPS J223702.8+342448	339.2618	34.4134	3.5	2.2×10^{-13}	13.9	S	1.2	5.1×10^{39}	0.41	0.00
2SXPS J223705.0+342443	339.2711	34.4122	1.6	4.4×10^{-13}	13.9	S	1.2	1.0×10^{40}	0.72	0.00
2SXPS J223718.4+342654	339.3267	34.4485	3.1	4.1×10^{-14}	94.0	S0/E	5.2	4.3×10^{40}	0.28	0.26
2SXPS J224513.7-224335	341.3073	-22.7264	2.8	2.0×10^{-14}	43.3	S	4.0	4.5×10^{39}	0.24	0.12
2SXPS J225710.0-410300	344.2918	-41.0501	2.7	3.3×10^{-13}	12.7	S	7.3	6.4×10^{39}	0.18	0.13
2SXPS J230313.8+085218	345.8077	8.8718	3.5	1.1×10^{-12}	69.6	S	9.1	6.4×10^{41}	0.76	0.66
2SXPS J230452.6+121954	346.2194	12.3318	2.3	7.8×10^{-14}	30.2	S	9.7	8.5×10^{39}	0.63	0.33
2SXPS J230939.4-362524	347.4145	-36.4235	3.3	5.5×10^{-14}	29.9	S	1.8	5.9×10^{39}	0.07	0.01
2SXPS J231821.9+432037	349.5914	43.3438	2.9	1.3×10^{-13}	51.9		4.0	4.1×10^{40}	0.16	0.13
2SXPS J235751.0-323726	359.4626	-32.6240	1.2	3.9×10^{-12}	3.9		2.3	7.2×10^{39}	0.47	0.00
2SXPS J235808.7-323403	359.5366	-32.5675	1.4	6.9×10^{-13}	3.9		4.8	1.3×10^{39}	0.88	0.01
2CXO J003738.8-334318	9.4117	-33.7219	0.4	2.4×10^{-15}	126.5	S	20.3	4.7×10^{39}	0.37	0.13
2CXO J003742.8-334209	9.4284	-33.7027	0.4	1.4×10^{-15}	128.2	S	5.7	2.7×10^{39}	0.87	0.03
2CXO J005950.5-073458	14.9607	-7.5828	0.4	2.2×10^{-13}	20.8	S	1.9	1.2×10^{40}	0.28	0.00
2CXO J010747.0-173029	16.9461	-17.5082	0.4	4.4×10^{-15}	83.8	S	3.3	3.7×10^{39}		
2CXO J011957.5-411400	19.9897	-41.2336	0.4	5.6×10^{-15}	76.5		2.8	3.9×10^{39}	0.78	0.03
2CXO J012341.0+331655	20.9210	33.2821	0.5	3.3×10^{-15}	72.9	S0/E	2.6	2.1×10^{39}		
2CXO J064302.5-741413	100.7607	-74.2371	0.4	2.0×10^{-15}	82.6	S	4.7	1.6×10^{39}	0.76	0.07
2CXO J072648.3+854548	111.7015	85.7636	0.4	5.2×10^{-14}	32.4		8.0	6.5×10^{39}		
2CXO J072648.3+854554	111.7013	85.7652	0.4	6.4×10^{-14}	32.4		8.8	8.0×10^{39}		

Table A.28: List of ULX candidates obtained in Chapter 4 (continued).

Name	RA	Dec	$POSERR$	F_X	D	Gal. type	Sep.	L_X	P_{XRB}	f_{cont}
	deg	deg	arcsec	erg cm^{-2} s^{-1}	Mpc		kpc	erg s^{-1}		
2CXO J074653.3+390051	116.7224	39.0144	0.4	7.8×10^{-15}	53.5	S	5.1	2.7×10^{39}	0.51	0.12
2CXO J103846.7+533013	159.6948	53.5037	0.4	1.3×10^{-13}	19.6	S	0.8	5.8×10^{39}		
2CXO J112830.6+583350	172.1277	58.5639	0.4	1.9×10^{-14}	35.3	S	1.7	2.8×10^{39}		
2CXO J145400.9+033132	223.5040	3.5257	0.4	4.1×10^{-14}	20.8	S	8.4	2.1×10^{39}		
2CXO J215707.3-694117	329.2806	-69.6881	0.4	1.8×10^{-14}	120.2	S0/E	5.4	3.1×10^{40}		
2CXO J153434.9+151149	233.6456	15.1972	0.4	1.3×10^{-14}	26.5	S	0.6	1.1×10^{39}	0.13	0.00
2CXO J010746.8-173026	16.9453	-17.5072	0.5	1.5×10^{-14}	83.8	S	4.0	1.3×10^{40}	0.15	0.11
2CXO J104413.0+064519	161.0546	6.7554	0.4	4.6×10^{-15}	84.3	S	6.9	3.9×10^{39}	0.87	0.03
2CXO J112830.6+583348	172.1279	58.5634	0.4	6.2×10^{-14}	35.3	S	1.4	9.3×10^{39}		
2CXO J003737.5-334256	9.4066	-33.7158	0.4	7.2×10^{-15}	126.5	S	25.5	1.4×10^{40}		
2CXO J224955.0+113640	342.4793	11.6113	0.5	4.2×10^{-15}	115.3	S0/E	6.3	6.7×10^{39}	0.58	0.07
2CXO J003743.0-334206	9.4292	-33.7017	0.4	3.2×10^{-15}	128.2	S	3.9	6.3×10^{39}	0.63	0.01
2CXO J003743.1-334204	9.4296	-33.7012	0.4	5.6×10^{-15}	128.2	S	3.6	1.1×10^{40}	0.63	0.01
2CXO J011957.3-411359	19.9889	-41.2333	0.5	1.2×10^{-14}	76.5		2.6	8.5×10^{39}	0.78	0.04
2CXO J125412.2+273729	193.5510	27.6247	0.4	3.2×10^{-15}	387.3	S0/E	9.1	5.7×10^{40}	0.30	0.10
2CXO J112830.6+583344	172.1279	58.5622	0.4	3.9×10^{-14}	35.3	S	0.9	5.9×10^{39}		
2CXO J003741.0-334331	9.4212	-33.7255	0.4	1.3×10^{-15}	126.5	S	19.2	2.5×10^{39}	0.56	0.11
2CXO J011957.2-411400	19.9886	-41.2336	0.5	9.4×10^{-15}	76.5		2.2	6.6×10^{39}	0.78	0.04
2CXO J010746.9-173025	16.9457	-17.5071	0.5	1.2×10^{-14}	83.8	S	3.4	1.0×10^{40}	0.15	0.11
2CXO J103844.6+533007	159.6859	53.5021	0.4	4.8×10^{-14}	19.6	S	1.1	2.2×10^{39}		
2CXO J112734.0+565222	171.8920	56.8728	0.4	1.2×10^{-14}	35.0	S	3.8	1.7×10^{39}		
2CXO J103844.7+533003	159.6866	53.5011	0.4	1.4×10^{-13}	19.6	S	1.2	6.4×10^{39}		

Table A.29: List of ULX candidates obtained in Chapter 4 (continued).

Acronyms

2MASS Two Micron All-Sky Survey.

2MASX 2MASS extended sources.

ACIS Advanced CCD Imaging Spectrometer.

AGN Active Galactic Nucleus.

ALMA Atacama Large Millimeter/submillimeter Array.

AMUSE AGN Multiwavelength Survey of Early-type galaxies.

APEC Astrophysical Plasma Emission Code.

ASCC All-Sky Compiled Catalogue of 2.5 million stars.

ATHENA Advanced Telescope for High ENergy Astrophysics.

BASS Beijing-Arizona Sky Survey.

BAT Burst Alert Telescope.

BH Black Hole.

BHB Black Hole Binary.

BHMF Black Hole Mass Function.

BPT Baldwin, Phillips & Terlevich.

CCD Charge Coupled Device.

CDS Centre de Données astronomiques de Strasbourg.

CIAO Chandra Interactive Analysis of Observations.

CLAXSON CLAssification of X-ray SOurces for Novices.

COSMOS Cosmic Evolution Survey.

CSC Chandra Source Catalogue.

CV Cataclysmic Variable.

CXB Cosmic X-ray Background.

CXC Chandra X-ray Center.

DCBH Direct Collapse Black Hole.

DES Dark Energy Survey.

DESI Dark Energy Spectroscopic Instrument.

DSS Digitized Sky Survey.

EAGLE Evolution and Assembly of GaLaxies and their Environments.

eFEDS eROSITA Final Equatorial-Depth Survey.

ELT Extremely Large Telescope.

EM Electromagnetic.

EPIC European Photon Imaging Camera.

eROSITA extended ROentgen Survey with an Imaging Telescope Array.

ETG Early-Type Galaxy.

EXOSAT European X-ray Observatory Satellite.

FIRST Faint Images of the Radio Sky at Twenty-centimeters.

FOV Field Of View.

FWHM Full Width at Half Maximum.

GALEX GALaxy evolution EXplorer.

GLADE Galaxy List for Advanced Detector Era.

GR General Relativity.

GW Gravitational Wave.

GWGC Gravitational Wave Galaxy Catalogue.

HARMONI High Angular Resolution Monolithic Optical and Near-infrared Integral field.

HEAO High Energy Astronomy Observatory.

HEASARC High Energy Astrophysics Science Archive Research Center.

HECATE Heraklion Extragalactic CATaloguE.

HID Hardness Intensity Diagram.

HLX HyperLuminous X-ray source.

HMXB High-Mass X-ray Binary.

HR Hardness Ratio.

HRC High Resolution Camera.

HST Hubble Space Telescope.

HyperLEDA Hypercat Lyon-Meudon Extragalactic Database.

HZQ High-redshift Quasar.

IMBH Intermediate-Mass Black Hole.

ISCO Innermost Stable Circular Orbit.

ISM InterStellar Medium.

JED Jet-Emitting Disc.

JWST James Webb Space Telescope.

KAGRA Kamioka Gravitational Wave Detector.

KDE Kernel Density Estimation.

LIGO Laser Interferometer Gravitational-Wave Observatory.

LINER Low-Ionization Nuclear Emission-line Region.

LISA Laser Interferometer Space Antenna.

LLAGN Low-Luminosity Active Galactic Nucleus.

LMXB Low-Mass X-ray Binary.

LSST Large Survey of Space and Time.

LTG Late-Type Galaxy.

MIR Mid-InfraRed.

MOS Metal Oxide Semiconductor.

NASA National Aeronautics and Space Administration.

NSA NASA Sloan Atlas.

NSC Nuclear Star Cluster.

OM Optical Monitor.

PanSTARRS Panoramic Survey Telescope and Rapid Response System.

PBH Primordial Black Hole.

PM Proper Motion.

PSF Point-Spread Function.

PULX Pulsating Ultraluminous X-ray Source.

QPE Quasi-Periodic Eruption.

RGS Reflection Grating Spectrometer.

RMS Root Mean Square.

ROSAT Röntgensatellit.

SAD Standard Accretion Disc.

SAS Science Analysis System.

SDSS Sloan Digital Sky Survey.

SED Spectral Energy Distribution.

SFR Star Formation Rate.

SIMBAD Set of Identifications Measurements and Bibliography for Astronomical Data.

SKA Square Kilometer Array.

SMBH SuperMassive Black Hole.

SSC Survey Science Center.

TDE Tidal Disruption Event.

TOPCAT Tool for OPerations on Catalogues And Tables.

TOV Tolman-Oppenheimer-Volkoff.

ULX UltraLuminous X-ray source.

USNO United States Naval Observatory.

UV Ultra-Violet.

UVOT Ulra-Violet Optical Telescope.

VLA Very Large Array.

VLASS Very Large Array Sky Survey.

WATCHDOG Whole-sky Alberta Time-resolved Comprehensive black-Hole Database Of the Galaxy.

WebPIMMS Web interface of the Portable, Interactive Multi-Mission Simulator.

WFI Wide Field Imager.

WISE Wide-field Infrared Survey Explorer.

XLF X-ray Luminosity Function.

XMM X-ray Multi-Mirror mission.

XRB X-Ray Binary.

XRT X-Ray Telescope.

YSO Young Stellar Object.

Bibliography

A. Einstein, Die Feldgleichungen der Gravitation, Sitzungsberichte der Königlich Preußischen Akademie der Wissenschaften (Berlin (1915) 844–847.

C. T. Bolton, Dimensions of the Binary System HDE 226868 = Cygnus X-1, Nature Physical Science 240 (1972) 124–127.

F. Wang, J. Yang, X. Fan et al., A Luminous Quasar at Redshift 7.642, Astrophysical Journal, Letters 907 (2021) L1.

K. Schwarzschild, Über das Gravitationsfeld eines Massenpunktes nach der Einsteinschen Theorie, Sitzungsberichte der Königlich Preußischen Akademie der Wissenschaften (Berlin (1916) 189–196.

M. Visser, The Kerr spacetime: A brief introduction, arXiv e-prints (2007) arXiv:0706.0622.

W. Anderson, Über die Grenzdichte der Materie und der Energie, Zeitschrift fur Physik 56 (1929) 851–856.

S. Chandrasekhar, The Maximum Mass of Ideal White Dwarfs, Astrophysical Journal 74 (1931) 81.

L. D. Landau, To the Stars theory, Phys. Zs. Sowjet 1 (1932) 285.

W. Baade, F. Zwicky, On Super-novae, Proceedings of the National Academy of Science 20 (1934) 254–259.

J. R. Oppenheimer, H. Snyder, On Continued Gravitational Contraction, Physical Review 56 (1939) 455–459.

R. C. Tolman, Static Solutions of Einstein's Field Equations for Spheres of Fluid, Physical Review 55 (1939) 364–373.

J. R. Oppenheimer, G. M. Volkoff, On Massive Neutron Cores, Physical Review 55 (1939) 374–381.

H. T. Cromartie, E. Fonseca, S. M. Ransom et al., Relativistic Shapiro delay measurements of an extremely massive millisecond pulsar, Nature Astronomy 4 (2020) 72–76.

T. E. Riley, A. L. Watts, P. S. Ray et al., A NICER View of the Massive Pulsar PSR J0740+6620 Informed by Radio Timing and XMM-Newton Spectroscopy, Astrophysical Journal, Letters 918 (2021) L27.

A. Heger, C. L. Fryer, S. E. Woosley, N. Langer, D. H. Hartmann, How Massive Single Stars End Their Life, Astrophysical Journal 591 (2003) 288–300.

P. Madau, M. J. Rees, Massive Black Holes as Population III Remnants, Astrophysical Journal, Letters 551 (2001) L27–L30.

T. Ohkubo, K. Nomoto, H. Umeda, N. Yoshida, S. Tsuruta, Evolution of Very Massive Population III Stars with Mass Accretion from Pre-main Sequence to Collapse, Astrophysical Journal 706 (2009) 1184–1193.

S. F. Portegies Zwart, S. L. W. McMillan, The Runaway Growth of Intermediate-Mass Black Holes in Dense Star Clusters, Astrophysical Journal 576 (2002) 899–907.

A. Loeb, F. A. Rasio, Collapse of Primordial Gas Clouds and the Formation of Quasar Black Holes, Astrophysical Journal 432 (1994) 52.

M. Mezcua, Observational evidence for intermediate-mass black holes, International Journal of Modern Physics D 26 (2017) 1730021.

B. Carr, F. Kühnel, Primordial Black Holes as Dark Matter: Recent Developments, Annual Review of Nuclear and Particle Science 70 (2020) 355–394.

K. Griest, A. M. Cieplak, M. J. Lehner, Experimental Limits on Primordial Black Hole Dark Matter from the First 2 yr of Kepler Data, Astrophysical Journal 786 (2014) 158.

V. Poulin, P. D. Serpico, F. Calore, S. Clesse, K. Kohri, CMB bounds on disk-accreting massive primordial black holes, Physical Review D 96 (2017) 083524.

G. Ballesteros, J. Coronado-Blázquez, D. Gaggero, X-ray and gamma-ray limits on the primordial black hole abundance from Hawking radiation, Physics Letters B 808 (2020) 135624.

A. Sicilia, A. Lapi, L. Boco et al., The Black Hole Mass Function Across Cosmic Times. I. Stellar Black Holes and Light Seed Distribution, Astrophysical Journal 924 (2022) 56.

L. A. C. van Son, S. E. De Mink, F. S. Broekgaarden et al., Polluting the Pair-instability Mass Gap for Binary Black Holes through Super-Eddington Accretion in Isolated Binaries, Astrophysical Journal 897 (2020) 100.

S. W. Hawking, Black hole explosions?, Nature 248 (1974) 30–31.

J. Wilms, A. Allen, R. McCray, On the Absorption of X-Rays in the Interstellar Medium, Astrophysical Journal 542 (2000) 914–924.

A. Cavaliere, R. Fusco-Femiano, X-rays from hot plasma in clusters of galaxies., Astronomy and Astrophysics 49 (1976) 137–144.

S. Klein, Suppression of bremsstrahlung and pair production due to environmental factors, Reviews of Modern Physics 71 (1999) 1501–1538.

T. W. Jones, S. L. O'Dell, W. A. Stein, Physics of Compact Nonthermal Sources. II. Determination of Physical Parameters, Astrophysical Journal 192 (1974) 261–278.

R. A. Sunyaev, L. G. Titarchuk, Comptonization of X-Rays in Plasma Clouds - Typical Radiation Spectra, Astronomy and Astrophysics 86 (1980) 121.

S. Russ, Hard and Soft X Rays , Archives of The Roentgen Ray 19 (1915) 307–337.

N. I. Shakura, R. A. Sunyaev, Black holes in binary systems. Observational appearance., Astronomy and Astrophysics 24 (1973) 337–355.

L. Titarchuk, Y. Lyubarskij, Power-Law Spectra as a Result of Comptonization of the Soft Radiation in a Plasma Cloud, Astrophysical Journal 450 (1995) 876.

M. Middleton, C. Done, N. Schurch, High-energy X-ray spectra of Seyferts and Unification schemes for active galactic nuclei, Monthly Notices of the RAS 383 (2008) 1501–1505.

HI4PI Collaboration, N. Ben Bekhti, L. Flöer et al., HI4PI: A full-sky H I survey based on EBHIS and GASS, Astronomy and Astrophysics 594 (2016) A116.

G. Risaliti, M. Elvis, F. Nicastro, Ubiquitous Variability of X-Ray-absorbing Column Densities in Seyfert 2 Galaxies, Astrophysical Journal 571 (2002) 234–246.

B. F. Liu, R. E. Taam, Application of the Disk Evaporation Model to Active Galactic Nuclei, Astrophysical Journal 707 (2009) 233–242.

R. P. Fender, T. M. Belloni, E. Gallo, Towards a unified model for black hole X-ray binary jets, Monthly Notices of the RAS 355 (2004) 1105–1118.

F. Meyer, B. F. Liu, E. Meyer-Hofmeister, Black hole X-ray binaries: a new view on soft-hard spectral transitions, Astronomy and Astrophysics 354 (2000) L67–L70.

J. M. Bardeen, W. H. Press, S. A. Teukolsky, Rotating Black Holes: Locally Nonrotating Frames, Energy Extraction, and Scalar Synchrotron Radiation, Astrophysical Journal 178 (1972) 347–370.

I. F. Mirabel, L. F. Rodríguez, Sources of Relativistic Jets in the Galaxy, Annual Review of Astron and Astrophys 37 (1999) 409–443.

H. Netzer, Revisiting the Unified Model of Active Galactic Nuclei, Annual Review of Astron and Astrophys 53 (2015) 365–408.

F. Ursini, G. Matt, S. Bianchi et al., Prospects for differentiating extended coronal geometries in AGNs with the IXPE mission, Monthly Notices of the RAS 510 (2022) 3674–3687.

G. Marcel, J. Ferreira, P. O. Petrucci et al., A unified accretion-ejection paradigm for black hole X-ray binaries. III. Spectral signatures of hybrid disk configurations, Astronomy and Astrophysics 617 (2018) A46.

P. Padovani, D. M. Alexander, R. J. Assef et al., Active galactic nuclei: what's in a name?, Astronomy and Astrophysics Reviews 25 (2017) 2.

S. Bianchi, V. Mainieri, P. Padovani, Active Galactic Nuclei and their demography through cosmic time, arXiv e-prints (2022) arXiv:2203.16846.

J. S. Collinson, M. J. Ward, H. Landt et al., Reaching the peak of the quasar spectral energy distribution - II. Exploring the accretion disc, dusty torus and host galaxy, Monthly Notices of the RAS 465 (2017) 358–382.

D. R. Wilkins, A. C. Fabian, Understanding X-ray reflection emissivity profiles in AGN: locating the X-ray source, Monthly Notices of the RAS 424 (2012) 1284–1296.

C. Bambi, Testing General Relativity with black hole X-ray data: a progress report, arXiv e-prints (2021) arXiv:2106.04084.

T. J. Turner, L. Miller, X-ray absorption and reflection in active galactic nuclei, Astronomy and Astrophysics Reviews 17 (2009) 47–104.

J. T. Stocke, S. L. Morris, I. M. Gioia et al., The Einstein Observatory Extended Medium-Sensitivity Survey. II. The Optical Identifications, Astrophysical Journal, Supplement 76 (1991) 813.

D. Lin, N. A. Webb, D. Barret, Classification of X-Ray Sources in the XMM-Newton Serendipitous Source Catalog, Astrophysical Journal 756 (2012) 27.

C. L. MacLeod, Ž. Ivezić, C. S. Kochanek et al., Modeling the Time Variability of SDSS Stripe 82 Quasars as a Damped Random Walk, Astrophysical Journal 721 (2010) 1014–1033.

S. Soldi, V. Beckmann, W. H. Baumgartner et al., Long-term variability of AGN at hard X-rays, Astronomy and Astrophysics 563 (2014) A57.

S. Kozłowski, C. S. Kochanek, M. L. N. Ashby et al., Quasar Variability in the Mid-Infrared, Astrophysical Journal 817 (2016) 119.

G. Yang, W. N. Brandt, B. Luo et al., Long-term X-Ray Variability of Typical Active Galactic Nuclei in the Distant Universe, Astrophysical Journal 831 (2016) 145.

G. Matt, M. Guainazzi, R. Maiolino, Changing look: from Compton-thick to Compton-thin, or the rebirth of fossil active galactic nuclei, Monthly Notices of the RAS 342 (2003) 422–426.

S. M. LaMassa, S. Cales, E. C. Moran et al., The Discovery of the First "Changing Look" Quasar: New Insights Into the Physics and Phenomenology of Active Galactic Nucleus, Astrophysical Journal 800 (2015) 144.

S. L. Shapiro, Spin, Accretion, and the Cosmological Growth of Supermassive Black Holes, Astrophysical Journal 620 (2005) 59–68.

A. S. Eddington, On the radiative equilibrium of the stars, Monthly Notices of the RAS 77 (1916) 16–35.

G. Wiktorowicz, M. Sobolewska, J.-P. Lasota, K. Belczynski, The Origin of the Ultraluminous X-Ray Sources, Astrophysical Journal 846 (2017) 17.

A. R. King, Ultraluminous X-ray sources and star formation, Monthly Notices of the RAS 347 (2004) L18–L20.

A. M. Stobbart, T. P. Roberts, J. Wilms, XMM-Newton observations of the brightest ultraluminous X-ray sources, Monthly Notices of the RAS 368 (2006) 397–413.

T. P. Roberts, X-ray observations of ultraluminous X-ray sources, Astrophysics and Space Science 311 (2007) 203–212.

J. C. Gladstone, T. P. Roberts, C. Done, The ultraluminous state, Monthly Notices of the RAS 397 (2009) 1836–1851.

H. Bondi, F. Hoyle, On the mechanism of accretion by stars, Monthly Notices of the RAS 104 (1944) 273.

H. Bondi, On spherically symmetrical accretion, Monthly Notices of the RAS 112 (1952) 195.

E. P. J. van den Heuvel, C. De Loore, The nature of X-ray binaries III. Evolution of massive close binaries with one collapsed component - with a possible application to Cygnus X-3., Astronomy and Astrophysics 25 (1973) 387.

H. J. Grimm, M. Gilfanov, R. Sunyaev, The Milky Way in X-rays for an outside observer. Log(N)-Log(S) and luminosity function of X-ray binaries from RXTE/ASM data, Astronomy and Astrophysics 391 (2002) 923–944.

S. Repetto, A. P. Igoshev, G. Nelemans, The Galactic distribution of X-ray binaries and its implications for compact object formation and natal kicks, Monthly Notices of the RAS 467 (2017) 298–310.

J. Iben, Icko, M. Livio, Common Envelopes in Binary Star Evolution, Publications of the ASP 105 (1993) 1373.

G. Nelemans, F. Verbunt, L. R. Yungelson, S. F. Portegies Zwart, Reconstructing the evolution of double helium white dwarfs: envelope loss without spiral-in, Astronomy and Astrophysics 360 (2000) 1011–1018.

K. Pavlovskii, N. Ivanova, K. Belczynski, K. X. Van, Stability of mass transfer from massive giants: double black hole binary formation and ultraluminous X-ray sources, Monthly Notices of the RAS 465 (2017) 2092–2100.

T. M. Tauris, E. P. J. van den Heuvel, Formation and evolution of compact stellar X-ray sources, in: Compact stellar X-ray sources, volume 39, 2006, pp. 623–665.

S. R. Kulkarni, P. Hut, S. McMillan, Stellar black holes in globular clusters, Nature 364 (1993) 421–423.

P. G. Jonker, K. Kaur, N. Stone, M. A. P. Torres, The Observed Mass Distribution of Galactic Black Hole LMXBs Is Biased against Massive Black Holes, Astrophysical Journal 921 (2021) 131.

G. Fabbiano, Populations of X-Ray Sources in Galaxies, Annual Review of Astron and Astrophys 44 (2006) 323–366.

K. Belczynski, V. Kalogera, A. Zezas, G. Fabbiano, X-Ray Binary Populations: The Luminosity Function of NGC 1569, Astrophysical Journal, Letters 601 (2004) L147–L150.

T. Fragos, B. Lehmer, M. Tremmel et al., X-Ray Binary Evolution Across Cosmic Time, Astrophysical Journal 764 (2013) 41.

M. Tremmel, T. Fragos, B. D. Lehmer et al., Modeling the Redshift Evolution of the Normal Galaxy X-Ray Luminosity Function, Astrophysical Journal 766 (2013) 19.

D.-W. Kim, G. Fabbiano, X-Ray Luminosity Function and Total Luminosity of Low-Mass X-Ray Binaries in Early-Type Galaxies, Astrophysical Journal 611 (2004) 846–857.

S. Mineo, M. Gilfanov, R. Sunyaev, X-ray emission from star-forming galaxies - I. High-mass X-ray binaries, Monthly Notices of the RAS 419 (2012) 2095–2115.

D. A. Swartz, R. Soria, A. F. Tennant, M. Yukita, A Complete Sample of Ultraluminous X-ray Source Host Galaxies, Astrophysical Journal 741 (2011) 49.

S. Wang, Y. Qiu, J. Liu, J. N. Bregman, Chandra ACIS Survey of X-Ray Point Sources in Nearby Galaxies. II. X-Ray Luminosity Functions and Ultraluminous X-Ray Sources, Astrophysical Journal 829 (2016) 20.

E. J. M. Colbert, R. F. Mushotzky, The Nature of Accreting Black Holes in Nearby Galaxy Nuclei, Astrophysical Journal 519 (1999) 89–107.

J.-F. Liu, J. N. Bregman, Ultraluminous X-Ray Sources in Nearby Galaxies from ROSAT High Resolution Imager Observations I. Data Analysis, Astrophysical Journal, Supplement 157 (2005) 59–125.

M. Bachetti, V. Rana, D. J. Walton et al., The Ultraluminous X-Ray Sources NGC 1313 X-1 and X-2: A Broadband Study with NuSTAR and XMM-Newton, Astrophysical Journal 778 (2013) 163.

P. Kaaret, H. Feng, T. P. Roberts, Ultraluminous X-Ray Sources, Annual Review of Astron and Astrophys 55 (2017) 303–341.

A. D. Sutton, T. P. Roberts, M. J. Middleton, The ultraluminous state revisited: fractional variability and spectral shape as diagnostics of super-Eddington accretion, Monthly Notices of the RAS 435 (2013) 1758–1775.

M. Bachetti, F. A. Harrison, D. J. Walton et al., An ultraluminous X-ray source powered by an accreting neutron star, Nature 514 (2014) 202–204.

F. Fürst, D. J. Walton, F. A. Harrison et al., Discovery of Coherent Pulsations from the Ultraluminous X-Ray Source NGC 7793 P13, Astrophysical Journal, Letters 831 (2016) L14.

G. L. Israel, A. Belfiore, L. Stella et al., An accreting pulsar with extreme properties drives an ultraluminous x-ray source in NGC 5907, Science 355 (2017) 817–819.

S. Carpano, F. Haberl, C. Maitra, G. Vasilopoulos, Discovery of pulsations from NGC 300 ULX1 and its fast period evolution, Monthly Notices of the RAS 476 (2018) L45–L49.

E. Quintin, N. A. Webb, A. Gúrpide, M. Bachetti, F. Fürst, A new candidate pulsating ULX in NGC 7793, Monthly Notices of the RAS 503 (2021) 5485–5494.

A. Gúrpide, O. Godet, F. Koliopanos, N. Webb, J. F. Olive, Long-term X-ray spectral evolution of ultraluminous X-ray sources: implications on the accretion flow geometry and the nature of the accretor, Astronomy and Astrophysics 649 (2021) A104.

F. Koliopanos, G. Vasilopoulos, O. Godet et al., ULX spectra revisited: Accreting, highly magnetized neutron stars as the engines of ultraluminous X-ray sources, Astronomy and Astrophysics 608 (2017) A47.

F. Koliopanos, G. Vasilopoulos, J. Buchner, C. Maitra, F. Haberl, Investigating ULX accretion flows and cyclotron resonance in NGC 300 ULX1, Astronomy and Astrophysics 621 (2019) A118.

P. Abolmasov, S. Fabrika, O. Sholukhova, T. Kotani, Optical Spectroscopy of the ULX-Associated Nebula MF16, arXiv e-prints (2008) arXiv:0809.0409.

C. T. Berghea, M. C. Johnson, N. J. Secrest et al., Detection of a Radio Bubble around the Ultraluminous X-Ray Source Holmberg IX X-1, Astrophysical Journal 896 (2020) 117.

A. Gúrpide, M. Parra, O. Godet, T. Contini, J.-F. Olive, MUSE spectroscopy of the ULX NGC 1313 X-1: a shock-ionised bubble, an X-ray photoionised nebula, and two supernova remnants, arXiv e-prints (2022) arXiv:2201.09333.

M. W. Pakull, L. Mirioni, Optical Counterparts of Ultraluminous X-Ray Sources, arXiv e-prints (2002) astro–ph/0202488.

C. T. Berghea, R. P. Dudik, K. A. Weaver, T. R. Kallman, The First Detection of [O IV] from an Ultraluminous X-ray Source with Spitzer. II. Evidence for High Luminosity in Holmberg II ULX, Astrophysical Journal 708 (2010) 364–374.

A. R. King, Masses, beaming and Eddington ratios in ultraluminous X-ray sources, Monthly Notices of the RAS 393 (2009) L41–L44.

G. Wiktorowicz, J.-P. Lasota, M. Middleton, K. Belczynski, The Observed versus Total Population of ULXs, Astrophysical Journal 875 (2019) 53.

J. Poutanen, G. Lipunova, S. Fabrika, A. G. Butkevich, P. Abolmasov, Supercritically accreting stellar mass black holes as ultraluminous X-ray sources, Monthly Notices of the RAS 377 (2007) 1187–1194.

M. J. Middleton, L. Heil, F. Pintore, D. J. Walton, T. P. Roberts, A spectral-timing model for ULXs in the supercritical regime, Monthly Notices of the RAS 447 (2015) 3243–3263.

M. H. Erkut, K. Y. Ekşi, M. A. Alpar, Ultra-luminous X-Ray Sources as Super-critical Propellers, Astrophysical Journal 873 (2019) 105.

A. G. Kuranov, K. A. Postnov, L. R. Yungelson, Population Synthesis of Ultraluminous X-ray Sources with Magnetized Neutron Stars, Astronomy Letters 46 (2020) 658–676.

G. Wiktorowicz, M. Sobolewska, A. Sądowski, K. Belczynski, Nature of the Extreme Ultraluminous X-Ray Sources, Astrophysical Journal 810 (2015) 20.

A. A. Mushtukov, V. F. Suleimanov, S. S. Tsygankov, J. Poutanen, On the maximum accretion luminosity of magnetized neutron stars: connecting X-ray pulsars and ultraluminous X-ray sources, Monthly Notices of the RAS 454 (2015) 2539–2548.

A. A. Mushtukov, V. F. Suleimanov, S. S. Tsygankov, A. Ingram, Optically thick envelopes around ULXs powered by accreating neutron stars, Monthly Notices of the RAS 467 (2017) 1202–1208.

J. Krticka, J. Kubat, I. Krtickova, X-ray irradiation of the stellar wind in HMXBs with B supergiants: Implications for ULXs, arXiv e-prints (2022) arXiv:2202.07072.

D.-W. Kim, G. Fabbiano, X-Ray Luminosity Function and Total Luminosity of Low-Mass X-Ray Binaries in Early-Type Galaxies, Astrophysical Journal 611 (2004) 846–857.

D. J. Walton, T. P. Roberts, S. Mateos, V. Heard, 2XMM ultraluminous X-ray source candidates in nearby galaxies, Monthly Notices of the RAS 416 (2011) 1844–1861.

R. Scott Barrows, J. M. Comerford, D. Stern, M. Heida, The Redshift Evolution of Ultraluminous X-Ray Sources out to z 0.5: Comparison with X-Ray Binary Populations and Contribution to the Cosmic X-Ray Background, Astrophysical Journal 932 (2022) 27.

S. A. Farrell, N. A. Webb, D. Barret, O. Godet, J. M. Rodrigues, An intermediate-mass black hole of over 500 solar masses in the galaxy ESO243-49, Nature 460 (2009) 73–75.

O. Godet, D. Barret, N. A. Webb, S. A. Farrell, N. Gehrels, First Evidence for Spectral State Transitions in the ESO 243-49 Hyperluminous X-Ray Source HLX-1, Astrophysical Journal, Letters 705 (2009) L109–L112.

M. Servillat, S. A. Farrell, D. Lin et al., X-Ray Variability and Hardness of ESO 243-49 HLX-1: Clear Evidence for Spectral State Transitions, Astrophysical Journal 743 (2011) 6.

S. W. Davis, R. Narayan, Y. Zhu et al., The Cool Accretion Disk in ESO 243-49 HLX-1: Further Evidence of an Intermediate-mass Black Hole, Astrophysical Journal 734 (2011) 111.

O. Godet, B. Plazolles, T. Kawaguchi et al., Investigating Slim Disk Solutions for HLX-1 in ESO 243-49, Astrophysical Journal 752 (2012) 34.

N. Webb, D. Cseh, E. Lenc et al., Radio Detections During Two State Transitions of the Intermediate-Mass Black Hole HLX-1, Science 337 (2012) 554.

O. Godet, J. C. Lombardi, F. Antonini et al., Implications of the Delayed 2013 Outburst of ESO 243-49 HLX-1, Astrophysical Journal 793 (2014) 105.

N. A. Webb, D. Barret, O. Godet et al., Chandra and Swift Follow-up Observations of the Intermediate-mass Black Hole in ESO 243-49, Astrophysical Journal, Letters 712 (2010) L107–L110.

N. A. Webb, A. Guérou, B. Ciambur et al., Understanding the environment around the intermediate mass black hole candidate ESO 243-49 HLX-1, Astronomy and Astrophysics 602 (2017) A103.

S. A. Farrell, M. Servillat, J. Pforr et al., A Young Massive Stellar Population around the Intermediate-mass Black Hole ESO 243-49 HLX-1, Astrophysical Journal, Letters 747 (2012) L13.

R. Soria, G. K. T. Hau, A. W. Graham et al., Discovery of an optical counterpart to the hyperluminous X-ray source in ESO 243-49, Monthly Notices of the RAS 405 (2010) 870–876.

D. Lin, J. Strader, E. R. Carrasco et al., A luminous X-ray outburst from an intermediate-mass black hole in an off-centre star cluster, Nature Astronomy 2 (2018) 656–661.

A. D. Sutton, T. P. Roberts, D. J. Walton, J. C. Gladstone, A. E. Scott, The most extreme ultraluminous X-ray sources: evidence for intermediate-mass black holes?, Monthly Notices of the RAS 423 (2012) 1154–1177.

M. Mezcua, T. P. Roberts, A. P. Lobanov, A. D. Sutton, The powerful jet of an off-nuclear intermediate-mass black hole in the spiral galaxy NGC 2276, Monthly Notices of the RAS 448 (2015) 1893–1899.

R. S. Barrows, M. Mezcua, J. M. Comerford, A Catalog of Hyper-luminous X-Ray Sources and Intermediate-mass Black Hole Candidates out to High Redshifts, Astrophysical Journal 882 (2019) 181.

I. Zolotukhin, N. A. Webb, O. Godet, M. Bachetti, D. Barret, A Search for Hyperluminous X-Ray Sources in the XMM-Newton Source Catalog, Astrophysical Journal 817 (2016) 88.

A. D. Sutton, T. P. Roberts, J. C. Gladstone, D. J. Walton, The hyperluminous X-ray source candidate in IC 4320: another HLX bites the dust, Monthly Notices of the RAS 450 (2015) 787–793.

M. J. Rees, Tidal disruption of stars by black holes of 10^6-10^8 solar masses in nearby galaxies, Nature 333 (1988) 523–528.

B. Mockler, J. Guillochon, E. Ramirez-Ruiz, Weighing Black Holes Using Tidal Disruption Events, Astrophysical Journal 872 (2019) 151.

R. Saxton, S. Komossa, K. Auchettl, P. G. Jonker, Correction to: X-Ray Properties of TDEs, Space Science Reviews 217 (2021) 18.

S. van Velzen, On the Mass and Luminosity Functions of Tidal Disruption Flares: Rate Suppression due to Black Hole Event Horizons, Astrophysical Journal 852 (2018) 72.

K. Bricman, A. Gomboc, The Prospects of Observing Tidal Disruption Events with the Large Synoptic Survey Telescope, Astrophysical Journal 890 (2020) 73.

K. Auchettl, J. Guillochon, E. Ramirez-Ruiz, New Physical Insights about Tidal Disruption Events from a Comprehensive Observational Inventory at X-Ray Wavelengths, Astrophysical Journal 838 (2017) 149.

C. Hazard, M. B. Mackey, A. J. Shimmins, Investigation of the Radio Source 3C 273 By The Method of Lunar Occultations, Nature 197 (1963) 1037–1039.

H. J. Smith, D. Hoffleit, Photographic History and Suggested Nature of the Radio Source 3C-48., Astronomical Journal 70 (1961) 295.

J. L. Greenstein, Red-Shift of the Unusual Radio Source: 3C 48, Nature 197 (1963) 1041–1042.

J. L. Greenstein, M. Schmidt, The Quasi-Stellar Radio Sources 3C 48 and 3C 273., Astrophysical Journal 140 (1964) 1.

E. E. Salpeter, Accretion of Interstellar Matter by Massive Objects., Astrophysical Journal 140 (1964) 796–800.

A. M. Wolfe, G. R. Burbidge, Black Holes in Elliptical Galaxies, Astrophysical Journal 161 (1970) 419.

G. R. Burbidge, The Nuclei of Galaxies, Annual Review of Astron and Astrophys 8 (1970) 369.

K. Makishima, R. Fujimoto, Y. Ishisaki et al., Discovery of an Obscured Low Luminosity Active Nucleus in the Spiral Galaxy NGC 4258, Publications of the ASJ 46 (1994) L77–L80.

Y. Tanaka, K. Nandra, A. C. Fabian et al., Gravitationally redshifted emission implying an accretion disk and massive black hole in the active galaxy MCG-6-30-15, Nature 375 (1995) 659–661.

J. Kormendy, L. C. Ho, Coevolution (Or Not) of Supermassive Black Holes and Host Galaxies, Annual Review of Astron and Astrophys 51 (2013) 511–653.

Event Horizon Telescope Collaboration, K. Akiyama, A. Alberdi et al., First M87 Event Horizon Telescope Results. I. The Shadow of the Supermassive Black Hole, Astrophysical Journal, Letters 875 (2019) L1.

J. Kormendy, D. Richstone, Inward Bound—The Search For Supermassive Black Holes In Galactic Nuclei, Annual Review of Astron and Astrophys 33 (1995) 581.

L. Ferrarese, H. Ford, Supermassive Black Holes in Galactic Nuclei: Past, Present and Future Research, Space Science Reviews 116 (2005) 523–624.

A. V. Filippenko, W. L. W. Sargent, Discovery of an Extremely Low Luminosity Seyfert 1 Nucleus in the Dwarf Galaxy NGC 4395, Astrophysical Journal, Letters 342 (1989) L11.

D. Kunth, W. L. W. Sargent, G. D. Bothun, A Dwarf Galaxy with Seyfert Characteristics, Astronomical Journal 93 (1987) 29.

A. E. Reines, J. E. Greene, M. Geha, Dwarf Galaxies with Optical Signatures of Active Massive Black Holes, Astrophysical Journal 775 (2013) 116.

E. C. Moran, K. Shahinyan, H. R. Sugarman, D. O. Vélez, M. Eracleous, Black Holes At the Centers of Nearby Dwarf Galaxies, Astronomical Journal 148 (2014) 136.

L. C. Ho, Nuclear activity in nearby galaxies., Annual Review of Astron and Astrophys 46 (2008) 475–539.

D. Asmus, P. Gandhi, A. Smette, S. F. Hönig, W. J. Duschl, Mid-infrared properties of nearby low-luminosity AGN at high angular resolution, Astronomy and Astrophysics 536 (2011) A36.

A. Merloni, S. Heinz, Evolution of Active Galactic Nuclei, in: T. D. Oswalt, W. C. Keel (Eds.), Planets, Stars and Stellar Systems. Volume 6: Extragalactic Astronomy and Cosmology, volume 6, 2013, p. 503.

X. Fan, M. A. Strauss, R. H. Becker et al., Constraining the Evolution of the Ionizing Background and the Epoch of Reionization with z$_\sim$6 Quasars. II. A Sample of 19 Quasars, Astronomical Journal 132 (2006) 117–136.

D. J. Mortlock, S. J. Warren, B. P. Venemans et al., A luminous quasar at a redshift of z = 7.085, Nature 474 (2011) 616–619.

G. Rauw, Y. Nazé, N. J. Wright, J. J. Drake, M. G. Guarcello, R. K. Prinja, L. W. Peck, J. F. Albacete Colombo, A. Herrero, H. A. Kobulnicky, S. Sciortino, J. S. Vink, X-Ray Emission from Massive Stars in Cyg OB2, ApJS 221 (2015) 1.

A. Levan, P. Crowther, R. de Grijs, N. Langer, D. Xu, S.-C. Yoon, Gamma-Ray Burst Progenitors, Space Science Reviews 202 (2016) 33–78.

P. Podsiadlowski, P. A. Mazzali, K. Nomoto, D. Lazzati, E. Cappellaro, The Rates of Hypernovae and Gamma-Ray Bursts: Implications for Their Progenitors, ApJ 607 (2004) L17–L20.

Y. Tanaka, N. Shibazaki, X-ray Novae, Annual Review of Astron and Astrophys 34 (1996) 607–644.

W. Chen, C. R. Shrader, M. Livio, The Properties of X-Ray and Optical Light Curves of X-Ray Novae, Astrophysical Journal 491 (1997) 312–338.

J. Krautter, F. J. Zickgraf, I. Appenzeller et al., Identification of a complete sample of northern ROSAT All-Sky Survey X-ray sources. IV. Statistical analysis, Astronomy and Astrophysics 350 (1999) 743–752.

M. C. i. Bernadich, A. D. Schwope, K. Kovlakas, A. Zezas, I. Traulsen, An expanded ultraluminous X-ray source catalogue, arXiv e-prints (2021) arXiv:2110.14562.

K. Gültekin, K. Nyland, N. Gray et al., Intermediate-mass black holes and the Fundamental Plane of black hole accretion, Monthly Notices of the RAS 516 (2022) 6123–6131.

B. Kızıltan, H. Baumgardt, A. Loeb, An intermediate-mass black hole in the centre of the globular cluster 47 Tucanae, Nature 542 (2017) 203–205.

J. Kormendy, The Stellar-Dynamical Search for Supermassive Black Holes in Galactic Nuclei, in: L. C. Ho (Ed.), Coevolution of Black Holes and Galaxies, 2004, p. 1.

I. V. Chilingarian, I. Y. Katkov, I. Y. Zolotukhin et al., A Population of Bona Fide Intermediate-mass Black Holes Identified as Low-luminosity Active Galactic Nuclei, Astrophysical Journal 863 (2018) 1.

C. A. Negrete, D. Dultzin, P. Marziani, J. W. Sulentic, Reverberation and Photoionization Estimates of the Broad-line Region Radius in Low-z Quasars, Astrophysical Journal 771 (2013) 31.

J. Guillochon, E. Ramirez-Ruiz, Hydrodynamical Simulations to Determine the Feeding Rate of Black Holes by the Tidal Disruption of Stars: The Importance of the Impact Parameter and Stellar Structure, Astrophysical Journal 767 (2013) 25.

R. M. Plotkin, S. Markoff, B. C. Kelly, E. Körding, S. F. Anderson, Using the Fundamental Plane of black hole activity to distinguish X-ray processes from weakly accreting black holes, Monthly Notices of the RAS 419 (2012) 267–286.

M. Nikolajuk, I. E. Papadakis, B. Czerny, Black hole mass estimation from X-ray variability measurements in active galactic nuclei, Monthly Notices of the RAS 350 (2004) L26–L30.

N. Kamizasa, Y. Terashima, H. Awaki, A New Sample of Candidate Intermediate-mass Black Holes Selected by X-Ray Variability, Astrophysical Journal 751 (2012) 39.

K. Vierdayanti, K.-Y. Watarai, S. Mineshige, On Black Hole Mass Estimation from X-Ray Spectra of Ultraluminous X-Ray Sources, Publications of the ASJ 60 (2008) 653.

M. Gliozzi, J. K. Williams, D. A. Michel, Estimating black hole masses in obscured AGN using X-rays, Monthly Notices of the RAS 502 (2021) 3329–3342.

A. Boehle, A. M. Ghez, R. Schödel et al., An Improved Distance and Mass Estimate for Sgr A* from a Multistar Orbit Analysis, Astrophysical Journal 830 (2016) 17.

Gravity Collaboration, R. Abuter, A. Amorim et al., A geometric distance measurement to the Galactic center black hole with 0.3% uncertainty, Astronomy and Astrophysics 625 (2019) L10.

K. C. Sahu, J. Anderson, S. Casertano et al., An Isolated Stellar-Mass Black Hole Detected Through Astrometric Microlensing, arXiv e-prints (2022) arXiv:2201.13296.

M. R. Garcia, R. Hextall, F. K. Baganoff et al., X-ray and Radio Variability of M31*, The Andromeda Galaxy Nuclear Supermassive Black Hole, Astrophysical Journal 710 (2010) 755–763.

J. E. Greene, L. C. Ho, Estimating Black Hole Masses in Active Galaxies Using the Hα Emission Line, Astrophysical Journal 630 (2005) 122–129.

R. Dong, J. E. Greene, L. C. Ho, X-Ray Properties of Intermediate-mass Black Holes in Active Galaxies. III. Spectral Energy Distribution and Possible Evidence for Intrinsically X-Ray-weak Active Galactic Nuclei, Astrophysical Journal 761 (2012) 73.

J. A. Baldwin, M. M. Phillips, R. Terlevich, Classification parameters for the emission-line spectra of extragalactic objects., Publications of the ASP 93 (1981) 5–19.

N. J. Secrest, R. P. Dudik, B. N. Dorland et al., Identification of 1.4 Million Active Galactic Nuclei in the Mid-Infrared using WISE Data, Astrophysical Journal, Supplement 221 (2015) 12.

R. J. Assef, D. Stern, G. Noirot et al., The WISE AGN Catalog, Astrophysical Journal, Supplement 234 (2018) 23.

K. N. Hainline, A. E. Reines, J. E. Greene, D. Stern, Mid-infrared Colors of Dwarf Galaxies: Young Starbursts Mimicking Active Galactic Nuclei, Astrophysical Journal 832 (2016) 119.

J. E. Greene, J. Strader, L. C. Ho, Intermediate-Mass Black Holes, Annual Review of Astron and Astrophys 58 (2020) 257–312.

A. Merloni, S. Heinz, T. di Matteo, A Fundamental Plane of black hole activity, Monthly Notices of the RAS 345 (2003) 1057–1076.

K. Gültekin, A. L. King, E. M. Cackett et al., The Fundamental Plane of Black Hole Accretion and Its Use as a Black Hole-Mass Estimator, Astrophysical Journal 871 (2019) 80.

M. A. Sobolewska, I. E. Papadakis, C. Done, J. Malzac, Evidence for a change in the X-ray radiation mechanism in the hard state of Galactic black holes, Monthly Notices of the RAS 417 (2011) 280–288.

R. M. Plotkin, E. Gallo, P. G. Jonker, The X-Ray Spectral Evolution of Galactic Black Hole X-Ray Binaries toward Quiescence, Astrophysical Journal 773 (2013) 59.

R. M. Plotkin, J. C. A. Miller-Jones, E. Gallo et al., The 2015 Decay of the Black Hole X-Ray Binary V404 Cygni: Robust Disk-jet Coupling and a Sharp Transition into Quiescence, Astrophysical Journal 834 (2017) 104.

Q.-X. Yang, F.-G. Xie, F. Yuan et al., Correlation between the photon index and X-ray luminosity of black hole X-ray binaries and active galactic nuclei: observations and interpretation, Monthly Notices of the RAS 447 (2015) 1692–1704.

Y. Tanaka, X-ray spectrum of low-mass X-ray binaries, in: E. Meyer-Hofmeister, H. Spruit (Eds.), Accretion Disks - New Aspects, volume 487, 1997, p. 1.

L. Stella, M. Vietri, Lense-Thirring Precession and Quasi-periodic Oscillations in Low-Mass X-Ray Binaries, Astrophysical Journal, Letters 492 (1998) L59–L62.

D. Psaltis, T. Belloni, M. van der Klis, Correlations in Quasi-periodic Oscillation and Noise Frequencies among Neutron Star and Black Hole X-Ray Binaries, Astrophysical Journal 520 (1999) 262–270.

A. A. Molla, S. K. Chakrabarti, D. Debnath, S. Mondal, Estimation of Mass of Compact Object in H 1743-322 from 2010 and 2011 Outbursts using TCAF Solution and Spectral Index-QPO Frequency Correlation, Astrophysical Journal 834 (2017) 88.

Y. Lu, Q. Yu, The relationship between X-ray variability and the central black hole mass, Monthly Notices of the RAS 324 (2001) 653–658.

E. S. Phinney, Manifestations of a Massive Black Hole in the Galactic Center, in: M. Morris (Ed.), The Center of the Galaxy, volume 136, 1989, p. 543.

L. E. Strubbe, E. Quataert, Optical flares from the tidal disruption of stars by massive black holes, Monthly Notices of the RAS 400 (2009) 2070–2084.

G. Lodato, A. R. King, J. E. Pringle, Stellar disruption by a supermassive black hole: is the light curve really proportional to $t^{-5/3}$?, Monthly Notices of the RAS 392 (2009) 332–340.

I. Khabibullin, S. Sazonov, R. Sunyaev, SRG/eROSITA prospects for the detection of stellar tidal disruption flares, Monthly Notices of the RAS 437 (2014) 327–337.

S. Campitiello, G. Ghisellini, T. Sbarrato, G. Calderone, How to constrain mass and spin of supermassive black holes through their disk emission, Astronomy and Astrophysics 612 (2018) A59.

L. Ferrarese, D. Merritt, A Fundamental Relation between Supermassive Black Holes and Their Host Galaxies, Astrophysical Journal, Letters 539 (2000) L9–L12.

K. Gebhardt, R. Bender, G. Bower et al., A Relationship between Nuclear Black Hole Mass and Galaxy Velocity Dispersion, Astrophysical Journal, Letters 539 (2000) L13–L16.

A. W. Graham, N. Scott, The M_{BH}-$L_{spheroid}$ Relation at High and Low Masses, the Quadratic Growth of Black Holes, and Intermediate-mass Black Hole Candidates, Astrophysical Journal 764 (2013) 151.

N. Sahu, A. W. Graham, B. L. Davis, Black Hole Mass Scaling Relations for Early-type Galaxies. I. M_{BH}-$M_{*,sph}$ and M_{BH}-$M_{*,gal}$, Astrophysical Journal 876 (2019) 155.

B. L. Davis, J. C. Berrier, D. W. Shields et al., Measurement of Galactic Logarithmic Spiral Arm Pitch Angle Using Two-dimensional Fast Fourier Transform Decomposition, Astrophysical Journal, Supplement 199 (2012) 33.

G. A. D. Savorgnan, Supermassive Black Holes and their Host Spheroids III. The Mbh-nsph Correlation, Astrophysical Journal 821 (2016) 88.

S. G. Djorgovski, S. Castro, D. Stern, A. A. Mahabal, On the Threshold of the Reionization Epoch, Astrophysical Journal, Letters 560 (2001) L5–L8.

T. E. Woods, B. Agarwal, V. Bromm et al., Titans of the early Universe: The Prato statement on the origin of the first supermassive black holes, Publications of the ASA 36 (2019) e027.

N. Y. Gnedin, J. P. Ostriker, Reionization of the Universe and the Early Production of Metals, Astrophysical Journal 486 (1997) 581–598.

R. Barkana, A. Loeb, In the beginning: the first sources of light and the reionization of the universe, Physics Reports 349 (2001) 125–238.

U. Maio, K. Dolag, B. Ciardi, L. Tornatore, Metal and molecule cooling in simulations of structure formation, Monthly Notices of the RAS 379 (2007) 963–973.

B. D. Smith, J. H. Wise, B. W. O'Shea, M. L. Norman, S. Khochfar, The first Population II stars formed in externally enriched mini-haloes, Monthly Notices of the RAS 452 (2015) 2822–2836.

S. McAlpine, J. C. Helly, M. Schaller et al., The EAGLE simulations of galaxy formation: Public release of halo and galaxy catalogues, Astronomy and Computing 15 (2016) 72–89.

S. Cole, A. Aragon-Salamanca, C. S. Frenk, J. F. Navarro, S. E. Zepf, A recipe for galaxy formation., Monthly Notices of the RAS 271 (1994) 781–806.

P. G. van Dokkum, M. Franx, D. Fabricant, D. D. Kelson, G. D. Illingworth, A High Merger Fraction in the Rich Cluster MS 1054-03 at Z = 0.83: Direct Evidence for Hierarchical Formation of Massive Galaxies, Astrophysical Journal, Letters 520 (1999) L95–L98.

P. F. Hopkins, L. Hernquist, T. J. Cox et al., A Unified, Merger-driven Model of the Origin of Starbursts, Quasars, the Cosmic X-Ray Background, Supermassive Black Holes, and Galaxy Spheroids, Astrophysical Journal, Supplement 163 (2006) 1–49.

C. J. Conselice, M. A. Bershady, M. Dickinson, C. Papovich, A Direct Measurement of Major Galaxy Mergers at $z<\sim 3$, Astronomical Journal 126 (2003) 1183–1207.

J. E. Barnes, Evolution of compact groups and the formation of elliptical galaxies, Nature 338 (1989) 123–126.

C. Villforth, T. Hamilton, M. M. Pawlik et al., Host galaxies of luminous $z \sim 0.6$ quasars: major mergers are not prevalent at the highest AGN luminosities, Monthly Notices of the RAS 466 (2017) 812–830.

A. Khalatyan, A. Cattaneo, M. Schramm et al., Is AGN feedback necessary to form red elliptical galaxies?, Monthly Notices of the RAS 387 (2008) 13–30.

M. Park, S. Tacchella, E. J. Nelson et al., On the formation of massive quiescent galaxies with diverse morphologies in the TNG50 simulation, Monthly Notices of the RAS 515 (2022) 213–228.

J. Silk, M. J. Rees, Quasars and galaxy formation, Astronomy and Astrophysics 331 (1998) L1–L4.

J. Aird, K. Nandra, E. S. Laird et al., The evolution of the hard X-ray luminosity function of AGN, Monthly Notices of the RAS 401 (2010) 2531–2551.

G. Kulkarni, G. Worseck, J. F. Hennawi, Evolution of the AGN UV luminosity function from redshift 7.5, Monthly Notices of the RAS 488 (2019) 1035–1065.

T. Xiao, A. J. Barth, J. E. Greene et al., Exploring the Low-mass End of the M $_{BH}$-σ_* Relation with Active Galaxies, Astrophysical Journal 739 (2011) 28.

D. J. Croton, V. Springel, S. D. M. White et al., The many lives of active galactic nuclei: cooling flows, black holes and the luminosities and colours of galaxies, Monthly Notices of the RAS 365 (2006) 11–28.

Y. Dubois, C. Pichon, J. Devriendt et al., Blowing cold flows away: the impact of early AGN activity on the formation of a brightest cluster galaxy progenitor, Monthly Notices of the RAS 428 (2013) 2885–2900.

C. Y. Peng, How Mergers May Affect the Mass Scaling Relation between Gravitationally Bound Systems, Astrophysical Journal 671 (2007) 1098–1107.

K. Jahnke, A. V. Macciò, The Non-causal Origin of the Black-hole-galaxy Scaling Relations, Astrophysical Journal 734 (2011) 92.

P. W. Hodge, Dwarf Galaxies, Annual Review of Astron and Astrophys 9 (1971) 35.

L. Mayer, F. Governato, M. Colpi et al., The Metamorphosis of Tidally Stirred Dwarf Galaxies, Astrophysical Journal 559 (2001) 754–784.

M. A. Norris, S. J. Kannappan, D. A. Forbes et al., The AIMSS Project - I. Bridging the star cluster-galaxy divide†‡§¶, Monthly Notices of the RAS 443 (2014) 1151–1172.

K. Gebhardt, T. R. Lauer, J. Kormendy et al., M33: A Galaxy with No Supermassive Black Hole, Astronomical Journal 122 (2001) 2469–2476.

N. Neumayer, C. J. Walcher, Are Nuclear Star Clusters the Precursors of Massive Black Holes?, Advances in Astronomy 2012 (2012) 709038.

A. V. Filippenko, L. C. Ho, A Low-Mass Central Black Hole in the Bulgeless Seyfert 1 Galaxy NGC 4395, Astrophysical Journal, Letters 588 (2003) L13–L16.

B. M. Peterson, M. C. Bentz, L.-B. Desroches et al., Multiwavelength Monitoring of the Dwarf Seyfert 1 Galaxy NGC 4395. I. A Reverberation-based Measurement of the Black Hole Mass, Astrophysical Journal 632 (2005) 799–808.

C. E. Thornton, A. J. Barth, L. C. Ho, R. E. Rutledge, J. E. Greene, The Host Galaxy and Central Engine of the Dwarf Active Galactic Nucleus POX 52, Astrophysical Journal 686 (2008) 892–910.

S. M. Lemons, A. E. Reines, R. M. Plotkin, E. Gallo, J. E. Greene, An X-Ray Selected Sample of Candidate Black Holes in Dwarf Galaxies, Astrophysical Journal 805 (2015) 12.

M. Volonteri, G. Lodato, P. Natarajan, The evolution of massive black hole seeds, Monthly Notices of the RAS 383 (2008) 1079–1088.

Y. Dubois, M. Volonteri, J. Silk et al., Black hole evolution - I. Supernova-regulated black hole growth, Monthly Notices of the RAS 452 (2015) 1502–1518.

M. Habouzit, M. Volonteri, Y. Dubois, Blossoms from black hole seeds: properties and early growth regulated by supernova feedback, Monthly Notices of the RAS 468 (2017) 3935–3948.

J. M. Bellovary, C. E. Cleary, F. Munshi et al., Multimessenger signatures of massive black holes in dwarf galaxies, Monthly Notices of the RAS 482 (2019) 2913–2923.

M. Geha, M. R. Blanton, R. Yan, J. L. Tinker, A Stellar Mass Threshold for Quenching of Field Galaxies, Astrophysical Journal 757 (2012) 85.

I. Martín-Navarro, M. Mezcua, Exploring the Limits of AGN Feedback: Black Holes and the Star Formation Histories of Low-mass Galaxies, Astrophysical Journal, Letters 855 (2018) L20.

M. Mezcua, H. Suh, F. Civano, Radio jets from AGNs in dwarf galaxies in the COSMOS survey: mechanical feedback out to redshift ∼3.4, Monthly Notices of the RAS 488 (2019) 685–695.

M. Molina, A. E. Reines, J. E. Greene, J. Darling, J. J. Condon, Outflows, Shocks, and Coronal Line Emission in a Radio-selected AGN in a Dwarf Galaxy, Astrophysical Journal 910 (2021) 5.

F. Davis, S. Kaviraj, M. J. Hardcastle et al., Radio AGN in nearby dwarf galaxies: the important role of AGN in dwarf galaxy evolution, Monthly Notices of the RAS 511 (2022) 4109–4122.

X. Fan, V. K. Narayanan, R. H. Lupton et al., A Survey of z>5.8 Quasars in the Sloan Digital Sky Survey. I. Discovery of Three New Quasars and the Spatial Density of Luminous Quasars at z∽6, Astronomical Journal 122 (2001) 2833–2849.

X.-B. Wu, F. Wang, X. Fan et al., An ultraluminous quasar with a twelve-billion-solar-mass black hole at redshift 6.30, Nature 518 (2015) 512–515.

E. Bañados, B. P. Venemans, C. Mazzucchelli et al., An 800-million-solar-mass black hole in a significantly neutral Universe at a redshift of 7.5, Nature 553 (2018) 473–476.

M. Volonteri, Formation of supermassive black holes, Astronomy and Astrophysics Reviews 18 (2010) 279–315.

C. L. Bennett, D. Larson, J. L. Weiland, G. Hinshaw, The 1% Concordance Hubble Constant, Astrophysical Journal 794 (2014) 135.

M. Volonteri, M. Habouzit, M. Colpi, The origins of massive black holes, Nature Reviews Physics 3 (2021) 732–743.

M. R. Mokiem, A. de Koter, J. S. Vink et al., The empirical metallicity dependence of the mass-loss rate of O- and early B-type stars, Astronomy and Astrophysics 473 (2007) 603–614.

F. Nakamura, M. Umemura, On the Initial Mass Function of Population III Stars, Astrophysical Journal 548 (2001) 19–32.

C. L. Fryer, S. E. Woosley, A. Heger, Pair-Instability Supernovae, Gravity Waves, and Gamma-Ray Transients, Astrophysical Journal 550 (2001) 372–382.

M. Spera, M. Mapelli, Very massive stars, pair-instability supernovae and intermediate-mass black holes with the sevn code, Monthly Notices of the RAS 470 (2017) 4739–4749.

G. Lodato, P. Natarajan, Supermassive black hole formation during the assembly of pre-galactic discs, Monthly Notices of the RAS 371 (2006) 1813–1823.

K. Omukai, Primordial Star Formation under Far-Ultraviolet Radiation, Astrophysical Journal 546 (2001) 635–651.

N. Yoshida, T. Abel, L. Hernquist, N. Sugiyama, Simulations of Early Structure Formation: Primordial Gas Clouds, Astrophysical Journal 592 (2003) 645–663.

J. H. Wise, J. A. Regan, B. W. O'Shea et al., Formation of massive black holes in rapidly growing pre-galactic gas clouds, Nature 566 (2019) 85–88.

E. Visbal, Z. Haiman, B. Terrazas, G. L. Bryan, R. Barkana, High-redshift star formation in a time-dependent Lyman-Werner background, Monthly Notices of the RAS 445 (2014) 107–114.

G. Dunn, J. Bellovary, K. Holley-Bockelmann, C. Christensen, T. Quinn, Sowing Black Hole Seeds: Direct Collapse Black Hole Formation with Realistic Lyman-Werner Radiation in Cosmological Simulations, Astrophysical Journal 861 (2018) 39.

M. A. Latif, D. J. Whalen, S. Khochfar, N. P. Herrington, T. E. Woods, Turbulent cold flows gave birth to the first quasars, Nature 607 (2022) 48–51.

M. Habouzit, M. Volonteri, M. Latif, Y. Dubois, S. Peirani, On the number density of 'direct collapse' black hole seeds, Monthly Notices of the RAS 463 (2016) 529–540.

M. Campanelli, C. Lousto, Y. Zlochower, D. Merritt, Large Merger Recoils and Spin Flips from Generic Black Hole Binaries, Astrophysical Journal, Letters 659 (2007) L5–L8.

C. L. Rodriguez, P. Amaro-Seoane, S. Chatterjee, F. A. Rasio, Post-Newtonian Dynamics in Dense Star Clusters: Highly Eccentric, Highly Spinning, and Repeated Binary Black Hole Mergers, Physical Review Letters 120 (2018) 151101.

M. Mapelli, M. Dall'Amico, Y. Bouffanais et al., Hierarchical black hole mergers in young, globular and nuclear star clusters: the effect of metallicity, spin and cluster properties, Monthly Notices of the RAS 505 (2021) 339–358.

C. L. Rodriguez, M. Zevin, P. Amaro-Seoane et al., Black holes: The next generation—repeated mergers in dense star clusters and their gravitational-wave properties, Physical Review D 100 (2019) 043027.

M. Mapelli, F. Santoliquido, Y. Bouffanais et al., Mass and Rate of Hierarchical Black Hole Mergers in Young, Globular and Nuclear Star Clusters, Symmetry 13 (2021) 1678.

I. Bartos, B. Kocsis, Z. Haiman, S. Márka, Rapid and Bright Stellar-mass Binary Black Hole Mergers in Active Galactic Nuclei, Astrophysical Journal 835 (2017) 165.

H. Tagawa, B. Kocsis, Z. Haiman et al., Mass-gap Mergers in Active Galactic Nuclei, Astrophysical Journal 908 (2021) 194.

J. E. Greene, Low-mass black holes as the remnants of primordial black hole formation, Nature Communications 3 (2012) 1304.

M. Volonteri, P. Natarajan, Journey to the M_{BH}-σ relation: the fate of low-mass black holes in the Universe, Monthly Notices of the RAS 400 (2009) 1911–1918.

F. Pacucci, A. Loeb, M. Mezcua, I. Martín-Navarro, Glimmering in the Dark: Modeling the Low-mass End of the M -σ Relation and of the Quasar Luminosity Function, Astrophysical Journal, Letters 864 (2018) L6.

D. Spinoso, S. Bonoli, R. Valiante, R. Schneider, D. Izquierdo-Villalba, Multi-flavour SMBH seeding and evolution in cosmological environments, arXiv e-prints (2022) arXiv:2203.13846.

Q. Yu, S. Tremaine, Observational constraints on growth of massive black holes, Monthly Notices of the RAS 335 (2002) 965–976.

F. Pacucci, P. Natarajan, M. Volonteri, N. Cappelluti, C. M. Urry, Conditions for Optimal Growth of Black Hole Seeds, Astrophysical Journal, Letters 850 (2017) L42.

K. Sugimura, T. Matsumoto, T. Hosokawa, S. Hirano, K. Omukai, The Birth of a Massive First-star Binary, Astrophysical Journal, Letters 892 (2020) L14.

J. P. Stott, D. Sobral, I. Smail et al., The merger rates and sizes of galaxies across the peak epoch of star formation from the HiZELS survey, Monthly Notices of the RAS 430 (2013) 1158–1170.

E. Noyola, K. Gebhardt, M. Bergmann, Gemini and Hubble Space Telescope Evidence for an Intermediate-Mass Black Hole in ω Centauri, Astrophysical Journal 676 (2008) 1008–1015.

N. Lützgendorf, M. Kissler-Patig, E. Noyola et al., Kinematic signature of an intermediate-mass black hole in the globular cluster NGC 6388, Astronomy and Astrophysics 533 (2011) A36.

R. Ibata, M. Bellazzini, S. C. Chapman et al., Density and Kinematic Cusps in M54 at the Heart of the Sagittarius Dwarf Galaxy: Evidence for A 10^4 M_{sun} Black Hole?, Astrophysical Journal, Letters 699 (2009) L169–L173.

B. B. P. Perera, B. W. Stappers, A. G. Lyne et al., Evidence for an intermediate-mass black hole in the globular cluster NGC 6624, Monthly Notices of the RAS 468 (2017) 2114–2127.

A. Zocchi, M. Gieles, V. Hénault-Brunet, Radial anisotropy in ω Cen limiting the room for an intermediate-mass black hole, Monthly Notices of the RAS 468 (2017) 4429–4440.

B. Lanzoni, A. Mucciarelli, L. Origlia et al., The Velocity Dispersion Profile of NGC 6388 from Resolved-star Spectroscopy: No Evidence of a Central Cusp and New Constraints on the Black Hole Mass, Astrophysical Journal 769 (2013) 107.

H. Baumgardt, N -body modelling of globular clusters: masses, mass-to-light ratios and intermediate-mass black holes, Monthly Notices of the RAS 464 (2017) 2174–2202.

H. Baumgardt, C. He, S. M. Sweet et al., No evidence for intermediate-mass black holes in the globular clusters ω Cen and NGC 6624, Monthly Notices of the RAS 488 (2019) 5340–5351.

C. R. Mann, H. Richer, J. Heyl et al., A Multimass Velocity Dispersion Model of 47 Tucanae Indicates No Evidence for an Intermediate-mass Black Hole, Astrophysical Journal 875 (2019) 1.

K. Gebhardt, R. M. Rich, L. C. Ho, A 20,000 M_{solar} Black Hole in the Stellar Cluster G1, Astrophysical Journal, Letters 578 (2002) L41–L45.

K. Gebhardt, R. M. Rich, L. C. Ho, An Intermediate-Mass Black Hole in the Globular Cluster G1: Improved Significance from New Keck and Hubble Space Telescope Observations, Astrophysical Journal 634 (2005) 1093–1102.

R. Pechetti, A. Seth, S. Kamann et al., Detection of a 100,000 $M_{\odot}$ black hole in M31's Most Massive Globular Cluster: A Tidally Stripped Nucleus, Astrophysical Journal 924 (2022) 48.

D. Pooley, S. Rappaport, X-Rays from the Globular Cluster G1: Intermediate-Mass Black Hole or Low-Mass X-Ray Binary?, Astrophysical Journal, Letters 644 (2006) L45–L48.

J. C. A. Miller-Jones, J. M. Wrobel, G. R. Sivakoff et al., The Absence of Radio Emission from the Globular Cluster G1, Astrophysical Journal, Letters 755 (2012) L1.

A. Franco, A. A. Nucita, F. De Paolis, F. Strafella, M. Maiorano, Searching for Intermediate Mass Black Holes in the Milky Way's galactic halo, arXiv e-prints (2021) arXiv:2110.11047.

G. Fragione, A. Gualandris, Hypervelocity stars from star clusters hosting intermediate-mass black holes, Monthly Notices of the RAS 489 (2019) 4543–4556.

T. Oka, S. Tsujimoto, Y. Iwata, M. Nomura, S. Takekawa, Millimetre-wave emission from an intermediate-mass black hole candidate in the Milky Way, Nature Astronomy 1 (2017) 709–712.

K. Tanaka, ALMA Images of the Host Cloud of the Intermediate-mass Black Hole Candidate CO-0.40-0.22*: No Evidence for Cloud-Black Hole Interaction, but Evidence for a Cloud-Cloud Collision, Astrophysical Journal 859 (2018) 86.

S. Takekawa, T. Oka, Y. Iwata, S. Tsujimoto, M. Nomura, Indication of Another Intermediate-mass Black Hole in the Galactic Center, Astrophysical Journal, Letters 871 (2019) L1.

S. Takekawa, T. Oka, Y. Iwata, S. Tsujimoto, M. Nomura, The Fifth Candidate for an Intermediate-mass Black Hole in the Galactic Center, Astrophysical Journal 890 (2020) 167.

A. Dressler, D. O. Richstone, Stellar Dynamics in the Nuclei of M31 and M32: Evidence for Massive Black Holes, Astrophysical Journal 324 (1988) 701.

A. E. Reines, Hunting for massive black holes in dwarf galaxies, Nature Astronomy 6 (2022) 26–34.

V. F. Baldassare, A. E. Reines, E. Gallo, J. E. Greene, A ∼50,000 $M_\odot$ Solar Mass Black Hole in the Nucleus of RGG 118, Astrophysical Journal, Letters 809 (2015) L14.

M. Mezcua, F. Civano, S. Marchesi et al., Intermediate-mass black holes in dwarf galaxies out to redshift ∼2.4 in the Chandra COSMOS-Legacy Survey, Monthly Notices of the RAS 478 (2018) 2576–2591.

L. F. Sartori, K. Schawinski, E. Treister et al., The search for active black holes in nearby low-mass galaxies using optical and mid-IR data, Monthly Notices of the RAS 454 (2015) 3722–3742.

S. Harish, S. Malhotra, J. E. Rhoads et al., Evidence for Black Holes in Green Peas from WISE colors and variability, arXiv e-prints (2021) arXiv:2105.13400.

K. Nyland, J. Marvil, J. M. Wrobel, L. M. Young, B. A. Zauderer, The Intermediate-mass Black Hole Candidate in the Center of NGC 404: New Evidence from Radio Continuum Observations, Astrophysical Journal 753 (2012) 103.

L. J. Latimer, A. E. Reines, R. M. Plotkin, T. D. Russell, J. J. Condon, An X-Ray + Radio Search for Massive Black Holes in Blue Compact Dwarf Galaxies, Astrophysical Journal 884 (2019) 78.

A. E. Reines, J. J. Condon, J. Darling, J. E. Greene, A New Sample of (Wandering) Massive Black Holes in Dwarf Galaxies from High-resolution Radio Observations, Astrophysical Journal 888 (2020) 36.

B. A. Groves, T. M. Heckman, G. Kauffmann, Emission-line diagnostics of low-metallicity active galactic nuclei, Monthly Notices of the RAS 371 (2006) 1559–1569.

J. M. Cann, S. Satyapal, N. P. Abel et al., The Limitations of Optical Spectroscopic Diagnostics in Identifying Active Galactic Nuclei in the Low-mass Regime, Astrophysical Journal, Letters 870 (2019) L2.

B. P. Miller, E. Gallo, J. E. Greene et al., X-Ray Constraints on the Local Supermassive Black Hole Occupation Fraction, Astrophysical Journal 799 (2015) 98.

R. She, L. C. Ho, H. Feng, Chandra Survey of Nearby Galaxies: A Significant Population of Candidate Central Black Holes in Late-type Galaxies, Astrophysical Journal 842 (2017) 131.

V. F. Baldassare, M. Geha, J. Greene, Identifying AGNs in Low-mass Galaxies via Long-term Optical Variability, Astrophysical Journal 868 (2018) 152.

V. F. Baldassare, M. Geha, J. Greene, A Search for Optical AGN Variability in 35,000 Low-mass Galaxies with the Palomar Transient Factory, Astrophysical Journal 896 (2020) 10.

C. Ward, S. Gezari, S. Frederick et al., AGNs on the Move: A Search for Off-nuclear AGNs from Recoiling Supermassive Black Holes and Ongoing Galaxy Mergers with the Zwicky Transient Facility, Astrophysical Journal 913 (2021) 102.

A. Einstein, Näherungsweise Integration der Feldgleichungen der Gravitation, Sitzungsberichte der Königlich Preußischen Akademie der Wissenschaften (Berlin (1916) 688–696.

A. Einstein, Über Gravitationswellen, Sitzungsberichte der Königlich Preußischen Akademie der Wissenschaften (Berlin (1918) 154–167.

B. P. Abbott, R. Abbott, T. D. Abbott et al. (LIGO Scientific Collaboration and Virgo Collaboration), Observation of gravitational waves from a binary black hole merger, Phys. Rev. Lett. 116 (2016) 061102.

R. Abbott, T. D. Abbott, S. Abraham et al., GW190521: A Binary Black Hole Merger with a Total Mass of 150 $M_\odot$, Physical Review Letters 125 (2020a) 101102.

R. Abbott, T. D. Abbott, S. Abraham et al., Properties and Astrophysical Implications of the 150 $M_\odot$ Binary Black Hole Merger GW190521, Astrophysical Journal, Letters 900 (2020b) L13.

M. Fishbach, V. Kalogera, Apples and Oranges: Comparing Black Holes in X-Ray Binaries and Gravitational-wave Sources, Astrophysical Journal, Letters 929 (2022) L26.

K. Belczynski, R. Hirschi, E. A. Kaiser et al., The Formation of a 70 $M_{\odot}$ Black Hole at High Metallicity, Astrophysical Journal 890 (2020) 113.

K. Belczynski, C. Done, J. P. Lasota, All Apples: Comparing black holes in X-ray binaries and gravitational-wave sources, arXiv e-prints (2021) arXiv:2111.09401.

W. H. Press, Long Wave Trains of Gravitational Waves from a Vibrating Black Hole, Astrophysical Journal, Letters 170 (1971) L105.

P. Amaro-Seoane, H. Audley, S. Babak et al., Laser Interferometer Space Antenna, arXiv e-prints (2017) arXiv:1702.00786.

M. C. Miller, Intermediate-mass black holes as LISA sources, Classical and Quantum Gravity 26 (2009) 094031.

K. Jani, D. Shoemaker, C. Cutler, Detectability of intermediate-mass black holes in multiband gravitational wave astronomy, Nature Astronomy 4 (2020) 260–265.

F. Pacucci, A. Loeb, The search for the farthest quasar: consequences for black hole growth and seed models, Monthly Notices of the RAS 509 (2022) 1885–1891.

R. Sánchez-Janssen, P. Côté, L. Ferrarese et al., The Next Generation Virgo Cluster Survey. XXIII. Fundamentals of Nuclear Star Clusters over Seven Decades in Galaxy Mass, Astrophysical Journal 878 (2019) 18.

S. van Wassenhove, M. Volonteri, M. G. Walker, J. R. Gair, Massive black holes lurking in Milky Way satellites, Monthly Notices of the RAS 408 (2010) 1139–1146.

A. H. Wright, A. S. G. Robotham, S. P. Driver et al., Galaxy And Mass Assembly (GAMA): the galaxy stellar mass function to z = 0.1 from the r-band selected equatorial regions, Monthly Notices of the RAS 470 (2017) 283–302.

N. Düchting, Supermassive black holes from primordial black hole seeds, Physical Review D 70 (2004) 064015.

J. L. Bernal, A. Raccanelli, L. Verde, J. Silk, Signatures of primordial black holes as seeds of supermassive black holes, Journal of Cosmology and Astroparticle Physics 2018 (2018) 017.

N. Cappelluti, G. Hasinger, P. Natarajan, Exploring the High-redshift PBH-ΛCDM Universe: Early Black Hole Seeding, the First Stars and Cosmic Radiation Backgrounds, Astrophysical Journal 926 (2022) 205.

S. L. O'Dell, R. J. Brissenden, W. N. Davis et al., High-resolution x-ray telescopes, in: A. M. Khounsary, S. L. O'Dell, S. R. Restaino (Eds.), Adaptive X-Ray Optics, volume 7803 of *Society of Photo-Optical Instrumentation Engineers (SPIE) Conference Series*, 2010, p. 78030H.

R. D. Saxton, O. König, M. Descalzo et al., HILIGT, upper limit servers I-Overview, Astronomy and Computing 38 (2022) 100531.

E. Pfeffermann, U. G. Briel, H. Hippmann et al., The focal plane instrumentation of the ROSAT Telescope, in: Soft X-ray optics and technology, volume 733 of *Society of Photo-Optical Instrumentation Engineers (SPIE) Conference Series*, 1987, p. 519.

E. Pfeffermann, U. G. Briel, M. J. Freyberg, Design and in-orbit-performance of the position sensitive proportional counter onboard the X-ray astronomy satellite ROSAT, Nuclear Instruments and Methods in Physics Research A 515 (2003) 65–69.

T. Boller, M. J. Freyberg, J. Trümper et al., Second ROSAT all-sky survey (2RXS) source catalogue, Astronomy and Astrophysics 588 (2016) A103.

M. C. Weisskopf, B. Brinkman, C. Canizares et al., An Overview of the Performance and Scientific Results from the Chandra X-Ray Observatory, Publications of the ASP 114 (2002) 1–24.

F. Jansen, D. Lumb, B. Altieri et al., XMM-Newton observatory. I. The spacecraft and operations, Astronomy and Astrophysics 365 (2001) L1–L6.

N. Gehrels et al., The Swift Gamma-Ray Burst Mission, ApJ 611 (2004) 1005–1020.

A. Merloni, P. Predehl, W. Becker et al., eROSITA Science Book: Mapping the Structure of the Energetic Universe, arXiv e-prints (2012) arXiv:1209.3114.

H. Brunner, T. Liu, G. Lamer et al., The eROSITA Final Equatorial Depth Survey (eFEDS). X-ray catalogue, Astronomy and Astrophysics 661 (2022) A1.

S. D. Barthelmy, Burst Alert Telescope (BAT) on the Swift MIDEX mission, in: K. A. Flanagan, O. H. W. Siegmund (Eds.), X-Ray and Gamma-Ray Instrumentation for Astronomy XIII, volume 5165 of *Society of Photo-Optical Instrumentation Engineers (SPIE) Conference Series*, 2004, pp. 175–189.

D. N. Burrows, J. E. Hill, J. A. Nousek et al., The Swift X-Ray Telescope, in: K. A. Flanagan, O. H. W. Siegmund (Eds.), X-Ray and Gamma-Ray Instrumentation for Astronomy XIII, volume 5165 of *Society of Photo-Optical Instrumentation Engineers (SPIE) Conference Series*, 2004, pp. 201–216.

P. W. A. Roming, T. E. Kennedy, K. O. Mason, J. A. Nousek, L. Ahr, R. E. Bingham, P. S. Broos, M. J. Carter, B. K. Hancock, H. E. Huckle, S. D. Hunsberger, H. Kawakami, R. Killough, T. S. Koch, M. K. McLelland, K. Smith, P. J. Smith, J. C. Soto, P. T. Boyd, A. A. Breeveld, S. T. Holland, M. Ivanushkina, M. S. Pryzby, M. D. Still, J. Stock, The Swift Ultra-Violet/Optical Telescope, Space Science Reviews 120 (2005) 95–142.

P. A. Evans, J. P. Osborne, A. P. Beardmore et al., 1SXPS: A Deep Swift X-Ray Telescope Point Source Catalog with Light Curves and Spectra, Astrophysical Journal, Supplement 210 (2014) 8.

S. Puccetti, M. Capalbi, P. Giommi et al., The Swift serendipitous survey in deep XRT GRB fields (SwiftFT). I. The X-ray catalog and number counts, Astronomy and Astrophysics 528 (2011) A122.

V. D'Elia, M. Perri, S. Puccetti et al., The seven year Swift-XRT point source catalog (1SWXRT), Astronomy and Astrophysics 551 (2013) A142.

P. A. Evans, K. L. Page, J. P. Osborne et al., 2SXPS: An Improved and Expanded Swift X-Ray Telescope Point-source Catalog, Astrophysical Journal, Supplement 247 (2020) 54.

Nasa High Energy Astrophysics Science Archive Research Center (Heasarc), HEAsoft: Unified Release of FTOOLS and XANADU, Astrophysics Source Code Library, record ascl:1408.004, 2014.

L. Strüder, U. Briel, K. Dennerl et al., The European Photon Imaging Camera on XMM-Newton: The pn-CCD camera, Astronomy and Astrophysics 365 (2001) L18–L26.

M. J. L. Turner, A. Abbey, M. Arnaud et al., The European Photon Imaging Camera on XMM-Newton: The MOS cameras, Astronomy and Astrophysics 365 (2001) L27–L35.

N. A. Webb, M. Coriat, I. Traulsen et al., The XMM-Newton serendipitous survey. IX. The fourth XMM-Newton serendipitous source catalogue, Astronomy and Astrophysics 641 (2020) A136.

M. G. Watson, J. L. Auguères, J. Ballet et al., The XMM-Newton Serendipitous Survey. I. The role of XMM-Newton Survey Science Centre, Astronomy and Astrophysics 365 (2001) L51–L59.

C. Gabriel, M. Denby, D. J. Fyfe et al., The XMM-Newton SAS - Distributed Development and Maintenance of a Large Science Analysis System: A Critical Analysis, in: F. Ochsenbein, M. G. Allen, D. Egret (Eds.), Astronomical Data Analysis Software and Systems (ADASS) XIII, volume 314 of *Astronomical Society of the Pacific Conference Series*, 2004, p. 759.

I. Pâris, P. Petitjean, É. Aubourg et al., The Sloan Digital Sky Survey Quasar Catalog: Fourteenth data release, Astronomy and Astrophysics 613 (2018) A51.

I. Traulsen, A. D. Schwope, G. Lamer et al., The XMM-Newton serendipitous survey. VIII. The first XMM-Newton serendipitous source catalogue from overlapping observations, Astronomy and Astrophysics 624 (2019) A77.

M. C. Weisskopf, H. D. Tananbaum, L. P. Van Speybroeck, S. L. O'Dell, Chandra X-ray Observatory (CXO): overview, in: J. E. Truemper, B. Aschenbach (Eds.), X-Ray Optics, Instruments, and Missions III, volume 4012 of *Society of Photo-Optical Instrumentation Engineers (SPIE) Conference Series*, 2000, pp. 2–16.

M. Markevitch, M. W. Bautz, B. Biller et al., Chandra Spectra of the Soft X-Ray Diffuse Background, Astrophysical Journal 583 (2003) 70–84.

M. Revnivtsev, A. Vikhlinin, S. Sazonov, Resolving the Galactic ridge X-ray background, Astronomy and Astrophysics 473 (2007) 857–862.

P. P. Plucinsky, A. Bogdan, H. L. Marshall, N. W. Tice, The complicated evolution of the ACIS contamination layer over the mission life of the Chandra X-ray Observatory, in: J.-W. A. den Herder, S. Nikzad, K. Nakazawa (Eds.), Space Telescopes and Instrumentation 2018: Ultraviolet to Gamma Ray, volume 10699 of *Society of Photo-Optical Instrumentation Engineers (SPIE) Conference Series*, 2018, p. 106996B.

I. N. Evans, F. A. Primini, K. J. Glotfelty et al., The Chandra Source Catalog, Astrophysical Journal, Supplement 189 (2010) 37–82.

I. N. Evans, C. Allen, C. S. Anderson et al., Chandra Source Catalog Release 2.0 - The State of the Art Serendipitous X-ray Source Catalog, in: AAS/High Energy Astrophysics Division, volume 17 of *AAS/High Energy Astrophysics Division*, 2019, p. 114.01.

J. D. Evans, M. Cresitello-Dittmar, S. Doe et al., The Chandra X-ray Center data system: supporting the mission of the Chandra X-ray Observatory, in: D. R. Silva, R. E. Doxsey (Eds.), Society of Photo-Optical Instrumentation Engineers (SPIE) Conference Series, volume 6270 of *Society of Photo-Optical Instrumentation Engineers (SPIE) Conference Series*, 2006, p. 62700N.

A. Fruscione, J. C. McDowell, G. E. Allen et al., CIAO: Chandra's data analysis system, in: D. R. Silva, R. E. Doxsey (Eds.), Society of Photo-Optical Instrumentation Engineers (SPIE) Conference Series, volume 6270 of *Society of Photo-Optical Instrumentation Engineers (SPIE) Conference Series*, 2006, p. 62701V.

P. A. Evans, K. L. Page, J. P. Osborne et al., 2SXPS: An Improved and Expanded Swift X-Ray Telescope Point-source Catalog, Astrophysical Journal, Supplement 247 (2020) 54.

M. B. Taylor, TOPCAT & STIL: Starlink Table/VOTable Processing Software, in: P. Shopbell, M. Britton, R. Ebert (Eds.), Astronomical Data Analysis Software and Systems XIV, volume 347 of *Astronomical Society of the Pacific Conference Series*, 2005, p. 29.

D. G. Monet, S. E. Levine, B. Canzian et al., The USNO-B Catalog, Astronomical Journal 125 (2003) 984–993.

Gaia Collaboration, T. Prusti, J. H. J. de Bruijne et al., The Gaia mission, Astronomy and Astrophysics 595 (2016) A1.

K. C. Chambers, E. A. Magnier, N. Metcalfe et al., The Pan-STARRS1 Surveys, arXiv e-prints (2016) arXiv:1612.05560.

R. M. Cutri, M. F. Skrutskie, S. van Dyk et al., 2MASS All Sky Catalog of point sources., 2003.

R. M. Cutri, et al., VizieR Online Data Catalog: AllWISE Data Release (Cutri+ 2013), VizieR Online Data Catalog (2014) II/328.

V. J. Mikles, S. S. Eikenberry, M. P. Muno, R. M. Bandyopadhyay, S. Patel, Identification of the Infrared Counterpart to a Newly Discovered X-Ray Source in the Galactic Center, Astrophysical Journal 651 (2006) 408–415.

Gaia Collaboration, A. G. A. Brown, A. Vallenari et al., Gaia Early Data Release 3. Summary of the contents and survey properties, Astronomy and Astrophysics 649 (2021) A1.

T. M. C. Abbott, F. B. Abdalla, S. Allam et al., The Dark Energy Survey: Data Release 1, Astrophysical Journal, Supplement 239 (2018) 18.

E. F. Schlafly, A. M. Meisner, G. M. Green, The unWISE Catalog: Two Billion Infrared Sources from Five Years of WISE Imaging, Astrophysical Journal, Supplement 240 (2019) 30.

M. Salvato, J. Buchner, T. Budavári et al., Finding counterparts for all-sky X-ray surveys with NWAY: a Bayesian algorithm for cross-matching multiple catalogues, Monthly Notices of the RAS 473 (2018) 4937–4955.

C. A. L. Bailer-Jones, J. Rybizki, M. Fouesneau, M. Demleitner, R. Andrae, Estimating Distances from Parallaxes. V. Geometric and Photogeometric Distances to 1.47 Billion Stars in Gaia Early Data Release 3, Astronomical Journal 161 (2021) 147.

G. Dálya, G. Galgóczi, L. Dobos et al., GLADE: A galaxy catalogue for multimessenger searches in the advanced gravitational-wave detector era, Monthly Notices of the RAS 479 (2018) 2374–2381.

G. Paturel, C. Petit, P. Prugniel et al., HYPERLEDA. I. Identification and designation of galaxies, Astronomy and Astrophysics 412 (2003) 45–55.

K. Kovlakas, A. Zezas, J. J. Andrews et al., The Heraklion Extragalactic Catalogue (HECATE): a value-added galaxy catalogue for multimessenger astrophysics, Monthly Notices of the RAS 506 (2021) 1896–1915.

M. F. Skrutskie, R. M. Cutri, R. Stiening et al., The Two Micron All Sky Survey (2MASS), Astronomical Journal 131 (2006) 1163–1183.

D. J. White, E. J. Daw, V. S. Dhillon, A list of galaxies for gravitational wave searches, Classical and Quantum Gravity 28 (2011) 085016.

G. Dálya, R. Díaz, F. R. Bouchet et al., GLADE+ : an extended galaxy catalogue for multimessenger searches with advanced gravitational-wave detectors, Monthly Notices of the RAS 514 (2022) 1403–1411.

H. Goddard, L. Shamir, A Catalog of Broad Morphology of Pan-STARRS Galaxies Based on Deep Learning, Astrophysical Journal, Supplement 251 (2020) 28.

M. E. Cluver, T. H. Jarrett, D. A. Dale et al., Calibrating Star Formation in WISE Using Total Infrared Luminosity, Astrophysical Journal 850 (2017) 68.

R. C. Kennicutt, N. J. Evans, Star Formation in the Milky Way and Nearby Galaxies, Annual Review of Astron and Astrophys 50 (2012) 531–608.

R. M. Cutri, et al., VizieR Online Data Catalog: WISE All-Sky Data Release (Cutri+ 2012), VizieR Online Data Catalog (2012) II/311.

F. Galliano, M. Galametz, A. P. Jones, The Interstellar Dust Properties of Nearby Galaxies, Annual Review of Astron and Astrophys 56 (2018) 673–713.

M. P. Véron-Cetty, P. Véron, A catalogue of quasars and active nuclei: 13th edition, Astronomy and Astrophysics 518 (2010) A10.

N. V. Kharchenko, S. Roeser, VizieR Online Data Catalog: All-Sky Compiled Catalogue of 2.5 million stars (Kharchenko+ 2009), VizieR Online Data Catalog (2009) I/280B.

R. A. Downes, R. F. Webbink, M. M. Shara et al., A Catalog and Atlas of Cataclysmic Variables: The Final Edition, Journal of Astronomical Data 11 (2005) 2.

H. Ritter, U. Kolb, The Ritter-Kolb Catalogue and its Impact on Research into CVs, LMXBs and related Objects, Acta Polytechnica CTU Proceedings 2 (2015) 21–25.

Q. Z. Liu, J. van Paradijs, E. P. J. van den Heuvel, A catalogue of low-mass X-ray binaries in the Galaxy, LMC, and SMC (Fourth edition), Astronomy and Astrophysics 469 (2007) 807–810.

A. Kundu, T. J. Maccarone, S. E. Zepf, Probing the Formation of Low-Mass X-Ray Binaries in Globular Clusters and the Field, Astrophysical Journal 662 (2007) 525–543.

P. J. Humphrey, D. A. Buote, Low-Mass X-Ray Binaries and Globular Clusters in Early-Type Galaxies. I. Chandra Observations, Astrophysical Journal 689 (2008) 983–1004.

Z. Zhang, M. Gilfanov, R. Voss et al., Luminosity functions of LMXBs in different stellar environments, Astronomy and Astrophysics 533 (2011) A33.

Q. Z. Liu, J. van Paradijs, E. P. J. van den Heuvel, Catalogue of high-mass X-ray binaries in the Galaxy (4th edition), Astronomy and Astrophysics 455 (2006) 1165–1168.

S. Sazonov, I. Khabibullin, Bright end of the luminosity function of high-mass X-ray binaries: contributions of hard, soft and supersoft sources, Monthly Notices of the RAS 466 (2017) 1019–1051.

J. M. Corral-Santana, J. Casares, T. Muñoz-Darias et al., BlackCAT: A catalogue of stellar-mass black holes in X-ray transients, Astronomy and Astrophysics 587 (2016) A61.

B. E. Tetarenko, G. R. Sivakoff, C. O. Heinke, J. C. Gladstone, WATCHDOG: A Comprehensive All-sky Database of Galactic Black Hole X-ray Binaries, Astrophysical Journal, Supplement 222 (2016) 15.

A. Moretti, S. Campana, D. Lazzati, G. Tagliaferri, The Resolved Fraction of the Cosmic X-Ray Background, Astrophysical Journal 588 (2003) 696–703.

S. W. Allen, R. W. Schmidt, A. C. Fabian, H. Ebeling, Cosmological constraints from the local X-ray luminosity function of the most X-ray-luminous galaxy clusters, Monthly Notices of the RAS 342 (2003) 287–298.

H. Tranin, O. Godet, N. Webb, D. Primorac, Probabilistic classification of X-ray sources applied to Swift-XRT and XMM-Newton catalogs, Astronomy and Astrophysics 657 (2022) A138.

M. Henze, W. Pietsch, F. Haberl, M. Middleton, Nova M31N 2012-05c found as a supersoft X-ray source with XMM-Newton, The Astronomer's Telegram 4511 (2012) 1.

P. Zhou, Y. Chen, X.-D. Li et al., Discovery of the Transient Magnetar 3XMM J185246.6+003317 near Supernova Remnant Kesteven 79 with XMM-Newton, Astrophysical Journal, Letters 781 (2014) L16.

K. K. Lo, S. Farrell, T. Murphy, B. M. Gaensler, Automatic Classification of Time-variable X-Ray Sources, Astrophysical Journal 786 (2014) 20.

D. Lin, N. A. Webb, D. Barret, Classification of X-Ray Sources in the XMM-Newton Serendipitous Source Catalog: Objects of Special Interest, Astrophysical Journal 780 (2014) 39.

F. Haberl, W. Pietsch, A ROSAT PSPC catalogue of X-ray sources in the LMC region, Astronomy and Astrophysics, Supplement 139 (1999) 277–295.

A. H. Prestwich, J. A. Irwin, R. E. Kilgard et al., Classifying X-Ray Sources in External Galaxies from X-Ray Colors, Astrophysical Journal 595 (2003) 719–726.

F. X. Pineau, C. Motch, F. Carrera et al., Cross-correlation of the 2XMMi catalogue with Data Release 7 of the Sloan Digital Sky Survey, Astronomy and Astrophysics 527 (2011) A126.

T. A. McGlynn, A. A. Suchkov, E. L. Winter et al., Automated Classification of ROSAT Sources Using Heterogeneous Multiwavelength Source Catalogs, Astrophysical Journal 616 (2004) 1284–1300.

S. A. Farrell, T. Murphy, K. K. Lo, Autoclassification of the Variable 3XMM Sources Using the Random Forest Machine Learning Algorithm, Astrophysical Journal 813 (2015) 28.

L. Breiman, Random Forests., Machine Learning 45 (2001) 5–32.

R. M. Arnason, P. Barmby, N. Vulic, Identifying new X-ray binary candidates in M31 using random forest classification, Monthly Notices of the RAS 492 (2020) 5075–5088.

F. X. Pineau, S. Derriere, C. Motch et al., Probabilistic multi-catalogue positional cross-match, Astronomy and Astrophysics 597 (2017) A89.

M. G. Watson, A. C. Schröder, D. Fyfe et al., The XMM-Newton serendipitous survey. V. The Second XMM-Newton serendipitous source catalogue, Astronomy and Astrophysics 493 (2009) 339–373.

F. X. Pineau, S. Derriere, L. Michel, C. Motch, Statistical Identification of 2XMMi Sources, in: D. A. Bohlender, D. Durand, P. Dowler (Eds.), Astronomical Data Analysis Software and Systems XVIII, volume 411 of *Astronomical Society of the Pacific Conference Series*, 2009, p. 259.

D. Primorac, Identification of the 1sxps catalog sources discovered by the swift-xrt, 2015.

I. N. Evans, F. A. Primini, K. J. Glotfelty et al., The Chandra Source Catalog, Astrophysical Journal, Supplement 189 (2010) 37–82.

G. Dalya, Z. Frei, G. Galgoczi, P. Raffai, R. S. de Souza, VizieR Online Data Catalog: GLADE catalog (Dalya+, 2016), VizieR Online Data Catalog (2016) VII/275.

I. Traulsen, A. D. Schwope, G. Lamer et al., The XMM-Newton serendipitous survey. X. The second source catalogue from overlapping XMM-Newton observations and its long-term variable content, Astronomy and Astrophysics 641 (2020) A137.

S. Allak, A. Akyuz, İ. Akkaya Oralhan et al., The transient ultraluminous X-ray source, ULX-4, in M51, Monthly Notices of the RAS 510 (2022) 4355–4369.

A. J. Izenman, Review papers: Recent developments in nonparametric density estimation, Journal of the American Statistical Association 86 (1991) 205–224.

S. J. Sheather, Density estimation, Statistical science (2004) 588–597.

Z. I. Botev, J. F. Grotowski, D. P. Kroese, Kernel density estimation via diffusion, arXiv e-prints (2010) arXiv:1011.2602.

B. W. Silverman, Density estimation for statistics and data analysis, volume 26, CRC press, 1986.

S. Raschka, Naive bayes and text classification i - introduction and theory, 2017.

K. P. Murphy, et al., Naive bayes classifiers, University of British Columbia 18 (2006) 60.

R. Storn, K. Price, Differential evolution–a simple and efficient heuristic for global optimization over continuous spaces, Journal of global optimization 11 (1997) 341–359.

V. Lukic, M. Brüggen, J. K. Banfield et al., Radio Galaxy Zoo: compact and extended radio source classification with deep learning, Monthly Notices of the RAS 476 (2018) 246–260.

M. Nikołajuk, R. Walter, Tidal disruption of a super-Jupiter by a massive black hole, Astronomy and Astrophysics 552 (2013) A75.

A. E. Truebenbach, J. Darling, The invisible AGN catalogue: a mid-infrared-radio selection method for optically faint active galactic nuclei, Monthly Notices of the RAS 468 (2017) 196–206.

J.-C. Guo, J.-F. Liu, S. Wang, Y. Wu, Y.-X. Qin, An active M star with X-ray double flares disguised as an ultra-luminous X-ray source, Research in Astronomy and Astrophysics 16 (2016) 34.

N. Secrest, J. Frouard, G. Hennessy, Quasar selection techniques going into the Gaia era, in: C. Bizouard (Ed.), Astrometry, Earth Rotation, and Reference Systems in the GAIA era, 2020, pp. 15–19.

C. J. Lintott, K. Schawinski, A. Slosar et al., Galaxy Zoo: morphologies derived from visual inspection of galaxies from the Sloan Digital Sky Survey, Monthly Notices of the RAS 389 (2008) 1179–1189.

C. Lintott, K. Schawinski, S. Bamford et al., Galaxy Zoo 1: data release of morphological classifications for nearly 900 000 galaxies, Monthly Notices of the RAS 410 (2011) 166–178.

C. Cardamone, K. Schawinski, M. Sarzi et al., Galaxy Zoo Green Peas: discovery of a class of compact extremely star-forming galaxies, Monthly Notices of the RAS 399 (2009) 1191–1205.

Y. I. Izotov, N. G. Guseva, T. X. Thuan, Green Pea Galaxies and Cohorts: Luminous Compact Emission-line Galaxies in the Sloan Digital Sky Survey, Astrophysical Journal 728 (2011) 161.

F. Bonnarel, P. Fernique, O. Bienaymé et al., The ALADIN interactive sky atlas. A reference tool for identification of astronomical sources, Astronomy and Astrophysics, Supplement 143 (2000) 33–40.

T. Boch, P. Fernique, Aladin Lite: Embed your Sky in the Browser, in: N. Manset, P. Forshay (Eds.), Astronomical Data Analysis Software and Systems XXIII, volume 485 of *Astronomical Society of the Pacific Conference Series*, 2014, p. 277.

A. C. Fabian, Observational Evidence of Active Galactic Nuclei Feedback, Annual Review of Astron and Astrophys 50 (2012) 455–489.

Z. Haiman, The Formation of the First Massive Black Holes, in: T. Wiklind, B. Mobasher, V. Bromm (Eds.), The First Galaxies, volume 396 of *Astrophysics and Space Science Library*, 2013, p. 293.

D. A. Swartz, K. K. Ghosh, A. F. Tennant, K. Wu, The Ultraluminous X-Ray Source Population from the Chandra Archive of Galaxies, Astrophysical Journal, Supplement 154 (2004) 519–539.

Q. Z. Liu, I. F. Mirabel, A catalogue of ultraluminous X-ray sources in external galaxies, Astronomy and Astrophysics 429 (2005) 1125–1129.

H. P. Earnshaw, T. P. Roberts, M. J. Middleton, D. J. Walton, S. Mateos, A new, clean catalogue of extragalactic non-nuclear X-ray sources in nearby galaxies, Monthly Notices of the RAS 483 (2019) 5554–5573.

K. Kovlakas, A. Zezas, J. J. Andrews et al., A census of ultraluminous X-ray sources in the local Universe, Monthly Notices of the RAS 498 (2020) 4790–4810.

Y. Inoue, K. Yabe, Y. Ueda, A fundamental plane in X-ray binary activity of external galaxies, Publications of the ASJ 73 (2021) 1315–1332.

D. J. Walton, A. D. A. Mackenzie, H. Gully et al., A multimission catalogue of ultraluminous X-ray source candidates, Monthly Notices of the RAS 509 (2022) 1587–1604.

G. de Vaucouleurs, A. de Vaucouleurs, J. Corwin et al., Herold G. et al., Third Reference Catalogue of Bright Galaxies, 1991.

I. D. Karachentsev, V. E. Karachentseva, W. K. Huchtmeier, D. I. Makarov, A Catalog of Neighboring Galaxies, Astronomical Journal 127 (2004) 2031–2068.

A. Wolter, P. Esposito, M. Mapelli, F. Pizzolato, E. Ripamonti, NGC 2276: a remarkable galaxy with a large number of ultraluminous X-ray sources, Monthly Notices of the RAS 448 (2015) 781–791.

P. G. Jonker, M. Heida, M. A. P. Torres et al., The Nature of the Bright ULX X-2 in NGC 3921: A Chandra Position and HST Candidate Counterpart, Astrophysical Journal 758 (2012) 28.

F. Ochsenbein, P. Bauer, J. Marcout, The VizieR database of astronomical catalogues, Astronomy and Astrophysics, Supplement 143 (2000) 23–32.

Gaia Collaboration, A. G. A. Brown, A. Vallenari et al., Gaia Early Data Release 3. Summary of the contents and survey properties, Astronomy and Astrophysics 649 (2021) A1.

T. M. C. Abbott, F. B. Abdalla, S. Allam et al., The Dark Energy Survey: Data Release 1, Astrophysical Journal, Supplement 239 (2018) 18.

A. S. Bolton, D. J. Schlegel, É. Aubourg et al., Spectral Classification and Redshift Measurement for the SDSS-III Baryon Oscillation Spectroscopic Survey, Astronomical Journal 144 (2012) 144.

R. Beck, L. Dobos, T. Budavári, A. S. Szalay, I. Csabai, Photometric redshifts for the SDSS Data Release 12, Monthly Notices of the RAS 460 (2016) 1371–1381.

P. Tarrío, S. Zarattini, Photometric redshifts for the Pan-STARRS1 survey, Astronomy and Astrophysics 642 (2020) A102.

H. Zou, J. Sui, S. Xue et al., Photometric Redshifts and Galaxy Clusters for DES DR2, DESI DR9, and HSC-SSP PDR3 Data, Research in Astronomy and Astrophysics 22 (2022) 065001.

Gaia Collaboration, C. A. L. Bailer-Jones, D. Teyssier et al., Gaia Data Release 3: The extragalactic content, arXiv e-prints (2022) arXiv:2206.05681.

R. M. Sambruna, M. Gliozzi, F. Tavecchio, L. Maraschi, L. Foschini, The Jet-Disk Connection in AGNs: Chandra and XMM-Newton Observations of Three Powerful Radio-Loud Quasars, Astrophysical Journal 652 (2006) 146–156.

A. R. Martel, W. B. Sparks, D. Macchetto et al., Discovery of an Optical Synchrotron Jet in 3C 15, Astrophysical Journal 496 (1998) 203–209.

J. Kataoka, J. P. Leahy, P. G. Edwards et al., Chandra discovery of an X-ray jet and lobes in 3C 15, Astronomy and Astrophysics 410 (2003) 833–845.

R. Urquhart, R. Soria, Optically thick outflows in ultraluminous supersoft sources, Monthly Notices of the RAS 456 (2016) 1859–1880.

S. K. Leggett, M. R. S. Hawkins, The infrared luminosity function for low-mass stars., Monthly Notices of the RAS 234 (1988) 1065–1090.

R. S. Stobie, K. Ishida, J. A. Peacock, Distance errors and the stellar luminosity function., Monthly Notices of the RAS 238 (1989) 709–727.

P. Kroupa, Unification of the nearby and photometric stellar luminosity functions, Astrophysical Journal 453 (1995) 358.

B. Binggeli, A. Sandage, G. A. Tammann, The luminosity function of galaxies., Annual Review of Astron and Astrophys 26 (1988) 509–560.

J. Loveday, B. A. Peterson, G. Efstathiou, S. J. Maddox, The Stromlo–APM Redshift Survey. I. The Luminosity Function and Space Density of Galaxies, Astrophysical Journal 390 (1992) 338.

R. J. Bouwens, G. D. Illingworth, P. A. Oesch et al., Ultraviolet Luminosity Functions from 132 z $\sim$7 and z $\sim$8 Lyman-break Galaxies in the Ultra-deep HUDF09 and Wide-area Early Release Science WFC3/IR Observations, Astrophysical Journal 737 (2011) 90.

D. Lynden-Bell, A method of allowing for known observational selection in small samples applied to 3CR quasars, Monthly Notices of the RAS 155 (1971) 95.

Y. Ueda, M. Akiyama, K. Ohta, T. Miyaji, Cosmological Evolution of the Hard X-Ray Active Galactic Nucleus Luminosity Function and the Origin of the Hard X-Ray Background, Astrophysical Journal 598 (2003) 886–908.

D.-W. Kim, G. Fabbiano, X-ray Properties of Young Early-type Galaxies. I. X-ray Luminosity Function of Low-mass X-ray Binaries, Astrophysical Journal 721 (2010) 1523–1530.

A. R. King, M. B. Davies, M. J. Ward, G. Fabbiano, M. Elvis, Ultraluminous X-Ray Sources in External Galaxies, Astrophysical Journal, Letters 552 (2001) L109–L112.

M. Gilfanov, H. J. Grimm, R. Sunyaev, L_X-SFR relation in star-forming galaxies, Monthly Notices of the RAS 347 (2004) L57–L60.

D. A. Swartz, R. Soria, A. F. Tennant, Do Ultraluminous X-Ray Sources Exist in Dwarf Galaxies?, Astrophysical Journal 684 (2008) 282–286.

K. Anastasopoulou, A. Zezas, V. Gkiokas, K. Kovlakas, Do sub-galactic regions follow the galaxy-wide X-ray scaling relations? The example of NGC 3310 and NGC 2276, Monthly Notices of the RAS 483 (2019) 711–733.

B. D. Lehmer, R. T. Eufrasio, A. Basu-Zych et al., The Metallicity Dependence of the High-mass X-Ray Binary Luminosity Function, Astrophysical Journal 907 (2021) 17.

R. A. Remillard, J. E. McClintock, X-Ray Properties of Black-Hole Binaries, Annual Review of Astron and Astrophys 44 (2006) 49–92.

R. Narayan, A. SaÌ§dowski, R. Soria, Spectra of black hole accretion models of ultraluminous X-ray sources, Monthly Notices of the RAS 469 (2017) 2997–3014.

J.-F. Liu, J. N. Bregman, Y. Bai, S. Justham, P. Crowther, Puzzling accretion onto a black hole in the ultraluminous X-ray source M 101 ULX-1, Nature 503 (2013) 500–503.

R. F. Shen, R. Barniol Duran, E. Nakar, T. Piran, The nature of ULX source M101 X-1: optically thick outflow from a stellar mass black hole., Monthly Notices of the RAS 447 (2015) L60–L64.

B. J. McLean, G. R. Greene, M. G. Lattanzi, B. Pirenne, The Status of the Second Generation Digitized Sky Survey and Guide Star Catalog, in: N. Manset, C. Veillet, D. Crabtree (Eds.), Astronomical Data Analysis Software and Systems IX, volume 216 of *Astronomical Society of the Pacific Conference Series*, 2000, p. 145.

R. F. Mushotzky, L. L. Cowie, A. J. Barger, K. A. Arnaud, Resolving the extragalactic hard X-ray background, Nature 404 (2000) 459–464.

A. Georgakakis, K. Nandra, E. S. Laird, J. Aird, M. Trichas, A new method for determining the sensitivity of X-ray imaging observations and the X-ray number counts, Monthly Notices of the RAS 388 (2008) 1205–1213.

M. Kim, B. J. Wilkes, D.-W. Kim et al., Chandra Multiwavelength Project X-Ray Point Source Number Counts and the Cosmic X-Ray Background, Astrophysical Journal 659 (2007) 29–51.

R. Soria, M. Kolehmainen, A. W. Graham et al., A Chandra Virgo cluster survey of spiral galaxies - I. Introduction to the survey and a new ULX sample, Monthly Notices of the RAS 512 (2022) 3284–3311.

B. D. Lehmer, R. T. Eufrasio, P. Tzanavaris et al., X-Ray Binary Luminosity Function Scaling Relations for Local Galaxies Based on Subgalactic Modeling, Astrophysical Journal, Supplement 243 (2019) 3.

C. Allende Prieto, D. L. Lambert, M. Asplund, The Forbidden Abundance of Oxygen in the Sun, Astrophysical Journal, Letters 556 (2001) L63–L66.

T. Maccacaro, I. M. Gioia, A. Wolter, G. Zamorani, J. T. Stocke, The X-Ray Spectra of the Extragalactic Sources in the Einstein Extended Medium-Sensitivity Survey, Astrophysical Journal 326 (1988) 680.

S. Jester, D. P. Schneider, G. T. Richards et al., The Sloan Digital Sky Survey View of the Palomar-Green Bright Quasar Survey, Astronomical Journal 130 (2005) 873–895.

A. Marconi, G. Risaliti, R. Gilli et al., Local supermassive black holes, relics of active galactic nuclei and the X-ray background, Monthly Notices of the RAS 351 (2004) 169–185.

E. F. Bell, D. H. McIntosh, N. Katz, M. D. Weinberg, The Optical and Near-Infrared Properties of Galaxies. I. Luminosity and Stellar Mass Functions, Astrophysical Journal, Supplement 149 (2003) 289–312.

A. E. Reines, M. Volonteri, Relations between Central Black Hole Mass and Total Galaxy Stellar Mass in the Local Universe, Astrophysical Journal 813 (2015) 82.

G. van de Ven, R. C. E. van den Bosch, E. K. Verolme, P. T. de Zeeuw, The dynamical distance and intrinsic structure of the globular cluster ω Centauri, Astronomy and Astrophysics 445 (2006) 513–543.

V. F. Baldassare, A. E. Reines, E. Gallo, J. E. Greene, X-ray and Ultraviolet Properties of AGNs in Nearby Dwarf Galaxies, Astrophysical Journal 836 (2017) 20.

H. Gong, J. Liu, T. Maccarone, An Extreme Luminous X-ray Source Catalog Based on Chandra ACIS Observations, Astrophysical Journal, Supplement 222 (2016) 12.

L. Tao, H. Feng, F. Grisé, P. Kaaret, Compact Optical Counterparts of Ultraluminous X-Ray Sources, Astrophysical Journal 737 (2011) 81.

M. Mezcua, Dwarf galaxies might not be the birth sites of supermassive black holes, Nature Astronomy 3 (2019) 6–7.

M. S. Polimera, S. J. Kannappan, C. T. Richardson et al., RESOLVE and ECO: Finding Low-metallicity z 0 Dwarf AGN Candidates Using Optimized Emission-line Diagnostics, Astrophysical Journal 931 (2022) 44.

A. E. Reines, G. R. Sivakoff, K. E. Johnson, C. L. Brogan, An actively accreting massive black hole in the dwarf starburst galaxy Henize2-10, Nature 470 (2011) 66–68.

A. J. Sargent, M. C. Johnson, A. E. Reines et al., Wandering Black Hole Candidates in Dwarf Galaxies at VLBI Resolution, Astrophysical Journal 933 (2022) 160.

E. Gallo, T. Treu, J. Jacob et al., AMUSE-Virgo. I. Supermassive Black Holes in Low-Mass Spheroids, Astrophysical Journal 680 (2008) 154–168.

M. Schramm, J. D. Silverman, J. E. Greene et al., Unveiling a Population of Galaxies Harboring Low-mass Black Holes with X-Rays, Astrophysical Journal 773 (2013) 150.

K. Pardo, A. D. Goulding, J. E. Greene et al., X-Ray Detected Active Galactic Nuclei in Dwarf Galaxies at $0 < z < 1$, Astrophysical Journal 831 (2016) 203.

K. L. Birchall, M. G. Watson, J. Aird, X-ray detected AGN in SDSS dwarf galaxies, Monthly Notices of the RAS 492 (2020) 2268–2284.

L. J. Latimer, A. E. Reines, A. Bogdan, R. Kraft, The AGN Fraction in Dwarf Galaxies from eROSITA: First Results and Future Prospects, Astrophysical Journal, Letters 922 (2021) L40.

A. A. Nucita, L. Manni, F. De Paolis, M. Giordano, G. Ingrosso, A Catalog Sample of Low-mass Galaxies Observed in X-Rays with Central Candidate Black Holes, Astrophysical Journal 837 (2017) 66.

B. D. Lehmer, A. R. Basu-Zych, S. Mineo et al., The Evolution of Normal Galaxy X-Ray Emission through Cosmic History: Constraints from the 6 MS Chandra Deep Field-South, Astrophysical Journal 825 (2016) 7.

M. Mezcua, M. Kim, L. C. Ho, C. J. Lonsdale, The extended radio jet of an off-nuclear low-mass AGN in NGC 5252, Monthly Notices of the RAS 480 (2018) L74–L78.

X. Yang, J. Yang, Z. Paragi et al., NGC 5252: a pair of radio-emitting active galactic nuclei?, Monthly Notices of the RAS 464 (2017) L70–L74.

X. Yang, S. Yao, J. Yang et al., Radio Activity of Supermassive Black Holes with Extremely High Accretion Rates, Astrophysical Journal 904 (2020) 200.

E. F. Bell, Estimating Star Formation Rates from Infrared and Radio Luminosities: The Origin of the Radio-Infrared Correlation, Astrophysical Journal 586 (2003) 794–813.

P. Schechter, An analytic expression for the luminosity function for galaxies., Astrophysical Journal 203 (1976) 297–306.

R. P. Norris, J. Afonso, P. N. Appleton et al., Deep ATLAS Radio Observations of the Chandra Deep Field-South/Spitzer Wide-Area Infrared Extragalactic Field, Astronomical Journal 132 (2006) 2409–2423.

J. M. Bellovary, S. Hayoune, K. Chafla et al., The origins of off-centre massive black holes in dwarf galaxies, Monthly Notices of the RAS 505 (2021) 5129–5141.

V. Parkash, M. J. I. Brown, T. H. Jarrett, N. J. Bonne, Relationships between HI Gas Mass, Stellar Mass, and the Star Formation Rate of HICAT+WISE (H I-WISE) Galaxies, Astrophysical Journal 864 (2018) 40.

P. van Dokkum, S. Danieli, A. Romanowsky, R. Abraham, C. Conroy, The Distance to NGC 1042 in the Context of its Proposed Association with the Dark Matter-deficient Galaxies NGC 1052-DF2 and NGC 1052-DF4, Research Notes of the American Astronomical Society 3 (2019) 29.

T. X. Thuan, F. E. Bauer, P. Papaderos, Y. I. Izotov, Chandra Observations of the Three Most Metal Deficient Blue Compact Dwarf Galaxies Known in the Local Universe, SBS 0335-052, SBS 0335-052W, and I Zw 18, Astrophysical Journal 606 (2004) 213–220.

P. Kaaret, J. Schmitt, M. Gorski, X-Rays from Blue Compact Dwarf Galaxies, Astrophysical Journal 741 (2011) 10.

G. Somers, S. Mathur, P. Martini et al., Discovery of a Large Population of Ultraluminous X-Ray Sources in the Bulgeless Galaxies NGC 337 and ESO 501-23, Astrophysical Journal 777 (2013) 7.

S. Avdan, A. Akyuz, A. Vinokurov et al., Optical Counterparts of ULXs and Their Host Environments in NGC 4490/4485, Astrophysical Journal 875 (2019) 68.

L. M. Oskinova, A. Bik, J. M. Mas-Hesse et al., ULX contribution to stellar feedback: an intermediate-mass black hole candidate and the population of ULXs in the low-metallicity starburst galaxy ESO 338-4, Astronomy and Astrophysics 627 (2019) A63.

T. Kettlety, J. Hesling, S. Phillipps et al., Galaxy and mass assembly (GAMA): the consistency of GAMA and WISE derived mass-to-light ratios, Monthly Notices of the RAS 473 (2018) 776–783.

V. Bonjean, N. Aghanim, P. Salomé et al., Star formation rates and stellar masses from machine learning, Astronomy and Astrophysics 622 (2019) A137.

B. H. Andrews, P. Martini, The Mass-Metallicity Relation with the Direct Method on Stacked Spectra of SDSS Galaxies, Astrophysical Journal 765 (2013) 140.

M. Mapelli, E. Ripamonti, L. Zampieri, M. Colpi, A. Bressan, Ultra-luminous X-ray sources and remnants of massive metal-poor stars, Monthly Notices of the RAS 408 (2010) 234–253.

M. Brorby, P. Kaaret, A. Prestwich, X-ray binary formation in low-metallicity blue compact dwarf galaxies, Monthly Notices of the RAS 441 (2014) 2346–2353.

N. Gehrels, Confidence Limits for Small Numbers of Events in Astrophysical Data, Astrophysical Journal 303 (1986) 336.

M. Brorby, P. Kaaret, A. Prestwich, I. F. Mirabel, Enhanced X-ray emission from Lyman break analogues and a possible L_X-SFR-metallicity plane, Monthly Notices of the RAS 457 (2016) 4081–4088.

M. Mezcua, Feeding and feedback from little monsters: AGN in dwarf galaxies, in: T. Storchi Bergmann, W. Forman, R. Overzier, R. Riffel (Eds.), Galaxy Evolution and Feedback across Different Environments, volume 359, 2021, pp. 238–242.

M. Mezcua, H. Domínguez Sánchez, Hidden AGNs in Dwarf Galaxies Revealed by MaNGA: Light Echoes, Off-nuclear Wanderers, and a New Broad-line AGN, Astrophysical Journal, Letters 898 (2020) L30.

J. W. Montano, H. Guo, A. J. Barth et al., Optical Continuum Reverberation in the Dwarf Seyfert Nucleus of NGC 4395, Astrophysical Journal, Letters 934 (2022) L37.

A. W. Graham, R. Soria, B. L. Davis et al., Central X-Ray Point Sources Found to Be Abundant in Low-mass, Late-type Galaxies Predicted to Contain an Intermediate-mass Black Hole, Astrophysical Journal 923 (2021) 246.

K. Nandra, D. Barret, X. Barcons et al., The Hot and Energetic Universe: A White Paper presenting the science theme motivating the Athena+ mission, arXiv e-prints (2013) arXiv:1306.2307.

J. A. Gaskin, D. A. Swartz, A. Vikhlinin et al., Lynx X-Ray Observatory: an overview, Journal of Astronomical Telescopes, Instruments, and Systems 5 (2019) 021001.

B. P. Abbott, R. Abbott, T. D. Abbott et al., GW170817: Observation of Gravitational Waves from a Binary Neutron Star Inspiral, Physical Review Letters 119 (2017) 161101.

J. Svoboda, V. Douna, I. Orlitová, M. Ehle, Green Peas in X-Rays, Astrophysical Journal 880 (2019) 144.

K. Inayoshi, E. Visbal, Z. Haiman, The Assembly of the First Massive Black Holes, Annual Review of Astron and Astrophys 58 (2020) 27–97.

S. E. I. Bosman, F. B. Davies, G. D. Becker et al., Hydrogen reionization ends by z = 5.3: Lyman-α optical depth measured by the XQR-30 sample, Monthly Notices of the RAS 514 (2022) 55–76.

Y. Matsuoka, K. Iwasawa, M. Onoue et al., Subaru High-z Exploration of Low-luminosity Quasars (SHELLQs). XVI. 69 New Quasars at $5.8 < z < 7.0$, Astrophysical Journal, Supplement 259 (2022) 18.

A. C. Seth, R. van den Bosch, S. Mieske et al., A supermassive black hole in an ultra-compact dwarf galaxy, Nature 513 (2014) 398–400.

C. Barber, J. Schaye, R. G. Bower et al., The origin of compact galaxies with anomalously high black hole masses, Monthly Notices of the RAS 460 (2016) 1147–1161.

P. Natarajan, A new channel to form IMBHs throughout cosmic time, Monthly Notices of the RAS 501 (2021) 1413–1425.

H. Inoue, Wandering of the central black hole in a galactic nucleus and correlation of the black hole mass with the bulge mass, Publications of the ASJ 73 (2021) 431–438.

L. Ma, P. F. Hopkins, X. Ma et al., Seeds don't sink: even massive black hole 'seeds' cannot migrate to galaxy centres efficiently, Monthly Notices of the RAS 508 (2021) 1973–1985.

D. D. Nguyen, A. C. Seth, N. Neumayer et al., Improved Dynamical Constraints on the Masses of the Central Black Holes in Nearby Low-mass Early-type Galactic Nuclei and the First Black Hole Determination for NGC 205, Astrophysical Journal 872 (2019) 104.

A. Ricarte, P. Natarajan, The observational signatures of supermassive black hole seeds, Monthly Notices of the RAS 481 (2018) 3278–3292.

S. Giodini, A. Finoguenov, D. Pierini et al., The galaxy stellar mass function of X-ray detected groups. Environmental dependence of galaxy evolution in the COSMOS survey, Astronomy and Astrophysics 538 (2012) A104.

R. M. Plotkin, E. Gallo, F. Haardt et al., The X-Ray Properties of Million Solar Mass Black Holes, Astrophysical Journal 825 (2016) 139.

F. Vito, W. N. Brandt, B. Luo et al., No evidence for an Eddington-ratio dependence of X-ray weakness in BALQSOs, Monthly Notices of the RAS 479 (2018) 5335–5342.

J. Aird, A. L. Coil, J. Moustakas et al., PRIMUS: The Dependence of AGN Accretion on Host Stellar Mass and Color, Astrophysical Journal 746 (2012) 90.

E. Pezzulli, R. Valiante, M. C. Orofino et al., Faint progenitors of luminous z $\sim$ 6 quasars: Why do not we see them?, Monthly Notices of the RAS 466 (2017) 2131–2142.

B. Agarwal, J. L. Johnson, E. Zackrisson et al., Detecting direct collapse black holes: making the case for CR7, Monthly Notices of the RAS 460 (2016) 4003–4010.

C. DeGraf, D. Sijacki, Cosmological simulations of massive black hole seeds: predictions for next-generation electromagnetic and gravitational wave observations, Monthly Notices of the RAS 491 (2020) 4973–4992.

Z. Schutte, A. E. Reines, Black-hole-triggered star formation in the dwarf galaxy Henize 2-10, Nature 601 (2022) 329–333.

S. Koudmani, N. A. Henden, D. Sijacki, A little FABLE: exploring AGN feedback in dwarf galaxies with cosmological simulations, Monthly Notices of the RAS 503 (2021) 3568–3591.

R. Nevin, L. Blecha, J. Comerford, J. Greene, Accurate Identification of Galaxy Mergers with Imaging, Astrophysical Journal 872 (2019) 76.

M. Dadina, N. Masetti, M. Cappi et al., Ultraluminous X-ray source XMMUJ132218.3-164247 is in fact a type I Quasar, Astronomy and Astrophysics 559 (2013) A86.

M. Mezcua, T. P. Roberts, A. D. Sutton, A. P. Lobanov, Radio observations of extreme ULXs: revealing the most powerful ULX radio nebula ever or the jet of an intermediate-mass black hole?, Monthly Notices of the RAS 436 (2013) 3128–3134.

L. J. Latimer, A. E. Reines, K. N. Hainline, J. E. Greene, D. Stern, A Chandra and HST View of WISE-selected AGN Candidates in Dwarf Galaxies, Astrophysical Journal 914 (2021) 133.

L. Jiang, I. D. McGreer, X. Fan et al., The Final SDSS High-redshift Quasar Sample of 52 Quasars at z>5.7, Astrophysical Journal 833 (2016) 222.

D. J. Mortlock, M. Patel, S. J. Warren et al., Probabilistic selection of high-redshift quasars, Monthly Notices of the RAS 419 (2012) 390–410.

S. L. Reed, R. G. McMahon, P. Martini et al., Eight new luminous z $\geq$ 6 quasars discovered via SED model fitting of VISTA, WISE and Dark Energy Survey Year 1 observations, Monthly Notices of the RAS 468 (2017) 4702–4718.

R. Nanni, J. F. Hennawi, F. Wang et al., Paving the way forEuclid and JWST via probabilistic selection of high-redshift quasars, Monthly Notices of the RAS 515 (2022) 3224–3248.

F. Vito, W. N. Brandt, G. Yang et al., High-redshift AGN in the Chandra Deep Fields: the obscured fraction and space density of the sub-L_* population, Monthly Notices of the RAS 473 (2018) 2378–2406.

F. Vito, W. N. Brandt, F. E. Bauer et al., The X-ray properties of z > 6 quasars: no evident evolution of accretion physics in the first Gyr of the Universe, Astronomy and Astrophysics 630 (2019) A118.

E. Lusso, R. Valiante, F. Vito, The Dawn of Black Holes, arXiv e-prints (2022) arXiv:2205.15349.

M. Johnston-Hollitt, M. Sato, J. A. Gill, M. C. Fleenor, A. M. Brick, Radio observations of the Horologium-Reticulum supercluster - I. A3158: excess star-forming galaxies in a merging cluster?, Monthly Notices of the RAS 390 (2008) 289–303.

E. J. Murphy, A. Bolatto, S. Chatterjee et al., The ngVLA Science Case and Associated Science Requirements, in: E. Murphy (Ed.), Science with a Next Generation Very Large Array, volume 517 of *Astronomical Society of the Pacific Conference Series*, 2018, p. 3.

J. Lazio, The Square Kilometre Array, in: Panoramic Radio Astronomy: Wide-field 1-2 GHz Research on Galaxy Evolution, 2009, p. 58.

F. Acero, J. T. Acquaviva, R. Adam et al., French SKA White Book - The French Community towards the Square Kilometre Array, arXiv e-prints (2017) arXiv:1712.06950.

G. Lanzuisi, A. Comastri, J. Aird et al., Surveys with Athena: results from detailed SIXTE simulations, in: J.-U. Ness, S. Migliari (Eds.), The X-ray Universe 2017, 2017, p. 127.

S. van Velzen, G. R. Farrar, S. Gezari et al., Optical Discovery of Probable Stellar Tidal Disruption Flares, Astrophysical Journal 741 (2011) 73.

F. B. Bianco, Ž. Ivezić, R. L. Jones et al., Optimization of the Observing Cadence for the Rubin Observatory Legacy Survey of Space and Time: A Pioneering Process of Community-focused Experimental Design, Astrophysical Journal, Supplement 258 (2022) 1.

C. J. Burke, Y. Shen, X. Liu et al., Dwarf AGNs from Variability for the Origins of Seeds (DAVOS): Intermediate-mass black hole demographics from optical synoptic surveys, arXiv e-prints (2022) arXiv:2207.04092.

D. Lin, J. Guillochon, S. Komossa et al., A likely decade-long sustained tidal disruption event, Nature Astronomy 1 (2017) 0033.

D. Lin, O. Godet, N. A. Webb et al., Follow-up Observations of the Prolonged, Super-Eddington, Tidal Disruption Event Candidate 3XMM J150052.0+015452: the Slow Decline Continues, Astrophysical Journal, Letters 924 (2022) L35.

G. Miniutti, R. D. Saxton, M. Giustini et al., Nine-hour X-ray quasi-periodic eruptions from a low-mass black hole galactic nucleus, Nature 573 (2019) 381–384.

R. Arcodia, A. Merloni, K. Nandra et al., X-ray quasi-periodic eruptions from two previously quiescent galaxies, Nature 592 (2021) 704–707.

G. Miniutti, M. Giustini, R. Arcodia et al., Disappearance of quasi-periodic-eruptions (QPEs) in GSN 069, simultaneous X-ray re-brightening, and predicted QPE re-appearance, arXiv e-prints (2022) arXiv:2207.07511.

J. E. Greene, A. Barth, A. Bellini et al., Astro2020 Science White Paper: The Local Relics of of Supermassive Black Hole Seeds, arXiv e-prints (2019) arXiv:1903.08670.

M. Onoue, N. Kashikawa, Y. Matsuoka et al., Subaru High-z Exploration of Low-luminosity Quasars (SHELLQs). VI. Black Hole Mass Measurements of Six Quasars at 6.1 $\leq$ z $\leq$ 6.7, Astrophysical Journal 880 (2019) 77.

N. M. Barrière, M. Bavdaz, M. J. Collon et al., Silicon Pore Optics, arXiv e-prints (2022) arXiv:2206.11291.

D. J. Whalen, M. Mezcua, A. Meiksin, T. Hartwig, M. A. Latif, Radio Power from a Direct-collapse Black Hole in CR7, Astrophysical Journal, Letters 896 (2020) L45.

Euclid Collaboration, R. Barnett, S. J. Warren et al., Euclid preparation. V. Predicted yield of redshift 7 < z < 9 quasars from the wide survey, Astronomy and Astrophysics 631 (2019) A85.

M. Arca Sedda, P. Amaro Seoane, X. Chen, Merging stellar and intermediate-mass black holes in dense clusters: implications for LIGO, LISA, and the next generation of gravitational wave detectors, Astronomy and Astrophysics 652 (2021) A54.

G. Fragione, I. Ginsburg, B. Kocsis, Gravitational Waves and Intermediate-mass Black Hole Retention in Globular Clusters, Astrophysical Journal 856 (2018) 92.

A. K. Mehta, A. Buonanno, J. Gair et al., Observing Intermediate-mass Black Holes and the Upper Stellar-mass gap with LIGO and Virgo, Astrophysical Journal 924 (2022) 39.

M. Dotti, M. Bonetti, F. Rigamonti et al., Optical follow-up of the tick-tock massive black hole binary candidate, arXiv e-prints (2022) arXiv:2205.06275.

T. Hartwig, B. Agarwal, J. A. Regan, Gravitational wave signals from the first massive black hole seeds, Monthly Notices of the RAS 479 (2018) L23–L27.

M. Maggiore, C. Van Den Broeck, N. Bartolo et al., Science case for the Einstein telescope, Journal of Cosmology and Astroparticle Physics 2020 (2020) 050.